Department of Civil Engineering

Proceedings of the International Conference on Non-destructive Evaluation of Concrete in Nuclear Applications

NDE NucCon 2023

Fahim Al-Neshawy, Miguel Ferreira, Edgar Bohner, Pirkko Kekäläinen, Tandré Oey, Vera Lay and Ernst Niederleithinger

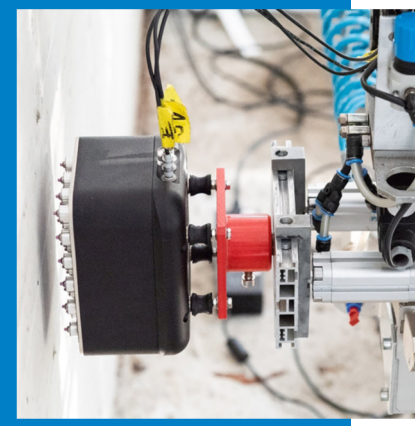

Aalto University

SCIENCE + TECHNOLOGY

CONFERENCE PROCEEDINGS

Aalto University publication series
SCIENCE + TECHNOLOGY /

Proceedings of the International Conference on Non-destructive Evaluation of Concrete in Nuclear Applications

NDE NucCon 2023

Fahim Al-Neshawy, Miguel Ferreira, Edgar Bohner, Pirkko Kekäläinen, Tandré Oey, Vera Lay and Ernst Niederleithinger

Aalto University
School of Engineering
Department of Civil Engineering
Mineral-based materials and mechanics

Fahim Al-Neshawy
E-mail: fahim.al-neshawy@aalto.fi
Phone: +358 50 564 9372

Aalto University publication series
SCIENCE + **TECHNOLOGY** /

ISBN (pdf)
ISSN 1799-490X (pdf)

https://www.aalto.fi/en/nde-nuccon-2023

Unigrafia Oy
Helsinki

Finland

TABLE OF CONTENTS

PREFACE

The most used material in terms of mass and volume in nuclear engineering is concrete. It is used for structures housing the reactors and all other components of a nuclear powerplant, to provide safety containments but also to wrap nuclear waste in packages and repositories. As all other materials used for a very long time span it need inspection and monitoring.

While non-destructive evaluation (NDE) of reinforced concrete structures (RCS) in civil engineering applications has a long history, as well as NDT of the pressurized (metallic) components of a nuclear power plant, testing of concrete constructions in nuclear installations has partly been neglected. At the same time there are many specific challenges to NDE that justify a dedicated international event.

The International Conference on Non-destructive Evaluation of Concrete in Nuclear Applications (NDE NucCon) was co-organized by VTT Technical Research Centre of Finland, Aalto University, Finland, and Bundesanstalt für Materialforschung und -prüfung (BAM), Germany. The event was sponsored by the Euratom projects ACES and PREDIS. In January 2023 about 70 participants gathered for three days in the Dipoli convention center in Espoo, Finland to listen to about 50 presentations from 15 countries, complemented by an exhibition with international instrument manufacturers and service providers.

This book includes all peer reviewed manuscripts submitted to the conference. The reader will find a large variety of subjects from basic research, new inspections methods and case studies in actual facilities. We, the organizers hope you will enjoy the read.

Dr. Ernst Niederleithinger,
NDE NucCon 2023 conference Co-Chair
Bundesanstalt für Materialforschung und -prüfung (BAM), Germany

COMMITTEES

Organising Committee

Dr. Miguel Ferreira, VTT Technical Research Centre of Finland, Finland, Chair

Dr. Edgar Bohner, VTT Technical Research Centre of Finland, Finland, Co-chair

Dr. Ernst Niederleithinger, BAM Federal Institute for Materials Research and Testing, Germany, Co-Chair

Dr. Fahim Al-Neshawy, Aalto University, Finland, Co-chair

Dr. Vera Lay, BAM Federal Institute for Materials Research and Testing, Germany, Co-Chair

Local Organizing Committee (*alphabetical order*)

Abdullah Al-Maisari, Aalto University, Finland.

Abobaker Ba Ragaa, Aalto University, Finland.

Akbar Numan, Aalto University, Finland.

Hassan Rubel, Aalto University, Finland.

Pirkko Kekäläinen, VTT Technical Research Centre of Finland, Finland

Dr. Tandré Oey, VTT Technical Research Centre of Finland, Finland.

Ville Sjöblom, VTT Technical Research Centre of Finland, Finland.

Scientific Committee (*alphabetical order*)

Dr. Amador Sillero, Tecnatom, Spain

Dr. Christoph Strangfeld, BAM, Germany

Dr. Edgar Bohner, VTT, Finland

Dr. Ernst Niederleithinger, BAM, Germany, Chair

Dr. Federico Navarro Castaño, Tecnatom, Spain

Prof. Iikka Virkkunen, Aalto University, Finland

Dr. Jacques Jabbour, IRSN, France

Dr. Javier Sanchez, IETCC, CSIC, Spain

Prof. Jean-Paul Balayssac, University of Toulouse, France

Prof. Jouni Punkki, Aalto University, Finland

Prof. Odile Abraham, Universite Gustave Eiffel, France

Dr. Phung Quoc Tri, SCK. CEN, Belgium

Prof. Rosa Lo Frano, Uni Pisa, Italy

Dr. Salvador Villalobos, EPRI, USA

Prof. Sylvia Keßler, Helmut Schmidt University, Germany

Tuomas Koskinen, VTT, Finland

Dr. Vera Lay, BAMGermany

Prof. Vincent Garnier, University of Marseille, France

Dr. Zbynek Hlavac, CVRez, Czech Republic

CONFERENCE PARTNERS

Aalto University School of Engineering

Civil Engineering Department

Website: https://www.aalto.fi/en/department-of-civil-engineering

The Department of Civil Engineering aims to build the structures of tomorrow through research, education and collaboration. The department conducts both basic scientific research as well as applied research, both of which are required for high-quality education at the graduate and undergraduate levels.

VTT Technical Research Centre of Finland

Website: https://www.vttresearch.com/en

VTT is one of Europe's leading research institutions. VTT is owned by the Finnish state. VTT advances the utilisation and commercialisation of research and technology in commerce and society.

BAM Division 8.2 – Non-destructive Testing Methods for Civil Engineering

Website: https://www.bam.de

The division Non-Destructive Testing Methods for Civil Engineering promotes the practical application of non-destructive testing (NDT) methods for all areas of civil engineering, improves existing methods, develops new methods and supports the development of regulations.

ACES project

Website: https://aces-h2020.eu/

The purpose of ACES is to advance the assessment of safety performance of safety-critical concrete infrastructure by addressing remaining scientific and technology gaps for the safe and long term operation of nuclear power plants.

The pre-disposal management of radioactive waste – PREDIS

Website: https://predis-h2020.eu/

The PREDIS project targets the development and implementation of activities for pre-disposal treatment of radioactive waste streams other than nuclear fuel and high-level radioactive waste.

aci – American Concrete Institute

Website: https://www.concrete.org/contactus.aspx

The American Concrete Institute is a leading global authority for the development, dissemination, and adoption of its consensus-based standards, technical resources, and educational, training, & certification programs.

European Atomic Energy Community (Euratom)

Website: https://commission.europa.eu/index_en

Euratom regulates the European civil nuclear industry, which produces almost 30 % of energy in the EU. Euratom's work safeguards nuclear materials and technology, facilitates investment, research and development, and ensures equal access to nuclear supplies, as well as the correct disposal of nuclear waste and the safety of operations.

CONFERENCE EXHIBITORS
(ALPHABETICAL ORDER)

Screening Eagle Technologies

Contact: Ana González
Phone: +41 79 470 44 96
E-mail: ana.gonzalez@screeningeagle.com
Website: https://www.screeningeagle.com/

Screening Eagle is a technology platform for intelligent inspection of the built environment with sensors, software, and data.

Germann Instruments

Contact: Claus Germann Petersen
Phone: +45 39 67 71 17
E-mail: germann-eu@germann.org
Website: https://www.germanninstruments.com/

Germann Instruments is a pioneer of innovative nondestructive test systems for concrete. For over a quarter of a century, Germann Instruments has been at the forefront in developing tools for on-site nondestructive evaluation (NDE) and mixture optimization in reinforced concrete structures.

ACS-Solutions GmbH

Contact: Sergey Nazhestkin
Phone: +79 03 2361 635
E-mail: info@acs-international.com
Website: https://acs-international.com/

Acoustic Control Systems – ACS Group – established in 1991 – is the international provider of innovative ultrasonic testing equipment and professional inspection and engineering services.

Hilti Oy

Contact: Teemu Rissanen
Phone: +358 207 999 332
E-mail: teemu.rissanen@hilti.com
Website: https://www.hilti.fi/en

Hilti services the professional construction industry. Hilti offers software for design, products and tools for work onsite, training, testing and consultancy.

CONFERENCE EXHIBITORS
(ALPHABETICAL ORDER)

Screening Eagle Technologies

Contact: Ana González
Phone: +41 79 470 44 96
E-mail: ana.gonzalez@screeningeagle.com
Website: https://www.screeningeagle.com/

Screening Eagle is a technology platform for intelligent inspection of the built environment with sensors, software, and data.

Germann Instruments

Contact: Claus Germann Petersen
Phone: +45 39 67 71 17
E-mail: germann-eu@germann.org
Website: https://www.germanninstruments.com/

Germann Instruments is a pioneer of innovative nondestructive test systems for concrete. For over a quarter of a century, Germann Instruments has been at the forefront in developing tools for on-site nondestructive evaluation (NDE) and mixture optimization in reinforced concrete structures.

ACS-Solutions GmbH

Contact: Sergey Nazhestkin
Phone: +79 03 2361 635
E-mail: info@acs-international.com
Website: https://acs-international.com/

Acoustic Control Systems – ACS Group – established in 1991 – is the international provider of innovative ultrasonic testing equipment and professional inspection and engineering services.

Hilti Oy

Contact: Teemu Rissanen
Phone: +358 207 999 332
E-mail: teemu.rissanen@hilti.com
Website: https://www.hilti.fi/en

Hilti services the professional construction industry. Hilti offers software for design, products and tools for work onsite, training, testing and consultancy.

kiwa inspecta

Contact: Jukka Hietikko
Phone: +358504061280
E-mail: fi.asiakaspalvelu@kiwa.com
Website: https://www.kiwa.com/en/

Kiwa is an autonomous global organization in Testing, Inspection and Certification (TIC), training and consultancy services.

CONFERENCE PAPERS

Multi-sensory monitoring and ultrasound for quality assurance at underground sealing structures

Vera Lay[1,*], Frank Mielentz[1], Prathik Prabhakara[1], Franziska Baensch[1], Sergej Johann[1], Detlef Hofmann[1], Patrick Sturm[1], Michael Stamm[1], and Ernst Niederleithinger[1]

[1] Bundesanstalt für Materialforschung und -prüfung (BAM), Berlin, Germany

ABSTRACT

Within the safety concepts of underground disposal sites of nuclear waste, engineered barriers play an important role. As these sealing structures have high demands concerning integrity, we aim at advancing the available construction materials, monitoring, and inspection techniques within the project SealWasteSafe. A specifically developed alkali-activated material is compared to classical salt concrete. A comprehensive multi-sensory monitoring scheme is used at 150-340 l specimens to monitor setting and hardening of both materials. All sensors are demonstrated to resist the highly alkaline environments. Besides cabled and wireless temperature and humidity of the materials, strain variations using fibre optic sensors and acoustic emissions are recorded over periods of at least 28 days, partly for more than eight months. After hardening of the specimens, further non-destructive evaluations using ultrasonic echo and thermographic measurements are conducted. Preliminary results proof the suitability of the tested sensors and clearly highlight differences between the tested materials. Particularly, the newly developed alkali-activated material shows lower acoustic emission activity indicating less cracking activity. Additionally, unique ultrasonic methods will enable better images of potential internal objects and cracks at in-situ sealing structures. A large-scale ultrasonic system is optimised to reliably detect objects at a depth exceeding 9 m while still obtaining a good resolution. Modelling studies show the potential of further increasing the distance between individual transducer arrays. Additionally, a new ultrasonic borehole probe using phased arrays allowing for beam focussing is constructed and tested. Laboratory measurements at a half-cylindrical concrete specimen coincide well with the previous modelling. In total, the presented safe materials, detailed monitoring approaches and ultrasonic quality assurance methods will help to obtain safe sealing structures within salt as a host rock. The concepts can partly be transferred to sealing structures in alternative host rocks and will also be valuable for non-nuclear waste repositories.

Keywords: engineered barriers; monitoring; embedded sensors; ultrasonic imaging

1. INTRODUCTION

Underground sealing structures are a crucial element in safe waste disposal planned for nuclear waste repositories. The existing geological barriers are complemented by engineered barrier systems [1]. For evaporites as one of the potential host rocks in Germany, salt concretes are under test to construct the engineered barrier. In general, salt concretes shall have (chemical) characteristics similar to the evaporite host rocks to provide high durability and are generally based on blended Portland cements with a high amount of supplementary cementious materials or concretes based on magnesium oxychloride cement ([2] and references therein).

Existing sealing concepts by the federal company for radioactive waste disposal in Germany (BGE) use specific salt concrete (SC) [3] that is tested e.g. at Morsleben mine. Although this salt concrete is fitted for the occurring evaporites, it shows significant heat of reaction with associated potential for deformation and cracking compromising the integrity of the constructed sealing structures.

* Corresponding author: vera.lay@bam.de; +49 30 8104 4749

Consequently, we aim at improving the construction material, provide suitable monitoring techniques, and offer complementary non-destructive quality assurance methods within the project SealWasteSafe. The applicability of alkali-activated materials (AAM) with a significantly lower heat of reaction is analysed in detail [2]. Due to the smoother temperature development of the AAM, less cracking activity is expected while mechanical strength and permeability are still within the required range for sealing structures.

After successful laboratory analysis on the cm-scale, cylindrical and cuboid specimens on the m-scale are produced from the newly developed AAM "F1" [2] and the salt concrete "M2" [3] as reference. These specimens are used to test a multi-sensory monitoring scheme to observe the hydration phase and potential cracking activity. Furthermore, complementary quality assurance methods will help to construct engineered barriers as safe as possible. These methods are applied at the same laboratory specimens used for monitoring but are particularly aiming at the inspection of in-situ structures.

2. MONITORING WITH A MULTI-SENSORY SETUP

2.1. Multi-sensory system at laboratory specimens

Making use of the results of previous material research [2], a series of large specimens was manufactured. Besides the newly developed alkali-activated material (AAM), the salt concrete (SC) is also analysed as a reference. A comprehensive multi-sensory monitoring scheme is applied to compare the setting process of both materials and to demonstrate the sensors' resistance to highly alkaline environments. For both materials, specimens with a cylindrical (height 1.2 m, diameter 0.4 m) and a cuboid shape (all lengths 0.7 m) were casted (Figure 1). Advanced formwork made sure to appropriately place the sensors. All sensors recorded over periods of at least 28 days. For selected specimens, the monitoring period reached more than eight months (Table 1).

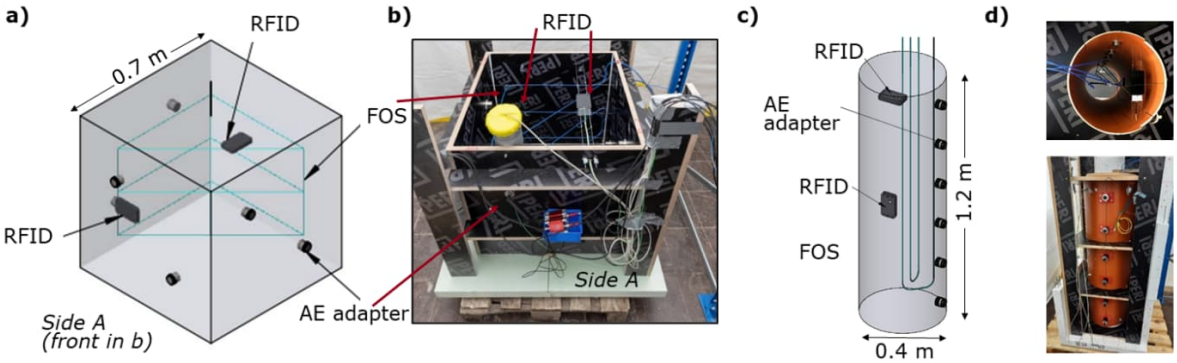

Figure 1. Specimens used for multi-sensory monitoring: a+b) cuboid, c+d) cylinder.

Table 1 Overview of specimen used for multi-sensory monitoring

	Specimen				
	1	2	3	4	5
Casting date	10.03.21	21.04.21	05.05.21	19.05.21	21.06.21
Material	SC	AAM	SC	SC	AAM
Geometry	Cylinder	Cylinder	Cuboid	Cylinder	Cuboid
Monitoring period	49 days	28 days	253 days	28 days	183 days

The multi-sensory setup involves a variety of sensors to monitor parameters such as temperature, humidity, strain, and acoustic emissions. A detailed description and analysis of the cylindrical specimens and the involved sensors is available [4].

Passive sensor systems based on radiofrequency identification technology (RFID) embedded in the concrete provide a wireless interface that allows for measurements with different sensors. Here, temperature and humidity measurements are conducted. Temperature and humidity sensors were embedded in the concrete with the cabled reference sensors directly beside the RFID-based

sensors. Although previous analysis of the humidity sensors embedded in concrete have been successful [5], particularly early humidity measurements are difficult for the casted specimens. High pH-values and potential salt reaction are challenging in both analysed materials here and demand further research to develop a reliable sensor system also for long-term monitoring [6].

Coated fibre optic cables found to be resistant to the highly alkaline environment (pH >13) are embedded in the concrete to monitor temperature and strain with the cable acting as continuous sensor [7]. To analyse the strain in detail, a temperature compensation is applied. The observed strain rates help to understand the reaction kinetics of the materials as different shrinkage occurs during the hardening phase [4].

Acoustic emissions (AE) are recorded by partly embedded adapters that record occurring acoustic events from within the concrete specimens with the aim to detect early cracking during the hydration phase of the materials [8, 9]. For each specimen, a set of six acoustic emission sensors was used as shown in Figure 1. Primarily, the occurring acoustic emission hits above a defined threshold are recorded but additional sophisticated analysis of the continuously recorded data offers detailed insights in the underlying processes within the specimens [4].

2.2. Monitoring results

Exemplary monitoring results of the cylindrical specimens for both the salt concrete and the alkali-activated material for the first 28 days after casting are shown in Figure 2 and discussed in detail by Baensch et al. [4]. Overall, the temperature curves in Figure 2a proof the lower heat of reaction for the newly developed AAM in accordance with [2]. Generally, a distinct temperature peak is observed for the SC in contrast to smooth transitions for the AAM. After reaching the equilibrium stage between sensor interior and concrete, the embedded RFID-based sensors successfully allow for cableless temperature measurements and measured values correlate well with the reference sensors [6].

Cumulative acoustic emission hits are plotted in Figure 2b for three sensors at different heights within the cylinder (bottom S1, centre S3, top S6). Summing the recorded acoustic emissions from all sensors, the SC has significantly more single and first hits (16740) in comparison to the AAM (6105 hits) during the first 28 days [4]. For the AAM, the uppermost sensor S6 shows unusually high acoustic emission hits in comparison to the other five sensors in the same material, which is only associated to a boundary effect at the top of the specimens [4]. Correcting for this effect, the number of total acoustic emission hits in the AAM is even decreasing thus indicating substantially less crack activity in comparison to the salt concrete.

Overall, the applied sensors withstand the highly corrosive and alkaline environment of the used materials. The early hydration and hardening phase have successfully been monitored with the used multi-sensory monitoring scheme.

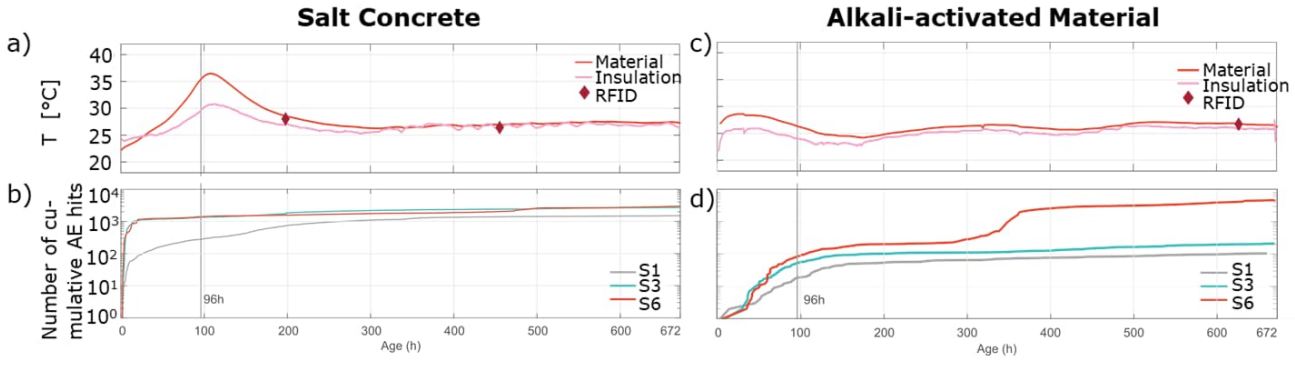

Figure 2. Monitoring results for the first 28 days for the cylindrical specimens showing results for the materials SC (a+b) and AAM (c+d). a+c) Temperature from cabled and RFID sensors. b+d) cumulative acoustic emission hits for selected sensors.

3. QUALITY ASSURANCE

Besides the monitoring, mainly ultrasonic methods are improved to be used for quality assurance to detect obstacles, potential cracks and delamination at in-situ sealing structure scale. Additionally, non-destructive evaluations using ultrasonic echo and thermographic measurements are conducted at the cuboids (Table 1) after hardening and removal of the outer casings. These analyses aim to identify potential cracks and check on the integrity of the installed sensors.

3.1. External ultrasonic inspection of laboratory specimens

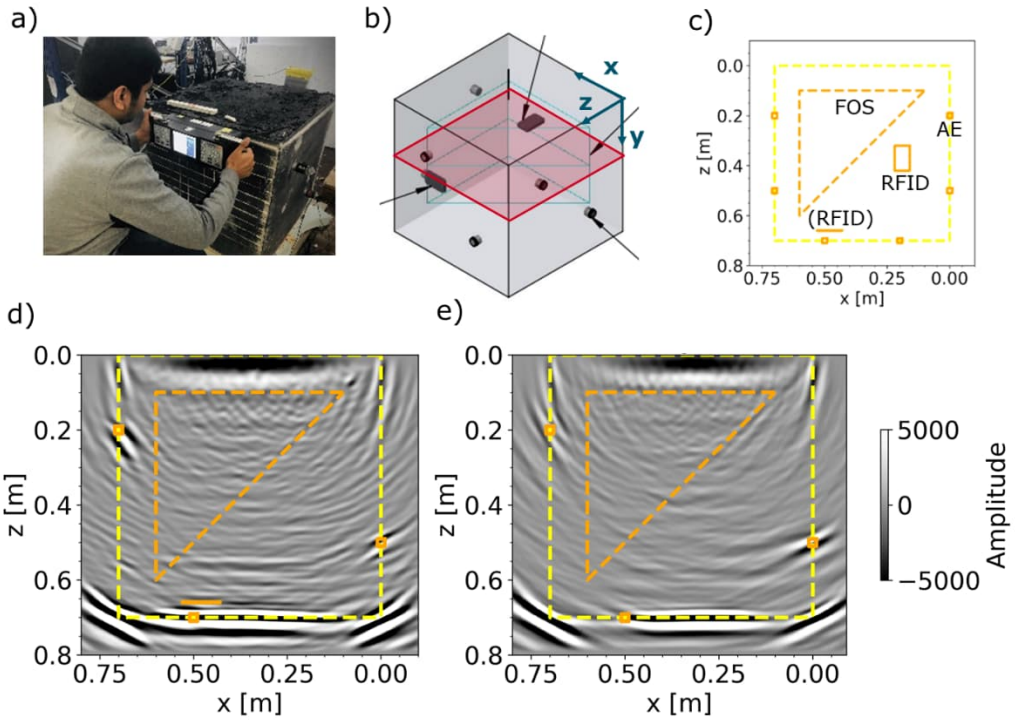

Figure 3. Inspection of the cuboids with ultrasonic impulse echo measurements. a) measurement b) geometry with the plotted area indicated in red, c) top view (i.e., parallel to red area in b) of the embedded sensors; reconstruction results for d) salt concrete and e) AAM.

Ultrasonic measurements were conducted after striking of the cuboid specimens. A commercial system (A 1040 MIRA) working at a frequency of 50 kHz was used that consists of a linear array of transverse transducers. The data was acquired from the side where no acoustic emission adapters were embedded (Figure 1 and Figure 3). Measurements were undertaken on a regular grid to obtain the image of the internal 3D volume of the cuboid. The reconstructions with the software InterSAFT [10] use a constant velocity (v_{s_SC} = 1970 m/s and v_{s_AAM} = 1950 m/s).

The exemplary 2D slices in Figure 3 (at y = 0.3 m) show clear reflectors at the backwall for both materials. Strong reflectors coincide well with the expected sensor locations. Particularly, the AE adapters (orange squares) can clearly be identified and show an opposite impedance contrast in comparison to the backwall reflector as expected for concrete/steel boundary in contrast to concrete/air boundary. No major reflectors indicating cracks are observed. Two comparison measurements were done with the first immediately after removing the casing, the second one at the end of an additional monitoring (AE and FOS) period of 3-6 weeks. No major differences that would indicate internal changes or additional cracking are observed.

3.2. External thermographic inspection of laboratory specimens

Thermographic measurements on concrete structures are an additional method of detecting defects below the surface [11]. Therefore, the specimens shown here were also examined with thermography for possible defects such as cracks and the embedded sensor technology. To do this, the specimens were first heated from above with a radiant heater for twenty minutes. Afterwards, the temperature profile at the surface was measured with an infrared camera for 120 minutes. The thermal measurements were carried out with the long-wave infrared camera ImageIR 8800 from

Infratec GmbH, which has a sensitive wavelength range of 8-9.4 µm. The distance between the camera and the specimen was 2.12 m and the frame rate was five seconds. The experimental setup can be seen in Figure 4a. To lower edge effects due to horizontal heat radiation from the specimen sidewalls, the sides of the specimens were wrapped with insulating Styrofoam sheets on the top 20 cm.

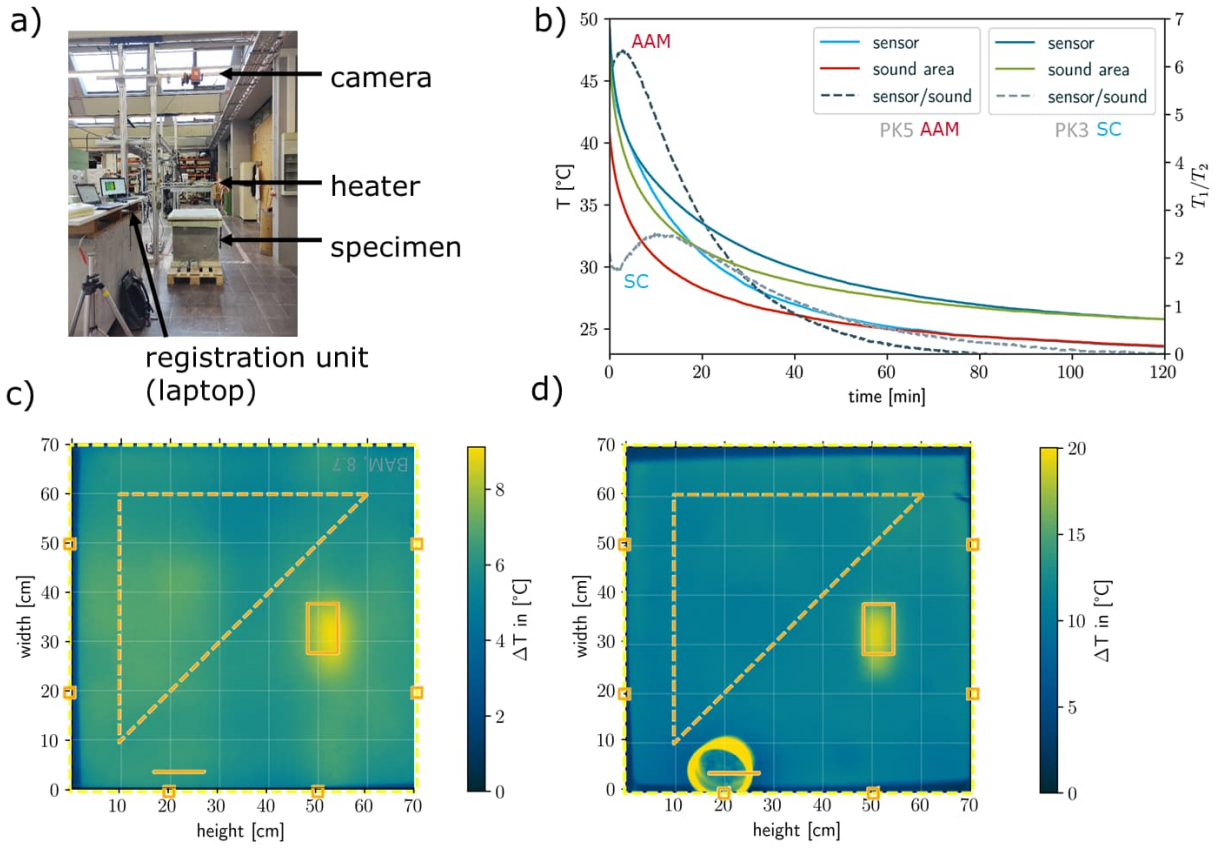

Figure 4. Inspection results for the thermographic measurements. a) measurement layout, b) absolute temperatures, maximal differential temperature for c) SC and d) AAM overlain by sensor locations.

Figure 4 summarises the thermographic results. Figure 4b shows temperature profiles during the cooling for the two specimens. For each material, a temperature profile of a sound area (red/green) and a temperature profile for the sensor area is plotted (light/dark blue). Additionally, the temperature difference between the sound and sensor area are plotted (dashed lines). The times of the maximum temperature differences are considered for the visualization of the sensors. To minimize the influence of inhomogeneous heating, the temperature distribution after 120 minutes is considered as refence image and subtracted from the temperature distribution. The resulting temperature differences are shown Figure 4c and 4d for the salt concrete ($T_{20\,min} - T_{120\,min}$) and alkali-activated material ($T_{3\,min} - T_{120\,min}$) respectively. In both cases, the location of the RFID-sensor (expected about 5 cm below the surface) can clearly be identified due to its low thermal diffusivity compared to concrete and a resulting hot spot (yellow) in the thermal images. The location coincides well with the expected location (see Figure 3c) of the sensors. The thermographic images also indicate the different material properties of SC and AAM and the varying porosity, both resulting in a varying maximal temperature and heat dissipation.

3.3. Optimisation for large-scale ultrasonic analysis

A unique large aperture ultrasonic system (LAUS) [12] with depth penetration as large as 9 m has already successfully been applied at the test site in Morsleben, Germany, of the federal company for radioactive waste disposal (BGE) [13]. The LAUS consists of an array of 12 units, each unit consisting of 32 horizontal shear wave transducers polarised perpendicular to the test plane and operating at a frequency of 25 kHz to 150 kHz [12]. Modelling studies help to further optimise the measurement layout later-on also tested at in-situ objects to potentially increase depth penetration

and resolution at specific depth ranges. To find the optimal spacing between the units for specific testing purposes, the following conditions are modelled:

- Probe units close together, varying the size of the reference flaw,
- Probe units close together, varying the depth of the reference flaw,
- Vary the distance between the probe units, keep the reference flaw constant.

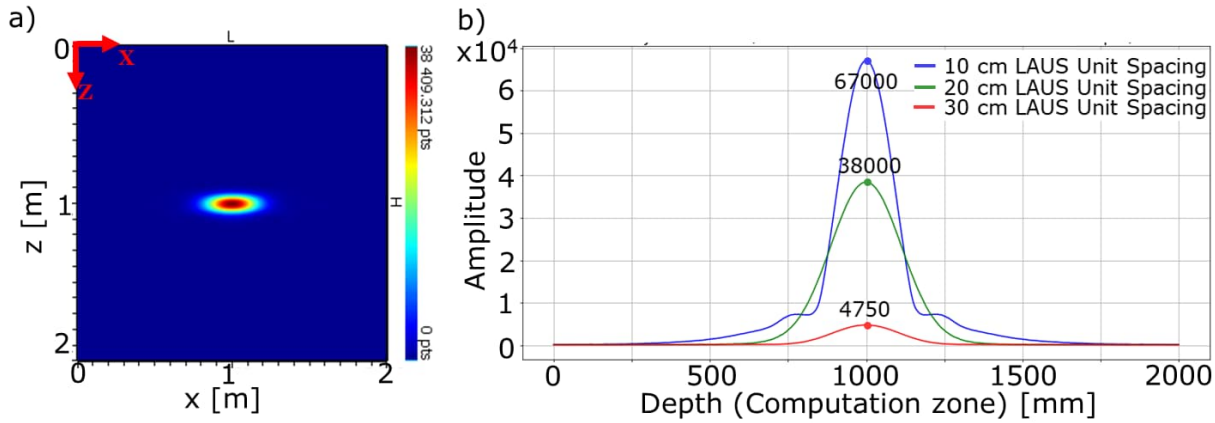

Figure 5. Simulation of LAUS configuration on salt concrete model with a 133 mm diameter reference hole a) SAFT reconstruction of 20 cm unit spacing b) Amplitude from reference hole for different unit spacing.

The simulation data is analysed using the SAFT reconstruction technique with an area of interest 2 m along the x and z directions, as shown in Figure 5a. The maximum amplitude from the reconstruction results is then compared to find the optimal condition for the current application.

Figure 5b shows the comparison of the maximum amplitude for 10 cm, 20 cm, and 30 cm distance between units, keeping the reference flaw at a constant depth. The graph shows that amplitudes decrease drastically when increasing the distance between individual probe units. For a distance of 30 cm the amplitude is 14 times smaller than for the smallest possible distance of 10 cm. However, increasing the distance between the units can further improve the penetration depth and will also affect the signal-to-noise ratio. To detect an obstacle/flaw at great depths, sufficient spatial resolution at that depth is required. For the axial resolution of the ultrasound image, the wavelength is the most important factor determining the resolution. Longer wavelength yielding a lower resolution are principally preferred here due to their weaker damping allowing for deep penetration. All these aspects will be studied in detail making use of various modelling scenarios and will help to validate studies at in-situ concrete test specimens.

3.4. Development of a sophisticated ultrasonic borehole probe

Figure 6. Ultrasonic borehole probe: a) phased array probe, b) specimen to test directivity, c) measurement results (grey scale) for 45° focussed beam overlain on respective beam simulation (colour plot).

An ultrasonic borehole probe is developed and constructed using phased arrays to further enhance the detection of potential cracks [14]. The probe consists of 32 shear wave transducers

working at a frequency of 50 kHz (Figure 6a). Modelling and preliminary results from laboratory specimens prove the feasibility and potential of the directional response even in heterogeneous material such as concrete [15].

To analyse the directional response pattern of the new borehole probe, a specifically made half-cylindrical concrete specimen was used (Figure 6b). The borehole probe is attached below, and a single contact-ultrasonic transducer records the transmission amplitude. Amplitudes depending on the angle are plotted in grey in Figure 6c for an example focussing the beam to 45°. The results correlate well with the simulated beam focussing plotted in comparison. Thus, the implemented phased-array technique can reliably focus the beam to a dedicated direction.

4. CONCLUSION AND OUTLOOK

In the project SealWasteSafe, two potential materials - salt concrete and alkali-activated material - to construct safe engineered barriers for nuclear waste repositories are investigated in detail with adequate monitoring and non-destructive inspection tools. The applied methods are valuable to monitor the hydration and hardening of concrete and inspect internal structures of existing structures.

The comprehensive multi-sensory monitoring schemes proofs to withstand challenging conditions for the used sensors for RFID-based temperature/humidity sensors, fibre-optic sensors, and acoustic emission adapters. The applied monitoring scheme is capable to monitor the setting and hardening phase of both the salt concrete and the alkali-activated material. Innovative embedded sensors help to gather information to characterise the materials and occurring cracking. Fibre-optic sensors provide insights into temperature and strain distribution within the object with high spatial resolution. Recorded acoustic emission events indicate a significantly lower hit rate and thus connected crack activity for the AAM in comparison to the salt concrete.

External non-destructive testing with ultrasound and thermography at the laboratory specimens used for monitoring confirms the sensor locations but does not indicate major cracks. For verification, cores are taken from the specimens to characterise SC and AAM in detail with radiographic computer tomography and microscopy. At the cuboids, continuous monitoring over more than six months is currently analysed. Additionally, long-term monitoring is on-going for the embedded RFID-based sensors.

Quality assurance is a key factor to develop and enable safe in-situ underground sealing structures through (frequent) inspection on structural integrity. For this, two unique ultrasonic test devices are improved and tested for the tailored use at these massive concrete structures. First, the measurement configuration for the existing large aperture ultrasonic system (LAUS) is optimised such that a greater depth penetration exceeding 9 m is possible. On top, reflectors at greater depth can be better imaged with higher amplitude contrasts to the background reflectivity and better resolution for adapted transducer distances as shown in modelling studies. Dedicated measurements at a thick (>4 m) concrete foundation with these adapted configurations are currently analysed. Using sophisticated imaging techniques [16, 17] will provide further potential to improve the image quality of internal structures within the engineered barrier system.

Second, an ultrasonic borehole probe making use of phased arrays to focus the ultrasonic energy is constructed and validated. Detailed modelling studies show how the imaging of cracks, particularly those perpendicular to the boreholes, can successfully be identified. Measurements at a half-cylindrical concrete specimen confirm the modelled beam focussing. Further characterization of the near-field properties of the borehole probe are on-going. Finally, a test application at a real test barrier in Morsleben is envisaged in late 2022. These in-situ measurements will be particularly valuable to proof the enhanced opportunities for ultrasonic methods to serve as quality assurance at sealing structures when combining innovative sensor and analysis methods.

Overall, the project SealWasteSafe improves the construction material, multi-sensory monitoring, and ultrasound for quality assurance to allow for the development of safe nuclear sealing structures. Although the techniques are tailored for sealing structures within salt as a host rock, they are transferrable to a wider field of applications and alternative disposal conditions.

ACKNOWLEDGEMENTS

The authors are grateful for funding by BAM enabling the research project SealWasteSafe. We thank our colleagues for their valuable support in form of advanced formwork, sophisticated concreting and solving challenging technical (sensor) tasks: Marco Lange, Sean Smith, Kerstin Borchert-Giers, Frank Haamkens, Hans-Carsten Kühne, Carlo Tiebe, Frank Basedau, Samuel Pötschke, Matthias Behrens, Heiko Stolpe.

REFERENCES

[1] Bundesamt für Strahlenschutz, "Endlager Morsleben: Hintergründe, Maßnahmen und Perspektiven der Stilllegung," Salzgitter, 2015. [Online]. Available: https://archiv.bge.de/archiv/www.endlager-morsleben.de/SharedDocs/Downloads/Morsleben/DE/broschueren/morsleben-stilllegung-neuf4b0.pdf?__blob=publicationFile&v=9

[2] P. Sturm, J. Moye, G. J. Gluth, N. Vogler, A. Taffe, and H.-C. Kühne, "Properties of alkali-activated mortars with salt aggregate for sealing structures in evaporite rock," *Open Ceramics,* vol. 5, p. 100041, 2021, doi: 10.1016/j.oceram.2020.100041.

[3] Deutsche Gesellschaft zum Bau und Betrieb von Endlagern für Abfallstoffe mbH (DBE), "Verfüllmaterial für Strecken mit hohen Anforderungen Materialeigenschaften und Materialkennwerte Salzbeton M2," Bundesamt für Strahlenschutz, Salzgitter, 2004.

[4] F. Baensch, D. Hofmann, S. Johann, C. Tiebe, F. Basedau, P. Sturm, V. Lay, and E. Niederleithinger, "Multi-sensor conception for safe sealing structures in underground repositories," in *26th International Conference on Structural Mechanics in Reactor Technology, SMiRT 26*, Berlin/Potsdam, 10-15.07.2022 2022.

[5] C. Strangfeld, S. Johann, M. Müller, and M. Bartholmai, "Embedded passive RFID-based sensors for moisture monitoring in concrete," in *2017 IEEE SENSORS*, 2017: IEEE, pp. 1-3, doi: 10.1109/ICSENS.2017.8234166.

[6] S. Johann, F. Baensch, P. Sturm, C. Tiebe, S. Pötschke, and V. Lay, "HF RFID-based measurement comparison for method optimization in M2 concrete and alkali-activated mortars," *Materials Today: Proceedings,* 2022, doi: 10.1016/j.matpr.2022.03.465.

[7] W. R. Habel and K. Krebber, "Fiber-optic sensor applications in civil and geotechnical engineering," *Photonic sensors,* vol. 1, no. 3, pp. 268-280, 2011.

[8] S. Pirskawetz, F. Weise, and P. Fontana, "Detection of early-age cracking using acoustic emission," in *International RILEM Conference on Volume Changes of Hardening Concrete: Testing and Mitigation*, 2006: RILEM Publications SARL, pp. 385-392, doi: 10.1617/2351580052.041.

[9] K. Van Den Abeele, W. Desadeleer, G. De Schutter, and M. Wevers, "Active and passive monitoring of the early hydration process in concrete using linear and nonlinear acoustics," *Cement and concrete research,* vol. 39, no. 5, pp. 426-432, 2009, doi: 10.1016/j.cemconres.2009.01.016.

[10] K. Mayer and P. M. Cinta, "User Guide of Graphical User Interface interSAFT," University of Kassel, Department of Computational Electronics and Photonics, 2012.

[11] C. Maierhofer, R. Arndt, M. Röllig, C. Rieck, A. Walther, H. Scheel, and B. Hillemeier, "Application of impulse-thermography for non-destructive assessment of concrete structures," *Cement and Concrete Composites,* vol. 28, no. 4, pp. 393-401, 2006, doi: 10.1016/j.cemconcomp.2006.02.011.

[12] H. Wiggenhauser, A. Samokrutov, K. Mayer, M. Krause, S. Alekhin, and V. Elkin, "Large aperture ultrasonic system for testing thick concrete structures," *Journal of Infrastructure Systems,* vol. 23, no. 1, p. B4016004, 2017, doi: 10.1061/(ASCE)IS.1943-555X.0000314.

[13] U. Effner, F. Mielentz, E. Niederleithinger, C. Friedrich, R. Mauke, and K. Mayer, "Testing repository engineered barrier systems for cracks-a challenge," *Materialwissenschaft und Werkstofftechnik,* vol. 52, no. 1, pp. 19-31, 2021, doi: 10.1002/mawe.202000118.

[14] F. Mielentz, H. Stolpe, U. A. Effner, M. Behrens, T. Bernstein, and E. Niederleithinger, "Entwicklung einer Bohrlochsonde für Ultraschalluntersuchungen an Abschlussbauwerken in Endlagern," in *Jahrestagung Deutsche Gesellschaft für Zerstörungsfreie Prüfung (DGZfP)*, 2021, vol. 176.

[15] P. Prabhakara, F. Mielentz, H. Stolpe, M. Behrens, V. Lay, and E. Niederleithinger, "Simulation and construction of a focussing borehole probe for ultrasonic investigations at sealing structures for radioactive waste repositories," in *ISNT NDE 21*, 2021.

[16] C. Büttner, E. Niederleithinger, S. Buske, and C. Friedrich, "Ultrasonic Echo Localization Using Seismic Migration Techniques in Engineered Barriers for Nuclear Waste Storage," *Journal of Nondestructive Evaluation,* vol. 40, no. 4, pp. 1-10, 2021, doi: 10.1007/s10921-021-00824-3.

[17] M. Grohmann, S. Müller, E. Niederleithinger, and S. Sieber, "Reverse time migration: Introducing a new imaging technique for ultrasonic measurements in civil engineering," *Near Surface Geophysics,* vol. 15, no. 3, pp. 242-258, 2017, doi: 10.3997/1873-0604.2017006.

Monitoring of durability parameters of the reinforced concrete structure for the disposal of low and intermediate level radioactive waste

Nuria Rebolledo[a], Julio E. Torres[a], Servando Chinchón[a], Javier sánchez[a*], Sylvia de Gregorio[b], Inmaculada López[b] and Manuel Ordóñez[b]
[a] Instituto de Ciencias de la Construcción "Eduardo Torroja" (IETcc-CSIC). Madrid, Spain.
[b] ENRESA. Madrid, Spain.
* javier.sanchez@csic.es

ABSTRACT

Durability is one of the main uncertainties of reinforced concrete structures. Moreover, one of the main causes of the reduction of this durability is the corrosion of reinforcement. In the literature, several authors provide mechanisms and models that allow predicting the behaviour of structures. However, due to the very heterogeneity of the structures and the dispersion of the parameters taken into account in the models, it is necessary to calibrate or validate these models with direct measurements on the structures or, more precisely, the monitoring of durability-related parameters. Additionally, monitoring structures allow decisions to be taken at early stages and even before any pathology occurs.
Since 1995, a mockup has been monitored at El Cabril, Cordoba (Spain), where sensors for temperature, deformation, corrosion potential, resistivity, oxygen availability and corrosion rate have been installed. The data have been analyzed and filtered using machine learning algorithms.
The analysis of the data obtained during these years allows us to appreciate the evolution of the different parameters and their daily and seasonal variation. The sensors that were successfully installed are still active. To date, no corrosion problems have been reported in the structure.

Keywords: Durability; Corrosion; Monitoring; Concrete; Radioactive waste.

1. INTRODUCTION

Durability is one of the most issue and challenge in reinforced concrete structures. And the main cause is the reinforcement corrosion that plays a prominent role in limiting durability. A number of authors have published mechanisms and models for predicting structural performance[1]–[6]. Nonetheless, given the enormous variety of the structures involved and the parameters addressed, models must be calibrated or validated with direct measurements or, for more accurate estimation, by monitoring durability-related parameters. Structural monitoring also supports early stage decision-making, prior even to the appearance of any pathology [7], [8].

For singular structures with a target service life of over 300 years such as the El Cabril disposal facility, monitoring is crucial to determining the structure's performance and back-feeding the data into the durability models to verify the assumptions involved.

The structure analysed here, along with the sensors used and their location on the structure, are described in earlier articles [9]–[11]. A pilot container bearing six series of 27 embedded electrodes each was built and buried in the subsoil in 1994, but connected to an above-grade chamber housing the corrosion datalogger. The parameters monitored included concrete temperature, strain, corrosion potential, resistivity, oxygen availability and corrosion current density. Fewer than 10% of the sensors, all embedded in the structure's walls and drums, failed [10]. Therefore, this article describes and analyses the results delivered by the sensors over a period of 25 years.

2. METHODOLOGY

After construction and instrumentation, the pilot container was buried under conditions very similar to those prevailing in the actual containers at El Cabril. The structure is located in the Spanish province of Córdoba with temperatures ranged from 6 °C to 32 °C, yearly precipitation from 28 cm to 71 cm and the mean relative humidity was 58%.

A specimen housing reference sensors and a data logging facility was stored in an adjacent enclosure. Further information on this set-up can be found in [9], [12]. The drawing in Figure 1 shows the pilot container, the position of the 21 sensors of each type in the container walls and the six on the surface of one of the drums.

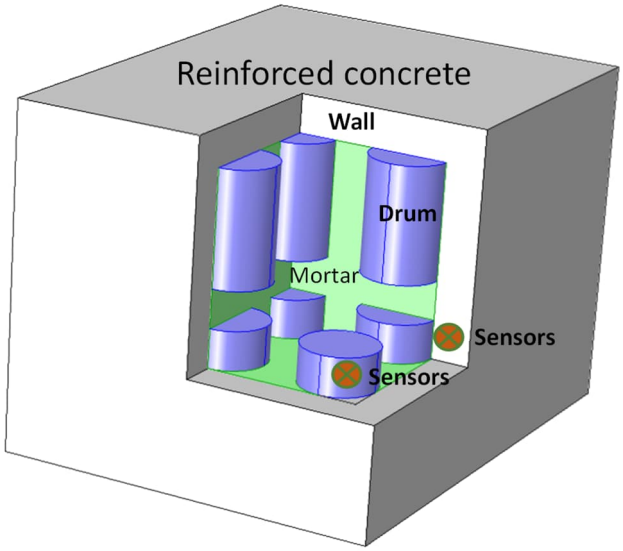

Figure 1. Sensor position in the pilot container: walls and drums

The sensors installed measured temperature, strain, corrosion potential, resistivity, oxygen availability and corrosion current density [9], [12]. The container was fitted with a total of 27 sensors of each of the aforementioned types, except temperature and strain, 15 of which were embedded each. In the correlations between temperature and other parameters, the same temperature sensor was assumed to have been used throughout. Table 1 lists the six types of sensors and the sensors, by number, included in each location, wall or drum. All the sensors are group in families in order to correlate it. More information is given in [9], [12].

Table 1. Sensor group location by container component

		WALL SERIES	DRUM SERIES
	Group No.	1 2 3 4 5 6 7 8 9 10 11 12 13 14 15 16 17 18 19 20 21	22 23 24 25 26 27
Sensor No.	Temperature	1 1 4 4 4 4 4 2 2 5 5 5 8 8 3 3 6 6 6 9 9	10 11 12 13 14 15
	Strain	1 1 4 4 4 7 7 2 2 5 5 5 8 8 3 3 6 6 6 9 9	10 11 12 13 14 15
	Resistivity	1 2 3 4 5 6 7 8 9 10 11 12 13 14 15 16 17 18 19 20 21	22 23 24 25 26 27
	Oxygen avail.	1 2 3 4 5 6 7 8 9 10 11 12 13 14 15 16 17 18 19 20 21	22 23 24 25 26 27
	Potential (E_{corr})	1 2 3 4 5 6 7 8 9 10 11 12 13 14 15 16 17 18 19 20 21	22 23 24 25 26 27
	Current density (I_{corr})	1 2 3 4 5 6 7 8 9 10 11 12 13 14 15 16 17 18 19 20 21	22 23 24 25 26 27

The data were analysed with Wolfram Mathematica software, which deployed machine learning algorithms to eliminate any outlying values (see for more information: https://reference.wolfram.com/language/ref/DeleteAnomalies.html). Such cleansing entailed outlier elimination only; i.e., data were neither otherwise modified or rounded (see figure 2 as an example).

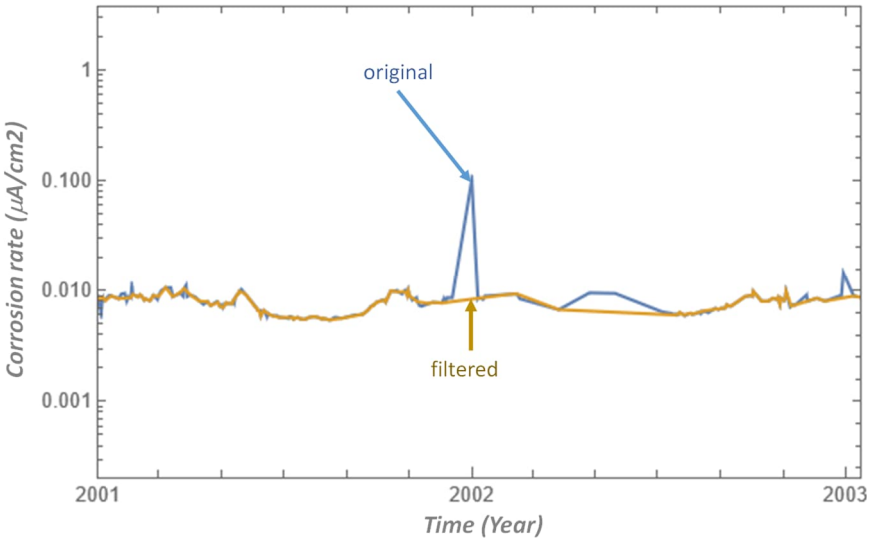

Figure 2. Temperature data from three sensors, No. 0, 1 and 2

3. RESULTS

The results obtained for each type of sensor are shown below.

3.1. Temperature

The temperature sensor data were more reproducible and reliable than either of the other types. The readings recorded by temperature sensors Nos 0, 1 and 2 illustrate the similarity among all the readings. Seasonal trends were as expected. Due to datalogger issues, data are missing for October 2007 to October 2010 and January 2015 to June 2016 (figure 3).

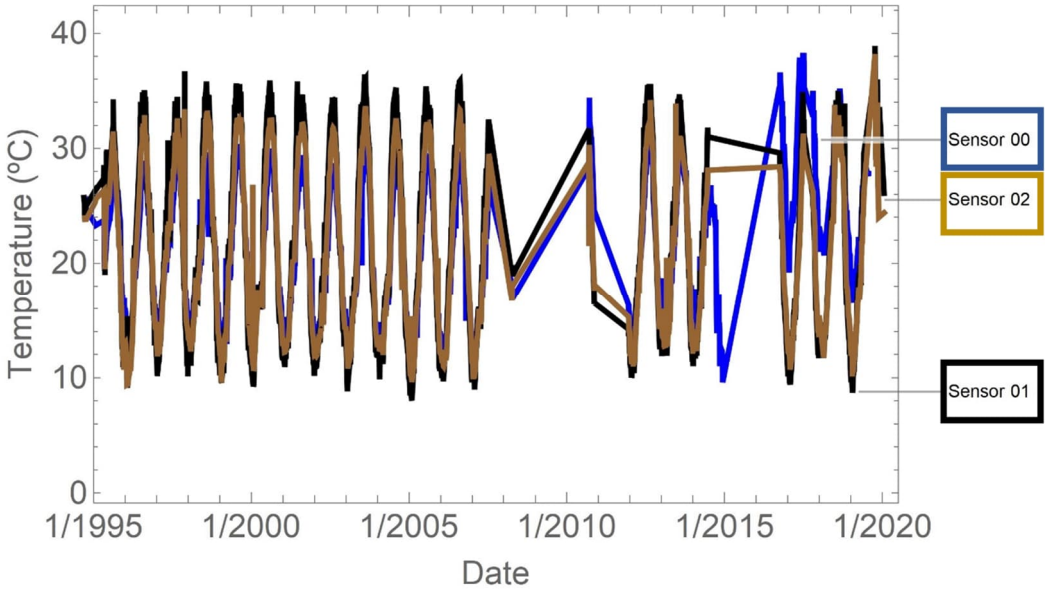

Figure 3. Temperature data from three sensors, No. 0, 1 and 2

A box and whisker plot for each sensor is graphed on the left of Figure 4 and the location of the sensors in the container and drums monitored is depicted on the right. Sensor No. 0 recorded data for the reference specimen. All the sensors delivered readings of around 20 °C, most ranging from 15 °C to 30 °C with extreme values of around 10 °C and 40 °C. The absolute minimum for the entire series was 7.6 °C and the absolute maximum 45.6 °C. The absence of any significant differences between sensors, whether housed in the adjacent chamber (sensor No. 7), the reference specimen

(sensor No. 0), container walls (1 to 6, 8 and 9) or drums (sensors Nos 10 to 15) was indicative of thermal stability in the entire facility throughout the study.

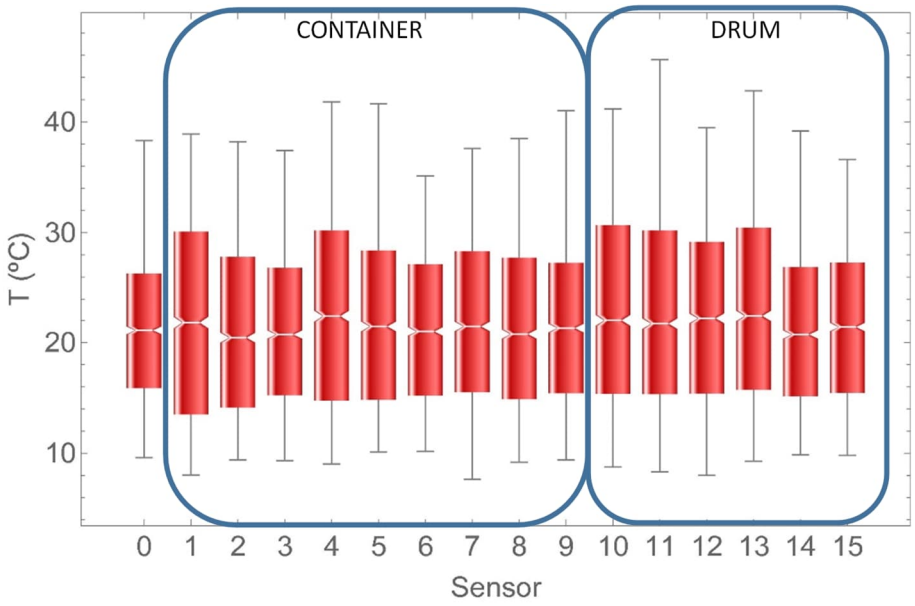

Figure 4. Temperature. Box and whisker plot

3.2. Deformation

As with other sensors, readings were missing for certain periods and the log changed beginning in 2010 when the datalogger was replaced. Those circumstances and seasonal variations aside, strain measurements stabilised after the first 10 years of service. A box and whisker plot for all the sensors is graphed in Figure 5, which also shows the outliers. The data scatter observed is characteristic of variation in this concrete parameter and the effect of temperature, as discussed later. All the readings were indicative of shrinkage within the range expected for concrete.

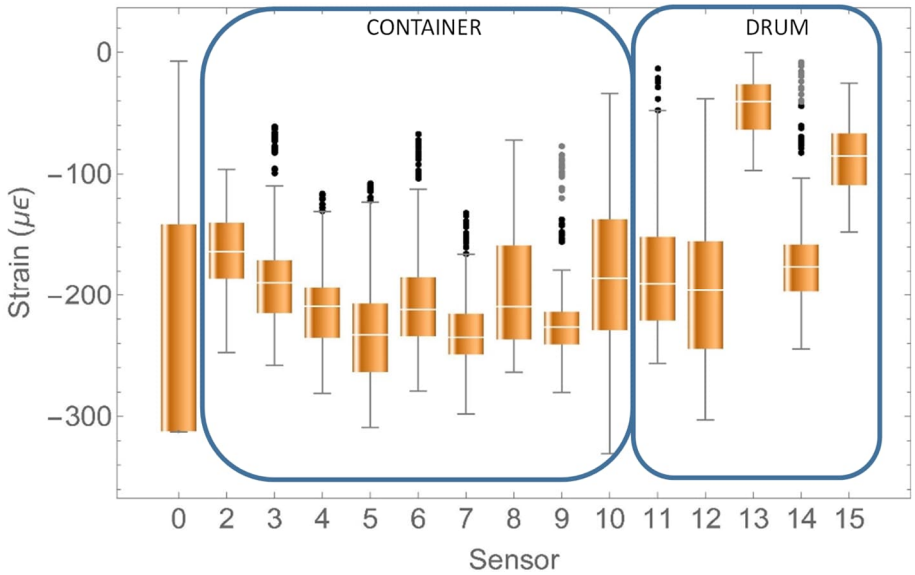

Figure 5. Deformation. Box and whisker plot

3.3. Oxygen availability

The values recorded are indicative of sufficient oxygen availability for the cathodic semi-reaction, with oxygen levels higher than the corrosion current density logged. Sensors Nos 1, 4, 11 and 18 were excluded from the analysis because they were damaged during container construction and implementation. A box and whisker plot for all the other strain sensors is graphed in Figure 6, which also shows the outliers. This type of measurements was widely scattered, with a considerable number of outliers.

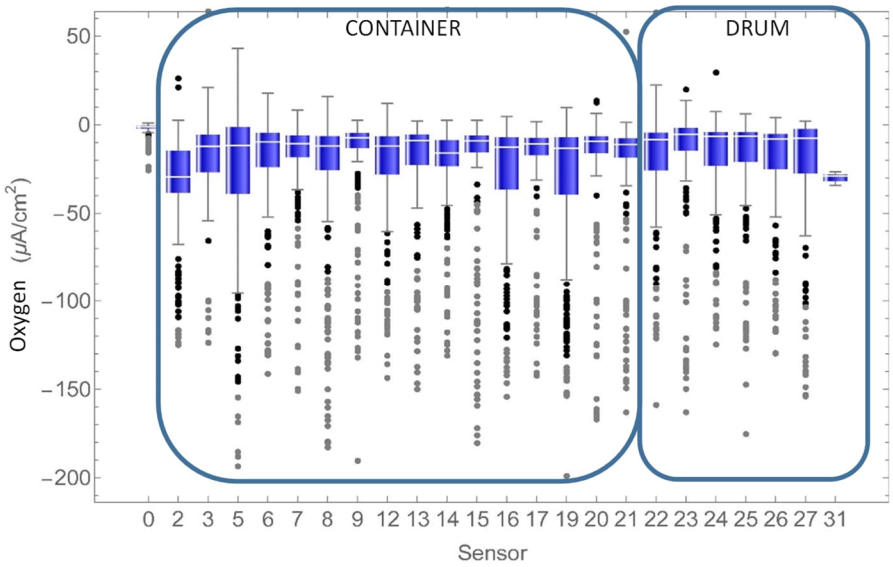

Figure 6. Oxygen. Box and whisker plot

3.4. Concrete resistivity

Resistivity values rose slightly in the latter years of the series due to concrete ageing and seasonal temperature variations. The figure also shows that the readings logged were less stable after January 2015 than previously. Resistivity sensors Nos 4, 10 and 11 failed. The box and whisker plot in Figure 7 gives the mean, maximum and minimum values for the resistivity sensors, along with the outliers. A very similar mean resistivity of around 20 kΩ cm to 80 kΩ cm was observed in all the sensors, although the readings recorded by the ones in the buried container were higher than in all the others.

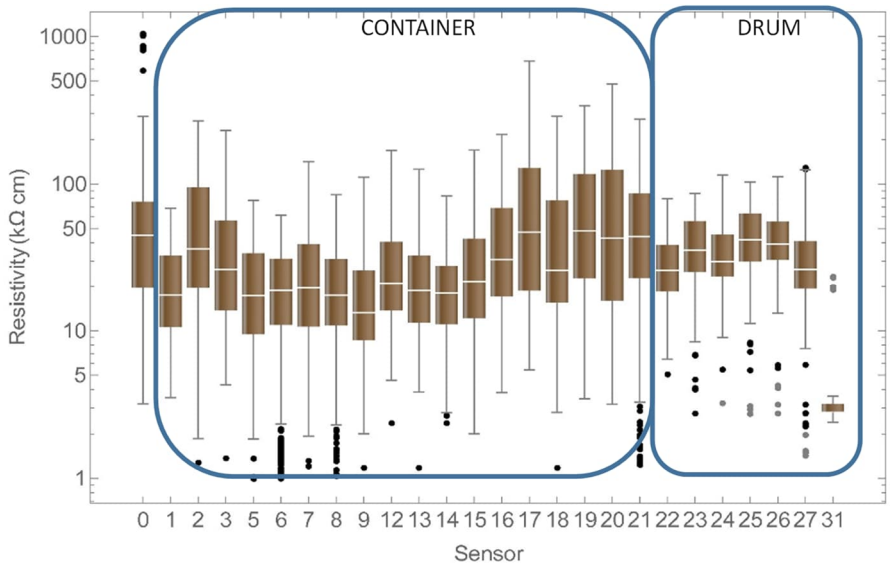

Figure 7. Concrete resistivity. Box and whisker plot

3.5. Corrosion potential

Corrosion potential relative to the manganese electrode (Mn/MnO) is registered. Sensors Nos 10 and 11 logged no readings from the outset. Further to the box and whisker plot for corrosion potential in Figure 8, the sensors located in the drums (sensors Nos 22 to 27) logged the most negative readings. No values smaller than -375 mV were recorded, denoting scant likelihood of corrosion

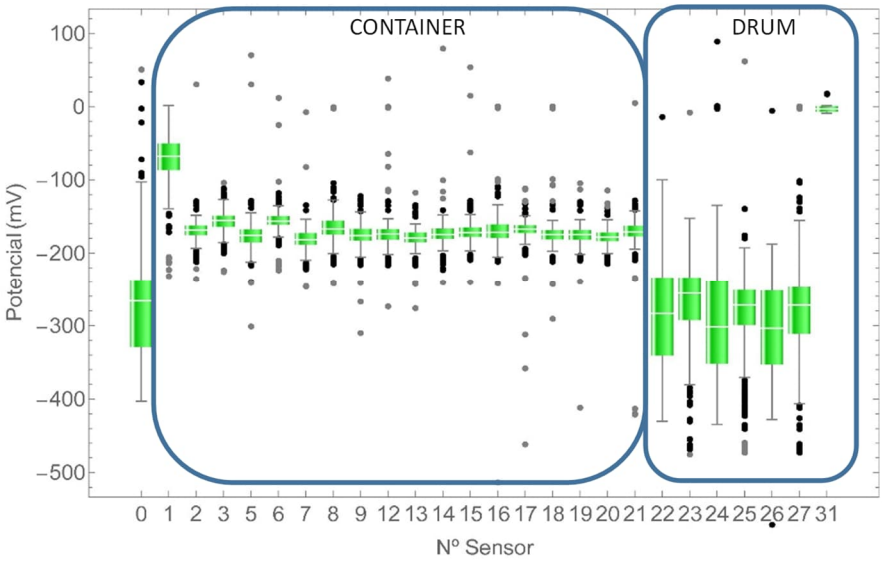

Figure 8. Corrosion potential. Box and whisker plot

3.6. Corrosion rate

The corrosion rate values recorded were lower than 0.10 µA/cm², the threshold above which corrosion is deemed to begin and the steel to become active [13], [14]. The box and whisker plots for all the corrosion current density sensors in Figure 9 show the mean and extreme values, along with the outliers. All the sensors exhibited mean values of under 0.02 µA/cm² and most approximately to 0.01 µA/cm².

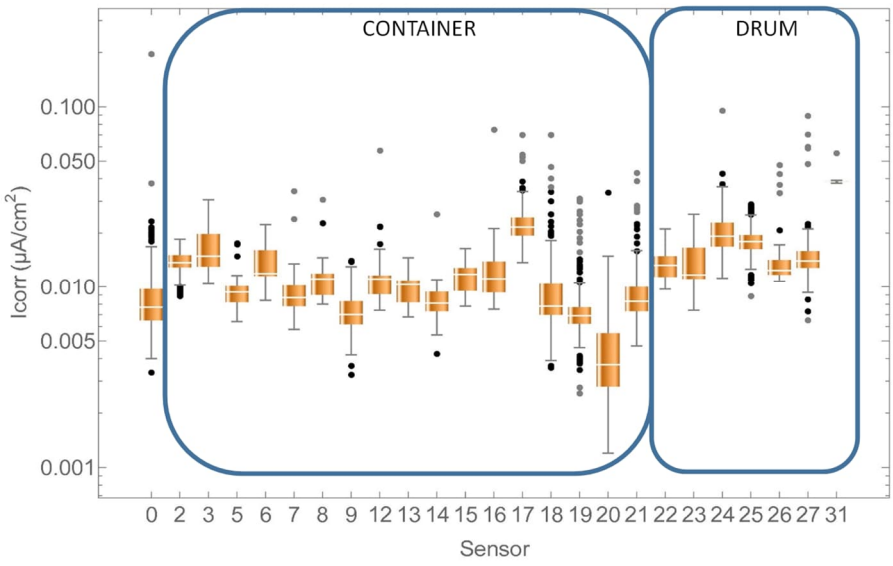

Figure 9. Corrosion rate. Box and whisker plot

4. DISCUSSION

The most significant correlations between parameters used to determine possible reinforced concrete corrosion are discussed in this section.

The relationship between resistivity and temperature are defined by Arrhenius equation, see equation 1.

$$\rho = \rho_0 Exp^{\left[\frac{-Ea}{RT}\right]} \qquad \text{Equation 1}$$

where ρ_0 is a constant and *Ea* is process activation energy.

The values declined with rising temperature, yielding negative activation energy when the data were fitted to Equation 1. The activation energy values for all the sensors in operation (i.e., all except Nos 4, 10 and 11) are shown in Figure 10, according to which this parameter adopted values ranging from -20 kJ/mol to 60 kJ/mol with a mean of -45 kJ/mol.

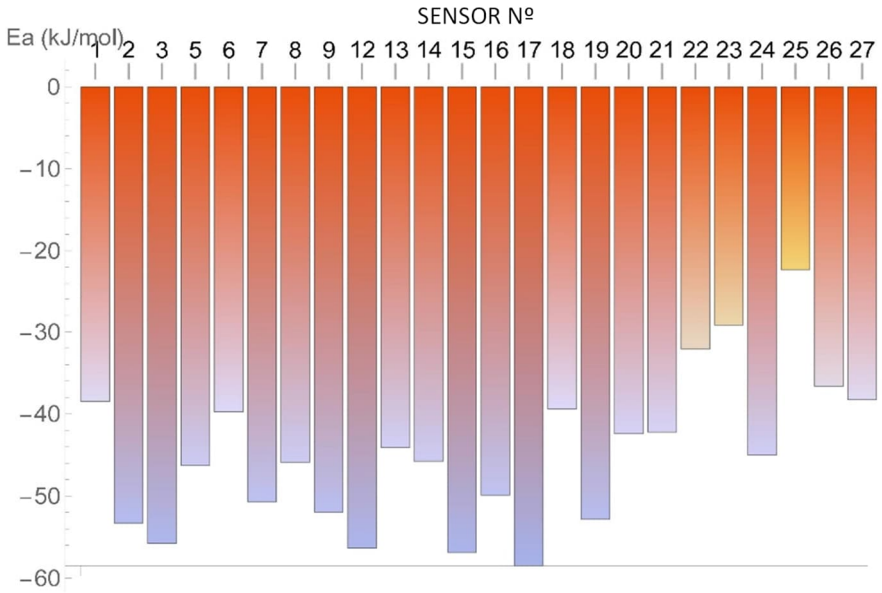

Figure 10. Activation energy for concrete resistivity. Sensors Nos 1 to 21 in container wall and Nos 22 to 27 in drums

One of the parameters that governed the corrosion rate, even in the presence of depassivation agents, is concrete resistivity [15]–[19]. Figure 11 graphs the mean sensor readings in a double log plot where corrosion rate is plotted against resistivity. The dotted orange line on the upper right delimits the area in which the structure may lie [17], [20], whilst the dotted red lines depict the range of values above which corrosion may be deemed to be active. All the most recent readings denoted passivity. With values lower than 100 kΩ·cm, resistivity did not limit corrosion current density. In other words, were the steel to move from the passive to the active state with a concomitant rise in corrosion current density, resistivity would remain unaltered.

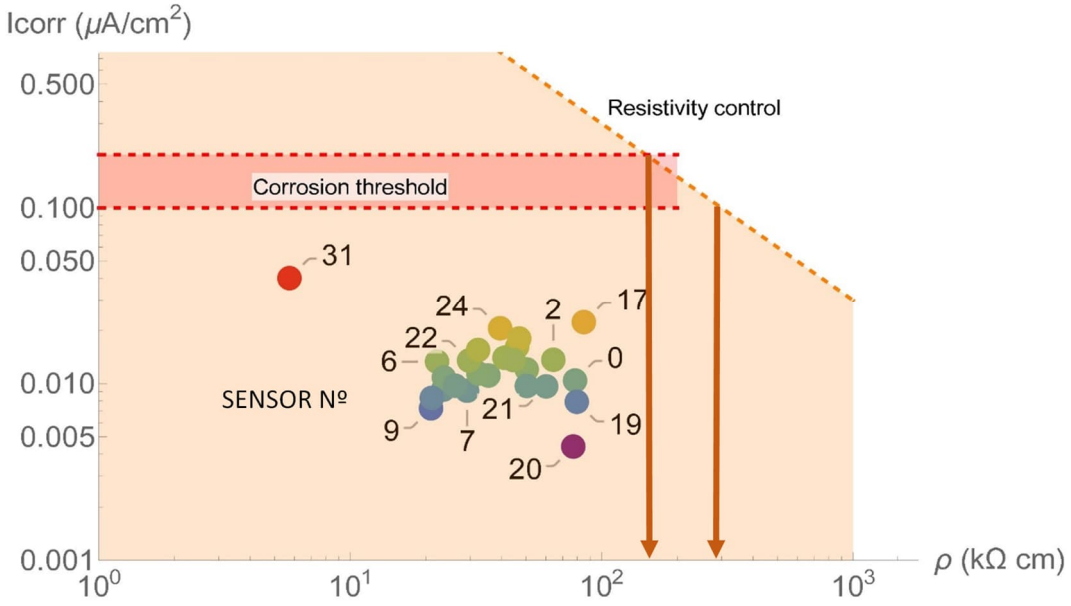

Figure 11. Mean corrosion rate vs mean concrete resistivity

Mean corrosion potential (vs Mn/MnO) is plotted against corrosion current density for each sensor in Figure 12. All the sensors recorded passive values, with corrosion potential readings ranging from -300 mV to 100 mV. The same graph shows the variation in oxygen (blue line) and in hydrogen (orange line) [21], [22]. The activation threshold is likewise plotted (green line). If the sensors were in a wholly anoxic environment the readings would denote the most negative potential (-800 mV) and density values lower than 0.2 µA/cm2 [23]. That scenario would appear to be unlikely in light of the oxygen availability sensor readings.

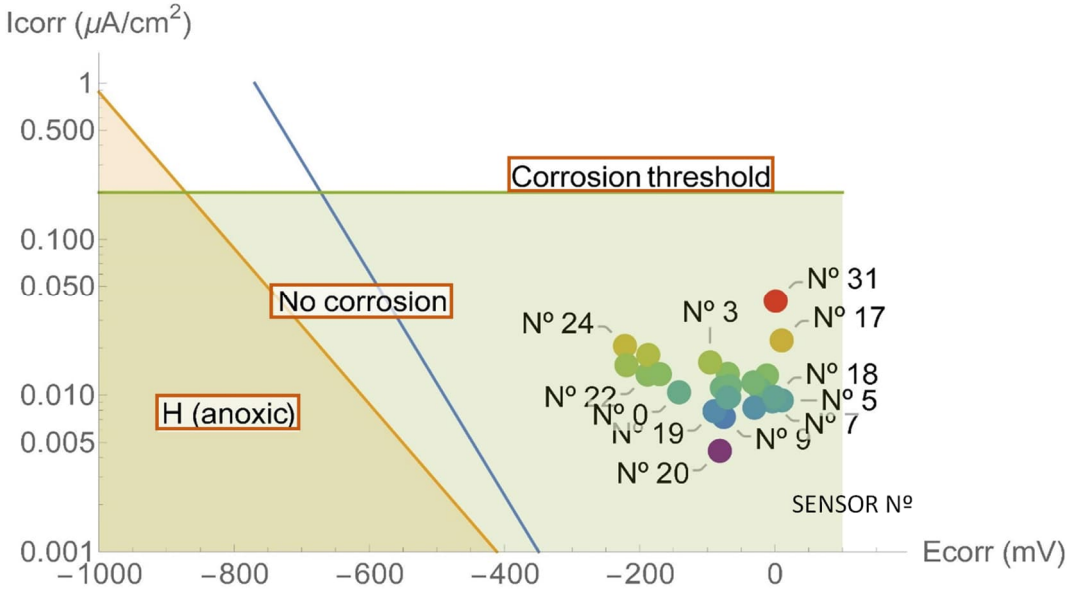

Figure 12. Corrosion current density vs corrosion potential

5. CONCLUSIONS

Monitoring reinforced concrete structures is technologically challenging, for it entails working with sensors with a service life longer than the structure itself. This article reports the findings after over 25 years of operation, in which artificial intelligence methodology was deployed to filter the data.

The sensors furnished valuable information on the variation in the parameters associated with reinforced concrete structure durability, which could then be used to validate long-term durability models.

The structure instrumented was exposed to daily and yearly temperature cycles that had a substantial impact on structural strain and concrete resistivity. Those thermal variations had no significant effect on corrosion current density, however, which was observed to vary indistinctly either directly or inversely relative to temperature.

The values for electrical parameters such as corrosion potential and corrosion current density recorded at all the measuring points confirmed that the structure remained passive, with a negligible corrosion-induced section loss in the reinforcement after 25 years of service life.

ACKNOWLEDGEMENTS

The data and funding provided by ENRESA under agreement No. 079-ES-IN-2019-0004 are gratefully acknowledged.

REFERENCES

[1] M. Alexander and H. Beushausen, “Durability, service life prediction, and modelling for reinforced concrete structures – review and critique,” *Cem. Concr. Res.*, vol. 122, pp. 17–29, 2019, doi: https://doi.org/10.1016/j.cemconres.2019.04.018.

[2] Y. Cao, C. Gehlen, U. Angst, L. Wang, Z. Wang, and Y. Yao, “Critical chloride content in reinforced concrete — An updated review considering Chinese experience,” *Cem. Concr. Res.*, vol. 117, pp. 58–68, 2019, doi: https://doi.org/10.1016/j.cemconres.2018.11.020.

[3] J. J. W. Gulikers, *A simplified and practical approach regarding design for durability of reinforced concrete structures based on probabilistic modeling of chloride ingress*. 2009.

[4] D. S. Dugdale, H. E. Enahoro, and G. T. Burstein, “Experimental investigation and numerical modeling of carbonation process in reinforced concrete structures: Part II. Practical applications,” *Cem. Concr. Res.*, vol. n/a, no. 3, pp. 337–344, 2020, doi: 10.1617/s11527-012-9968-1.

[5] U. Angst *et al.*, “Corrosion of steel in carbonated concrete: mechanisms, practical experience, and research priorities – a critical review by RILEM TC 281-CCC,” *RILEM Tech. Lett.*, vol. 5, no. 0 SE-, pp. 85–100, Dec. 2020, doi: 10.21809/rilemtechlett.2020.127.

[6] K. Li, P. Wang, Q. Li, and Z. Fan, “Durability assessment of concrete structures in HZM sea link project for service life of 120 years,” *Mater. Struct.*, vol. 49, no. 9, pp. 3785–3800, 2016, doi: 10.1617/s11527-015-0754-8.

[7] J. Sanchez-Montero *et al.*, “Ten years study of the hygrothermal behaviour of the Prado museum’s roof,” *Inf. la Construcción*, vol. 66, no. 535, 2014, doi: e02710.3989/ic.12.121.

[8] J. Sanchez, C. Andrade, and J. Fullea, “Hydrothermal monitoring using embedded sensors of the actual roof system of the Prado Museum,” *Constr. Build. Mater.*, vol. 24, no. 12, pp. 2579–2589, 2010, doi: 10.1016/j.conbuildmat.2010.05.018.

[9] C. Andrade, S. Briz, J. Sanchez, P. Zuloaga, M. Navarro, and M. Ordoñez, “Evolution of corrosion parameters in a buried pilot nuclear waste container in el Cabril,” in *Materials Research Society Symposium Proceedings*, 2014, vol. 1665, pp. 215–224, doi: 10.1557/opl.2014.648.

[10] C. Andrade, P. Zuloaga, I. Martinez, A. Castillo, and S. Briz, “Effect of temperature on corrosion parameters and apparent activation energy measured by embedded sensors in pilot container in El Cabril repository,” *Corros. Eng. Sci. Technol.*, vol. 46, no. 2, pp. 182–189, 2011, doi: 10.1179/1743278211y.0000000007.

[11] P. Zuloaga *et al.*, “Ageing management program for the Spanish low and intermediate level waste disposal and spent fuel and high-level waste centralised storage facilities,” in *Amp 2010 - International Workshop on Ageing Management of Nuclear Power Plants and Waste Disposal Structures*, vol. 12, V. Lhostis, K. Philipose, R. Gens, and C. Galle, Eds. 2011, p. 01003.

[12] C. Andrade, I. Martinez, M. Castellote, and P. Zuloaga, “Some principles of service life calculation of reinforcements and in situ corrosion monitoring by sensors in the radioactive waste containers of El Cabril disposal (Spain),” *J. Nucl. Mater.*, vol. 358, no. 2–3, pp. 82–95, 2006, doi: 10.1016/j.jnucmat.2006.06.015.

[13] J. Sanchez, J. Fullea, and C. Andrade, “Corrosion-induced brittle failure in reinforcing steel,” *Theor. Appl. Fract. Mech.*, vol. 92, no. Supplement C, pp. 229–232, 2017, doi: https://doi.org/10.1016/j.tafmec.2017.08.006.

[14] Ø. Vennesland, M. Raupach, and C. Andrade, “Recommendation of Rilem TC 154-EMC: ‘Electrochemical techniques for measuring corrosion in concrete’—measurements with embedded probes,” *Mater. Struct.*, vol. 40, no. 8, pp. 745–758, 2007, doi: 10.1617/s11527-006-9219-4.

[15] P. Azarsa and R. Gupta, “Electrical Resistivity of Concrete for Durability Evaluation: A Review,” *Adv. Mater. Sci. Eng.*, vol. 2017, 2017, doi: 10.1155/2017/8453095.

[16] S. Feliu, C. Andrade, J. A. Gonzalez, and C. Alonso, “A new method for in-situ measurement of electrical resistivity of reinforced concrete,” *Mater. Struct.*, vol. 29, no. 190, pp. 362–365, 1996.

[17] J. Gulikers, “Theoretical considerations on the supposed linear relationship between concrete resistivity and corrosion rate of steel reinforcement,” *Mater. Corros.*, vol. 56, no. 6, pp. 393–403, 2005, doi: 10.1002/maco.200403841.

[18] K. Hornbostel, C. K. Larsen, and M. R. Geiker, “Relationship between concrete resistivity and corrosion rate – A literature review,” *Cem. Concr. Compos.*, vol. 39, no. 0, pp. 60–72, 2013, doi: http://dx.doi.org/10.1016/j.cemconcomp.2013.03.019.

[19] J. Sanchez, C. Andrade, J. Torres, N. Rebolledo, and J. Fullea, “Determination of reinforced concrete durability with on-site resistivity measurements,” *Mater. Struct.*, vol. 50, no. 1, Feb. 2017, doi: 10.1617/s11527-016-0884-7.

[20] J. Warkus, M. Raupach, and J. Gulikers, “Numerical modelling of corrosion – Theoretical backgrounds –,” *Mater. Corros.*, vol. 57, no. 8, pp. 614–617, 2006, doi: 10.1002/maco.200603992.

[21] E. Garcia, J. Torres, N. Rebolledo, R. Arrabal, and J. Sanchez, “Corrosion of Steel Rebars in Anoxic Environments. Part I: Electrochemical Measurements,” *Materials* , vol. 14, no. 10. 2021, doi: 10.3390/ma14102491.

[22] E. Garcia, J. Torres, N. Rebolledo, R. Arrabal, and J. Sanchez, “Corrosion of Steel Rebars in Anoxic Environments. Part II: Pit Growth Rate and Mechanical Strength,” *Materials* , vol. 14, no. 10. 2021, doi: 10.3390/ma14102547.

[23] P. Lu, B. Kursten, and D. D. Macdonald, “Deconvolution of the Partial Anodic and Cathodic Processes during the Corrosion of Carbon Steel in Concrete Pore Solution under Simulated Anoxic Conditions,” *Electrochim. Acta*, vol. 143, no. Supplement C, pp. 312–323, 2014, doi: https://doi.org/10.1016/j.electacta.2014.08.027.

Electrochemical techniques for non-destructive evaluation of corrosion damage on steel liners in concrete

Miha Hren[1,*], Nina Gartner[1], Tadeja Kosec[1] and Andraž Legat[1]
[1] Slovenian National Building and Civil Engineering Institute (ZAG), Ljubljana, Slovenia

ABSTRACT

Concrete structures with embedded steel are a considerable part of the Nuclear Power Plant (NPPs) infrastructure. Although concrete enables passivation of the steel surface due to its alkalinity, many corrosion processes can still occur due to environmental conditions (e.g. chlorides, carbonation) and geometry on the steel surface (e.g. crevice). Many of these corrosion processes are hidden inside the concrete until the mitigation of damage is very complex and costly.
One of the safety concerns in NPPs is chloride-induced corrosion of steel cylinder concrete pipes (SCCPs). Objective within EC H2020 ACES project is to find and evaluate suitable non-destructive inspection techniques (NDTs) for early detection of corrosion inside SCCPs. Electrochemical methods for corrosion inspection on reinforced concrete structures are cost effective, portable, robust, and relatively easy to use in more complex conditions. In this study, commercially available portable instrument for half-cell potential mapping was evaluated. Additionally, stationary laboratory galvanostat will be used for a more detailed study of the galvanostatic pulse technique, and to further substantiate the results of field equipment.
Larger scale test specimens were produced, mimicking the properties of real SCCP. Carbon steel liner was covered with 15 mm or 25 mm concrete cover containing different concentrations of chlorides. Specimens were exposed to wet/dry cycles with tap water, measurements were performed once per each cycle.
The measurements show that the differences between initially measured potentials on different specimens are very evident; half-cell potentials are influenced by the concentration of chlorides and the thickness of concrete cover. The half-cell potential mapping is a valuable method for fast qualitative corrosion risk estimation, showing weak spots on steel liner surface. The galvanostatic pulse technique is slower method, but can also provide quantitative indication of the corrosion rate.

Keywords: steel liner in concrete; corrosion inspection; non-destructive techniques; half-cell potential mapping; galvanostatic pulse technique.

1. INTRODUCTION

Concrete structures with embedded steel liners are a considerable part of the Nuclear Power Plants (NPPs) infrastructure. Steel in concrete is normally protected from corrosion by high pH of the concrete. However, the depassivation of the carbon steel reinforcement can occur due to the reaction of the concrete with atmospheric CO_2 (carbonation) and/or ingress of aggressive ions (Cl^-) to the steel surface [1]–[3]. Apart from the crevice corrosion of steel liner embedded in concrete of containment building, the chloride-induced corrosion of steel cylinder concrete pipes (SCCP) is also a part of NPPs where safety is the major concern [4]. Since corrosion initiates on the internal part of the liner, it is necessary to perform inspections from the inside of pipes to detect corrosion on early stages. This requires the non-destructive corrosion inspection from the inside of pipes. There are several commercially available, cost effective, portable, robust, fast and relatively easy-to-use non-destructive techniques (NDTs) for corrosion inspection of reinforced concrete

* Corresponding author: +386 1 2804 504, miha.hren@zag.si

structures, which could be used also in more complex conditions, e.g. half-cell potential mapping and galvanostatic pulse measurements [5], [6].

Half-cell potential mapping (PM) is a NDT, which can be used for evaluation of steel corrosion in laboratory and on real concrete structures. The basic idea of the potential field measurement is to measure the potentials on multiple locations of the concrete surface, in order to get a characteristic map of the steel corrosion state inside the concrete. For this purpose, a reference electrode (usually Cu/CuSO4 or Ag/AgCl) is connected via a high-impedance voltmeter to the steel, and is moved in a grid pattern over the concrete surface [7]. The numerical value of the measured potential difference between the steel in concrete and the reference electrode depends on the type of reference electrode used and on the corrosion condition of the steel in concrete. Since the potential cannot be measured directly on the steel surface, the result is also influenced by the ohmic drop (i*R*) in the concrete cover, by macro-cell current and possibly by junction potentials. Potentials are interpreted in the context of complementary data from the concrete structure (chloride content, carbonation, porosity, concrete cover etc.) [5]. The correlation between measured half-cell potential ranges (vs. Cu/CuSO4) and the probability of steel corrosion in concrete are provided in ASTM standard C876-15 [8]. The Galvanostatic Pulse (GP) technique is somehow an upgrade of PM technique. It is a fairly rapid non-destructive polarization technique. In addition to half-cell corrosion potentials, GP also gives the information on the polarisation resistance and the resulting corrosion currents (corrosion rate by polarization) on the steel surface in concrete [6], [9]–[12].

The aim of this study is to address the strengths and limitations of selected commercially available electrochemical NDTs, i.e. half-cell potential mapping and galvanostatic pulse measurements, which are able to detect the occurrence and location of early corrosion on the inside of SCCP.

2. EXPERIMENTAL

Laboratory tests were performed to evaluate selected electrochemical NDTs for their use in specific SCCP environments. Laboratory scale test specimens were produced, mimicking the properties of the real SCCP and enable controlled evaluation of NDT's abilities. The mock-up specimens' properties are listed in Table 1, and the specimen sketch is presented in Figure 1 (left).

For half-cell potential mapping (PM) the device Profometer Corrosion (rod and 1-wheel electrode) from the producer Proceq was used. This technique was also selected as the most appropriate electrochemical NDT for the use in SCCP, concerning multiple evaluation criteria, e.g. the resolution, geometrical limitations, duration of measurement, operational skills needed, sensitivity to the environment and compatibility with the robotic manipulation platform. Galvanostatic pulse (GP) measurements were also performed, but the results are not presented in this paper.

Table 1. The properties of mock-up specimens.

Steel plate (liner)	Type:	SS355
	Size:	400 mm × 400 mm
	Thickness:	4 mm
	Surface:	As received
	Defects:	4 different mechanical holes in the corner of each plate (Φ / depth [mm]): 5 / 1, 5 / 2, 20 / 1, 20 / 2
Steel mesh	Type:	B 500A
	Dimensions:	Φ5 mm, 150 mm between individual bars
Concrete	W/C/A:	0.6/1/4
	Cement:	CEM I 42,5N
	Sand & Aggregates:	0/4 4/8 mm (lime stone)
	Chemical additives:	None
	Cover thickness:	15 mm or 25 mm
	Defects:	Artificial crack of concrete cover by bending
	Chlorides:	Mixed-in – concentrations [wt. % NaCl on the mass of cement]: 0, 1, 4
	Carbonation:	Only natural
Design	length × width × thickness:	1) 500 mm × 500 mm × 40 mm (15 mm concrete cover) 2) 500 mm × 500 mm × 50 mm (25 mm concrete cover)
	Construction:	3 layers: concrete base (25 mm) + steel plate (4 mm) + concrete cover (15 or 25 mm)

Seven types of specimens were used for this study, differing on thickness of concrete cover, content of chlorides and presence of a steel mesh:

- Steel liner + 15 mm concrete cover with 0, 1 or 4 % NaCl (mixed-in)
- Steel liner + 25 mm concrete cover with 0, 1 or 4 % NaCl (mixed-in)
- Steel liner & mesh + 25 mm concrete cover with 0 % NaCl (mixed-in)

Specimens were exposed to wet/dry cycles with tap water in normal room conditions – drip-wetted for 1 day (~1 dL/hour) and dried for 6 days (1 cycle = 1 week). PM measurements with rod and 1-wheel electrode were performed once per cycle on wetted specimens in an 8x8 matrix (rod) and in 8 rolling lines (Figure 1 middle and right).

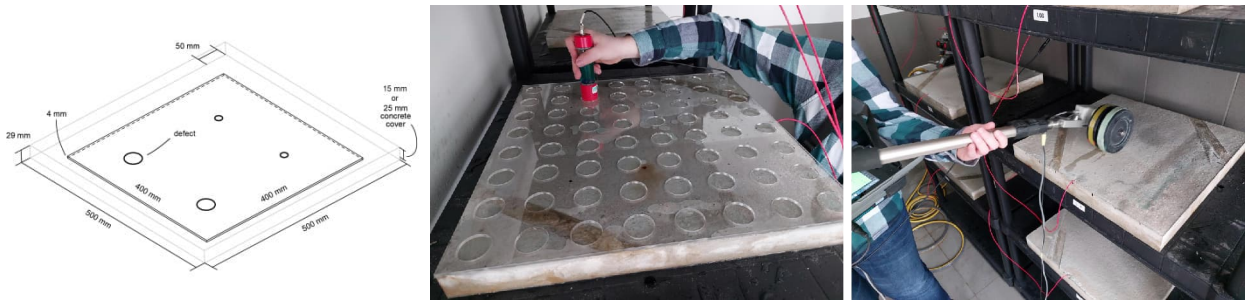

Figure 1. Sketch of the specimen (left), PM measurements with rod electrode (middle) and 1-wheel electrode (right) on the mock-up specimen.

3. RESULTS AND DISCUSSION

This study shows that results of half-cell potentials measured with Profometer Corrosion (Proceq SA). The presented results for specimens without the mesh were measured 230 days after the start of the cyclic wetting, while only a single mesh specimen is presented at select times. The results are fairly comparable between discrete measurements (rod electrode) and continuous measurements (wheel electrode), therefore only results measured with rod electrode are presented in this study.

The difference between initial half-cell potentials measured on different specimens is very evident (Table 2). This indicates that the half-cell potentials on average are significantly influenced by the concentration of mixed-in chlorides, where higher Cl^- concentrations result in more negative potentials. To a smaller extent, the thickness of concrete cover also results in different average potentials, but this varies based on the amount of chlorides present (Figure 2 and 3).

Table 2. Approximate average half-cell potential values measured before the exposure on mock-up specimens with different chloride contents and different thicknesses of concrete cover.

Concrete cover \ NaCl	0 %	1 %	4 %
15 mm	–250 mV	–350 mV	–500 mV
25 mm	–200 mV	–400 mV	–500 mV
25 mm with steel mesh	–200 mV	-	-

The values of half-cell potentials measured across the steel surface differ for about 100 mV for all chloride concentrations and concrete covers (Figure 2, 3 and 4), indicating locations more or less prone to corrosion. These deviations in potential roughly coincide with larger 20 mm defects drilled in the bottom part of the specimens (Figure 1 left), where slightly less negative potential was measured. This indicates less chance of active corrosion in these areas.

Figure 2. Results of half-cell potential measurements performed after 230 days of exposure with rod electrode on mock-up specimens without the steel mesh, with 15 mm concrete cover and a) 0 % NaCl b) 1 % NaCl and c) 4 % NaCl.

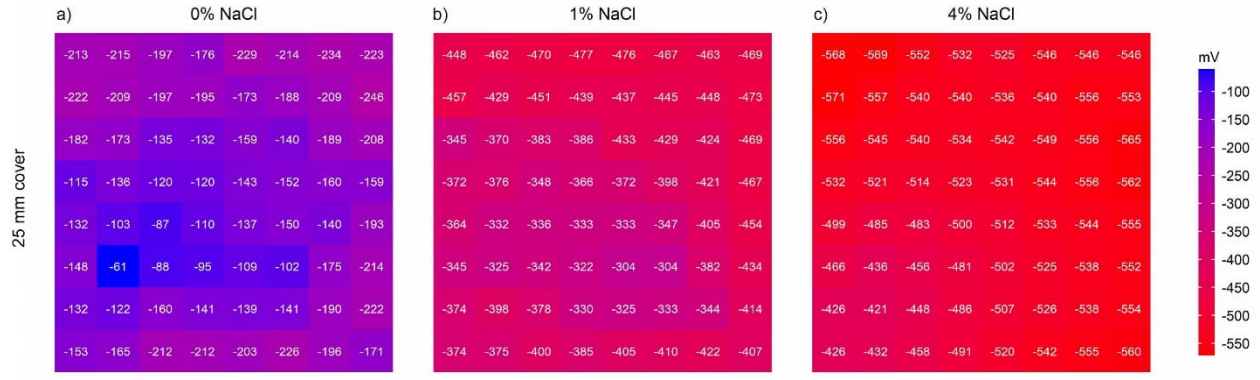

Figure 3. Results of half-cell potential measurements performed 230 days of exposure with rod electrode on mock-up specimens without the steel mesh, with 25 mm concrete cover and a) 0 % NaCl b) 1 % NaCl and c) 4 % NaCl.

Potential values measured on mock-up specimen with the embedded mesh is also presented at select times (Figure 4). Although the specimen after 229 days shows almost no change in potentials from the initial measured values (42 days), it does show a significant increase in potentials towards more positive values in between those timeframes (138 days). This phenomenon

was also observed on other specimens and is likely the result of significant moisture reaching the steel surface, initiating the start of active corrosion.

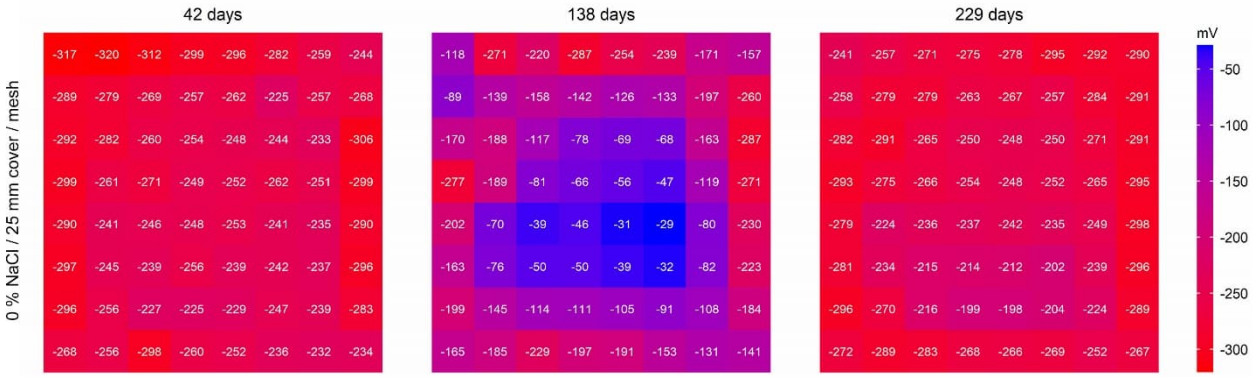

Figure 4. Results of half-cell potential measurements performed over time with rod electrode on mock-up specimen with the steel mesh, with 25 mm concrete cover and 0 % NaCl.

4. CONCLUSIONS

Half-cell potential mapping (PM) does not provide quantitative information on the actual corrosion rate of the steel; it only indicates the likelihood of the corrosion process at the point of measurement, and the risk of corrosion may then be related empirically to the measured potential [5]. This technique was found to be easy to use (both rod and one-wheel electrode), with fast measurements and results that indicate corrosion weak spots on the surface of steel inside concrete. The main limitation of this technique is comparison between values measured in different corrosion conditions, i.e. level of chlorides and concrete cover.

In our further activities, the results from PM method will be compared with the results obtained using the galvanostatic pulse method (GP) measured with Gamry Reference 600+ potentiostat. This is more complex laboratory device and therefore less suitable to use in large reinforced structures. Its advantage towards some portable GP devices (e.g. GalvaPulse from Germann Instruments A/S) is that the interpretation of results is not limited to Randles equivalent circuit model. GP results will give additional information of concrete currents on the surface, and consequently provide quantitative information on locations with increased corrosion rates.

ACKNOWLEDGEMENTS

This work has been performed in the scope of the EC H2020 ACES project.

REFERENCES

[1] L. Bertolini, B. Elsener, P. Pedeferri, E. Redaelli, and R. B. Polder, *Corrosion of Steel in Concrete: Prevention, Diagnosis, Repair*, 2nd ed. Weinheim, Germany: Wiley-VCH, 2013. Accessed: Dec. 05, 2017. [Online]. Available: http://www.wiley.com/WileyCDA/WileyTitle/productCd-3527331468.html

[2] H. Böhni, Ed., *Corrosion in Reinforced Concrete Structures*, 1st ed. Cambridge, England: Woodhead Publishing Limited, 2005. Accessed: Dec. 05, 2017. [Online]. Available: https://www.elsevier.com/books/corrosion-in-reinforced-concrete-structures/bohni/978-1-85573-768-6

[3] J. P. Broomfield, *Corrosion of Steel in Concrete: Understanding, investigation and repair*. CRC Press, 1996. Accessed: Dec. 07, 2017. [Online]. Available: https://www.crcpress.com/Corrosion-of-Steel-in-Concrete-Understanding-investigation-and-repair/Broomfield/p/book/9780203475287

[4] V. L'Hostis and R. Gens, Eds., *Performance Assessment of Concrete Structures and Engineered Barriers for Nuclear Applications, Conclusions of RILEM TC 226-CNM*, vol. 21.

Springer Nature, 2016. Accessed: Jul. 28, 2022. [Online]. Available: https://link.springer.com/book/10.1007/978-94-024-0904-8

[5] B. Elsener, C. Andrade, J. Gulikers, R. Polder, and M. Raupach, 'Half-cell potential measurements—Potential mapping on reinforced concrete structures, RILEM TC 154-EMC Recommendations', *Mat. Struct.*, vol. 36, no. 7, pp. 461–471, Aug. 2003, doi: 10.1007/BF02481526.

[6] T. Luping, 'Calibration of the electrochemical methods for the corrosion rate measurement of steel in concrete', SP Technical Research Institute of Sweden, NORDTEST Project No. 1531-01 NT TR 521, Nov. 2002. Accessed: Dec. 07, 2017. [Online]. Available: http://www.nordtest.info/index.php/technical-reports/item/calibration-of-the-electrochemical-methods-for-the-corrosion-rate-measurement-of-steel-in-concrete-nt-tr-521.html

[7] Proceq SA, 'Profometer - Operating Instructions', 2017. https://www.screeningeagle.com/en/products/profometer-corrosion (accessed Jan. 26, 2022).

[8] ASTM Subcommittee 14, *ASTM Standard C876-15, Standard Test Method for Corrosion Potentials of Uncoated Reinforcing Steel in Concrete*. Torrance, California, USA: American Society for Testing and Materials - ASTM International, 2015.

[9] B. Elsener, O. Klinghoffer, T. Frolund, E. Rislund, Y. Schiegg, and H. Böhni, 'Assessment of reinforcement corrosion by means of galvanostatic pulse technique', *Repair of Concrete Structures*, pp. 391–400, 1997.

[10] Germann Instruments, 'Corrosion rates by various authors', *GalvaPulse*. https://www.germann.org/Publications/GalvaPulse/1.%20Corrosion%20rates%20by%20various%20authors.pdf (accessed Jun. 09, 2020).

[11] M. Hren, T. Kosec, and A. Legat, 'Characterization of stainless steel corrosion processes in mortar using various monitoring techniques', *Construction and Building Materials*, vol. 221, pp. 604–613, Oct. 2019, doi: 10.1016/j.conbuildmat.2019.06.120.

[12] S. Sathiyanarayanan, P. Natarajan, K. Saravanan, S. Srinivasan, and G. Venkatachari, 'Corrosion monitoring of steel in concrete by galvanostatic pulse technique', *Cement and Concrete Composites*, vol. 28, no. 7, pp. 630–637, Aug. 2006, doi: 10.1016/j.cemconcomp.2006.03.005.

Calibration process of a capacitive probe for monitoring of reinforced concrete nuclear structures

Houssein Ibrahim[1,2*], Géraldine Villain[1], Narintsoa Ranaivomanana[2], Xavier Dérobert[3], Sérgio Palma Lopes[3], Cyrille Fauchard[4], Vincent Guihard[5] and Jean-Paul Balayssac[2]

[1] Univ Gustave Eiffel, MAST-LAMES, Campus de Nantes, F-44344 Bouguenais
[2] Université de Toulouse INSA/UPS, LMDC, F-31077 Toulouse
[3] Univ Gustave Eiffel, GERS-GEOEND, Campus de Nantes, F-44344 Bouguenais
[4]Cerema, F-76121 Le Grand-Quevilly
[5]EDF, F-78401 Chatou

ABSTRACT

Nuclear and civil engineering structures are subjected to environmental conditions (rain, wind, temperature variations, etc.), as well as to various physical, mechanical and chemical aggressions that affect their durability.
In our work, we are interested in the development of an embedded capacitive sensor in order to determine the water content gradient as a durability indicator. Thus, in this paper, we propose the use of standard liquids (with well-known permittivity values) in order to carry out a prior calibration of the sensor which will be embedded later in reinforced concrete structures. Liquids were selected for their relative permittivities that cover the concrete range (2 to 30) at the frequency range of capacitive method. Liquid permittivities are extracted on one hand from literature review. On the other hand, measurements were performed with two coaxial probes. These probes were developed in research works and their principle consists on an open-ended coaxial line connected to a network analyzer. The obtained dispersion curves of the permittivities were adjusted then with the Debye model. Results show that Debye's model can adjust our measurements with a good correlation. Permittivity values in the working frequency range of the capacitive probe are thus extracted and compared to values published in literature. Once calibration is done, capacitive sensor is ready to be embedded in concrete to monitor reinforced concrete nuclear structures.

Keywords: Dielectric permittivity measurement, Capacitive probe, Calibration, Durability

1. INTRODUCTION

Durability of a structure conveys to a set of technical specifications based on destructive (D) or non-destructive (ND) test methods. In this work, we are in an intermediate situation since we aim to develop a sensor to be drown in reinforced concrete nuclear structures in order to determine the water content gradient, an essential information for the development of most water content pathologies, in particular corrosion of reinforcements. Thus, such sensor is somewhat intrusive, but still provides ND measurements.
As part of the of the French ANR-SCaNING project, the aim is to monitor concrete using three sensors: capacitive, resistive and ultrasonic. Concerning our study, the final objective is to design an embedded capacitive sensor to follow the evolution of the water content gradient by measuring dielectric permittivity over time.
The capacitive method is considered as an electromagnetic method sensitive to water content [1].
Many studies have been published on capacitive surface probes domain [2]. Its principle in civil engineering consists in applying an alternating current between two electrodes placed on the surface of a sample and measuring the resonance frequency of the electrode-concrete system. Our capacitive measurement RLC circuit called "SYMECC" oscillates at a frequency close to 33 MHz in order to minimize the influence of temperature and ion conduction [2].
Therefore, and before embedding the sensor and casting the concrete, a first calibration procedure should be performed in standard materials with well-known permittivities in order to relate the measured resonance frequency to the permittivity values. Once this calibration is done, frequency measurements in concrete are performed by SYMECC apparatus and then converted to permittivity

values due to the empirical model. A second calibration is then needed to convert permittivity to water content gradient. In this article, a study was established to find standard liquids useful for our first calibration initially based on the literature. In a second step, an experimental campaign was carried out in order to verify the permittivity values of the calibration materials with two open coaxial probes [3,4].
Hence, the definition of the permittivity, the coaxial probes and the dielectric models will be presented in section 2. Next, the different bibliographic permittivity results obtained for the standard materials will be shown. Then, we move on to the experimental campaign. We will define the two probes used to measure the permittivity values. The dispersion curves obtained are presented in section 4. A comparison between the results of the bibliographic and experimental study is performed at the end.

2. DIELECTRIC PERMITTIVITY

2.1. Definition

The dielectric permittivity, noted ε, is related to the phenomena of electrical polarization and results from a relative displacement of the bound charges of the matter exposed to an external electric field [5]. It is expressed in Farad per meter (F/m) and appears in the constitutive relation $\vec{D} = \varepsilon \vec{E}$ where $\vec{D}$ is the electric displacement field (C/m²) and $\vec{E}$ the electric field (V/m).
In lossy materials like concrete, permittivity is represented by a complex quantity such as $\varepsilon = \varepsilon' - j\,\varepsilon''$. Real and imaginary parts of the complex permittivity can be divided by the vacuum permittivity $\varepsilon_0 = 8.854187 \times 10^{-12}$ (F/m) in order to obtain the relative permittivity. The real relative part ε'_r called dielectric constant takes into account the polarization potential of concrete and the imaginary relative part ε''_r represents losses (both dielectric and by conduction) in concrete during electromagnetic wave propagation [2].
As mentioned in [6], the capacitance is the ability of the material to store electric energy and it depends on the real part of the complex permittivity. Therefore, we are interested in working on the real part more than the imaginary one.
Throughout the paper, we will work only on the relative permittivity. Thus, for simplification purposes, the real relative part of the permittivity will be noted as ε' and the imaginary relative part as ε''.

2.2. Dielectric permittivity measurement probes

Dielectric permittivity can be measured indirectly using capacitive probes. The principle consists in measuring a resonance frequency which is converted to ε' by a calibration process [7]. Otherwise, permittivity can be derived directly from the analysis of the transmission and reflection coefficients methods [8]. Coaxial transmission methods provide the advantage of measuring both dielectric constant and magnetic susceptibility. However, those methods are not applicable in many fields such as ND domains because they require the extraction of samples [9]. Reflection methods are used as a solution to this problem. A lot of work has been achieved with reflection methods [8], they proved the capacity of these methods specially in non-magnetic materials. Open coaxial probes are one of these methods, they offer the ability to perform permittivity measurement over a wide frequency band.
Two open coaxial probes are used in this work for measuring selected standard liquids permittivities. The first probe [3] consists on a device characterized by a core radius of 1.2 mm and a metallic shield radius of 4.5 mm built by abrading the surface of a connector (Figure 1.a). This device is connected to a vector network analyser (VNA) that delivers an electromagnetic signal that propagates in the material under test. The reflected signal is then collected and transformed to a value of ε' and ε'' by means of a capacitive model [10]. This probe will be called later as Probe 1. The second one [4] consists on a HP 85070B Hewlett Packard dielectric probe kit connected to an HP network analyser, under control of a personal computer (Figure 1.b). The measurements were carried out by ensuring the contact between the surface of the sample and the probe. The apparatus measures a coefficient of reflection which is converted to ε' and ε'' by a theoretical approach suggested by [11]. This probe will be called Probe 2. Both apparatuses can't measure under 50 MHz, thus a dielectric model is required in order to obtain permittivity at our interesting frequency 33 MHz.

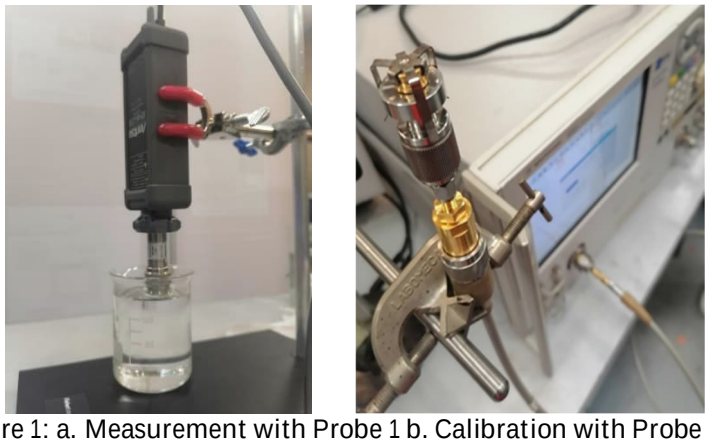

Figure 1: a. Measurement with Probe 1 b. Calibration with Probe 2

2.3. Dielectric models

The first dielectric expression was derived by Debye [12] based on permanent dipole moments in dielectric materials (equation 1). Others models was then developed based on Debye's theory such as Cole-Cole (CC), Davidson-Cole (DC)

$$\varepsilon_r = \varepsilon_\infty + \frac{\varepsilon_s - \varepsilon_\infty}{1 + j\,\omega\,\tau} \quad (1)$$

where ε_s and ε_∞ are respectively the static permittivity and the optical permittivity. ω (rad/s) is the angular frequency and τ (s) is the relaxation time.

Debye's model is adopted in this work. In order to simulate the frequency behaviour of the real and imaginary parts of the permittivity at low frequencies (<1 GHz) a conductivity term σ is added to equation 1, so equation (1) becomes:

$$\varepsilon_r = \varepsilon_\infty + \frac{\varepsilon_s - \varepsilon_\infty}{1 + j\,\omega\,\tau} + \frac{\sigma}{j\,\omega\varepsilon_0} \quad (2)$$

2.4. Standard liquids selection

Several solid standard materials were already used (Teflon, PVC...) to calibrate the surface capacitive probes [6]. For the present application, we are working with sensors to be embedded in concrete, thus this calibration procedure needs to be adapted. The idea proposed is to first drown the capacitive sensor in liquids or gels with known relative permittivity values in the range of concrete ones ($2<\varepsilon'<35$) at the frequencies of the capacitive method (~33 MHz). The search for gels or liquids is summarized in the following table.

Table 1: Standard liquids, references and characteristics

Liquids	References	Frequency range	ε'	T (◦C)
Methanol	[13]	0 to 100 MHz	32	22
	[14]	10 MHz	34.8	20
	[15]	1 KHz-1 MHz	33.64	20
Ethanol	[13]	0 to 100 MHz	24	22
	[16]	975 MHz	23.6	25
	[17]	50 KHz	25.3	20
Liquid Paraffin	[18]	38 MHz	2.7	-
	[19]	3 GHz	2.25	-
Acetone	[20]	Very Low frequencies	21.13	20
	[21]	1 GHz	22	-
	[22]	0 to 2 GHz	20.5	20
Amyl Alcool	[23]	DC to 5 GHz	15.152	20
	[24]	10 MHz to 32 MHz	15	25
	[25]	10 MHz to 10 GHz	15.6	20

3. STANDARD LIQUIDS PERMITTIVITY MEASUREMENT

3.1. Measurement process principle

Before starting measurements, a calibration process is required for the two probes. Measurements were performed in Methanol, Ethanol, Acetone, Amyl Alcohol, Liquid paraffin and a Methanol-Ethanol mixture (50%-50% proportion to obtain $\varepsilon' \simeq 28$) with the two probes defined in section 2.2.
Once measurements are performed, results appear in the form of ε' and ε'' as function of the frequency. The frequency range for the Probe 1 is [50 MHz, 2 GHz] with 3900 measurement points and for Probe 2 [200 MHz, 2 GHz] with 200 points. After that, dispersion curves obtained are adjusted by Debye's model presented in section 2.3. Since we are interested in the value of permittivity at 33 MHz, an extrapolation process has been done in order to extract the value of ε' at 33 MHz. Dispersion curves, extrapolation results and a comparison with literature results are shown in the next section.

3.2. Results and discussion

Optimisation was computed over the whole frequency range for both probes and for each standard liquid. Figure 2 shows the results for Methanol and Acetone. The same analysis was conducted for the four other liquids defined above (not shown here). Results for Probe 1 and Probe 2 are shown in Figure 2 with the respective indexes (1 and 2), where Re and Im stand for the real and imaginary part respectively, and "mes" or "extra" stand for measured or extrapolated (adjusted) respectively.

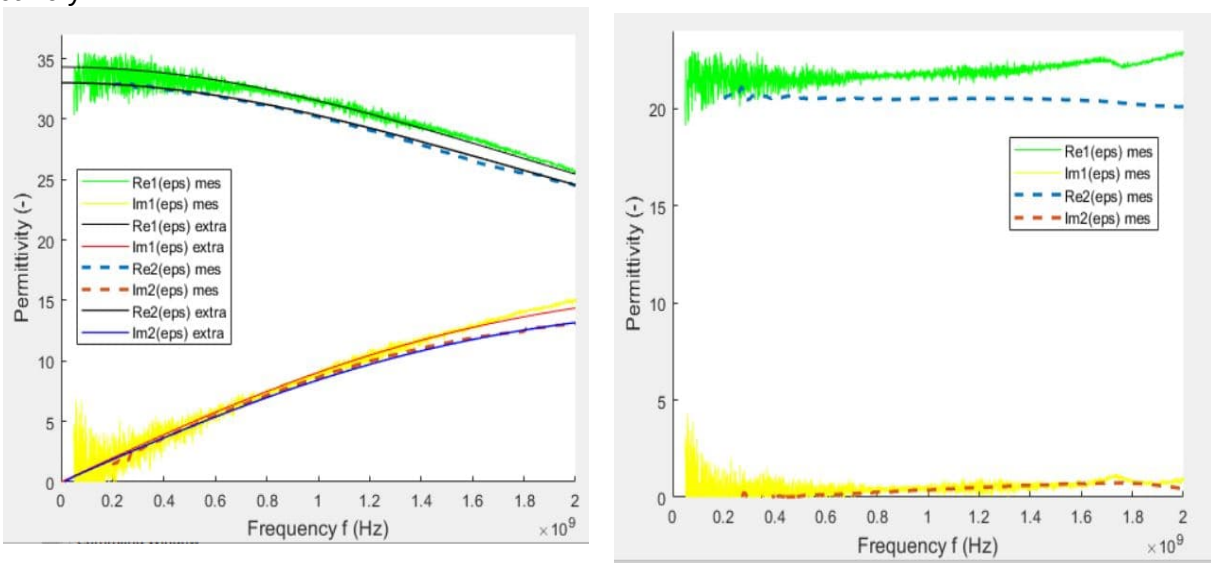

Figure 2: Dispersion curves for measured and adjusted permittivities for a) Methanol and b) Acetone.

Results show that Debye's Model can fit the dispersion curves for Methanol, Ethanol, Methanol+Ethanol mixture and Amyl Alcohol. The curves of Acetone and Paraffin show a trend that is not adjustable by Debye's model due to the limited frequency range insufficient for fitting the optimised curves for these liquids. Even though, those curves tend to the literature values (Table 1) at low frequencies. For the other liquids, Table 2 shows the normalized residual "R_n" defined in equation 3 for each curve as well as the extrapolated ε' at 33 MHz compared to the minimum and maximum ε' values of the literature (detailed in Table 1).

$$R_n = \frac{\sum(\varepsilon'_{mes} - \varepsilon'_{extra})^2}{N} \quad (3)$$

where N is the number of measurement points defined in section 3.1

Table 2: Comparison of extrapolated and literature values of ε'

Product	ε' extrapolated at 33 MHz Probe 1	ε' extrapolated at 33 MHz Probe 2	ε' minimum literature	ε' maximum literature	R_{n1} (Probe 1)	R_{n2} (Probe2)
Methanol	34.3	32.9	32	34.8	0.57	0.06
Methanol +Ethanol	29.9	28.9	27.8	30.1	0.5	0.02
Ethanol	24.9	24.3	23.6	25.3	0.27	0.05
Amyl Alcohol	15.2	15.8	15	15.6	0.09	0.18
Acetone	-	-	20.5	22	-	-
Liquid paraffin	-	-	2.25	2.7	-	-

It can be deduced from Table 2 that the relative permittivity values ε' of our liquids are in agreement with the literature given. The average of the two extrapolated values obtained with these two probes will be adopted in the calibration process of our embedded capacitive sensor.

4. CONCLUSION

This study aimed to measure the dielectric permittivity of standard liquids that will serve as a calibration input for future measurements with our capacitive sensor in reinforced concrete nuclear structures. To do this, we started by bibliographic research on standard liquids. Some liquids were selected for their relative permittivity values ε' that cover the concrete ones at working frequencies of the capacitive method. At a later time, measurements with two coaxial probes were conducted. Adjustment with Debye's model was the third step. At last, an extrapolation process was performed in order to obtain permittivity values at working frequencies of the capacitive method. Values obtained with the two probes were confirmed by the literature. For the future steps, the average of the two extrapolated values obtained with the two probes will be considered for the calibration process of our capacitive sensor that will be embedded in reinforced concrete nuclear structures.

ACKNOWLEDGEMENTS

The authors would like to thank the French Agence Nationale de la Recherche for the financial support of the project ANR-2020-CE22-015 SCaNING.

REFERENCES

[1]. Balayssac, J. P., Garnier, V. (Eds.). (2017). Non-destructive testing and evaluation of civil engineering structures. ISTE Press - Elsevier, London, United Kindom,355.

[2]. Dérobert, X., Iaquinta, J., Klysz, G., Balayssac, J. P. (2008). Use of capacitive and GPR techniques for the non-destructive evaluation of cover concrete. NDT & E International, 41(1), 44-52.

[3]. Guihard, V. (2018). Homogénéisation de grandeurs électromagnétiques dans les milieux cimentaires pour le calcul de teneur en eau. PhD thesis, Université Paul Sabatier-Toulouse III, France,198.

[4]. Godio, A. (2007). Open ended-coaxial cable measurements of saturated sandy soils. American Journal of Environmental Sciences, 3(3), 175-182.

[5]. Derobert, X., (2012). Presentation of common non destructive techniques, capacitive technique, in: D. Breysse (Ed.), Non-destructive Assessment of Concrete Structures: Reliability and Limits of Single and Combined Techniques, pp. 71–77, chapter 2. Toulouse.

[6]. Fares, M., Fargier, Y., Villain, G., Derobert, X., & Lopes, S. P. (2016). Determining the permittivity profile inside reinforced concrete using capacitive probes. NDT & E International, 79,

[7]. Ibrahim, H., Villain, G., Balayssac, J.P., Dérobert, X., Lopes, S.P., Devie, T. (2022). Calibration procedure for the development of an embedded capacitive sensor, Congrès Francais de Mécanique CFM, Nantes, France, accepted.
[8]. Chen, L. F., Ong, C. K., Neo, C. P., Varadan, V. V., & Varadan, V. K. (2004). Microwave electronics: Measurement and materials characterization. John Wiley & Sons, 28,29,32,38,39,166.
[9]. Guihard, V., Taillade, F., Balayssac, J. P., Steck, B., Sanahuja, J., & Deby, F. (2017, May). Modelling the behaviour of an open-ended coaxial probe to assess the permittivity of heterogeneous dielectrics solids. In 2017 Progress In Electromagnetics Research Symposium-Spring (PIERS) (pp. 1650-1656). IEEE.
[10]. Stuchly, M. A., & Stuchly, S. S. (1980). Coaxial line reflection methods for measuring dielectric properties of biological substances at radio and microwave frequencies-A review. IEEE Transactions on instrumentation and measurement, 29(3), 176-183.
[11]. Stuchly, M., M. Brady, S. Stuchly and G. Gajda, (1982). Equivalent Circuit of an Open-Ended Coaxial Line in a Lossy Dielectric, IEEE Transactions on Instrumentation and Measurement, IM-31: 116–119.
[12]. Debye, P. (1945). Polar Molecules. New York: Dover.
[13]. Ouiza, A. (2008). Caractérisation diélectrique des mélanges alcools primaires-eau par la spectroscopie fréquencielle (Doctoral dissertation). Université des sciences et de la technologie Houari Boumediene « U.S.T.H.B », Algérie,101.
[14]. Jordan, B. P., Sheppard, R. J., & Szwarnowski, S. (1978). The dielectric properties of formamide, ethanediol and methanol. Journal of Physics D: Applied Physics, 11(5), 695.
[15]. Gregory, A. P., & Clarke, R. N. (2012). Tables of the complex permittivity of dielectric reference liquids at frequencies up to 5 GHz,NPL REPORT MAT 23,93.
[16]. Sato, T., Buchner, R. (2005). Cooperative and molecular dynamics of alcohol/water mixtures: the view of dielectric spectroscopy. Journal of molecular liquids, 117(1-3), 23-31. https://doi.org/10.1016/j.molliq.2004.08.015.
[17]. Wu, J., Stark, J. P. W. (2005). A low-cost approach for measuring electrical conductivity and relative permittivity of liquids by triangular waveform voltage at low frequencies. Measurement Science and Technology, 16(5), 1234.
[18]. Gaudu, J. C., Mathieu, J. M., Fumanal, J. C., Bruckler, L., Chanzy, A., Bertuzzi, P., Guennelon, R. (1993). Mesure de l'humidité des sols par une méthode capacitive: analyse des facteurs influençant la mesure. Agronomie, 13(1), 57-73. https://hal.archives-ouvertes.fr/hal-00885528.
[19]. Paletto, J., Goutte, R., Eyraud, L. (1971). Théorie approchée de la permittivité diélectrique d'un mélange. Journal of Solid State Chemistry, 6(1), 58-66.
[20]. Onimisi, M. Y., Ikyumbur, J. T., Abdu, S. G., Hemba, E. C. (2016). Frequency and temperature effect on dielectric properties of acetone and dimethylformamide. Phys. Sci. Int. J., 11(4), 1-8.
[21]. Maunder, A., Taheri, O., Fard, M. R. G., Mousavi, P. (2015). Calibrated layer-stripping technique for level and permittivity measurement with UWB radar in metallic tanks. IEEE Transactions on microwave theory and techniques, 63(7), 2322-2334.
[22]. Cataldo, A., Catarinucci, L., Tarricone, L., Attivissimo, F., Trotta, A. (2007). A frequency-domain method for extending TDR performance in quality determination of fluids. Measurement science and technology, 18(3), 675.
[23]. Jiménez, J. M., Forniés-Marquina, J. M., Rodríguez, D. D., Lacarra, S. O. (2008). Dielectric behaviour and molecular polarization process in some polar-non polar mixtures: Alcohol+ n-alkane. Journal of Molecular Liquids, 139(1-3), 48-54.
[24]. García-Garabal, S., Segade, L., Domínguez-Pérez, M., Cabanas, M., Yañez-Vilar, S., & Cabeza, O. (2015). Excess molar enthalpies of the binary systems:(Dibutyl ether+ isomers of pentanol) at T=(298.15 and 308.15) K. The Journal of Chemical Thermodynamics, 87, 52-57.
[25]. Gestblom, B., & Sjoblom, J. (1984). Dielectric relaxation studies of aqueous long-chain alcohol solutions. Acta chemica Scandinavica. Series A. Physical and inorganic chemistry, 38(1), 47-56.

Comparison of simulations and measurements of radar and ultrasound inspections of concrete structures

Jean-Marie Henault[1,*], Denis Vautrin[1], Adrian Luca[1], Frédéric Taillade[1], Alexandre Boule[2] and Salvador Villalobos[3]

[1] EDF R&D, PRISME, Chatou, France
[2] EDF DI, TEGG, Aix-en-Provence, France
[3] EPRI, Charlotte, USA

ABSTRACT

Reinforced concrete structures are inspected with different Non-Destructive Evaluation (NDE) techniques. Commonly, radar devices and ultrasound tomographs are used to detect and localize internal elements like rebar grids and tensioning ducts, and defects of concrete like delamination, voids, and honeycombs. Radar and Ultrasound techniques are based on wave propagation, electromagnetic waves for radar and mechanical waves for ultrasound. Considering the usual working frequencies and the wave velocity in concrete, for both techniques the wavelength is around a few centimeters. Therefore, these techniques are affected by wave multi-scattering by the aggregates of the material. Moreover, an additional attenuation could come from the mortar matrix.

Modelling the wave propagation and simulating different cases to better understand the inspection results, to confirm the limitation of the actual techniques and to find ways to optimize the measuring conditions represents a challenging task. Two modelling tools were chosen to make 2D-simulations: gprMax for radar and COMSOL Multiphysics for ultrasound. Both enable the user to define the geometry of the inspected piece, the materials (e.g. homogenized concrete or concrete composed by aggregates in a mortar matrix, steel for the rebars and ducts), and the NDE device characteristics like the wave polarization and the emitting signal.

Different configurations were simulated corresponding to measurements made with commercial radar and ultrasound devices on concrete mock-ups containing rebars, ducts, voids and honeycombs. Simulation and experimental results show a good consistency.

Keywords: concrete, ultrasound, radar, inspection, experimental measurements, simulation

1. INTRODUCTION

EDF, like the other power plant operators, must ensure the sustainability of its civil engineering structures and power generation-related equipment and especially all the civil engineering buildings present in nuclear power plant installations. EDF and EPRI have been working on the imaging of flaws within reinforced concrete structures. Recent studies at EDF and EPRI in the field of flaw detection using non-destructive techniques (NDT) led to the further use of numerical modelling tools in addition to experimental measurement campaigns.

Modelling aims at determining the capabilities and limitations of NDT with respect to the device technical characteristics as well as the medium under test properties (material characteristics, flaws size, etc.). Modelling also offers the opportunity to evaluate in advance the relevance of on-site measurement campaigns, to design data processing tools, and could also be used as training tools.

One way to validate a simulation tool is to compare numerical simulation results and real measurements in a controlled environment. For that, NDT investigations were carried out on different reinforced concrete mock-ups (cf. Figure 1) [1]. They were designed and built to include controlled features like rebar splices, misaligned rebars, delaminations, voids and honeycombs. Specific mockups with a metallic liner were also built.

In this paper, two NDT devices are considered: a Ground-Penetrating Radar (GPR) and an Ultrasonic Tomograph (UT). These two techniques are based on wave propagation, electromagnetic

* Corresponding author: jean-marie.henault@edf.fr

waves for GPR and mechanical waves for UT. Considering the usual working frequencies and the wave velocity in concrete, for both techniques the wavelength is around a few centimeters.

In the following, the measurement devices used on the mock-ups as well as the simulation softwares are described. Then real acquisitions are compared to simulation results considering specific singularities or defects.

First results of the on-going study are presented. Further works are already planned to improve GPR and UT simulations and also to compare and combine the results obtained with the two techniques on identical configurations.

Figure 1. Acquisitions on one of the mock-ups with an ultrasound tomograph

2. MEASURING CONDITIONS

2.1. Concrete mock-ups

Several mock-ups were built both by EDF and EPRI with similar characteristics. They were designed to include typical singularities and defects that can appear on real buildings during construction and operation. For instance, double rebars are present in normal conditions whereas mis-aligned rebars and inclined rebar grids are construction defects. Concerning the concrete part, voids and honeycombs come from a flawed concrete mixing and pouring and delamination could appear in concrete during operation.

The mock-up size was set to 1.2 m × 1 m × 0.5 m to minimize edge effects during measurements and to enable to move the mock-ups easily. The singularities and defects were spaced to minimize measurement interferences.

Standard concrete was used. During the mock-up construction (cf. Figure 2), concrete samples were poured for complementary analysis. After 28 days, Young's modulus and compression strength values were measured by EDF to around 30 GPa and 30 MPa.

(a) (b) (c) (d)

Figure 2. Pictures during mock-up construction: (a) void defect made with a polystyrene ball, (b) honeycomb defect made with concrete with a lack of aggregates and covered with mortar, (c) concrete pouring and (d) concrete samples.

As aggregate size could influence NDT measurements, samples were cut and images of 2D sections were analyzed (cf. Figure 3). A size threshold was set to 2 mm corresponding to a value ten times smaller than the smallest wavelength of the propagating electromagnetic and ultrasound waves used in this study. In this condition, the surface ratio corresponding to aggregates is 27 %. Aggregates distribution parameters were calculated replacing aggregates by disks with similar surface areas. In this condition, the maximum diameter value is 14 mm.

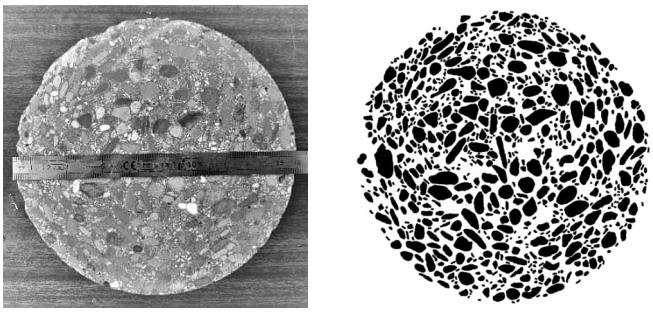

(a) (b)

Figure 3. (a) Picture of a concrete sample section and (b) a processed image for aggregate size analysis

2.2. GPR measurements

GPR devices are mainly characterized by their central frequency, which depends on its antenna's dimensions. The higher the central frequency, the better the resolution, but the shallower the investigation depth. Indeed, for a given material, high frequencies are more attenuated than low frequencies. Thus, a compromise must be found between the expected investigation depth and the minimum size of elements to be imaged. For applications relating to the localization of concrete reinforcements, the central frequencies usually range from 1 to 3 GHz.

Here, investigations on mock-ups were carried out using a TR-HF 2 GHz antenna from IDS GeoRadar. Continuous measurements were performed on the two largest faces of each mock-up, both in the horizontal and the vertical direction following a 10 cm × 10 cm marking grid.

2.3. UT measurements

Compared to GPR, UT devices for concrete inspection are more recent but this technology has gained increased popularity and further development. Here, we consider UT equipped with shear wave dry point contact sensors assembled in a matrix antenna array where sensors are connected by blocks.

Here, investigations on mock-ups were carried out using a A1040 MIRA from ACS. The array is composed by 48 sensors assembled in 12 blocks, each containing 4 elements. The block lines are 3 cm spaced. Sensor nominal frequency is 50 kHz.

Measurements were performed on the two largest faces of each mock-up, both in the horizontal and the vertical direction following a 10 cm × 10 cm marking grid. The device was moved between two successive acquisitions by a step of 10 cm.

3. SIMULATION TOOLS

3.1. GPR simulations

GPR simulations were performed using the open-source software gprMax. It enables to simulate the propagation of an electromagnetic wave through a medium in 2D or in 3D, by means of a finite-difference time-domain approach.

In the following, several comparisons between real data and 2D simulations are presented. In each case, the medium consists of a 1 m × 0.5 m concrete block, including two rebar grids of 25 mm

and 16 mm diameter, and surrounded by a 10 cm thick air layer. Absorbing conditions are introduced at these whole domain boundaries.

Depending on the configuration, other internal elements or defects are also introduced: two tensioning ducts, a void, or the splicing of two 25 mm diameter bars (one horizontally and one vertically). The case of delaminations and honeycombs is not addressed here since these defects are known to be undetectable by means of GPR measurements. Simulations of acquisitions are performed from the two faces of the concrete block, with a step of 1 cm. This is summarized in Figure 4.

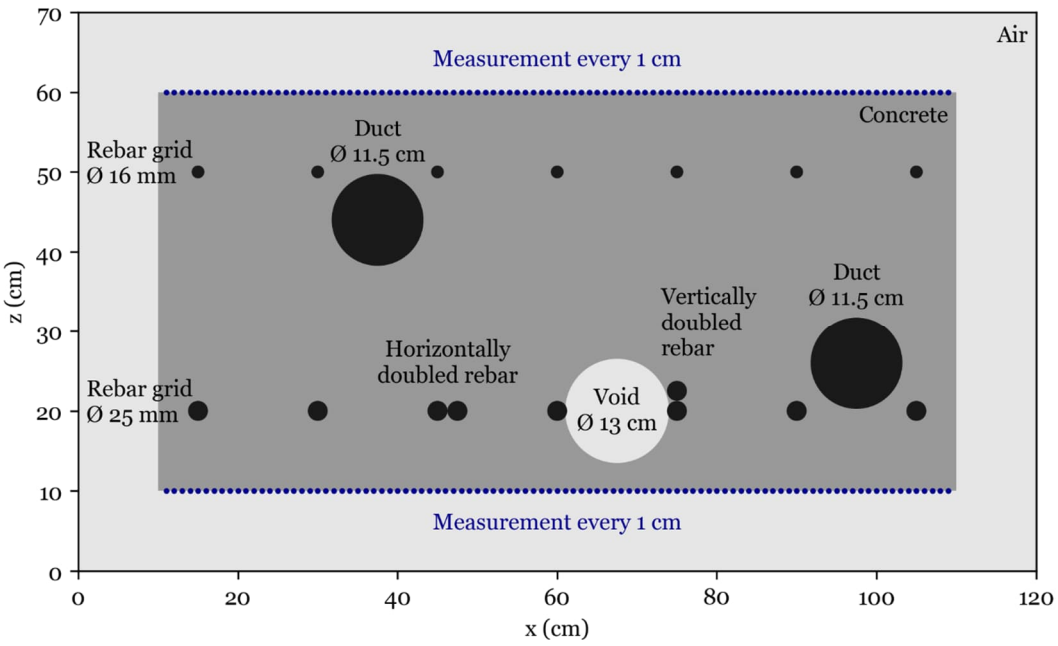

Figure 4. Scheme of the GPR simulation configurations

The electromagnetic characteristics of materials are given in Table 1. Two cases were considered in this study: concrete was modelized either by homogenized medium or by aggregates in a mortar matrix.

The permittivity of homogenized concrete was set by comparison between an experimental acquisition and the theoretical hyperbolas corresponding to reflections on the rebars. The estimated value ($\varepsilon_r = 11$) is consistent with the one that can be obtained from its constituents' characteristics using a homogenization model [2].

Considering the aggregates and mortar assembly, aggregates size distribution was set based on the image analysis presented in paragraph 2.1.

Table 1. Material characteristics for GPR simulations

	Permittivity	Conductivity (S/m)
Homogenized concrete	$\varepsilon_r = 11$	$\sigma = 0.001$
Mortar	$\varepsilon_r = 12$	$\sigma = 0.001$
Aggregates	$\varepsilon_r = 4.5$	$\sigma = 0$
Rebars, ducts	Perfect electric conductor	
Air, void	Free space	

At each measurement point, the source-receiver distance is 2 cm. Only the orthogonal component of the electric field is considered for emission and reception. The source signal is a Ricker pulse. Its central frequency f_R was set to 1.2 GHz based on a comparison with the median spectrum of measurements on mock-ups.

Given that the spatial discretization step should be at least ten times smaller than the smallest wavelength of the propagating electromagnetic fields, it was set to 2 mm.

3.2. UT simulations

UT simulations were performed using Comsol Multiphysics. As for GPR, we consider 2D simulations in planes corresponding to mock-up sections perpendicular to its surface and along horizontal measurement lines. As the shear wave sensors are polarized perpendicularly to these planes, waves correspond to SH waves for which displacements are orthogonal to the propagation plane. As SH waves are decorrelated from P and SV waves for which wave displacements are in the propagation plane, SH wave propagation equation corresponds to acoustic wave equation. Therefore, we use the acoustic module in Comsol Multiphysics by doing an analogy between SH displacements and pressure. The acoustic module enables time-dependent finite element simulations.

A 1 m × 0.5 m 2D geometry, including two rebar grids of diameter 25 mm and 16 mm, was considered. Free space conditions are introduced at the whole domain boundaries Depending on the configuration, other internal elements are also introduced: a 9 cm diameter void and a 15 cm diameter honeycomb as illustrated in Figure 5.The measurement device consists of 12 lines of dry point contact sensors. They are associated to a set of 12 specific points in the geometry. For one specific acquisition, these points are successively source and receiving locations. A line of measurements is simulated by moving the 12 points set by 10 cm increments. The image is reconstructed by a specific algorithm which is described in paragraph 5.

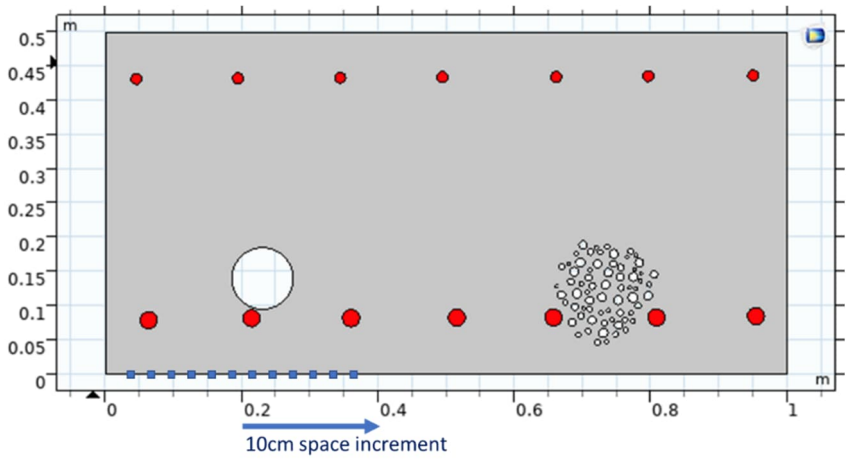

Figure 5. Scheme of the UT simulation configuration (rebars in red and point sensors in blue)

Material characteristics are indicated in Table 2. As for GPR simulations, we consider either homogenized concrete or aggregates randomly distributed in a mortar matrix. The homogenized concrete velocity was set by comparison with experimental results. The aggregates characteristics were set based on [3]. For this first study, we chose to set the mortar properties equal to the homogenized concrete properties. Considering the aggregates and mortar assembly, aggregates size distribution was set based on the image analysis presented in paragraph 2.1.

Table 2. Material characteristics for UT simulations

	Shear wave velocity (m/s)	Density (kg/m^3)
Homogenized concrete	2250	2050
Mortar	2250	2050
Aggregates	2475	2610
Steel	3050	7850
Air in void and honeycomb	Free space	

The source signal is a SinGauss function with a 45 kHz nominal frequency and a 100 kHz maximum frequency based on analysis of measurement data. Triangles were used for meshing. Their size varies between two values corresponding to the smallest wavelength divided by 10 and by 5. The smallest wavelength is 2.25 mm considering the smallest velocity in Table 2 and the maximum frequency of the source function. Time step value is set to 2.10^{-7} s to satisfy stability condition.

4. GPR RESULTS

In this section, a comparison between GPR measurements and simulations results is given. For the simulations, first a homogeneous concrete and then a medium composed by aggregates in a mortar matrix were considered. In all cases, B-scans after Automatic Gain Control (AGC) pre-processing as well as migration images are presented.

4.1. Simulations with a homogeneous concrete

Firstly, the medium is composed of two rebar grids, including the horizontally and the vertically doubled rebars, inside a homogeneous concrete area. Figure 6 shows a comparison between numerical and experimental data, considering measurements from the 25 mm diameter bars side only. The vertical dotted lines in Figure 6.a are introduced because the real-measurement images come from two separate acquisitions.

If we consider the rebar grid closest to the measurement line, the observations are the same for real measurements and for simulations: the rebar grid is easily detected both on the B-scans and on the migration images. Additional comparisons showed that rebars can be easily localized even if some of them are misaligned or out-of-plane (not presented here). The horizontal doubling is also easily detectable since it is parallel to the measurement line. However, the vertical doubling appears as one single rebar and is thus undetectable.

If we compare on-site acquisitions and simulations, the B-scans show that the simulated signals are less attenuated and less noisy than the experimental signals. This makes the reflections on the distant rebar grid more visible. Its signature in the migration image is thus slightly visible.

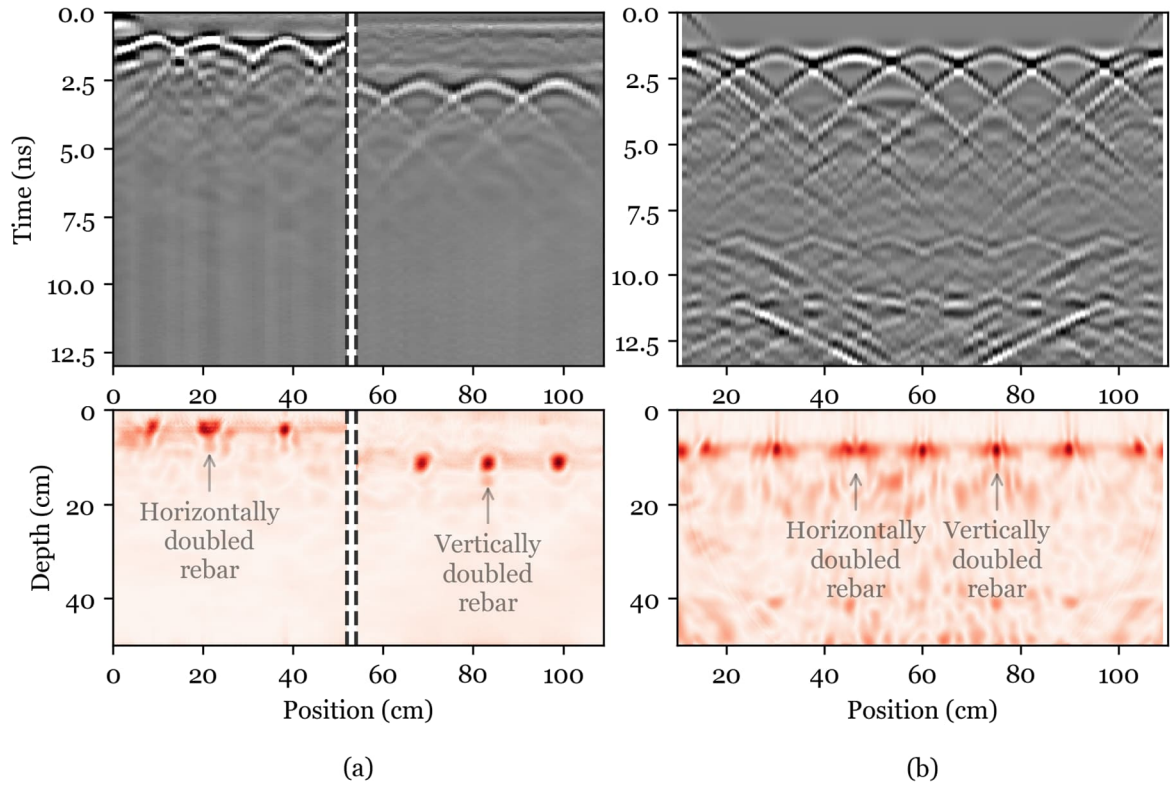

Figure 6. Comparison between real measurements (a) and simulation (b). The structure includes two rebar grids, with one horizontally and one vertically doubled rebars. In the two cases, a B-scan of the data after AGC pre-processing (top) and the migration image (bottom) are presented.

Secondly, we consider that the medium is composed of a homogeneous concrete area with the two regular rebar grids without doubled rebars, as well as the two tensioning ducts and the void. Figure 7 shows a comparison between numerical and experimental data, considering measurements from the 25 mm diameter bars side only. A B-scan of the data after AGC pre-processing and the migration image are also presented.

If we consider the duct closest to the measurement line and the void, they are easily detected both on the simulated and the on-site B-scans. They do not appear so distinctly in the migration images. This can be explained by the fact that the migration algorithm is suited to the detection of punctual reflectors.

The signature of the deepest duct is also detectable in the simulated signals, but not in the real measurements. As before, this is due to the lower attenuation and noise amplitude than for the real acquisitions.

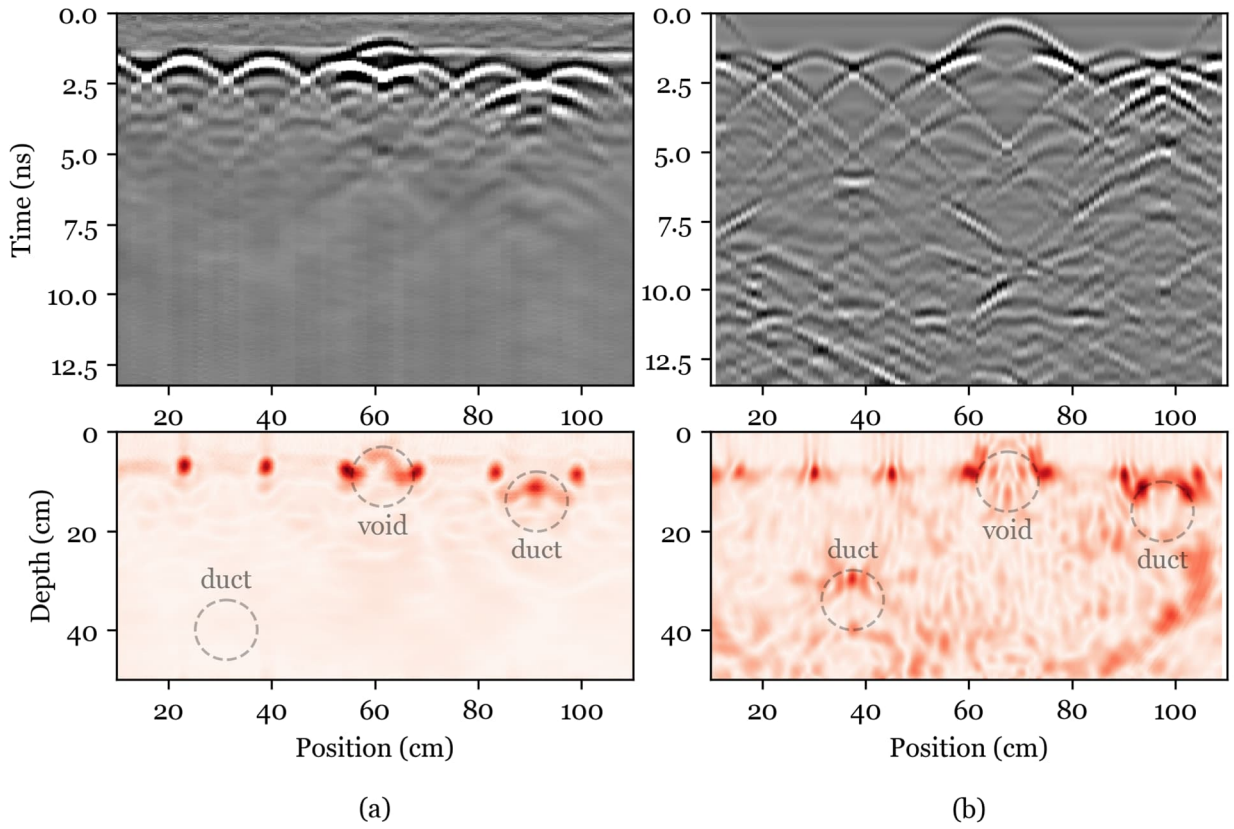

Figure 7. Comparison between real measurements (a) and simulation (b). The structure includes two regular rebar grids, two ducts and one void. In the two cases, a B-scan of the data after AGC pre-processing (top) and the migration image (bottom) are presented.

These first comparisons show a good agreement between simulation results and real measurements. They confirm that GPR is suitable for the detection of metallic elements such as rebars and ducts, on the condition that they are not too distant from the antenna, and not masked by a closer rebar grid. Voids close to the measurement line can also be detected, even if the contrast in the electromagnetic characteristics is lower.

It can be noticed that simulated signals with homogeneous concrete differ from measurements in that they are less attenuated and with less noise. This makes deep reflectors more easily detectable in the simulations.

4.2. Simulations with concrete composed by mortar and aggregates

In the previous section, simulations were performed considering concrete as a homogeneous material. This is an approximate representation of this material since it actually consists of a mix of

mortar and aggregates. It is worth noting that the biggest aggregates size is comparable to the smallest wavelength, and that mortar and aggregates highly differ from each other in terms of electromagnetic properties. In this case, the electromagnetic wave propagation is affected by multi-scattering. This results in a “structural noise” component in the measurements, which partly explains the “noisy” aspect of real acquisitions.

Additional simulations were performed to take this heterogeneous aspect into account. For that, a block of mortar in which aggregates were introduced was considered.

Figure 8 shows a comparison between numerical (Figures 8.a and 8.c) and experimental data (Figure 8.b). The probed medium is simply composed of the two regular rebar grids, and measurements are performed from the 16 mm diameter bars side. Simulations are presented with distinction between mortar and aggregates (Figure 8.a) and considering a homogeneous material (Figure 8.c).

The two simulation results show that distinguishing between mortar and aggregates clearly has an impact on the signals. This confirms that multi-scattering of the electromagnetic wave on aggregates is not negligeable.

However, this does not make the simulated signals completely representative of measurements:

- The “structural noise” level due to the explicit introduction of aggregates is more important. This can be explained by the 2D approach in the simulations, which implicitly consider that material properties are invariant in the orthogonal direction. This is not representative of a wave propagation in a 3D distribution of aggregates. Instead of performing 3D simulations, which would make the computational cost prohibitive, the simulation could be modified by finding a compromise between a homogeneous and a heterogeneous description of the concrete material.
- Simulated signals remain less attenuated, making late arrivals associated to deep reflectors more visible than for real acquisitions. This is probably due to the material characteristics, and more particularly the conductivity of mortar which was chosen rather low for the simulations.

5. UT RESULTS

In this section, we compare UT measurements and simulations results. For simulations, we consider first a homogeneous concrete and then a medium composed by aggregates in a mortar matrix.

The UT device has a sampling frequency of 1 MHz. It is delivered with a specific software to process the data to image the inspected zone. The data processing is described in [4] and Matlab codes are available on github [5][6]. The processing is composed by successive steps: [20 kHz; 80 kHz] pass-band filtering, surface Rayleigh waves suppression resulting in blindness over the first centimeters, Synthetic Aperture Focusing Technique (SAFT) migration, Hilbert transform and normalization. For one acquisition, the result is a B-scan image of the inspected zone. In the case where several successive acquisitions are performed, elementary images are overlayed and maximum intensities from all images are selected.

Measured and simulated data are processed the same way. Simulation results are sampled every 1 µs to be consistent with measurements. A-scans are normalized. B-scans are produced with a Python code which was developed based on [6] to reproduce the described steps.

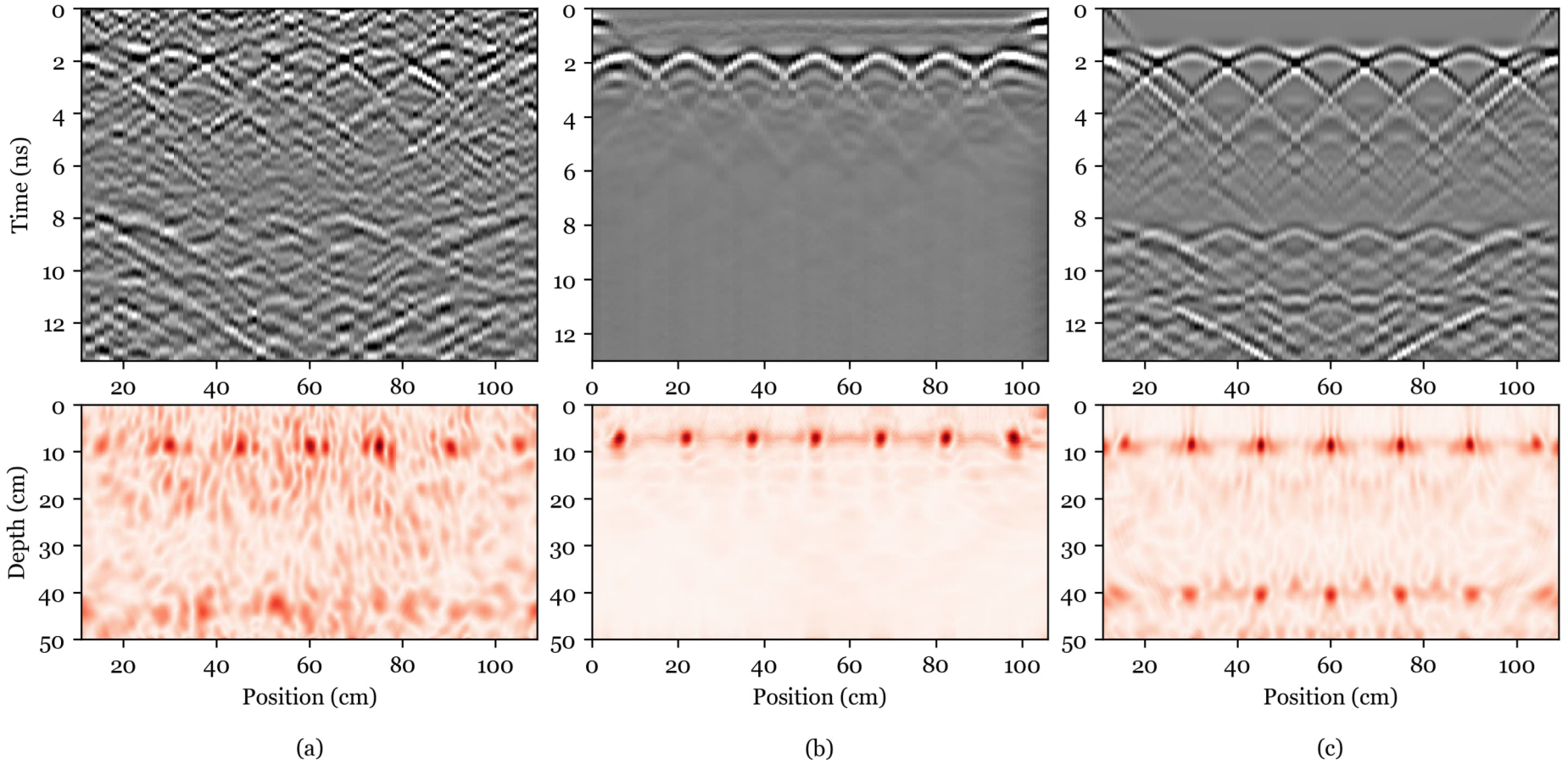

Figure 8. Comparison between real measurements (b) and two simulation results: with distinction between mortar and aggregates (a) and with homogenization of concrete (c). The structure includes two regular rebar grids. In the three cases, a B-scan of the data after AGC pre-processing (top) and the migration image (bottom) are presented.

5.1. Simulations with a homogeneous concrete in a sound structure

First, simulations of acquisitions in a medium composed of a homogeneous concrete with two rebar grids were performed (cf. Figure 9). The UT device was located at the central position.

Snapshots of simulation results obtained with the source in position 1 can be observed in Figure 10. Comparison between measurement and simulation of the A-scan obtained with the source in location 1 and the receiver in position 2 is given in Figure 11. Experimental and simulation results are consistent in terms of arrival time. Simulation snapshots enable to explain different echoes on the A-scans: echoes from surface wave, from the rebar in front of the source location, from the two contiguous rebars, from the right side of the structure and from its upper right corner are identified. Nevertheless, echo amplitudes differ: echoes in measurement are more attenuated than in simulation.

This amplitude difference is also visible in the corresponding B-scan images in Figure 12 where echoes from the 3 closest 25mm rebars and backwall echo are visible. Rebar echoes are more intense than backwall echo for experimental results (cf. Figure 12.a) while this is the opposite for simulation results (cf. Figure 12.b).

Simulations were performed considering a homogeneous concrete with elastic properties. Studies like [3][7] showed that the heterogenous structure of concrete made of aggregates in a matrix mortar, Interfacial Transition Zone (ITZ) at the interface between mortar and aggregates and mortar visco-elasticity enhance signal attenuation. Moreover, beam geometrical divergence is not completely considered as simulations are performed in 2D and not in 3D.

A first approach consists in adding an analytical attenuation to the simulation results. Each A-scan from the simulation is multiplied by a decreasing exponential function which parameter is fitted to adjust the contrast between echoes from the closest rebars and from the backwall. Resulting B-scan (cf. Figure 12.c) is very consistent with the experimental B-scan. In all cases, the 16 mm rebars from the layer close to the backwall are not visible.

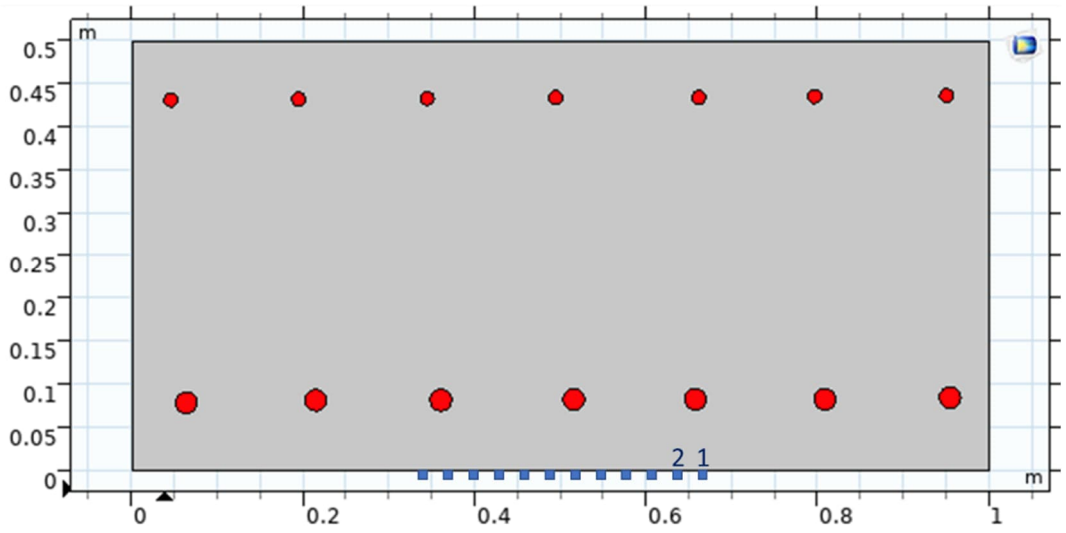

Figure 9. Scheme of the UT simulation configuration without defects
(rebars in red and point sensors in blue).

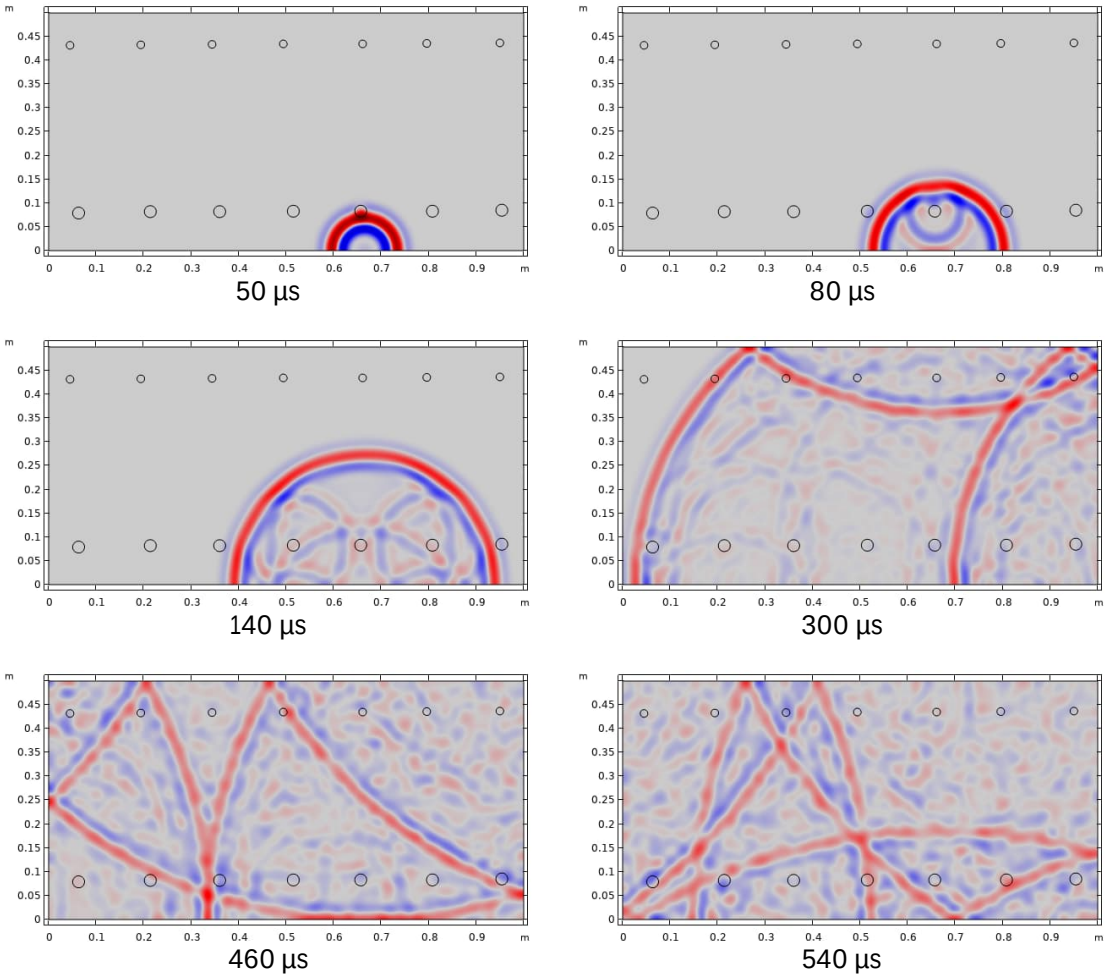

Figure 10. Snapshots at different time steps of the simulation results
for the configuration described on Figure 9. The source is located in position 1

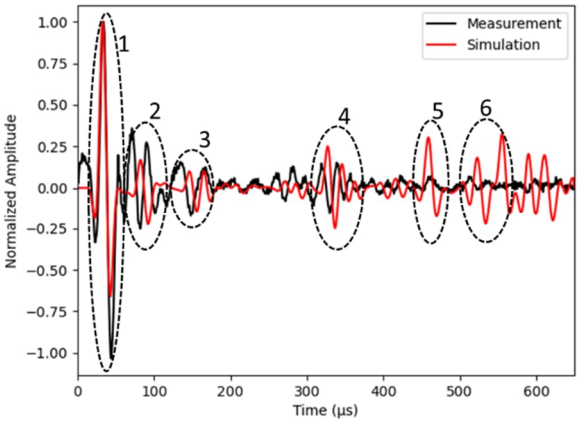

1. Surface wave echo
2. Echo from the rebar in front of the source
3. Echoes from the two adjacent rebars
4. Echo from the right edge
5. Backwall echo
6. Echo from the upper right corner

Figure 11. A-scans from measurement and simulation for the configuration described in Figure 9,
with the source in position 1 and the receiver in position 2

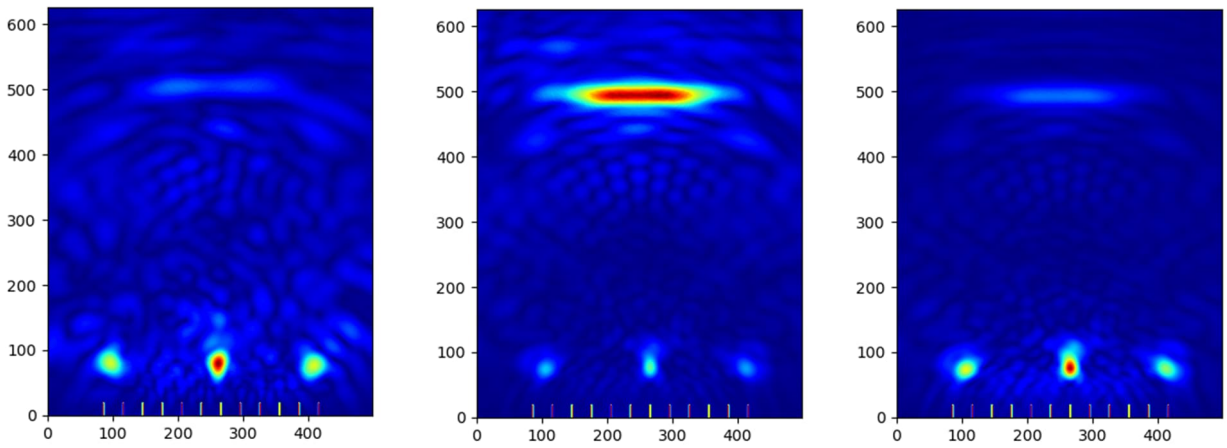

(a) (b) (c)

Figure 12. B-scans images for the configuration described in Figure 9, from (a) measurement, (b) simulation and (c) simulation with added exponential attenuation

5.2. Simulations with a homogeneous concrete in a structure with defects

For this simulation, the medium is comprised of homogeneous concrete with 2 rebar layers, a 9 cm diameter air void, and a 15 cm diameter honeycomb, represented in Figure 13.a.

Seven acquisitions are considered by successively moving the device by 10 cm steps along the measurement line. Resulting B-scans are assembled to image the structure. Results from measurements are shown in Figure 13.b. For simulation, raw B-scans (cf. Figure 13.c) and B-scans processed with attenuated A-scans (cf. Figure 13.d) are considered. The attenuation parameter value is the one deduced from the simulation without defects (cf. paragraph 5.1).

B-scans from measurements and simulations are consistent. In all B-scans, the first rebar layer is visible and the second, close to the backwall, is not. Concerning the 9 cm void placed near a rebar, it appears in B-scans as a diffraction point with a signature similar to a rebar but with a higher backwall echo attenuation. These two elements indicate the presence of a defect but its size cannot be precisely estimated.

Concerning the 15 cm honeycomb detection, acquisitions in front of the default also show more attenuated backwall echoes, both for experimental measurements and simulations. There is no other visible signature in the measured B-scan whereas a signature is visible in the simulated B-scans. As shown in Figure 13.a, honeycomb was modeled by circular macro-porosities in a 15 cm diameter zone, which may not be representative.

5.3. Influence of concrete description

In the previous sections, simulations were performed considering concrete as a homogeneous material. This is an approximate representation since it consists of a mix of mortar and aggregates. Moreover, mortar is a visco-elastic material and interfaces between aggregates and mortar are not perfect.

Additional simulations were performed to evaluate individually and qualitatively the influence of these parameters on A-scans and B-scans. For that, we considered the configuration composed of a block of concrete with 2 rebar layers without defects, and a central positioning of the device, as described in Figure 9. For the A-scans, the source is in position 1 and the receiver in position 2.

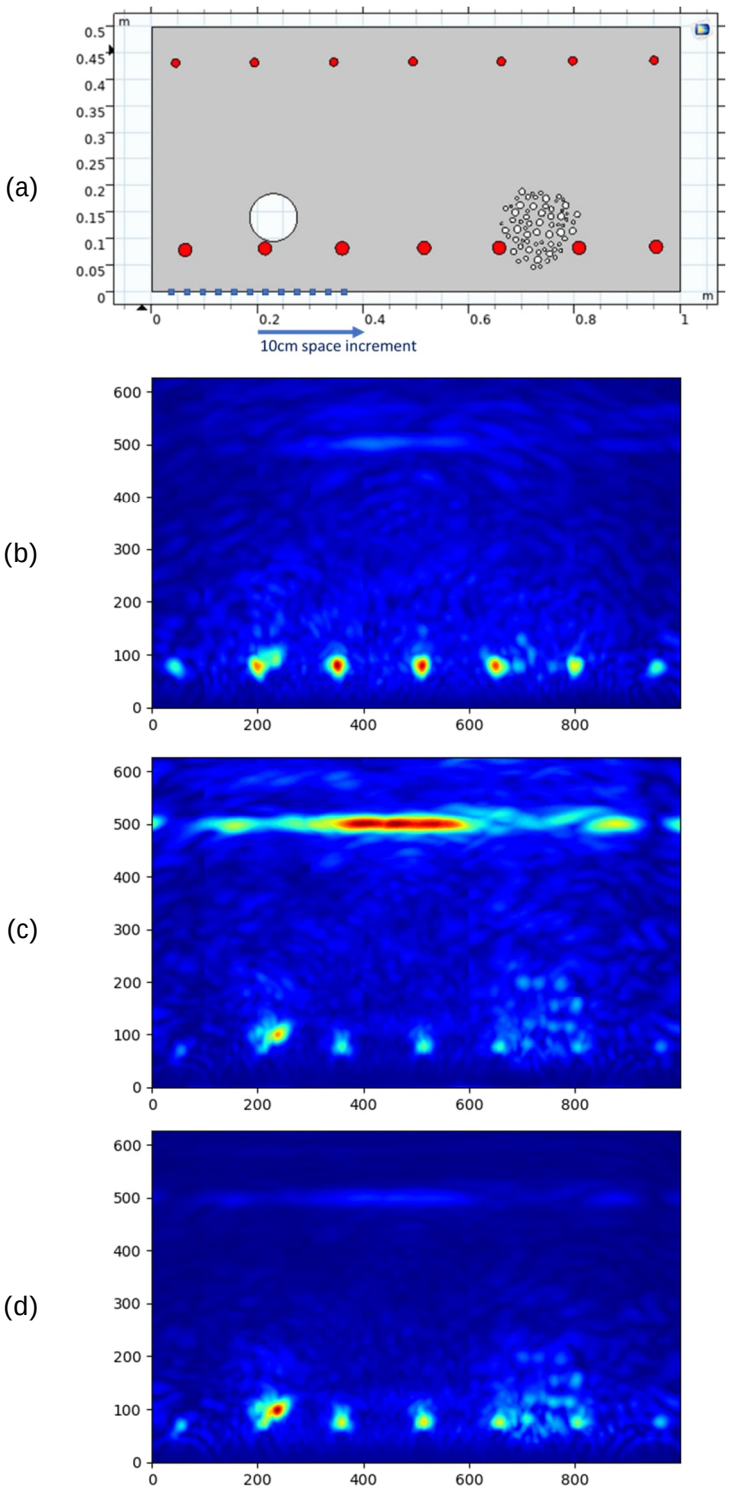

Figure 13. (a) Configurations with 2 rebar layers, a 9 cm void and a 15 cm honeycomb, and B-scans images from (b) measurements, (c) simulations and (d) simulations with added exponential attenuation

5.3.1. Visco-elasticity

Concrete was modelized by homogeneous visco-elastic material. Increasing the viscous parameter results in decreasing the signal amplitude. The parameter value was set so that the backwall echo amplitude in A-scan was comparable to the one observed in the measurement (cf. Figure 14). B-scans are compared in Figure 15. It can be noticed that visco-elasticity involves echoes spreading.

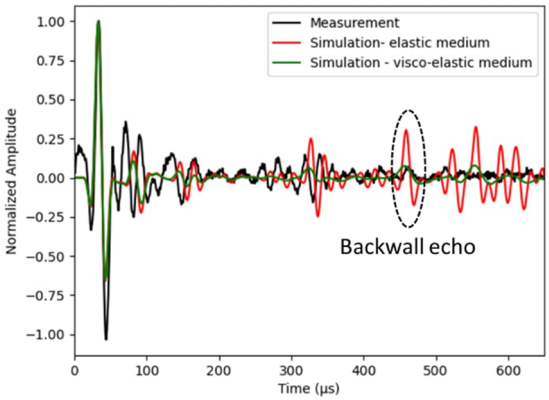

Figure 14. A-scans from measurement and simulations considering concrete as an elastic and a visco-elastic medium, for the configuration described in Figure 9, the source in position 1 and the receiver in position 2

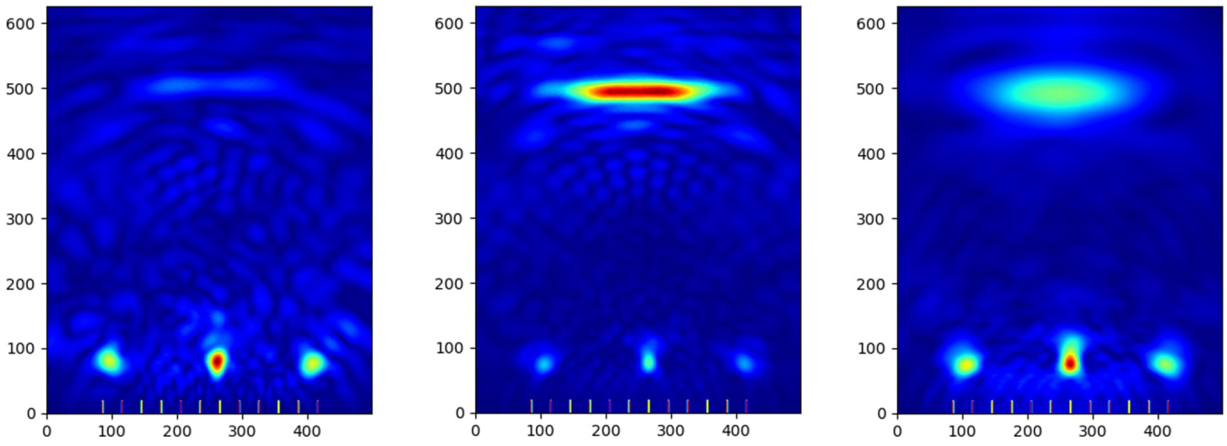

(a) (b) (c)

Figure 15. B-scans images for the configuration described in Figure 9, from (a) measurement, (b) simulation with a homogeneous elastic medium and (c) simulation with a homogeneous visco-elastic medium

5.3.2. Aggregates in a mortar matrix

Concrete was modelized by aggregates in a mortar matrix with properties set from image analysis (cf. Figure 3). The aggregate surface ratio is 27 % and the maximum aggregate diameter is 14 mm. The resulting configuration is shown in Figure 16. Mortar and aggregates have elastic properties given in Table 2. It is worth noting that the biggest aggregates size is comparable to the smallest wavelength, and that mortar and aggregates slightly differ from each other in terms of mechanical properties.

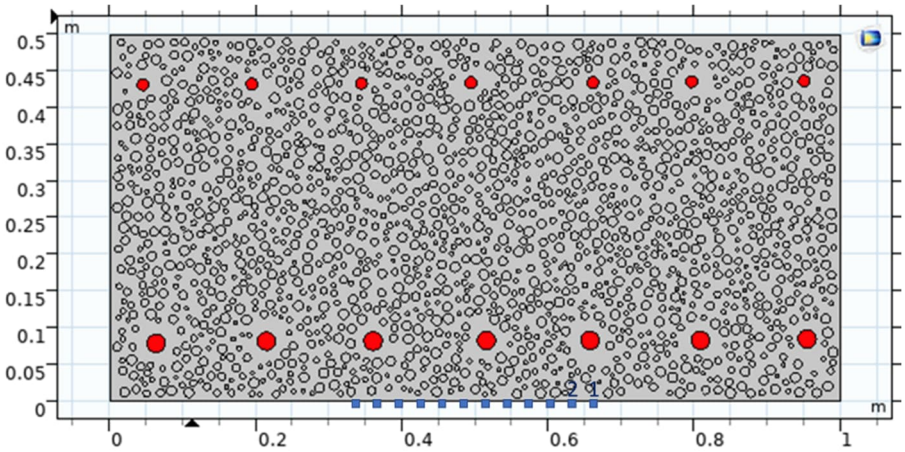

Figure 16. Scheme of the UT simulation configuration with aggregates (rebars in red and point sensors in blue).

The influence of aggregates is shown in Figure 17 for A-scan signal and in Figure 18 for B-scan. Mechanical wave propagation is affected by multi-scattering. This results in a slight increase in the mean velocity value and an added “structural noise”. Nevertheless, as presented in Figure 17, the relative amplitude of specific echoes, like backwall echo, remains comparable with the case where concrete is modelized by a homogeneous medium. The heterogeneous structure of concrete does not explain the signal higher attenuation in measurements. This is confirmed in B-scan in Figure 18.c where structural noise is visible but backwall echo remains prominent compared to rebar echoes. Figure 18.d corresponds to simulation results with heterogeneous concrete with an added exponential attenuation. In this case, the B-scan is more consistent with experimental B-scan of Figure 18.a.

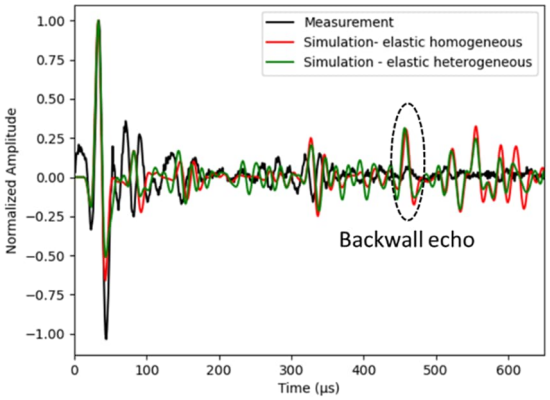

Figure 17. A-scans from measurement and simulations considering concrete as a homogenous and a heterogeneous elastic medium, for the configuration described in Figure 16, the source in position 1 and the receiver in position 2

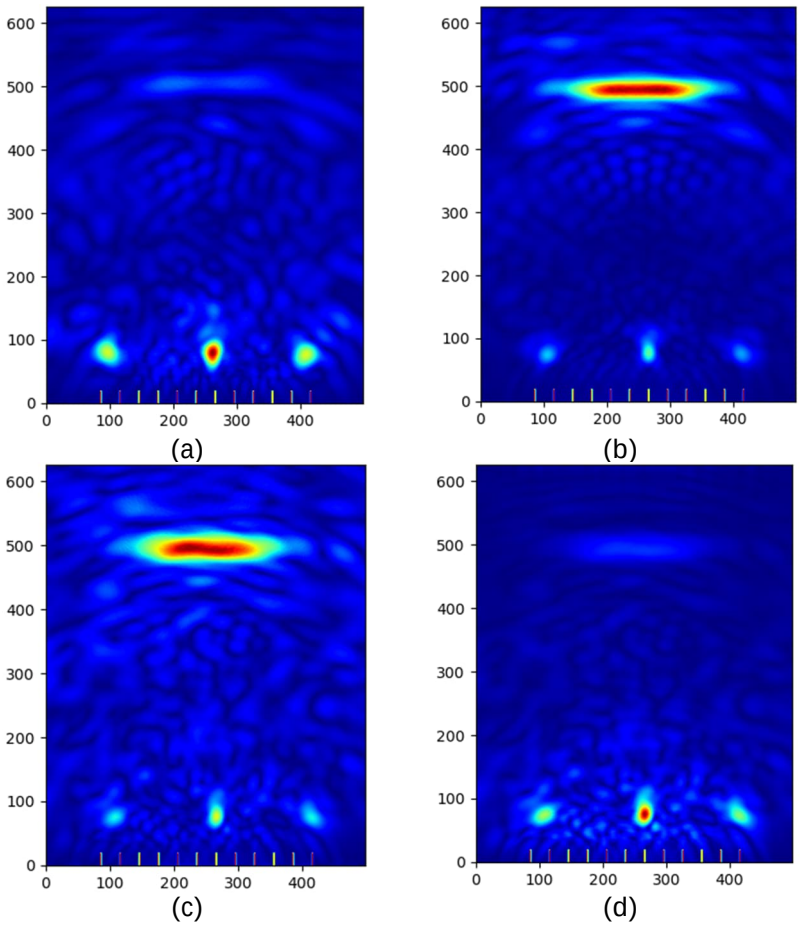

Figure 18. B-scans images for the configuration described in Figure 16, from (a) measurement, (b) simulation with a homogeneous elastic medium, (c) simulation with a heterogeneous elastic medium and (d) simulation with a heterogeneous elastic medium with an added attenuation

5.3.3. Interfacial Transition Zone

Interfacial Transition Zone (ITZ) refers to the zone at the interface between aggregates and mortar, where mortar has lower properties than bulk mortar over a thickness between 10µm and 150 µm. ITZ modeling is an issue. In [3][7], non-perfect limit conditions were introduced to avoid explicitly meshing the ITZ for each aggregate.

In this study, for the sake of simplicity, ITZ around each aggregate was defined with a thickness of 2.25 mm. This corresponds to the lowest mesh size, i.e. the minimum wavelength divided by 10. The resulting ITZ thickness is not representative, but the computation time remains unchanged. As a consequence, the simulation results are only qualitative. In future works, ITZ thickness will be reduced to make it more representative.

Simulations were performed by decreasing mortar properties in ITZ, from 100 % (no ITZ) to 50 % of bulk mortar properties given in Table 2, by steps of 10 %. It is observed that the mean velocity value decreases while ITZ properties decrease. This was considered in the SAFT migration post-processing. The velocity was adjusted so that the backwall echo corresponds to a 500mm thickness. Results in terms of B-scans are given in Figure 19. It can be noticed that the “structural noise” amplitude increases while ITZ properties decreases. Consequently, echoes from rebars and backwall are less and less defined. In the case where ITZ properties are 60 % of bulk mortar properties, “structural noise” is prominent and rebars and backwall are not visible anymore.

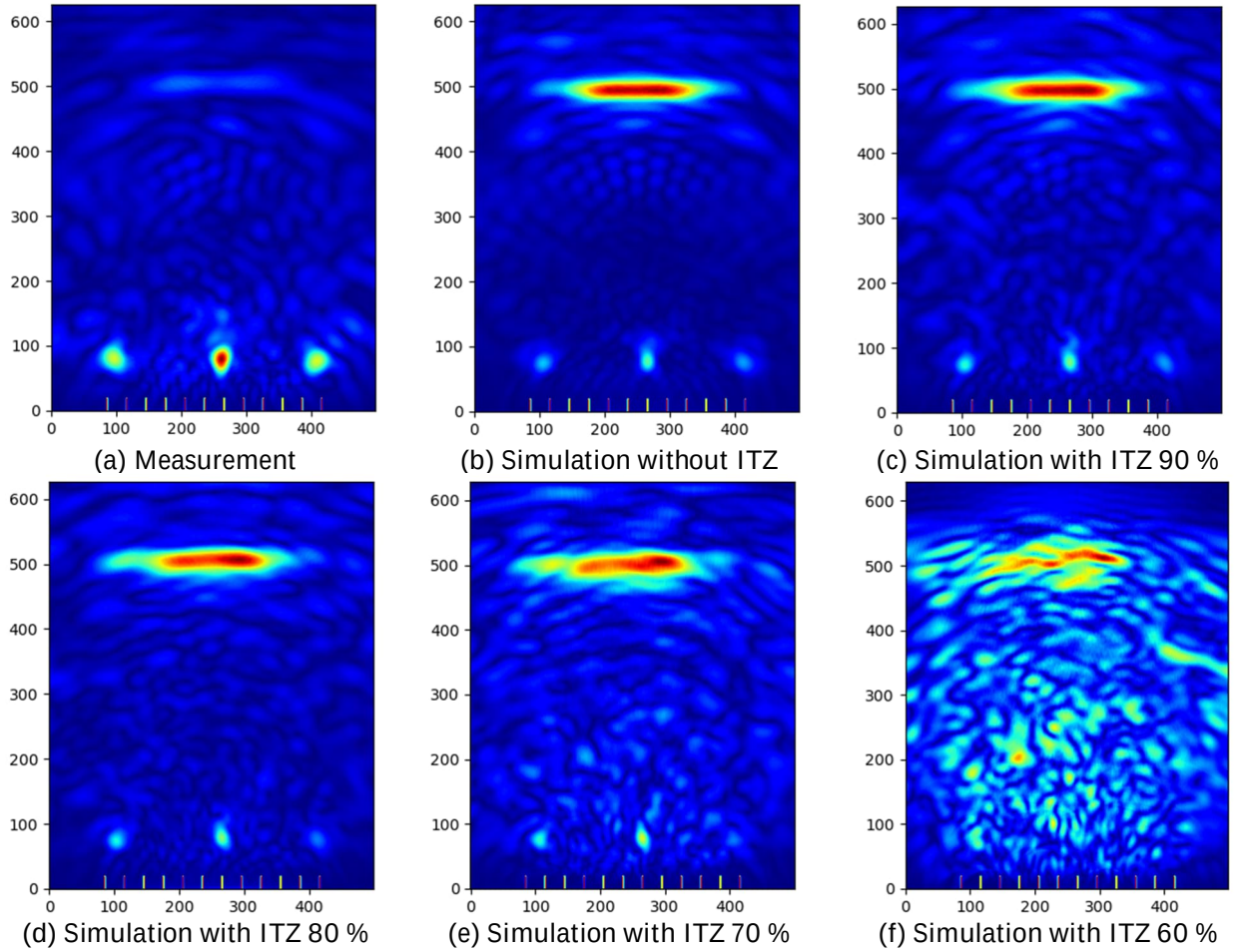

Figure 19. B-scans images for the configuration described in Figure 16, from (a) measurement, (b) simulation with a heterogeneous elastic medium, and (c) to (g) simulations with a heterogeneous elastic medium with ITZ with decreasing properties.

5.3.4. Discussion

In the previous paragraphs, we studied the individual influence of different modelling choices on the simulation results: exponential attenuation, medium visco-elasticity, heterogeneous concrete and ITZ around aggregates. In each case, we compared the simulation results to experimental data. These parameters have an influence on the amplitude attenuation and/or the presence of structural noise. However, we observed that experimental results cannot be fully explained by taking into account only one of these phenomena. Future works will be dedicated to the combination of these choices to better represent the experimental results. An issue is to determine the relative contribution of each phenomenon.

6. CONCLUSION AND PERSPECTIVES

In the framework of NDT investigations, simulation helps to determine the capabilities and limitations of devices, to evaluate in advance the relevance of on-site measurement campaigns and to design data processing tools. In this paper, two techniques commonly used for reinforced concrete structure inspections were considered: GPR and UT.

In the two cases, simulations results were compared to real measurements performed on different mock-ups. These were specially designed and built to include controlled singularities and defects that can be encountered on real civil engineering structures.

Different measurement configurations were considered. The results show a good agreement between simulations and real acquisitions. With the two investigation techniques, the closest of the two rebar grids are easily imaged. Voids are also detectable if they are close enough to the measurement surface. GPR is also suitable for the detection of ducts, and honeycombs can be detected with UT.

Simulations were first carried out considering concrete as a homogeneous medium, but other concrete descriptions were also considered for comparison. In particular, distinguishing between mortar and aggregates allows to make the simulated signals more realistic since electromagnetic and ultrasonic wave propagations are affected by multi-scattering. This leads to the introduction of a “structural noise” component in the acquisition signals.

However, in the case of GPR, simulation results show that a heterogeneous description of concrete make the structural noise component prominent. This may be due to the 2D-simulation approach. Finding a compromise between a homogeneous and a heterogeneous description of the concrete material would certainly be more suitable. Moreover, increasing the mortar conductivity would help to attenuate the signals in a more realistic way.

In the case of UT, introducing a visco-elastic model of concrete causes attenuation of the signal, but also results in echoes spreading. An alternative approach is to introduce a multiplicative exponential law. When considering concrete as a heterogeneous material, it seems necessary to also introduce ITZ at the interface between aggregates and mortar. The ITZ characteristics have an impact on the structural noise amplitude.

Further works are planned to improve GPR and UT simulations and also to compare and combine the results obtained with the two techniques on identical configurations.

REFERENCES

[1] S. Villalobos, J.-M. Henault, A. Boule, "Capability Demonstration of NDE Methods for Evaluating Concrete”, in *NDT-CE Conference*, Zurich, 2022.

[2] V. Guihard, F. Taillade, J.-P. Balayssac, B. Steck, J. Sanahuja, F. Deby, “Prediction of Cement-Based Materials' Water Content with the Use of Electromagnetic Homogenisation Schemes,” in *2018 Progress in Electromagnetics Research Symposium (PIERS-Toyama)*. IEEE. p. 164-168.

[3] T. Yu, “Modélisation de la propagation des ondes ultrasonores dans le béton pour l’amélioration du diagnostic des structures de génie civil ”, *PhD thesis, Université Aix-Marseille*, 2018.

[4] J. S. Popovics, J. R. Roesler, J. Bittner, A. N. Amirkhanian, A. S. Brand, P. Gupta, K. Flowers, “Ultrasonic imaging for concrete infrastructure condition assessment and quality assurance”, in *Research Report No. FHWA-ICT-17-007, Illinois Center for Transportation*, 2017.

[5] J. Bittner, A. Spalvier, J. S. Popovics, “Internal Imaging of Concrete Elements.” In *Concrete International*, April 2018, 57–63.

[6] https://github.com/Jabittner/openSAFT

[7] M. Ramaniraka, S. Rakotonarivo, C. Payan, V. Garnier, “Effect of the Interfacial Transition Zone on ultrasonic wave attenuation and velocity in concrete”, in *Cement and Concrete Research*, vol. 124, 2019, 105809.

Evaluation of anisotropic material parameters in damaged concrete using ultrasound velocity measurements

Kim Calonius[1], Alexis Fedoroff[1*], and Antti Forsström[1]
[1] VTT Technical Research Centre of Finland Ltd., Espoo, Finland

ABSTRACT

It is well known, that under uniaxial compression, a concrete specimen undergoes very different damage patterns depending on the considered direction: on a qualitative level, the concrete is compacted in the direction of loading while cracks tend to form in the direction orthogonal to the loading. Quantitatively, however, the description of anisotropic damage in concrete is far from being well understood. Continuum material models that are well suited for anisotropic damage description are referred to as tensorial elastic-damage or elastic-damage-plastic models. Calibration of such models requires, however, experimental data from sophisticated material tests that adequately describe the evolution of damage patterns in different directions of the tested concrete specimen. In an orthotropic media, using the eigensolutions of the Kelvin-Christoffel matrix, one can solve out nine components of the tangent stiffness tensor as a function of soundwave velocity measurements in different wavefront directions and polarization directions. This study shows how, using the pitch-catch method for the determination of first time arrival, one can evaluate the soundwave velocities in different directions and compute the stiffness tensor components for a damaged concrete specimen. Plotting the stiffness value components as a function of non-recoverable strain gives a qualitative measure of the anisotropic strain degradation process. The results found in this study are valuable in structural design and analysis of critical concrete infrastructures, in particular for the civil nuclear industry, since they enable the use of advanced material models that are needed in beyond design basis analyses and simulations, as prescribed by the Finnish YVL nuclear regulation code in DEC-C loading scenarios.

Keywords: Anisotropic damage in concrete, ultrasound velocity measurement, Kelvin-Christoffel eigenproblem.

1. INTRODUCTION

Despite the fact that concrete has been used for a long time in building industry, the exact physical mechanisms that lead to uniaxial loading failure are very difficult to model in continuum material models. The basic failure mechanisms have been studied both from the fracture mechanics perspective at a micro-scale, [1], [2], [3], and from continuum scalar damage perspective at a continuum scale, [4], [5], [6]. However, studies based on continuum tensorial damage theory, which is necessary to grasp the anisotropic behaviour that occurs during uniaxial loading, are rather scarce in the context of concrete modelling, [7]. One of the challenges in continuum tensorial damage modelling is the large amount of model parameters that need to be calibrated. In particular, it is of primary importance to have a quantitative assessment of the tangential stiffness tensor degradation in a concrete sample undergoing uniform loading. For materials other than concrete (additively manufactured materials, ceramics) both initially isotropic and anisotropic, a stiffness tensor degradation measurement methodology has been developed based on ultrasound velocity measurement, [8], [9], [10], [11]. The proposed methodology uses ultrasound probes immersed in thermoregulated water tank that also contains the dog-bone specimen undergoing tensile loading. The longitudinal wave ultrasound transducers provide therefore soundwave velocity measurements

* Corresponding author: +358 408487103, alexis.fedoroff@vtt.fi

in different angles and without direct contact with the specimen. The eigenproblem induced by the Kelvin-Christoffel matrices is not solved directly for the eigenvalues, but rather using least square optimization that gives directly the values of the nine stiffness matrix components as a function of the measured soundwave velocities. A second methodology, proposed in [12] and [13], uses a chamfered cube specimen for initially orthotropic material to determine soundwave velocities in the three principal directions of the specimen and in nine diagonal directions using both longitudinal wave and shear wave contact probes. The Kelvin-Christoffel eigenproblem is solved analytically for the eigenvalues, which gives the expression of soundwave velocities as a function of stiffness tensor components. Then the relations are inverted to get analytical expressions of stiffness tensor components as a function of measured soundwave velocities.

The methodology based on chamfered cube specimens has been adopted in this work for the investigation of concrete samples, which have undergone various degrees of uniaxial compressive loading. Previous feasibility studies, presented in [14] and [15] show that using both longitudinal wave 54 kHz transducers and shear wave 40 kHz transducers are applicable to damaged concrete. Further, experiments on uniaxially loaded concrete specimens with post-loading chamfering show that the method can be extended to evaluate all nine stiffness tensor components if orthorhombic material symmetry is assumed, [16].

In this work, it is shown that the proposed methodology based on ultrasound velocity measurement is valid for the determination of stiffness tensor of damaged concrete by comparing results provided using ultrasound methods to results obtained from mechanical stress-strain measurements. After validation, the aim is to use the proposed method to draw conclusions on the anisotropic character of stiffness degradation of uniaxially loaded concrete.

2. TEST SETUP DESCRIPTION

Concrete cube samples of 200mm are cast using C40/50 ready mixed concrete with evaluated air content of 2.1% and maximum aggregate size of 8mm. The age of concrete at test date was 88 days, and the concrete samples were immersed in room temperature water for a total of 82 days. The loading surfaces of the cubes were smoothed and parallelized with a diamond grinding apparatus prior to testing. Three standard compression tests with average concrete strength of f_{cm}=62.72MPa (standard deviation 1.26MPa) were carried out to identify the reference loading capacity of the concrete batch. The engineering strain measured between the loading plates and corresponding to the peak load has an average value of ε_{c1}=0.4383% (standard deviation 0.0011%). The experimental test setup consists of the following equipment:

- A hydraulic press suitable for uniaxial compression of concrete specimens and instrumented with a load cell for engineering stress measurement and two displacement sensors for engineering strain measurement between the loading plates in the loading direction.
- A digital image correlation (DIC) system, consisting of two cameras with 35mm focal distance lenses, computer hardware for data acquisition and software (LaVision StrainMaster) for data processing. The DIC data enables the computation of the strain tensor field at selected time frames from one of the free surfaces of the concrete cube. After post-processing, the strain field data can be used to compute the engineering strain measured by virtual extensometers and/or virtual strain gauges placed between arbitrary points on the specimen surface.
- An ultrasonic measurement device (Proseq Pundit) with 54 kHz longitudinal wave transducers (used with couplant gel) and 40 kHz shear wave transducers (used without couplant gel).

The uniaxial compression tests were conducted on a total number of 18 concrete specimens with displacement control at a rate of 0.1 mm/min to obtain a controlled loading and unloading portion of the stress-strain curve. Table 1 shows the test matrix for the compressive pseudo-cyclic tests. By a “pseudo-cycle” it is referred here to a loading pattern consisting of a single constant rate loading up to the target displacement value and a constant rate unloading down until the applied force is zero. Six target displacement values were chosen, corresponding to undamaged concrete, concrete in elastic range, small damage, medium damage, heavy damage around peak load, and specimen fragmentation. For each target displacement three repetitions were carried out.

Table 1. Test matrix for compressive displacement driven pseudo-cyclic tests

Test # (Specimen #)			Target displacement	Remark
1 (K24)	2 (K25)	3 (K26)	0.00 ε_{c1}	undamaged concrete
4 (K01)	5 (K02)	6 (K03)	0.25 ε_{c1}	in elastic range
7 (K23)	8 (K20)	9 (K21)	0.50 ε_{c1}	small damage
10 (K19)	11 (K08)	12 (K09)	0.75 ε_{c1}	medium damage
13 (K10)	14 (K11)	15 (K12)	1.00 ε_{c1}	at peak load, heavy damage
16 (K13)	17 (K15)	18 (K22)	1.20 ε_{c1}	specimen fragmentation

2.1. Measurements during the compressive tests

Two displacement sensors, d_1 and d_2, located on each side of the concrete specimen measure the displacement between the loading plates as shown in Figure 1. The engineering strain in the direction of loading averaged over the entire specimen is calculated as the mean value of the two displacement sensors divided by the initial height of the specimen. The advantage of measuring the strain between the loading plates is that the measurement is not prone to errors due to localized cracking, as opposed to strain measurements across the specimen. Notice, however, that due to surface roughness at the interface between the loading plates and the concrete, there is a lag in the stress-strain curve due to the crushing of the interface layer, which has to be compensated by an appropriate offset.

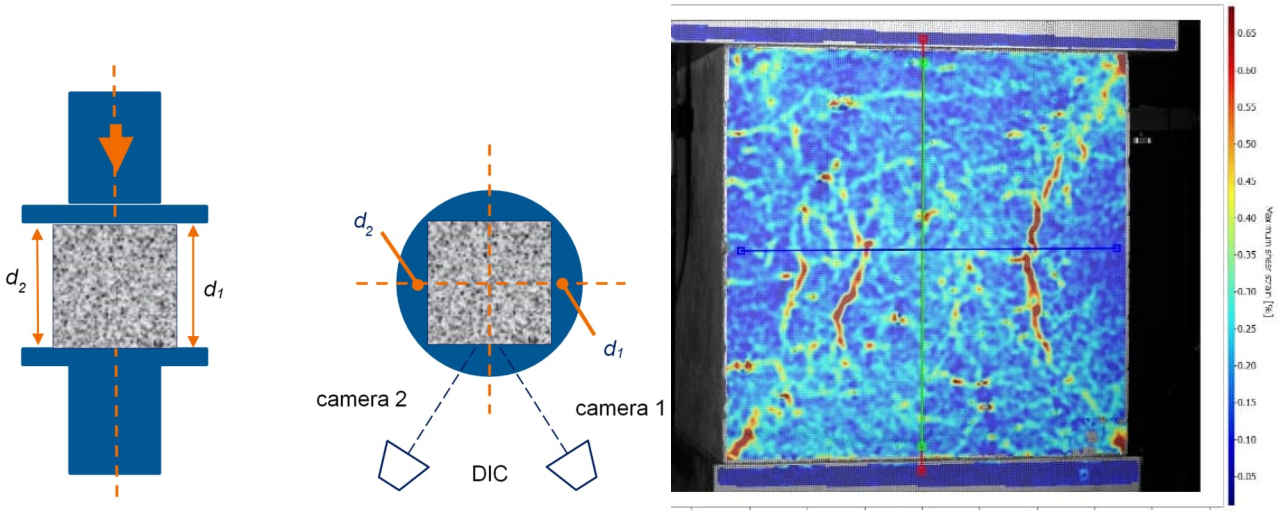

Figure 1. Left: Measurement device placement (front and top view), Right: DIC camera strain field

In addition to the displacement sensors, strain is also measured using digital image correlation (DIC) on one of the non-loaded surfaces of the tested specimen. DIC image data taken at regular time intervals is post processed to get strain field evolution at the examined surface. In Figure 1, on the right hand side, there is an example plot from one of the tests where red colour represents maximum shear strain values larger than 0.55%. Virtual extensometers are used to combine load data and strain field data for obtaining engineering stress strain curves. As per Figure 2, the virtual extensometer SG198 (red) is used to measure strain in loading direction averaged between the loading plates, SG199 (green) is used to measure strain in loading direction averaged across the specimen, and SG200 (blue) is used to measure strain in lateral direction averaged across the specimen.

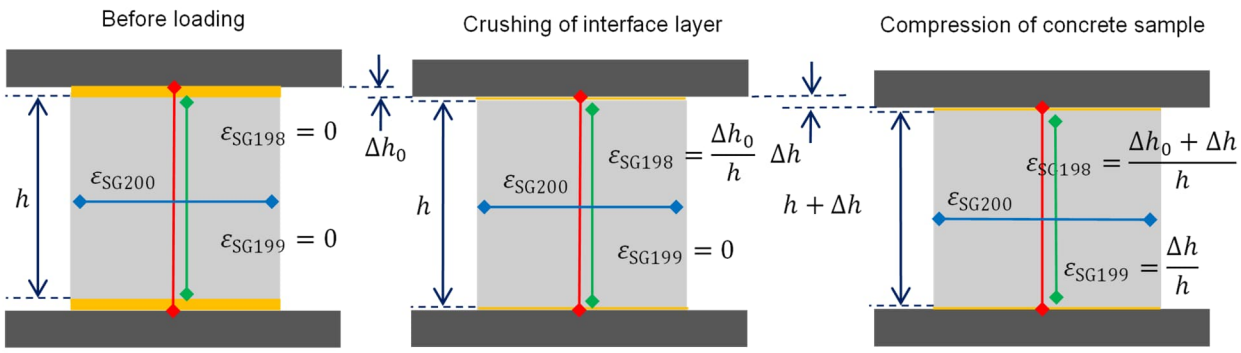

Figure 2. Schematic view of virtual extensometer location

The advantage of measuring strain averaged between the loading plates is that the strain values are not perturbed by local strain data, whereas strain values averaged across the specimen may provide unreliable data especially after the onset of large macroscopic cracks. The schematic stress-strain curves in Figure 3 show the effect of the lag along the horizontal axis for strain measured between the plates and the effect of a jump along the vertical axis for strain measured across the specimen.

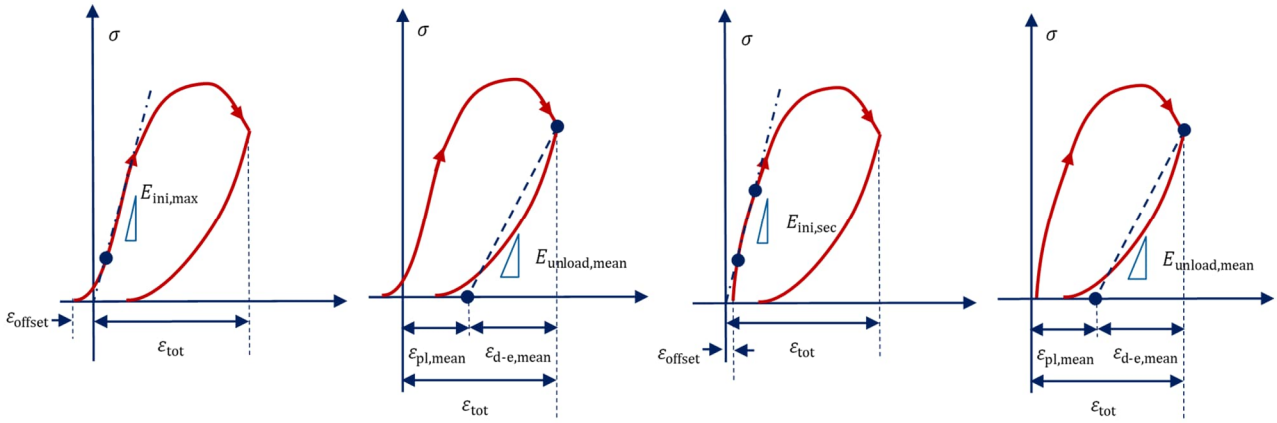

Figure 3. Left: strain averaged between loading plates; right: strain averaged across specimen

2.2. Measurements with ultrasound after compressive tests

After the compressive tests, the concrete sample cubes are cut with a diamond saw along the edges to obtain a chamfered cube shape (see Figure 4). The ultrasound measurements are carried out by placing the emitter and receiver probes on opposite sides of the specimen along three principal directions and six diagonal directions. The direction numbering nomenclature is shown in Figure 5. The first time arrival (flight time) of the emitted signal is recorded by the ultrasound device as per Figure 4. The first time arrival in the wavefront direction *I* and in the polarization direction *j* is denoted by t_{ij}. The specimen dimension in the wavefront direction is denoted by l_i. The soundwave velocity is then defined as: $v_{ij} = l_i/t_{ij}$. In order to obtain statistical average over the specimen in a given direction, multiple time arrival and dimension readings are performed on each face of the chamfered cube.

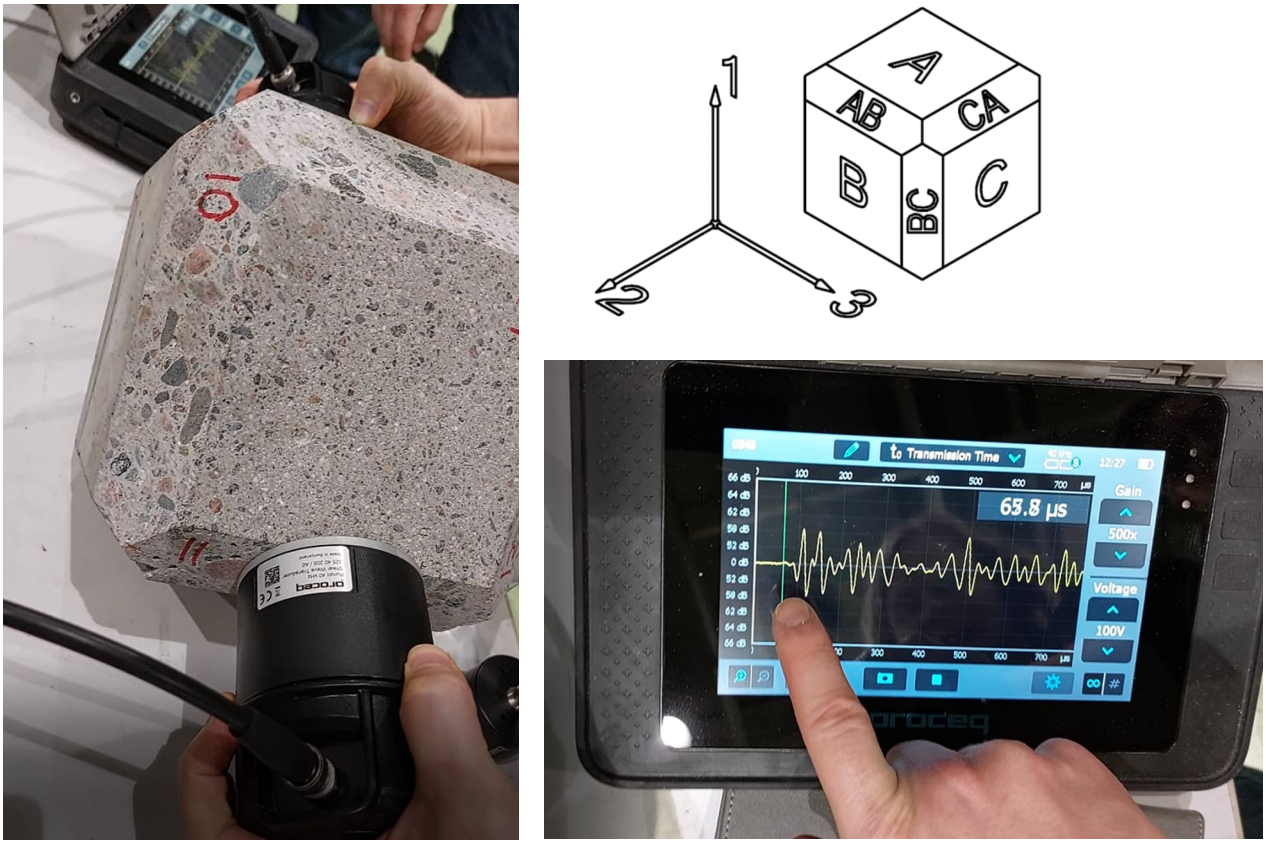

Figure 4. Views of a chamfered cube specimen and the first time arrival determination

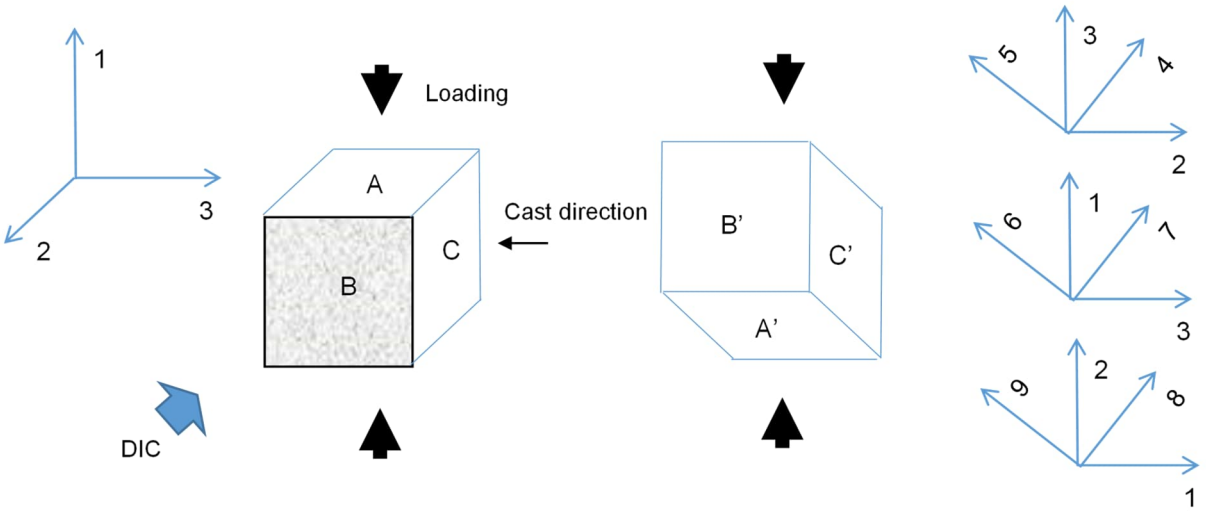

Figure 5. Schematic view of principal direction and diagonal direction nomenclature

The Kelvin-Christoffel eigenproblem can be considered as the solution of the elastodynamics equation $\rho\partial_t^2 u_i = E_{iklj}\partial_k\partial_l u_j$ without the source term, where ρ denotes the density and E_{iklj} the stiffness tensor. One can consider, without a loss of generality, a plane wave eigenmode solution of the form $\boldsymbol{u}(\boldsymbol{x},t) = a\,\boldsymbol{p}\exp\left(\mathrm{i}\omega(v^{-1}\boldsymbol{n}\cdot\boldsymbol{x}-t)\right)$, where a is an arbitrary amplitude, $\boldsymbol{p}$ the polarization unit vector, $\boldsymbol{n}$ the wavefront unit vector and v the wave velocity. Substitution of the plane wave eigenmode solution in the elastodynamics partial differential equation yields the following algebraic eigenproblem: $n_k E_{iklj} n_l p_j = \rho v^2 p_i$. Setting $\Gamma_{ij} = n_k E_{iklj} n_l$, one gets the Kelvin-Christoffel eigenproblem: $\boldsymbol{\Gamma}\cdot\boldsymbol{p} = \lambda\,\boldsymbol{p}$. For a material with orthorhombic symmetry, the nine non-zero stiffness tensor components can be expressed as functions of the measured soundwave velocities (Voigt's notation is used here, $11 \leftrightarrow 1, 22 \leftrightarrow 2,\ 33 \leftrightarrow 3, 23 \leftrightarrow 4, 31 \leftrightarrow 5, 12 \leftrightarrow 6$):

$$E_{11} = \rho {v_{11}}^2 , \quad E_{22} = \rho {v_{22}}^2 , \quad E_{33} = \rho {v_{33}}^2 ,$$

$$E_{44} = \rho ({v_{23}}^2 + {v_{32}}^2)/2 , \quad E_{55} = \rho ({v_{31}}^2 + {v_{13}}^2)/2 , \quad E_{66} = \rho ({v_{12}}^2 + {v_{21}}^2)/2 ,$$

$$E_{23} = \rho \left(\sqrt{\left(2\frac{{v_{44}}^2 + {v_{55}}^2}{2} - \frac{{v_{23}}^2 + {v_{32}}^2}{2} - \frac{{v_{22}}^2 + {v_{33}}^2}{2} \right)^2 - \left(\frac{{v_{22}}^2 - {v_{33}}^2}{2} \right)^2} - \frac{{v_{23}}^2 + {v_{32}}^2}{2} \right),$$

$$E_{13} = \rho \left(\sqrt{\left(2\frac{{v_{66}}^2 + {v_{77}}^2}{2} - \frac{{v_{31}}^2 + {v_{13}}^2}{2} - \frac{{v_{11}}^2 + {v_{33}}^2}{2} \right)^2 - \left(\frac{{v_{33}}^2 - {v_{11}}^2}{2} \right)^2} - \frac{{v_{31}}^2 + {v_{13}}^2}{2} \right),$$

$$E_{12} = \rho \left(\sqrt{\left(2\frac{{v_{88}}^2 + {v_{99}}^2}{2} - \frac{{v_{12}}^2 + {v_{21}}^2}{2} - \frac{{v_{11}}^2 + {v_{22}}^2}{2} \right)^2 - \left(\frac{{v_{11}}^2 - {v_{22}}^2}{2} \right)^2} - \frac{{v_{12}}^2 + {v_{21}}^2}{2} \right).$$

Notice, that the stiffness in the direction of loading (corresponding to the Young's modulus in the isotropic case) is obtained as a function of the stiffness components E_{11}, E_{22}, E_{33}, E_{23}, E_{13}, E_{12} from:

$$E_{\text{axi}} = E_{11} - \frac{{E_{12}}^2 E_{33} + {E_{13}}^2 E_{22} - 2E_{23}E_{13}E_{12}}{E_{22}E_{33} - {E_{23}}^2}.$$

3. RESULTS

Only a summary of the most important results is presented here. A more complete display of results can be found in [16]. The presented results can be summarized as follows:

- Selected soundwave velocity mean values v_{ij} are shown in Figure 6 as a function of the wavefront direction i and polarization direction j. The loading mentioned in the headings of each chart refers to the target displacement shown in Table 1. One can observe a clear decrease of soundwave velocity measurement values for highly damaged concrete. One can also observe the following pattern in soundwave velocity evolution: p-wave velocities in diagonal directions v_{66}, v_{77}, v_{88} and v_{99} follow the same evolution pattern as the p-wave velocity in the direction of loading, v_{11}. In addition, p-wave velocities in diagonal directions v_{44} and v_{55} follow the same evolution pattern as the p-wave velocity in the lateral directions v_{22} and v_{33}.
- The stiffness tensor component mean values E_{pq}, are shown in Figure 7 as a function of the component index pq using Voigt's notation. The ratio of off-diagonal component values (E_{23}, E_{13}, E_{12}) to diagonal components values relative to the lateral direction (E_{22}, E_{33}) tends to increase with compressive loading. The shear-related components E_{44}, E_{55} and E_{66} tend to decrease by a comparable amount.
- Comparative plot of stiffness in loading direction vs. non-recoverable strain in loading direction is shown in Figure 8. The plot enables the comparison of stiffness data obtained from various sources (stress-strain plot from displacement sensor data, stress-strain plot from DIC data and stiffness values computed from soundwave velocity measurements). One can observe that the results from various sources of measurement are comparable. Due to internal compliance, mechanical test device such as displacement sensors tend to produce smaller values of stiffness than measurement device without mechanical contact (DIC, ultrasound measurement)

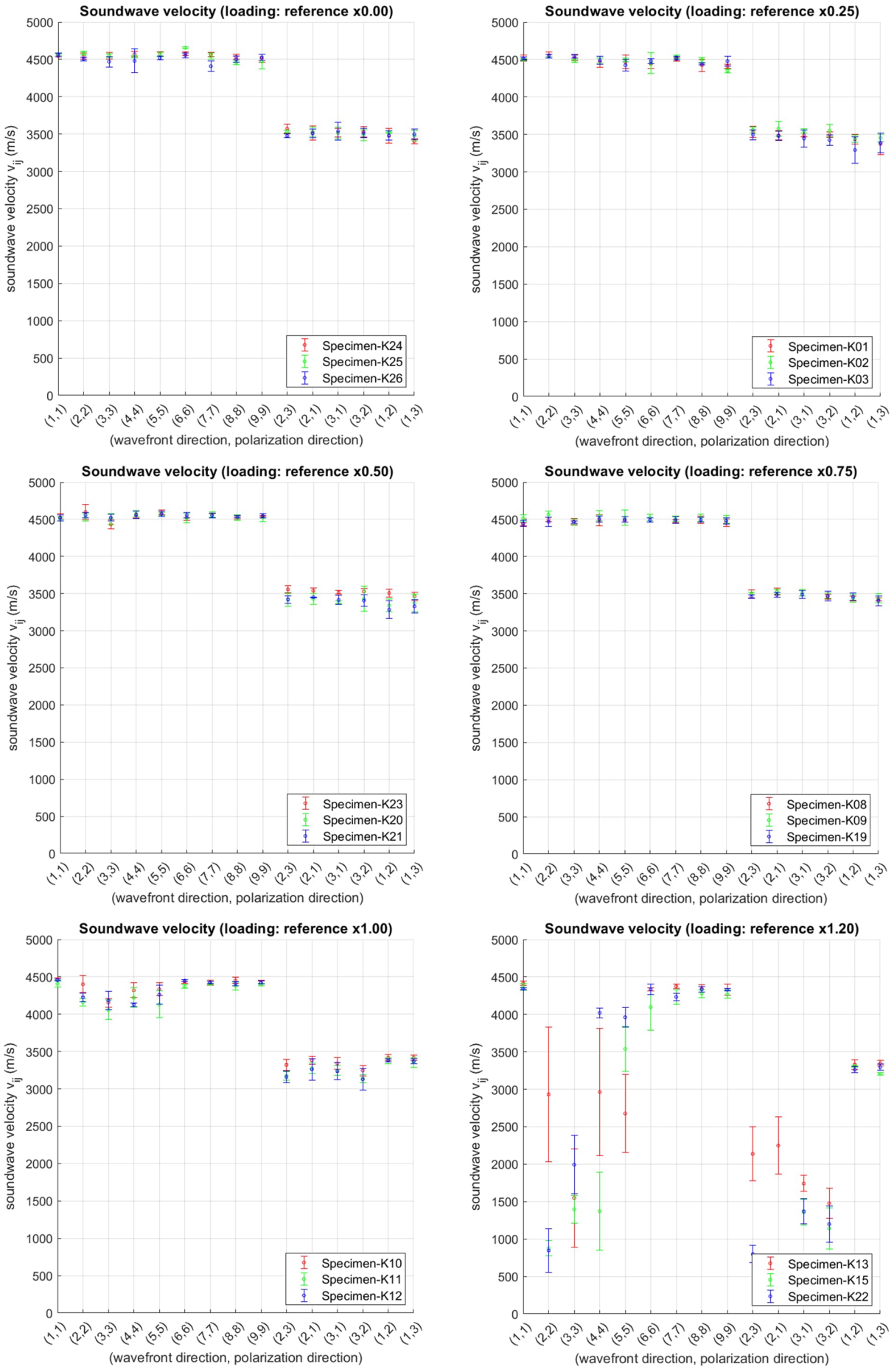

Figure 6. Soundwave velocity mean values ± one standard deviation (N=8)

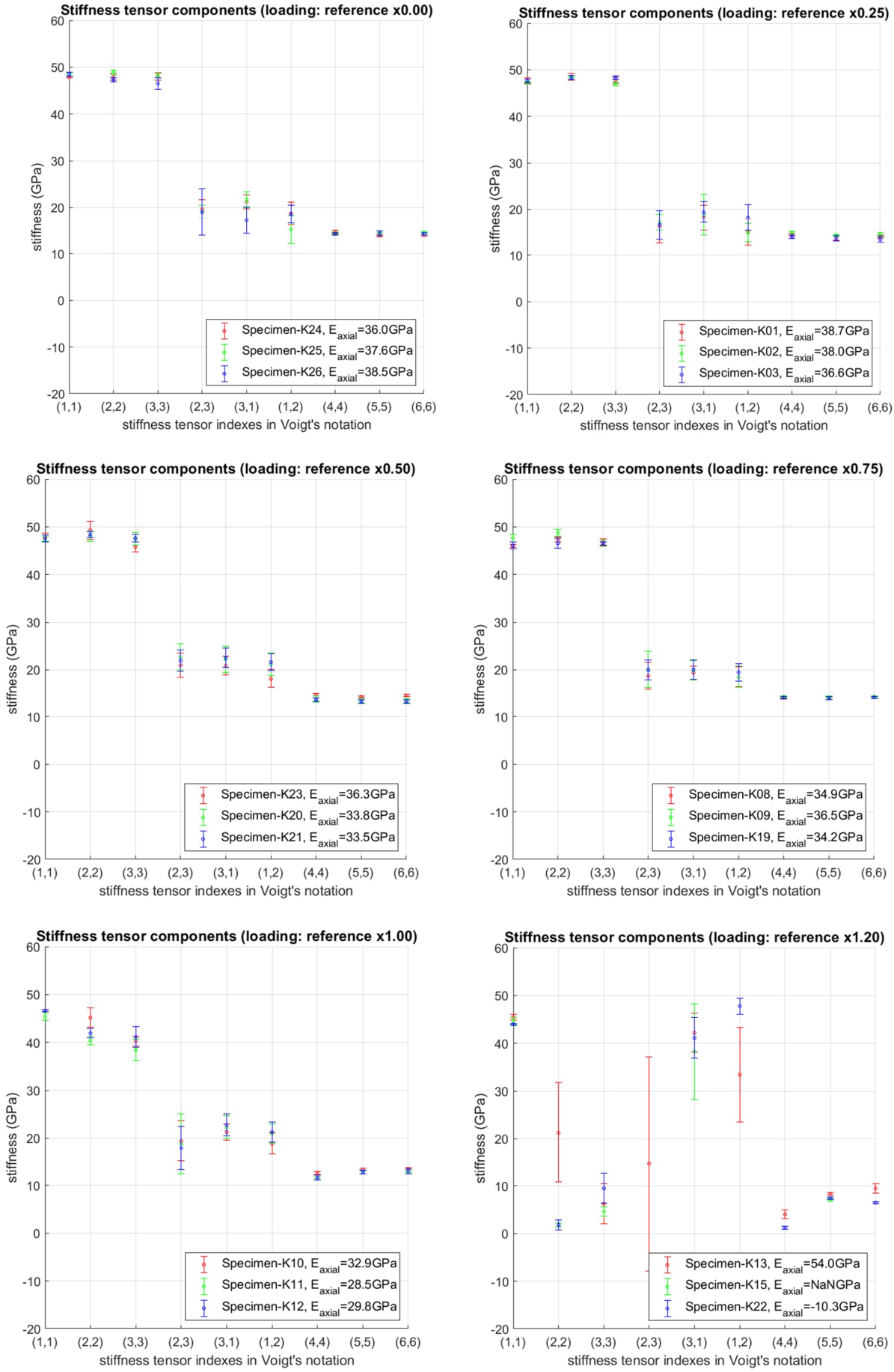

Figure 7. Stiffness tensor component mean values ± one standard deviation (N=8)

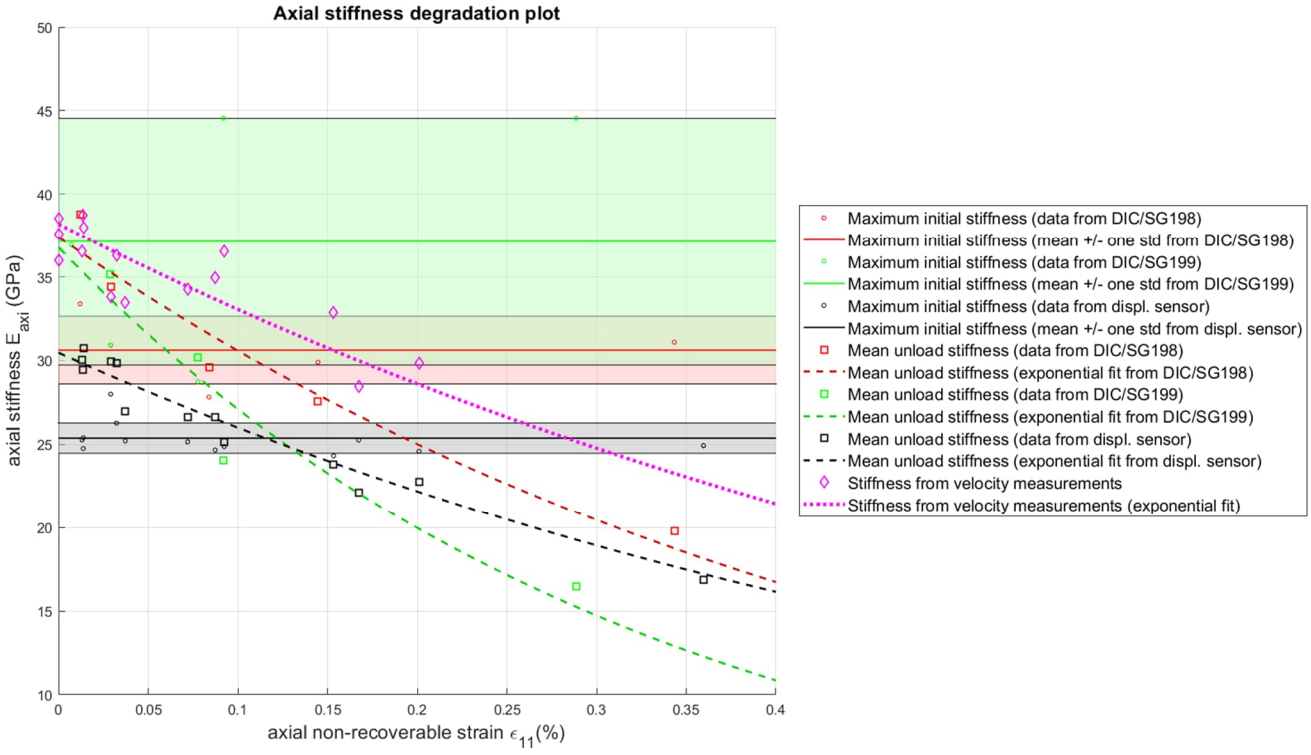

Figure 8. The plot shows: a) initial stiffness mean values from various data sources (solid lines), b) unload stiffness values as a function of non-recoverable strain from various data sources (dashed lines), and c) stiffness values from ultrasound velocity measurements (dotted magenta line). Comparison of stiffness values from ultrasound velocity measurements to unload stiffness values from DIC measurements indicates rather good correspondence.

4. CONCLUSIONS

In this research, a novel method of evaluating material stiffness parameters using ultrasound measurements on compressively damaged concrete cube specimens has been carried out. The method consists in measuring the soundwave velocity in principal and diagonal directions, both with longitudinal and shear waves, and computing the stiffness tensor components as a function of the measured soundwave velocities. Application of this ultrasonic method to concrete specimens with variable degree of damage during uniaxial compressive tests shows that the method works and is capable of producing stiffness degradation profiles comparable to the stiffness degradation profiles obtained from traditional means of measurement from stress-strain data.

The evolution of strain tensor components evaluated from ultrasound velocity measurements shows a pattern that is compatible with the damage expected in a uniaxial compressive stress state. In the future, the ultrasonic method can, therefore, be used to characterize the stiffness tensor degradation pattern in other type of simple stress states (biaxial and triaxial compression, pure shear, uniaxial tension, etc.).

REFERENCES

[1] A. Hillerborg, M. Modéer and P. Petterson, “Analysis of crack formation and crack growth in concrete by means of fracture mechanics and finite elements,” *Cem. Concr. Res.,* vol. 6, pp. 773-781, 1976.

[2] K. Kendall, “Complexities of compression failure,” *Proc. R. Soc. Lond. A361245-263,* 1978.

[3] M. Adams and G. Sines, “Crack extension from flaws in a brittle material subjected to compression,” *Tectonophysics,* vol. 49, pp. 97-118, 1978.

[4] M. Basista, “Micromechanics of damage in brittle solids,” in *Anisotropic Behaviour of Damaged Materials, volume 9 of Lecture Notes in Applied and Computational Mechanics*, Springer-Verlag, 2003, pp. 221-258.

[5] A. Litewka, J. Bogucka and J. Debinski, “Anisotropic Behaviour of Damaged Concrete and Fiber Reinforced Concrete, Chapter 6,” in *Lecture Notes in Applied and Computational Mechanics, Volume 9*, Springer-Verlag, 2003.

[6] J. Mazars and G. Pijaudier-Cabot, “From damage to fracture mechanics and conversely: a combined approach,” *Int. J. Solids Struct.,* vol. 33, pp. 3327-3342, 1996.

[7] J. Vilppo, R. Kouhia, J. Hartikainen, K. Kolari, A. Fedoroff and K. Calonius, “Anisotropic damage model for concrete and other quasi-brittle materials,,” *International Journal of Solids and Structures,* vol. 225, 2021.

[8] B. Audoin and S. Baste, “Ultrasonic evaluation of stiffness tensor changes and associated anisotropic damage in a ceramic matrix composite,” *J. Appl. Mech,,* vol. 61:399, 1994.

[9] S. Baste and C. Aristégui, “Induced anisotropy and crack systems orientations of a ceramic matrix composite under off-principal axis loading,” *Mech. Mater.,* vol. 29:19, 1998.

[10] L. Olsen-Kettle, “Quantifying the orthotropic damage tensor for composites undergoing damage-induced anisotropy using ultrasonic investigations,” *Compos. Struct.,* vol. 204, pp. 701-711, 2018.

[11] L. Olsen-Kettle, “Using ultrasonic investigations to develop anisotropic damage models for initially transverse isotropic materials undergoing damage to remain transverse isotropic,” *Int. J. Solids Struct.,* vol. 138, pp. 155-165, 2018.

[12] S. P. Cheadle, R. J. Brown and D. C. Lawton, “Orthorhombic anisotropy: A physical seismic modeling study,” vol. 56, no. 10, 1991.

[13] R. J. Brown, “Relationships between the velocities and the elastic constants of an anisotropic solid possessing orthorombic symmetry,” CREWES project, 2001.

[14] K. Calonius, A. Fedoroff, A. Forsström and O. Jessen-Juhler, “Comparison of ultrasonic, imaging and mechanical measurements for concrete stiffness determination in cyclic compression tests,” VTT report, VTT-R-00926-21, Espoo, 2021.

[15] K. Calonius, Fedoroff, A., Forsström, A. ja Jessen-Juhler, O., ”Calibration of tensorial damage concrete material model with cyclic compression tests and ultrasound measurements,” tekijä: *Transactions, SMiRT-26, Berlin/Potsdam, July 10-15*, Germany, 2022.

[16] K. Calonius, A. Fedoroff, A. Forsström, V.-A. Hakala and J. Piironen, “Determination of concrete stiffness tensor at different levels of damage,” VTT report, VTT-R-00692-22, Espoo, 2022.

Where durability analysis can benefit from NDT?

Arto Köliö[1,*] and Jaakko Koskinen[1]
[1] Renovatek Oy, Tampere, Finland
*corresponding Author arto.kolio@renovatek.fi

ABSTRACT

The main goal of condition assessment and durability analysis of concrete structures is from a subject structure to assess i) the current condition, damage and degradation, ii) material properties and durability, iii) propagation of the degradation in near future and iv) suitable repair methods. For this task, a multitude of inspection, investigation and test methods are available including both destructive (DT) and non-destructive methods (NDT). This paper presents the current feedback from practice from condition assessment projects of the authors.

NDT-methods have the unrivalled benefit over conventional testing that the subject structure is not spoiled during testing. Ie. for instance information from compressive strength is gained from ultrasonic pulse velocity, impact echo or rebound instead of destructive compression testing. The reverse side to this is that the information gained is often indirect from the actual information needed.

Condition assessment information is utilized in assessing the residual service life of a structure, setting up maintenance strategies and verifying of the fulfilment of durability requirements. Often calculative models are used in the analysis, which operate on input data difficult to obtain from existing structures. Therefore some very specific material tests are often required for a reliable analysis including e.g. the concrete grade, assessment of water to binder -ratio and the measurement of reinforcement cover depth.

This paper discusses feedback from the objectives and test methods of recent condition investigation projects for industrial concrete structures. NDT methods are often in practice complemented or even replaced with conventional destructive test methods. This is due to lack of credibility and reliability of NDT methods. Partly this just may be due to a convention of using destructive methods instead. This increases control over reliability issues but simultaneously hinders the possible benefits of NDT.

Keywords: concrete, durability analysis, condition assessment, NDT.

1. INTRODUCTION

The objectives of an owner of degrading concrete structure does not include the development of novel non-destructive test methods. Instead, the owner is invested in maintaining functionality, maintaining safe use, minimising life cycle costs and preserving the residual value of the structure.

The owner uses timely scheduled repairs which have been properly designed and dimensioned to the renovation needs. To enable sufficient means, the renovation and services must be budgeted and planned beforehand. The owner must mind the current and future service lives i.e. the current and possible future uses of the building and care for preservation of service and condition information of the structure. These are all examples of very different focuses from actual test methods. It just happens to be that tests are that what provides the owner the information which is essential for all the maintenance actions.

Service life estimation in finnish practice is based on the factor approach defined in ISO 15686 standards [1]. A normal target service life is 50 to 200 years. The analysis gives requirements for

* Corresponding author: phone and email

design and materials. These requirements are then used in the design and construction of the structure [2].

An application in renovation of the service life estimation focuses on i) assessing the residual service life of a structure, ii) set up maintenance strategies or iii) prove the fulfillment of durability requirements.

The main goal of condition assessment and durability analysis of concrete structures is to assess i) the current condition, damage and degradation, ii) material properties and durability, iii) propagation of the degradation in near future and iv) suitable repair methods for the subject structure. A multitude of inspection, investigation and test methods are available for use in different combinations to achive this goal.

This paper discusses feedback from the objectives and test methods of recent condition investigation projects for industrial concrete structures conducted by the authors in 2015-2022.

2. NON-DESTRUCTIVE TESTING OF CONCRETE

Numerous test methods are specified and used in determining material and structural properties of concrete structures. Among these, non-destructive tests (NDT) are such that can be considered non-invasive and do not require dismantling or removing of the material tested. NDT methods are beneficial since they are fast and effective, but in contrast they require special knowledge and training to facilitate [3]. A classification of NDT methods is presented in table 1 [3].

Table 1 Compilation of NDT methods (not exhaustive) from [3]

Method	Description
Impact echo	Seismic or stress wave based
Ultrasonic pulse velocity	Ultrasonic (acoustic) stress wave based
Impulse response	Transient dynamic or mechanical impedance based, extension of vibration
Acoustic emission	Transient elastic waves
Ground penetrating radar	Electromagnetic waves, echo
Half-cell potential	Electrochemical detection
Electrical resistivity	Voltage and current measurement of corrosion cell
Infrared thermography	Electromagnetic wave in infrared region, emitted from material surfaces, related to temperature variation
Hammer sounding or chain drag	Based on the sound characteristic of the structure surface

It must be especially mentioned that Rehman et al. considered visual inspection as one of the most versatile and powerful NDT methods for inspecting visible surfaces even though its effectiveness depends on the experience and knowledge of the investigator. The author must agree fully to this argument.

Another key aspect of NDT methods is, that they provide measurement on the studied property indirectly and the difficulty to correlate the values of physical NDT measurements with the mechanical properties has been pointed out for a long time [4].

The benefits usually reported with the use of NDT methods in the investigation of concrete structures include that [3, 5]:

- the test procedure causes little or no damage at all to the subject structure,
- as a consequence of the former the test can be performed without interfering the mechanical performance of the subject structure
- the test procedure does not require heavy equipment,
- the test can be repeated easily.

The challenges usually reported with the use of NDT methods include:

- indirect nature of the methods [4, 5, 6],
- challenges in the calibration of measurements [4, 7, 8]
- reliability [6, 8, 9]
- the need to combine at least two test methods [4].

3. DURABILITY ANALYSIS

3.1. Service life estimation

The estimated service life is calculated separately for freeze-thaw and corrosion of reinforcement and the shorter of these two is regarded as terminal service life [2]. The model was analysed to find out the most influencing parameters for the service life estimate. Regarding the use of NDT techniques, these material and design level properties are the most important properties to investigate. The reliability and accuracy in which these properties are investigated is of key importance!

As given in ISO 15686 standards, the structure's properties that have an influence on the estimated service life are inherent material properties, design level, work execution level, indoor environment, outdoor environment, usage conditions and maintenance level as compiled in table 2. As an application from these, the Finnish approach of the factor method most commonly includes: A material properties, B detailing and design of structures (regarding coatings and how massive the structure is), C curing of concrete, E environmental exposure class, facing and geographical location of the structure and G maintenance schedule.

Table 2 Service life influencing factors compiled from [1] and their description

Factor	Factor category	Description
A	inherent performance level	Is defined as the grade of the component in the time on delivery. Is interpreted as durability properties of the material.
B	design level	Reflects the component's installation in the building. The design choices made can provide shelter and protection from degradation agents.
C	work execution level	Considers the level of skill and control in sitework. Storage, protection during installation, ease of installation, manufacturer's recommendations, etc.
D	indoor environment	Considers the exposure of component to indoor degradation agents.
E	outdoor environment	Considers the exposure of component to outdoor degradation agents. The effect of weather conditions and microclimate surrounding the component should be taken into account.
F	usage conditions	Takes into account the wear that occurs during the use of the building.
G	maintenance level	Represents the level of maintenance of the component. Includes cleaning, maintenance, repair, replacement, etc. and how accessible the component is for maintenance.

The impact of indoor environment and usage conditions are not currently taken into account in the Finnish code and their factor is set to 1. The value ranges of the relevant factors for freeze-thaw and for corrosion are shown in figures 1 and 2. The material properties and design level, namely concrete cover, (factors A and B) are in the described methodology given more weight over the other factors (fig. 1 and 2). Also in the same magnitude is the factor E to describe the environment exposure. The defined factors have more tendency in lengthening the RSL rather than shortening it. This is visible in the numerical values which are weighed more above 1 than below (fig. 1 and 2).

The calculative model operates on input data which may be difficult to define for new construction, let alone obtain from existing structures. Specific material tests are required to obtain input data. The essential tests include e.g. the concrete grade, assessment of w/c -ratio and the measurement of reinforcement cover depth.

Material properties (A), design level (B) and outdoor environment (E) have the most significant influence on service life estimates. The Focus of conventional condition assessment is also on issues regarding the same factors.

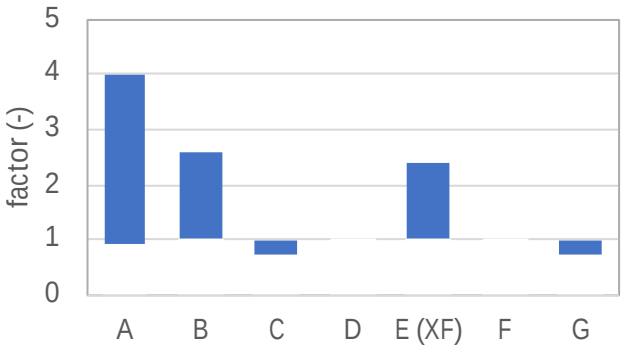

Figure 1. Relative weights of service life parameters A-G considering freeze-thaw durability

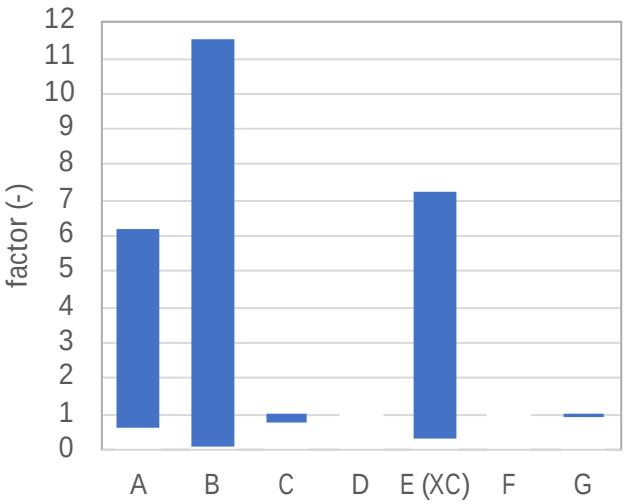

Figure 2. Relative weights of service life parameters A-G considering corrosion durability

4. PRACTICAL EXPERIENCE

4.1. Testing of material properties

The owner of industrial concrete structures is only indirectly interested in material properties. The interest lies in the effects of these properties, whether good or adverse, on the capabilities of the structure to sustain the intended use of the building.

A few boundary conditions exist in the testing of material properties:

- the material properties and their meaning have to be analysed and interpreted as part of the testing contract. This means, that the responsibility for the conclusions drawn remains on the consultant
- Usually the risks and costs of a possible structural failure are so large that the budget for condition assessments allows thorough investigation and testing
- The material testing is not usually allowed to interfere with the facility processes. Also the processes and protocols may greatly affect how the test equipment may be transported and operated on site

- Some structures in a facility are more critical to the process than others. These have to be identified
- Some structures are more easily accessible for study than others. Time window for studies may be very limited. Structures may be accessible for study only with special means (high-rise structures, narrow spaces, submerged spaces etc.) Also some parts of structures may be completely inaccessible.
- Some critical structures may have restrictions on destructive methods. The integrity may not be compromised by coring but the structure, as a critical one, regardless requires a service life estimation.

The choice of test methods is not dictated by the owner. The choice is made by considering the technically feasible test methods against the abovementioned boundaries or restrictions.

Guidelines for the use of rebound hammer have been accessible in Finland as publications of the Finnish Transport Infrastructure Agency and lately as a part of a standard SFS-EN 13791 on the assessment of in-situ compressive strength in structures. The method has been accessible for forensic engineers for decades. And still, the utilisation of this method in practice is quite restricted.

The estimation of concrete strength merely on rebound data is not allowed, and it has to be complemented with core testing data. Considering reliability, this is a very good rule. As pointed out also in literature, e.g. [9], a sound universal correlation between concrete strength and rebound number may not even exist. On the other hand it at the same time hinders the possible benefits of NDT, since conventional DT-methods cannot entirely be left out.

Comparison between concrete compressive strength tests and rebound hammer studies have been conducted in 13 indvidual cases between 2015-2021. The compressive strength tests were carried out according to SFS-EN 12390-3. The rebound hammer tests were all conducted with the same procedure described in [10]. The subject structures were 25...40 years old. In majority of the cases (11 out of 13) the estimate given of the compressive strength by rebound hammer testing was lower (by average -23 %, max. -43 %) than that of determined with test specimen. In two cases the estimate given by the rebound hammer was considerably higher than that of the compressive test. These overestimates were +56 % and +12 %. The general tendency of underestimating compressive strength is safe and gives credit that the procedure used is sound for practice. In the single overestimated cases the subject structure has been a column or a beam. In a column structure the casting direction may cause large variation in the compression of the concrete and make the estimation of strength more difficult.

When existing structures and their degradation is studied, the alterations (descent) in strength originates from degradation phenomena and not cement hydration, as is the case in concrete hardening. This is important to be kept in mind when degradation is studied with NDT methods whose calibration mainly is done using concrete specimens of new concrete. The progression of freeze-thaw damage of concrete samples was followed with ultrasonic pulse velocity measurements (Figure 3). A clear correlation with residual strength and UPV was noted, which seems to be of similar form than relationships between UPV and compressive strength.

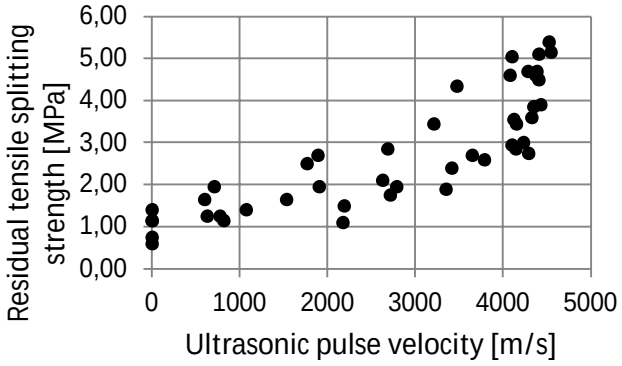

Figure 3. Comparison of the residual tensile splitting strength and ultrasonic pulse velocity in freeze-thaw damaged concrete.

Rebar cover measurements have been in use in studies of concrete structures for a long time. Also in Finland literature and guidelines exist in performing the measurements and the analysis as well as the utilisation of the cover measurement data in service life assessments.

The rebar cover meter is not in any way different from other NDT apparatus. It locates the depth of rebar with detecting the effects and differentials in the field of a two-coil electromagnet. Thereby, the cover meter does not measure length but this is induced from the altered magnetic field.

Cover depth measurements are utilised in nearly every assessment which is taken on reinforced concrete structures. It is the foundation to analysing the risk of reinforcement corrosion with statistical analyses.

Information on the concrete microstructure cannot be reliably acquired with any non-destructive methods. The petrographic analysis of concrete thin section samples is unrivalled in its detail of information. This test requires destructive sampling.

5. CONCLUSIONS

NDT methods have undisputed advantages and in some cases they can be the only alternative. Some NDT methods already have a long history and convention (e.g. cover meter) in condition investigation and some have not stabilised in practice. The following concluding remarks can be drawn:

- Durability analysis relies mainly on factors related to material properties (A), design level (B) and outdoor environment (E). This conclusion is drawn from the factor approach in concrete codes (by 65 2016) but in conventional condition assessment and durability analysis these are also the key points. Material properties, design level and outdoor environment are the factors that in minimum have to be determined with good reliability. The test method, whether DT or NDT, is from this viewpoint irrelevant. NDT methods, if chosen, should not compromise the reliability in which the physical properties of the structure need to be known.
- In industry facilities, the accessibility, level of criticality to the process and the process itself give restrictions to testing.
- Visual inspection done by an experienced engineer can also be considered as a very valuable NDT tool
- The current convention in Finland does not allow the use of NDT-methods alone. This evades reliability issues but simultaneously hinders the possible benefits of NDT.
- The current procedure of rebound hammer testing tends to underestimate compressive strength according to the authors own studies. The estimate seems therefore to be on the safe side. In single cases overestimation has occurred. No single reason was identified as a cause of this.
- The investigation of the degradation of existing structures will require calibration of its own, since alteration in the measured surface hardness or sound wave penetration is affected by degradation phenomena and not cement hydration. However, a relationship of similar form can be found also to degradation.
- Information on the concrete microstructure cannot be reliably acquired with any non-destructive methods.

REFERENCES

[1] ISO 15686-1. 2011. Buildings and constructed assets, Service life planning part 1: General principles and framework

[2] by 65, Betoninormit 2016 (Concrete code 2016), Finnish Concrete Association.

[3] Rehman, S.K.U., Ibrahim, Z., Memon, S.A., Jameel, M. 2016. Nondestructive Test Methods for Concrete Bridges: a Review. Construction and Building Materials 107(2016). Pp. 58-86

[4] Breysse, D., 2012. Nondestructive Evaluation of Concrete Strength: An Historical Review and a New Perspective by Combining NDT Methods. Construction and Building Materials 33(2012). Pp. 139-163

[5] Desa, M.S.M, Ibrahim, M.H.W, Shahidan, S., Ghadzali, N.S., Misri, Z. 2018. Fundamental and assessment of concrete structure monitoring by using acoustic emission technique testin: A review. IOP Conf. Series: Earth and Environmental Science 140(2018). doi:10.1088/1755-1315/140/1/012142

[6] McCann, D.M., Forde, M.C. 2001. Review of NDT methods in the assessment of concrete and masonry structures. NDT&E International 34 (2001) 71–84

[7] Breysse, D., Martınez-Fernandez, J.L., 2014. Assessing concrete strength with rebound hammer: review of key issues and ideas for more reliable conclusions. Materials and Structures (2014) 47:1589–1604. DOI 10.1617/s11527-013-0139-9

[8] Szilágyi, K., Borosnyói, A., Zsigovics, I. 2011. Rebound surface hardness of concrete: Introduction of an empirical constitutive model. Construction and Building Materials 25 (2011) 2480–2487

[9] Ali-Benyahia, K., Sbartaï, Z.-M., Breysse, D., Ghrici, M., Kenai, S. Improvement of nondestructive assessment of on-site concrete strength: Influence of the selection process of cores location on the assessment quality for single and combined NDT techniques. Construction and Building Materials 195 (2019) 613–622

[10] Liikennevirasto (eng. Finnish Transport Infrastructure Agency). 2014. Kimmovasaran käyttäjän ohje. 4905/080/2013, Liikennevirasto, Helsinki. In Finnish.

DIN 4871: Qualification of NDT Personnel in Civil Engineering (NDT-CE)

Sascha Feistkorn[1]*, Daniel Algernon[2], Ralf W. Arndt[3], Gino Ebell[4], Martin Friese[5], Christian U. Grosse[6], Ralf Holstein[1], Ernst Niederleithinger[4], Martin Schickert[7], Sebastian Schulze[8], Alexander Taffe[9], Andrei Walther[10], Julia Wolf[11], Andreas Zoëga[12], Michael Zwanzig[1]

[1]German Society for Non-Destructive Testing (DGZfP), Berlin, Germany
[2]SVTI - Swiss Association for Technical Inspections, Nuclear Inspectorate, Wallisellen, Switzerland
[3]FH Erfurt - University for Applied Sciences Erfurt, Erfurt, Germany
[4]BAM - Federal Institute for Materials Research and Testing, Berlin, Germany
[5]DZSF Dresden, Germany
[6]TUM - Technische Universität München, München, Germany
[7]MFPA Weimar - Materialforschungs- und -prüfanstalt an der Bauhaus-Universität Weimar, Weimar, Germany
[8]Hupfer Ingenieure, Hamburg, Germany
[9]HTW Berlin - University for Applied Sciences, Berlin, Germany
[10]Kiwa GmbH, Berlin, Germany
[11]DB Engineering & Consulting GmbH, Bremen, Germany
[12]TFI - Institut für Bodensysteme an der RWTH Aachen e.V., Aachen, Germany

**Corresponding author: Sascha Feistkorn; fe@dgzfp.de*

ABSTRACT

Non-destructive testing, in particular of concrete components, plays an increasingly important role in civil engineering (NDT-CE). Especially in nuclear power plants, the application of different inspection methods is indispensable to ensure the integrity of concrete components during the manufacturing process or regarding the extension of the lifespan. Therefore, different methods have been commercialized and are now applied for the structural assessment on-site to serve as valuable tools in the process of ensuring safety and durability. This growing importance of NDT-CE methods for concrete inspections requires measures to ensure the reliability of the information provided by NDT.

Among other aspects of an inspection system such as the equipment or the procedure, the reliability and the comparability of the results depend largely on the person who applies the inspection technique and evaluates the results.

To ensure a high quality of non-destructive concrete evaluation as well as to keep the uncertainty caused by the inspection personnel to a minimum, structured, consistent, and regulated theoretical as well as practical training of inspection personnel is essential. To close this gap, the subcommittee of education and training (UA-A) within the committee for NDT-CE of the German Society for Non-Destructive Testing (DGZfP) has been committed in recent years establishing uniform training standards for NDT-CE.

So far, the national standard DIN 4871 “Non-destructive testing - Qualification of NDT personnel in Civil Engineering (NDT-CE)” was developed in the standards committee for Materials Testing (NA 062) of the German Institute for Standardization DIN (DIN NMP). Furthermore, an additional standard DIN 4873 “Non-destructive testing - Certification of NDT personnel in Civil Engineering (NDT-CE)” is in preparation. This committee work could be an initial step for regulated concrete inspections, especially for the nuclear industry, where the requirements for standardization are particularly high.

Within this presentation, an overview of the German standardization activities, the concepts of both standards, and their connections to ISO 9712 as well as to other standards will be presented.

Keywords: NDT-CE; DIN 4871; Personnel; Qualification; Training; Education; Standard; Modules; Syllabus;

1. INTRODUCTION

The inspection of safety-relevant components such as containment structures or cooling towers becomes more relevant due to the discussion of lifetime extension and the related ageing process. Other relevant infrastructures such as bridges are additionally faced with increased traffic load. Therefore, gaining reliable information is essential to ensure the integrity and safety of these civil structures. To be as precise and reliable as possible, the performance of the inspection system containing the inspection technique, the inspection procedure, and the inspection personnel has to be well known. Therefore, valuable tools such as the GUM (Guide to the Expression of Uncertainty in Measurement) [1] or the POD (Probability of Detection) [2], [3] were successfully transferred to non-destructive testing in civil engineering (NDT-CE) several years ago [4], [5].
However, the reliability of the results depends to a large extent on the personnel who apply the non-destructive testing methods. To become indispensable for the monitoring of the manufacturing process or the periodic in-service inspection of concrete components, standardized qualification and certification of personnel are required to keep the uncertainty caused by the inspection personnel as small as possible. This leads to the conclusion, that uniform and standardized education and training for inspection personnel in NDT-CE would be valuable. This was the main goal by reactivating the subcommittee for education and training (UA-A) within the committee for NDT-CE of the German Society for Non-destructive Testing (DGZfP) in 2018. Representatives of universities, service providers, research institutes, and other public institutions joined this subcommittee (see Figure 1) to work together on how a uniform training standard should be designed to fulfil the specific requirements for non-destructive concrete inspections.

Figure 1: Organizations working on DIN 4871

One specific requirement to be considered is the fact of unique concrete structures in practice, so the majority of inspection scenarios can be described as a case-by-case examination of components made of reinforced or prestressed concrete. In addition, concrete is a relatively inexpensive material compared to steel. This leads to the fact, that NDT-CE must compete with destructive testing in many cases, which means that a certain cost efficiency must be taken into account. As one result both aspects according to DIN EN ISO 9712 [6] - the extensive amount of training and the level definition for inspection personnel - would not find acceptance in the civil industry. To establish mandatory training for NDT-CE personnel, a different approach has to be developed, also regarding the aspect that DIN EN ISO 9712 [6] does not regulate all NDT methods applied for concrete inspections. Additionally, the basic requirement for including the civil industry sector in the DIN EN ISO 9712 [6] - a complete NDT-CE method-standardization - is also not fulfilled.
On the other hand, various existing inspection standards, such as DIN 1076 [8], VDI Guideline 6200 [9] or RI-ZFP-TU [10] have to be considered to avoid parallel standardization with these regulations as well as to avoid a parallel standardization of some NDT methods such as VT (Visual Testing) or TT (Thermographic Testing). Therefore, the UA-A pursued the goal of developing a standard that takes these specific conditions of the civil industry into account. Nevertheless, the existing approaches of DIN EN ISO 9712 [6] and DIN CEN ISO/TS 25107 [7] contain also valuable ideas such as the responsibilities, the level system, the clear definition of training amounts or the uniform syllabus structure, which should be transferred and adapted to the qualification of ND-CE inspection personnel.
A concept considering all these aspects was developed in the subcommittee for education and training (UA-A) and presented to the responsible working committee NA 062-08-21 AA of the DIN (German Institute for Standardization) Standards Committee for Materials Testing (NMP) in 2019. After intensive discussions and internal coordination work, the standardization project "DIN 4871" was set up in mid-2020. In addition to the high level of motivation and identification for this topic in the UA-A, the corona pandemic can also be seen as a driver of the standard. In the following months, more than 20 online meetings were held to develop the DIN 4871. As part of the regular publication process for the development of a DIN standard and the associated discussion in the

responsible working committee DIN NMP, the draft of DIN 4871 was published in September 2021. During the two-month objection period, numerous comments were received, which were subsequently discussed and partially adopted. After further revision work, the standard was successfully voted on in May 2022. The standardization project "DIN 4871: Qualification of NDT personnel in Civil Engineering (NDT-CE)" was successfully completed with its publication in September 2022 [11].

2. DIN 4871 – OVERVIEW

Based on the boundary conditions explained before as well as on the typical inspection tasks in the field, the following inspection methods were identified in so-called method-related modules regarding theoretical and practical training contents (see *[11]* chapter 1):

a. Rebound hammer
b. Magneto-inductive methods
c. Potential mapping
d. Ground penetrating radar
e. Ultrasonics
f. Impact-echo

Since some inspection tasks in the civil industry are frequently requested and carried out, two inspection task-related modules were also defined:

g. Proof of compressive strength
h. Proof of reinforcement

To cover the essential basic knowledge, which is required in any case before applying different inspection methods, basic modules which have to be completed during the qualification process were also established:

- Overview of non-destructive testing in civil engineering
- Measurement technology
- Wave theory and physical basics
- Damage mechanisms and structural specifics
- Quality assurance
- Combination of inspection methods

An overview of the general structure of DIN 4871 is given in Figure 2 (*[11]* chapter 1).

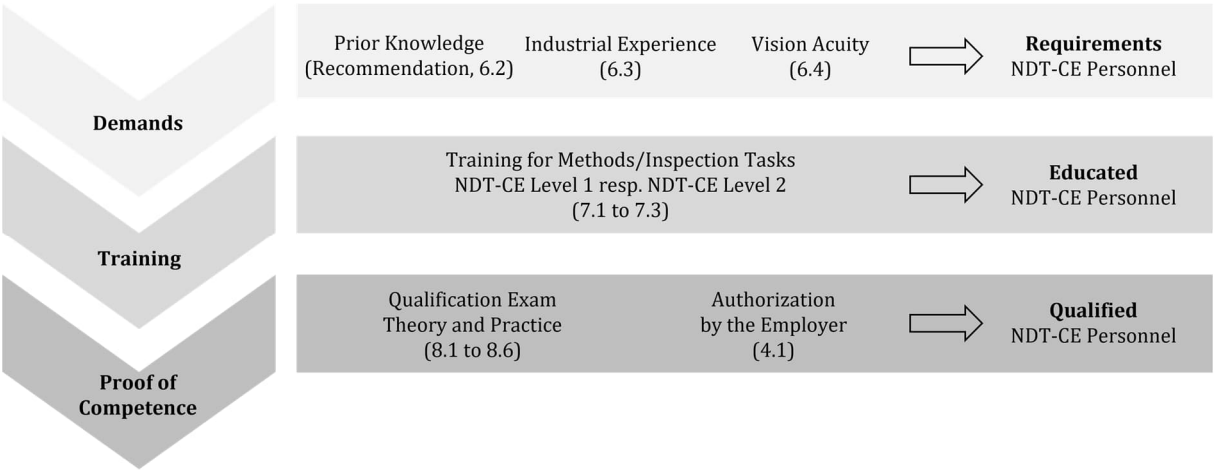

Figure 2: Overview over the regulated contents of DIN 4871 [11]

3. LEVEL DEFINITION OF NDT-CE INSPECTION PERSONNEL

After an intensive discussion about an adequate definition of levels for the civil industry, considering both, the DIN EN ISO 9712 [6] level definition and the specifics of the civil industry, the subcommittee concluded, that two levels fulfil these criteria and represent the relevant inspection tasks of NDT-CE inspection personnel in the field in contrast to the three levels defined in DIN EN ISO 9712 [6] (compare [11] subchapter 3.1/3.2).

3.1. NDT-CE Level 1

From the subcommittees point of view, the main purpose of NDT-CE Level 1 personnel to be performed in the field is data acquisition with its related tasks. Therefore, the following definition was created (see *[11]* chapter 5.1; Please note: currently not yet officially translated; this translation was provided by the authors of this paper):

"*A person qualified in NDT-CE Level 1 has demonstrated the ability to perform NDT-CE in accordance with a procedure and under the supervision of NDT-CE Level 2 inspection personnel. NDT-CE Level 1 personnel must be operationally authorized by their employer within the specified scope to perform the following in accordance with procedures:*

a) *Adjustment of NDT-CE equipment in accordance with procedures.*
b) *Execution of measurements and their adjustment to the boundary conditions.*
c) *Recording of measurement results as well as their preliminary evaluation and classification based on written criteria.*
d) *Report on measurement results to NDT-CE Level 2 inspection personnel.*

NDT-CE Level 1 personnel are not permitted to make a selection of the inspection method or the inspection technique, nor are they take responsibility for the final evaluation and assessment."

3.2 NDT-CE Level 2

From the subcommittee's point of view, the main purpose of NDT-CE Level 2 personnel to be performed in the field is the data evaluation with its related tasks and the supervision of NDT-CE Level 1 personnel. Therefore, the following definition was created (see *[11]* chapter 5.2; Please note: currently not yet officially translated; this translation was provided by the authors of this paper):

"*A person qualified in NDT-CE Level 2 has demonstrated the ability to perform and supervise NDT-CE activities. The NDT-CE Level 2 inspection personnel may perform operationally authorized the following activities within the specified scope:*

(a) *All NDT-CE Level 1 activities.*
(b) *Guidance of NDT-CE level 1 inspection personnel.*
(c) *Selection of the inspection method and the inspection technique as well as determining the limit of application.*
(d) *Development of procedure and interpretation of standards, regulations, and guidelines.*
(e) *Supervision of measurements.*
(f) *Evaluation and assessment of measurement results.*
(g) *Documentation.*
(h) *Technical responsibility for the inspection result generated from the measurements and their evaluation.*"

4. REQUIREMENTS

Besides specifying an approach containing theoretical and practical training to ensure comparable competence in the application of NDT-CE and to be able to evaluate these competencies, one main goal of introducing a standard was to keep the entry barrier to NDT-CE as low as reasonable. Therefore, a minimum set of requirements were defined regarding prior knowledge and industrial NDT-CE experience (see [11] chapter 6). Accordingly DIN 4871 recommends demonstrating prior

knowledge of the candidate through technical vocational training or a relevant study prior to the training. The minimum industrial NDT-CE experience before the training must be as indicated in Table 1 at the time of training. If a candidate seeks training in more than one inspection method or inspection task, the industrial NDT-CE experience time must equal the sum of the industrial NDT-CE experience times in each inspection method or inspection task.

Table 1: Minimum industrial NDT-CE Experience

NDT-CE Method or NDT-CE Inspection Task	Industrial NDT-CE Experience in days[a]	
	NDT-CE Level 1	NDT-CE Level 2
Rebound Hammer	5	20
Magneto-inductive Methods	10	30
Potential Mapping (Half Cell Potential)	10	30
Ground Penetrating Radar	10	30
Ultrasonics	10	30
Impact-Echo	10	30
Proof of Compressive Strength	15	30
Proof of Reinforcement	15	30

[a] One-day duration is at least seven hours, which can be achieved on a single day or by accumulating hours. The maximum allowable hours in any one day is 12 hours. Experience in days is achieved by dividing the total accumulated hours by 7.

In addition, the candidate shall provide documentary evidence of acceptable vision in accordance with their employer's requirements. Depending on the inspection method or inspection task, near vision acuity and, if applicable, colour vision has to be tested. The employer shall document the requirements in writing.

5. AMOUNT OF TRAINING AND EXAMINATION

The minimum duration of training is given in Table 2 for the respective inspection method or inspection task (see [11] chapter 7). The duration is based on the candidate having adequate mathematical skills and knowledge of material properties and manufacturing processes. Training includes both practical and theoretical elements.

Table 2: Minimum Training Requirements

NDT-CE Method or NDT-CE Inspection Task	Training Amount in days[a]	
	NDT-CE Level 1	NDT-CE Level 2
Rebound Hammer	1	2
Magneto-inductive Methods	2	2
Potential Mapping (Half Cell Potential)	1	2
Ground Penetrating Radar	2	2
Ultrasonics	2	2
Impact-Echo	2	2
Proof of Compressive Strength	2	2
Proof of Reinforcement	2	2

[a] One-day duration is at least seven hours, which can be achieved on a single day or by accumulating hours. The maximum allowable hours in any one day is 12 hours. Training in days is achieved by dividing the total accumulated hours by 7.

Prior to the initial qualification for an NDT-CE Level 1, the one-day basic module “Overview of non-destructive testing in civil engineering” shall be completed.
Before the initial qualification for an NDT-CE Level 2, the basic modules according to Table 3 must be completed.

Table 3: Minimum Training Requirements for the Basic Modules NDT-CE Level 2

Basic Modules for NDT-CE Level 2	Training Amount in days[a]
Measurement Technology	1
Wave Theory and Physical Basics	1
Damage Mechanisms and Constructive Specifics	1
Quality Assurance	1
Combination of Inspection Methods	1
Overall	5

[a] One-day duration is at least seven hours, which can be achieved on a single day or by accumulating hours. The maximum allowable hours in any one day is 12 hours. Training in days is achieved by dividing the total accumulated hours by 7.

The qualification examination (see [11] chapter 8) consists of a theoretical and a practical element and must cover a specific NDT-CE inspection method or a specific NDT-CE inspection task. Theoretical and practical qualification exams must be supervised by an examiner, who shall meet certain requirements (see [11], chapter 4.3). The theoretical and practical parts of the examination must be evaluated separately.
The theoretical exam may only consist of multiple-choice examination questions randomly selected from the collection of questions for qualification exams. These questions must be confirmed and approved by an examiner. A minimum number of multiple-choice examination questions specified in DIN 4871 must be answered by the candidate. The theoretical qualification exam is considered passed if the candidate achieves a score of at least 70%.
In practical exams, the NDT-CE Level 1 candidate must demonstrate his ability to perform and to document NDT on a test specimen unknown to him. The NDT-CE Level 2 candidate must also demonstrate his ability to evaluate and assess measurement results and to prepare a procedure.
The practical exam shall include the application of the inspection method or inspection task for the specified test specimens and the recording of the results. The practical exam has to be performed on areas of test specimens whose test situation differs from the test situations during training. For the test specimens used for the qualification exams, documentation must be available containing the geometry as well as the properties relevant to the respective inspection task in a representative manner. During the practical exam, the NDT-CE Level 1 candidate shall follow the procedure provided by the examiner. The NDT-CE Level 2 candidate has to select an NDT-CE method suitable for the inspection task and define the procedure in relation to given regulations, standards or specifications. In addition, NDT-CE Level 2 candidates shall design at least one procedure appropriate for NDT-CE Level 1 personnel for a test specimen selected by the examiner. The practical qualification exam is considered passed if the candidate achieves a score of at least 70%.

6. SYLLABUS ON THE EXAMPLE OF THE REBOUND HAMMER

For each inspection method and inspection task as well as for each basic module contents for theoretical and practical training were defined (see [11] Appendix A, B, C and D). Therefore, a syllabus containing the theoretical aspects was created according to the scheme introduced with DIN CEN ISO/TS 25107 [7] for each inspection method and inspection task. The example of the developed syllabus for the “Rebound Hammer”, covering the theory can be found in Table 4, taken from [11] Appendix A.1.

Table 4: Theoretical Contents of the Rebound Hammer Module (normative)

Contents of the theoretical NDT-CE Method Training Rebound Hammer			
Contents		NDT-CE Level 1	NDT-CE Level 2
A.1.1 Introduction to Terminology and historical Background	Historical Development of the Methods	X	
	Tasks of the NDT-CE personnel	X	X
	Standards and Guidelines	X	X
	Hardness, Compressive Strength, Carbonation	X	X
	Hardness Testing, Spring Hammer, Rebound Hammer	X	X
A.1.2 Physical Principle	Measurement Principles and Impact Energy (Rebound Distance und Quotient of Velocity)	X	
	Correlation Hardness – Compressive Strength Correlation Rebound Hammer – Cores Depth of Influence, Correlation Curves, Correlation Tables, Regressions	X	
	Core Taking (Basic Idea, Requirements such as Number, Geometry, etc.)	X	
A.1.3 Product Knowledge (Correlation between Method and Product, Method Capabilities and Limitations)	Rebound Values and Compressive Strengths, comparative Measurements with the Rebound Hammer	X	X
	Factors affecting the Measurement Result (a. o. Carbonation, Gravitation, Friction, Component Thickness, Surface, Moisture, Temperature, Load, Aggregates, etc.)	X	X
	Options: only Rebound Hammer without Cores; Correlation of Rebound Hammer and Cores; Only Cores	X	X
	Component Properties and Parameters affecting the Concrete Quality (a.o. Hardness, Compressive Strength, Effect of Frost and Weathering)	X	X
A.1.4 Equipment	Rebound Hammer (compliant with Standards: with R- and Q-Values), Anvil, Grinding Stone	X	
	Cores (Requirements and Taking)	X	
A.1.5 Information prior Data Acquisition	Aim of the Inspection	X	X
	Carbonation State, Year of Construction (Structure or Component)	X	
	Inspection Area and Surface Condition	X	
A.1.6 Data Acquisition	Standards for the Data Acquisition	X	X
	Definitions, Inspection Conditions, Functional Checks	X	
	Requirements for the Number of Measurements	X	
	Data Acquisition with the Rebound Hammer	X	
	Taking Cores	X	
	Determination of the Carbonation Depth	X	

Contents of the theoretical NDT-CE Method Training Rebound Hammer			
Contents		NDT-CE Level 1	NDT-CE Level 2
A.1.7 Data Evaluation, Interpretation and Documentation	Standards for the Data Evaluation	X	X
	Definitions, Overview about the different Evaluation Approaches	X	X
	Comparative Evaluation (Rebound Hammer)		X
	Evaluation with Correlation Curves and Correlation Tables		X
	Evaluation in Correlation with Cores		X
	Destructive Compressive Strength Estimation		X
A.1.8 Assessment and Inspection Statement	Comparison of the Results with additional Information (a. o. Soundings, Plans, Drawings)		X
	Concept of Compressive Strength Evaluation		X
	Compressive Strength Evaluation based on Results gained from non-destructive Tests with Correlation Curves and -tables		X
	Compressive Strength Evaluation based on the Combination of Results gained from destructive and non-destructive Tests		X
	Compressive Strength Evaluation based on Results gained from destructive Tests		X
	Localization of Concrete Qualities and -Differences		X
	Inspection Report		X
A.1.9 Quality Assurance	Concept and essential Parts of Procedures	X	X
	Application of Procedures	X	
	Development of Procedures		X
	Creation of Tender Contents		X
	Additional Investigations		X
	Further Quality Assurance Measures		X
	Examples for Laboratory and in-situ Measurements and Inspections	X	X
A.1.10 New Developments	Automated Data Evaluation		X
	Additional Concepts such as the Combination or Ultrasonics and Rebound Hammer (SONREB)		X
	New Approaches from Research and Development		X

The minimum requirements for the practical Rebound Hammer training are exemplarily summarized in Table 5, taken from [11] Appendix D.1.

Table 5: Practical Contents of the Rebound Hammer Module (informative)

Contents of the practical NDT-CE Method Training Rebound Hammer		
Inspection Task	Requirements	Tasks
D.1.1 Concrete Compressive Strength Estimation applying Rebound Hammer and/or Cores	— Calibration Anvil — Set of Rebound Hammers measuring the Rebound Distance (R-Value) and the Quotient of Velocity (Q-Value) — Concrete Test Block with a minimum Thickness of 10 cm (better of 30 cm minimum) with smooth Surface (horizontal and vertical) — Suitable Pairs of Values to calculate a Regression Curve	— Calibration at the Anvil — Determination of R- and Q-Values — Differences of R- and Q-Values gained on horizontal and vertical Surfaces considering the Impact Direction — Calculation of a Regression Curve from given Measurement Data supported by a software
D.1.2 Detection of qualitative Differences in Concrete Compressive Strength	— Calibration Anvil — Set of Rebound Hammers measuring the Rebound Distance (R-Value) and the Quotient of Velocity (Q-Value) — Concrete Test Block or in-situ Component with obviously different Concrete Compressive Strengths	— Calibration at the Anvil — Application of Rebound Hammers (R- and Q-Values) and capture the qualitative Differences of the measured Values

It has to be considered, that the minimum requirements for theoretical training are normative whereas the practical training contents are informative due to the complexity of test block manufacturing.

8 SUMMARY AND OUTLOOK

In more than 25 meetings during the last years, the subcommittee of education and training (UA-A) within the committee for NDT-CE of the German Society for Non-Destructive Testing (DGZfP) has developed the first standard for the training and qualification of personnel in Civil Engineering (NDT-CE). Members of different organizations such as service providers, universities, or research institutes containing scientists, practitioners, authorities, and clients were actively involved to comply with the national standardization project “DIN 4871” under the roof of the standards committee for Materials Testing (NA 062) within the German Institute for Standardization DIN (DIN NMP). The German national standard DIN 4871 passed the mandatory objection period in November 2021. All submitted comments have been addressed, so the document was officially released in September 2022.
In parallel, the official translation of DIN 4871 into English has been started. Furthermore, a second complementary standard - DIN 4873: “Non-destructive testing - Certification of NDT personnel in Civil Engineering (NDT-CE)” - is in preparation to establish a certification process for NDT-CE inspection personnel.

Please note, that all excerpts taken from DIN 4871 *[11]* are currently not yet officially translated. The presented translation was provided by the authors of this paper.

REFERENCES

[1] Guide to the Expression of Uncertainty in Measurement. (deutsche Übersetzung: Leitfaden zur Angabe der Unsicherheit beim Messen) Beuth-Verlag, Berlin, 1995

[2] Department of Defence: MIL-HDBK-1823A Nondestructive Evaluation System Reliability Assessment. 7. April 2009

[3] A. P. Berens: NDE Reliability Analysis, Reprinted from Metals Handbook Volume 17, 9th Edition: Nondestructive Evaluation and Quality Control. University of Dayton Research Institute, ASM International, 1989

[4] S. Feistkorn: Gütebewertung qualitativer Prüfaufgaben in der zerstörungsfreien Prüfung im Bauwesen am Beispiel des Impulsradars. In: Schriftenreihe des Deutschen Ausschusses für Stahlbeton, Heft 603, Beuth Verlag, Berlin, 2012, Dissertation

[5] A. Taffe: Zur Validierung quantitativer zerstörungsfreier Prüfverfahren im Stahlbetonbau am Beispiel der Laufzeitmessung. In: Schriftenreihe des Deutschen Ausschusses für Stahlbeton, Heft 574, Beuth Verlag, Berlin, 2008, Dissertation

[6] DIN EN ISO 9712:2012-12: Zerstörungsfreie Prüfung - Qualifizierung und Zertifizierung von Personal der zerstörungsfreien Prüfung
(Non-destructive testing - Qualification and certification of NDT personnel)

[7] DIN CEN ISO/TS 25107:2022-04: Zerstörungsfreie Prüfung - Leitfaden für Ausbildungs-Syllabus der zerstörungsfreien Prüfung; Deutsche Fassung CEN ISO/TS 25107:2019
(ISO/TS 25107:2019: Non-destructive testing - NDT training syllabuses);

[8] DIN 1076:1999-11: Ingenieurbauwerke im Zuge von Straßen und Wegen - Überwachung und Prüfung
(Engineering structures in connection with roads - inspection and test)

[9] VDI 6200:2010-02: Standsicherheit von Bauwerken - Regelmäßige Überprüfung
(Structural safety of buildings - Regular inspections)

[10] RI-ZFP-TU:2002-03: Richtlinie für die Anwendung der zerstörungsfreien Prüfung von Tunnelinnenschalen
(Guideline for the Application of non-destructive Testing for Inner Tunnel Shells)

[11] DIN 4871:2022-09: Zerstörungsfreie Prüfung – Qualifizierung von Personal der zerstörungsfreien Prüfung im Bauwesen (ZfPBau)
(Non-destructive testing – Qualification of NDT personnel in Civil Engineering (NDT-CE))

Reliability Assessment of NDT in Civil Engineering – the German Approach for Standardization (normPOD)

Sylvia Keßler[1,*], Vamsi Krishna Rentala[2], Fabian Dethof[1] and Daniel Kanzler[2]
[1] Helmut Schmidt University/University of the Federal Armed Forces Hamburg, Chair of Engineering Materials and Building Preservation, Hamburg, Germany
[2] Applied Validation of NDT (AV-NDT), Berlin, Germany

ABSTRACT

Over the last decades, non-destructive testing (NDT) became an indispensable element of condition assessment in civil infrastructure, automotive, nuclear and many other safety-related industries. Each NDT method has its unique strengths and weaknesses, and there is increased interest in using them in concert to provide the best overall assessment. However, the use of the full potential of NDT data is constrained by a lack of standardization to estimate the reliability of NDT. Most often, the capability of a NDT system for a certain inspection task remains unknown. In addition, this situation limits the application of NDE 4.0 in which the knowledge about the reliability of a non-destructive test plays a critical role.
This paper emphasizes the urgent need for standardization of reliability assessment of NDT on an international level and shows the outcome of the joint research project 'Standardization for probabilistic evaluation of the reliability of non-destructive testing systems (*normPOD*)' funded by the German government. The overall objective of the proposal is the preparation of a national standard on the reliability assessment of NDT. This standard specifies the procedure for the evaluation of NDT including: (i) the definition of the application, (ii) development and production of test specimens, (iii) statistical evaluation test results, (iv) the consideration of human factors and much more. In this way, the standard ensures comparability of reliability assessments and increases the acceptability of reliability assessments. In the current paper, reliability evaluation in terms of Probability of Detection (POD) is discussed based on a model-based approach for ultrasonic inspection of concrete structure with and without reinforcement and with different defect conditions. This work is carried out as one of the case studies under the civil engineering scenario as part of the development of *normPOD* standard for the reliability of NDT.

Keywords: Probability of Detection (POD); Standardization; Reinforced Concrete; Non-destructive testing (NDT).

1. MOTIVATION

Evaluation and assessment of existing structures becomes more and more important especially with regard to the increasing age of our infrastructure. In light of progressing deterioration, regular inspection and continuous monitoring form the basis to assess reliable data on the current condition of structures. Additionally, testing and monitoring provide model input parameters for existing structures or validate the model outcome. All these information enable decision making for further maintenance and undertaking interventions. The portfolio of available non-destructive testing and monitoring methods for condition assessment is constantly growing. However, even though the methods are more and more elaborated the comprehensive evaluation of their reliability receive none or only minor attention. Major reason for this neglect is the lack of knowledge on how to assess and interpret measurement reliability. To overcome this deficiency, there is a standard in preparation based on the research outcomes of the German *normPOD*-project [1],[2]. This standard provides the basic requirements on what to consider, how to perform and how to evaluate measurement reliability with respect to qualitative test methods. The generally accepted parameter

* Corresponding author: +49 - (0)40 - 6541 35 56, sylvia.kessler@hsu-hh.de

to quantify the measurement reliability of qualitative tests according to its detectability is the Probability of Detection (POD). Here, this paper highlights the specific challenges when applying the standard to NDT in civil engineering in order to assess a Probability of Detection.

2. BACKGROUND

A proper quality process requires the knowledge of the gap between defect indication and defect characteristic. Only with this knowledge, the construction and the maintenance of a safe component is possible as well as the determination of its end of service life. Thus, the evaluation of the Probability of Detection (POD) is the embodiment of reliability assessment.

The reliability of NDT systems is the result of several factors affecting the whole NDT process. Major factors are [3],[4]: (i) the *Intrinsic Capability,* which unites the physical principle and their limits to detect defects; (ii) the *Application Parameters*, which considers boundary condition during the time of measurement, (iii) the *Human Factors* describing the influence of any person involved in the process and (iv) the *Organizational Context*, which takes into account the complete process of the in-service inspection. In addition, if applied, also deep learning algorithms contribute to the reliability of NDT, which is defined as part of the *Algorithms*, which includes influences of different algorithms [5],[6]. This so-called modular model leads to a holistic description of the quality of a testing system. The neglect of one factor might affect the reliability evaluation. The response of the testing system while testing is only an indication. Due to the influences of the modular model, the result of the systems indicates, but does not prove the existence of a flaw.

This can be mainly due to variety of reasons such as the noise signals or the false alarms or false positives resulting an indication. These kinds of indications have to be dealt carefully otherwise, the components or the test objects might be rejected or replaced unknowingly resulting in the loss of money. These kinds of errors generally referred as type 1 errors. Alternatively, there could also be situations where there is no indications upon inspecting a test object that contains a defect. This can be due to different reasons such as the NDT technique used is not being capable or sensitive enough, also due to lot of uncertainties involved in the process, technique or methodology adopted. These kinds of errors are referred as false negatives or type 2 errors. From these two types of errors follows that the outcomes of any NDT technique have lot of uncertainties in providing consistent results. For example, when different number of flaws of same size are inspected, the NDT outcomes have different detection probabilities. Alternatively, repeated inspections of same flaw also do not provide consistent hit (detected) or miss (not detected) indications. Hence, it the NDT outcomes are influenced by several uncertainties and are probabilistic in nature [7]. This kind of probabilistic nature of NDT outcomes as well as its capability and reliability can be assessed using POD techniques. In order to account for all the uncertainties due to which the outcomes of NDT techniques vary, it is important to consider all the different influences as explained from the modular model. However, research on quantifying the influences due to human factors and organizational context are still in its infant stage while carrying out the reliability evaluations of the test systems [8]. Moreover, reliability evaluations of the NDT techniques especially used in the field of civil engineering is very limited. Hence, this contribution focusses on the evaluation of the Intrinsic Capability with some references to the Application parameters.

3. NDT IN CIVIL ENGINEERING

3.1 Inspection tasks in reinforced concrete structures

Most often, the application of NDT systems is the only tool to prevent failures. As such, the task of NDT is to get information from the tested object, which might indicate a threat for the later or current use of the component. Structural irregularities, degradation, flaws, constructive elements or material properties are typical tasks. For Civil Engineering (CE), typical inspection tasks at reinforced concrete structures with corresponding flaws are [9], see Table 1:

Table 1 Inspection tasks in reinforced concrete structures with corresponding flaws

Task	Flaw
Concrete cracks (vertical, horizontal)	Crack width, Crack length, Crack depth
Honeycombs	Volume, Diameter
Spalling	Area, Depth
Delamination	Area, Depth
Reinforcement corrosion	Area, Volume, Depth
Localization of metallic parts	Size
Cracks in tendons	
Incomplete grouting	Volume, Diameter

3.2 Reinforced concrete test specimens for POD evaluation

The reference specimens represent a model intending to provide a representation of selected characteristics regarding an application scenario for NDT. First, the definition of the flaw and its corresponding size is necessary in order to enable a POD evaluation. Then, the evaluation of the detectability demands specific individual reference specimens for the type of flaw of interest. The inspection test conditions should be representative of those that will be present at the time of typical inspections on-site. Unflawed specimen are also indispensable to preclude guessing and to estimate the rate of false indications. The aim is to establish the relationship between POD and target size that defines the capability of a NDT system under representative application conditions [10]. In addition, it is mandatory to know the true value of the value and its determination is often the most challenging step.

In general, the development of reference specimens is independent on the measurement method since some flaws are detectable with multiple methods. However, some inspection methods are prone to scaling effects and interferences due to the limitation from the size of the test specimen, which never occur under on-site conditions. These kind of boundary effects require special consideration.

For the design of specimens, numerical simulations might be helpful [11]. Here, geometry effects can be predicted accurately and structural noise levels can be adjusted for different concrete mix designs. Such simulations have proven to give quite realistic results, even when the simulation was only performed in two dimensions [12]. Especially for NDT methods like Impact Echo, where geometry effects are not easy to predict but have a strong effect on the inspection result, additional simulations can support the design of experiment. In this way, the creation of poorly designed specimens may be avoided, which also have positive ecological and economic effects as less concrete will be used in total. For the purpose of creating specimens with defects that may only be detected in some cases, which is the objective here, an understanding of the measuring equipment as well as a numerical model for the defect is necessary.

However, it is indispensable that the reference specimens represent the flaw as realistic as possible even though the implementation of the flaw is artificial. Therefore, this flaw type is a so-called “artificial defect”. The specimens should be designed in a way that the targets can be inserted, and the final geometry obtained by machining or other forming methods that will not change the target characteristics (size, shape, and orientation and intended location) [10],[13]. Flaws from specimens from on-site condition are “real defects”. The reliability analyses benefits from field-

removed specimens with real flaws. However, to collect sufficient number of field-removed specimens including certain flaw types for a specific scenario is unrealistic. Further limitations result from constraints, which prohibit providing the fully realistic geometry. These can be size limitations for transportability, which might provoke artefacts in the NDT results obtained.

The reliability evaluation of one flaw type requires multiple reference specimens. However, at the beginning of the reliability evaluation the range of the needed flaw sizes is usually unknown. Thus, the preparation of the reference specimens is an iterative process starting with a fixed flaw size and performing the first NDT measurement. Depending on the detectability of the flaw, further adaption in the next generation of test specimen is necessary. This iterative process could be very time-consuming and cost-intensive that are the main two reasons why data of reliability assessment of NDT in CE is scarce. However, preliminary numerical simulation of the test scenario can confine the required real flaw sizes. The target-oriented realistic and reproducible implementation of the flaw in the specimen is of vital importance. The description of the specimens design has to be as precise as possible to enable the reproduction of the specimens everywhere, to repeat the reliability evaluation and to enhance the basic data set and to achieve given confidence levels.

3.3 Challenges in production of reinforced test specimens

The design and production of reference specimen from reinforced concrete is a challenge. Reinforced concrete show a huge variation in reinforcement density, reinforcement layout, concrete type, geometry, etc. If a structure is built with cast in-situ procedure, the concrete varies from one batch to another; even though ordering the same concrete composition. Normally, each component in a structure demands other prerequisite regarding durability and load-bearing capacity. Therefore, most components have different concrete compositions. However, the reconstruction of the used concrete composition is very difficult as soon as the concrete is in a progressed hydration stage.

The environment and load history is specific for each structure/ component. Among other factors, most concrete properties are moisture, temperature and load dependent. Consequently, concrete properties change constantly over time and deterioration processes progress in different rates with high spatial variability. All these factors influence the reliability of the NDT system as well. No structure and no component equals another, each reinforced concrete structure is unique.

The specimens should closely mimic the local geometries. However, reference specimens are always a simplification due to several reasons such as limitations and constraints in the fabrication capabilities, limited understanding of the scenario, but also due to an intentional reduction of complexity, which requires awareness in order to keep the testing situation as realistic as possible [14].

After the preparation of the specimens, its storage or conditioning in a specific climate is of vital importance since the material properties should be in a range, which is expected on-site. Real civil engineering structures show parts, which are exposed to precipitation and chlorides while other parts of the same structure are sheltered. However, the exposure condition determines the deterioration processes, which in turn might affect the NDT. Therefore, the definition of representative storage condition is an important step. Additionally, most parts of a civil engineering structure are under static load conditions such as tension and compression and due to traffic, wind, etc. exposed to dynamic loading. If the reference specimens needs to be tested under static or dynamic loads, is to be discussed for each measurement scenario individually. Another issue is the surface condition of the reference specimens, which has a huge impact on the Application Parameter. Under real exposure condition, the surface suffers from scaling due to mechanical impact or freeze/ freeze-thaw attack. Normally the cement stone matrix deteriorates first or single aggregates pop out. Consequently, the concrete surface is no longer a flat, even surface which could impair the coupling of the inspection method.

3.4 POD-Analysis

After the performance of the measurements, it is necessary to specify the suitable stochastic POD approach for the evaluation of the data set. These POD studies can be carried out using both non-parametric and parametric based approaches. The non-parametric POD approaches are based on binomial distributions for example, the 29/29 method [15] etc. However, these methods are highly dependent on very large number of sample sizes for obtaining reasonable confidence bounds on the POD curve. Under the absence of large number of samples, parametric based POD functions

such as a log odds function or cumulative log normal distribution functions can be used [16]. However, these parametric methods are mainly divided in to two types such as the binary [17] and the signal response [18] methods depending on the type of NDT outcome i.e., either qualitative or quantitative. In the case of NDT techniques producing qualitative outcome in terms of the binary responses such as the “1 or HIT” (defect detected) or “0 or MISS” (defect undetected) (in case of penetrant inspection, magnetic particle, etc.), HIT-MISS methods are used. In the case of NDT techniques producing quantitative outcome in terms of a signal response such as an amplitude (in case of Ultrasonic inspection) or volt (in case of eddy current inspection), â (signal response) vs. a (defect size) approaches are used. Both approaches like hit-miss or signal response methods aim to produce POD curves and the outcome of a POD curve is the $a_{90/95}$ (reliably detectable crack size with 90% probability and 95% confidence) value. This $a_{90/95}$ value helps in taking right decisions for approving components during inspection, identifying maintenance schedules, etc. This $a_{90/95}$ value is obtained from the intersection of the lower 95% confidence curve of the POD curve at 90% probability level as shown in Figure 1 [19].

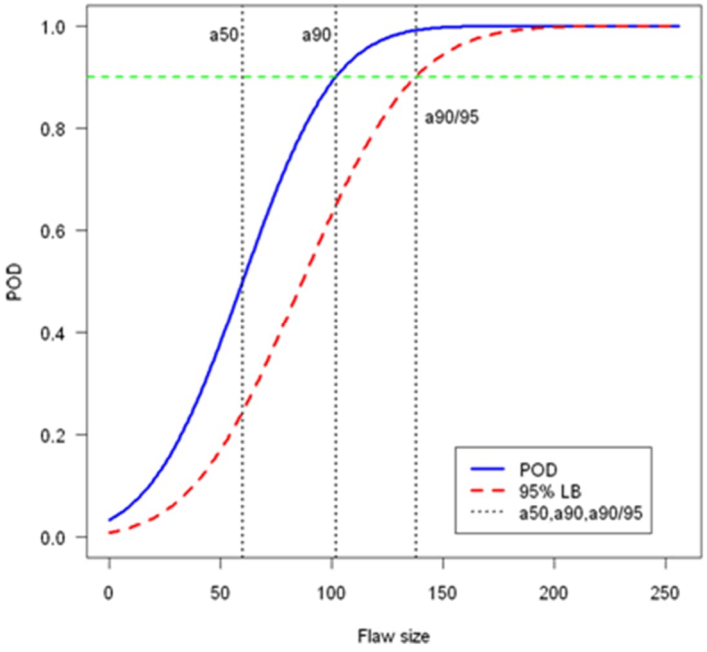

Figure 1: POD curve showing a_{50}, a_{90} and $a_{90/95}$ points

Conventionally, POD curves of NDT techniques are only a function of one defect parameter such as crack length. However, for many of the quantitative NDT techniques the defect response is often a function of multiple defect parameters. For example, in the case of ultrasonic inspection of fatigue cracks, the crack orientation plays a vital role in estimating the POD of the technique. If the crack orientation is parallel to the incoming sound beam, the amplitude of the reflections of the waves is smaller when compared to the perpendicular orientation of the crack. Accordingly, the resulting POD of the technique could be higher or lower. In addition, for the cases where defect length alone does not correspond to the defect severity, the POD of the NDT technique cannot be determined only as a function of defect length. Hence, estimating the POD as a function of defect length alone is not a reliable estimate in cases where other defect parameters such as width, depth, orientation etc. have large influence on the POD. If the POD was estimated as a function of crack length alone even under the influence of various defect parameters, there might be a risk in accepting a component with a critical defect or rejecting a component with a defect, which is not critical for the application. Hence, in the case of influences by many different parameters of the defects, multi-parametric POD approaches [20]-[22] provide viable solutions. However, majority of the POD approaches requires huge number of samples in order to account for all the statistical uncertainties. In case of a limited data base due to insufficient number of measurements advanced POD approaches can still enable the POD evaluation. It is obvious, that that the variety of the reliability approaches offers the possibility on the one hand to choose the right method for each situation. On the other hand, it is a complex process to select the useful models. Therefore, the standard will help for the selection of the approaches and understanding the results of the integration of the statistical model.

The standard allows a specific procedure, how to perform a useful analysis. Especial in the case of integration of the statistical framework a number of software tools and a large amount of scientific literature can help to choose the right procedure. However, the general procedure would excess the content of this article.

A new approach of the standard is the context-related characteristics. Through the recent past, a large number of reliability evaluations were developed. However, just for an example, the POD number is not comparable with another POD number. The main information is related to the context and the question raised before starting the evaluation. Due to the standard, it is possible to have variety of characteristics can be created over the process of developing a testing method, or within the introduction of the testing method into the technical use. Therefore, the understanding of the characteristics and the assessment of the context, after calculating the characteristics is as important as the collecting of the data or the choosing of the right statistical model. However, the standards also allows to calculated POD-curves beside the strong requirements of the structural integrity evaluation normally used in e.g. for NDT evaluation of components in nuclear industry.

4. CASE STUDY

In a first case study, the aim is to create POD curves for ultrasonic inspection solely from simulation data. The numerical simulations apply the elastodynamic finite integration technique (EFIT) [23] on a fictional specimen with dimensions $1.2 \cdot 1.2 \cdot 0.45\ m^3$. The specimen contains concrete with 75 vol.-% aggregates following an A/B16 grading curve. The porosity of the specimen is 2 vol. %. [24],[25] shows a detailed description of the numerical concrete generation. There are two variations of this specimen: (i) the specimen containing only concrete and (ii) the specimen containing also steel reinforcement. The steel reinforcement consists of rebar with a diameter of 10 mm and a cover depth of 55 mm. The distance between the rebar is 12 cm.

The simulations are carried out in a way, that the source and receiver positions have the same configuration as the used device. Defects are assumed spherical cavities in order to reduce the amount of degrees of freedom, so that only the location and size of the defects vary, while the spatial orientation remains the same. The position of the defect depths are 10 cm or 20 cm measured from the top of the defect, respectively. The defects are located at three different positions with respect to the source locations: POS1, where the defects are located right underneath the source, POS3, where the defects are located underneath the receiver farthest away from the source and POS2, where defects are located right in the middle between POS1 and POS3, see Figure 2.

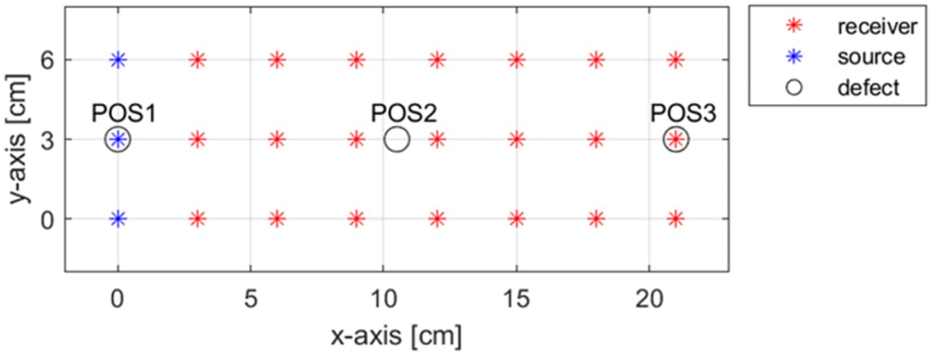

Figure 2. Top view of the simulation setup. The defects vary in size and depth, but their lateral position is restricted to one of the three possible positions

For each scenario, the numerical simulation considers as well one defect-free scenario as a reference measurement for every configuration. For every simulation, the theoretical arrival time of the defect reflection signal is calculated and the maximum amplitude is picked from a time window starting at the arrival time and having the same duration as the source wavelet. The normalization of the amplitudes obtained considers the maximum signal amplitude multiplied by 100 to obtain the percentage of the maximum amplitude.

This kind of amplitude data with respect to different defect sizes that are simulated are processed using signal response based parametric POD approach as explained earlier using cumulative lognormal distribution function. In order to obtain the $a_{90/95}$ value, 95% lower confidence bound of the POD curve is plotted using Wald method or Cheng and Iles confidence interval method [7].

Figure 3 shows the POD curves obtained for different numerical conditions. Figure 3 (a) and (b) shows the a_{90} and $a_{90/95}$ values obtained from POD curves for a defect located at 10 cm depth at POS1 position in both - without (a_{90} = 1.24 cm and $a_{90/95}$ = 1.47 cm) and with (a_{90} = 2.51 cm and $a_{90/95}$ = 4.16 cm) steel in the concrete. Figure 3 (c) shows the a_{90} and $a_{90/95}$ values obtained from the POD curve for a defect located at 20 cm depth at POS1 without steel with 3.91 cm and 4.54 cm, respectively. Comparing the results with and without reinforcement, Figure 3 (a) and (b), it can be noticed that the concrete with reinforcement obtains larger a_{90} and $a_{90/95}$ values i.e., the detectability decreases with respect to the detectability in concrete without reinforcement. One possible explanation is the decrease in the signal amplitudes in reinforced concrete due to additional scattering, transmission and damping of the waves as well as the geometrical spreading due to the reinforcement in the concrete [26]. However, reinforcement is an indispensable component in most concrete structures. Thus, the inspection technologies, methodologies, etc. require further improvement and further research is needed to identify the best ways of decreasing the scattering and damping of waves in structures due to the reinforcement. Figure 3 (c) shows the a_{90} (3.91 cm) and $a_{90/95}$ values (4.54 cm) obtained for defects at 20 cm depth without steel. Hence, the deeper the defects is in the structure, the more difficult is its detection as the a_{90} and $a_{90/95}$ values are larger for defects at 20 cm deep in concrete without steel when compared to the defects at 10 cm deep in concrete without steel.

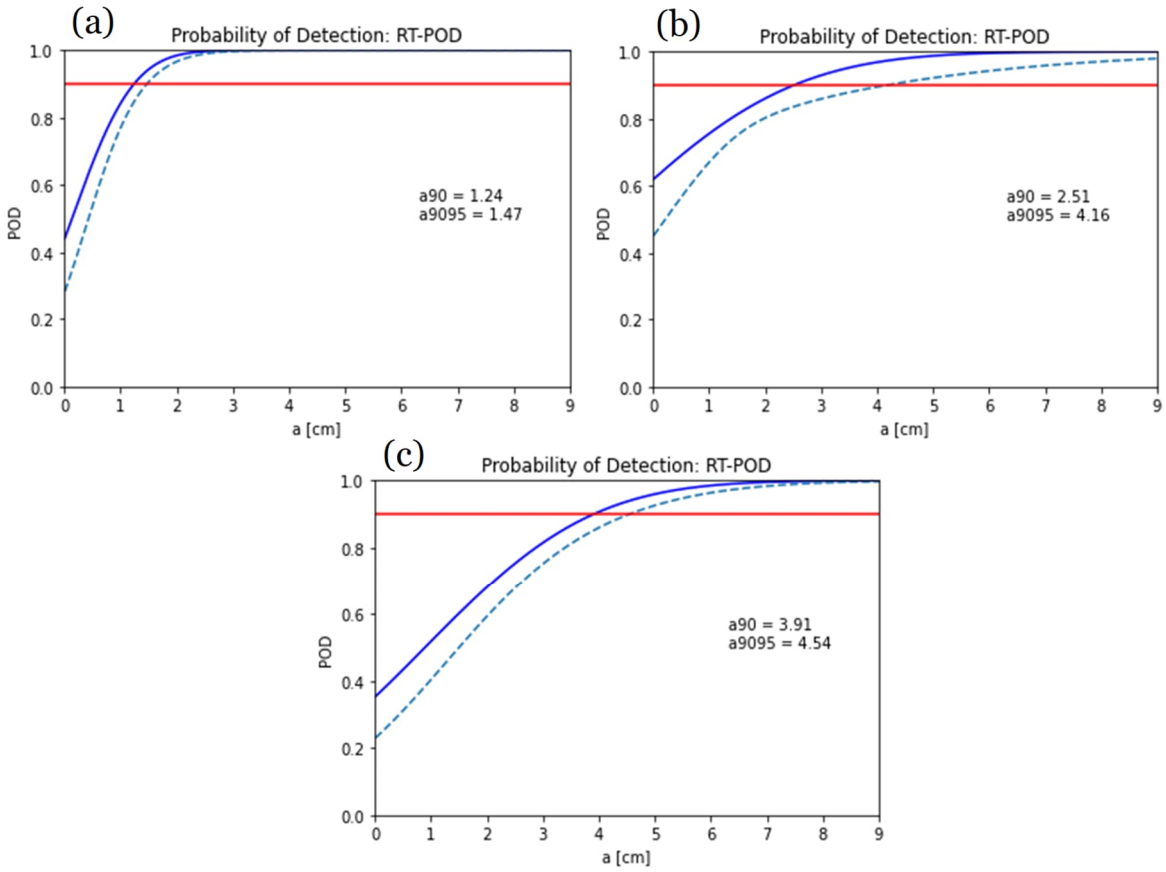

Figure 3. POD curves obtained for different conditions (a) defect located at 10 cm depth in concrete and without reinforcement (b) defect located at 10 cm depth in concrete and with reinforcement and (c) defect located at 20 cm depth in concrete and without reinforcement

Moreover, Table 2 shows the a_{90} and $a_{90/95}$ values obtained for all the different conditions of simulations performed such as for the defects at both 10 cm and 20 cm depths and at different positions in concrete with and without steel. From Table 2, it can be observed that the a_{90} and $a_{90/95}$ values of POS1 are better i.e., smaller when compared to the a_{90} and $a_{90/95}$ values of both POS2 and POS3. In addition, the largest a_{90} and $a_{90/95}$ values are for the defect positions at POS3. This signifies that the detectability or the POD is much sensitive to the defects present at position POS 1 when compared to position POS3. This is mainly due to the presence of defects much closer to the source in the case of position POS1 and hence, it can receive and transmit higher magnitudes of signals when compared to the position POS3, which is located far away from the source location. In addition, as the POS2 is the position that is exactly half way between the positions POS1 and positions POS3,

the a_{90} and $a_{90/95}$ values are exactly in between the a_{90} and $a_{90/95}$ values obtained from both POS1 and POS3 positions.

Table 2: a_{90} and $a_{90/95}$ values obtained for different boundary conditions

	10cm_no steel		10cm_steel		20cm_no steel	
	a_{90} [cm]	$a_{90/95}$ [cm]	a_{90} [cm]	$a_{90/95}$ [cm]	a_{90} [cm]	$a_{90/95}$ [cm]
POS1	1.24	1.47	2.51	4.16	3.91	4.54
POS2	1.67	2.16	NA	NA	4.55	5.53
POS3	1.93	3.6	2.14	4.85	4.14	5.52

5. ROUGH OVERVIEW ON THE FUTURE STANDARD

As the case study illustrates, each step in the reliability evaluation is generalizable in order to include probability studies in quality management. Consequently, the future standard compiles all the knowledge to provide a guideline on how to obtain comparable and trustworthy reliability evaluations see Figure 4.

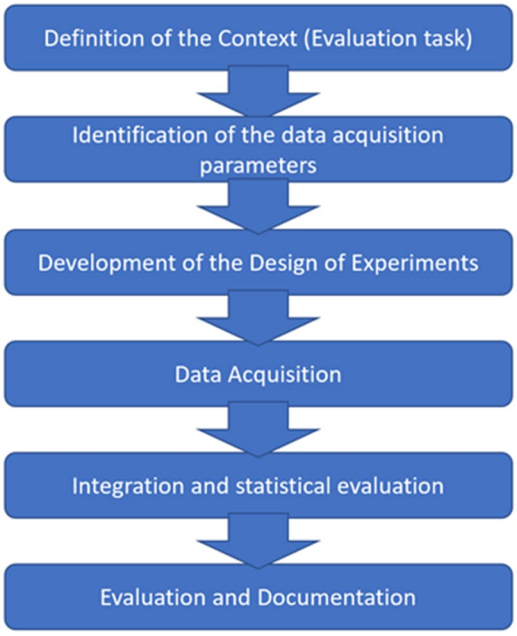

Figure 4. Schematic for a generalized reliability evaluation approach

5.1 Definition of the context - evaluation task

The first essential step is the definition of the context. There are multiple mistakes, which might influence the result of the evaluation, i.e. the neglect of essential parameters or the insufficient number of data for statistical requirements. The following list provides a selection of criteria, which reflect also the future content of the standard:

- Evaluated testing application: Besides the selection of the testing method (ultrasonic testing, radiographic testing or eddy current testing etc.), there shall be a description of the equipment, used probes and sensors.
- Tested components: Design, production process, possible defects and the variation of the component geometry are essential parameters (e.g. material variation within one component).
- Evaluation aim: The aim of the evaluation requires a precise description. For example, is it the aim to validate a new technology or is it the comparison of two testing application to each other? Is it the aim to get a rough estimation according its

realisation or is it necessary to answer safety critical question for the structural integrity?
- Level of development of the testing application: Is there a specific framework for the evaluation or is it possible to have an overview over all relevant influences (tests in laboratory vs. in the field).

The specification of the testing task reduces the costs of the evaluation and focuses on the evaluation and the context of the application.

5.2 Identification of the Data Acquisition Parameters

The second step of the evaluation is the identification of the parameters for the data acquisition based on the evaluation task.

- Identification of the NDT/E response: binary (indication / no indication) or continues signal
- Definition of the true value
- Identification and handling of other influences, see modular model
- Definition of the Key Performance Indicators (KPIs): $a_{90/95}$ of a POD evaluation, False Alarm Rate, Precision etc.
- Inclusion of Human Factors

5.3 Development of the Design of Experiments

The focus of the Design of Experiments is the definition of necessary steps to accomplish the evaluation:

- Defect geometries, positions, types (defect sizes, real/realistic/artificial defects)
- Number of components (real or simplified components)
- Definition of the testing environment
- Number of operators and experts for the data acquisition and evaluation
- Limitation of specific environmental influences (usage of robots)
- Method of evaluating Human Factors

5.4 Data Acquisition

Besides experimental data, also the inclusion of results from simulation and technical assessments also known as a-priori knowledge is possible.

- Recording of the data
- Outlier test
- Statements about physical relationships
- Evaluation of potential noise sources
- Definition of thresholds (e.g. decision, reporting, saturation threshold)

5.5 Integration and Statistical evaluation

In the integration of the statistical methods, commercial software packages might be useful as long as the specific method, how the program is doing the statistical calculations, e.g. approximation approaches, is transparent:

- Estimation of the mathematical models (e.g. logistic regression for Hit/Miss)
- Estimation of the statistical confidence (e.g. confidence intervals of 95%)
- Evaluation of the data (e.g. with MIL-HDBK-1823a software program [10])

5.6 Evaluation and Documentation

The final step is the evaluation of the statistical results with respect to the context:

- Assessment of the statistical statement
- Evaluation with respect to the context and according to the defined aim

- Transparent and comprehensive documentation in regard to the decision aims
- Final decision making

The presented steps suggest a successive procedure. However, in reality, the process exists of feedback and decision loops. A typical example is that during the influence analyses unknown influences pop up, which were not under consideration during the preparation of the analysis.

6. CONCLUSIONS

The periodic inspection and/or continuous monitoring of our infrastructure plays a critical role in ensuring its safety, serviceability and reliability. The focus is to assess the likelihood of damage and to evaluate the potential consequence in terms of safety and serviceability. Nowadays, the inspection strategy considers the structure type, age, condition, importance, environment, loading, prior problems, and other characteristics that contribute to the reliability and durability of reinforced concrete structures.

Thus, the decision-makers responsible for the preservation and maintenance or our infrastructure need to understand the importance of the reliability of a NDT system including the influence of the NDT reliability on the decision-making process. Moreover, knowing the POD leads to the outstanding advantage that the Bayesian Updating of conditions states is possible [27],[28]. Therefore, in future the inspection strategy should consider the reliability of the used testing methods as well. Otherwise, the inspection resources are not used effectively.

Each POD evaluation starts with the definition of the NDT task, the identification of the data acquisition parameters and the design of the corresponding reference specimen and eventually, with the design of complementary numerical simulations. After the data acquisition follows the statistical analyses complemented by the proper interpretation and documentation. The upcoming standard addresses all these steps in detail and provides further guidance in order to obtain comparable and trustworthy reliability evaluations for NDT also in civil engineering.

However, much more research needs to be dedicated to this issue especially in the field of civil engineering since reinforced concrete is one of the most used and most diverse materials. The evaluation of inspection or monitoring reliability needs time, expert knowledge and financial foundation. In civil engineering, we are just at the beginning of understanding the detectability of our NDT systems.

ACKNOWLEDGEMENT

The authors gratefully acknowledge the funding of the project ‘Standardization for probabilistic evaluation of the reliability of non-destructive testing systems (*normPOD*)’ by the German Federal Ministry for Economic Affairs and Climate Action under the signature 03TN0006A.

REFERENCES

[1] D. Kanzler, V.K. Rentala, M. Bertovic, T. Heckel, V. Tkachenko, J. Given, S. Keßler, F. Dethof, A. Jüngert, J. Vrana, „Lasst uns mal POD standardisieren!“ *DGZfP-Jahrestagung* 2022, Kassel, May, Germany (DGZfP 2022)

[2] Dethof, F.; Rabe, U.; Keßler, S. “Numerical investigation of near and far field ultrasound transducer radiation characteristics in concrete”. *The International Symposium on Nondestructive Testing in Civil Engineering* (NDT-CE 2022), 16.-18. August 2022, Zürich, Switzerland

[3] Holstein, R., Bertovic, M., Kanzler, D., Müller, C (2014). „NDT Reliability in the Organizational Context of Service Inspection Companies”. *Materials Testing* 56, 7-8, 607–610.

[4] Müller, C., et al. (2016). “Conclusions of the 6th European American Workshop on reliability of NDE”. *AIP Conference Proceedings*. Vol. 1706. No. 1. AIP Publishing.

[5] D. Kanzler, V.K. Rentala, (2021) “Reliability Evaluation of Testing Systems and Their Connection to NDE 4.0”, Meyendorf N., Ida N., Singh R., Vrana J. (eds*) Handbook of Nondestructive Evaluation 4.0*, pp 1-34. Springer, Journal of Nondestructive Evaluation.

[6] V.K. Rentala, D. Kanzler, P. Fuchs, “POD Evaluation: The Key Performance Indicator for NDE 4.0”, *Journal of Nondestructive Evaluation*, 41, 20, 2022

[7] Berens, A.P.: “NDE reliability data analysis: non-destructive evaluation and quality control”. *Metals Handbook*. 9./17, pp. 689–701. Materials Park, Ohio: ASM International (1989).

[8] M. Bertovic, J. Given, V.K. Rentala, J. Lehleitner, D. Kanzler, T. Heckel, V. Tkachenko, “Human Factors in der POD - ist das möglich?” *DGZfP Jahrestagung 2022*, Kassel, May, Germany (DGZfP 2022). More info about this article: http://www.ndt.net/?id=27036

[9] Wiggenhauser, H.; Azari, H. (2017). “Classification of Nondestructive Evaluation Tasks for Reinforced Concrete Structures”. *Journal of Infrastructure Systems* 23, 4, S. 4017021 https://doi.org/10.1061/(ASCE)IS.1943-555X.0000378 .

[10] MIL-STD-1823 (2009). “Non-destructive evaluation system reliability assessment”. U.S. Department of Defense.

[11] Kessler, S., Gehlen, C., (2017). „Reliability evaluation of half-cell potential measurement using POD”. *J. of Infrastructure Sys* 23 (2), doi.org/10.1061/(ASCE)IS.1943-555X.0000334

[12] Dethof, F., Alernon, D., Thrunherr, C., Keßler, S. “How to conduct Impact Echo simulations for non-destructive testing at concrete structures for the nuclear industry” *NDE NucCon 2023 - International Conference on Non-destructive Evaluation of Concrete in Nuclear Applications* January 25-27, 2023, Espoo, Finland

[13] ENIQ RECOMMENDED PRACTICE 5 (2011). “Guidelines for the design of test pieces and conduct of test piece trials”. Issue 2, *ENIQ report No 42*, doi:10.2790/33727

[14] Algernon, D., Walther, A., Denzel, W., Ebsen, B., Feistkorn ,S., Friese, M., Grosse, C.U., Kathage, S., Kessler, S., Köpp, C., Krause, M., Maack, S., Schickert, M., Taffe, A., Timofeev, J., Wilcke, M., Wolf, J. (2018). „Test Specimen Concepts in Regard to Quality Assurance and Validation of Nondestructive Testing in Civil Engineering”. *International Symposium Non-Destructive Testing in Civil Engineering* (NDT-CE 2018), New Brunswick, USA.

[15] Rummel Ward, D., Rathke Richard, A.: “Flaw Detection Reliability Assessment and Analysis”. *DTIC Report*-ADP000013 (1982).

[16] V.K. Rentala, P. Mylavarapu, A. Kumar, J.P. Gautam, G. Kakkropath, T. Jaya Kumar, “POD of NDT Techniques Using High Temperature Oxidized Fatigue Cracks in an Aero Engine Alloy”, *Journal of Nondestructive Evaluation*, 40, 41 (2021).

[17] V.K. Rentala, P. Mylavarapu, J.P. Gautam, V. Kumar, “Generation of POD Curves in the Absence of Service Induced Cracked Components - An Experimental Approach”, *Insight-Nondestructive testing and condition monitoring*, Vol 61, No 1, January 2019.

[18] V.K. Rentala, P. Mylavarapu, J.P. Gautam, “Issues in Estimating Probability of Detection of NDT Techniques – A Model Assisted Approach”, (Elsevier) *Ultrasonics* 87 (2018) 59–70.

[19] Meeker, W.Q.: “R.B.Thompson’s contribution to model assisted probability of detection”. *AIP Conf. Proc*. 1430, 83–94 (2012)

[20] M. Pavlovic, K. Takahashi, U. Ronneteg, C. Müller, “Multi-Parameter Influence on the Response of the Flaw to the Phased Array Ultrasonic NDT System. The Volume POD”, *4th European-American Workshop on Reliability of NDE*, (2009).

[21] D Kanzler, C Müller, J Pitkänen. „Probability of detection for surface-breaking holes with low-frequency eddy current testing - a non-linear multi-parametric approach”, *Insight* 56 (2014). DOI: 10.1784/insi.2014.56.12.664.

[22] N. Yusa, J.S. Knopp, “Evaluation of probability of detection (POD) studies with multiple explanatory variables”, *J Nucl Sci Technol* 53 (2016) 574–9.

[23] Fellinger, P., Marklein, R., Langenberg, K. J., & Klaholz, S. (1995). „Numerical modeling of elastic wave propagation and scattering with EFIT—elastodynamic finite integration technique". *Wave motion*, 21(1), 47-66.

[24] F. Schubert and B. Köhler, "Numerical time-domain simulation of diffusive ultrasound in concrete," *Ultrasonics,* no. 42(1-9), pp. 781-786, 2004.

[25] F. Dethof und S. Keßler, „Simulation von Impakt Echo Inspektionen in Beton zur Analyse der Detektionswahrscheinlichkeit," in *DGZfP Jahrestagung*, Kassel, 2022.

[26] L. Fülöp, M. Ferreira, A. Tuhti, G. Rapaport, "Assessing the challenges of condition assessment of steel-concrete (SC) composite elements using NDE", *Case Studies in Construction Materials*, Volume 16, June 2022, e00887

[27] Tang, W.H. (1973). "Probabilistic Updating of Flaw Information". *Journal of Testing and Evaluation*. Vol. 1, No. 6, 1459-467.

[28] Kessler, S., Gehlen, C. (2015) "Probability of Detection of Potential Mapping and its Impact on Service Life Prediction". *Proceeding 12th International Conference on Applications of Statistics and Probability in Civil Engineering*, ICASP12 Vancouver, Canada, http://hdl.handle.net/2429/53300

ACES: A Teleoperated Robotic Solution to Pipe Inspection from the Inside

Eric Lucet* and Farès Kfoury
Université Paris-Saclay, CEA List, F-91120 Palaiseau, France
{eric.lucet, fares.kfoury}@cea.fr

ABSTRACT

This paper presents the definition of a teleoperated robotic system for non-destructive corrosion inspection of Steel Cylinder Concrete Pipes (SCCP) from the inside. A general description of in-pipe environment and a state of the art of in-pipe navigation solutions are exposed, with a zoom on the characteristics of the SCCP case of interest (pipe dimensions, curves, slopes, humidity, payload, etc.). Then, two specific steel corrosion measurement techniques are described. In order to operate them, several possible architectures of inspection system (mobile platform combined with a robotic inspection manipulator) are presented, depending if the mobile platform is self-centred or not and regarding the robotic manipulator type, namely a basic cylindrical manipulator, a self-centred one, or a force-controlled 6 degrees of freedom (DoF) robotic arm. A suitable mechanical architecture is then selected according to SCCP inspection needs. This includes relevant interfaces between the robot, the corrosion measurement Non-Destructive Testing (NDT) device and the pipe. Finally, possible future adaptation of the chosen solution are exposed.

Keywords: Robotic NDE; steel cylinder concrete pipes; remote inspection.

1. INTRODUCTION

This work is carried out in the scope of the ACES European research project. The mission of ACES is to assess the integrity of concrete infrastructure of nuclear power plants. In particular, one task focuses on inspection of SCCP from the inside by means of robotic mobile manipulator, aiming to assess chloride induced corrosion of steel in SCCP. Several types of inspection are usually carried out from the outside whenever possible, as they are confined areas, difficult to access by an operator. However, since steel corrosion initiates on internal surface of the steel liner, it is necessary to perform inspection from the inside of pipes to detect corrosion on early stages, before waterproofing provided by the steel liner is broken. Within this work, a prototype of a mobile robotic platform suitable for carrying out steel corrosion inspection from the inside of SCCP is designed, implementing a NDT technique.

The definition of such a mobile manipulator depends on mainly two critera, namely:

1) The inspected section geometry and its changing, like T sections, elbows, diameter change, etc.

2) The device and the process of corrosion measurement with their constraints; for example the acquisition time and the footprint of one measurement, the number of measurements in one position, the need of contact, angle position, etc.

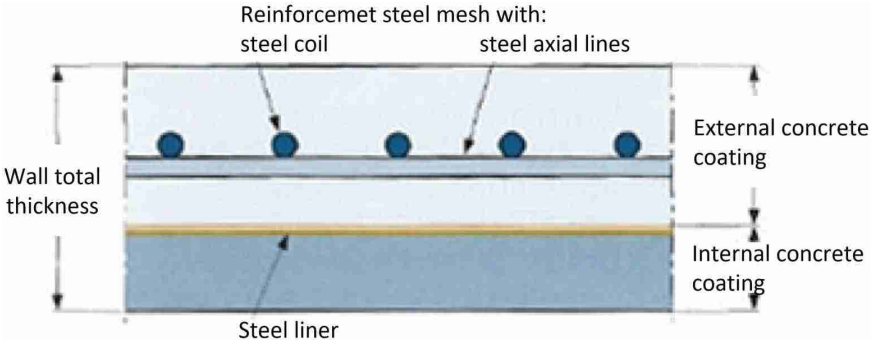

Figure 1. SCCP structure diagram

2. STATE OF THE ART IN-PIPE NAVIGATION SOLUTIONS

2.1. In-pipe environment

If many solutions for navigation in pipe exist, it is mainly because of the different possible geometries of the navigation environment and the necessary functionalities. Indeed, the network may vary in diameter range, material, fluid inside, with different joint configurations. Furthermore, each of these in-pipe configurations could be found in any orientation and possibly even consecutively, for example encountering two consecutive bends. Developing a single mobile platform to solve all of these problems in a wide range of diameters would require a fleet of multiple systems in different class sizes (example of modular and articulated-segmented design solution in [1]. Similar issues would be encountered for a robotic arm. Common encountered in-pipe bends and joints are the following [2]:

- Horizontal constant-diameter sections are the baseline for in-pipe complexity.
- Changes in diameter are a common occurrence; many robots take measures to prepare for this obstacle specifically.
- Elbows are commonly encountered and are often described in terms of their bend radius; lower radius bends being harder to navigate.
- T-Sections are challenging obstacles due to their lack of wall support; only sophisticated robotic platforms can navigate these (example of suitable two wheel chains mobile platform design in [3]).
- Vertical sections require a traction method that must also overcome gravity.
- Valves are particularly difficult because such plug valves can split the cross-section in two, obstructing full passage robots.

The context of this study includes the four first configurations, the last two being out of scope. It is in the light of these types of constraints and also of targeted applications that possible designs of mobile platforms and robotic arms are considered.

Preventive corrosion measurement is to be performed in areas where it is constrained to send people, to plan in advance the replacement of sections or repairing that will limit the deterioration of the concrete. Curative aspects are not considered here.

Considering an operational SCCP pipe network, different configurations might be encountered:

- High percentage of humidity (95 %) inside the pipes which, apart from maintenance operations, are usually filled with salt water.
- Slope up to 30° (vertical section parts not considered).
- Pipe inner diameter range from 600mm to 1000mm with a conical connecting part of a maximum angle to be set (example of this angle in blue Figure 2).
- 90° horizontal elbows with a minimum radius of curvature of about 3 times the pipe diameter (known as 3D Elbows).
- Passage by junctions such as T-sections or merging area (only navigation, no measurement).
- Hard bumps and irregularities up to 25mm thick at pipe joints.

Last constraint is especially true since the measurement at these joints is necessary. Start and end joints as well as the inside of bends and diameter change cones are also critical measurement areas. In addition, clearance issues are to be investigated with regard to these irregularities, which may also be caused by vegetation in pipes.

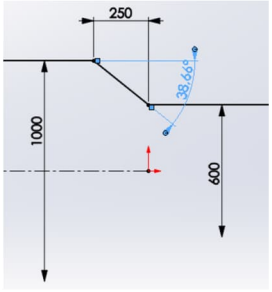

Figure 2. Lateral section of a diameter-varying pipe (lengths in mm)

2.2. Sate of the art of locomotion solutions

The pipe considered here is a SCCP as part of a nuclear power plant's concrete infrastructure. However, the need would remain similar in oil and gas pipelines, water pipelines, sewerage system or any piping systems that require specific inspection.

Main remaining weaknesses of existing solutions to be overcome are their maneuverability, meaning difficulties maneuvering inside a pipe with different diameters, curves or bends, and T joints, causing robots to be regularly found stuck during an operation because of a lack of stability and motion efficiency. Then, such issues of geometric changes in the pipe have also to be addressed.

We do not consider here specifically pipe climbing robots in vertical pipes, a review of 41 of such systems being available in [4]. Similarly, outer-pipe robots are not a topic of interest here, focusing on in-pipe robots. On the other hand, some robotic solutions designed for pipe diameters whose values are outside our scope are reported anyway, as relevant mechanical architecture examples can still be considered to be used at different diameters.

The first objective of the robotic platform is to be able to move inside a cylindrical pipe, meaning to generate traction in such an environment. For that, four in-pipe traction methods are possible [2]. Firstly, the gravity to propel on the floor restricts to only horizontal and slightly inclined pipes. Mass of the robot, as well as the geometry and composition of its contact zone affect the in-pipe wall adhesion. Secondly, wall-pressing consists of using the reaction force from the enclosed walls, usually in combination with a diameter adjustment mechanism. Third, wall magnetic adhesion is possible in ferrous pipelines that allow the production of reaction force through magnetics. Fourth, fluid Flow with the use of the transport medium to move, usually in combination with a passive Pipeline Inspection Gauge (PIG) or propeller device. In the context of this study, only the first two solutions are available, the pipes being made of concrete with an integrated steel sheet that is difficult to access for a reaction, and the measurements being made in a pipe emptied of any fluid.

Thus, based on a recent article [5], that is an extension of previous surveys on in-pipe robotic approaches for the inspection of unpiggable pipelines [2], on water in-pipe inspection robots [6], on in-pipe inspection robots from 1994 to 2010 [7], and on in-pipe hybrid locomotion robots from 1994 to 2012 [8], and completing it with other scientific papers about large-diameter in-pipe robots [9] and industrial solutions, a review of possible types of in-pipe inspection mobile robotic systems is proposed in the aim of direct to a choice of mobile platform solution for our needs. In addition, this gives inputs for a more complex optimized next generation inspection robotics system solution. This review is presented in the following by mobile platform architecture categories.

2.2.1. Wheel type robot

Wheeled robots are the simplest method of in-pipe locomotion. They are the most prevalent method because of their adaptability and ease of combination with other locomotion types, excluding tracks, to create hybrid in-pipe systems. Wheeled systems are also predominantly used with wall-press traction methods.

One of the first wall-pressing systems was the MOGRER in-pipe robot, developed by Niigata University around 1987 [10] for climbing angled pipes against gravity, from 520mm to 800mm in-pipe diameter. It was an improvement of the previous FERRET-1 design with the spring system forming a scissor structure similar to a pantograph mechanism (see Figure 3). Only one of the three wheels is actuated, and the robot is turning automatically following the pipe shape by wall-pressing. As another example of wheeled robot architecture, the two-modules NTU-Navigator robot was developed by National Taiwan University [11]. Its driving module consists of a worm gear, a DC motor and a driving wheel, and its steering module is composed of a servo motor and two steering wheels. The height of the robot is self-adjustable by a spring linked to the upper wheel (see Figure 4) for in-pipe diameter from 180mm to 250 mm. A concept from the University of California Irvine (see Figure 5) is proposed to apply a carbon-fiber coating to the in-pipes walls in order to fix them. A sensor is used to measure contact pressure against the pipe wall.

Figure 3. MOGRER in-pipe robot [10]

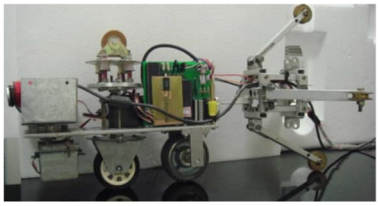

Figure 4. NTU-Navigator robot [11]

Figure 5. UCI pipe repair robot

One can also cite the MRINSPECT robots for 130mm to 180mm in-pipe diameter (see Figure 6) from Sungkyunkwan University of Suwon, Korea [12], or the flat two wheel chains robot [3] with one steering wheel and one driving wheel at each wheel chain, suitable for T-sections from 80mm to 100mm in-pipe diameter (see Figure 7).

Figure 6. MRINSPECT VI and VI+ robots [13]

Figure 7. Flat robot with two wheel chains [3]

The SVM-RS robot [14] was designed by the Fraunhofer in Germany to clean and measure damage of large concrete pipes diameter between 1600mm to 2600 mm. It is four-wheel driven (see Figure 8). Its three degrees of freedom servo-controlled arm (see Figure 9) can pivot around a main axis and has two independent telescopic arms, a nozzle bank on the upper end of the arm and an ejector nozzle on the lower end. Navigation sensors are cameras and position relative to the pipe measuring sensors including inclinometer and seven light section sensors that use laser lines. The robot is linked to a cable with fibre optics and electrical wires for communication and energy, that is reinforced to be able to pull it in case of failure.

Figure 8. SVM-RS robot front view [14]

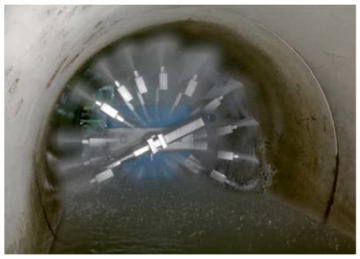

Figure 9. SVM-RS cleaning tool at rear [14]

2.2.2. Track / caterpillar / crawler type robot

Tracked robots, also known as caterpillars or crawlers, are used as an alternative to wheeled systems. Their large surface contact area generates high friction and reduce chances of losing wall contact. Tracks are more stable but also generally larger than wheels. They are used mainly for wall-pressing, and also for gravity alone. A classical design can be illustrated with a sewer cleaning and inspection robot (see Figure 10) designed by the department of Mechatronics of the University of Technical Education of Ho Chi Minh City, Viet Nam [15]. It is able to work underwater in pipes with diameters ranging from 300mm to 600 mm. As a more complex example, Paroys-II robot [16] is using an actively controlled pantograph mechanism with a partially passive spring mechanism, and a second set of articulated caterpillar tracks for an increased adaptive range from 400mm to 700mm in-pipe diameter.

Figure 10. Sewer cleaning and inspection Robot [17]

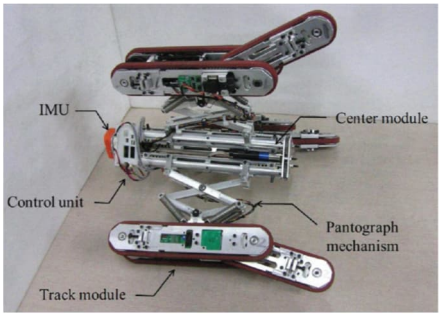

Figure 11. Paroys-II robot [16]

A pipeline cleaning robot (see Figure 12 and Figure 13) from the Chinese Wuhan University of Technology [18] is able of self-adaption to variable cross-section pipe diameter from 150mm to 450mm by using an umbrella-like and lifting structure. Touch sensors at umbrella arms extremity are used for a closed-loop regulation of both lift and open-and-close motors. Also, the stability of the robot body posture is ensured by using a three-arms tail positioning empennage system. A strain gauge measuring the pressure is pasted on the robot tail to collect the tail curvature signal for controlling the tail open-closed angle.

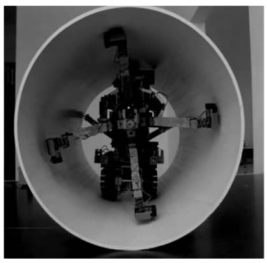

Figure 12. SVM-RS robot front view [18]

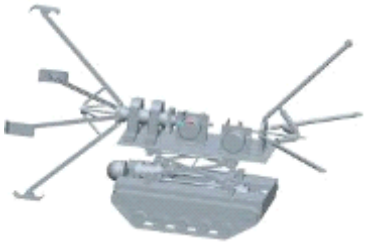

Figure 13. SVM-RS cleaning tool at rear [19]

The ILI crawler (see Figure 14 and Figure 15) from US Diakont company [20] is equipped with two Pulsed Eddy Current (PEC) probes in contact of the internal surface of a metallic pipe, with attached wheels and connected to a rigid, mechanical arm that extends from the crawler. The two arms rotate 180 degrees of the pipe circumference to cover the entire internal surface. Collected probe data, along with on-board camera images, operator's navigational instructions, and electrical power, are transmitted via an umbilical cable. It is able to support inspections for piping with diameters of 24 to 55 in (600mm to 1400 mm), being demonstrated on site in an operator's 36- and 42-in (900mm to 1100mm) diameter test cylinders.

Figure 14. Diakont inline inspection (ILI) robotic crawler with 2 PEC probes inside a 42 in (1067 mm) diameter metallic pipe

Figure 15. Zoom on a probe and the top crawler deployed against the pipe inner surface

2.2.3. Screw / helical type robot

Screw robots use a rotary motion to move forward along a spiral inspection path in a pitched circle. They are always wall-pressing and generally difficult to move backward due to their angled wheels or tracks. They perform well in vertical sections and are resistant to slip due to their angled approach, even against an in-pipe flow. As an example, Shenyang University designed a robot capable of

250mm to 300mm pipeline diameter exploration using a passively adaptive four bar linkage [21] (see Figure 16). Or the China Nuclear Power Engineering Company of Shenzhen designed a screw-type drive unit [17] for 260mm in-pipe diameter, able to handle large payload (see Figure 17).

Figure 16. Helicoidal robot [21]

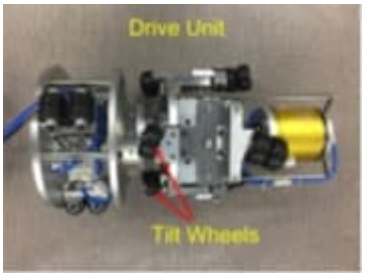

Figure 17. Screw-type drive robot [17]

2.2.4. Snake type robot

Snake robots take advantage of the length of the pipe. They are generally modular and adaptable to many in-pipe environments. They are composed of articulated modules equipped with wheels or tracks for locomotion. Such articulation allows many degrees of freedom making these robots very versatile in their approach to obstacles. For example, the BioInMech laboratory of the department of Robotics from Faculty of Science and Engineering of Ritsumeikan University, Japan, developed the AIRo-5.1 robot [22] consisting of two passive compliant joints and a single active compliant joint that is actuated by a series elastic actuator (see Figure 18), for 100mm to 130mm in-pipe diameter. Or the SINTEF ICT department of applied cybernetics of Trondheim, Norway, designed the PIKo snake-like robot [23] for horizontal and vertical pipes of varying diameter (see Figure 19).

Figure 18. AIRo-5.1 snake robot [22]

Figure 19. PIKo snake-like robot [23]

2.2.5. Inchworm type robot

Inchworm robots are only wall-pressing, they generate traction through large normal force applied at a front or back module while a central module alternately contracts and extends. The use of point contact and the removal of wheels or tracks makes them more stable than other designs. They are slower than other types but can generally carry higher payloads due to their need for high wall-traction forces. They are useful in industrial transport tasks where speed is not important. The school of mechanical engineering from Yonsei University of Seoul, Korea, designed a steerable inchworm type in-pipe robot [24] dimensioned for 205mm to 305mm in-pipe diameter with the ability to traverse T-sections (see Figure 20). Another kind of design is the Compliant Modular Mesh Worm (CMMWorm) robot [25] designed by the Biologically Inspired Robotics laboratory of the Department of Mechanical Engineering of Case Western Reserve University, Cleveland, USA, that creates peristaltic motion with a continuously deformable exterior surface, dimensioned for 180mm to 220mm in-pipe diameter (see Figure 21).

Figure 20. Inchworm inspection robot [24]

Figure 21. CMMWorm robot [25]

2.2.6. Walking type robot

Walking robots use multiple DoF legs to move inside the pipe. Their end effectors have low surface areas, which is useful for passing through in-pipe wall contaminants. Their wall-pressing functions sacrifice mobility for increased stability, being generally slower but with the ability to deliver heavier payloads. MORITZ robot, built at the Technical University of Munich, was one of the first walking style robots [26], capable of travelling through 600mm to 700mm diameter pipes and hold up to 20 kg payloads (see Figure 22). One can cite also more recent legged robots developed for more general robotics purposes, as for example the Mini Cheetah 3 from the MIT Biomimetic Robotics Laboratory that is a research prototype developed in 2018 [27].

Figure 22. MORITZ pipe crawling robot [26]

Figure 23. Mini cheetah 3 robot from MIT [27]

2.2.7. Hybrid wall-pressing

Previous basic locomotion elements are often used in conjunction with another, forming a hybrid system, wall-pressing being the most popular method of generating in-pipe traction. These systems mostly consist of a chassis that is kept concentric with the pipe, using usually tracks or wheel locomotion subsystems that are mounted perpendicular to the chassis. Such a concentric system would be an advantage for the integration of a robotic manipulator that would no longer need to adapt its distance to the pipe inner wall during its 360-degree rotation. However, the drawback is that such system would not adapt to pipe change in diameter, T-section, and also elbow in case of rigid longitudinal body.

2.2.8. Summary of the different in-pipe robotic systems

Then, Table 1 summaries the advantages and disadvantages of the pipeline robotic systems presented above.

Table 1 Summary table of in-pipe robotic systems

Type	Advantages	Drawbacks
Wheels	• Common design • Low maintenance costs	• Complex steering mechanism • Poor traction performance on slippery terrains

	• Lower cost than crawler	• High centering over uneven terrain
Crawler	• Handles more aggressive terrain	• Less energy efficiency • Expensive
Helical	• Relatively less actuators needed • Able to move forward and backward freely in small diameter pipe	• Low speed • Mainly suitable for precise motion in small pipe • Not suitable for complex pipes with low payload
Snake	• No need of motor for wheels • Move horizontally	• Needs more energy for operation
Inchworm	• Light weight • Cheap • Carry higher payloads	• Low speed • Poor reliability
Walking	• Able to cope with different in-pipe environment	• Relatively complicated for practical application • Instability during locomotion • Generally slower
Hybrid wall-pressing	• Able to move forward and backward in small diameter pipe • Adaptable to small pipes with different diameters	• Calibration at the center of pipe is needed • Mainly suitable for precise motion in small pipe • Not suitable for complex pipes with low payload

The main function of the navigation platform is to provide a pose (position and orientation) of the frame linked to the sensor manipulator in relation to a frame linked to the SCCP. The latter must be defined each time the navigation platform encounters a new bend or joint. Figure 24 displays examples of navigation platforms and SCCP frames for cylindrical and elbow-shaped SCCP. Specification of the manipulator system depends on the ability of the navigation platform to position itself relative to the SCCP, which depends on its own locomotion architecture.

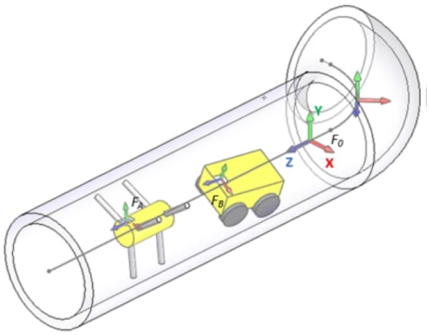

Figure 24. F_A and F_B frames provided by two navigation platforms

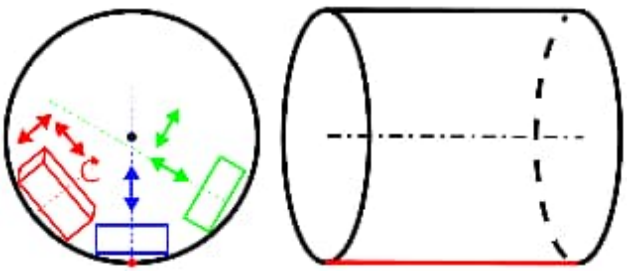

Figure 25. Robot position inside a pipe - cylinder front (left) and side (right) views

Thus, navigation platforms can be classified into two categories, whether they provide constant positions and orientation around lateral and vertical axes with respect to SCCP frame, meaning self-centred navigation platform (the central axis of the cylinder is the black point on the front view or the dotted line on the side view in Figure 25), or not, meaning non-centred navigation platform. The latter class of navigation platforms may be in different situations in the pipe, namely aligned with the pipe central axis and properly oriented (blue drawing on Figure 25), properly oriented (green drawing on Figure 25) or misoriented (red drawing on Figure 25).

3. CHOICE OF A **ROBOTIC INSPECTION SYSTEM SOLUTION**

3.1. Steel corrosion measurement process

In addition to environmental constraints, corrosion measurement NDT (see a review in [28]) is a key element for specifying the robotic system. This refers mainly to the measuring device and the complete measuring process description.
In particular, two steel corrosion measurement devices are considered. The first one is a rod electrode using potential field mapping technique (see an example Figure 6 in [29]). The second one is a commercial single-element Pulsed Eddy Current (PEC) probe. The selected measurement process, suitable for both techniques, is pointing and pressing with the measurement device over evenly spaced points along a 360° circle on the inner wall representing a cross section of the SCCP. The distance between measurement points is about 50mm. A cross section is said inspected when 3 circles are inspected, all located within a 200mm length of SCCP, that is about 150 inspection points per cross section. The next cross section to be inspected may be about 1 meter far from the previous cross section. Elbows being critical components (erosion, cracks and creep will most likely appear in elbows and at joints), it is necessary to perform some measurements there. Point by point process allows handling irregular areas or when a particular zone of interest needs to be inspected. Cross-sections do not have to be perfectly circular, and a bit elliptical inspection lines are acceptable. Contact of the sensor against the pipe inner wall is necessary, and inclination is to be avoided. A slight pressure on contact area should be assured by the robotic manipulator. These devices need a cable between them and the pipe entrance. Also, a screen outside is wired to the sensor for remote measurement activation and data observation.

3.2. Possible architectures for robotic inspection systems

Several possible architectures of inspection system (mobile platform combined with a robotic inspection arm) are presented, depending if the mobile platform is self-centered or not and regarding the robotic arm type, namely a basic cylindrical manipulator, a self-centered arm or a force-controlled 6 DoF robotic arm.

3.2.1. Cylindrical manipulator

This manipulator has a serial architecture, and comprises two actuated joints: one infinite revolution or at least with a range greater than one revolution, and a limited translation whose axis is perpendicular to the axis of the revolution joint. This architecture is the simplest and lightest for given sensor and SCCP specifications and may be typically associated with a navigation platform that centers the revolution joint axis in the SCCP, meaning a self-centered navigation platform. An example of such a cylindrical manipulator is given in Figure 9.

3.2.2. Self-centering manipulator

Compared to a cylindrical manipulator, the self-centring manipulator additionally includes an actuated centering system. The centering system is of the “wall-pressing” type with “legs” at the front and rear of the navigation platform pushing against the inner wall of the SCCP to center and orient the manipulator. For example, Figure 13 refers to such kind of system. The link between the centered manipulator and the navigation platform must remain passive, at least the 4 DoF around the lateral and vertical axes, or the whole system becomes hyperstatic in the SCCP. Then, this centering system is used as measurement manipulator only. Otherwise, with wheels it can become a self-centering navigation platform.

3.2.3. Force-controlled 6 DoF robotic arm

This manipulator is a serial robotic arm of at least 6 DoF including a contact sensor capable of detecting and locating contact points at its end effector with respect to its base frame. When the navigation platform carrying the manipulator stops at a point of interest, the manipulator detects 5 different contact points on the cylinder, provided that in any set of 4 points selected from those 5

points, the 4 points are not coplanar. Knowing the coordinates of these 5 points in the robot base frame, the inner cylinder of the SCCP is fully determined in this frame. Recognition of elbows or T sections may be more complex using this method. The measurement path, a circle whose center is on the axis of the inner cylinder, is then traveled by the measurement tool using the robotic arm. Despite its apparent genericity, drawbacks of such a solution are its high price and the complexity of control. Additional degrees of freedom may be required to control the arm internal configuration, for example to avoid collision situations with the navigation platform and/or the SCCP inner wall.

3.3. Chosen solution

The objective is a prototype mobile platform that allows the implementation of stable navigation functionalities in a pipe network, and carries a corrosion sensor manipulator. It must therefore have a sufficient payload, sufficient energy, one or more controllers with associated communication network, and a number of perceptual sensors of its environment. For all these reasons, and with a limited budget, it is out of scope to consider a commercial existing rover solution dedicated to the inspection of pipes in a nuclear environment, being waterproof and protected against radiation. Thus, according to SCCP inspection environment (see section 2.1) and process (see section 3.1), wheeled and tracked platforms may be suitable, the tracked solution allowing a better grip on the ground but also being more expensive and more energy consuming. Nevertheless, even if a complex solution, a legged mobile platform (see Figure 23) would still be an interesting category of solution to consider.
Then, in the particular case of navigation in a 600 mm to 1000 mm inner diameter pipe, a possible choice is the Clearpath Jackal [30] mobile robotic platform, this mobile base having a suitable size with sufficient clearance capacity (see Figure 26).

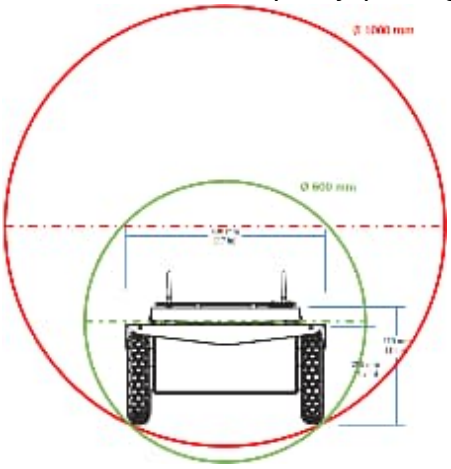

Figure 26. Jackal drawing in pipes of 600 mm and 1000 mm inner diameter

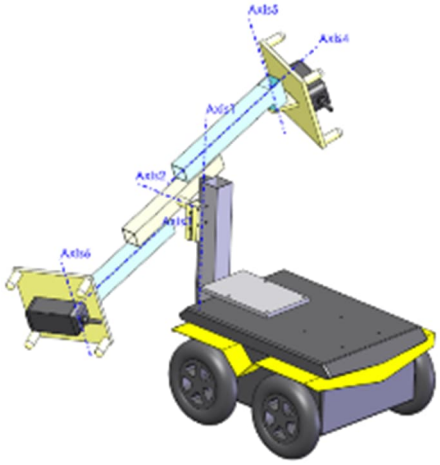

Figure 27. Manipulator integration into the mobile platform

For the manipulator specification, main challenges are appropriate measurement in elbow-shaped sections and in conical sections of pipes varying in diameter. With such requirements and if a wheeled navigation mobile platform is chosen, a simple cylindrical manipulator is not an option. Therefore, either a custom self-centering manipulator or a 6 DoF robotic arm is required.

If a commercial 6 DoF robotic arm is chosen, its generic mechanical architecture already physically allows the desired measurement areas to be reached, at least theoretically. Indeed, some situations of the end effector lead to unreachable joint positions due to contact between robot bodies and the SCCP inner wall. Thus, a redundant 7 or more DoF robotic arm may be necessary. On the other hand, the challenge is shifted to the perception and controller development, which need to robustly adapt to all types of configurations encountered.

A custom solution allows reduced complexity, both mechanically and for the control part, being specifically adapted to SCCP inspection requirements. Drawbacks of such solution are that complex pipe configurations would be difficult to manage and can also lead to a high number of degrees of freedom required, which will need to be controlled. As an example, the ILI robot manipulator architecture (see Figure 14) is not suitable for elbow pipes or conical parts.

Thus, finally the following customized mechanical architecture (see Figure 27) is proposed. For the correct centering of the manipulator, a vertical translation (Axis 1) is provided in relation to

the mobile platform. This translation allows adaptation to a variation in pipe diameter. A lateral translation and a yaw rotation along the vertical axis that would also be needed for an accurate manipulator centering, are to be ensured by the mobile platform. Then, the Axis 2 horizontal rotation to be concentric with the pipe axis is actuated with an absolute rotation angle measurment. Axis 3 and 4 coupled radial translations are dedicated to the deployment of the 2 measuring end-effectors. They are compliant and reversible to adapt to surface roughness and allow sliding against the wall. Inclination of the two yellow plates, rotation movement about Axis 5 and Axis 6, perpendicular to the pipe axis, is symmetrical, and mechanically coupled, possibly operated by a motor. Any deviation from the tilt symmetry is subject to elastic return. Four contacts on ball joints are made between each plate and the pipe wall. This system, with 3 motors, can be centered in a tube, cone and elbow, and is compatible with pipe inner diameter in a range of 600mm to 1000 mm, allowing the use of 1 or 2 NDTs types simultaneously. The advantages of such a solution are its diameter adjustment capability and tolerance to surface irregularities, and its light weight. The drawback is that the rotation Axis 2 will not be merged with the axis of an elbow or conical pipe, the section covered by the manipulator being not fully orthogonal to the axis of a pipe with such a geometry. The magnitude of this orthogonality error will depend on the curvature of an elbow or the variation in diameter of a cone, with complementary point by point measurements still possible after a mobile platform shift.

4. CONCLUSIONS AND PERSPECTIVES

This paper deals with the design of a sensor manipulation robotic system dedicated to the measurement of corrosion from the inside of a pipe. Based on the specifications of the corrosion measuring NDT task to be performed and on a state of the art of existing systems, a robotic mobile manipulator solution is proposed as a compromise between reachability and adaptability on one side and overall weight and size, complexity and operability on the other side

This technical solution also allows future adaptation taking into account other likely scenarios of use. In particular, the current system performance may be improved by:

- 1 to 2 additional rotations to cope with elbows and conical parts in case of a correct roll, pitch, yaw positioning of the mobile platform;
- 2 additional rotations and 1 additional translation to cope with elbows and conical parts in case of roll and/or pitch and/or yaw positioning error from the mobile platform;
- Extra degrees of freedom to cope with high irregularities and holes.

ACKNOWLEDGEMENTS

This work was carried out in the scope of ACES project. This project has received funding from the Euratom research and training programme 2014-2018 under grant agreement N° 900012.

REFERENCES

[1] H. Schempf, E. Mutschler, A. Gavaert, G. Skoptsov and W. Crowley, "Visual and nondestructive evaluation inspection of live gas mains using the Explorer family of pipe robots," *Journal of Field Robotics,* vol. 27, p. 217–249, 2010.

[2] G. H. Mills, A. E. Jackson and R. C. Richardson, "Advances in the Inspection of Unpiggable Pipelines," *Robotics,* vol. 6, p. 36, December 2017.

[3] Y. Kwon, B. Lee, I. Whang, W. Kim and B. Yi, "A flat pipeline inspection robot with two wheel chains," in *2011 IEEE International Conference on Robotics and Automation*, 2011.

[4] P. Chattopadhyay, S. Ghoshal, A. Majumder and H. Dikshit, "Locomotion methods of pipe climbing robots: a review," *J. Eng. Sci. Technol. Rev. 11 (4),* p. 154–165, 2018.

[5] M. Z. A. Rashid, M. F. M. Yakub, S. A. Z. bin Shaikh Salim, N. Mamat, S. M. S. M. Putra and S. A. Roslan, "Modeling of the in-pipe inspection robot: A comprehensive review," *Ocean Engineering,* vol. 203, p. 107206, 2020.

[6] J. M. Mirats Tur and W. Garthwaite, "Robotic devices for water main in-pipe inspection: A survey," *Journal of Field Robotics,* vol. 27, pp. 491-508, 2010.

[7] I. N. Ismail, A. Anuar, K. S. M. Sahari, M. Z. Baharuddin, M. Fairuz, A. Jalal and J. M. Saad, "Development of in-pipe inspection robot: A review," in *2012 IEEE Conference on Sustainable Utilization and Development in Engineering and Technology (STUDENT)*, 2012.

[8] N. S. Roslin, A. Anuar, M. F. A. Jalal and K. S. M. Sahari, "A Review: Hybrid Locomotion of In-pipe Inspection Robot," *Procedia Engineering,* vol. 41, p. 1456 – 1462, 2012.

[9] W.-C. Law, I.-M. Chen, S.-H. Yeo, G.-L. Seet and K.-H. Low, "A Study of In-pipe Robots for Maintenance of Large-Diameter Sewerage Tunnel," *Proceedings of the 14th IFToMM World Congress,* January 2015.

[10] T. Okada and T. Sanemori, "MOGRER: A vehicle study and realization for in-pipe inspection tasks," *IEEE Journal on Robotics and Automation,* vol. 3, p. 573–582, December 1987.

[11] C. Lu, H. Huang, J. Yan and T. Cheng, "Development of a Pipe Inspection Robot," in *IECON 2007 - 33rd Annual Conference of the IEEE Industrial Electronics Society*, 2007.

[12] S. U. Yang, H. M. Kim, J. S. Suh, Y. S. Choi, H. M. Mun, C. M. Park, H. Moon and H. R. Choi, "Novel robot mechanism capable of 3D differential driving inside pipelines," in *2014 IEEE/RSJ International Conference on Intelligent Robots and Systems*, 2014.

[13] K. Sungkyunkwan University, *MRINSPECT robots.*

[14] J. Saenz, N. Elkmann, T. Stuerze, S. Kutzner and H. Althoff, "Robotic systems for cleaning and inspection of large concrete pipes," in *2010 1st International Conference on Applied Robotics for the Power Industry*, 2010.

[15] N. Truong-Thinh, N. Ngoc-Phuong and T. Phuoc-Tho, "A study of pipe-cleaning and inspection robot," in *2011 IEEE International Conference on Robotics and Biomimetics*, 2011.

[16] J. W. Park, W. Jeon, Y. K. Kang, H. S. Yang and H. Park, "Instantaneous kinematic analysis for a crawler type in-pipe robot," in *2011 IEEE International Conference on Mechatronics*, 2011.

[17] D. Zhu, H. Chen, D. Wang, W. Shu, D. Meng, X. Hu and S. Fang, "Design and Analysis of Drive Mechanism of Piping Robot," *Journal of Robotics and Automation,* vol. 3, November 2019.

[18] Z. Li, J. Zhu, C. He and W. Wang, "A new pipe cleaning and inspection robot with active pipe-diameter adaptability based on ATmega64," in *2009 9th International Conference on Electronic Measurement Instruments*, 2009.

[19] Z. X. Li, H. W. Li and Z. H. Li, "A New Air-Conditioning Pipeline Cleaning Robot System," in *Functional Manufacturing Technologies and Ceeusro II*, 2011.

[20] K. R. Larsen, *Inspection Technology Assesses Unpiggable Pipelines,* 2020.

[21] C. Ye, L. Liu, X. Xu and J. Chen, "Development of an in-pipe robot with two steerable driving wheels," in *2015 IEEE International Conference on Mechatronics and Automation (ICMA)*, 2015.

[22] A. Kakogawa and S. Ma, "A Multi-Link In-Pipe Inspection Robot Composed of Active and Passive Compliant Joints," in *IEEE/RSJ International Conference on Intelligent Robots and Systems (IROS)*, Las Vegas, NV, USA (Virtual), 2020.

[23] S. A. Fjerdingen, P. Liljeback and A. A. Transeth, "A snake-like robot for internal inspection of complex pipe structures (PIKo)," in *2009 IEEE/RSJ International Conference on Intelligent Robots and Systems*, 2009.

[24] W. Jeon, J. Park, I. Kim, Y. Kang and H. Yang, "Development of high mobility in-pipe inspection robot," in *2011 IEEE/SICE International Symposium on System Integration (SII)*, 2011.

[25] A. S. Boxerbaum, K. M. Shaw, H. J. Chiel and R. D. Quinn, "Continuous wave peristaltic motion in a robot," *The International Journal of Robotics Research,* vol. 31, p. 302–318, 2012.

[26] A. Zagler and F. Pfeiffer, ""MORITZ" a pipe crawler for tube junctions," in *2003 IEEE International Conference on Robotics and Automation (Cat. No.03CH37422)*, 2003.

[27] G. Bledt, M. J. Powell, B. Katz, J. Di Carlo, P. M. Wensing and S. Kim, "MIT Cheetah 3: Design and Control of a Robust, Dynamic Quadruped Robot," in *2018 IEEE/RSJ International Conference on Intelligent Robots and Systems (IROS)*, 2018.

[28] R. F. Wright, P. Lu, J. Devkota, F. Lu, M. Ziomek-Moroz and P. R. Ohodnicki, "Corrosion Sensors for Structural Health Monitoring of Oil and Natural Gas Infrastructure: A Review," *Sensors,* vol. 19, 2019.

[29] D. Luo, Y. Li, J. Li, K.-S. Lim, N. A. Mohd Nazal and H. Ahmad, "A Recent Progress of Steel Bar Corrosion Diagnostic Techniques in RC Structures," *Sensors,* vol. 19, no. 34, 2019.

[30] Clearpath Jackal, [Online]. Available: https://clearpathrobotics.com/jackal-small-unmanned-ground-vehicle/.

Improvement of numerical tools for the ultrasonic NDE of concrete: the fundamental role of the Interfacial Tranzition Zone

M. Ramaniraka[1*], C. Payan[1], S. Rakotonarivo[1], J-F. Chaix[1] and V. Garnier[1]
[1] Aix Marseille Univ, CNRS, Centrale Marseille, LMA, Marseille, France

ABSTRACT

This paper is an overview of the progress made in the consideration of the ITZ effects on wave propagation in concrete. During its service life, concrete can be subjected to different damages. Firstly, as it is not chemically inert, pathologies as swelling reactions (Alkali Silica Reaction (ASR), Delayed Ettringite Formation (DEF)) and carbonation (reaction with CO2) can occur, leading to concrete's cracking. Secondly, mechanical and thermal solicitations can also lead to cracks apparitions when they are beyond the design values. All those damages arise from one location: the Interfacial Tranzition Zone (ITZ), which is the thin and very porous layer around each aggregate. With a thickness ranging from 10µm to 150µm, it governs the concrete mechanical behavior (linear and nonlinear) and durability.

Ultrasonic waves are excellent candidates for an early detection of damages. In fact, at the scale of investigation (wavelength ~ aggregates sizes), the wave/medium interaction is maximized (stochastic regime). It is thus obvious that ITZ plays an important role within those interactions, and consequently on the measured parameters. However, despite the significant development of numerical tools for the ultrasonic NDE of concrete, the ITZ was less or not considered. The importance of modeling it and its effects on different ultrasonic parameters were recently demonstrated: velocity/attenuation and diffusivity.

Having a robust "numerical concrete" as support for ultrasonic NDE research is thus the aim of this study. Since few years, an elastic model developed within Prospero code (LMA) and considering ITZ through jump conditions at interfaces has been available. It is to be permanently improved. Firstly, an extensive campaign of concrete samples manufacturing and characterization (mechanical, chemical, microscopy, ...) is launched to collect data as input for the model, especially concerning the ITZ. Secondly, it is known that the non-linear behavior of concrete is largely attributed to the aggregates interfaces. The role of ITZ in nonlinear acoustics is investigated.

Keywords: numerical concrete, ultrasound, Interfacial Tranzition Zone (ITZ), damages.

1. INTRODUCTION

An early detection of concrete damages is very important to ensure a high level of safety on nuclear powerplants. During its service life, concrete is not chemically inert. Different kinds of reactions can occur depending on the surrounding environment and/or concrete's composition: Alkali Silica Reaction (ASR), Delayed Ettringite Formation (DEF), carbonation, ... Those reactions are considered as pathologies for concrete as they lead to the formation of cracks that can, in fine, compromise the structure's integrity. Other solicitations can also damage the concrete such as freeze-thaw cycles, overheating or overloading. The common point of the damage mechanisms is that they generally take birth at the Interfacial Tranzition Zone (ITZ). This layer around each aggregate is considered as the "weakest link" of the concrete.

Numerical simulations are now essential part of research and development work – beside theory and experiments – on ultrasonic NDE of concrete. In fact, they allow to test quasi-infinite number of configurations (of medium, of sensors, ...) at lower cost as there is no need to manufacture a large amount of concrete specimens or to get a multitude of devices. The ITZ was less or not considered within those tools until recent years. However, to be relevant and robust, they have to

* Corresponding author: phone and email

consider a “numerical concrete” as representative as possible of a real one. Taking into account ITZ effects seems thus legitimate in order to fit with reality.

This paper synthetises the main achievements recently done about ITZ implementation in numerical simulations of ultrasound propagation in concrete. Such precursor works allowed to have a much better fit between measured parameters from numerical simulations and from experiments.

Firstly, the role played by the ITZ within the concrete material is presented (Section 2). Secondly, the numerical model developed for this purpose is presented (Section 3). After that, the main results obtained about the ITZ effects on ultrasonic wave velocity and attenuation (Section 4) and diffusivity (Section 5) are synthetized. Current works on those linear parameters are also addressed. Finally, the outlook on the ITZ effects on nonlinear parameters is also addressed (Section 6).

2. ITZ EFFECTS ON CONCRETE PROPERTIES

2.1. What is ITZ?

ITZ is the thin porous layer surrounding each aggregate, materializing the aggregate/cement paste interfaces within concrete (Figure 1). Negligible for sand particles, its thickness grows with the aggregate’s size. In fact, wall effect reduces the cement paste packing, that increases the water content at this zone. Higher water content at the fresh state means higher porosity at hardened state. ITZ thickness depends on many parameters: the aggregate’s shape, its chemical composition, the type of cement, the mix formulation, etc. Many authors agree to say that the ITZ thickness for a “common” concrete is about 40-50µm [1]. It is also known that the ITZ properties exhibit a gradient profile from the aggregate surface to the cement paste bulk [6]. In terms of chemical composition, ITZ has higher calcium hydroxide $Ca(OH)_2$ (Portlandite) content compared to the cement paste [1].

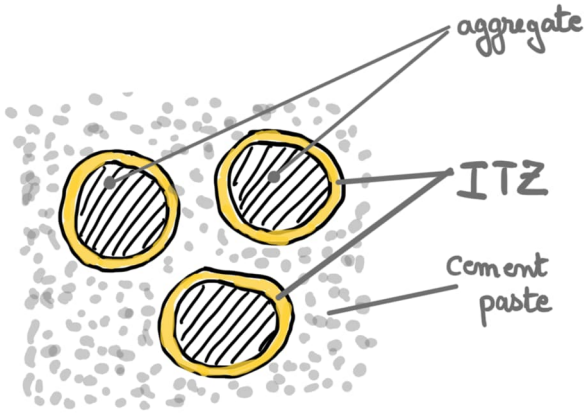

Figure 1 : Illustration of ITZ in concrete

2.2. ITZ and concrete’s mechanical properties

Several studies showed that ITZ governs the concrete’s strength. In fact, the compressive strengths of aggregate alone or cement paste alone are higher than the obtained concrete [1] [2]. Due to its high porosity, ITZ exhibits very low mechanical properties. That is thus legitimate to affirm that ITZ is the “weakest link” of concrete. Its high porosity leads to microcracks formation that are densifying under increasing loads.

ITZ is also involved in the nonlinear behaviour of concrete under dynamic loads. In any granular materials, as rocks, nonlinearity comes from different contacts conditions at grains interfaces and different microcracks [7]. Once again, due to its high porosity/microcracks density and its localisation around each aggregate, ITZ governs a great part of the nonlinear behaviour of concrete.

2.3. ITZ and concrete's durability

The ITZ doesn't only impacts concrete's strength, it may also boost some pathologies. Its high porosity and microcracks density increase transport of chemical elements (CO_2, Cl^-, ...) within concrete [2] and constitute a potential water supply for swelling reactions such as ASR and DEF.

ASR occurs when alkali ions (Na^{2+} and K^{2+}) within the cement paste react with reactive silica present in some types of aggregates to form an alkali silica gel, which swells in presence of moisture. This growth creates stresses within concrete that can lead to cracks, that increase water supply, accelerating the damage mechanism [8].

High temperatures at early age of the concrete inhibits the formation of ettringite, a classical product of cement hydration. DEF occurs later when water supply activates the delayed formation of ettringite within the hardened concrete. As with ASR, this swelling reaction creates stresses and cracks within concrete, accelerating the damage mechanism [9].

External solicitations impact also firstly ITZ. For example, the freeze-thaw cycles effects will be accentuated with the high water content of ITZ, while overloads will densify the microcracks inside the ITZ [10]. It is thus clear that ITZ plays a crucial role in concrete's durability.

3. ITZ IMPLENTATION IN NUMERICAL SIMULATIONS

The previous section allowed to realize the fundamental role of ITZ in concrete material. Despite all of this, its effects on ultrasonic wave propagation were less studied, while such technics are widely used in Non Destructive Evaluation of concrete. Especially, in numerical simulations of wave propagation in heterogenous materials as concrete, ITZ was often neglected.

Ramaniraka *et al* [4] suggested to implement it with the simplest way possible: an imperfect contact between matrix and aggregates. The ITZ was modelled within Prospero software through "spring-mass jump" conditions as described below [11].

$$[u_N(A,t)] = \frac{1}{K_N}\sigma_{N0}(A,t)\ ; \quad [\sigma_N(A,t)] = M_N\frac{\partial^2}{\partial t^2}u_{N0}(A,t)$$
$$[u_T(A,t)] = \frac{1}{K_T}\sigma_{T0}(A,t)\ ; \quad [\sigma_T(A,t)] = M_T\frac{\partial^2}{\partial t^2}u_{T0}(A,t) \qquad (Eq.1)$$

where $[u_N(P,t)]$, $[u_T(P,t)]$, $[\sigma_N(P,t)]$ and $[\sigma_T(P,t)]$ are respectively the normal displacement, the tangential displacement, the normal stress and the tangential stress jumps across the interface at the point A and at time t, from the medium 0 to the medium 1; and $K_N > 0$, $K_T > 0$, $M_N \geq 0$ and $M_T \geq 0$ are respectively the normal stiffness, the tangential stiffness, the normal mass and the tangential mass of the interface.

Thus, one single parameter was defined to simply describe the quality of the interface between the aggregate and the mortar: the Contact Level (CL). This parameter includes the Young modulus and the thickness of the ITZ, and the Young modulus of the surrounding mortar [4]:

$$CL = \frac{E(ITZ)/E(mortar)}{\text{thickness (ITZ)}} \qquad (Eq.2)$$

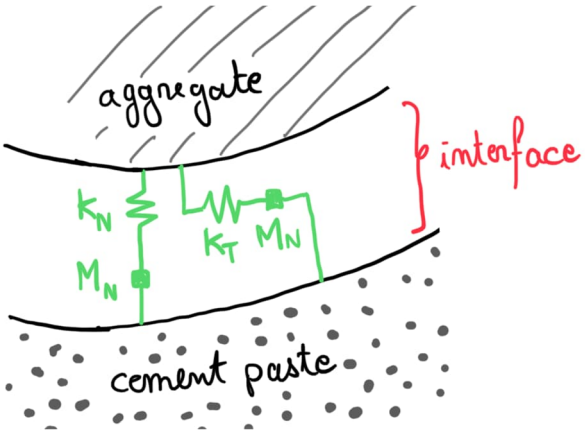

Figure 2 : spring-mass modelling of ITZ

4. ITZ EFFECTS ON CLASSICAL LINEAR PARAMETERS

It is important to notice at the beginning that viscoelastic effects are not implemented in the model. So, only the multiple scattering affects the propagating signal. The comparison with the experimental results is still possible as the contributions of the two phenomena are easily separable [13]. In addition, the comparison between 2D numerical simulations and 3D experimental measurements was justified at the frequency range of auscultation (≈500kHz) [4].

4.1. Simulations and experimental setups

The computational domain is 40cm x 25cm mortar rectangle filled with 40% by aggregates. The aggregates consist in randomly positioned discs of 12mm diameter (monodisperse). Plane P-wave with Ricker signal centered at 500kHz is propagated through the medium. A grid of 31 lines by 16 rows, that means 496 receivers, allows to record wave propagation on the first 15cm. Coherent signals are then computed (see details in [4]).

The materials properties (aggregates and mortar) presented in Table 1 are common values chosen for simulations in many studies [4]. Concerning the modelling of ITZ, different CL parameter (Eq. 2) values were tested during those studies, ranging from 0 (contact free) to infinite (perfect contact).

Table 1 : Simulated materials properties

	Mortar	Aggregate
P-wave velocity (m/s)	3950	4300
S-wave velocity (m/s)	2250	2475
Density (kg/m3)	2050	2610

Experimental values of velocity and attenuation used in this part of the study came from literature [4].

4.2. The ITZ effects on attenuation

Numerical simulations that didn't take into account ITZ (perfect contact: CL=inf) exhibited very low multiple scattering attenuation values compared to experiments. At 500kHz, this represents a gap of about 14Np/m (Figure 3). Considering realistic ITZ properties (thickness and Young modulus) in numerical simulations allowed to reach the experimental attenuation values [4]. This result can quantify the effect of ITZ.

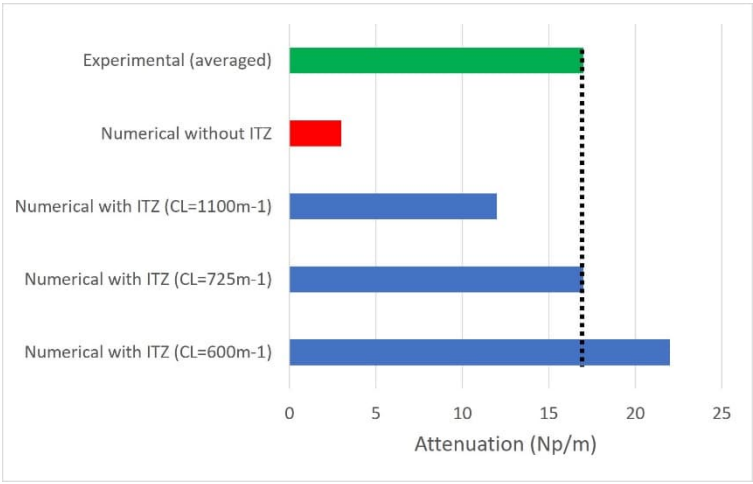

Figure 3. Attenuation values at 500kHz: experimental vs numerical

4.3. The ITZ effects on velocity

The ITZ effect on wave's velocity was not quantitatively measured (the exact velocities for mortar and for aggregate were not assessed) but qualitative observations were performed. Wave velocities were measured on concrete specimens with different thermal damage levels [4]. The decreasing trend of the velocity (when the damage increases) was reproduced by the numerical simulations (when the parameter CL decreases) (Figure 4). This result confirms the previous affirmation: damage mechanisms firstly affect the ITZ interface.

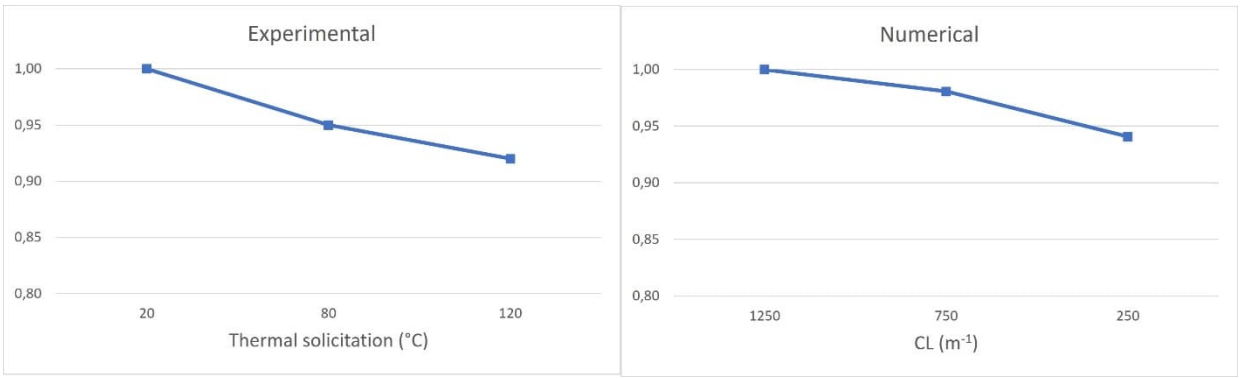

Figure 4 : Evolution of relative velocity values at 500kHz: experimental vs numerical

4.4. Ongoing improvements

Those promising results paved the way for an inversion tool. However, as previously mentioned: ITZ is highly variable, even for sound concretes. It becomes crucial to be able to distinguish a normal situation from an abnormal one. A sufficient amount of data on ITZ characteristics is thus needed for an accurate interpretation.

To collect the necessary data, an extensive experimental campaign is currently ongoing. This consists in manufacturing several specimens from different concrete batches (different origins of aggregates, different types of cement and different water/cement ratios). A monodispersed aggregates size was chosen to get closer to the numerical configuration (12mm diameter aggregates within mortar).

First, MEB observations and microhardness measurements are planned to collect ITZ characteristics (thickness, Young modulus). Ultrasonic measurements (velocity and attenuation) will be performed on the different concrete batches. Then, concrete specimens will be gradually damaged (thermally and/or chemically and/or mechanically). For each damage level, the process is repeated: MEB observation + microhardness + ultrasonic velocity and attenuation. This will constitute a considerable database for the numerical tool.

5. ITZ EFFECTS ON DIFFUSE LINEAR PARAMETER

5.1. Simulations and experimental setups

In this part of the study, 9cm x 9cm x 26cm specimens from the same batch but exposed to different thermal damages (20°C, 120°C, 250°C, 400°C) were inspected. The emitter consisted in a 500kHz transducer placed at the center of one of the small faces while a laser vibrometer recorded signals at the center of the four lateral faces (perpendicularly).

The numerical setup was designed in order to reproduce the experimental one. 9cm x 26cm rectangular specimens were modelled with similar materials properties (aggregates and mortar) as mentioned in Table 1. The different ITZ qualities were obtained by tuning the CL parameter. A point source with a central frequency of 500kHz is used. A row of 19 receivers located at the center of the numerical specimen allowed to compute an averaged diffusivity.

5.2. Main progress and ongoing improvements

For the diffusivity parameter study, two main results can be highlighted [5]. The first result is that the diffusivity values obtained from the numerical simulations are in the same order of magnitude than the experimental measurements (Figure 5), considering CL parameters used in the velocity and attenuation study. That means the numerical model, considering realistic ITZ characteristics, validated with the classical parameters is still relevant in the diffusion regime.

The second result is that the numerical tool was able to reproduce the evolution of the measured diffusivity values for an increasing level of thermal damage. The affirmation that the *higher the damage level, the lower the interface quality, the higher the multiple scattering, the lower the diffusivity value* was well validated.

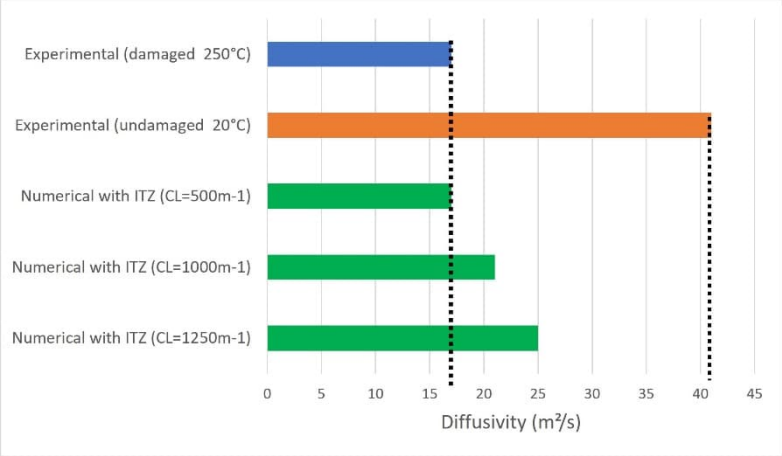

Figure 5 : Diffusivity values at 500kHz: experimental vs numerical

Again, those results confirm the potential of the numerical tool for inverse problem. And as for velocity and attenuation study, that needs a sufficient database to avoid any misinterpretation of the diagnostic. So, diffusivity parameter measurements will be also performed on the different concrete batches discussed in (4.4).

6. WHAT'S NEXT? : ITZ EFFECTS ON NONLINEAR ACOUSTICS PARAMETERS

On one hand, it was said that ITZ is at the heart of the nonlinear mechanical behaviour of concrete (hysteresis) as the case of fractures in rocks [7]. On the other hand, it was perfectly demonstrated that ITZ affects the multiple scattering of ultrasound within concrete [4] [5]. Effects on velocity, attenuation and diffusivity were shown and evaluated by the developed numerical tool. So, it is legitimate to ask the question: what are ITZ effects on nonlinear acoustics? Nonlinear technics have shown great potentials for NDE of concrete over the recent years. They exhibit a very high sensitivity to minor modification compared to linear parameters [12].

6.1. Observation of nonlinear multiple scattering

Nonlinear acoustics generally analyse the wave propagation within a "disturbed" medium. The same experimental process as for diffusivity study (Section 5) was realized, only the wave's amplitude was changed – sufficiently to activate material's nonlinearity. A difference on diffusivity values is observed. More precisely, the measured diffusivity increases as the amplitude increases (Figure 6). In other words, the ultrasound is less multiply scattered when the amplitude increases.

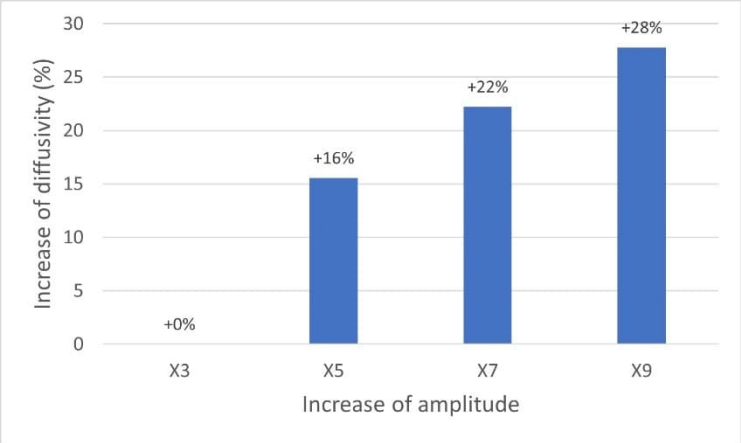

Figure 6 : Evolution of diffusivity values according to wave's amplitude

6.2. A first explanation of the role of ITZ

As a recall, in classical heterogeneous medium, multiple scattering of ultrasound is governed by the frequency and the impedance contrast between the inclusions and the matrix [13]. However, it was shown that the interface (ITZ) between the inclusions (aggregates) and the matrix (mortar) within concrete greatly impacts the aggregates scattering sections [4] [5]. In the case of linear acoustics, as all the results previously discussed, the ITZ state does not evolve during the acquisition. In the case of nonlinear experiment, a sufficient increase of amplitude can modify the structure of the interface. As the amplitude increases, the material is "compressed"; such compression inevitably consolidates the ITZ. And it was demonstrated that the higher the ITZ modulus, the lower the multiple scattering, the higher the diffusivity values [5]. So, from this first short explanation, we can assume that ITZ plays also an important role in nonlinear acoustics. This role has to be analysed and quantified in order to enhance the accuracy of the numerical tool.

7. CONCLUSION

This paper highlighted the fundamental role of ITZ in the improvement of numerical tools for the NDE of concrete. It allowed to make an overview of the different properties and impacts of such thin layer on the whole concrete behaviour and durability. A review of the recent advances in ITZ consideration within numerical simulations was addressed. It is confirmed that ITZ impacts wave propagation in concrete for both classical and diffuse parameters. The model developed through those studies will constitute a real inversion tool. Current works consist in building a large database about ITZ characteristics of sound concretes as well as of damaged concrete. Microscopic observations, microhardness measurements, ultrasonic velocity and attenuation measurements, diffusivity measurements are planned for the different concrete batches and damage levels. Such database is needed to enhance the accuracy of the numerical tool. Finally, the effect of ITZ in nonlinear acoustics, especially in nonlinear multiple scattering is investigated. First observations and analysis confirm the role of ITZ in such approach. Further analysis is planned to build a robust numerical tool for both linear and nonlinear acoustics. Such tool will be the *ideal ally* for a reliable ultrasonic NDE of concrete in nuclear applications, as the objective is *to detect as early as possible any damage initiation*.

REFERENCES

[1] G. Prokopski et al., “Interfacial transition zone in cementitious materials”, Cement and Concrete Research, vol. 30, pp. 579-584, 2000

[2] K. Wu et al., “Microstructural characterization of ITZ in blended cement concretes and its relation to transport properties”, Cement and Concrete Research, vol. 79, pp. 243-256, 2016

[3] I.F. Sáez del Bosque et al., “Properties of interfacial transition zones (ITZs) in concrete containing recycled mixed aggregate”, Cement and Concrete Research, vol. 81, pp. 25-34, 2017

[4] M. Ramaniraka et al., “Effect of the Interfacial Transition Zone on ultrasonic wave attenuation and velocity in concrete”, Cement and Concrete Research, vol. 124, no. 105809, 2019

[5] M. Ramaniraka et al., “Effect of Interfacial Transition Zone on diffuse ultrasound in thermally damaged concrete”, Cement and Concrete Research, vol. 152, no. 106680, 2022

[6] [6] J.P. Ollivier et al., “Interfacial transition zone in concrete”, Cement and Concrete Research, vol. 2, pp. 30-38, 1995

[7] R.A. Guyer and P.A. Johnson, « Nonlinear mesoscopic elasticity: the complex behaviour of rocks, soil, concrete”, Ed. Wiley VCH, 2009

[8] A. Zahedi et al., “Condition assessment of alkali-silica reaction affected concrete under various confinement conditions incorporating fine and coarse reactive aggregates”, Cement and Concrete Research, vol. 153, no. 106694, 2022

[9] M. Thomas et al., “Diagnosing delayed ettringite formation in concrete structures”, Cement and Concrete Research, vol. 38, pp. 841-847, 2008

[10] A. Zahedi et al., “Global assessment of concrete specimens subjected to freeze-thaw damage”, Cement and Concrete Composites, vol. 133, no. 104716, 2022

[11] B. Lombard et al., “Numerical modeling of elastic waves across imperfect contacts”, Society for Industrial and Applied Mathematics, vol. 28, pp. 172-205, 2006

[12] J.-P. Balayssac and V. Garnier, “Non-destructive Testing and Evaluation of Civil Engineering Structures”, first ed., ISTE Press, 2017

[13] A. Derode et al., “Random multiple scattering of ultrasound. I. Coherent and ballistic waves”, Physical Review E 64, 2001

How to conduct Impact Echo simulations for non-destructive testing at concrete structures for the nuclear industry

Fabian Dethof[1*], Daniel Algernon[2], Claudia Thurnherr[2] and Sylvia Keßler[1]
[1] Helmut Schmidt University/University of the Federal Armed Forces Hamburg, Chair of Engineering Materials and Building Preservation, Hamburg, Germany
[2] SVTI Swiss Association for Technical Inspections, Wallisellen, Switzerland

ABSTRACT

The Impact Echo testing method probably is one of the easiest non-destructive testing (NDT) methods to conduct for the detection of defects in concrete. However, its results are usually quite difficult to interpret. Artifacts can arise which result from the geometry of the investigated structure, from wave scattering or simply from the presence of multiple resonance modes. These might be some of the reasons why in the past, numerical simulations of Impact Echo testing have been very rare.

Here, we present a way of conducting large scale 3D Impact Echo simulations that are able to capture geometry as well as scattering effects. The simulations are performed using the elastodynamic finite integration technique (EFIT), which is a staggered-grid finite differences code for elastic wave propagation. The code is validated by recreating inspections conducted on two different test specimens. Here a good agreement between simulation and inspection results was found. For the simulations not only the correct resonance frequency, but also a realistic noise level was desired. Therefore, different parameter studies were conducted to investigate the effect of wave scattering on the resonance frequency depending on the share of pores and aggregates inside the concrete. Also, the spatial resolution for these kinds of simulations must be chosen carefully as it was found that it can have an influence on the resonance frequency if chosen too large.

These simulations are applicable to very thick concrete structures, similar to those used in the nuclear industry. Because of the quite accurate noise level, applications for reliability assessments concerning the Probability of Detection (PoD) are likely possible and will be investigated in future studies.

Keywords: Impact Echo, simulation, concrete

1. INTRODUCTION

Impact Echo (IE) testing is a valuable tool for condition assessment of various structures in civil engineering as well as in the nuclear industry. One of the big advantages of IE testing is, that it uses lower frequencies than Ultrasonic testing or Ground Penetrating Radar, which allows the waves to travel further and results in a higher sensitivity at greater depth. For the nuclear industry the large penetration depth and sub-wavelength resolution capability of Impact Echo make it applicable for the inspection of thick and highly reinforced concrete structures like nuclear reactors [1] as well as for the estimation of prestresses on bonded tendons [2]. In order to get a better understanding and visualization of the inspections and the underlying physical phenomena, numerical simulations are a commonly used tool [3] [4] [5].

In the past, numerical simulations of Impact Echo testing have been very rare. However, some studies that have been carried out can be found in [5] and [6]. These studies show that numerical simulations can accurately simulate the resonance frequencies [6] and geometry effects during IE inspections [5]. Further reasons for the scarcity of IE simulations may be a consequence from the fact that the simulated time for IE inspections is much longer than for Ultrasonic testing. Whereas for Ultrasonic testing, the waves only have to travel to the backwall and back to the source once, for

* phone: +49 40 6541-2788, e-mail: dethoff@hsu-hh.de

IE testing the waves have to travel that distance several times in order to give a stable frequency spectrum. This means for a specimen of 50 cm thickness, the ultrasonic waves would travel about 1 m, whereas waves for Impact Echo testing would have to travel this distance at least ten to fifteen times in order to give a well resolved frequency spectrum. Additionally, it was found that pores do affect the frequency spectrum in IE simulations even though their size is much smaller than the dominating wavelength [6]. For that reason, it might also be necessary to discretize pores explicitly for the simulations to allow for scattering inside the medium.

In this paper, a way to carry out numerical simulations of IE testing at concrete structures is presented. For this, the staggered-grid finite differences code EFIT is used [7], which has shown in the past that it is capable of simulating IE measurements [5] [6]. Different parameters that influence the outcome of the simulation are analysed in section 2. In section 3 real-life inspections from two test specimens are recreated using 2D and 3D simulations. These results are then discussed with the conclusion following at the end.

2. SIMULATION CODE AND INFLUENCING FACTORS

The numerical simulations in this paper follow the elastodynamic finite integration technique (EFIT). This code uses the integral form of the Cauchy equation of motion as well as the deformation rate equation [7]. Therefore, it is very robust for strongly heterogeneous media like (reinforced) concrete [8]. As it was found that scattering, which is mainly caused by concrete pores [6], has an influence on the wave propagation during IE testing, aggregates and pores within the concrete are discretized explicitly. Both aggregates and pores are assumed to have an ellipsoidal shape and are distributed randomly in the medium. Aggregate size follows a given grading curve. As the minimum aggregate and pore size is limited by the grid cell size of the simulation domain, which can be up to 2 mm depending on the size of the simulation domain, only the larger aggregates and pores can be incorporated into the simulations. The procedures described in [9] and [10] are used for a fast generation of the numerical concrete, as computation time can be a problem for large scale 3D simulations.

When modelling concrete, the process requires the assignment of elastic parameters to both the cement matrix and the aggregates. Concrete pores are treated as a vacuum, which is a valid assumption if the pores are filled with air since the reflection coefficient at a concrete-air interface is close to one [8]. In case of water-filled pores, wave propagation inside the pores might have to be considered explicitly, but this situation is not covered in this paper.

Once the generation of the numerical concrete was completed, the model was complemented by steel reinforcement, which was placed at its respective position assuming a cylindrical shape. Material parameters in this area were changed corresponding to those of homogeneous, isotropic steel. Isotropy is assumed to keep computation times low as otherwise calculations would have to be performed with more than two independent elastic parameters in the entire simulation domain. Also, the wave propagation inside the steel reinforcement is assumed to have a rather small impact on the results due to the high reflection coefficients at the concrete-steel interface ($R \approx 0.65$ for both P- and S-waves).

2.1. Wave propagation velocity

For a medium as heterogeneous as concrete the phase velocities that result from the elastic parameters given to each grid cell associated with aggregates or cement matrix are not equal to the wave speed that will be observed in the IE measurement. Since wavelengths for IE inspections are in the order of the specimen thickness and therefore much larger than the maximum aggregate size (typically 8 mm – 32 mm), the phase velocity typically will be a mixture of the phase velocity inside the aggregate and the cement matrix. However, experimental studies have shown that concrete shows a dispersive behaviour at frequencies below 100 kHz [11]. In the frequency regions typically used for Ultrasonic testing and Impact Echo, the phase velocities are smaller than for higher frequencies. Due to the large number of scatterers inside the medium, the effective phase velocity will be smaller than the average velocity inside the medium.

To demonstrate this effect, a 2D medium is generated, in which cement matrix and aggregates do have the same phase velocity, but their densities differ from each other, in order to enable scatter.

The total grid size is 200 x 1000 grid cells with absorbing boundaries [12] at the short sides and periodic boundaries [8] at the long sides. The spatial resolution is 1 mm resulting in a total grid size of 0.2 m x 1 m. The simulation setup is shown schematically in fig. 1. A plane wave with a centre frequency of 5 kHz, which is a typical frequency for IE testing is inserted into the medium. In this case, the P-wave velocity is 4000 m/s meaning a wavelength of 80 cm. Due to the fine spatial discretization (here: about 160 grid cells per smallest wavelength) numerical accuracy is ensured as only eight grid cells per smallest wavelength are required [8].

The aggregates follow an A/B16 grading curve and cover 70 vol.% of the simulation domain. By taking the wave arrival time at two different grid points the wave propagation velocity can be determined. Here, the wave arrival time is the time of the first maximum in the wavelet. This simulation is repeated several times for different aggregate densities and therefore different reflection coefficients at the aggregate-cement interface. By keeping the wave velocities and the overall setup constant, the results can be compared against each other. Due to near field effects which alter the waveform of the signal the calculated wave speeds may differ from the theoretical values given by the material parameters used as the same distinct phase of the signal has to be picked at each receiver.

In this study we found that the wave velocity decreases with higher reflection coefficients. For a reflection coefficient of R = 0.3, which is a realistic value for the cement-aggregate interface [13], the P-wave velocity decreases by about 3% just due to the aggregates (see table 1). The presence of pores reduces the velocity even more, since the pores already lower the average wave speed within the medium due to their low wave speed (0 m/s for air – in the simulations). These factors must be kept in mind when trying to calibrate the correct wave speed for the simulation. Table 1 shows that the P-wave velocity for a homogeneous medium is not exactly at 4000 m/s. The reason is that the waveform will change with larger distance to the source when the far field term becomes more dominant and the near field terms, which are proportional to $1/r^2$ and $1/r^4$ respectively, vanish [14]. As the time of the maximum is picked for all simulations, the waveform change influences the obtained wave speed directly.

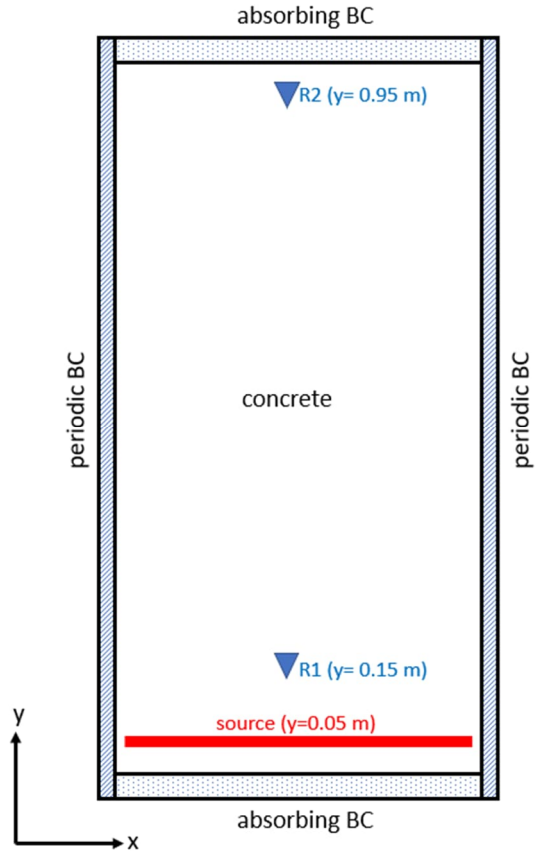

Figure 1. Simulation setup to determine the pore influence on the wave speed. Waveforms will be recorded at two locations R1 and R2 80 cm apart from each other. In order to minimize S-wave amplitudes, a line source is chosen, so that only P-waves will be recorded.

Table 1 Time delays and resulting velocity changes due to scattering. Time delays are measured over a distance of 80 cm. The nominal P-wave velocity is 4000 m/s.

Aggregate density [kg/m³]	$\Delta\rho$ [kg/m³]	Reflection coefficient R	Δt [μs]	P-wave velocity [m/s]
2300	0	0	201.6	3963
2800	500	0.10	202.1	3958
3300	1000	0.18	203.9	3923
4300	2000	0.30	208.0	3846

2.2. Spatial resolution

In this section, the effect of the grid cell size on the IE resonance frequency is under investigation. The grid cell size (or spatial resolution) most often will be the most restricting factor to IE simulations in concrete-like media. Due to the large bandwidth in aggregate size, not all of them will actually be resolved as ellipsoids since EFIT generally only allows cuboid grid cells. Therefore, the geometrical shape of the ellipsoids will be discretized using a staircase approximation. The actual simulation error made by this approximation is hard to quantify as real aggregates are not shaped perfectly ellipsoidal.

However, the spatial resolution and therefore the shape of the aggregate or pore does affect the signal amplitude reflecting from a single one of them. For IE testing, as wavelengths are usually much larger than the maximum dimension of the scatterer, the scattering occurs in the Rayleigh limit, which is most often disregarded due to its small reflection amplitudes.

In order to demonstrate the dependence of reflection amplitudes from differently fine resolved scatterers, a 2D simulation was carried out, in which a plane wave travels in a homogeneous medium and is reflected by a circular structure, which is embedded in the medium. This scatterer here shall resemble a single steel rebar located inside a homogeneous concrete-medium. With this scatterer size this simulated scenario can also be viewed as scattering at a single aggregate. The surrounding medium has concrete-like properties with a P-wave velocity of c_p = 4000 m/s, a S-wave velocity of c_s = 2400 m/s and a density of ρ = 2500 kg/m³, while the circular structure has material properties comparable to those of steel (c_p = 6000 m/s, c_s= 4000 m/s, ρ = 3800 kg/m³) and a diameter of 16 mm. The incident wave has a centre frequency of 10 kHz, so that the dimensions of wavelength and scatterer size are resembling those that are common during IE testing for the concrete-steel interface as well as for the cement-aggregate interface. Here material properties of steel were chosen due to the higher reflection amplitudes compared to aggregates. Figure 2 shows the reflected P-waves for different spatial resolutions. It can be observed that the reflection amplitude increases with a coarser grid. In fact, in this case the reflection amplitude increases by about 20% (measured at the second maximum of the reflection signal) when comparing a grid resolution of 0.5 mm with a 5 mm resolution.

This simulation setup was chosen due to the availability of an analytical solution for this scattering problem [15]. In fig. 3 one can see that the analytical solution for this particular scenario leads to much larger reflection amplitudes than the simulated one. The reason for this might be that some of the coefficients in the calculation for the analytical solution increase very large for small values of ka, with k being the wavenumber and a being the radius of the scatterer. For this scattering scenario the value of ka for P-waves is approx. 0.126, which is well below the lower limit of 0.5, for which the applicability is demonstrated in the paper [15]. This same scattering scenario with a frequency of 50 kHz (ka = 0.628) was also simulated (fig. 3). Here the calculated waveform matched much better with the simulated one. When comparing the maximum amplitudes with each other, the amplitudes for the EFIT simulation are still approx. 12% lower than the analytically calculated amplitude. However, it is observable that the overall waveforms still do not match perfectly with each other as the minimum amplitudes in the EFIT simulation are approx. 36% larger than the analytical one. A possible reason for the non-matching results at 10 kHz might also be that scattering amplitudes are measured in the near field for this scenario, but an additional simulation at a distance

of 5 m gave similar results. Even though the results for 10 kHz do not match, it can still be concluded that scattering amplitudes are likely not overestimated for EFIT simulations of IE inspections.

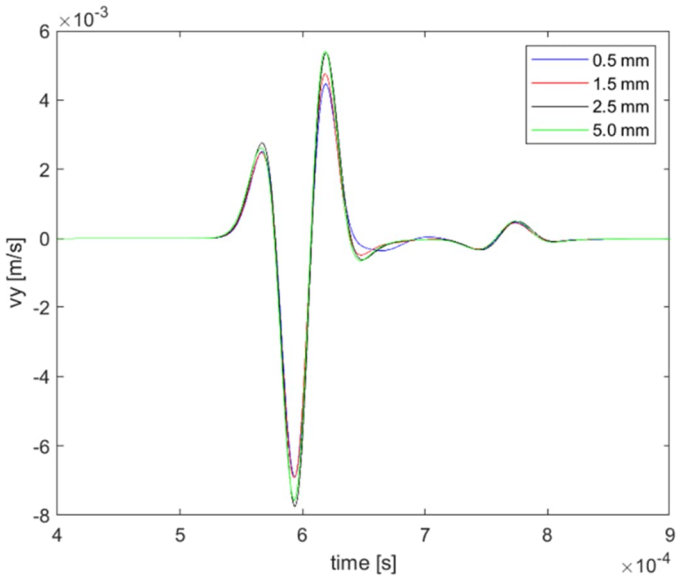

Figure 2. Reflection signals caused by a circular inclusion with a 16 mm diameter for different grid cell sizes [16]. The incident wave has a centre frequency of 10 kHz. The small reflection at about $7.5 \cdot 10^{-4}\ s$ belongs to the reflected and mode converted S-wave.

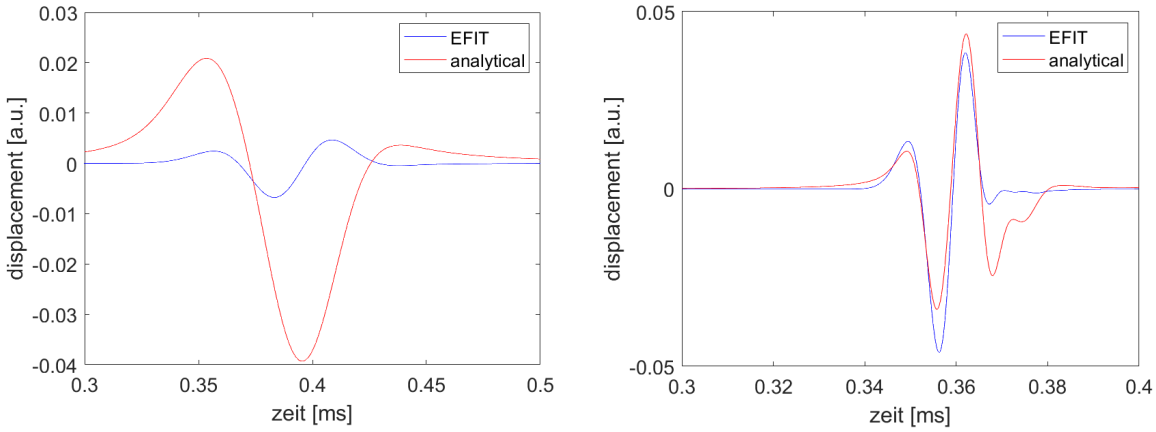

Figure 3. Comparison of analytical and simulated signals for a spatial resolution of 1.5 mm. Scatterer size in this example was 16 mm in diameter with a centre wave frequency of 10 kHz (left) and 50 kHz (right). Analytical solutions were calculated up to an order of 100 to obtain stable and converged waveforms [15].

In order to evaluate the influence of spatial resolution on IE simulations, 3D simulations with different spatial resolutions were carried out for a slab with 20 cm thickness and infinite lateral dimensions (absorbing boundaries at the sides). A schematic sketch of the simulation setup can be found in fig. 4. The wave velocities again were the same for cement matrix and aggregates (here: c_p = 4519 m/s and c_s = 2712 m/s). The density of the cement paste is ρ = 2294 kg/m³, while those for the aggregates vary uniformly in a range of ρ = 2294 ± 1700 kg/m³ to increase the scattering effect and to compensate for the absence of pores in these simulations. For comparison, the same simulations were not only carried out for the described inhomogeneous medium but also for a homogeneous one. Figure 5 presents the obtained frequency spectra from the simulations. Here, a significant frequency shift can be observed for the inhomogeneous medium, while the spatial resolution does not seem to have an influence on the resonance frequency for the homogeneous reference medium. This observation agrees with the previous results presented in this paper as higher reflection amplitudes again cause the wave velocity to decrease and therefore a lower resonance frequency will be observed. However, in contrast to the previous result, this is an additional numerical effect caused only by the grid cell size. The actual frequency shift due to

scattering is likely close to the difference between the frequency peak of the red curve and the vertical black line, which marks the theoretical resonance frequency calculated using $f = (\beta\, c_P)/(2\, d)$ with $\beta = 0.96$.

What also is worth mentioning here is, that the amount of noise in both simulations is similar. This is likely caused by the fact that all the energy which is scattered to one of the sides will essentially get lost due to the absorbing boundaries. Therefore, the noise levels in these simulations are similar for both, the homogeneous and heterogeneous medium.

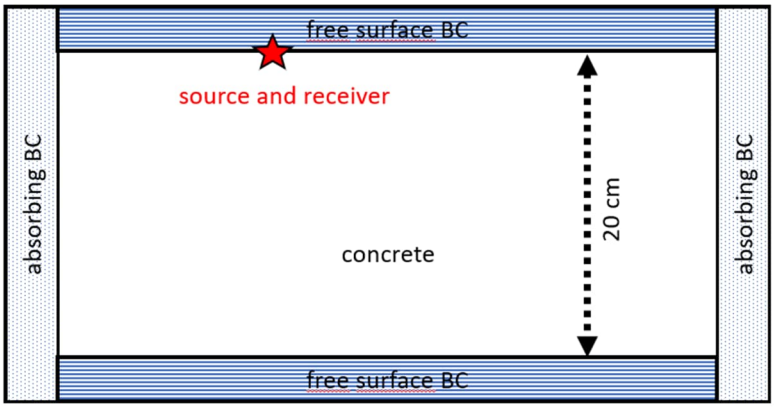

Figure 4. Simulation setup for the 3D simulations to determine the influence of aggregates on the IE resonance frequency. The dimensions of the free plates in both lateral directions are equal with absorbing boundaries surrounding them at all sides.

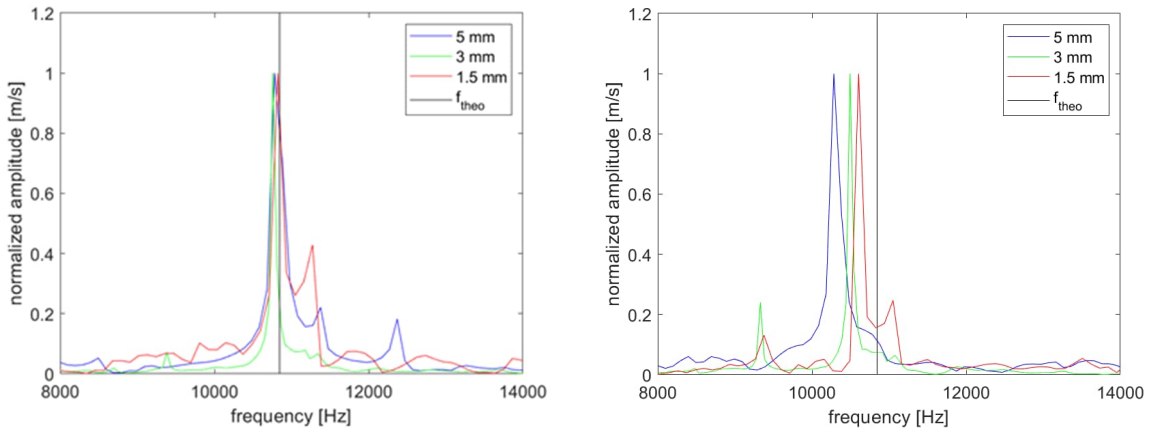

Figure 5. Frequency spectra for IE testing at a slab with 20 cm thickness for a homogeneous (left) and inhomogeneous medium (right) [16]. The signals were recorded at the impact point. The different colours express different grid cell sizes, while the black vertical line marks the theoretical resonance frequency. The centre frequency of the signal was 10 kHz.

2.3. Source function

For IE testing some parameters, which are required for modelling, are usually unknown. An example for this is the source function. According to Goldsmith [17], the force-time relationship for an elastic impact between a steel ball and a concrete plate can be approximated by a half-sine curve. The time between the start and the end of the half-sine curve in the force-time function is called the contact time, which can be determined by evaluating the width of the first Rayleigh wave [18]. For numerical simulations information on the exact force-time function generally is not available and therefore a suitable model has to be chosen. As previously mentioned, the typical assumption made for the source function in IE testing is assuming a half-sine curve [17]. In the EFIT IE simulations performed here, a Gaussian wavelet $f(t) = e^{\omega t - 2\pi} e^{-0.5(\omega t - 2\pi)^2}$ instead of a half sine curve was used. This source function was chosen because of numerical instabilities that occurred when using the half-cycle sine curve. Probably, these instabilities result from the non-differentiability at the end of the signal leading to numerical dispersion. In order to avoid numerical dispersion, the maximum signal frequency (i.e., the smallest signal period) must cover at least eight grid cells [8]. Usually,

numerical dispersion should not play a significant role for IE simulations, but in this case, the end of the signal seems to act locally as a Dirac pulse.

The centre frequency for all 3D simulations presented here is always in the vicinity of the theoretical expected resonance frequency (± 2 kHz) in order to compensate for the smaller bandwidth of the signals. Therefore, when comparing the signal response to actual measurements, only parts of the frequency spectrum are comparable. This effect was not as strong as for 2D simulations. Here, always the same frequency was used for all measurements at a certain specimen.

3. RECREATION OF TEST SPECIMEN INSPECTIONS

In order to validate the simulation code, real inspections from two different test specimens were recreated. The first test specimen was produced by the Florida Department of Transportation (FDOT) [20] and is a concrete block with 7 different sections of varying thickness. The second specimen belongs to the company TFB AG Wildegg and contains artificially generated honeycombs of different sizes in sections with and without steel reinforcement [21]. The geometry of both test specimens is shown in fig. 6.

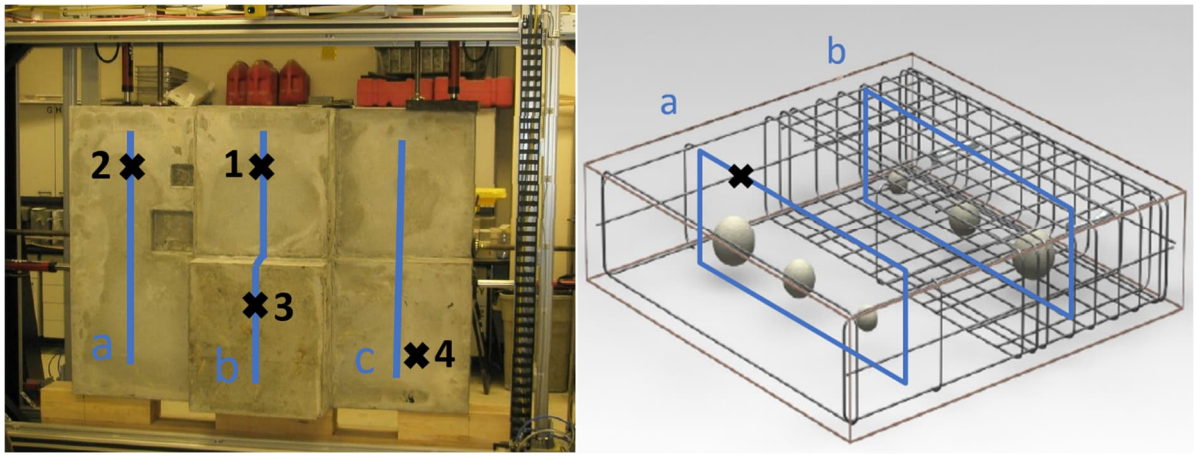

Figure 6. Test specimen 1 [20] is shown on the left side. The four simulated single point measurements are marked with black crosses while the three simulated B-Scans are indicated with blue lines. Test specimen 2 [21] is depicted on the right. Here, simulated B-Scans are marked with blue lines, while the simulated A-Scan is marked with a black cross.

3.1. Specimen 1

This specimen was produced by the Florida Department of Transportation (FDOT) in order to compare the quality of IE and ultrasonic measurements for thickness determination at a concrete part with a complex geometry [20]. Here, accurate thickness estimations could be obtained for ultrasonic measurements, while IE measurements were strongly influenced by geometry effects. Using EFIT the IE inspections at this specimen are recreated numerically to validate the described approach to IE simulations. Therefore, single point 3D simulations (A-Scans) as well as several 2D simulations (B-Scans) were conducted.

For the 3D simulations, a spatial resolution of 1.5 mm was chosen to avoid the additional frequency shift described in section 2.2. As the size of the specimen is 1.5 m x 2.1 m with a maximum thickness of 0.51 m, the total simulation domain contained 1406 x 1006 x 346 (= 489 million) grid cells (on each side three grid cells were added to simulate the free surface boundary condition). The material properties of the concrete and aggregates as well as the porosity can be found in table 2. In chapter 2.1 and 2.2 it was shown that scattering lowers the obtained resonance frequency. As the P-wave velocity was determined experimentally from the resonance frequency of a control specimen with a uniform thickness, this velocity already includes scattering effects. Therefore, a higher velocity would be needed for the material parameters in the simulation. However, as the inspected parts are relatively thick, an exact velocity calibration is not possible, especially if the frequency resolution in the obtained spectra is coarse. With frequency resolutions (3D simulation) of about 190 Hz even a single sample of difference in the resonance frequency would already mean a difference of more about 1.5% in resonance frequency for the thinnest part of the specimen. Therefore, an exact velocity

calibration may only be possible for thinner specimens. As pores decrease the average wave speed inside the medium [22], P- and S-wave velocities were adjusted, nevertheless. Here, they were increased by 2% keeping the Poisson's ratio constant.

Table 2 Parameters used for the simulations described in chapter 3. The percentage for the porosity and the share of aggregates refers to volume percent for 3D simulations and to the area percentage for 2D simulations.

Simulation	c_P [m/s]	c_S [m/s]	ρ_{agg} [kg/m³]	ρ_{cem} [kg/m³]	Porosity	Grid cell size [mm]	Share of aggregates
Specimen 1, 2D	4609	2766	1294-3294	2294	2%	1	75%
Specimen 1, 3D	4609	2766	1294-3294	2294	2%	1.5	75%
Specimen 2, 2D	4000	2650	1300-3300	2300 200 for honeycombs	2%	1	75%
Specimen 2, 3D	4000	2650	1300-3300	2300 200 for honeycombs	2%	2	75%

Using this setup, the IE inspection result of one measuring point (here: point 3) is compared to the simulation result at this point for four different scenarios using a homogeneous medium (i), a homogeneous medium only containing pores (ii), a medium without any pores but with aggregates (iii) and a medium with pores and aggregates (iv). For these simulations, the ones containing pores consider the increased velocity. The results are shown in fig. 7 and even though, all simulation results exhibit the same resonance frequency, only those where pores are included also exhibit strong local frequency peaks which are similar to those found in the inspection data. Therefore, they show best agreement with the real data, which is in line with previous results suggesting that pores, apart from geometry effects, are a major source of noise in IE measurements [6]. Even though the addition of aggregates does not change the frequency spectrum as much, it still has a significant influence. In the results shown here, it seems that the presence of aggregates leads to a smoother spectrum. However, this conclusion requires further investigation in detail for the sake of verification.

The simulation results for four different single point measurements are compared to the real inspection results in fig. 8. Here, all four simulation results show a good agreement in resonance frequency to the measurement results. As the results from measurement point 1 and 4 show quite significant differences from the theoretical resonance frequency. This leads to the assumption that also geometry effects, which can have a significant influence on IE results, are simulated correctly. When calculating the estimated thickness from the simulated resonance frequencies and comparing it to the thicknesses calculated from the measurement at that spot alongside with the standard deviation obtained within this specific section of the specimen, one finds that for two out of the four simulated scenarios, the thickness calculated from the simulations lies within the standard deviation (see table 3). For measurement no.3 the simulation gives a resonance frequency much closer to the actual specimen thickness, but does not lie within the standard deviation of the measurements. At measurement no. 1 it can already be seen in fig.8 that there are multiple resonance frequencies of approximately the same intensity in the spectrum. This holds true for both the actual measurement as well as the simulation. Because of this the correct frequency may not be easy to identify. This might also be the reason why both simulation and measurement do not match with the standard deviation of the thickness range in this section, but give results very close to one another.

To better investigate the geometry effects, simulations of entire B-Scans would be necessary. However, as these 3D simulations took three days of computation time on 160 cores, the recreation of B-Scans would be impractical. For this reason, 2D simulations are carried out to further investigate the geometry effects.

Table 3 Obtained specimen thicknesses from measurement and 3D simulations. The mean values and standard deviations are taken from [20] using the evaluation method with the smallest standard deviation that also considers the theoretical resonance frequency. Standard deviations for the simulation result are based on the frequency resolution of the obtained spectrum.

Measurement No.	Specimen thickness [cm]	Calculated thickness from measurements [cm]	Calculated thickness from simulations [cm]	Mean thickness in this section from all measurements [cm]
1	36.9	41.9	41.3 ± 1.5	33.1 ± 3.3
2	31.9	28.6	30.3 ± 0.8	28.5 ± 2.9
3	51.0	45.7	50.6 ± 2.2	44.0 ± 6.2
4	27.1	25.1	24.9 ± 0.5	24.9 ± 2.0

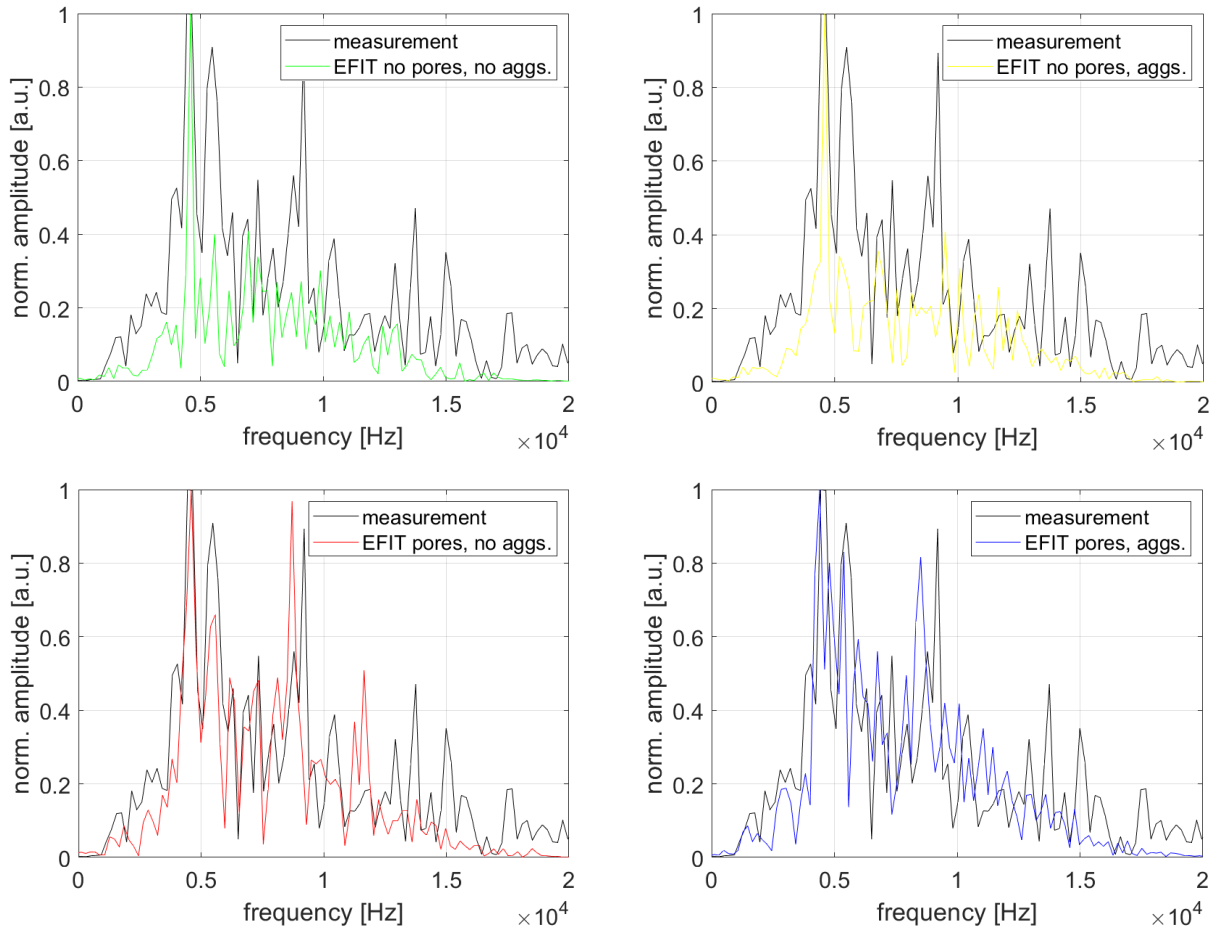

Figure 7. Comparison of the simulated (3D) and the experimentally obtained frequency spectra at measurement point 3 (see fig. 6 left) for four different scenarios that include or exclude pores and aggregates. The upper two results use the experimentally obtained velocities, while the two bottom simulations consider the increased velocities due to pores.

The 2D simulations were carried out using a 1 mm spatial resolution for 66 measurement points along the 1.5 m long side of the specimen, starting 10 cm from the edge with an increment of 2 cm between them. With these simulations, an entire IE B-Scan can be recreated. The simulation results for the right cross section (cross section c, see fig. 6 left) of the specimen is shown in fig. 9. In order to enhance the inspection results comparability and to eliminate effects caused by imprecise single point measurements, seven B-Scans located near the centre of the simulated section are stacked in the time domain before the Fourier transform is calculated. Additionally, a 2 kHz high pass filter was applied as a strong low frequency signal was masking the inspection result.

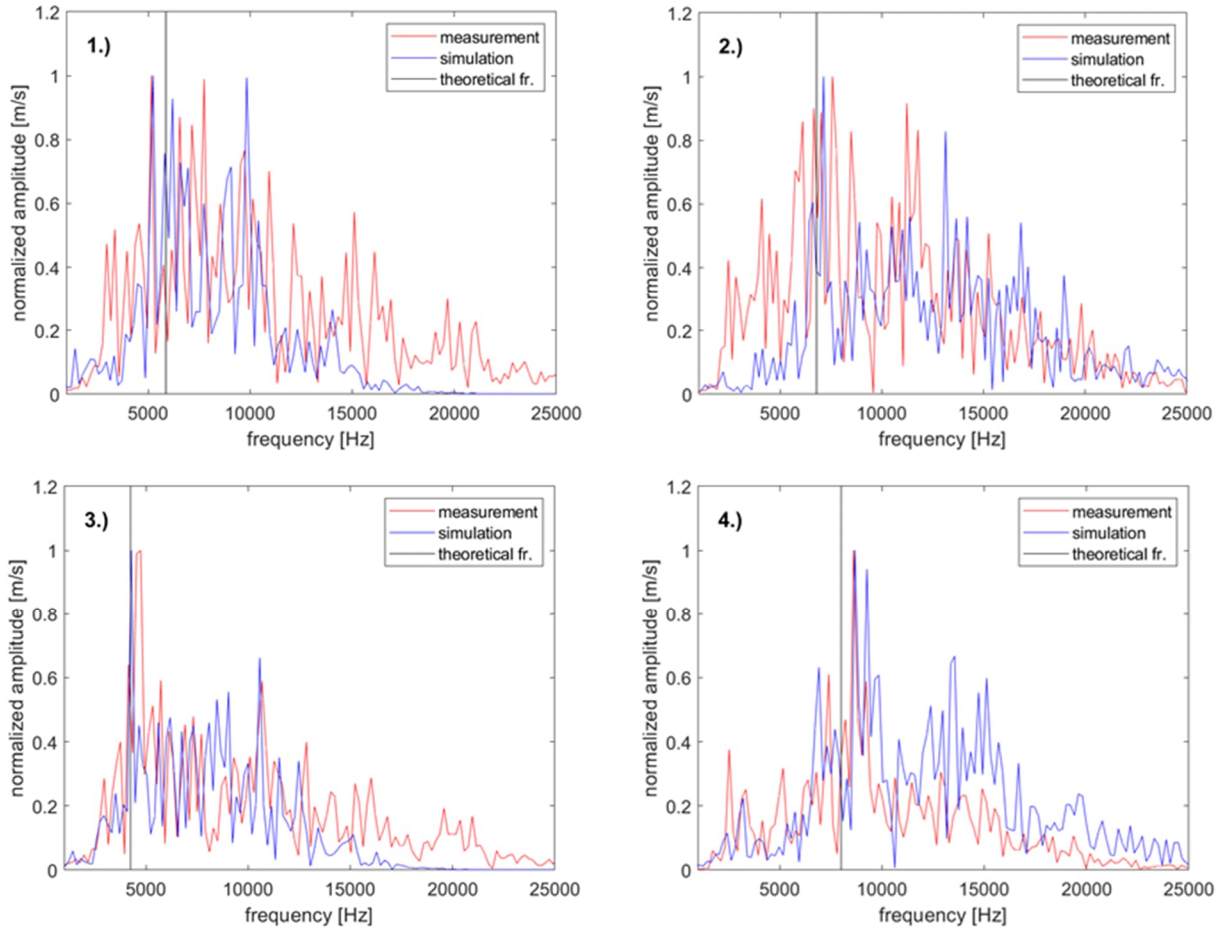

Figure 8. Comparison of the simulated (3D) and the experimentally obtained frequency spectra for four randomly selected measurement points (see fig. 6 left) [16].

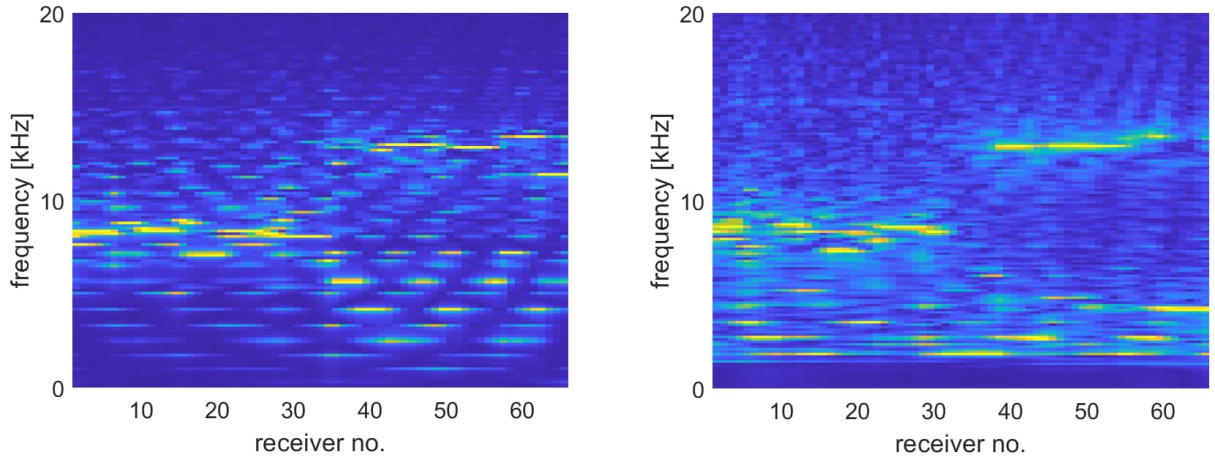

Figure 9. Frequency spectra for the cross section along the short side of specimen 1 with thicknesses of 27.1 cm between measurement point 1 and 33 and 16.9 cm for points 34 to 66. On the left side is the 2D simulation result whereas the actual inspection result can be found on the right. Processing includes clipping of the onset as well as a 2 kHz high pass filter for the inspection result due to resonance effects caused by the device itself.

For the 2D simulations, the noise seems to be smaller than for the 3D simulation. The reason for this could be that all the scattered waves coming in from the third dimension are disregarded in the 2D simulations. Overall, the simulation results show a very good agreement with the inspection in the vicinity of the resonance frequency. Even very complex patterns in the resonance frequency are reproduced almost identically. The only significant difference between the simulation and inspection is the limited bandwidth of the simulation signal, which was discussed in section 2.3.

Besides, EFIT has proven to be a very effective tool for simulating IE inspections at specimens with complex geometries.

3.2. Specimen 2

The second specimen is a 2 x 2 x 0.5 m^3 large concrete block containing steel reinforcement and artificially produced honeycombs. In the specimen a total of six honeycombs with three different sizes (two honeycombs per size) are placed at least 0.5 m from each side. Steel reinforcement can only be found in one half of the specimen, so that one honeycomb of each size is located in a region with and without steel reinforcement (see fig. 6, right). The specimen was originally designed to test the capabilities of Ultrasonic and IE testing to detect honeycombs. While some of the honeycombs could be detected with Ultrasonic testing, no honeycomb was reliably detectable with IE testing due to the strong geometry effects, which are masking the signals [21].

3D simulations for this specimen were carried out with a spatial resolution of 2 mm. As no velocity measurements were available for this specimen, literature values for the material properties were chosen (see table 2). The inspection was also carried out twice with different sensors, so that each simulation result can be compared to two inspections.

An ultra-low-density zone represented the honeycombs in the simulations. In the honeycombing areas the density of the cement matrix was assumed to be 200 kg/m^3, while the material parameters of aggregates were unchanged. For ultrasonic testing scenarios this modelling exhibited the same features as an assumed cluster of voids, which was used for finite element simulation of this specimen in a previous study [21]. Such a cluster led to numerical instabilities for EFIT simulation and therefore is not expedient.

Simulation results for this specimen (see fig. 10) show a slight difference in terms of resonance frequency compared to the simulations from section 3.1. Since no information on P- and S-wave velocity is available, also no velocity calibration is possible. Overall, the simulation results still show a good agreement within the frequency range covered by the source function (here: up to 12 kHz). A significant difference for frequency spectra of inspections in regions with and without honeycombing cannot be detected from the 3D simulations.

2D simulations have been carried out in the same way as for the previous specimen in order to compare entire B-Scans against each other. In figs. 11 and 12 the simulated B-Scans for the sections right on top of the honeycombs (cross section a and b) can be compared with each other. The most striking feature of the honeycomb IE signals seems to be the relatively low amount of higher frequencies compared to the signals right next to it. Such a feature can also be found in the simulations. As the actual velocities for P- and S-waves are not known exactly, a comparison of resonance frequencies is not possible. Overall, the simulation looks quite similar to the measurements for both sensors up to a frequency of about 14 kHz, but still has a smaller bandwidth than the actual measurement.

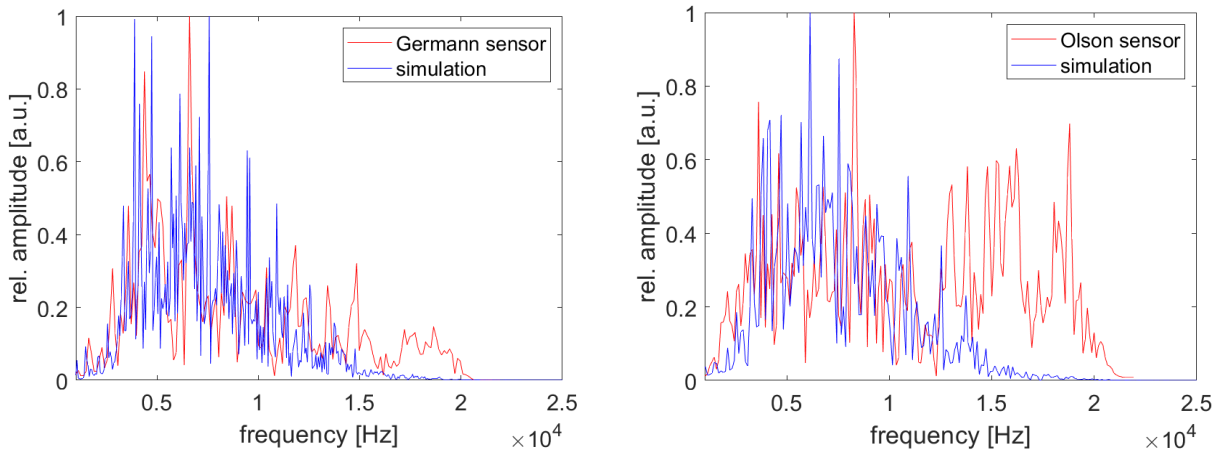

Figure 10. Comparison of the frequency spectra of the EFIT simulation (blue) and the two inspection results (red) for the measurement point right above the bottom left honeycomb (see fig. 4 right).

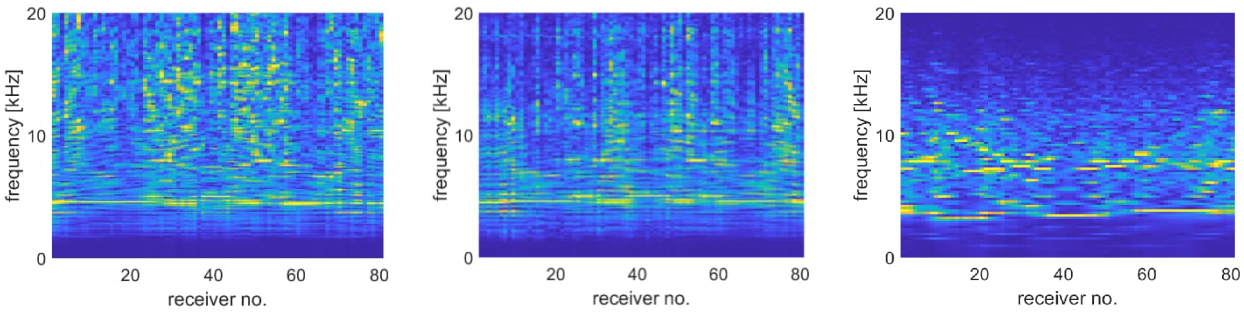

Figure 11. Frequency spectra for IE testing at specimen 2 in a region without steel reinforcement (y = 0.5 m). Inspection results from the Germann sensor are on the left, results from the Olson sensor are in the middle and 2D simulation results are on the right.

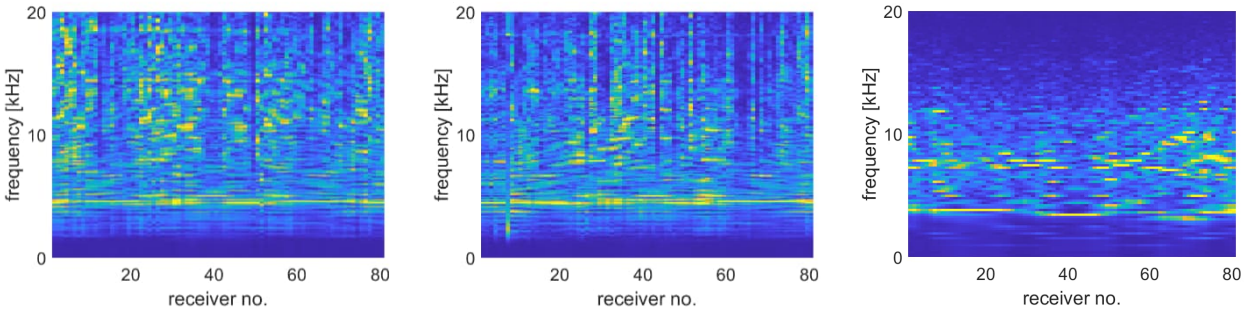

Figure 12. Frequency spectra for IE testing at specimen 2 in a region with steel reinforcement (y = 1.5 m). Inspection results from the Germann sensor are on the left, results from the Olson sensor are in the middle and 2D simulation results are on the right.

4. DISCUSSION

The simulation results have proven to be quite realistic. However, their verification is difficult since a lot of the factors, which are relevant for the simulation, are unknown when performing inspections. Such features include the exact shape, size and location of each aggregate and pore in the concrete, the exact source function, signal modulation effects caused by the device itself and background noise.

For 2D simulations, it must also be considered that geometrical spreading leads to an amplitude-distance proportionality of $1/\sqrt{r}$, instead of $1/r$. This means that waves arriving at later times will have a larger impact on the Fourier spectrum than they would have in 3D. Additionally, it has been shown that scattering for 2D simulations is more pronounced than for 3D simulations under the same circumstances [8]. This results from the fact that scatterers in 2D simulations would have to be infinitely large in the third dimension to achieve the same scattering amplitude.

When evaluating the 2D IE simulations from this work, it was found that, even though scattering amplitudes are larger for the 2D case than for 3D, the signal-to-noise ratio during IE simulations in 2D tends to be overestimated. A reason for this might be the fact that during IE inspections usually the S1 Lamb wave mode is being measured, which has a group velocity of zero. It therefore acts as an energy trap. When simulating in only two dimensions, the energy gets trapped even stronger as wave propagation in the third dimension is restricted.

Velocity calibrations are likely not necessary for large specimens as the change in resonance frequency that would be caused by pores and aggregates is too small to make difference large enough to be resolved with typical IE frequency resolutions. As Impact Echo uses frequencies, in which group and phase velocities are dispersive [11], some experimentally obtained velocities have to be adjusted in the numerical model to cover for the dispersion effect. For thinner specimens this effect might look differently as frequencies are higher and the transition zone between effective medium and ray theory will be reached at wavelength to scatterer size ratios of about 10 [22].

It is possible to explicitly discretize concrete and achieve realistic results. In the simulations it made a significant impact to the frequency spectrum if the medium was assumed to be heterogeneous instead of homogeneous (see fig. 7 and [6]). If this approximation reflects reality can

certainly be debated. According to the two-phase diffusion model by Anugonda et al. [23] diffusivity increases drastically at frequencies below 200 kHz, which would suggest that scattering should not play a huge role at typical IE frequencies. However, applicability of this model to scattering within the Rayleigh limit has, to the author's knowledge, not yet been proven.

In order to produce IE simulations with a realistic noise level, it is inevitable that the code is capable to correctly calculate reflection amplitudes and waveforms within the Rayleigh scattering limit. However, the analytical solution for scattering at a single infinitely long cylinder gave significantly larger scattering amplitudes than the EFIT simulation (see fig. 3). If this difference is a result of the simulation or the fast-growing coefficients in the analytical solutions in the Rayleigh scattering limit cannot be proven. Based on the direct comparison with real measurements, it can be concluded that the concrete model somewhat creates realistic measurement condition, whilst the comparison with the analytical solution suggests that EFIT underestimates scattering amplitudes. However, due to the lack of benchmark tests for this problem, the results cannot be verified.

One drawback of performing such numerical simulations with an explicit concrete model is the required computational power. As was shown in chapter 2.2 the spatial resolution might influence the obtained resonance frequency. Therefore, a fine resolved grid would be required, which drastically increases the amount of computational resources required for the simulations. In the case of specimen 1 (chapter 3.1) nearly half a billion grid cells were required and calculations took 72 hours with 160 processes on a high-performance computer. A computationally more efficient code is currently being developed.

5. CONCLUSION

A possible way to carry out Impact Echo simulations in concrete was presented. The effects of performing such simulations for inhomogeneous media were discussed regarding the porosity, spatial resolution and the reflection coefficient between aggregates and cement matrix. When comparing the simulations with inspection results several features, such as the resonance frequency as well as the noise level and other strong resonance modes were in good agreement, especially if pores and aggregates were considered in the simulation domain. However, the explicit discretization of the concrete does make the choice of velocity for the simulations more difficult, as dispersion effects occur. Also, 2D simulations have shown to reproduce the most pronounced features of B-Scans, while noise will not be as realistic as for 3D simulations. For future studies EFIT might also be used for inspections of nuclear reactors as well as for training artificial intelligence to enhance the detectability of defects.

ACKNOWLEDGEMENTS

All simulations were performed using the finite difference EFIT code, which was implemented as part of the WIPANO project "Normung für die probabilistische Bewertung der Zuverlässigkeit für zerstörungsfreie Prüfverfahren". This project is funded by the German Federal Ministry for Economic Affairs and Climate Action under the signature 03TN0006A.

REFERENCES

[1] A. Kumar, B. Raj, P. Kalyanasundaram, T. Jayakumar and M. Thavasimuthu, "Structural integrity assessment of the containment structure of a pressurised heavy water nuclear reactor using impact echo technique," *NDT & E International,* no. 35(4), pp. 213-220, 2002.

[2] B. H. Kim, I. K. Lee and S. J. Cho, "Estimation of existing prestress level on bonded strand using impact-echo test," in *Proceedings of the 6th European Workshop on Structural Health Monitoring*, Dresden, 2012.

[3] G. Vu, J. Timothy, D. Singh, L. Saydak, E. Saenger and G. Meschke, "Numerical-Simulation-Based Damage Identification in Concrete," *Modelling,* vol. 2(3), p. 19, 2021.

[4] K. Nakahata, G. Kawamura, T. Yano and S. Hirose, "Three-dimensional numerical modeling of ultrasonic wave propagation in concrete and its experimental validation," *Construction and Building Materials,* vol. 78, pp. 217-223, 2015.

[5] F. Schubert, R. Lausch and H. Wiggenhauser, "Geometrical effects on impact-echo testing of finite concrete specimens," in *Proceedings of international symposium non-destructive testing in civil engineering (NDT-CE)*, 2003.

[6] F. Schubert and B. Köhler, "Ten lectures on impact-echo," *Journal of Nondestructive Evaluation,* no. 27(1), pp. 5-21, 2008.

[7] P. Fellinger, R. Marklein, K. J. Langenberg and S. Klaholz, "Numerical modeling of elastic wave propagation and scattering with EFIT—elastodynamic finite integration technique," *Wave motion,* no. 21(1), pp. 47-66, 1995.

[8] F. Schubert and B. Köhler, "Three-dimensional time domain modeling of ultrasonic wave propagation in concrete in explicit consideration of aggregates and porosity," *Journal of computational acoustics,* no. 9(04), pp. 1543-1560, 2001.

[9] F. Schubert and B. Köhler, "Numerical time-domain simulation of diffusive ultrasound in concrete," *Ultrasonics,* no. 42(1-9), pp. 781-786, 2004.

[10] A. Asadollahi and L. Khazanovich, "Numerical investigation of the effect of heterogeneity on the attenuation of shear waves in concrete," *Ultrasonics,* no. 91, pp. 34-44, 2019.

[11] T. Philippidis and D. Aggelis, "Experimental study of wave dispersion and attenuation in concrete," *Ultrasonics,* no. 43(7), pp. 584-595, 2005.

[12] D. Komatitsch and R. Martin, "An unsplit convolutional perfectly matched layer improved at grazing incidence for the seismic wave equation," *Geophysics,* no. 72(5), pp. SM155-SM167, 2007.

[13] DGZfP Merkblatt B04, Ultraschallverfahren zur Zerstörungsfreien Prüfung im Bauwesen, Überarbeitete Auflage 67 S. ed., Berlin: Deutsche Gesellschaft für Zerstörungsfreie Prüfung (DGZfP), August 2018.

[14] K. Aki and P. G. Richards, "Plane waves in homogeneous media," in *Quantitative Seismology - second edition*, Mill Valley, California, University Science Books, 2009, pp. 76-78.

[15] Y. Liu, R. Wu and C. Ying, "Scattering of elastic waves by an elastic or viscoelastic cylinder," *Geophysical Journal International,* vol. 142(2), pp. 439-460, 2000.

[16] F. Dethof and S. Keßler, "Simulation von Impakt Echo Inspektionen in Beton zur Analyse der Detektionswahrscheinlichkeit," in *DGZfP Jahrestagung*, Kassel, 2022.

[17] W. Goldsmith, Impact: the theory and physical behavior of colliding, E.Arnold, 1960.

[18] N. Carino, "Impact echo: The fundamentals," in *Proceedings of the International Symposium Non-Destructive Testing in Civil Engineering (NDT-CE)*, Berlin, Germany, 2015.

[19] H. Chai, K. Liu, A. Behnia, K. Yoshikazu and T. Shiotani, "Development of a tomography technique for assessment of the material condition of concrete using optimized elastic wave parameters," *Materials,* no. 9(4), p. 291, 2016.

[20] D. Hiltunen, D. Algernon and Ferraro, "Validation of nondestruvtive testing equipment for concrete," University of Florida, 2010.

[21] D. Algernon, S. Feistkorn, Y. Schiegg and B. Mühlan, "Zerstörungsfreie Detektion von Kiesnestern in Stahlbetonbauteilen," Eidgenössisches Departement für Umwelt, Verkehr, Energie und Kommunikation UVEK, 2021.

[22] D. Marion, T. Mukerji and G. Mavko, "Scale effects on velocity dispersion: From ray to effective medium theories in stratified media," *Geophysics,* no. 59(10), pp. 1613-1619, 1994.

[23] P. Anugonda, W. J. Turner and J. Turner, "Diffusion of ultrasound in concrete," *Ultrasonics,* no. 39(6), pp. 429-435, 2001.

Assessment procedure of determining compressive strength of hardened reinforced concrete structures

Antti Wallenius[1], Fahim Al-Neshawy[2] and Jouni Punkki[2]
[1] Nodetec Oy, Helsinki, Finland
[2] Department of Civil Engineering, Aalto University, Espoo, Finland

ABSTRACT

As a heterogenous material, hardened concrete has several properties which have influence to the quality, compressive strength and service life. As there are several properties to examinate, there are multiple examination methods for different properties. Scope of this research was to introduce testing methods which are related to the examination of the concrete compressive strength, and furthermore to create a procedure for conducting effective examination of the compressive strength of structural concrete.
During the carrying out of this research, application of standard SFS-EN 13791 in Finland was in progress. Standard SFS-EN 13791 was published in 2019 and its scope is assessment of in-situ compressive strength in structures and precast concrete components. As concrete compressive strength is the most important property of concrete, a special attention was given to the determination of in situ compressive strength. This was done in accordance with the standard SFS-EN 13791 clause 8 and its Finnish application standard SFS 7508.
By carrying out the experimental examinations, it concretely helped to create understanding of the procedure of determining properties of hardened reinforced concrete. The procedure should be done systematically, where analysing the results of first examination can lead to the next needed examination method.
As a final result of this research, a flowchart was produced. The flowchart was produced in respect with standard SFS-EN 13791 clause 8 and its Finnish application standard. Scope of the flowchart was to introduce how many cores need to be extracted with possible indirect testing, in respect with the size of test region and the examination method.

Keywords: Concrete, In-situ compressive strength, examination methods, deterioration, indirect testing.

1 INTRODUCTION

There are times when it is considered necessary to assess the in situ characteristic compressive strength ($f_{ck,is}$) for structural assessment of an existing structure. The most practical procedure set out in SFS-EN 13791 Clause 8: Estimation of compressive strength for structural assessment of an existing structure [1]. This determination of the characteristic in situ compressive strength for application with EN 1992-1-1 [2]. For clause 8 it is assumed there is little or no prior information on the concrete and that the value generated is an estimate of the in situ characteristic strength.

For an assessment of an existing structure, there is no limit on the volume of concrete under consideration, and a minimum of eight ≥ 75 mm diameter cores with length : diameter ratios of either 2:1 or 1:1 are required. It is strongly recommended to obtain at least 10 cores due to the possibility that one or two core results may be rejected e.g., due to excess voidage or reinforcement inclusions.

1.1 Testing of the existing concrete structures

Indirect testing where use is either by rebound number in accordance with EN 12504-2 [3] or ultrasonic pulse vibration (UPV) in accordance with EN 12504-4 [4]. Core testing should be carried out in accordance with EN 12504-1 [3] where specimens are stored in sealed containers, apart from when they are either trimmed to length or the ends are capped ready for testing. The density of each core should be determined in accordance with EN 12390-7 and recorded as it is useful when interpreting core results.

Figure 1. Testing methods for concrete structures. (a) Ultrasonic Pulse Velocity (UPV), (b) Rebound Hammer and (c) drilled cores.

Cores with a trimmed length: diameter ratio of 2:1 or 1:1 and a diameter ≥ 75 mm should be used. The permitted range of 2:1 cores is 0,90:1 to 1,10:1 and the permitted range of 1:1 cores 0,90:1 to 1,10:1. Where 1:1 cores are used the core test result is converted to the equivalent value of a 2:1 core using the core length factor (CLF). For normal-weight and heavyweight concrete the CLF for converting a 1:1 core to a 2:1 core is 0,82 unless a different value is justified by testing. The characteristic in situ compressive strength for every test region was determined as follows:

$$f_{ck,is} = CLF * f_{c,1:1core,mean} \quad (1)$$

where

$f_{ck,is}$ is the characteristic in situ compressive strength of test region [MPa]

CLF is the core length factor 0.82

$f_{c,1:1core,mean}$ is the mean of the individual test measurements, where every individual test measurement is first multiplied with the diameter factor [MPa]

Cores should be free from reinforcement. Where a core contains reinforcement that is arranged perpendicular to the direction of loading, this shall be recorded and evaluated separately. Any core that contains reinforcement in the direction of coring or close to the direction of coring shall be rejected immediately and a further core taken from around same test location [5], [6].

1.2 Characteristic in situ compressive strength for test regions

The test regions should be defined, where it may comprise a series of similar elements, one large element or a defined volume associated with a source or time period where this is known. Different concretes should have separate test regions. Where there is little or no information about the concrete strengths in a structure then engineering judgement shall be applied to group elements into test regions, e.g., concrete columns may be a different strength class to concrete in floors. Test results should be checked to see whether they comprise more than one concrete.

Small test region < 10 m³

A small test region may be considered one to three elements and a total volume not exceeding approximately 10 m³ (a volume of concrete up to 10 m³). At least three drilled cores ≥ 75 mm diameter are taken including at least one core from every element in the test region and the in situ compressive strengths ($f_{c,is}$) are calculated. Where the core locations represent concrete that will remain in the structure, and where the spread of test results is not more than 15 % of the mean value, the lowest value of three or more cores may be considered in situ compressive strength ($f_{ck,is}$) for structural assessment purposes. If the spread of results is more than 15 % of the mean, this is an indication that more information about the test region should be sought.

Small test region <30 m³

Where there are no issues over the compressive strength of the supplied concrete and where indirect testing is used for an initial survey the test region may be considered as up to approximately 30 m³ of concrete. The variability and locations of lower compressive strength should be identified with the initial survey. From the locations or location with the lowest indirect test result at least three

≥ 75 mm diameter cores are taken and the in situ compressive strength ($f_{c,is}$) calculated. If the core locations represent concrete that will remain in the structure, and provided the spread of test results is not more than 15 % of the mean value, the mean value of three or more cores may be assumed to be the characteristic in situ compressive strength ($f_{ck,is}$) for structural assessment purposes.

Where the spread of the test results is higher than 15 % of the mean value, and if an investigation provides a justified reason for rejecting one of the core tests results, the in situ compressive strength ($f_{ck,is}$) may be taken as being the mean of the remaining valid values.

The Standard SFS-EN 13791 [1] was published in 2019 and its scope is for assessment of in-situ compressive strength in structures and precast concrete components. As concrete compressive strength is the most important property of concrete, in this research, special attention was given to the determination of in situ compressive strength. This was done in accordance with the standard SFS-EN 13791 clause 8 and its Finnish application standard SFS 7508.

The objectives of this research were:

1) to create a procedure for conducting effective and systematic examination of structural concrete.
2) to create a flowchart of the procedure of determining the compressive strength of hardened reinforced concrete from structures
3) to introduce the assessment of in-situ compressive strength in accordance with the standard SFS-EN 13791 and its Finnish application standard SFS 7508

2 EXPERIMENTAL PROGRAM

Understanding hardened concrete properties is the basis for using concrete in construction and design. Many standards and tests are used in the concrete industry and these tests ensure the quality of the concrete structures.

2.1 Indirect testing of concrete structures

To assess the compressive strength of hardened reinforced concrete structures and create a flowchart of the procedure of determining the characteristic compressive strength of hardened reinforced concrete from structures, three tests were performed:

1) Rebound hammer test – compressive strength and selecting the location of drilled samples.
2) Ultrasonic pulse velocity (UPV) test – quality of concrete
3) Compressive strength from cored specimen – compressive strength of concrete

2.1.1 Rebound hammer test

Rebound hammer is the mostly used non-destructive (NDT) method for assessing the compressive strength of hardened concrete. The rebound numbers are influenced by a number of factors like types of cement and aggregate, surface condition and moisture content, age of concrete and extent of carbonation of concrete [7].

Table 1. Influencing factors on average rebound measurements [8], [9].

Influencing Factors	Material	Factors	Influence
Concrete mix	Aggregate	Maximum aggregate size	Average
		Type (hardness/density)	High
	Cement paste	Content (percentage)	Moderate
		Type of cement	Moderate
Humidity			Average
Factors influencing surface and near-surface condition		Age/carbonation	High
		Surface smoothness	Average
		Type of formwork and curing	Average
Others		Rigidity of the component (thickness)	Average
		Temperature	Moderate
		Air voids	High
		Steel reinforcement	High

To select coring location, rebound hammer Proceq Silver Schmidt hammer (Q) Type N was used. In standard SFS-EN 13971 clause 8.3 there is no exact specification for minimum number of test locations for indirect test measurement for the test region. Therefore, SFS-EN 13791 Table 9 was adopted for determining the minimum number of test locations. According to SFS-EN 13791 Table 9, nine is the minimum number of indirect test locations when the volume of test region is less than 30 m^3. Therefore, nine rebound test locations were examined for each test region (structure), as shown in Figure 2. All the structures had similarly arranged test locations with identical numbering system [10].

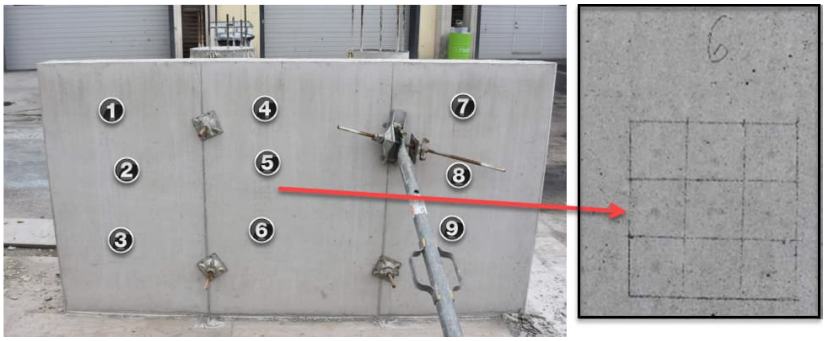

Figure 2. Nine rebound hammer test locations were marked for each test region.

Each rebound test location was divided into three-by-three grids as shown in Figure 2 and the median of nine valid readings was used as the rebound number of that location. Location with the lowest rebound number of the test region was determined as coring location. Due to the reinforced structures, rebar detector was used to locate the rebars to avoid any rebars in the cored specimens.

2.1.2 Ultrasonic pulse velocity (UPV) test

Ultrasonic pulse velocity (UPV) is a testing technique where high-frequently elastic waves are fed into concrete. The pulse is generated by a transmitter and received by a receiver. It is used to detect surface and subsurface discontinuities by measuring the pulse velocity (v) when transit time (T) and path length (L) are known [11]. Additionally, UPV can be used to determine concrete material properties such as compressive strength.

It is well known that the factors which significantly affects to the UPV measurement have a little influence on the concrete strength. As a result, when estimating the compressive strength, it is essential touse pre-established calibration curves for specific concrete [12].

Table 2. Influencing factors on UPV measurements [13].

Influencing Factors	Material	Factors	Influence
Concrete mix	Aggregate	Content (percentage)	High
		Maximum aggregate size	Average
		Type (density)	High
	Cement paste	Content (percentage)	Moderate
		Type of cement	Moderate
		Water/cement ratio	High
Humidity			Moderate
Others		Age of concrete	Average
		Air voids and cracks	Average
		Steel reinforcement	High

With indirect transmission there is uncertainty regarding the exact length of the transmission path, because of the significant size of the areas of contact between the transducers and the concrete. Therefore, standard SFS-EN 12504-4 (2004)[4] specifies that four testing should be carried out by using fixed increments along the chosen line on the surface as shown in Figure 3. The results of four locations should be plotted as points on a graph. The mean pulse velocity is determined by the slope of the best straight line drawn though the points (tan Φ).

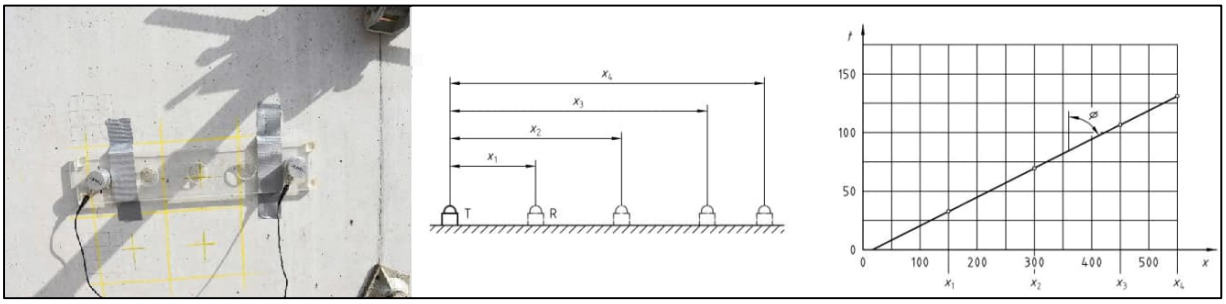

Figure 3. Determination of pulse velocity by indirect (surface) transmission [4].

The ultrasonic pulse velocity of concrete can be related to its density and modulus of elasticity. It depends upon the materials and mix proportions used in making concrete as well as the method of placing, compacting, and curing of concrete. If the concrete is not compacted thoroughly and having segregation, cracks or flaws, the pulse velocity will be lower as compared to good concrete, although the same materials and mix proportions are used. The quality of concrete in terms of uniformity can be assessed using the guidelines given in Table 3.

Table 3. General Guidelines for Concrete Quality based on UPV [14].

Longitudinal pulse velocity (km/s)	Quality of concrete
>4.5	Very good to excellent
3.5–4.5	Good, slight porosity may exist
3.0–3.5	Doubtful, but loss of integrity is suspected
2.0–3.0	Poor and loss of integrity exist
<2.0	Very poor

2.1.3 Compressive strength from cored specimen

Concrete compressive strength determined by compression testing machine is the only permitted testing method according to SFS-EN standards. According to SFS-EN 13791:2019 standard, there is three different options for estimation of compressive strength for structural assessment of an existing structure. The used method is depending on the size of test region and if indirect testing is used along core test data.

The thickness of the walls was 200 mm thick with two layers of reinforcing mesh, bars have diameter of 8 mm at 150 mm centres. To avoid any reinforcing in the final compressive strength three test specimens with diameter of 94 mm were drilled from each wall. The slab thickness was 150 mm. A similar mesh was used for slabs as walls and the mesh was located approximately in the lower third of the slab. For smaller thickness compared to the walls and the location of the reinforcement mesh, smaller cores with diameter of 78 mm were drilled. All the specimens had diameter to length ratio 1:1. Two different specimen sizes where used, diameter of 94 mm and diameter of 78 mm. The compressive strength test was carried out with a universal hydraulic compression machine (Toni Technik) with capacity of 5000 kN.

Figure 4. Drilling of the concrete cores. (a) Drilling setup and (b) specimens sealed with plastic bags after coring.

To align with the design standard SFS-EN 1992-1-1 [2], where the compressive strength is based on 2:1 cylinder and the in-situ strength is based in 2:1 core. This has to be considered when 1:1 cores are used in compressive strength test. To convert 1:1 core ($f_{c,1:1core}$) to equivalent 2:1 ($f_{c,2:1core}$) cores, the 1:1 core has to be multiplied with core length factor CLF = 0,82. In exception to SFS-EN 13791, in the Finnish application of standard SFS-EN 13791 to determine the fc,1:1 core, the tested result has to be first multiplied with diameter factor. The diameter factor is determined as follows:

- cylinder specimen's nominal diameter is within 100…150 mm → factor 1.05
- cylinder specimen's nominal diameter is within 75…80 mm → factor 1.10
- cylinder specimen's nominal diameter is within 80…100 mm → factor is linearly interpolated in range 1.10-1.05

2.2 Test region and test locations

Total of four reinforced concrete structures where cast in situ for education purposes. These structures were allowed to be utilized to simulate existing structures where no information of the properties was known. When these structures were prepared, purposely good and poor compaction were carried out for each structure as presented in Figure 5. In this research, the two walls and two slabs were investigated.

Figure 5. Investigated reinforced concrete structures.

Table 4. Properties of the investigated hardened concrete.

Concrete	Density (kg/m³)	Total porosity [%]	Air content [%]
TL1	2318	19.5	3.5
TL2	2225	22.8	6.9
TL3	2290	20.3	4.8
TL4	2193	23.2	8.3

3 RESULTS AND DISCUSSION

Table 5 represents rebound numbers (medians) from every test region. The lowest median result which determined the coring location for that test region is labelled for each test structure. In test region TL3, there was five test locations with the same lowest median value. From rebound test results points of view, the rebound value from all test locations in the test region was rather constant. Taking nine rebound locations from each structure when total volume of concrete was approximately 1.7 m^3 was probably too conservative. Especially, when it was known that structures TL1 and TL3 were cast from same batch, similarly TL2 and TL4 were from same batch. However, due to relatively small structure sizes and test regions TL2 and TL4 were compacted purposely poorly, every structure was investigated as own test region.

Table 5. Rebound hammer median test results.

Test location	Test structure (region)			
	TL1	TL2	TL3	TL4
1	52	53	51	46
2	53	45	55	47
3	52	48	55	46
4	50	52	51	46
5	50	50	52	45
6	47	48	51	42
7	51	50	51	48
8	51	49	54	51
9	58	48	51	48

Figure 6 represents the ultrasonic pulse velocity test results. Test regions TL2, (TL2) and TL3 had very small coefficient of variation – CoV of 1,70 %, 2,16 % and 0,02 %, respectively. Two UPV areas were tested for test region TL2. TL2 without brackets was the main UPV location which was determined to be coring location by using rebound hammer. (TL2) with brackets was additional UPV location where the poor labour working joint was able to be seen. As expected, (TL2) had the lowest average UPV which was most likely due to poor concrete labour and the higher porosity of concrete. Most of the velocities were under 3,5 km/s which according to Table 3 is the threshold between good and doubtful concrete quality. Therefore, the measured results predicted that air entraining agent would have been used in the concrete mix. This prediction was verified when the porosity tests were done.

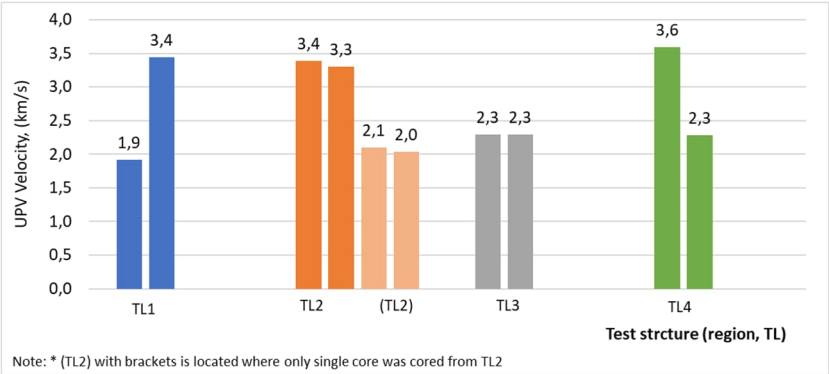

Figure 6. UPV measurement result for the test structures.

Table 6 represents results of drilled specimens' compressive strength test results. In test region TL2 the standard deviation was the greatest 3,2 MPa with 9.2 % CoV. This was predictable due to poor labouring which was possible to notice onsite. Surprisingly, standard deviation for other poor laboured test region TL4 was the second lowest. Probably poor labouring work is more affected to vertical structures than to horizontal structures as segregation is more critical to higher structures.

Table 6. Compressive strength test measurements of the drilled samples.

	Test structure (region)			
	TL1	TL2	TL3	TL4
Drilled sample – 1	40,5	32,5	42,8	41,3
Drilled sample – 2	40,6	38,3	41,6	42,6
Drilled sample – 3	39,6	33,2	40,6	41,8
Average (MPa)	40,3	34,7	41,7	41,9
Standard Deviation SD (MPa)	0,5	3,2	1,1	0,7
Coefficient of Variation CoV (%)	1,3	9,2	2,7	1,6

It is important to remember that the compressive strength determination was based on the standard SFS-EN 13791 clause 8, where there was no doubt of the concrete quality. The main purpose was to determine characteristic in situ compressive strength for every test region, which can further be utilized in design of concrete structures according with standard SFS-EN 1992-1-1.

Assessment of compressive strength for concrete structures

Flowchart offers combined guidance of standard SFS-EN 13791 clause 8 Estimation of compressive strength for structural assessment of an existing structure with the Finnish application standard. This is only based on how to determinate compressive strength and does not include deterioration. The examination is governed by two main factors: (i) volume of the test region and (ii) usage of indirect testing. The difference can be seen on how many extracted cores are needed and, in some cases, how many indirect testing locations are needed.

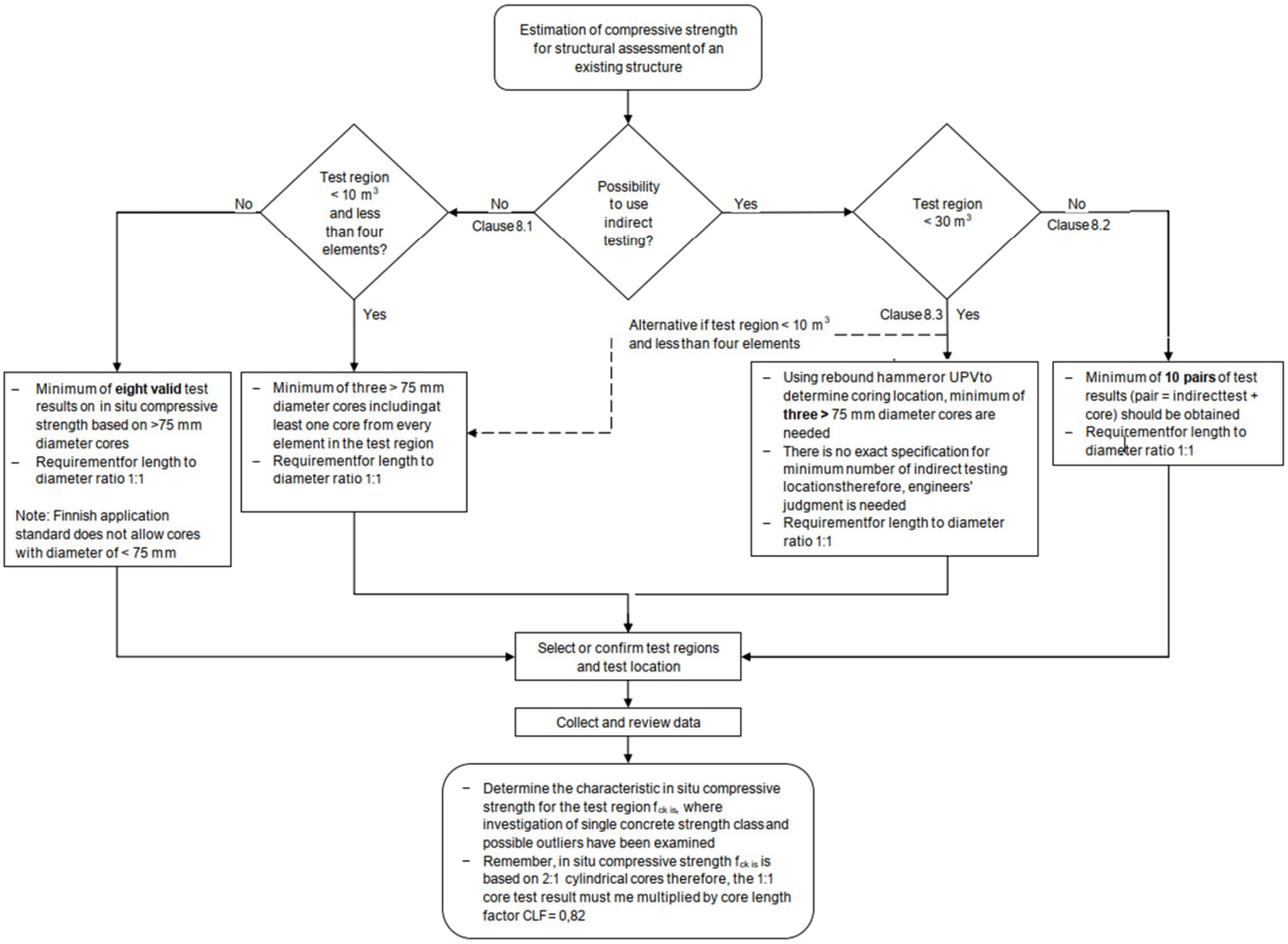

Figure 7. Flowchart for assessment of compressive strength in accordance with standard SFS-EN 13791 clause 8 and its Finnish application standard.

Scope of the flowchart was to offer easily approachable guidance on how many extracted cores or/and indirect testing locations are needed, in respect with the size of test region and the examination method. The flowchart does not specify how the actual compressive strength examination is carried out and therefore the flowchart should be used with the standard SFS-EN 13791. The flowchart is presented in Figure 7.

4 CONCLUSION

This research presents the determination of in-situ compressive strength of existing concrete structures. Three testing methods were used: (i) rebound hammer testing for locating the weakest location of the concrete structures, (ii) ultrasonic pulse velocity (UPV) for determining the location of poorest quality of the concrete in the structure and (iii) drilling of concrete cores for compressive strength test.

- During the compressive strength assessment, where the coring locations was to be determined according to the standard SFS-EN 13791, it was found that a quite challenging to get an overall picture, as there were multiple alternative ways how the determination can be done, in terms of test region volume and if indirect testing can be used.
- Therefore, flowchart for assessment of compressive strength was created. Scope of the flowchart was to introduce easily approachable flowchart on how many cores need to be extracted with possible indirect testing, in respect with the size of test region and the examination method. The flowchart does not specify how the actual compressive strength examination is carried out and therefore the flowchart should be used with the standard SFS-EN 13791 and its Finnish application standard SFS 7508.

In the experimental examination, rebound hammer was used as the indirect testing method to locate the coring locations. However, rebound hammer only concerns the surface layer of concrete structure and therefore its influence to present the whole structure is debatable. Therefore, in the future, comparison between rebound hammer and UPV could be done in terms of locating the core locations for compressive strength testing. Additionally, could be investigated if ground penetrating radar (GPR) could be used to locate the coring locations.

REFERENCES

[1] EN 13791, *Assessment of in-situ compressive strength in structures and precast concrete components*. 2019.

[2] EN 1992-1-1, “Eurocode 2: Design of concrete structures - Part 1-1: General rules and rules for buildings,” *305/2011 Directive 98/34/EC*. The European Union Per Regulation 305/2011, 2004.

[3] EN 12504-1, *Testing concrete in structures Part 1: Cored specimens - Taking, examining and testing in compression*. The European Committee for Standardisation (CEN), 2009, pp. 1–20.

[4] EN 12504-4, “Testing concrete - Part 4: Determination of ultrasonic pulse velocity.” The European Committee for Standardisation (CEN), 2004.

[5] C. A. Clear, “Estimation of compressive strength for structural assessment of an existing structure,” *BRMCA GUIDE BS EN 13791:2019, Clause 8*. The Mineral Products Association (MPA), 2021.

[6] R. Sefrin and C. Glock, “Characteristic concrete compressive strength of existing structures—Evaluation of EN 13791:2019 for small sample sizes,” *Structural Concrete*, vol. 23, no. 2, pp. 822–835, Apr. 2022, doi: 10.1002/SUCO.202100207.

[7] Proceq, “Rebound Measurement and Carbonation,” 2003. Accessed: Dec. 05, 2020. [Online]. Available: https://www.pcte.com.au/images/pdf/Original Schmidt Hammer/Data-Sheet-(Effects-of-Carbonation).pdf

[8] D. Breysse and J. L. Martínez-Fernández, “Assessing concrete strength with rebound hammer: Review of key issues and ideas for more reliable conclusions,” *Materials and Structures/Materiaux et Constructions*, vol. 47, no. 9, pp. 1589–1604, 2014, doi: 10.1617/S11527-013-0139-9.

[9] D. Breysse, “Nondestructive evaluation of concrete strength: An historical review and a new perspective by combining NDT methods,” *Constr Build Mater*, vol. 33, pp. 139–163, Aug. 2012, doi: 10.1016/j.conbuildmat.2011.12.103.
[10] A. Wallenius, “Procedure of determining properties of hardened reinforced concrete from structures,” Aalto University School of Engineering, Espoo, 2022. Accessed: Aug. 27, 2022. [Online]. Available: https://aaltodoc.aalto.fi:443/handle/123456789/112661
[11] P. Burrascano, S. Callegari, A. Montisci, M. Ricci, and M. Versaci, *Ultrasonic nondestructive evaluation systems: Industrial application issues*. Springer International Publishing, 2015. doi: 10.1007/978-3-319-10566-6/COVER.
[12] Y. Lin, “Investigation of pulse velocity-strength relationship of hardened concrete,” *ACI Mater J*, vol. 104, no. 4, pp. 344–350, Jun. 2007, Accessed: Aug. 27, 2022. [Online]. Available: https://www.researchgate.net/publication/287762473_Investigation_of_pulse_velocity-strength_relationship_of_hardened_concrete
[13] D. Breysse, “Nondestructive evaluation of concrete strength: An historical review and a new perspective by combining NDT methods,” *Constr Build Mater*, vol. 33, pp. 139–163, Aug. 2012, doi: 10.1016/j.conbuildmat.2011.12.103.
[14] J. P. Balayssac and V. Garnier, *Non-destructive Testing and Evaluation of Civil Engineering Structures*. Elsevier Inc., 2017. doi: 10.1016/C2016-0-01227-5.

Towards a harmonization of permeability measurements under pressure and in vacuum

H. Cagnon[1,*], J. Verdier[1], A. Nehme[1] and S. Multon[1]
[1] Université de Toulouse, UPS, INSA, LMDC (Laboratoire Matériaux et Durabilité des Constructions), 135, avenue de Rangueil, F-31 077, Toulouse Cedex 04, France
* cagnon@insa-toulouse.fr

ABSTRACT

To measure the tightness of nuclear containment structures and their durability, air permeability measurement is of particular interest. It allows to estimate leakage rates quickly and has the advantage of being non-destructive. However, the devices used in the laboratory and those used in situ differ. The CEMBUREAU permeameter is the subject of a standard (XP-P18-463) whereas this technique is limited to the laboratory and requires a particular sampling and confinement, inadequate to the real structures. This implies that a core sampling of the structure is necessary but that is not always possible, hence the interest to develop new techniques of non-destructive measurement on site. In this perspective, many works have been carried out and several approaches have been apprehended. One of these techniques is the measurement of permeability by the Torrent apparatus which is widely studied today. These two techniques rely on different equipment and different physical phenomena. The CEMBUREAU permeameter operates under pressure, i.e., the gas passing through the sample is injected at a pressure higher than atmospheric pressure, whereas the Torrent permeability measurement is performed in vacuum (Torrent, 1992). The tests therefore give variable results that do not allow an easy comparison (Sogbossi et al., 2019). A standardization or at least a harmonization of the results from different tests is necessary for a better analysis and estimation of the durability of the structures. Five measurement techniques will be presented here:
- Two techniques carried out in laboratory working in steady state (CEMBUREAU under pressure and a technique in vacuum). They consist in measuring an air flow through a cylindrical specimen confined in a cell and subjected to a constant pressure gradient.
- Two new laboratory approaches developed at LMDC operating in transient regime (simple cell with a vacuum time of sixty seconds and another with a longer vacuum time). They consist in measuring a pressure rise in a cell stuck to the surface of a confined specimen in which a vacuum has been initially made.
- An on-site measurement technique (Torrent, 1992) which works like the two previous ones in vacuum and in transient regime.

The reference value of the literature being that of the CEMBUREAU, the objective is to manage, from the four other tests, to go back to this permeability. The measurement from the Torrent shows still important differences, which originate from the technique or the interpretation of the results, whereas the four other tests lead, after calculation of the systematic error, to convincing results.

Keywords: Permeability, CEMBUREAU, Torrent, Durability

1. INTRODUCTION

Controlling and guaranteeing the tightness of the containment of nuclear power plants is a worldwide challenge, and even more so in France, with more than fifty reactors currently in operation. Nuclear power plants are regularly inspected to verify their tightness in case of an accident. These conditions correspond to an increase in internal pressure and temperature of up to +0.5 MPa and 180°C respectively for two weeks.

* Hugo Cagnon: 05 62 25 89 57 and cagnon@insa-toulouse.fr

To test the tightness, the reactor building (inner vessel) is pressurized to the design pressure and the leakage is evaluated by following the mass loss over time. At the same time, single leakage measurements are performed in the space between the reactor vessels using collection boxes. The difference between the global leakage rate leaving the enclosure and the rate associated with the singularities constitutes the diffuse leakage in the healthy zone. There are still large uncertainties in the evaluation of the singular leakage, which results in a poor estimation of the diffuse leakage. In addition, these tests are restrictive and require a high level of logistics and are only carried out about once a decade in France, which could prove problematic in the context of rapid leak detection.

The tests classically carried out in laboratory under pressure (CEMBUREAU), are destructive techniques, which require the taking of samples on site representative of the structure. However, the small size of the samples and the impossibility to come and core a power plant makes these tests obsolete. A technique developed in the 1990's, allows to make in situ measurements. The Torrent permeameter, developed by the engineer of the same name, makes it possible to measure surfaces permeability in vacuum in a non-steady state, which is difficult to interpret. Moreover, the investigated zones are small in diameter (about 5 cm) and in depth. This raises questions about the representativeness of tests on walls that can reach several tens of centimeters of thickness, as is the case for nuclear power plants.

To propose a new interpretation of these under vacuum tests, a laboratory methodology has been developed. It consists in determining the apparent permeability of reference under pressure and steady state (CEMBUREAU) for several concretes in variable states of saturation, then to compare this value with those obtained in vacuum and steady state, then in vacuum and transient state, configuration which is the closest to the in-situ measurement Finally, correlations are proposed to harmonize the different techniques.

2. MATERIALS AND METHODS

In this part, the materials used, and the concrete mix-designs are presented. The protocols used as well as all the pre-conditioning of the samples are also explained, since these have a strong impact on the results.

2.1. Materials and conditioning prior to testing

The mix-designs were chosen so that the concretes studied cover the range of porosity representative of site concretes from the point of view of transport. The variation of the saturation state also allows to act on the porosity accessible to the gas and to widen the study range. The work is part of the global framework of the project Non-Destructive Evaluation of Nuclear Power Plant Containment (NDEN), the concrete formulated is the one used on Vercors (Multon et al., 2022), which is the 1/3 scale nuclear power plant model, representative of the double-walled containment of a 1300 MWe nuclear power plant. The two other mix-designs are: an ordinary concrete (OC) and a high-performance concrete based on CEM I (HPC). The formulations of the different concretes studied are presented in Table 1.

Table 1 Concrete mix-designs (in kg/m^3)

Constituents	NDEN	HPC	OC
Sand 0/4 rec GSM LGP1	830	-	-
Sand 0/4 R Garonne	-	858	941
Aggregate 4/11 R GSM LGP1	445	-	-
Aggregate 8/16 R BALLOY	550	-	-
Aggregate 5/12.5	-	945	-
Aggregate 4/14 R Garonne	-	-	1020
CEM I 52.5 NCE CP2 NF Gaurain	320	400	280
Techno 80 Sika plast	2.4	-	-
Masterglenium Sky 537	-	3	-
Chryso Optima 175	-	-	1.96
Total water	198	172	180

The concrete is poured into cylindrical moulds of 15 cm diameter and 20 cm height which are vibrated on a vibrating table in two layers. The covered moulds are stored in a humid chamber at 20 ± 2°C for twenty-four hours, the demoulding then takes place, and the samples are kept in lime water as soon as they are demoulded. To obtain a relatively stable material with respect to hydration, the duration of this water cure is fixed at 60 days minimum (Saul, 1951; Waller et al., 2004). The different permeability measurements were made on specimens in given states of saturation, given the strong dependence of this measurement on the internal humidity of the samples. The preconditioning adopted to limit the thermal damage and to reach the saturation states is the following (Carcasses and Abbas, 2001) start drying in a ventilated oven at 40°C until a degree of saturation of 80% is obtained, continue drying at 50°C until a degree of saturation of 45-40% is obtained, then drying at 60°C until a degree of saturation of 20% is obtained, then drying at 80°C until constant mass (less than 0.05% mass variation over 24 hours), Finally drying at constant mass at 105°C, reference for updating the real saturation states of the samples.

The objective of such a drying is to limit the part of cracking induced by too important hydric and thermal gradients. The capillary depressions generated by a complete drying lead to stresses exceeding the tensile strength of the concrete, resulting in uncontrolled cracking.

2.2. Characterization of the studied materials

The fresh and hardened properties determined on 3 samples are reported in the following Table 2.

Table 2 Characterization of materials in fresh and hardened states (standard deviation in brackets)

Concretes	NDEN	HPC	OC
Density ρ (kg/m3)	2417	2433 (17.54)	2390
Slump (mm)	215	190	-
Air content (%)	2.4	2.1	-
Compressive strength 60d (MPa)	46.8 (1.66)	57.8 (1.31)	40.2 (0.68)
Young Modulus (MPa)	39200 (1450)	38800 (444)	31700 (415)
Water accessible porosity Φ (%)	15.2	13.5	18.0

2.3. Steady-state measuring devices for in vacuum and under pressure

The CEMBUREAU permeameter is used to perform in vacuum and under pressure tests. In steady state, the pressure gradient is maintained until a constant flow rate is obtained. An air flow point is recorded every 5 seconds by a computer linked to a digital thermal mass flowmeter system to ensure that the steady state is established (Sogbossi, 2017). The apparent permeability at a given pressure is obtained using the Hagen-Poiseuille equation:

$$k_a = \frac{2\mu L P_2 Q_{v2}}{A(P_1^2 - P_2^2)} \quad \text{(Eq. 1)}$$

With: P1: the absolute injection pressure (Pa) P2: Atmospheric pressure (Pa), Q_{v2}: Flow rate measured at the sample outlet (m^3/s), k_a: Apparent permeability (m^2), A: Surface crossed by the flow (m^2), L: Length of the sample (m), μ: Dynamic viscosity of the fluid (Pa.s).

The apparent reference permeability k_{aref} is obtained from the flow rate Qv measured with the CEMBUREAU for an inlet pressure of 2 bar of absolute pressure, i.e., a pressure differential of 1 bar.

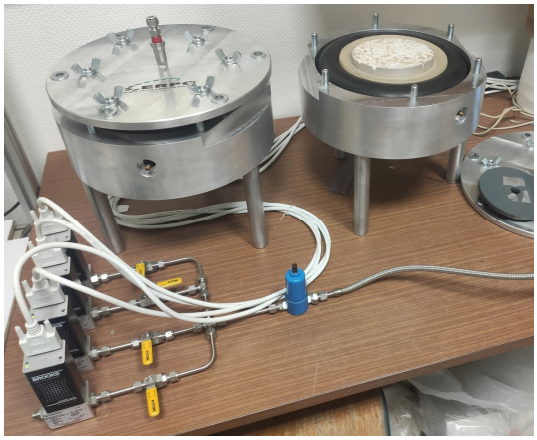

Figure 1. Cembureau apparatus for concrete permeability measurement in laboratory

2.4. Transient and steady state measurement devices under controlled flow conditions

To study the influence of the flow regime, the CEMBUREAU cell is also used in vacuum and in transient regime by making the time of vacuum in the upper volume, then by measuring the speed of pressure rise in the system. The pressure in the upstream volume (bell) is fixed at 15 mbar to represent the same vacuum as in the TPT[†] test. The following figure shows the schematic diagram of the CEMBUREAU apparatus in vacuum.

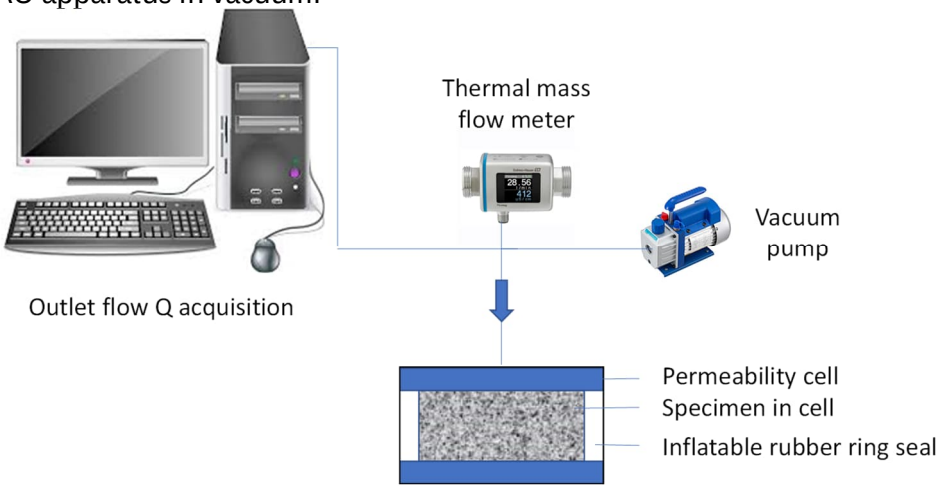

Figure 2. Cembureau apparatus for concrete permeability measurement in laboratory and in vacuum

Two vacuum times are studied: a time at least equal to the time of establishment of the steady state (TESS[‡]), which allows the use of the relation (Eq.2) and a time of 60 s, the same as in the TPT[§] test. In this case there is no analytical exact solution to the mass transport problem because the test takes place in transient regime. The solution can be approximated by a simplified method similar to that of Torrent or by a numerical approach using finite elements. The exact depth mobilized during the test with a vacuum time of 60 seconds is not known. The permeability calculation equation (Eq.3) must consider the thickness investigated during the measurement (Sogbossi, 2017). Sogbossi proposed to evaluated the apparent permeability in transient conditions by (Sogbossi, 2017.):

$$k_{ac} = \frac{2\mu L}{A(P_a^2 - P_c^2)} V_c \dot{P}_c \qquad \text{(Eq. 2)}$$

With k_{ac}: permeability coefficient (m^2) according to the bell method, P_c: Pressure in the bell (Pa), $\dot{P}_c$: Initial velocity of pressure rise in the bell, V_c: Volume of the bell (m^3), A: Cross-section of the specimen (m^2).

[†] Time Permeameter Torrent
[‡] Time of Establishment of the Steady State
[§] Time Permeameter Torrent

$$k_{aT0} = \frac{8\mu}{\emptyset}\left(\frac{V_c}{A}\right)^2 \frac{P_a}{\left(P_a^2 - P_c^2\right)^2} \dot{P}_c^2 (t_v + t) \quad \text{(Eq. 3)}$$

t_v: vacuum time; t = time at which the ascent rate is taken; ∅ air accessible porosity of the concrete (%).

Due to the great thickness of the walls of real structures, and in particular for the containments of nuclear power plants, the vacuum time required is too long to perform a permeability measurement under controlled conditions. The main difficulty is then to evaluate the concrete depth impacted by the air flow. In this approach, Torrent proposed to evaluate this depth, L_0, from the mass balance of the moles of air passing through the concrete to reach the central cell during the Eq. 4:

$$L_0 = \sqrt{\frac{2 \cdot k_{a_t} \cdot P_{atm} \cdot (t_v + t)}{\varphi \cdot \mu}} \quad \text{(Eq. 4)}$$

with: k_{at} the unknown permeability of concrete crossed by the air flow, t_v, the vacuum time, t, the time after the stop of pumping, φ, the porosity of concrete and μ, the air viscosity.

Equation (Eq.3) is used for short vacuum times or low permeability concretes, if the total thickness of the sample is not crossed by the air flow. It allows to estimate the permeability, because of the pressure profile present in the thickness at the time of the measurement. This effect fades as the measurement progresses, which is why the rate of ascent is taken at the end of the pressure acquisition curves. Finally, this equation can also be used on the upwellings obtained with the Torrent permeameter, which allows to compare permeability obtained by the various approaches.

2.5. In-situ Torrent permeameter

The Torrent permeameter creates a vacuum for 60 seconds in two concentric bells, one which will be called the inner bell and the other the outer bell. The inner bell is used to make the measurement and the outer bell to confine the flow in a single direction. The depression is then maintained in the external bell and cut in the internal. With the help of a membrane the pressure difference between the bells is kept constant. The recording of the pressure rise in the inner bell is carried out continuously at intervals of 20 mbar and for a maximum duration of 12 minutes. All the details are given in (Torrent, 1992).

Figure 3. Torrent apparatus for concrete permeability measurement in field

3. RESULTS

All tested configurations are listed in the following table. To facilitate the understanding of the reader, especially concerning the graphs and their interpretations, we recommend that the reader refer to this table.

Table 3. Names and explanations of the acronyms used for the results obtained

Type of permeability	Type of pressure	Type of state	Vacuum time	Designation
Apparent permeability measured	Under Pressure	Steady State	Time of Establishment of the Steady State	$k_{aref\ UP\ SS}$
Apparent permeability measured	In Vacuum	Steady State	Time of Establishment of the Steady State	$k_{a\ IV\ SS}$
Apparent permeability measured	In Vacuum	Transient State	Time of Establishment of the Steady State	$k_{a\ IV\ TS}$
Torrent permeability measured	In Vacuum	Transient State	60 seconds	$K_{T\ IV\ TS\ corrected}$

3.1. Permeability in steady states: CEMBUREAU under pressure and in vacuum

Figure 4 shows the relationship between the reference measurements, k_{aref}, and permeability measured under vacuum with the same equipment: the CEMBUREAU. Based on the relation of Klinkenberg (Klinkenberg 1941), a coefficient of pressure is used (Sogbossi et al., 2019) to relate k_{aref} to the apparent permeability obtained in vacuum for the various states of saturation. This coefficient depends theoretically on the characteristic size of the pore network. In this study, it can be evaluated at 0.56, as shown for the experimental measurements (Fig. 1). In order to evaluate the air leakage of a structure under pressure, it is therefore necessary to determine both the intrinsic permeability and the slope of Klinkenberg's law which are given by the following equation:

$$k_a = k_i \left(1 + \frac{b_k}{P_m}\right) \quad \text{(Eq. 5)}$$

With k_a, the apparent permeability, k_i, the intrinsic permeability, P_m, the mean pressure between the atmospheric pressure and the pressure of the test, and b_k, the Klinkenberg gas slippage factor.

For low permeability, i.e., below 2.10^{-17} m², the results are scattered. This is associated with measurements in vacuum and with measuring devices which are then used at their limit in terms of flow measurement. This is also because the pressure gradient in vacuum is lower than the gradient obtained for measurement under pressure.

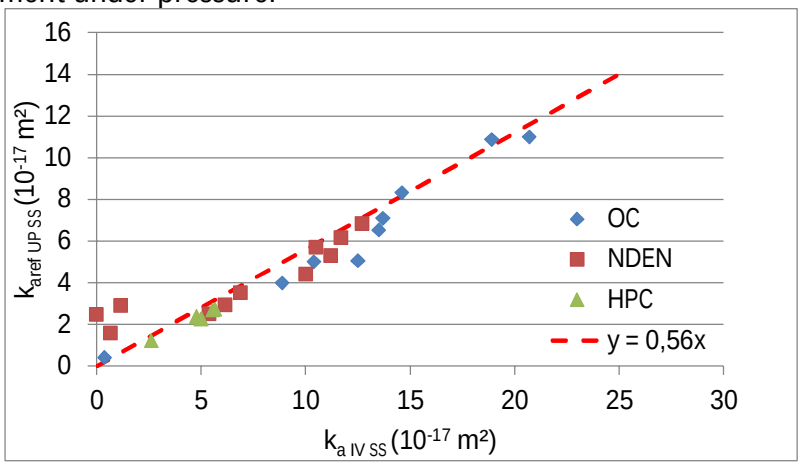

Figure 4. Apparent permeability at CEMBUREAU, k_{aref} Under Pression Steady State ($k_{aref\ UP\ SS}$) vs. apparent permeability k_a In Vacuum Steady State ($k_{a\ IV\ SS}$) P=15mbar

These results show the possibility of switching from apparent permeability under pressure to apparent permeability in vacuum, and vice versa, in the context of unidirectional steady state testing.

It is therefore possible to make accurate predictions of permeability results from either under pressure or vacuum tests. In the case of nuclear power plants, it is then possible to find the normative value under pressure from tests under vacuum.

3.2. Vacuum measurement: steady state and transient state after a vacuum time = TESS

Figure 5 shows the apparent permeability under vacuum and steady state conditions as a function of the apparent permeability under vacuum and transient conditions calculated by the previous equation Eq. 2, since the vacuum time is long, and the sample is crossed by the air flow. The graph seems to show that the type of regime does not influence the permeability results since the relationship between the two results is the line of equality. Obviously, this must be moderated for low permeability which are highly affected by experimental artefacts in this range of measurements.

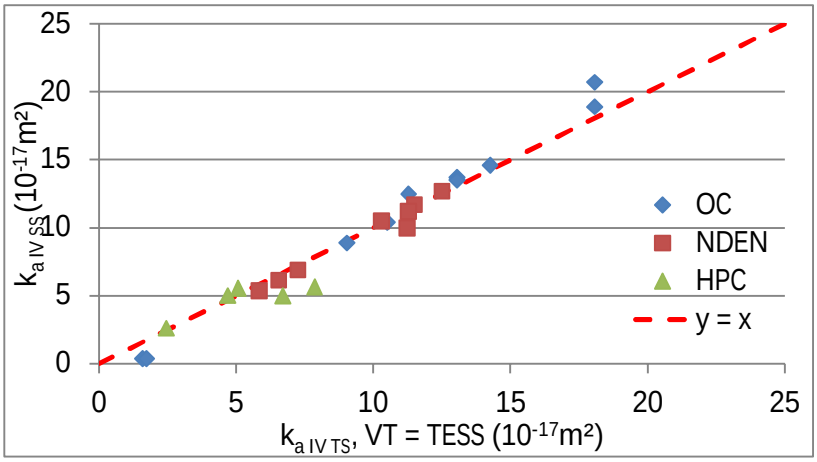

Figure 5. Apparent permeability in vacuum and steady state ($k_{a\ IV\ SS}$) and in vacuum and transient state ($k_{a\ IV\ TS}$) with a vacuum time = TESS

These results show the possibility to go from the apparent permeability obtained in transient to the apparent permeability obtained in steady state for a measurement in depression. In view of the conclusions given in part 3.1, it is therefore possible to use the apparent permeability in transient regime with a long vacuum time measured in vacuum to find the measurement at CEMBUREAU.

3.3. Vacuum measurement: transient state after a vacuum time = TESS and a vacuum time = 60 s.

Figure 6 shows the permeability obtained in vacuum and transient conditions after a vacuum time equal to the steady state time (TESS) and a vacuum time of 60 seconds (as used for in field apparatus). In this case, the flow can cross the thickness of the sample during the vacuum. If it happens, equation 2 is used to calculate the permeability if it does pass through or equation 3 if it does not. Therefore, if the L_0 calculated from equation 4 is greater than the thickness of the sample, equation 2 is used, otherwise equation 3 is used. The curve shows some deviations, especially in the central area of the graph, i.e., for permeability values between 5 and 15.10^{-17} m². However, the general trend is never more than 30% away from the equality line. In view of the possible deviations for the same permeability measurement on one sample, this is within the measurement uncertainty. Moreover, when drying creates additional percolation, the difference in analysis area as a function of the duration of the vacuum leads to the development of local heterogeneities that can create dispersion.

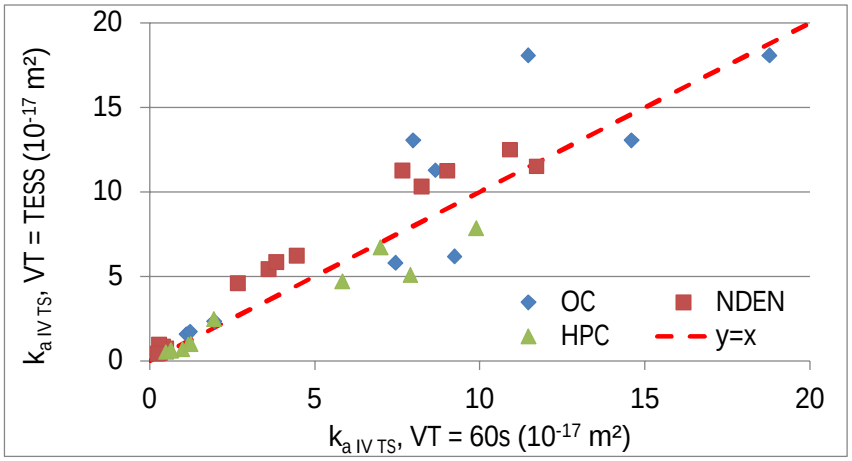

Figure 6. Apparent permeability in vacuum and steady state and in vacuum and transient state with a vacuum time = 60 s

These results show the possibility to switch from the apparent permeability obtained in transient regime and in vacuum for short or long vacuum time. Because of the previous conclusions, exposed in 3.1 and 3.2, within the framework of a 1D measurement in laboratory, i.e., with a good control of the direction of the flow, it is possible to determine the traditional CEMBUREAU measurement and thus a normative value.

3.4. Measurement with the Torrent permeameter and in vacuum and in transient regime after a vacuum time = 60 s in laboratory cell.

The previous steps have shown the possible correlation of the different techniques for the estimation of a reference permeability, from the CEMBUREAU and the previous equations. The final objective is to make the link between the *in-situ* measurement technique, the Torrent permeameter, and the tests carried out in the laboratory, those which are the closest to this technique, i.e., in transient regime after a vacuum time of 60 s. The permeability calculated from the Torrent permeameter ($k_{T\ IV\ TS\ corrected}$) considers the pressure rise rates provided by the Torrent permeameter combined with the equations proposed previously (Eq. 2 and Eq. 3 depending on the depth investigated) and corrected for the real porosity. These values are compared to the k_{AT0} or k_{aC} determined in (Sogbossi et al., 2019).

What emerges from this graph is that the results obtained by the Torrent permeameter are almost systematically inferior to those obtained by the CEMBUREAU. This translates into experimental results below the equality line (Figure 6)

In addition to the fact that the analysis area is not the same between the Torrent (5 cm diameter cylinder) and the CEMBUREAU (15 cm diameter cylinder), which can lead to errors in representativeness due to possible heterogeneities, it is difficult to consider the evolution of pressure in the thickness of the samples in a transient regime. It is possible that very porous paste/aggregate interfaces are over-represented in the case of small diameter samples, which is the case of the Torrent permeameter. Moreover, parasitic fluxes are involved in the Torrent permeameter measurement, whereas they are controlled in by the CEMBUREAU cell by the rubber ring (Figure 2) for the measurement in laboratory. Their estimation is being investigated with numerical simulations of the Torrent permeameter test. The modelling is based on the equations for the transport by permeability of air developed by Verdier et al. (Verdier et al., 2002). After calibration, the pressure isobars in the concrete samples were plotted to assess the direction of airflow during the test. The air flow is perpendicular to the lines shown. The isobars were nearly perpendicular to the axis of symmetry of the central cell throughout the pressure rise, as assumed by analytical methods (Sogbossi, 2017; Torrent, 1992) with some inflection below the joint between the cells. All the results are presented in Figure 7.

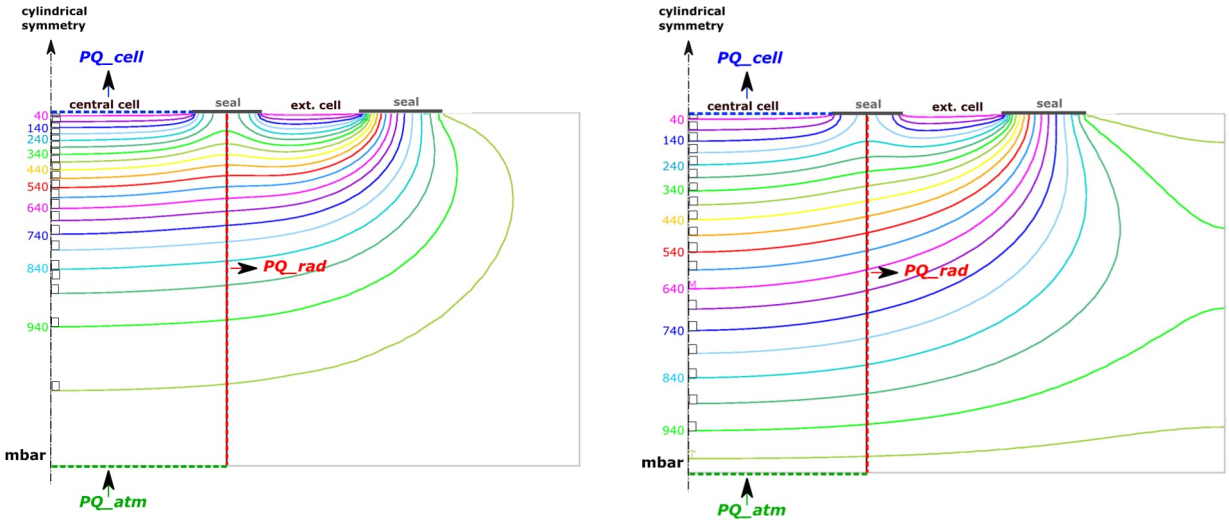

Figure 7. Isobars in the concrete sample (50 mm thick). On the left at the end of the period of vacuum (60 seconds), on the right at the end of the period of measurement (330 seconds after the end of the vacuum in the central cell) for a sample of concrete at 30% of saturation

The model can then be used to evaluate the part of the radial flow entering the investigated area and assumed to be zero by the analytical methods. For this purpose, three mass fluxes were determined by the modelling during the pressure rise: PQ_cell, the flux entering the central cell, PQ_atm, the flux passing through the investigated surface of the sample on the face at atmospheric pressure, and PQ_rad, the air entering (negative flux) or leaving (positive flux) the investigated volume along the radial direction (Figure 7). Figure 8 represents the evolution of the three fluxes during the pressure increase throughout the test. At the end of the 60 seconds of vacuum, once the pump is stopped, the flow entering the cell is maximal: the air present in the concrete porosity before the test enters the cell, it is at this moment that the pressure gradient is maximal. Gradually, the air must come from further into the concrete, the air flow entering the cell decreases and the air flows through the other surfaces increase. For a thin sample (50 mm) with a low degree of saturation (30%), the three flows change little after 200 seconds of testing.

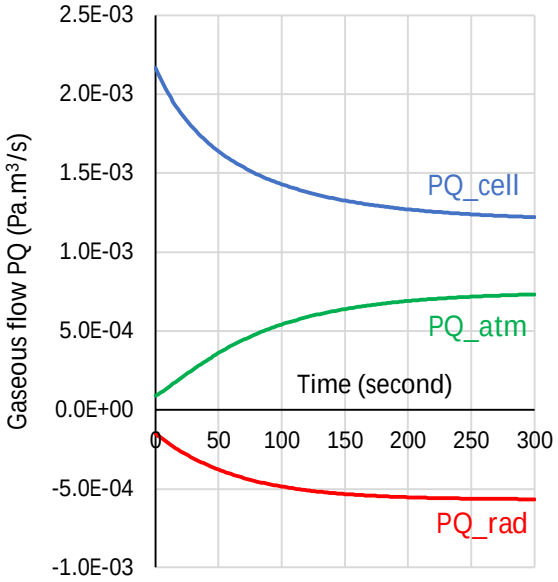

Figure 8. Gaseous flows during the pressure increase: in the cell, PQ_cell, at the external surface, PQ_atm, and at the mean radius between the two cells, PQ_rad, for one sample of concrete at 30% of saturation

To take all this into account, and in particular the through-flow, Torrent corrects its measurement by a double flow when the flow crossed the samples (which corresponds to the case when the investigated thickness indicated by the apparatus is larger than the thickness of the concrete element).

4. RESULTS AND CONCLUSIONS

The permeability under pressure or in vacuum in steady state with the CEMBUREAU cell give the same results whatever the type of concrete (Figure 4). This means that the type of measurement does not influence the permeability results. Nevertheless, the possible measurement range is smaller in terms of saturation for vacuum test due to the lower pressure gradient than under pressure.

The permeability in vacuum in permanent or transient regime with the CEMBUREAU cell also give similar results (Figure 5) whatever the type of concrete. The regime does not influence the permeability results if the air flow direction is controlled by an external cell in laboratory.

The permeability in vacuum after a long vacuum time (vacuum time to reach the steady state) and a vacuum time of 60 seconds give once again the same results (Figure 6) in laboratory cell. This means that a vacuum of 60 seconds is sufficient to estimate the permeability of the material.

The problem is the comparison between the results of permeability in vacuum in transient regime between the Torrent permeameter and the laboratory cell. There is a slight tendency to overestimate the permeability with the Torrent permeameter. The size of the samples and the parasitic flows present on these tests could partly explain this difference, as developed in section 3.4. A corrective factor of 0.6 is proposed for the moment to consider the parasitic flow and thus recover the good correlation between the two measurement techniques which seems to provide satisfactory results.

Figure 9 groups all the measured or calculated permeability values in relation to the reference value taken as being the value under pressure and in steady state. Some values have been corrected for the effects of the pressures and depths investigated, those measured with the Torrent permeameter after a vacuum of 60 seconds. From Figure 9, it seems possible to relate the permeability in vacuum and under pressure. The proportionality around the straight line of equality between the reference points and all the other measurements, whether under pressure, in vacuum, in steady state or transient, is well observed. Most of the experimental points are within a range of 50% of the mean, which is still within the uncertainty due to the heterogeneity of the concrete and the degree of saturation.

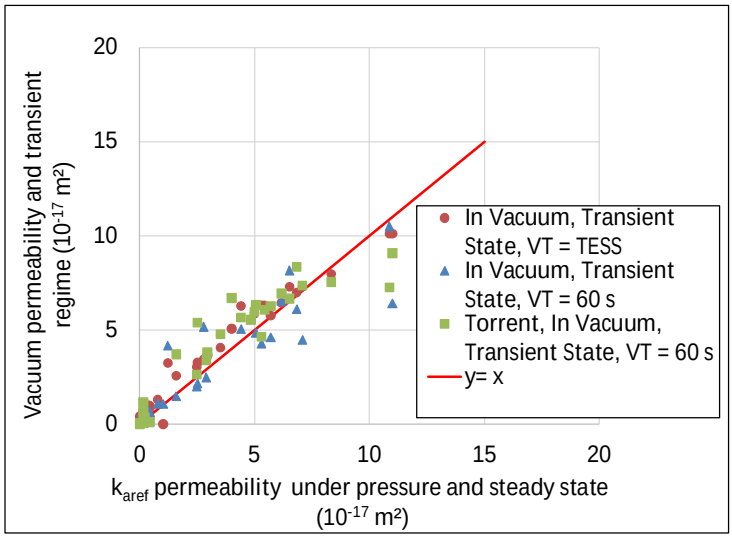

Figure 9. Corrected permeabilities obtained by the different measurement techniques in vacuum and in transient state as a function of the reference permeability obtained under pressure and in steady state.

Based on these results, the objective now is to be able to carry out in situ tests on larger surfaces to be representative of the structure. The extension of the void time and the increase of the size of the apparatus to investigate larger depths as well as the consideration of the saturation profile in the thickness of the studied structure are avenues of improvement of these tests.

ACKNOWLEDGEMENTS

The authors thank the ANR ENDE for its financial support and Vincent Garnier of the LMA Aix Marseille for steering the project

REFERENCES

Carcasses, M., Abbas, A., 2001. An optimised preconditioning procedure for gas permeability measurement 6.

Multon, S., Verdier, J., Villain, G., Sogbossi, H., Dérobert, X., Cagnon, H., Balayssac, J.-P., 2022. Non-destructive measurements for the evaluation of the air permeability of concrete structures. Measurement 196, 111204. https://doi.org/10.1016/j.measurement.2022.111204

Saul, A.G.A., 1951. Principles underlying the steam curing of concrete at atmospheric pressure. Mag. Concr. Res. 2, 127–140. https://doi.org/10.1680/macr.1951.2.6.127

Sogbossi, H., n.d. Etude de l'évolution de la perméabilité du béton en fonction de son endommagement: transposition des résultats de laboratoire à la prédiction des débits de fuite sur site 251.

Sogbossi, H., Verdier, J., Multon, S., 2019. New approach for the measurement of gas permeability and porosity accessible to gas in vacuum and under pressure. Cem. Concr. Compos. 103, 59–70. https://doi.org/10.1016/j.cemconcomp.2019.04.032

Torrent, R.J., 1992. A two-chamber vacuum cell for measuring the coefficient of permeability to air of the concrete cover on site. Mater. Struct. 25, 358–365. https://doi.org/10.1007/BF02472595

Verdier, J., Carcasses, M., Ollivier, J.P., 2002. Modelling of a gas flow measurement Application to nuclear containment vessels. Cem. Concr. Res. 10.

Waller, V., d'Aloı̈a, L., Cussigh, F., Lecrux, S., 2004. Using the maturity method in concrete cracking control at early ages. Cem. Concr. Compos. 26, 589–599. https://doi.org/10.1016/S0958-9465(03)00080-5

Non-destructive testing of mock-up of reactor pressure vessel cavity

Jan Patera[1], Jiri Zdarek[2], Edita Zarybnicka[3], Vaclav Svoboda[4], Vlastimil Habrcetl[1], Marek Postler[2], and Zbynek Hlavac[1,*]
[1]Centrum vyzkumu Rez s.r.o., Husnec - Rez, Czechia
[2]UJV Rez a.s., Husinec - Rez, Czechia
[3]CEZ a.s., Temelin, Czechia
[4]Preditest, Praha, Czechia

ABSTRACT

Two concrete blocks 1000×600×300 mm, each lined from one side by 10 mm thick carbon steel liner, were designed to simulate concrete cavity around reactor pressure vessel (RPV) in Temelin nuclear power plant (NPP). Each block contained two cylindrical holes with 6.5 mm thick carbon steel liners representing channels for ionization chamber in concrete biological shield (CBS). Both blocks were curved as a section of a tube.
Parallel work was development of non-destructive testing methods able to determine any defect in the block. Four concrete tubes with artificial defects were designed and manufactured for this purpose. Each tube was surrounded from inside by 6 mm thick carbon steel plate and from outside by 7 mm thick polyethylene tube.
Ultrasonic pulse-echo, impact-echo, magnetic memory method (MMM), indirect ultrasonic pulse method and non-linear wave modulation spectroscopy (NWMS) were employed.
The best result were reached by MMM and NWMS.
Simple one-axis manipulators were developed for both methods to be applied in the tubes.
Moreover, NWMS was used for testing of irradiated concrete block from the fifth unit of NPP Greifswald.

Keywords:concrete biological shield; nonlinear wave modulation spectroscopy; ultrasonic pulse-echo; magnetic memory method; mechanical manipulator.

1. INTRODUCTION

Safety of nuclear power plants is one of the most guarded areas in energetics or even whole industry.

A mock-up of the nuclear reactor pressure vessel cavity was designed and manufactured in order to qualify the non-destructive testing (NDT) methods able to check concrete biological shield of nuclear power plant. Five NDT methods were chosen for this purpose: ultrasonic pulse-echo, impact-echo, MMM, indirect ultrasonic pulse method and NWMS.

After the experiments, NWMS method was selected for real structure testing. The angularsection of RPV cavity was brought from the fifth unit of NPP Greifswald in eastern Germany. Mechanical manipulator Horymir was developed as a robotic system applying NWMS in CBS and its ionization chamber channels.

2. MOCK-UPS OF RPV CAVITY

A total of 6 concrete mock-up have been designed and manufactured in cooperation with Czech Technical University in Prague. First two mock-ups simulated the shape and dimensions of RPV cavity section brought from Germany (Figure 1).

*Corresponding author: phone +420 723 946 561,e-mail zbynek.hlavac@cvrez.cz

Figure 1.The mock-up of angular section of concrete biological shield with two holes inside

The dimensions of the mock-upswere 1000×600×300 mm,each edged by 10 mm thick carbon steel liner. Bothcontained two cylindrical holes with a 6.5 mm thick carbon steel liner representing ionization chamber channels.

Four concrete tubes with artificial defects were designed and manufactured to qualify various NDT methods capable of detecting honeycombs, cracking, purely compacted concrete or air voids. Each tube was lined with a 6 mm thick carbon steel plate on the inside and a 7 mm thick polyethylene layer on the outside the tube (Figure 2).

Figure 2.The mock-up of ionization chamber channel surrounded by concrete with various types of defects.

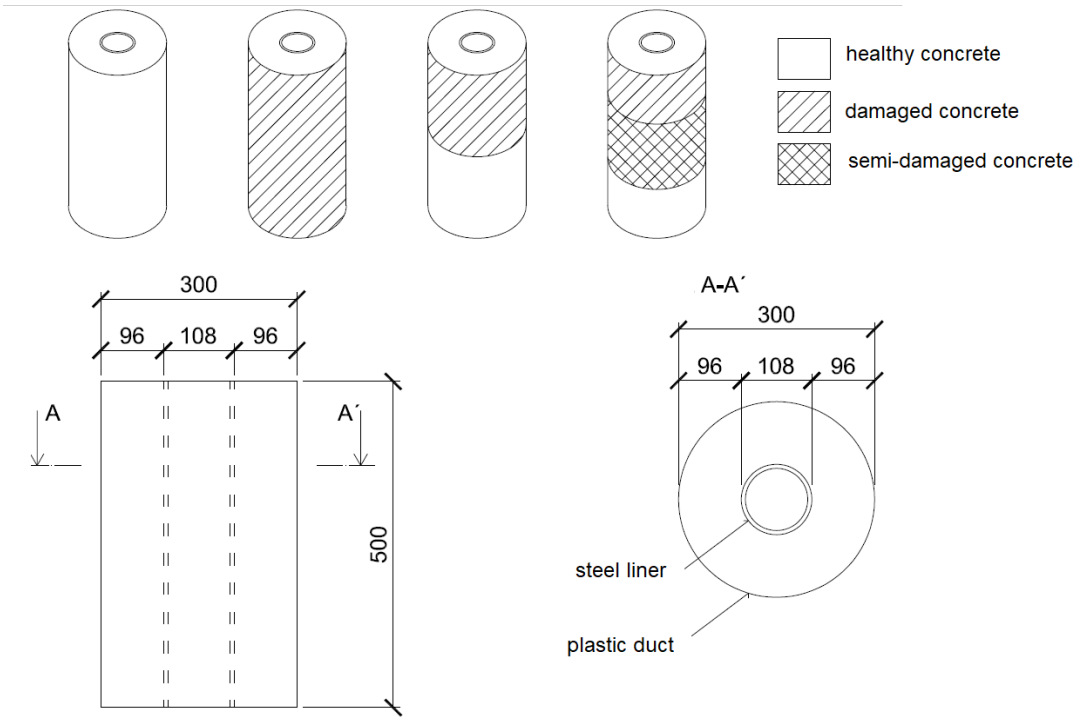

Figure 3.Ionization chamber channels surrounded by concrete in variouslevel of deterioration

3. SELECTED METHODS

Five non-destructive testing methods have been chosen for detection of artificial defects in mock-ups of reactor pressure vessel cavity.

First method applied on the mock-ups of the RPV cavity was ultrasonic pulse-echo, where 24 transducers generate sinus pulses, received echo shows interfaces reflecting the signals. The method is suitable for large air voids, ducts, rebars or honeycomb detection. Smaller elements, cracks or delamination are hardly detectable, see Figure 4.

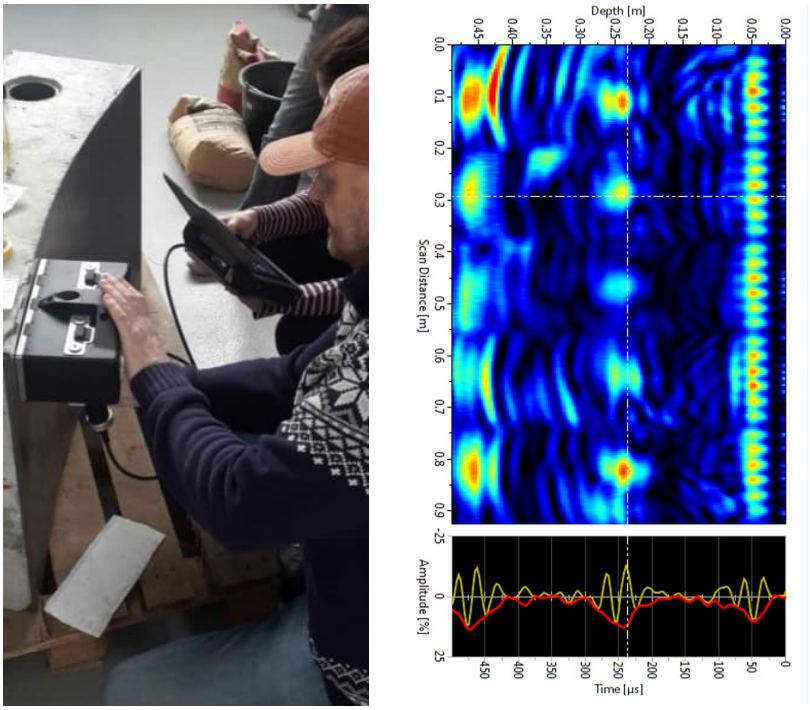

Figure 4.Ultrasonic Pulse-Echo instrument PUNDIT PL200 PE

The second method was impact-echo.It is a well-known NDT method which is capable of finding delaminations or other discontinuities. Impact-echo uses a hard impactor (e.g. impact hammer) to generate the pulse. Receiving hardware can be various, containing an accelerometer and an oscilloscope. The software uses mostly Fast Fourier transform (FFT) to analyse the results. In the given case the impact was placed at the top of the mock-up but the receiver was inside the tube. Outcome of the measurement can be a frequency domain (Figure 5).

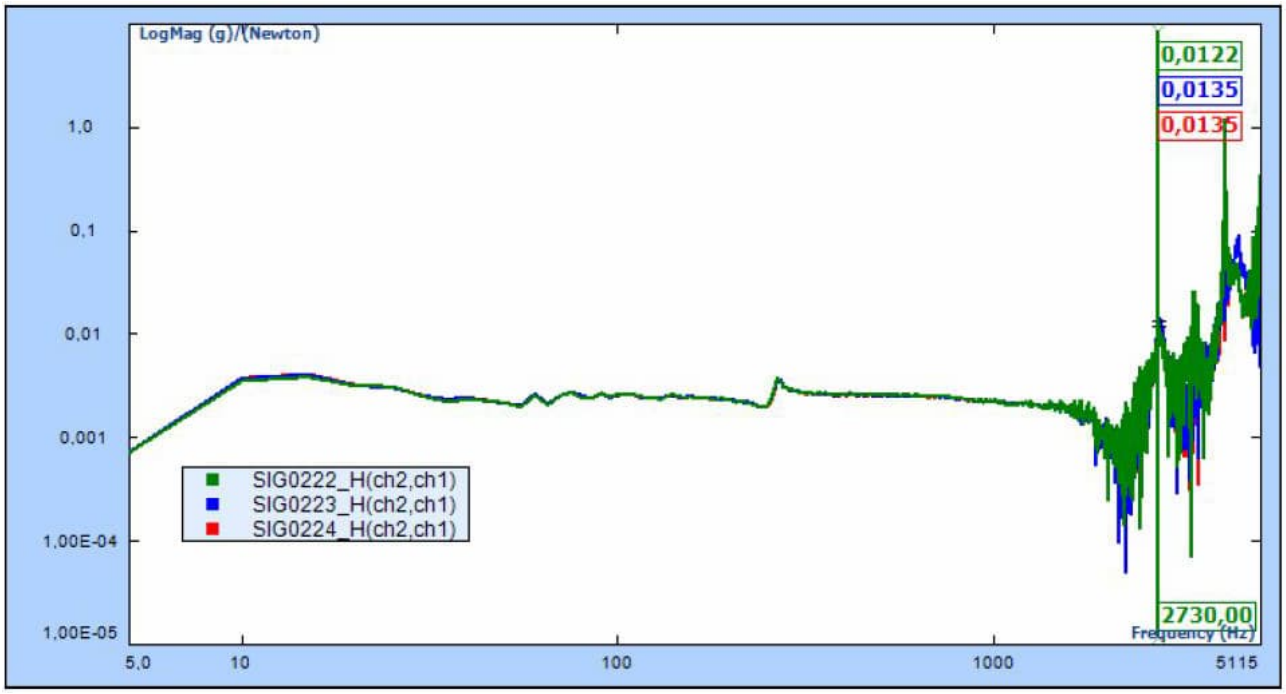

Figure 5.Frequency domain of the measurement of biological shielding concrete mock-up

Magnetic memory method (Figure 2) shows differences in the magnetic field of ferromagnetic materials due to the change in internal pressure. This method is suitable not only for steel-reinforced concrete structures but also for steel constructions, pipelines, etc. In the given case, the change of the pressure was caused by poor quality of concrete and thus the lower compression of the inner tube that was measured (Figure 6).

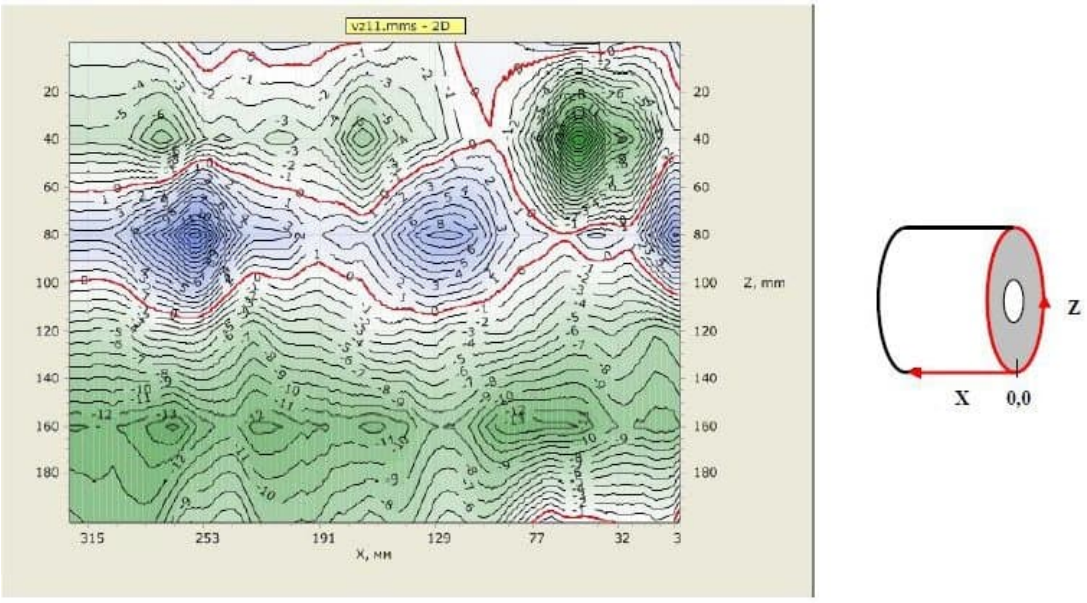

Figure 6.Magnetic memory method applied in ionization chamber channel of the CBS mock-up

Indirect ultrasonic pulse method allows the structure to be tested with access from only one side (Figure 7). This type of method is suitable for homogeneity or quality testing. Large defects such as honeycombs or poorly compacted concrete can be detected as well.

Figure 7. Indirect ultrasonic pulse testing of RPV cavity mock-ups using PUNDIT PL200 instrument

Nonlinear wave modulation spectroscopy is a quite new method for material testing. Two sinusoidal signals with two different frequencies f_1 and f_2 are transmitted into the tested material. There the signals are combined into one resulting signal containing oscillations f_1, f_2, their modal frequencies $2f_1$, $3f_1$,... , $2f_2$, $3f_2$, ... and their intermodulations $f_1 + f_2$, $2f_1 + f_2$, $3f_1 + f_2$, ..., $f_1 + 2f_2$, $f_1 + 3f_2$, ... Concrete damaged by micro-cracks or meso-cracks generates many intermodulations with higher amplitudes (Figure 8). The higher the amplitudes of the intermodulations, the more micro-cracks or meso-cracks.

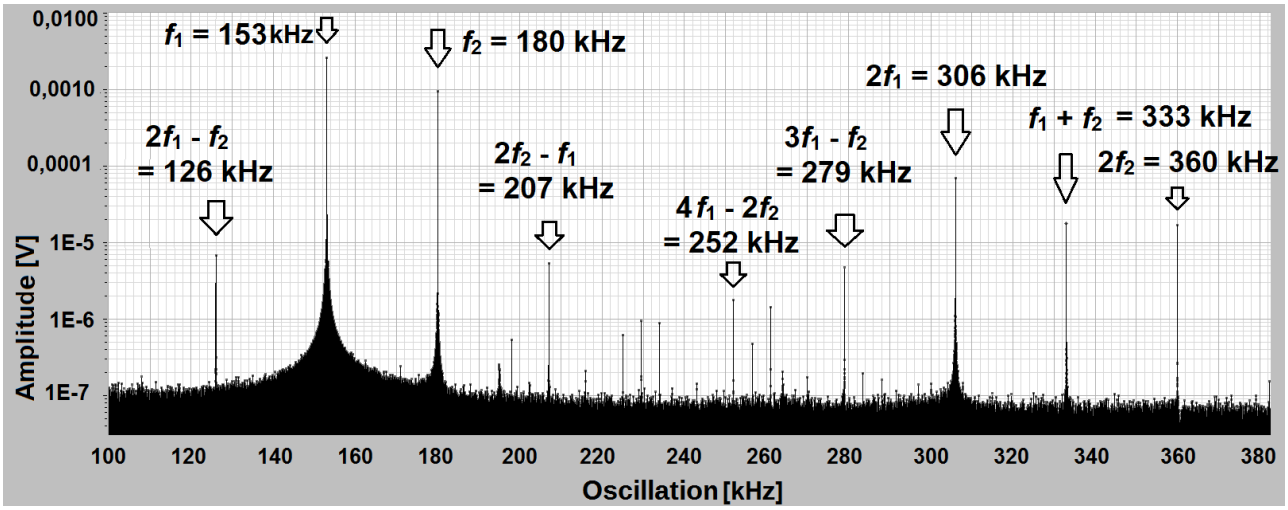

Figure 8. NWMS: two main peaks with oscillations f_1 and f_2, their modal frequencies and intermodulations

4. REAL STRUCTURE TESTING

Two uniaxial manipulators were developed for the application of the methods MMM and NWMS in the real structure of the reactor pressure vessel cavity (Figure 2 andFigure 1 respectively). Both manipulators were able to enter the channel of the ionization chamber, press the transducers onto the steel liner and send or receive the signal. However, only Horymir was selected for NDT inspection of Greifswald NPP RPV cavity using NWMS (Figure 9,Figure 10 and Figure 11).

Figure 9. Angular section of reactor pressure vessel cavity of Greifswald's NPP NORD

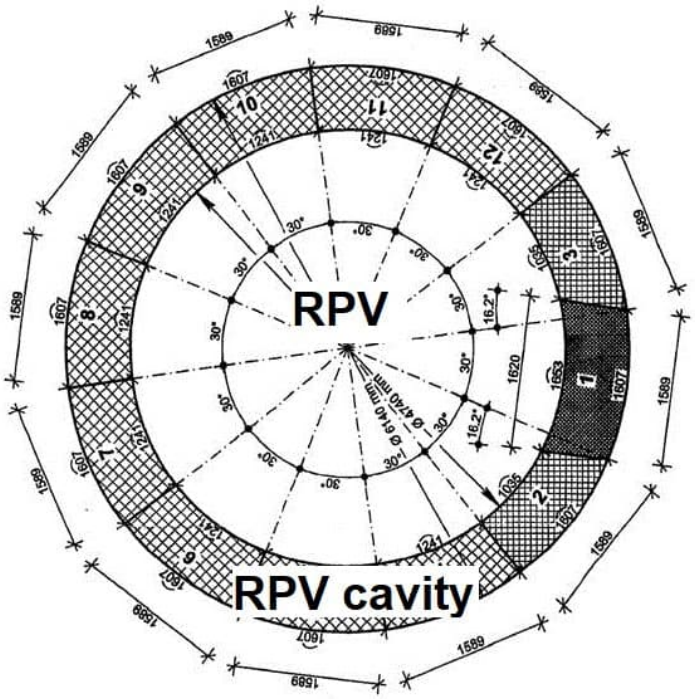

Figure 10. Scheme of cutting the angular section of nuclear reactor pressure vessel cavity in NPP NORD

Figure 11. Manipulator Horymir during NDT inspection of Greifswald NPP RPV cavity

5. CONCLUSION

Five non-destructive testing methods have been validated to investigate the cavity of nuclear reactor pressure vessel. 5 methods were tested in six RPV cavity mock-ups with various artificial defects. The NWMS method and the Horymir manipulator were chosen to test the real structure, a section of the nuclear power plant NORD, located near Greifswald in eastern Germany.

Measurement was carried out in a controlled area, the radiation was monitored by dosimeters. Safety clothes and boots were worn.

The conclusion of the long-term experiment was, that there is no degradation of the concrete biological shield imposed due to radiation or subsequent effects. The NWMS or MMM methods should be capable of in-situ application.

Manipulators developed for NDT testing of RPV cavity mock-up have been validated and might be adapted for a real power plant.

ACKNOWLEDGEMENTS

This paper was created by financial support of the project VI20192022154 Biological shielding concrete testing after irradiation in nuclear reactor and the Security research program of the Czech Republic 2015-2022.

Assessing the concrete of Nuclear Power Plants containment by NDT

V. Garnier[1], J. Verdier[2], M Sbartai[3], JF Chaix[1], O Abraham[4], C Payan[1], E Larose[5], B Piwakowski[6], JM Henault[7], JP Balayssac[2], G Villain[4], X Derobert[4], F Dufour[8], J Eiras[1]

[1] Aix Marseille University, LMA, CNRS UPR 7051, IUT, Bd Gaston Berger, 13625 Aix en Pce
[2] University of Toulouse; UPS, INSA; LMDC;135, avenue de Rangueil, 31077 Toulouse
[3] I2M, University of Bordeaux, 351 Cours de la Libération 33405 Talence
[4] University Gustave Effeil, Route de Bouaye, CS4, 44344 Bouguenais, France
[5] ISTerre, CNRS, University of Grenoble Alpes, CS 40700, 38058 Grenoble, France
[6] IEMN, Ecole Centrale de Lille, 59651 Villeneuve d'Ascq Cedex, France
[7] EDF-R&D-STEP, 6 Quai Watier, BP 49, 78401 Chatou, France
[8] Univ. Grenoble Alpes, CNRS, Grenoble INP, 3SR, 38000, France

ABSTRACT

The aging of prestressed concrete containments wall of nuclear power plants is experimentally modelled by a 1/3 scale mock-up of 15 m in diameter and 20 m in high carried out by EDF within the VeRCoRs project. This aging leads to the modification of the concrete properties as well as to possible mechanical damage during a pressurization cycle at 4.2 bars of the containment. This pressurisation carried out annually on the mock up, represents the conditions of the ten-year inspections imposed by the French regulations for Nuclear Power Plants (NPP).
On the basis of several previous projects having developed Non Destructive Techniques (NDT) for civil engineering in laboratory and structured their transfer on site, a consortium made up of 9 partners participated in the monitoring of this double-walled containment within the framework of the ENDE project (Non Destructive Evaluation of the NNP containment walls). NDTs have been implemented with two objectives: assessing the physical (water content, porosity) and mechanical (strength, modulus of elasticity) properties of concrete over time and monitoring structure damage (depth and opening closing of cracks) more specifically when the containment vessel is under pressure. The techniques used for characterization are: ultrasonic waves (linear, diffuse and nonlinear acoustics), electromagnetic and electric fields and permeability. A statistical selection of the most efficient measured parameters is associated with a fusion of multi-technical data to assess the concrete properties.
To monitor the damage, the NDTs are implemented on an area with cracks. They are surface ultrasounds for deep auscultation, acoustic emission, and diffuse waves.
A third approach is developed with a global analysis of the structure by follow of modal analysis and vibration.
The article presents the auscultation strategies and measurement methodologies for the three objectives, the proposed innovations, and the results. We focus on the evolution of the water content that we can quantify as well as on the control of cracks length and opening.
We intend to propose a strategy of Structural Health Monitoring of the containment walls with a global-local approach based on the modal analysis of the enclosure.

Keywords: NDT, Cracks Control, Concrete Characterization, Containment Walls, Data fusion

1. INTRODUCTION

The containments of the power plants constitute the last barrier in the event of an accident such as the rupture of the primary pipeline or during a major external mechanical event. It is important that their tightness and mechanical resistance be assessed during operation or during ten-year inspections of nuclear power plants. In the event of a rupture of the primary pipe, the pressure rises to 4.2 bar and the temperature to 180°C in 20 s, which generates the opening of existing cracks or the creation of new ones, especially since the mechanical properties of the concrete have evolved.

The ENDE project (Non Destructive Evaluation of Nuclear Power Plant Containment Walls 2014-2022) aims to characterize the concrete as well as the cracks. It follows several projects [1-2]. It is based on a 1/3 scale mock up (VerCoRs) of a containment building. The dimensional homothety of the thickness (0.4 m for 1 m) and therefore of the saturation conditions of the walls makes it possible to simulate the Integrated Leak Rate Test (ILRT), scheduled each Ten Years in France, by a test each year. The project is built on 4 stages from laboratory measurement to on-site measurement:

The first stage consisted in the laboratory of studying the sensitivity of the parameters resulting from the non-destructive testing (NDT) regarding the properties of the concrete: saturation, thermal damage and stress applied. The objective is to select the NDT measurements most capable of characterizing the concrete.

The second time allowed in the laboratory to follow the diffused damage in the concrete then the generation of cracks in different cases of loading by acoustic and imaging techniques. Some tests have been realized to follow the opening and the closing of cracks.

The third phase enabled laboratory techniques to be transferred to on site. This change of the structure dimensions was implemented through the VeRCoRs mock up measurements.

The fourth step led during the extension of the project to make NDT techniques operational for industrial measurements. It also made it possible to structure part of the links between the END measurements and the thermo-hydromechanical modeling (THM).

After a reminder on the laboratory tests and the general principles of the transfer, we target here the on-site tests and their applicability on a real structure.

2. LABORATORY TESTS

2.1. Characterization of the concrete

To follow the evolutions of the parameters which can evolve during the ILRT or a primary accident, NDTs were carried out, on a type of concrete of NPP, under press to take into account the evolution of the potential stress from 0 to 12 MPa, with specimens at different states of thermal damage (heating at 80, 150 and 200°C) and different states of saturation (30, 60, 100%). Conversion models were determined between the observables (NDT measures) and the targeted reliability indicators (Strength, Modulus of elasticity, Saturation, Damage, Porosity, Stress)

10 NDT techniques were implemented following an approach described in [3] (linear and non-linear acoustics, radar, capacitive, electrical, permeability). 62 observables deduced from these tests were correlated to the changes of the indicators (Strength, Modulus of elasticity, Saturation, Damage, Porosity, Stress).

Figure 1 shows 3 examples of the capability of measuring stress and thermal damage and saturation with very different coefficients of variation from 1 to 500%. The observables

sensitivities are very different regarding the indicators. Especially the stress evolutions are difficult to measure.

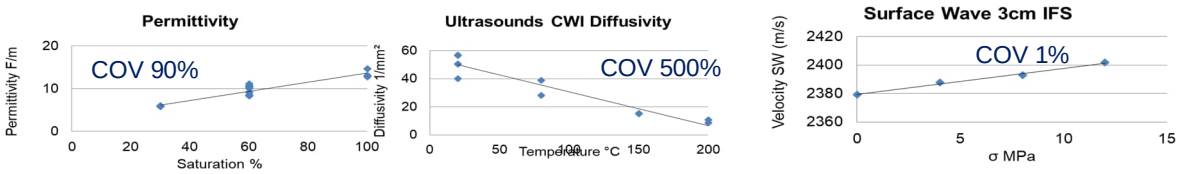

Figure 1. Examples of evolution for 3 observables according to 3 indicators

A statistical selection process made it possible to retain the most efficient observables that will be transferred to on-site measurements. Table 1 shows the sensitivities identified by technique. We can note that the first 4 techniques (italics), usually used in Civil Engineering, make it possible to mainly evaluate the saturation and that the last 3 (bold) which are techniques in the making complete the previous ones by improving the capability of measuring the stress and thermal damage.

Tabel 1. Sensitivity of NDT to Saturation, Stress, Thermal Damage indicators

Technics	Saturation	Stress	Thermal Damage
Capacity	+++	+	+
Radar	+++	*0*	*0*
Resistivity	+++	*0*	++
Ultrasounds	++	+	++
Permeability	+++	+	++
Ultrasound Multi Diffusion	++	++	+++
Non Linéaire Acoustique	+	+++	+++

Figure 2 shows the evaluations resulting from the inversion of the ENDs of the saturation and the damage temperature of the concrete for the ENDE specimens tested in the laboratory. The inversion consists in data fusion process integrating the readjustment of the conversion models [4]. The quality of the evaluation is good in both cases.

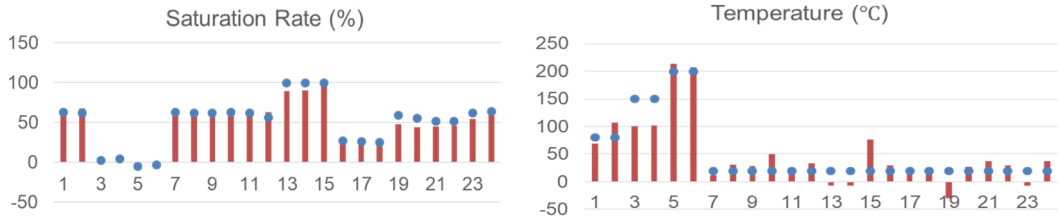

Figure 2. Evaluation of saturation and damage temperature of concrete by inversion and data fusion ENDs (merged red – measured blue)

2.2. Control of the cracks

Ultrasonic tests by diffuse waves, acoustic emission, linear and non-linear acoustics, and image correlation, were carried out in press during bending tests of two types of specimens. NDTs made it possible to follow the formation of diffuse mechanical damage in the form of microcracks then their coalescence in macro-cracks [5].

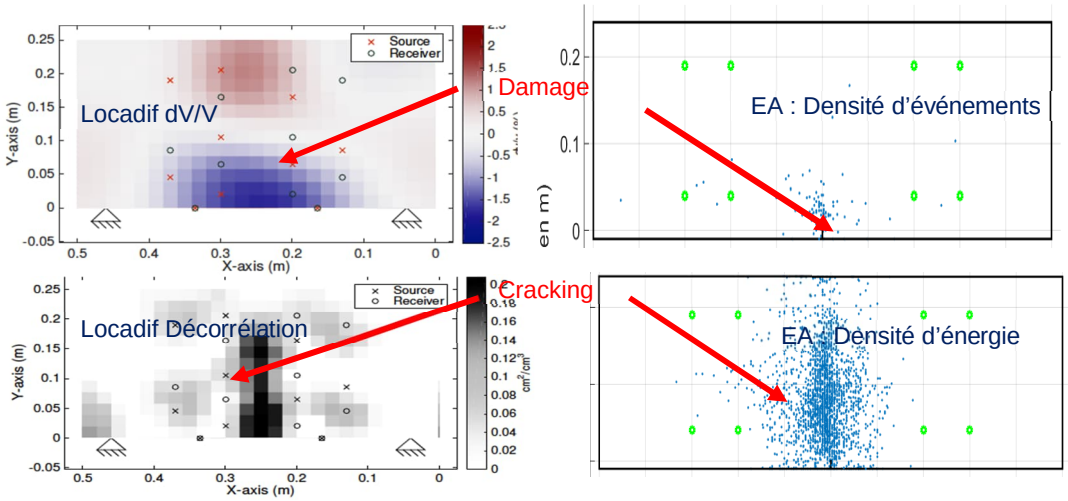

Figure 3. Suivi de l'endommagement mécanique puis de la propagation d'une fissure

Figure 3 shows the parallel between 2 techniques, by diffuse waves and by acoustic emission (AE). The relative ultrasonic velocity variations of the diffuse waves (Locadiff) and the density of events in acoustic emission make it possible to detect and position the damage which appears before the initiation of the crack. The decorrelation of the diffuse waves for Lodaciff and the energy density for AE make it possible to identify the position of the crack in the space of the specimen. A test on a beam with a prestressing cable showed that it is also possible to follow the opening and closing of a crack.

These data can be associated by fusion with logical operators to identify the length of a crack.

3. ON SITE TRANSFER

3.1. Characterization of the concrete

The transfer is made on the VeRCoRs mockup developed by EDF. It is 1/3 scale in terms of dimensions and 1/10 in terms of saturation evolution. It therefore undergoes each year the equivalent of a ten-year inspection ILRT which consists of carrying out a pressurization cycle of the containment walls up to 4.2 bar and then decompression over a week (figure 4).

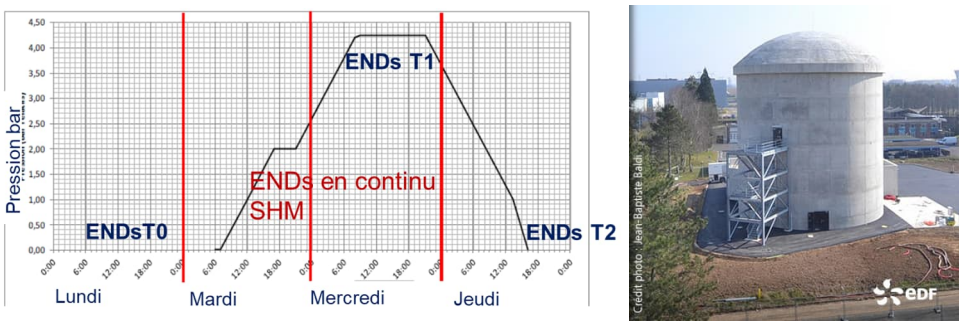

Figure 4. Pressurization cycle and VeRCoRs mockup

The first objectives are to characterize the concrete on the structure and to follow the evolution of the cracks. Initially, the measurements were carried out in June 2016, December 2016, and March 2017 outside the pressurization cycle, then during the pressurization cycle in March 2017. Due to the measurement times and the time available to make them, they are performed only on 2 points.

Figure 5. Location of measurement points for characterization.

The NDTs technics transferred on site are Surface ultrasonic waves, UPE, Capacity, Radar, Permeability, Non-Linear Acoustics. These techniques are not very automated in these testing campaigns. They had to be optimized for rapid implementation. They made it possible to estimate the evolution of the observables and to follow the properties of the concrete.

As an example, figure 5 shows the evolutions of the dynamic modulus of elasticity and of the saturation from June 2016 to March 2017 for the points in blue and during the pressure cycle in red.

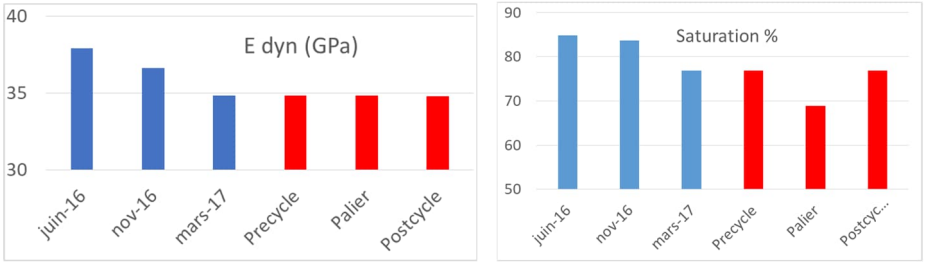

Figure 5. Evolution of the elasticity modulus and saturation with time (blue) and then with pressure (red)

The mock-up is maintained approximately at 33° C to approximate concrete aging conditions in service. During pressurization, for reasons of accessibility, the temperature is not regulated. This results in a drop of around 15°C which generates a bias. We took it into account [6] to correct the raw NDT measurements.

We note that we can follow the saturation and elasticity modulus that decreases over time. Then we observe during the pressurization that the modification of the stress generates a bias that must be integrated into the inversion for the saturation assess.

A more general mapping of ENDs data has been built on the entire containment with 114 points examined by 6 techniques: Surface ultrasound, UPE, Impact Echo, capacity and more partially resistivity and permeability. The points are distributed over 3 verticals and 2 circular horizontals and are subsequently merged to go up for each point to a value of the properties of the concrete. For example, we can see on the cartography below the saturation and the modulus

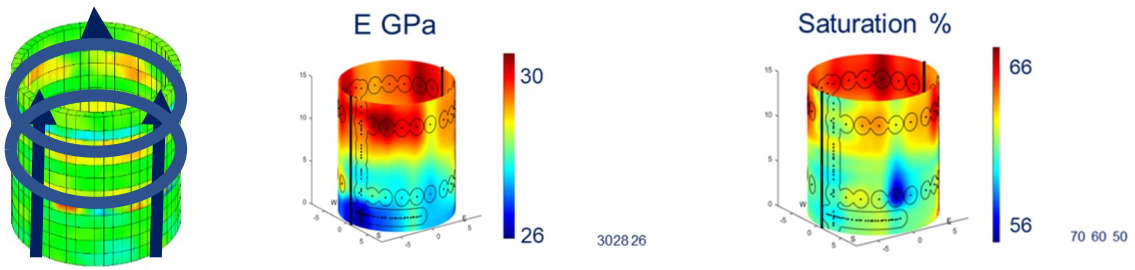

Figure 6. Mapping of the modulus of elasticity and saturation without pressurization of the VeRCoRs containment

It appears that these 2 indicators vary according to the height and the angular position therefore the variations in temperature and associated partial vaporization pressures as well as according to the polar orientation. It should be noted that these parameters can introduce biases in the context of the natural aging of the concrete or during stress on the containment, but also during its construction, which lasted 6 months with highly variable water and thermal conditions.

The points to remember in the context of these on-site concrete characterization tests are:

- All the indicators sought can be assessed by NDTs. Data fusion is an important element for converging all the measurements towards quantitative values by separating the cross effects of the different indicators on the observables. The absolute stress value is not accessible by NDT on site.
- To achieve quantitative measurements, it is not possible to readjust the inversion processes on destructive tests on concrete samples from the structure because these are prohibited. It is necessary to adjust the inversion process on hypothesis, embedded probes or/and modeling results.
- Saturation can be measured using surface or bulk ultrasonic velocity techniques, the diffusivity of ultrasonic waves as well as resistivity and capacitive techniques.
- The monitoring of the stress is possible by the ultrasonic waves in velocity and diffusivity as well as by the permeability. The low variation of the observables with the stress don't allow to assess absolute stress.
- The 2 points that have been monitored are 5 m apart and come from 2 different lifts. The two materials are different with the more porous for C3 point.
- Saturation depth gradients are highlighted by calculations or measurements by implemented probes. A difference of 20% between the core and the surface is observed. This bias must be also integrated into the inversion.

3.2. Control of the cracks

Important advances made during these tests on VeRCoRs concern the monitoring of cracks.

Three types of measurements were implemented with a fully monitored process (figure 7). The area studied is 3 * 2 m² located at the bottom of the barrel and making the link with the gusset. Cracks have already been identified in this area. The technics are Acoustic Emission, Locadiff (diffused waves), Surface wave robot.

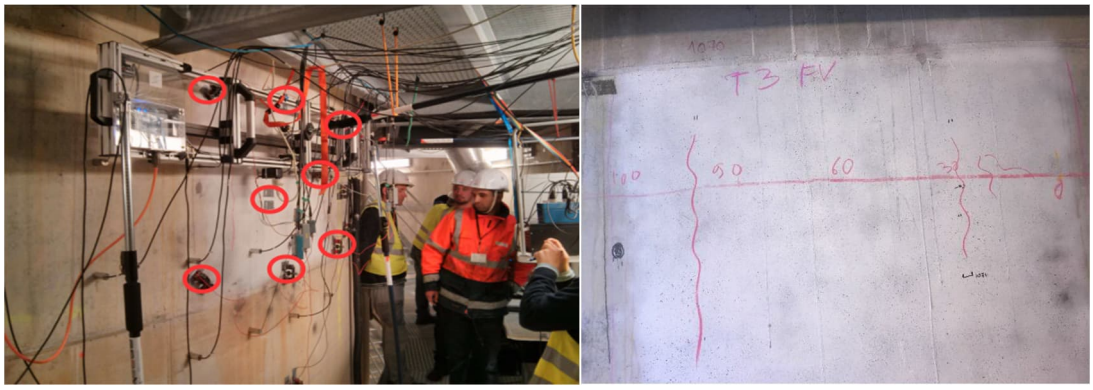

Figure 7. Instrumentation for acoustic emission, diffuse waves (Locadiff) and surface wave robot set up to monitor to follow the cracks: Inspected zone with in red vertical cracks.

During the pressurization of the containment and despite the initial prestressing, the opening and even the generation and growth of the cracks are monitored in real time.

Acoustic Emission and the Lodadiff technique, which is based on the multi-scattering of ultrasonic waves, make it possible to report in situ on the activity of crack opening and closing.

The links with the dimension and the opening of the cracks are not identifiable at this level of information. Locadiff also makes it possible to follow the distribution and the evolution of the stresses in the structure as well as to identify the damage by the decorrelation of the signals.

During these same pressure cycles, the implementation of a robot using surface waves that can inspect the entire wall over a depth of 40 cm works on the basis of the attenuation of the propagated surface waves [6].

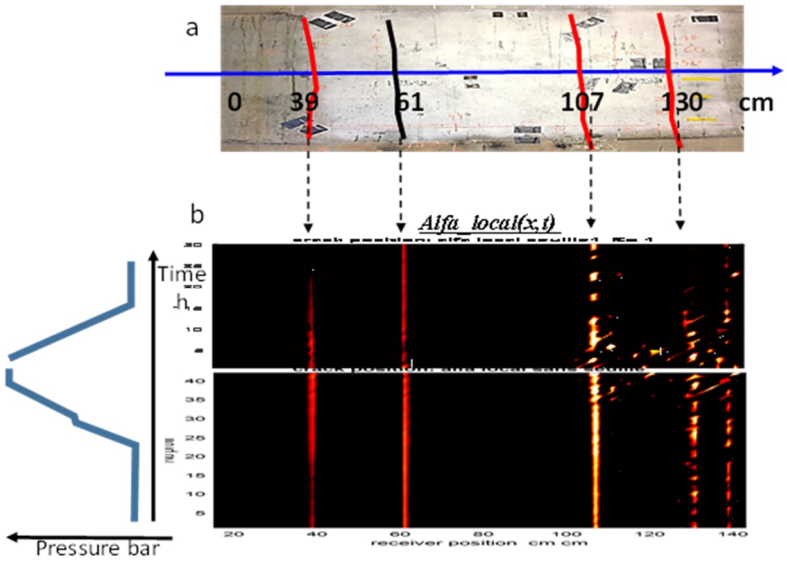

Figure 8. Evolution of the cracks opening during the pressure cycle.

This set allowed access in figure 8 to the opening of the cracks visible on the surface (red) for which the attenuation of the waves increases with their opening. This was correlated with fiber optic measurements. A subsurface crack was also identified (black) and its opening monitored. It is also possible to assess the cracks depth considering the length waves evolution.

The points to remember in the context of these on-site cracking monitoring tests are:

• Acoustic emission and diffuse waves (Locadif) are to be implemented as part of monitoring in a large, localized area. They make it possible to identify the existence of an activity either of modification of the constraints, or of opening and closing of cracks. It is not possible to evaluate the depth of the cracks.

• The surface wave inspection robot, developed as part of this project, can inspect a smaller localized area but in greater detail. It makes it possible to follow the opening and closing of even non-visible cracks and to position them in depth.

• These techniques can be covered in the following timeline. First, EA and/or Locadif to detect the existence of cracks then second, the surface waves to characterize them. This chronology can be done on a single pressurization cycle because the cracks detection can be obtained during the increase of the pressure and the cracks characterization during the decrease of the pressure.

3.2. Global approach

Finally, a third global approach has been implemented to highlight the possibilities offered by the vibration and modal analysis of the containment.

The recording of the noise generated by the air circulating in the pipes during the pressurization of the containment made it possible to identify recurring frequencies throughout the test. These increase with the pressure and return to their initial value when the pressure drops with a slight hysteresis. By selecting several of these, a multivariate regression model was deduced from the evolution of their value as a function of the pressure in the containment. This model makes it possible to estimate in real time the internal pressure during the pressure cycle [7] as shown in the following left figure 9.

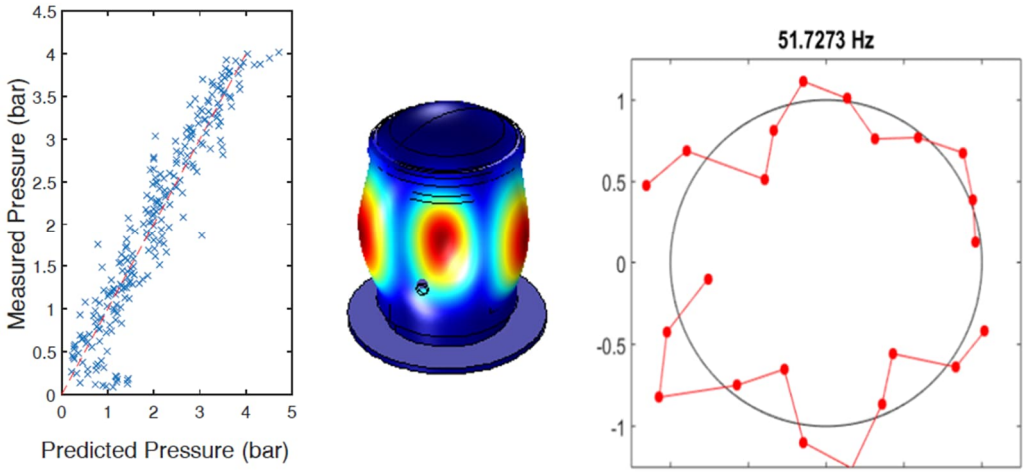

Figure 9. Comparison of numerical and experimental data : Predicted pressure ($Ppred$) vs. experimentally measured pressure ($Pexp$), Example of vibration mode

The modal analysis approach is more ambitious because it could be integrated into an SHN approach. It consisted of measuring, using simple instrumentation made up of 1 to 4 accelerometers depending on the tests carried out. The observables are the frequencies, shapes, and amplitudes of the vibration modes of the containment during pressurization, but also their evolution during the pressure cycle. An example of experimental numerical comparison is given by right figure 9.

It finally appears that modal analysis opens real potential. Up to date, it is difficult to work on exact descriptions of a complex and already partially damaged structure, real-time monitoring of these frequencies is possible à priori on the noise of air circulation within the framework of the ILRT of VeRCoRs. The evolutions of the modes and their amplitude could provide a significant alarm on an evolution of the local properties of the concrete or the structure. A numerical study of the sensitivity of this approach based on a Principal Analysis Component has been proposed on the data of VeRCoRs [8]. It shows the capability of the approach to provide statistical information on the modification of the modes linked to specific cases of concrete evolution.

4. CONCLUSIONS

The ENDE project has made it possible to apply NDTs to a nuclear civil engineering structure in the case of containment control during several phases of its life cycle. It is shown that NDTs are applicable for concrete characterization and crack control but also for structural monitoring. The developments have been made both on the technical aspects, operation, and link between the different scales. Versions of surface wave measurement robots and data fusion software have been proposed at a high level of TRL.

The ability of the different techniques to meet the expectations of the controls was studied in the laboratory, the on-site capability was shown as part of the measurements on the VeRCoRs mockup.

Parameters have been clearly identified as being able to integrate biases into the measures and inversion process. These are the temperature inside the containment wall, the temperature during the casting of the lifts as well as the gradients of properties such as saturation. Additional studies are necessary with an approach based on numerical studies such as the comparison between forecasts and capacitive measurements for saturation [9].

An auscultation approach can be developed around a multiscale approach. The SHN based on global auscultations either in service with the operating noise or in ILRT with the noise of the air flows can highlight a shift of the vibrations of the structure. The latter could be linked to positions of potential damage in the structure. A local measurement approach can then be associated with the detection by NDT of defects. The useful concrete characteristics can be assessed by NDT as well.

Such an approach could result of joint work between the owners and the measurers.

ACKNOWLEDGE

The authors thank the ANR ENDE-11 RSNR 009 for funding and the EDF compagny for making availablethe VeRCoRs mock-up and the assistance provided during the experimental campaigns.

REFERENCES

[1] Garnier V. and al, Project C2D2–ACDC, Final report and appendices, may 2014, http://temis.documentation.developpement-durable.gouv.fr/docs/Temis/0083/Temis-0083308/22288_A.pdf

[2] Balayssac J.P. and all Description of the general outlines of the French project SENSO – Quality assessment and limits of different NDT methods, CBM, Vol 35, October 2012

[3] Garnier V. and all, Non Destructive Testing applied to nuclear Civil Engineering, International Conference on Technological Innovations in Nuclear Civil Engineering, Paris, 2016

[4] Balayssac JP, Garnier V, Evaluation Non Destructive des ouvrages en génie civil, ISTE Press - Elsevier, Version française Mai, 2018

[5] Garnier V. and all, Garnier V. and all, Non-destructive Evaluation of Containment Walls in Nuclear Power Plants, Quantitative Non Destructive Evaluation, Atlanta, July 2016

[6] B Piwakowski, R Drelich, C Ciccarone, J Li, JM Henault, V Garnier, Non-destructive non-contact concrete evaluation using an automated surface wave scanner, Volume 38, Issue 1, Proceedings of Meetings on Acoustics ICU, Bruges 2019

[7] A. Spalvier, J. Eiras, G. Cetrangolon, V. Garnier, C. Payan Internal pressure monitoring in a post-tensioned containment building using operational vibration, Journal of Nondestructive Evaluation 39 (3), 1-13, 2020

[8] JN Eiras, C Payan, S Rakotonarivo, Agustin Spalvier, Vincent Garnier, Vibration monitoring of nuclear power plant containment buildings during the Integrated Leakage Rate Test for structural condition assessment Journal of Nondestructive Evaluation, 2021

[9] R.Guptaa, D.Rossat,X. Dérobert, J. Baroth, M. Briffaut, G.Villain, F. Dufour, Blind comparison of saturation ratio profiles on large RC structures by means of NDT and SFE—Application to the VeRCoRs mock-up, Engineering Structures, Volume 258, 1 May 2022, 114057

Effect of carbonation on non-destructive strength and durability assessment of limestone based concrete

Bart Craeye[1,2*], Neel Renne[1] and Patricija Kara-De Maeijer[1,3]
[1] University of Antwerp, Faculty of Applied Engineering, EMIB Research Group, Belgium
[2] Odisee University College, Applied Sciences and Technology, DUBiT Research Unit, Belgium
[3] Geos Laboratories, Belgium

ABSTRACT

For the condition assessment and determination of residual bearing capacity of existing concrete structures, strength and durability related properties of the reinforced element are of high importance. Assessment of these properties can be performed by (i) destructive testing of drilled cores and testing the extracted samples in lab environment for compressive strength evaluation and determination of carbonation depth and (ii) indirect methods by using non-destructive techniques such as rebound hammer, ultrasonic pulse velocity tester, resistivity meter and air permeability meter.
The experimental program is conducted on concrete slabs of different strength classes intended for various exposure classes according to EN206, based on a limestone aggregate matrix where different amounts of CEMI and CEMIII (260-340 kg) and alternating w/c-ratios (0.40-1.00) were used. The plates were tested at the age of 90 days and the test program was repeated at the age of 5.5 years, after exposing the elements in a sheltered outside environment to natural carbonation, in order to evaluate the effect of carbonation on the mechanical and durability related properties.
Best fit correlations between the output of these different techniques were established by means of regression analysis. By using UPV and air permeability testing devices the strength and carbonation coefficient can be obtained non-destructively. Furthermore, the effect of age (i.e. carbonation) on the established correlation curves and predictive models is clearly noticeable.

Keywords: Strength assessment, durability assessment, non-destructive testing, carbonation

1. INTRODUCTION

For characterization of existing concrete structures, insight in the strength and durability related properties are necessary in order to come to an adequate expert judgement and repair strategy (Hobbs *et al.* (2007)). By means of (i) time-consuming and labour-intensive destructive testing of drilled cores and testing in lab environment and/or (ii) indirect methods by using non- or semi-destructive techniques on site, as an alternative. In this study, an experimental program was conducted on concrete slabs with an approximate age of 5.5 years, intended for various exposure classes (variation in W/C-ratio, cement type and cement content), based on a limestone inert matrix, and frequently used for Belgian applications. These slabs were intensively investigated, both in 2014 (results discussed in Craeye *et al.* (2017)) and 2019, by means of destructive testing (compressive strength tests and determination of carbonation rate), and non-destructive techniques (the rebound hammer, the ultrasonic pulse velocity tester, the Wenner probe for concrete resistivity and the air permeability tester). Best fit correlations between the output of these different techniques were established. The effect of age (e.g. carbonation) on the established predictive models is being evaluated.

* Corresponding author: bart.craeye@uantwerpen.be

By measuring the propagation speed of ultrasound waves through the material, the concrete quality is investigated. A high pulse velocity will result in a good quality concrete and, therefore, a higher compressive strength and more durable material can be expected. In this study, only ultrasonic techniques were used to determine to ultrasonic pulse velocity (direct transmission), according to EN 12054-4. The main influencing parameters on the output of the UPV are the type, content and hardness of the aggregates, the presence of cracks/voids in the structure and the moisture content of the concrete (Breysse (2012)). The W/C-ratio also affects the readings in pulse velocity. Furthermore, relative humidity also influences the output. The pulse velocity might increase up to 5% between dry and saturated test specimens, according to Solís-Carcaño *et al.* (2008).

The rebound hammer measures the rebound of a spring-loaded mass impacting on the surface of a concrete sample or structure, generating the rebound number, according to EN 12504-2. The higher this number, the harder the surface, indicating a high concrete compressive strength. A correlation exists between the compressive strength of standard cubes and the rebound number obtained by the hammer. However, this correlation is not universal and has to be modified for different devices, different concrete mixes or different conditions of testing. The condition of the surface has a high influence on the readings. Furthermore the type and the hardness of the aggregate and the carbonation degree, as it increases the surface hardness of the concrete, will have a big influence on the rebound number (Kim et al. (2009)). The influence of carbonation on the rebound number varies considerably according to the strength level but the effect of carbonation on the strength evolution is negligible for medium and high strength concrete.

Measuring concrete resistivity on site can be performed in various ways. It is often measured with a Wenner probe consisting of four equally spaced point electrodes that are pressed onto the concrete surface, which makes the technique entirely non-destructive. Results show that there is no appropriate relationship between surface resistivity and strength, generally due to different mechanisms support compressive strength and electrical resistivity. Consequently, it is not recommended to use surface resistivity as an indicator for evaluation of compressive strength (Ramezanianpour *et al.* (2011)). Nevertheless, the electrical resistivity of concrete is an important parameter, e.g. used to describe the corrosion rate of reinforced concrete elements for durability assessment. This parameter is related to the water content, the cement type, the W/C-ratio of concrete and the hydration degree. Environmental conditions such as relative humidity and temperature also affect the resistivity of the concrete matrix.

Several researches have shown that the coefficient of air permeability k_T correlates quite well with other standardized durability related tests (Jacobs *et al.*, 2009, Torrent et al., 2012). For instance, carbonation depth of concretes after 500 days of natural exposure correlates well with their k_T values measured at 28 days: higher air permeability leads to higher carbonation rate. These concretes have W/C-ratios in the range 0.26-0.75 and are made with CEM I (except few mixes to which 5-8% silica fume was added). Furthermore, according to (Neves *et al.* (2015)), a reliable correlation exist between the carbonation rate and the coefficient of air permeability, of which the linear scale factor depends on the type of cement that is being used. As such this non-destructive method can be used to update the residual service life of an existing concrete structure.

2. MATERIALS AND METHODS

2.1. Concrete composition

The study was initiated in 2013, with the casting of 14 non-reinforced slabs using 7 concrete mixtures with strength classes varying from C12/15 up to C50/60. For each mix two slabs (600 x 100 x 100 mm^3) were cast and tested (destructive compressive strength and various non- or semi-destructive techniques, as mentioned in (Craeye et al., 2017)). The composition of these mixtures is given in Table 1. These concrete mixtures are frequently applied in Belgium for different exposure classes. Limestone aggregates are used (max. grain size 22 mm), except for mixture C25/30 (which used porphyry 8 mm). Blends of three different cement types are selected: Portland CEM I 52.5R and blast furnace slag CEM III/A 42.5N – CEM III/B 42.5N. The W/C-ratio varies from 0.40 up to

1.00, the cement content from 260 kg/m³ up to 340 kg/m³ depending on the required exposure classes.

Once this original research project was finished in 2014 (results available and discussed in Craeye *et al.*, 2017), the slabs were stored in an unconditioned but sheltered outside environment (no direct exposure to rain). Temperature and relative humidity were not registered, moisture level and saturation degree were not monitored during storage.

For this research study, the slabs are tested at an approximate age of 5.5 years. Note that the test program will be repeated in 2023-2024 to evaluate the effect of age and carbonation of concrete with age of 10 years.

Table 1 Concrete composition in different strength classes

Strength class	Exposure Class	Slump W/C	Aggregates Max. grain size	Cement Min. content
C12/15	X0	S4 1.00	Limestone 22 mm	CEM III/B 42.5N LH SR LA 260 kg/m³
C20/25	XC2	S3 0.60	Limestone 22 mm	CEM III/B 42.5N LH LA 280 kg/m³
C25/30	XC3-XF1	S3 0.55	Porphyry 8 mm	CEM III/B 42.5N LH LA 280 kg/m³
C30/37	XC4-XF1	S3 0.50	Limestone 22 mm	CEM I 52.5R + CEM III/B 42.5N LH LA 300 kg/m³
C35/45	XC4-XD3-XF4	S3 0.45	Limestone 22 mm	CEM III/A 42.5N LA 320 kg/m³
C40/50	XC4-XD3-XF4	S3 0.40	Limestone 22 mm	CEM I 52.5R + CEM III/A 42.5N LA 320 kg/m³
C50/60	XC4-XD3-XF4	S4 0.40	Limestone 22 mm	CEM I 52.5R + CEM III/A 42.5N LA 340 kg/³

2.2. Selection of testing methods

Out of each slab 7 cores (diameter 100 mm, height 100 mm) are drilled to perform compressive strength and carbonation tests. To determine the actual compressive strengths of the concrete slabs, 3 cores are tested per slab, according to EN 12504-1. The core strength is converted into the equivalent cube compressive strength ($f^*_{ccub150}$) by means of a shape factor (averaged value of 1.05, NBN B15-001).

Prior to the drilling the slabs are tested non-destructively: ultrasonic pulse velocity (via direct transmission), air-permeability, surface resistivity, and rebound hammer tests are executed, according to EN 12504-2, SIA 262/1, AASHTOT277 and EN 12504-4 respectively. The location of the tested area on the slab are identical for each test and the same procedure is followed for each slab to minimise measuring artefacts.

The depth of carbonation (or the carbonation coefficient) is determined on 1 core per slab, according to EN 14630, using a 1% phenolphthalein solution.

3. RESULTS AND DISCUSSION

3.1. Strength assessment

In Figure 1 the results of the individual tests on both slabs per strength class are given and compared to the results obtained in 2014. There is a time difference of 5.5 years in between the 2014 and 2019 results. In general, there is a slight decrease in strength, except for C20/25. Lower strength loss was observed for the lower strength classes: 1.3% and 4.9% for C12/15 and C20/25, while for C30/37-C35/45-C40/50-C50/60 the decrease is 20.9%-9.0%-4.4%-8.4% respectively. As the slabs were stored in a sheltered outdoor environment, variation in saturation degree and frost exposure might explain the decrease in strength.

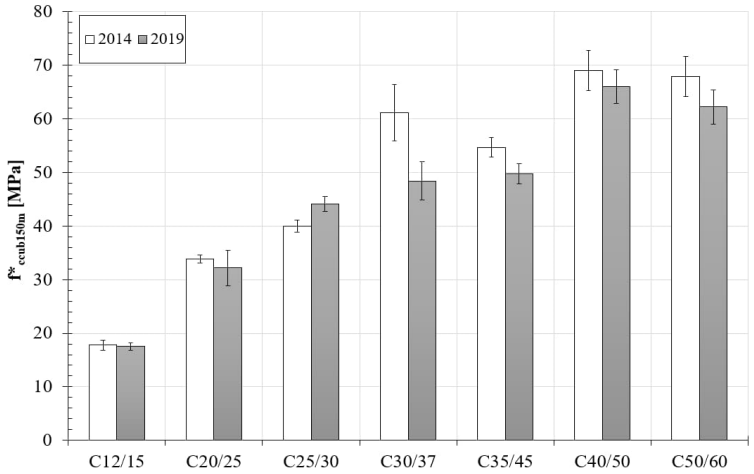

Figure 1. Equivalent cube compressive strength

The output of the equivalent cube compressive strength results is linked to the test results of the ultrasonic pulse velocity (direct transmission), the rebound hammer measurements and the air permeability measurements, as shown in Figure 2, Figure 3 and Figure 4. Note that the results of 2014 are only presented by means of the dotted line: the depicted data points and corresponding correlation line are representing the 2019 data.

Linear regression analysis is performed the obtain the best fitting curve between destructive and non-destructive test, and the reliability of the correlation of one method specifically, is quantified by means of the coefficient of determination (R^2-value) and the standard deviation (shown in the graphs). A linear correlation exists between cube compressive strength and the ultrasonic pulse velocity and compressive strength and the rebound number, with comparable correlation R^2 of 0.726 and 0.701 respectively. Compared to the 2014 study (dotted line), there is a noticeable drop in R^2 (0.957 for the rebound number, 0.886 for the ultrasonic pulse velocity): measurements on concrete surfaces that were subjected to environmental effects, have a significant lower linear coherence compared to tests performed on young concrete. It is known that carbonation has an effect on strength-hardness correlation (Kim *et al.*, 2009) which is also identified in this study. There is a noticeable shift in the correlation in between the 2014 and 2019 correlation curve (Figure 2, Figure 3). Furthermore, the difference in between the correlation provided by the provider of the supplier and the one obtained in this research is noticeable. For a given strength, the rebound number increases due to carbonation, and this effect is more prominent for higher strength classes. Comparable conclusions can be drawn regarding the correlation in between strength and ultrasonic pulse velocity. However, the effect of carbonation is less prominent. Furthermore, the compressive strength is inversely proportional with the air permeability (Figure 1c)): increasing the permeability of matrix leads to a decrease in strength. A good correlation is found in this project, R^2 equals 0.822.

As the resistivity meter is not designed for strength estimation, the measurements cannot be related to each other. In comparison with the 2014 study, it appears that the surface resistivity of the concrete slabs increased over a period of 5.5 years which can be linked to an increase in hydration degree and a decrease in saturation level (moisture content).

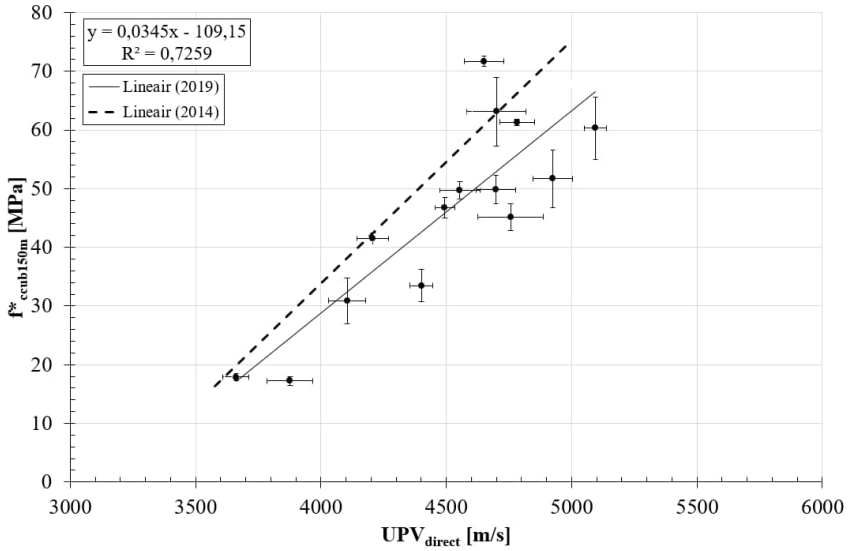

Figure 2. Correlation f*$_{ccub150m}$-ultrasonic pulse velocity

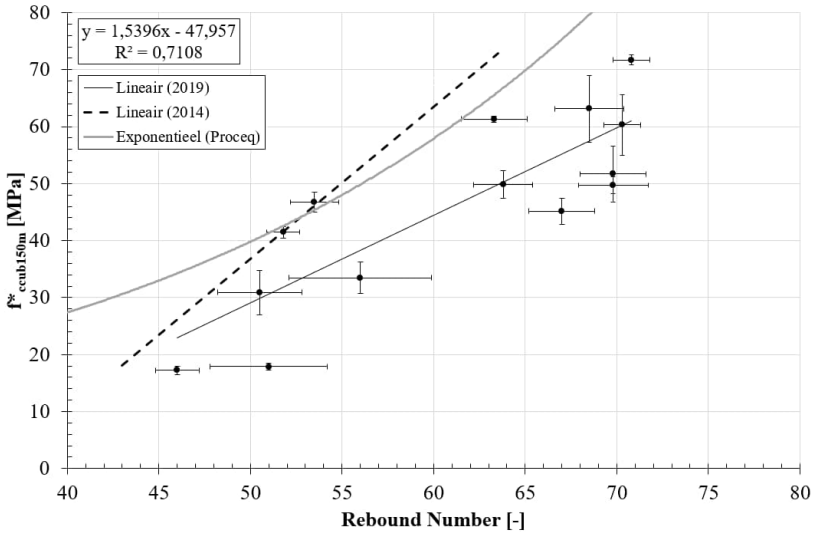

Figure 3. Correlation f*$_{ccub150m}$-rebound number

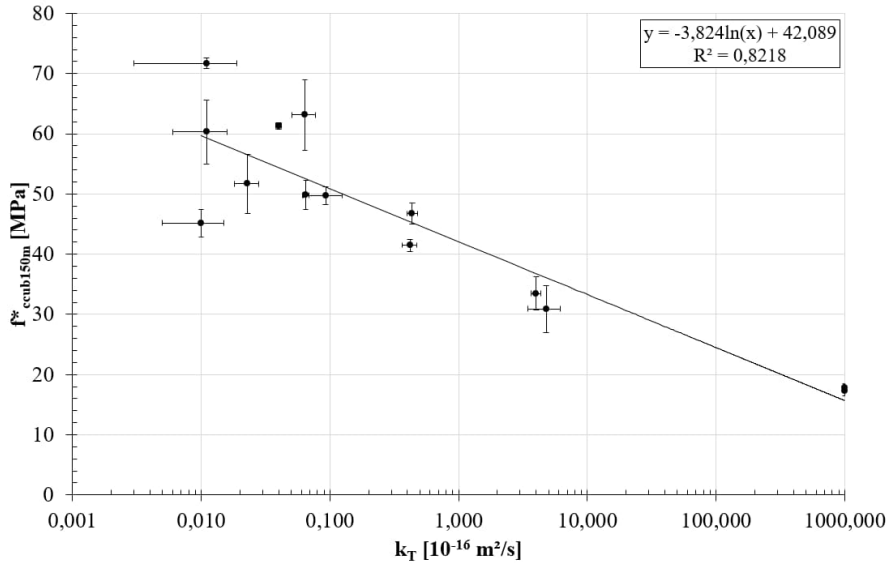

Figure 4. Correlation f*$_{ccub150m}$-air permeability

3.2. Durability assessment

The depth of the carbonation is determined destructively on the cores drilled out of the slabs. The results are presented in Figure 5. The effect of the strength class is clearly noticeable. However, as the cement type has a decisive effect on durability and corrosion related properties such as carbonation (Hiemer *et al.* (2018)) a subdivision of the results is needed. The carbonation coefficient decreases with increased strength class for the slabs with a lower strength class concrete (C12/16 to C25/30) with blast furnace slag cement (CEM III/B) (Figure 6). For the higher concrete strength classes, using blends of Portland CEM I 52.5 and blast furnace slag CEM III, no effect of strength class on carbonation is found. A higher carbonation coefficient is noticed for the slabs with strength class C35/45. This is due to the single use of blast furnace slag CEM III/A, which is known to be more susceptive to carbonation. Carbonation depends on several factors such as the penetrability of the concrete cover, the amount of carbonatable material in the matrix, the concentration of CO2 in the atmosphere, the exposure conditions (temperature, RH, rain, solar exposure), etc. (Neves *et al.*, 2018). It leads to precipitation of $CaCO_3$ which leads to an increase in hardness of the concrete surface and densification of the matrix, however without increasing the strength of the material. This might also effect the air permeability. The penetrability of the cover concrete is one of the main factors governing the carbonation rate. Air permeability is one of the most accepted properties to evaluate the penetrability of the cover concrete. The penetration of CO2 into concrete can be considered as a purely diffusive process, , which predicts a carbonation depth proportional to the square root of time (obeying Fick's 2nd Law). An increase in carbonation coefficient increases the air permeability of the matrix (Figure 8) and a decrease in pulse velocity can be identified (Figure 7), which confirms the findings of Neves *et al.* (2018). The permeability of concrete has an effect on the speed of propagation of the ultrasonic pulse and vice versa, which is shown in Figure 9). Elements with high permeability have a lower pulse velocity, mainly due to the scattering of the pulse through air present in the pores. It is important to note that the use of the air permeability meter can be a good alternative for the ultrasonic pulse velocity tester and both techniques can be useful for estimation the carbonation coefficient in a non-destructive way. The coefficient of determination of the established correlations is good: 0.836 and 0.939 for ultrasonic pulse velocity and air permeability respectively.

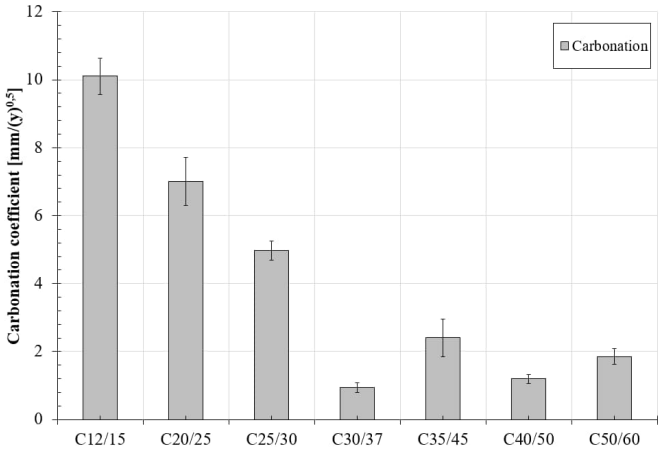

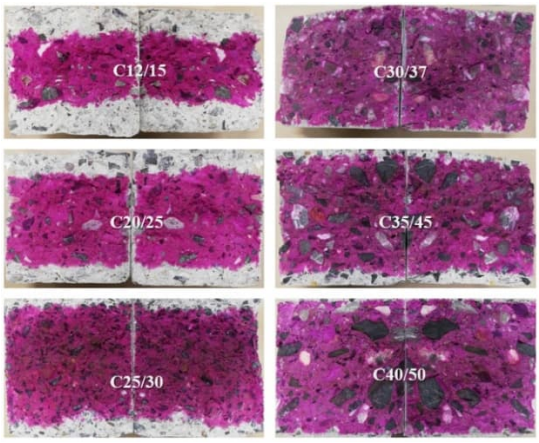

Figure 5. (left) Results of carbonation coefficient
Figure 6. (right) Carbonation depth of concrete with different strength classes

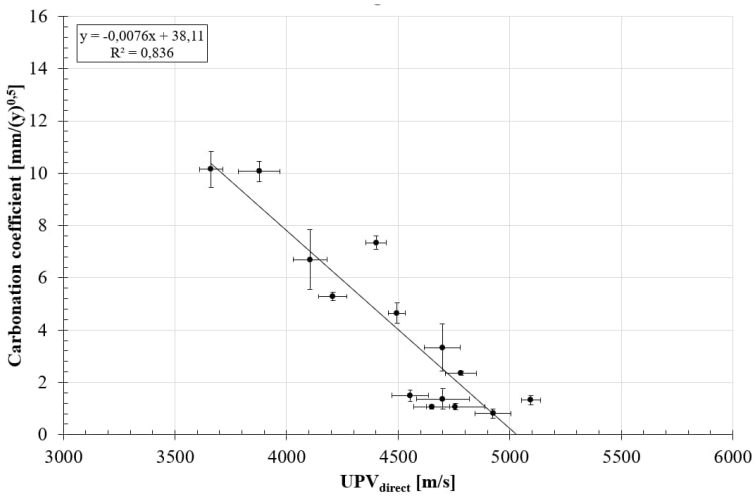

Figure 7. Correlation carbonation coefficient-ultrasonic pulse velocity

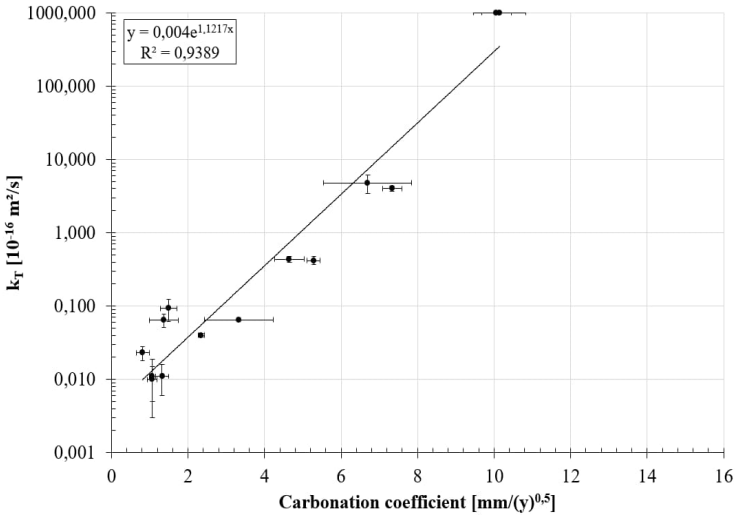

Figure 8. Correlation air permeability-carbonation coefficient

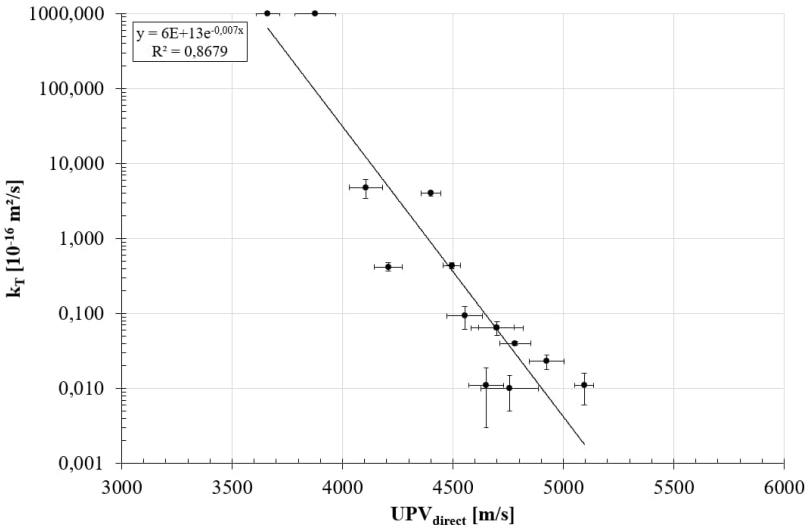

Figure 9. Correlation air permeability-ultrasonic pulse velocity

4. CONCLUSION

In this study an experimental program is conducted on concrete slabs of different strength classes intended for various exposure classes, based on a limestone aggregate matrix. The plates have an age of 5.5 years, are also characterized at younger stage (in 2014) and will be tested once more after 10 years of exposure to natural carbonation (2023-2024). Destructive core drilling and testing and several non-destructive techniques are used to assess strength and durability related properties of the slabs.

A slight strength decrease is found with higher strength loss for higher strength classes. Furthermore, the strength is linear proportional with surface hardness and ultrasonic pulse velocity and inversely proportional with air permeability. Compared to the results of 2014 (i) higher coefficient of determination on the obtained correlation curves is found and (ii) a shift on the correlation curves is noticeable, linked to the aging effect due to carbonation. This aging effect is more pronounced for the rebound hammer results. The effect of strength class on carbonation rate is clearly noticeable for slabs of lower strength classes (up to C25/30). For higher strength classes the effect of cement type is more pronounced. A linear correlation with high coefficient of determination is found between carbonation coefficient, air permeability (directly proportional) and ultrasonic pulse velocity (inversely proportional). Note that the air permeability test is a good non-destructive alternative for the ultrasonic pulse velocity test: elements with high permeability have a lower pulse velocity, mainly due to the scattering of the pulse through air present in the pores.

REFERENCES

Breysse, D. (2012). *Nondestructive evaluation of concrete strength: An historical review and a new perspective by combining NDT methods*, Construction and Building Materials, vol. 33, pp. 139–163.

Craeye, B., van de Laar, H., van der Eijk, J., Lauriks, L. (2017). *On-site strength assessment of limestone based concrete slabs by combining non-destructive techniques*, Journal of Building Engineering, vol. 13, pp. 216-223.

Hiemer, F., Jakob, D., Kessler, S., Gehlen, C. (2018). *Chloride induced corrosion in cracked and coated concrete: from experimental study to time-dependent modelling,* Materials and Corrosion, vol. 69, no. 11, pp. 1526-1538.

Hobbs, B., Tchoketch Kebir, M. (2007). *Non-destructive testing techniques for the forensic engineering investigation of reinforced concrete buildings*, Forensic Science International, vol. 167, no. 2–3, pp. 167–72.

Jacobs, F., Denarié, E., Leemann, A., Teruzzi, T. (2009). *VSS Report 641*, Office Fédéral de Routes, Bern, Switzerland.

Kim, J.-K., Kim, C.-Y., Yi, S.-T., Lee, Y.(2009). *Effect of carbonation on the rebound number and compressive strength of concrete*, Cement and Concrete Composites, vol. 31, no. 2, pp. 139–144.

Maierhofer, C., Reinhardt, H.-W., Dobmaan, G. (2010). *Non-destructive evaluation of reinforced concrete structures*, Woodhead Publishing in Materials, CRC Press, UK.

Neves, R., Sena da Fonseca, B., Branco, F., de Brito, J., Castela, A. and Montemor, M.F. (2015). *Assessing concrete carbonation coefficient resistance through air permeability measurements*, Construction and Building Materials, vol. 82, pp. 304-309.

Neves, R., Torrent, R. and Imamoto, K. (2018). *Residual service life of carbonated structures based on site-non-destructive tests,* Cement and Concrete Research, vol. 109, pp. 10-18.

Ramezanianpour, A.A., Pilvar, A., Mahdikhani, M., Moodi, F. (2011). *Practical evaluation of relationship between concrete resistivity, water penetration, rapid chloride penetration and compressive strength*, Construction and Building Materials, vol. 25 , no.5, pp. 2472–2479.

Solís-Carcaño, R., Moreno, E.I. (2008). *Evaluation of concrete made with crushed limestone aggregate based on ultrasonic pulse velocity*, Construction and Building Materials, vol. 22, no. 6, pp. 1225–1231.

Torrent, R., Denarié, E., Jacobs, F., Leemann, A., Teruzzi, T. (2012). *Specification and site control of the permeability of the concrete cover*, Materials and Corrosion, vol. 63, no. 12, pp. 1127-1133.

Detecting capability of NDE methods in steel-concrete (SC) structures

Ludovic Fülöp[1,*], Miguel Ferreira[2] and Guy Rapaport[3]
[1] VTT Technical Research Centre of Finland LTD, Finland
[2] VTT Technical Research Centre of Finland LTD, Finland
[3] Rambol Oy, Finland

ABSTRACT

This paper gives a summary of an exploratory study of different non-destructive evaluation (NDE) methods has been carried out on steel-concrete (SC) liner structures [1]. SC NDE present similar challenges as traditional liner-plate elements. The deployed NDE methods were based on ultrasonic measurements using: the pulse echo technique; radiographic inspection; ultrasound 3D tomographer; impact-echo (IE); impulse-response (IR) and ground penetrating radar (GPR). The study has highlighted severe limitations of several traditional NDE techniques used for concrete structures, especially the ultrasound-based methods. Mechanical impact-based testing systems revealed promising results to detect cracks and de-bonding. Radiographic testing was successful in detecting the presence of cracks in cases when these had sufficient opening and length.

Keywords: steel-concrete (SC) structures, liner structures, exploratory study,

1. INTRODUCTION

The concept of steel-concrete (SC) originated from earlier ideas of using steel plates bonded to the concrete as reinforcement for slabs [2]. Prefabricated SC element development for NPP structures continued in the 1990's, in Japan and South-Korea [3]. SC elements are also used in the Westinghouse AP1000 plant design, under construction or entering operations in China and the US [4]. As future perspective, use of SC elements is considered as a feasible construction method for small modular reactors [5].

Recent research and standardization efforts are directed to identify design changes, answer fundamental questions on the expected performance, optimise SC configurations for NPP, and provide standard for application in Europe [6].

The inspection of SC elements, especially when used in industrial setting such as NPPs, has different challenges from conventional concrete structures. Wall thickness can be in excess of one meter, both sides covered with continuous steel plates; the structures can have complex detailing with penetrations or cast-in-place items; accessibility may be limited due to the presence of other components; and elements are exposed to harsh environments or located below ground. This poses a challenge for non-destructive evaluation (NDE) of SC structures to undertake compliance testing, condition and damage assessment.

The goal of this study was to evaluate a range of possible NDE inspection methods for testing the integrity of SC elements. The expectation was to confirm some of the earlier findings and carry out trials with additional NDE methods to assess to what degree concrete damage can be detected. Several techniques have been explored and the results can guide selection of NDE for SC. Extensive description of the results, was published earlier [1].

* Corresponding author: +0358 40 5934698 and ludovic.fulop@vtt.fi

2. METHODS AND RESULTS

2.1. Tested SC members

The inspected SC elements had two steel plates with a concrete infill, in which welded studs and tie bars were used to connect steel and concrete (Figure 1). The SC beam elements were mechanically damaged. Two types of cracks were present in the specimens: bending cracks perpendicular to the steel plate and shear cracks with an angle of about 45 degrees. In addition, de-bonding of the top and bottom steel-plate may be present.

Figure 1 – The steel formwork of the SC beams, on the side during concreting.

2.1. NDE methods used

Ultrasonic, radiography, 3D tomography, impact-echo, impulse-Response (IR) and ground penetrating radar (GPR) was tried on the specimens. The GPR tests from the steel side were completely unsuccessful, due to extremely intense wave reflections and wave energy loss on the steel plate. Hence, the GPR tests are not presented here.

Ultrasonic testing was performed using pulse-echo technique and wet coupling. The main equipment was a Krautkrämer USM 35. Additionally, Krautkrämer USM 23 was used in a measurement with a low frequency ultrasonic transducer K0,1G (a straight beam transducer with frequency of 100 kHz).

Radiographic testing was using a cyclic induction electron accelerator producing high-energy radiation. The radiation source was a small-size cycle model accelerator (Betatron MIB 7.5) with a pulse supply and a focal spot of approximately 0.325×3 mm2, with a radiation beam spread angle of 22, and producing a continuous energy spectrum with peak energy of 7.5 MeV.

3D tomography was based on the pulse-echo principle and was conducted using MIRA from Germann Instruments, which can be used to create a three-dimensional representation of internal defects in a concrete object. The MIRA uses an array of 40 dry point contact (DPC) transducers to emit shear-horizontal (SH) waves into the surface.

Impact-echo tests were based on the monitoring reflected stress waves initiated by mechanical impact to detect internal reflecting interfaces in solids. IE can be used to determine the thickness of slab-like structures and detect internal damages. Short-duration (<100 μs) stress pulses are introduced into the solid by mechanical impact and high-fidelity displacement transducers are used to measure the surface displacement response.

The Impulse-Response (IR) test is suitable for screening of plate-like structures, providing information regarding the relative quality of concrete within a test area. The IR test measure the relative flexibility of a structure, aiming to evaluate integrity and identify suspicious areas for subsequent detailed analysis.

2.1. Highlighted results

The most promising methods were the radiographic testing and the mechanical impact-based methods, i.e. impact-echo (IE), impulse response (IR).

The X-raying was performed for four cracks visible on the concrete surface, selected based on their dimension and orientation in the direction of the X-ray (Figure 2.a). The SC's steel plate on the X-raying side was 10mm thick. On the opposite side the SC's steel plate was 15mm thick. The film plate was placed in contact with the 15mm plate and covered with an additional backing, to prevent X-ray scattering from background. Cracks were fully open in the concrete up to the steel plate on the X-raying side (Figure 2.b). The internal cracking of the concrete was observed on the radiograph of Crack 3 (Figure 2.c), but also in other cases where only the main crack was visible on the concrete surface. The detection of concentrated cracks was also very good. The X-raying technique was efficient to detect cracks behind the SC steel plates down to the crack width of 1 mm, for cracks near the side of the film and oriented roughly in the X-ray direction (i.e. perpendicular to the SC surface). Tests have shown that it is possible to X-ray cross sections of concrete/steel up to 900 mm thicknesses.

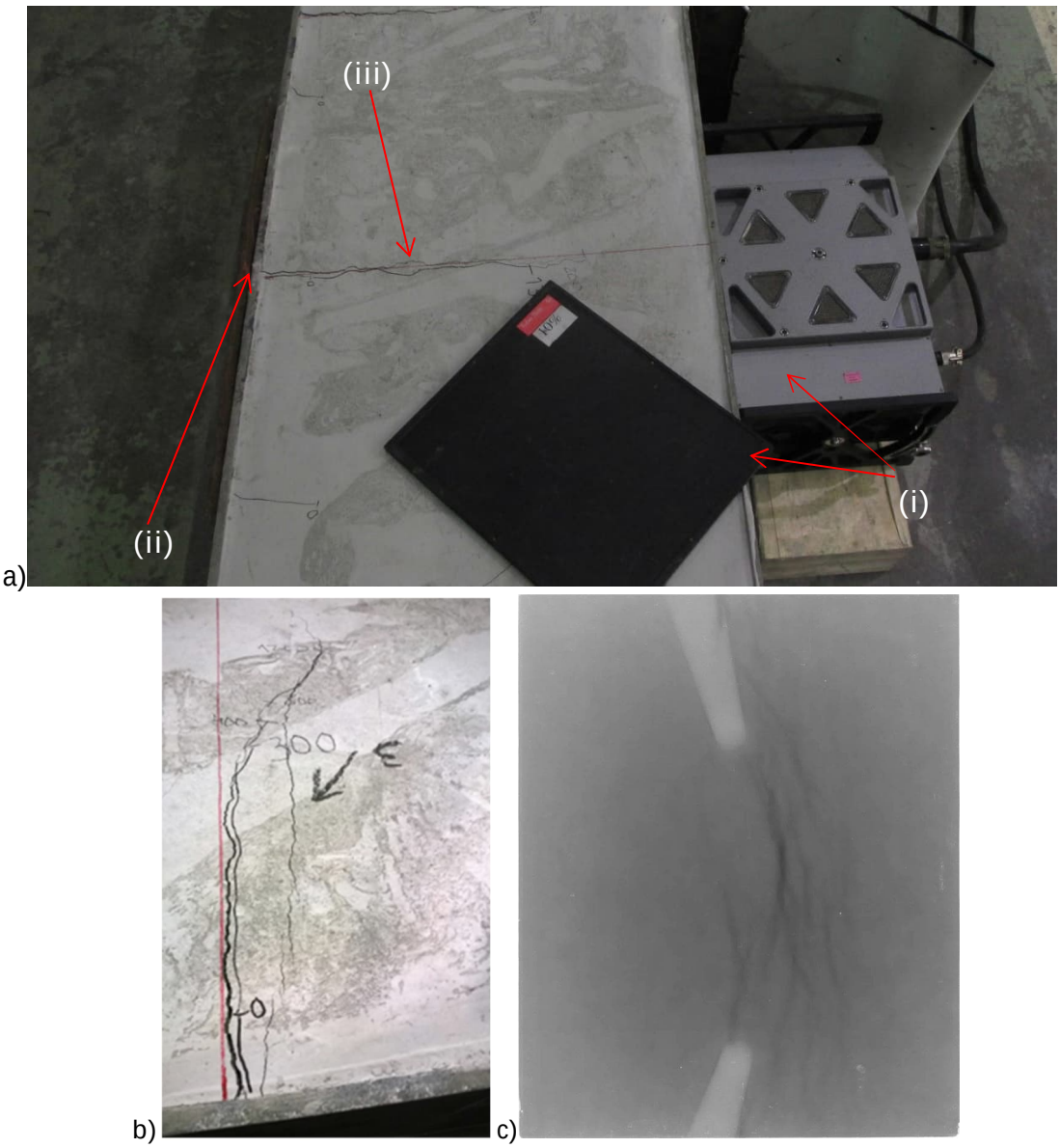

Figure 2 – (a) The betatron X-raying setup: (i) the radiator unit and digital film plate used, (ii) location of the film plate when X-raying and additional steel back-plate to prevent X-ray scattering from background, (iii) crack in the SC beam (b) View of Crack 3 from the side of the beam and (c) radiographic image through the steel-plate. Several cracks visible as darker lines in the 10% digital film plate with exposure 600 s, focal spot position 375 mm. Two tie bars are also identifiable as lighter spots.

The Impact-Echo technique (Figure 3.a) appears to be suitable for integrity evaluations of SC members, when damages are located mid-depth in the concrete and are oriented favourably to generate wave reflections.

For the intact beam, the anticipated frequency of the un-damaged slab was estimated between 2.19-2.23 kHz; using P-wave velocity of 5900 m/s and 3454 m/s, shear-wave velocity of 3250m/s and 2107m/s, Poisson ratio of 0.3 and 0.2, density of 7800kg/m^3 and 2400kg/m^3, for steel and concrete respectively. The detected frequency of the undamaged SC beam was 2.44 kHz.

Tests were performed at location with oblique cracks 565 mm and 650 mm from surface (Figure 3b), using the 12mm impactor as wave source on the steel surface. The anticipated frequency in these locations are 3.09 kHz and 2.66-2.68 kHz, while the detected frequency was 2.93 kHz and 2.44 kHz respectively.

a)  b) 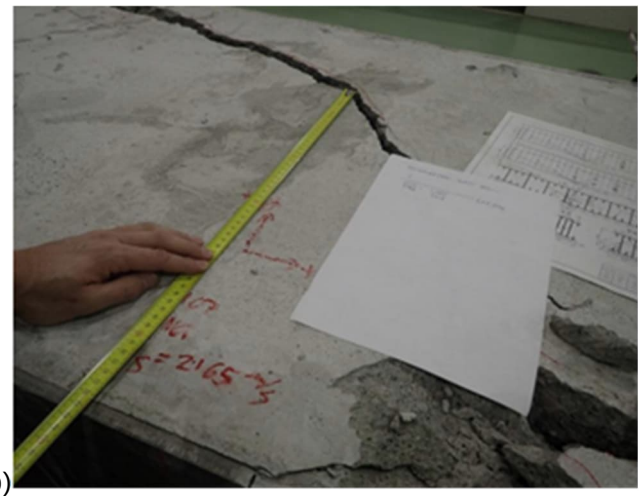

Figure 3 – (a) The Impact-Echo (IE) system components, and (b) testing at the location of an oblique crack at the depth of 565 mm from the steel plate surface

3. CONCLUSIONS

Ultrasonic pulse-echo, radiographic inspection, 3D tomography, impact-echo (IE), impulse response (IR) and ground penetrating radar (GPR) were tested on SC. The suitability of the different techniques to detect damages in SC structures is given in Table 1.

Table 1 – Suitability of different NDE techniques to investigate in SC elements.

	Detection capability for through steel plate testing in SC				
NDT method	Delamination of steel plate	Oblique crack	Perpendicular crack	Local fault /- Drilled holes	Embedded steel studs
Ultrasonic testing	No	-	-	No	-
Radiographic testing	-	Yes	Yes / >1mm	-	Yes
Ultrasound 3D topographer testing	No	No	No	-	-
Impact-Echo (IE)	-	Yes	-	-	-
Impulse-Response (IR)	Yes	Yes	Yes / If there is damage to steel bond	-	-
Ground Penetrating Radar (GPR)	No	No	No	-	No

With ultrasonic measurements, the signal could not be transmitted through the steel plates into the concrete, with the techniques used. Radiographic testing was applicable when the cracks had sufficient opening and length close to the film side. Stress-wave based methods were found to be applicable for SC. Impact-Echo (IE) is suitable for detecting cracks and concrete damage, with

limitations related to size and orientation of the crack to be detected. IE was used to detect oblique cracks creating extended reflection surfaces within the mid-depth of the SC member

ACKNOWLEDGEMENTS

The tests were performed in VTT's project "*NDE of NPP primary circuit components and concrete infrastructure (WANDA)*" of the Finnish Research Programme on NPP Safety (SAFIR 2018).

REFERENCES

[1] L. Fülöp, M. Ferreira, A. Tuhti, and G. Rapaport, "Assessing the challenges of condition assessment of steel-concrete (SC) composite elements using NDE," Case Studies in Construction Materials, vol. 16, p. e00887, Jun. 2022, doi: 10.1016/j.cscm.2022.e00887.

[2] H. Lerchenthal and I. Rosenthal, "Flexural behaviour of concrete slabs reinforced with steel sheet" Materiaux et Constructions, vol. 18, no. 88, pp. 279–282, 1982.

[3] S. Suzuki, Y. Shimazaki, K. Sekiguchi, W. Kokubo, "Introduction of 'large block prefabrication method'" Japan: Atomic Energy Society of Japan (1992)

[4] AP1000, AP1000 European Design Control Document, (2009).

[5] B. Burgan, C. Kyprianou, S. Bingham, S. Waterhouse, A novel steel-concrete composite system for modular nuclear reactors, in: Proc. Inst. Civ. Eng. Energy, 2017: pp. 80–90. https://doi.org/10.1680/jener.16.00022.

[6] L. Fülöp, J. Niepceron, and B. Burgan, "Steel Concrete for NPP applications," Nordic Concrete Research Seminar NUCCON 2016 – Concrete for Nuclear Structures, Espoo, Oct. 2016.

NDE to detect Concrete Flaws behind Steel Plates

Larry D. Olson[1,*], Dennis A. Sack[2] and Julia Tcherner[3]
[1] Chief Engineer, Olson Engineering, Inc., USA
[2] Principal Engineer, Olson Engineering, Inc., USA
[3] Specialist Engineer, Nuclear, SNC Lavalin, Canada

ABSTRACT

A variety of nondestructive evaluation (NDE) methods are available to evaluate the integrity of concrete structures, but the number of applicable methods is reduced when the access is limited to only one side of the structure and when no direct access to the concrete exists (e.g., steel lined containment structures, steel lined nuclear waste storage containers). A multi-year project was initiated to identify the methods that can be easily applied in the field to inspect these types of structures and to identify cracks, voids, delaminations, consolidation issues (e.g., honeycombing), concrete strength degradation and corrosion of steel in concrete behind steel liners. The NDE methods that showed the most application in the study were Impact Echo Scanning, Spectral Analyses of Surface Waves and Slab Impulse Response. Example NDE results are presented from a steel-plated concrete wall with various concrete flaws and bonded/debonded steel plates.

Keywords: Impact Echo: Surface Waves; Impulse Response; Steel Plates; and Concrete Flaws.

1. INTRODUCTION

Several NDE techniques are applicable for detection of degradation in concrete structures where the access is limited to only one side of the structure. Some of these methods, e.g., Impulse Response, Impact Echo, Ultrasonic Pulse Echo, Ground Penetrating Radar, Half Cell Potential [ACI 228.2R-2013].) are being successfully used in the field to evaluate integrity of concrete structures in nuclear installations While some NDE techniques are ready for deployment on the field, caution must be exercised when applying these techniques in the field as it is very important to select the right technique for the anticipated degradation type. Typically, the use of a combination of methods improves reliability.

Steel-concrete composite structures are used in nuclear as well as non-nuclear industry. Composite structures have a variety of applications in a non-nuclear industry, e.g., in bridge construction as steel-concrete slabs and rigid connections between piers and beams. Examples of steel-concrete composite structures in nuclear industry include concrete containment with a steel liner and certain designs of nuclear waste storage structures.

A few experiments were conducted over the recent years to test applicability of the NDE to detect defects in concrete behind steel plates (Haack, Wu, 2011, Clayton, 2013, Wiggenhauser, 2013, Yanagihara, 2015, CSNI, 2015 and Fülöp, 2016). It appears that it is possible to detect voids (delaminations) at the interface of the steel liner and concrete. However, it is very challenging to detect voids and other defects deeper inside the concrete, particularly when voids are present at the interface of the liner and concrete. A few NDE techniques such as impulse response, impact echo and surface wave method were identified as promising to detect flaws in concrete behind steel plate and were selected for further study by the authors [Tcherner et al, 2019]. This paper provides example results for these NDE methods from the research study that have not been previously presented.

* Larry D. Olson, 1+303-423-1212, Larry.Olson@OlsonEngineering.com

2. CONCRETE TEST WALL CONSTRUCTION

The mock-up test wall consisted of a composite 0.5 inch (127 mm) thick steel plate and concrete with a thickness of 12 inches (0.3048 m). A variety of nondestructive test methods were employed in the research, including: Ultrasonic Pulse Velocity (UPV), Impact Echo Scanning (IES), Slab Impulse Response (SIR), and Spectral Analysis of Surface Waves (SASW). The UPV tests were conducted directly through the wall from the steel side to the opposite concrete side in order to confirm that the defects were constructed as planned and therefore UPV results are not reported herein. The IES, SIR, and SASW tests were all conducted from the steel plate side of the wall in order to evaluate their ability to detect internal concrete defects behind the steel plate. Example test results and plots of the test results for the wall are presented in Sections 3 and 4, respectively.

2.1. Mock-Up Wall #1 Construction

The nominal dimensions for Wall #1 were 6x6x1 feet (1.8 x 1.8 by .30 m) with a 0.5-inch (12.7 mm) thick steel plate on the front wall face with 4-inch (102 mm) embedded steel studs on 1-foot (0.305 m) centers. Wall #1 was built with grade 60 steel reinforcement (#4 bars) and nominally 6000 psi (41.4 MPA) strength high slump self-consolidating concrete with ¾ inch (19 mm) aggregate-6-inch (152 mm) slump pea gravel. Wall #1 was initially cast as a flat slab (steel plates down) to facilitate concrete placement and flaw installation. Constructed flaws within Wall #1 are described in Table 1 and are shown in a construction drawing in Figure 1 below. Figure 2 shows photographs of Wall #1 construction and the locations of the constructed flaws prior to casting the wall and after concrete placement.

Table 1: Wall #1 - Constructed Flaw Descriptions

Constructed Flaw number	Flaw name/type	Simulation material	Construction	Notes
1	4 mm vertical crack	Closed cell foam	5 in deep	Some areas of minor loss of contact with steel plate
2	Weak concrete	Watered down concrete	Full wall thickness	Some areas of minor to moderate loss of contact with steel plate, plus visible cracking present
3	Air/Water void	Concrete box	2 in deep, 8 in thick	Air filled for all testing except for Impact Echo Scanning. In this case air vs. water filled were compared.
4	4 mm crack	Closed cell foam	on plane 45° from vertical	Some areas of minor loss of contact with steel plate
5	4 in thick honeycomb	Corse aggregate dipped in cement	4 in deep, 4 in thick	No fine aggregate included
6	corrosion delamination	Closed cell foam	10 in deep	Some areas of minor loss of contact with steel plate
7	corrosion delamination	Closed cell foam	10 in deep	Some areas of minor loss of contact with steel plate
8	Minor loss of contact over sound concrete	Thin plastic sheet	Attached to steel plate	
9	Moderate loss of contact over sound concrete	Thin paper sheet	Attached to steel plate	
10	4 mm horizontal crack	Closed cell foam	1.5 - 8 in deep	
11	4 mm horizontal crack	Closed cell foam	1.5 – 8 in deep	

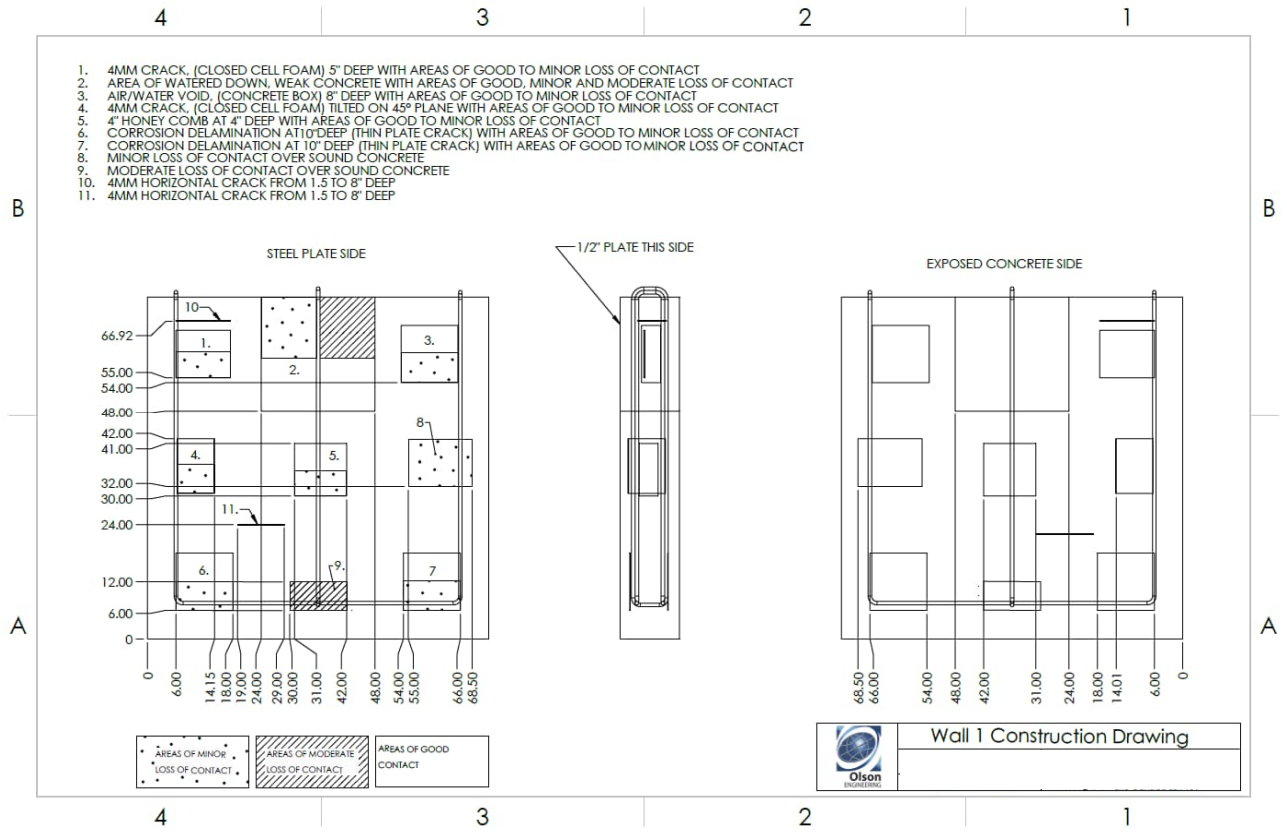

Figure 1: Wall #1 construction drawing showing locations and types of planned flaws.

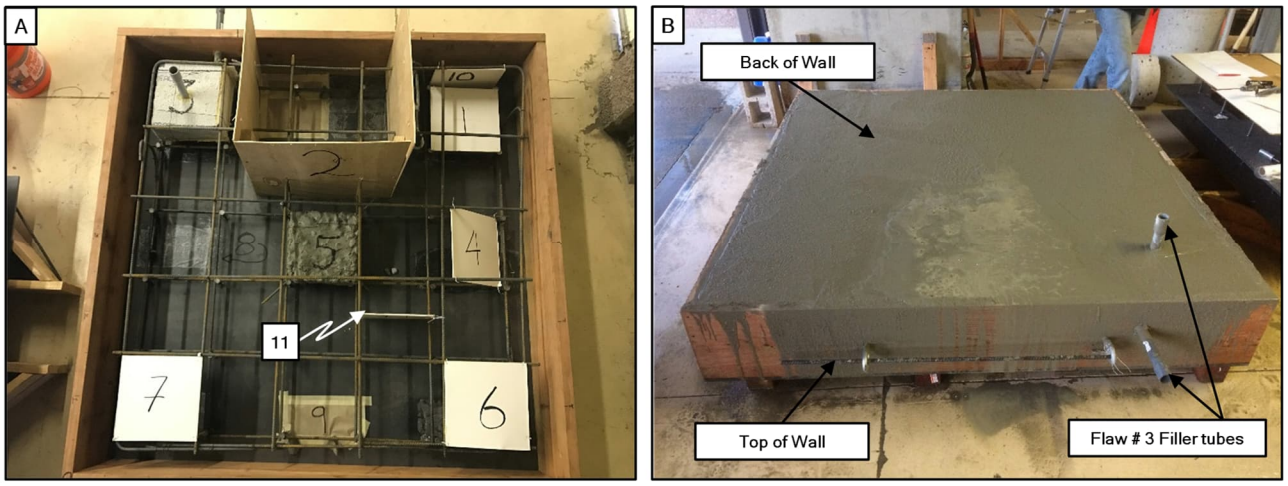

Figure 2: Photographs of Wall #1 construction before and after concrete placement.

3. NONDESTRUCTIVE EVALUATION (NDE) METHODS AND RESULTS

NDE results from Wall #1 are discussed and presented below for the IES, SIR and SASW tests.

3.1. Impact Echo Scanning (IES) Method and Results

The IES method involves hitting the concrete surface with a small or larger solenoid impactor and identifying the reflected wave energy with a displacement or accelerometer receiver mounted on the surface near (within 50 mm, 2 inches) the impact point. A photo of the scanning IE tests being

conducted along a line on the wall is presented in Figure 3 below, and a simplified diagram of the method is presented in Figure 4 (ASTM C1383) for point-by-point IE testing. In impact echo scanning (IES), a slow-rolling transducer wheel records data every inch (25.4 mm) along a scan line from a solenoid impact to the concrete. The resulting displacement response of the receiver is recorded. The resonant echoes are usually not apparent in the time domain. The resonant echoes are more easily identified in the frequency domain. Consequently, the time domain test data are processed with a Fast Fourier Transform (FFT) which allows identification of frequency peaks (echoes). The displacement spectrum of the receiver or the transfer function (receiver displacement output/hammer force input vs. frequency) are used to determine the resonant peaks. If the thickness of a structural member is known, the factored IE compressional wave velocity (V_P) and member echo thickness can be determined by the following equations:

$$V_P = 2*d*f/\beta \text{ and} \quad (1)$$

$$d = \beta*V_P/(2*f) \quad (2)$$

where d = slab thickness, f = resonant frequency peak. The above equation is modified by a β (Beta) factor of 0.96 for walls and slabs. Furthermore, flaws or other defects within the slab will produce anomalous echoes and corresponding resonant peaks in the frequency domain, making the IE method able to detect not only slab thickness, but slab integrity as well.

For surface delaminations and debonds, the IE test results are dominated by the low frequency flexural response (drum-like response) rather than by the true compression wave IE echoes. Thus, standard processing of IE data results in shallow debonds and delaminations appearing as very thick (deeper than the actual maximum thickness) areas on the wall or slab. The results of the IE tests on the specimen show these debonded areas clearly, and verify that the IE method is very well suited for locating steel debonds as well as for deeper flaws.

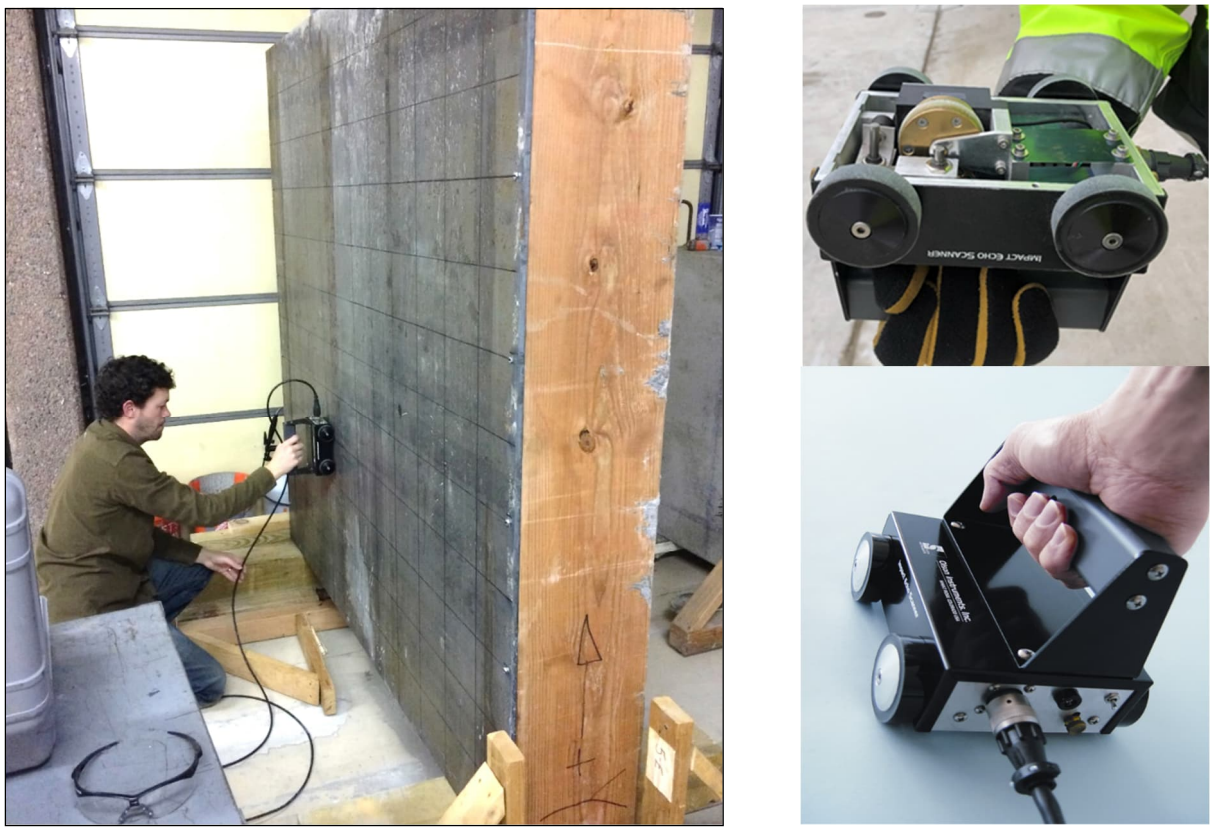

Figure 3: Impact Echo Scanning (IES) on steel side of Wall #1 and view of underside of IES unit with rolling displacement transducer on spring and normal and large solenoid impactors for tests every 1 inch (25.4 mm) and a close-up view of the IES unit.

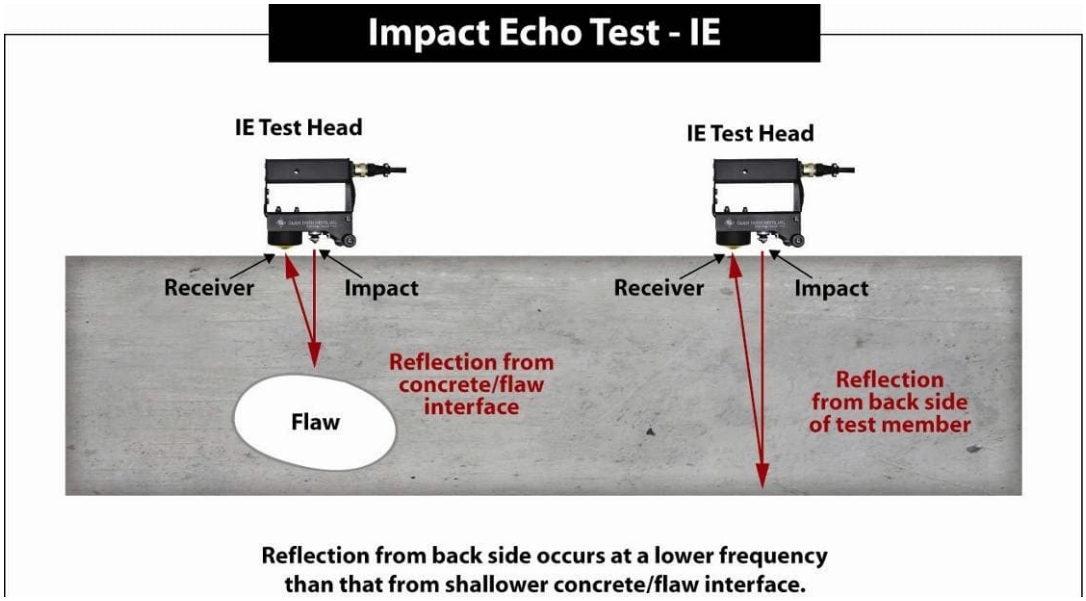

Figure 4: Impact Echo Test Diagram for point-by-point testing with solenoid impactor and displacement transducer.

Impact Echo Scanning (IES) was performed on nominally 0.5 ft (0.15 m) spaced vertical lines over the steel plated side of Wall 1. Impact Echo (IE) measurements were recorded at 1-inch (25.4 mm) intervals along each scan line. An example IES scan and IE record are presented in Figure 5 below. The wall IES results are plotted in Figure 6 with the constructed defects overlain on the results for comparison purposes.

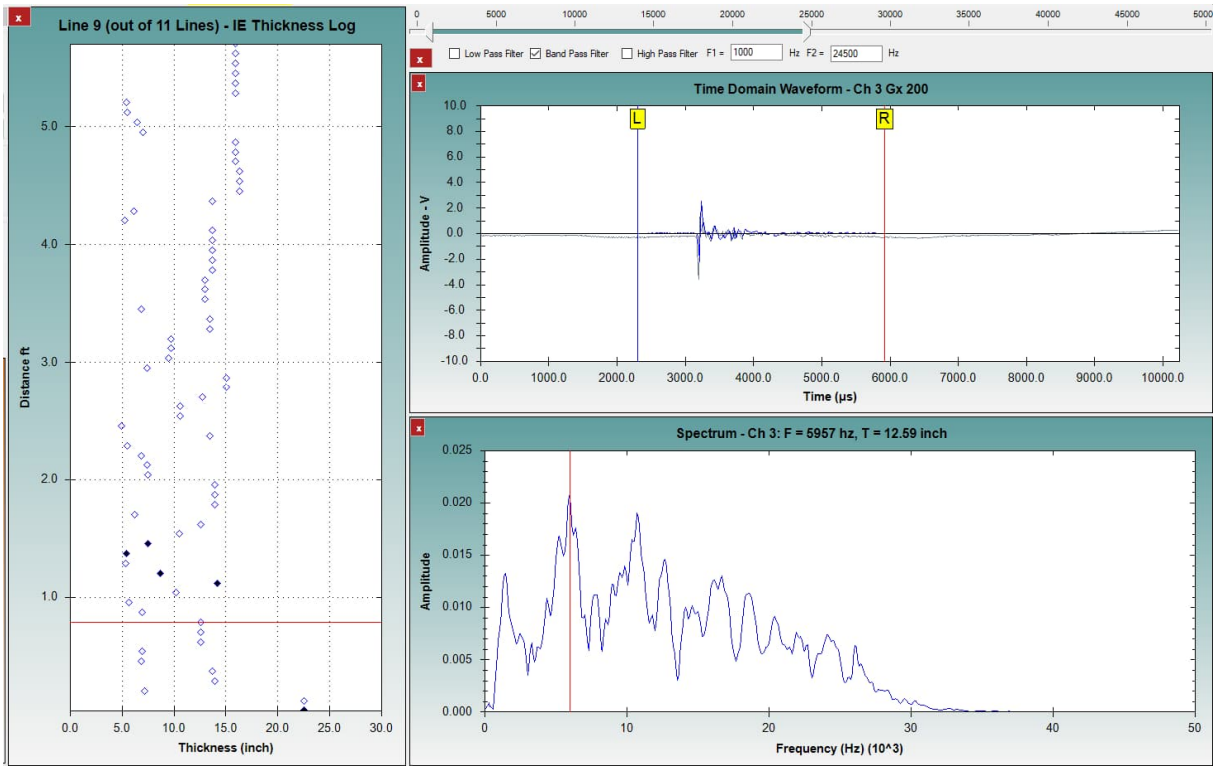

Figure 5: Example IES record. Left plot - IE thickness/echo depth log for scan 9: x=4.5 ft scan line. Top right plot - Time domain record for IE point indicated by red line in left echo depth plot. Bottom right - Frequency domain plot of time domain record in showing resonant echo peak at 12.59 inches.

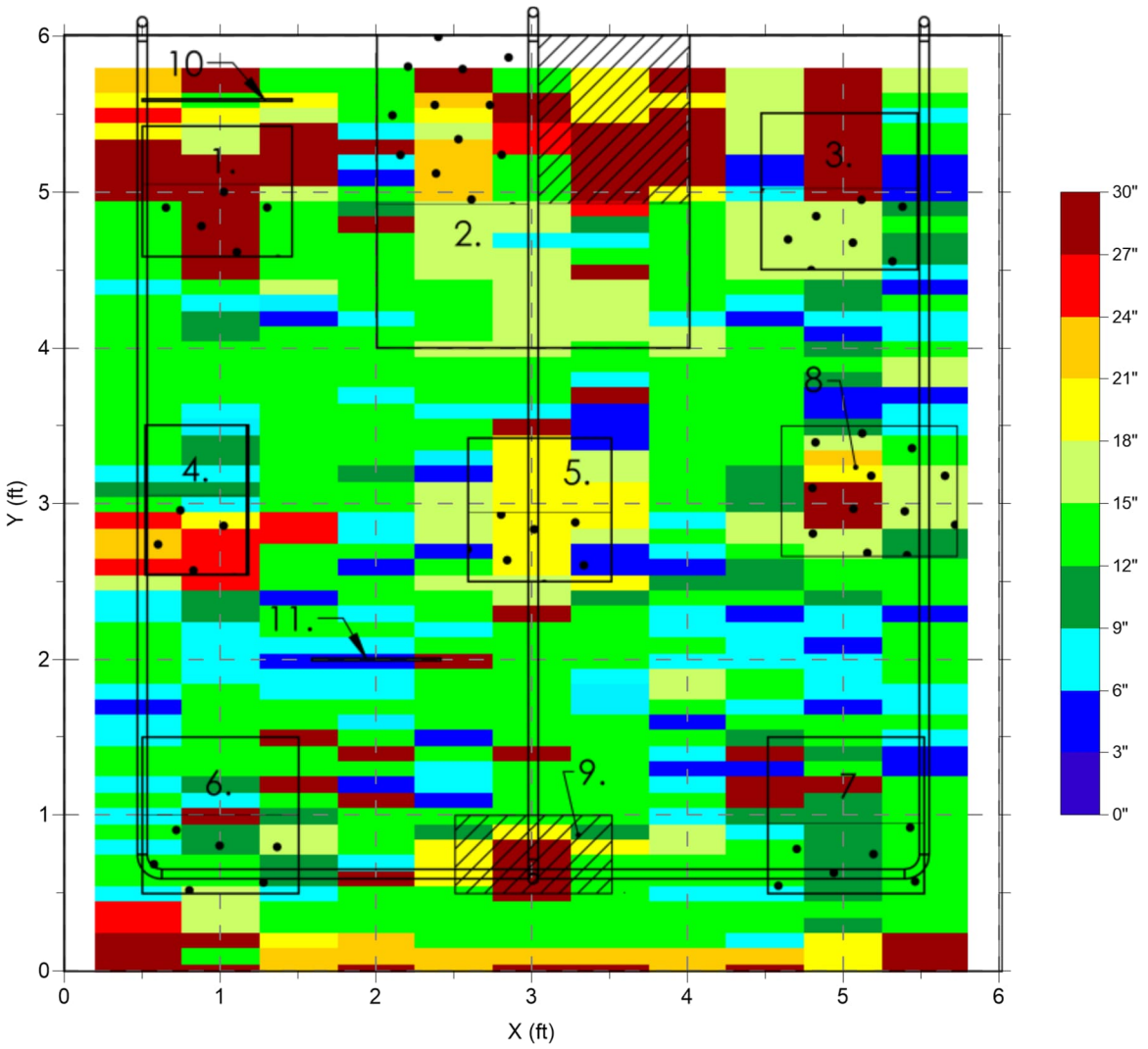

Figure 6: IES test results on Wall #1 with constructed defects overlain.

The IES testing results are displayed with color coding representing apparent thickness as observed by the dominant frequency peak in the IE spectrum (see Figure 5). Figure 6 indicates that many of the constructed features can be detected with the Impact Echo method. Steel plate delaminations (constructed flaws 8 and 9) and thin shallow cracks (constructed flaws 1 and 4) are well imaged with IES. Ringing vibrations caused by these flaws shift the resonant frequency peak to lower values, therefore increasing the calculated apparent thickness. In addition, the IES testing was able to detect the honeycombing flaw (constructed flaw 5) as well as the air void flaw (constructed flaw 3). The honeycombing flaw results in a slower bulk concrete velocity, which manifests as somewhat larger apparent thicknesses in the IES results. The air void flaw produces low frequency vibrations during testing, also causing an increase in the apparent thickness. Also, delaminations and cracking in the area of watered-down weak concrete (constructed flaw 2) were imaged with the IES testing. The deeper “corrosion delaminations” (constructed flaws 6 and 7) also show up well in the data, in this case as thinner than expected back side reflections. This is not shown as clearly in the IES results image map due to the very wide range in apparent thicknesses seen which stretched out the color scale.

Constructed flaw 3 (air/water void) was filled with water and additional IES testing was performed in 4 scan lines crossing the flaw. Results of these test are shown in Figure 7 with the wall construction defects drawn on top of the IES results for the water-filled void.

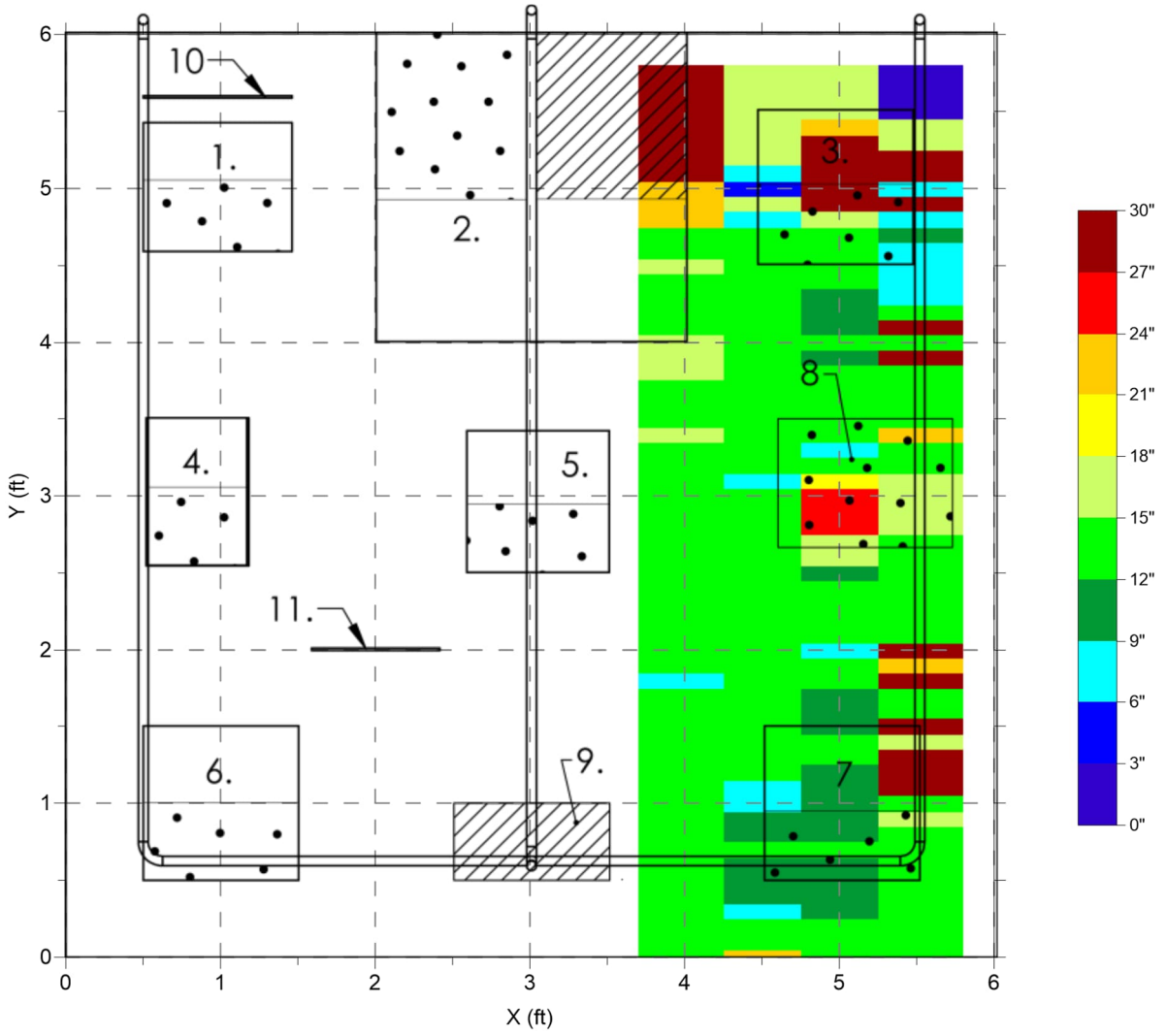

Figure 7: IES test results on Wall #1, Flaw #3 filled with water, with constructed defects overlain.

Compared to the IES testing results with constructed flaw 3 filled with air, the results after filling flaw 3 with water are very similar. A distinct anomaly is still observable in the location of flaw 3, with no significant change in apparent thickness or extent. This suggests that a void behind a steel plate is detectible with IE / IES, but it is not possible to determine if the void is air or water filled. It should be noted that this flaw also had a partial debond zone under part of it. The IE results in this zone would be dominated by the debond and thus would not be sensitive to deeper flaws such as the water filled void.

3.2. Slab Impulse Response (SIR) Method and Results

The Slab Impulse Response (SIR) method (ASTM C1740) detects and defines the extent of good versus void/poor support conditions of a concrete slab and, in the application for this project, delamination of steel plating bonded to concrete. The method was developed from a force-response vibration test for investigating the integrity of deep foundations and was originally adapted for a slab by a European group.

A photo of the SIR testing presented in Figure 8 below. Testing equipment for the SIR method equipment includes an impulse hammer, velocity transducer, and an Olson Instruments Freedom Data PC SIR-1 system as shown in Figure 9. The method involves hitting the test surface to generate vibration energy. The 3-lb impulse hammer has a built-in load cell with a plastic head to measure the force of the impact. The vibration response

of the concrete slab to the impact is measured with the velocity transducer held in contact with the slab close to the point of impact.

Figure 8: SIR Testing with 3-lb impulse hammer and Wilcoxon velocity transducer on Wall #1.

The Olson Instruments Freedom Data PC SIR-1 system performs the Fast Fourier Transform (FFT) operation on the time domain data to produce the mobility (velocity/force) plots in the frequency domain. Delamination (debonding) of steel plating from concrete is evaluated based on several measured parameters. First, the presence of a high-amplitude, low frequency peak in the mobility plot corresponds to a high flexibility (displacement/force) and low stiffness (force/displacement). High flexibility/low stiffness almost always indicates the presence of delamination/poor bonding of steel plating with the concrete slab. Second, the mean mobility ($in \cdot sec^{-1} \cdot lbf^{-1}$) provides a general indication of the steel plate bonding conditions. The higher the mobility, the more flexible the steel plating with respect to the concrete slab generally is. Also, the shape of the mobility plot is another indicator of delamination. The response curve is more irregular and has a greater mobility for debonded versus well bonded conditions due to the decreased damping of the steel plate vibration response for a delamination.

Other factors typically considered in the SIR method include the geometry and thickness of the slab and associated steel plating, the boundary conditions in the vicinity of a test location (including cracks and joints), and any reinforcement. Findings and conclusions on delamination conditions can usually be drawn based on SIR results, comparison of data from similar conditions, and/or by correlation with destructive (e.g., core) results. The shape of a mobility curve from a point with good steel bonding is generally

smooth with no large, low frequency peaks. A diagram of the SIR method for steel-concrete delamination (debonding) testing is presented below in Figure 9.

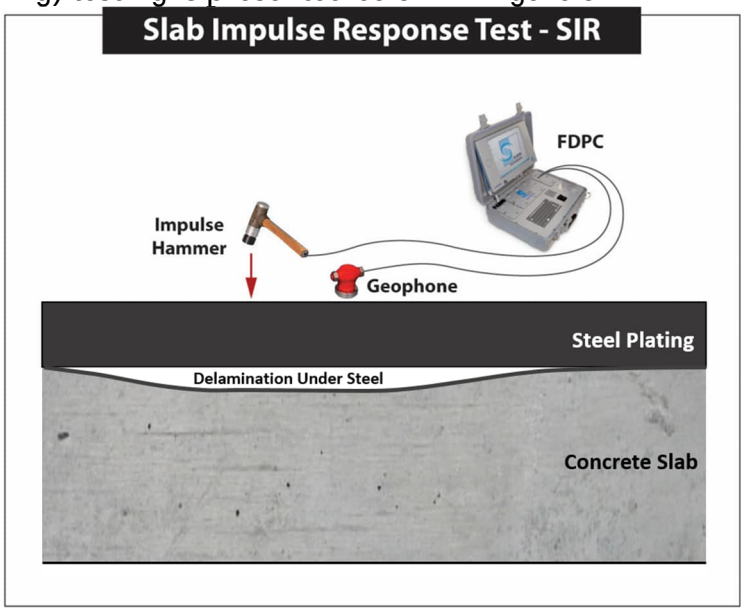

Figure 9: Slab Impulse Response (SIR) test method diagram.

The Slab Impulse Response (SIR) testing was performed on a 0.5 x 0.5 ft (0.15 x 0.15 m) grid over the steel plated side of Wall #1. The SIR method was expected to be particularly useful in mapping out steel plate delamination (debond) areas. An example test record for the SIR data is presented in Figure 10 below.

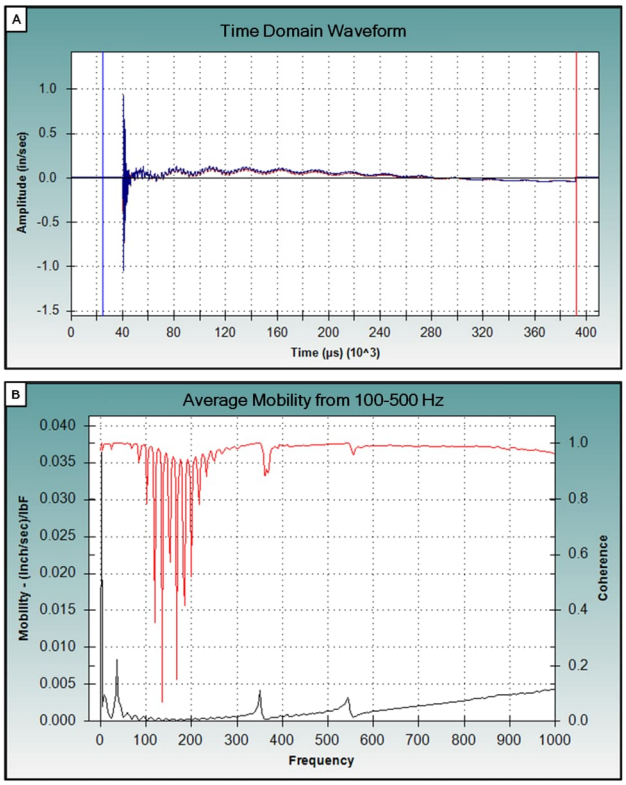

Figure 10: Example SIR record in area of debonding/delamination at test location x=5 ft, y=3ft. Plot A - Time domain record, showing two repeated tests (red and blue signals). Plot B - Mobility vs. frequency plot showing a low-frequency/high-mobility peak, indicative of steel plate debonding/ delamination. Red curve is coherence between the two tests in (a) with 1.0 being excellent coherence at a given frequency.

A map of the SIR results on the steel plated side of Wall #1, as well as the SIR results overlain by the planned flaws construction drawing are presented in Figures 11 and 12, respectively, below. The color scale for the SIR results presented in Figure 11 and Figure 12 displays average mobility over the steel plated side of Wall #1 (in/sec/lbf), with warmer colors representing higher mobility. The Slab Impulse Response method is sensitive to debonding/delamination of the steel plating from the concrete wall, and several high mobility areas in the results correlate with constructed loss-of-contact flaws. Constructed flaws 8 and 9, both explicitly designed with minor and moderate loss of contact respectively, are well identified in the SIR results. In addition, the minor to moderate loss of contact over the vertical cracks and voids (constructed flaws 1, 3, and 4) are distinguishable. It is important to note that mobilities are generally higher near the edges of the wall. This is due to the free boundary condition of the wall edge being in closer proximity to the test location, resulting in more flexure during testing.

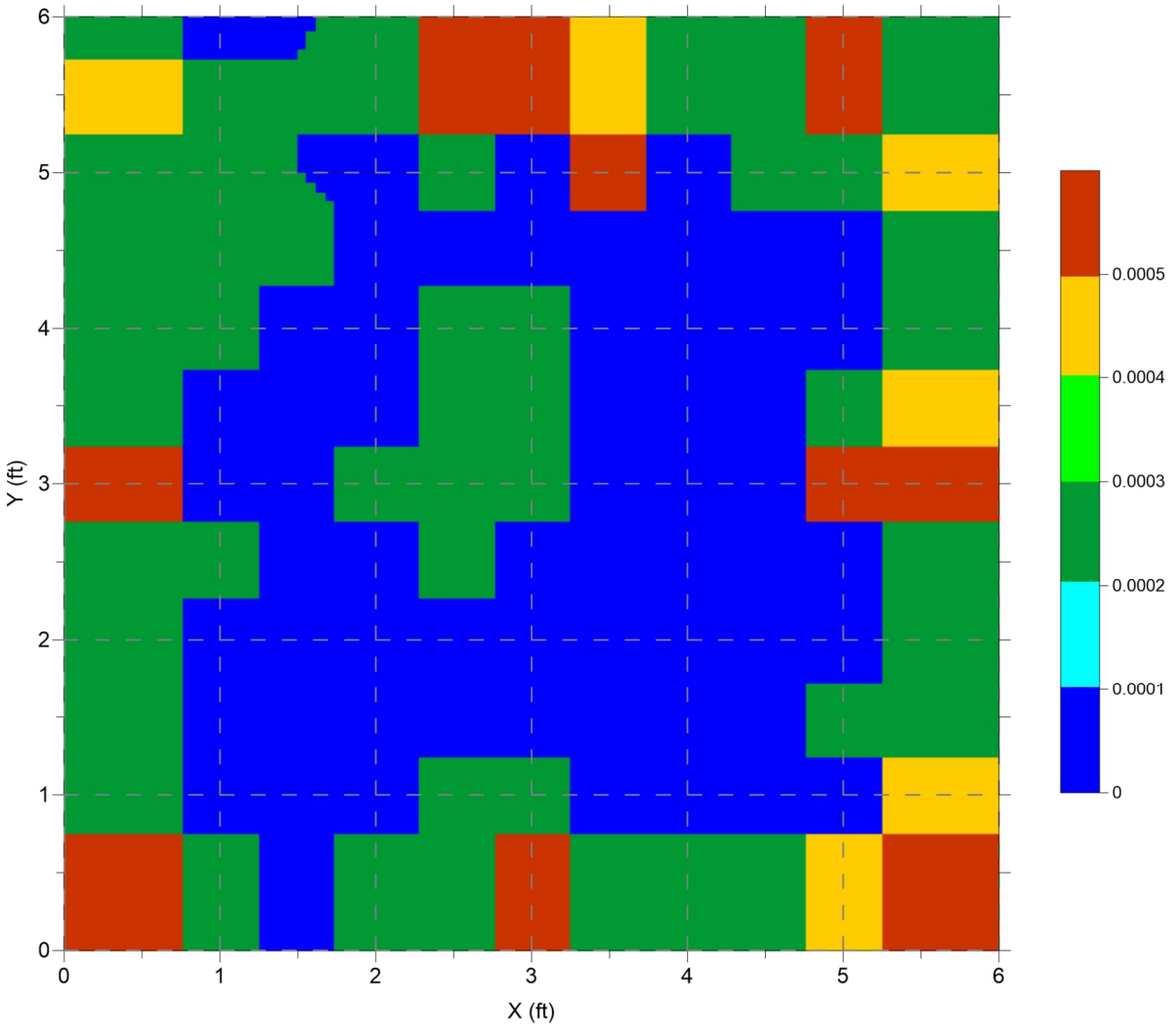

Figure 11: SIR testing results over steel plated side of Wall #1. Higher average mobility values (see color scale legend on the right in units of in/sec/lbf) are indicative of debonding/delamination of the steel plate from the concrete.

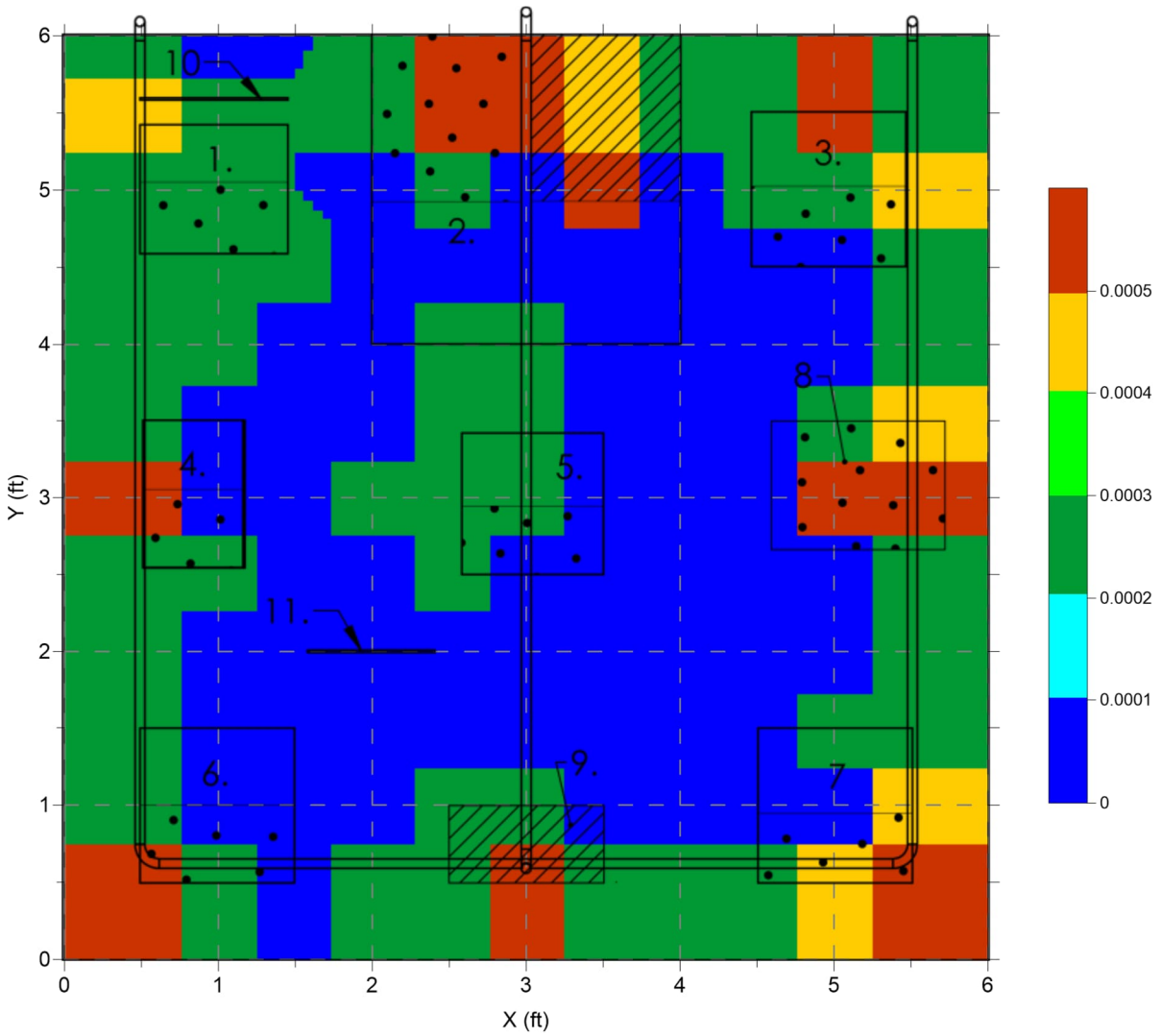

Figure 12: SIR testing results over steel plated side of Wall #1 with constructed defects overlain. Higher average mobility values (see color scale legend on the right in units of in/sec/lbf) are indicative of debonding/delamination of the steel plate from the concrete.

The simulated corrosion delaminations are not identifiable in the SIR test results, as they are located deeper in the specimen and would not be expected to affect the surface mobility values as measured from the steel plate side. Similarly, the honeycomb flaw (constructed flaw 5) was also not identifiable in the SIR results, again due to its depth as well as small relative size. The zone of watered-down concrete (constructed flaw 2) was not identifiable in the SIR results either. However, areas of minor to moderate delamination over constructed flaw 2 are identifiable in the SIR results. In addition, the low strength and visible cracking of the watered-down concrete may have contributed to the higher edge mobility in the vicinity of constructed flaw 2 as well (Figure 12).

3.3. Spectral Analyses of Surface Waves (SASW) Method and Results

The SASW method is based upon measuring surface waves propagating in layered elastic media. A photo of the SASW testing on the wall is illustrated in Figure 13, and is shown in a photo in Figure 14. The ratio of surface wave velocity to shear wave velocity varies with Poisson's ratio. However, reasonable estimates of Poisson's ratio and mass density for concrete and other materials can be made. Therefore, knowledge of the surface wave velocity combined with reasonable estimates of mass density and Poisson's ratio allows calculation of shear moduli for low-strain amplitudes.

Surface wave (also termed Rayleigh; R-wave) velocity will vary with frequency in a layered system with differing material velocities. This variation in velocity with frequency is termed dispersion. A plot of surface wave velocity versus wavelength is called a dispersion curve. In a semi-

homogeneous material such as concrete the wavelength of the surface wave is approximately equal to the penetration depth, therefore the dispersion curve can be evaluated as a plot of material velocity versus depth from the test surface. However, during data interpretation it is important to understand that longer wavelength velocities are affected by all material between the associated wavelength (depth) and the test surface.

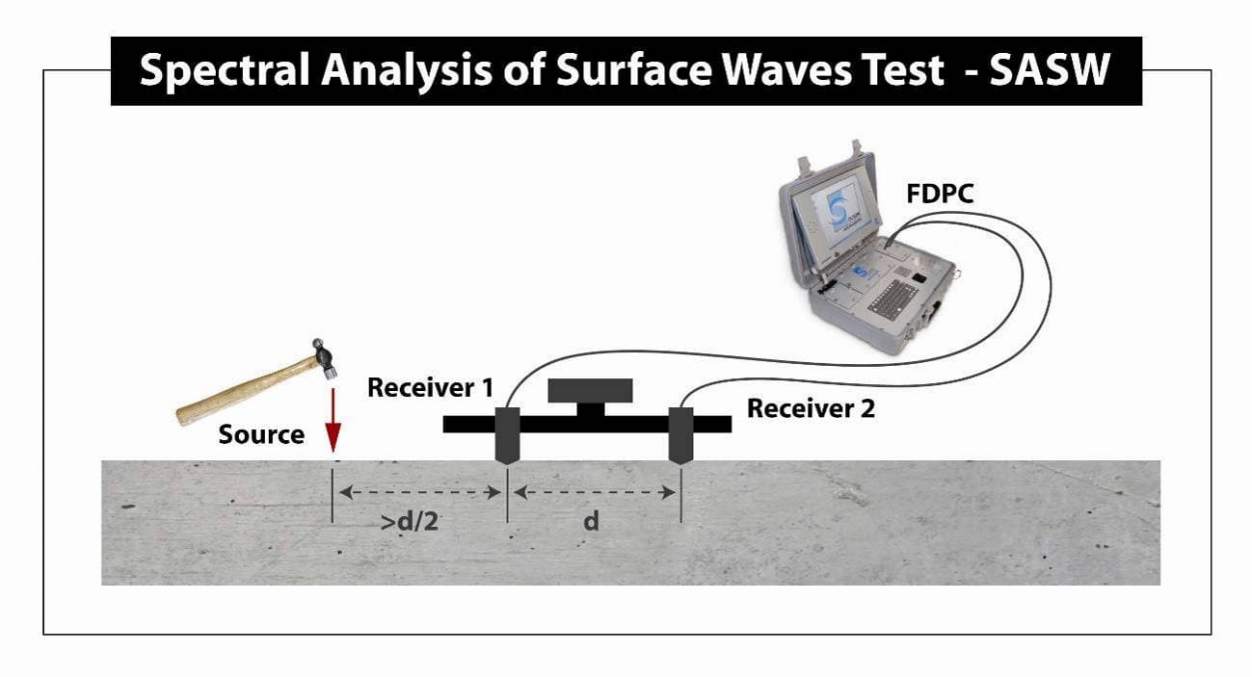

Figure 13: Spectral Analysis of Surface Waves (SASW) Test Diagram.

Figure 14: Spectral Analysis of Surface Waves (SASW) Testing on Wall #1 (Horizontal Test Direction) with SASW-S bar with 2 displacement transducers and IE-1 solenoid impact source at left end of bar.

The distance between receivers affects the penetration depth of the test, typically wavelengths of 1.5 – 2.0 times the receiver spacing can be evaluated depending upon the noise level in the data. A metal impactor is typically used as an impact source to induce the measured surface waves. The impactor strike must be in-line with the two transducers in order to ensure that the wave travel distance between receivers is accurate. The impactor size is chosen based upon the frequencies of interest (desired penetration depth) and is therefore also correlated with the receiver spacing. For greater penetration wider receiver spacings and larger impact hammers are used.

Wavelength (λ), frequency (f), and wave velocity (V_r), are related as follows:

$$V_r = f*\lambda \quad (3)$$

The SASW testing and analyses included collection of field data in situ and the construction of experimental dispersion curves at each test point from the field data. The dispersion curve plots were used during data analysis to evaluate the bonding condition between the topping and structural slabs and the condition of both slabs. The phase information of the transfer function (cross power spectrum) between the two receivers for each frequency was the key spectral measurement.

The experimental dispersion curve is developed from the phase data for a given test point by knowing the phase (φ) at a given frequency (f) and then calculating the travel time (t) between receivers of that frequency/wavelength by:

$$t = \varphi / 360*f \quad (4)$$

Surface wave velocity (V_r) is obtained by dividing the receiver spacing (X) by the travel time at a frequency:

$$V_r = X / t \quad (5)$$

The wavelength (λ) is related to the velocity and frequency as shown in equation 3 above.

By repeating the above procedure for any given frequency, the surface wave velocity corresponding to a given wavelength is evaluated, and the dispersion curve is determined. The phase data was viewed on the PC data acquisition system in the field to ensure that acceptable data was being collected. The phase data were then returned to our office for further processing. The phase of the cross-power spectrum (transfer function) between the two receivers are used to create the dispersion curves by masking unwanted (noisy or nonlinear) portions of the phase record from the data set for each test location and then performing the above calculations to determine the surface wave velocity for all relevant frequencies.

The dispersion curve plots are the basis of the data analysis and are used to determine the concrete's overall condition, the average surface wave velocity of the concrete and any areas or zones throughout the depth of the concrete structure that indicate varying conditions. The SASW test can be used to locate delamination or debonded concrete layers as well as deteriorated layers that reduce the velocity/modulus of the concrete. The SASW tests evaluates the average velocity or condition between the two receivers, therefore the further apart the receivers (greater penetration depth) the larger the area evaluated. As in many kinds of testing, an increase in penetration depth also yields a loss in resolution (average over greater distance).

The SASW test method uses an analysis of surface wave propagation velocity versus wavelength to look at the condition profile of a test member versus depth. The result of a single SASW test is a "dispersion curve", which is a plot of velocity versus wavelength. For concrete, wavelength is very close to depth, and thus the dispersion curve is essentially a velocity versus depth profile. Two example records from steel plate over concrete are as follows: one from a "sound" location and the other from a location with a drop in surface wave velocity followed by an increase (a "dip" in velocity) are presented in Figures 15 and 16. The plot seen in Figure 15 is typical of that seen at a sound location, where the steel is well-bonded to the concrete and there are no anomalies present in the concrete that can be sensed by this method. As seen in the far right plot (the dispersion curve), the velocity is essentially constant for the entire depth range of the tested wall. The average

velocity of about 2,500 m/s is typical of the surface wave velocity of sound concrete. In Figure 16, there is a drop in the velocity at relatively shallow depths of from 60 to 120 mm and the velocity increases at greater depths (wavelength is approximately depth in the dispersion curve plot). This corresponds to a defect in the concrete but not one that is right at the back side of the steel.

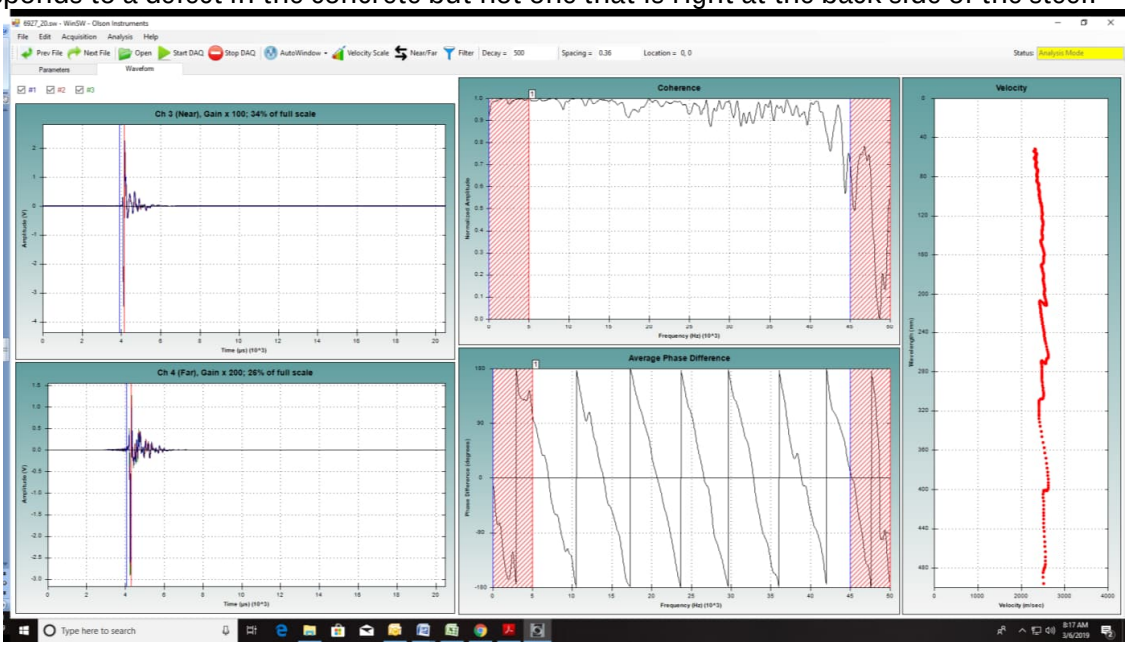

Figure 15: SASW Sample Record. Sound Conditions with bonded steel over concrete.

- The top left and bottom left signals are the time domain responses of the SASW bar near and far displacement transducer receivers to the in-line solenoid impacts (typically 5 impacts are recorded and averaged).
- The top center plot is coherence of the receiver responses and a coherence near 1 indicates good quality data.
- The bottom center plot is the wrapped phase plot and at 360 degrees of phase (from 0 to -180 and +180 to 0 degrees) that is one wavelength between the receivers spaced 0.375 m apart at ~7500 Hz so that is about a surface wave velocity of 2500 m/s which can be seen in the dispersion curve plot of surface wave velocity vs. wavelength in the right plot above.

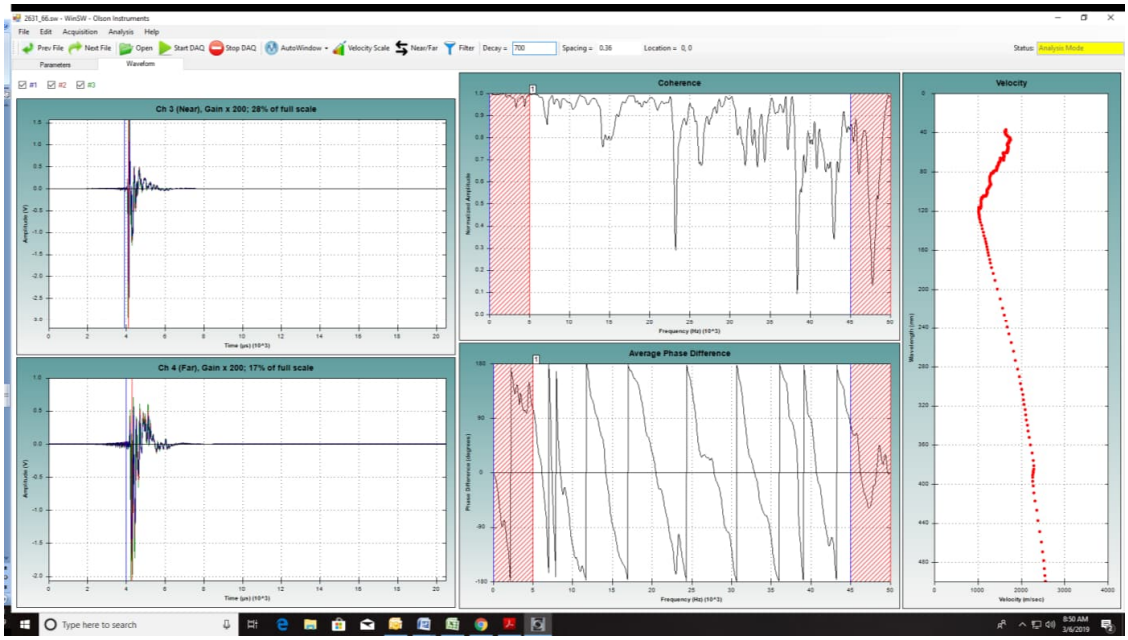

Figure 16: SASW Sample Record. Velocity Drop at depth of 60 mm to 120 mm indicating a concrete defect that is deeper in the concrete and not right behind the steel plate.

The SASW testing was performed in the horizontal direction from the steel plate side on the same 0.5 x 0.5 foot grid as the SIR testing. Figure 17 shows the average surface wave velocity at each grid point over the steel side of Wall 1, and Figure 18 shows these same results overlain by the planned flaws from the construction drawing. The results of the SASW testing are displayed in Figure 17 and Figure 18 with color coding representing surface wave velocity in ft/s. Sound concrete typically has surface wave velocities between 5,500 and 7,500 ft/s depending on specific concrete strength. All of the constructed anomalies were designed to either reduce the strength/integrity of the concrete or to create discontinuities in the concrete. The SASW test method is sensitive to both low strength zones as well as discontinuities. It is expected to be especially sensitive to discontinuities (cracks and voids) that are oriented in the direction perpendicular to the test surface. Based on this, it was expected that most of the constructed defects would present themselves as reductions in surface wave velocity at some depth, with an overall drop in average velocity at the given test point. With these considerations, the SASW test results correlate well with the locations of the constructed defects (as shown in Figure 18). The SASW method appears to be most sensitive to loss-of-contact flaws. This is evidenced by a larger drop in surface wave velocity over areas of minor to moderate loss of contact compared to areas of good contact atop the zone of weak concrete (flaw 2). This observation is intuitive because, as surface waves need an elastic medium to propagate, waves that attempt to propagate across the steel-concrete interface are attenuated when bonding between the steel and concrete is poor. Surface waves that encounter air voids are similarly attenuated, as seen at the location of flaw 3 in Figure 18, allowing for the detection of these type of defects with the SASW method.

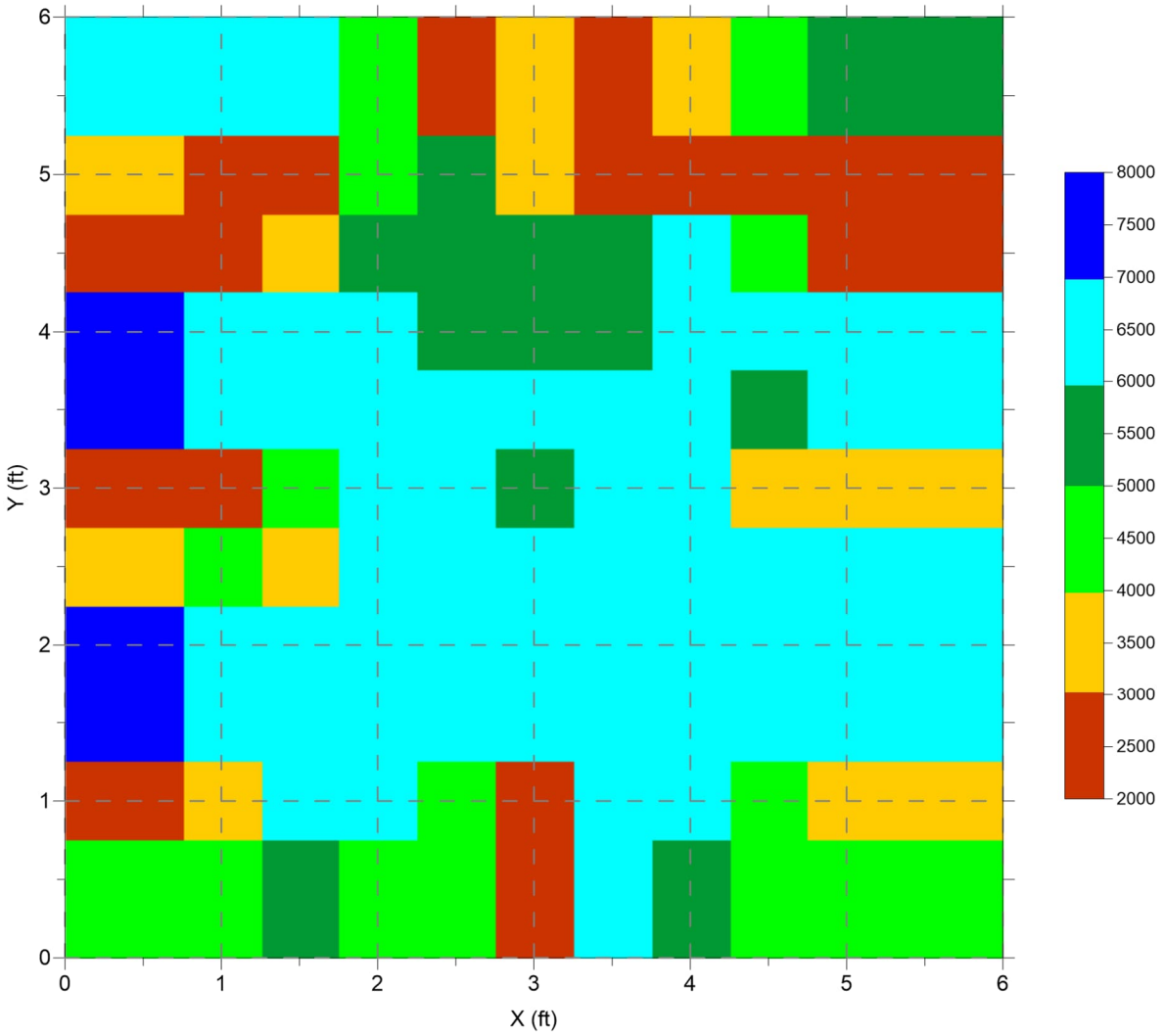

Figure 17: SASW testing results over steel plated side of Wall #1. Color scale surface wave velocity legend is in ft/sec. Higher velocity values indicate better concrete conditions.

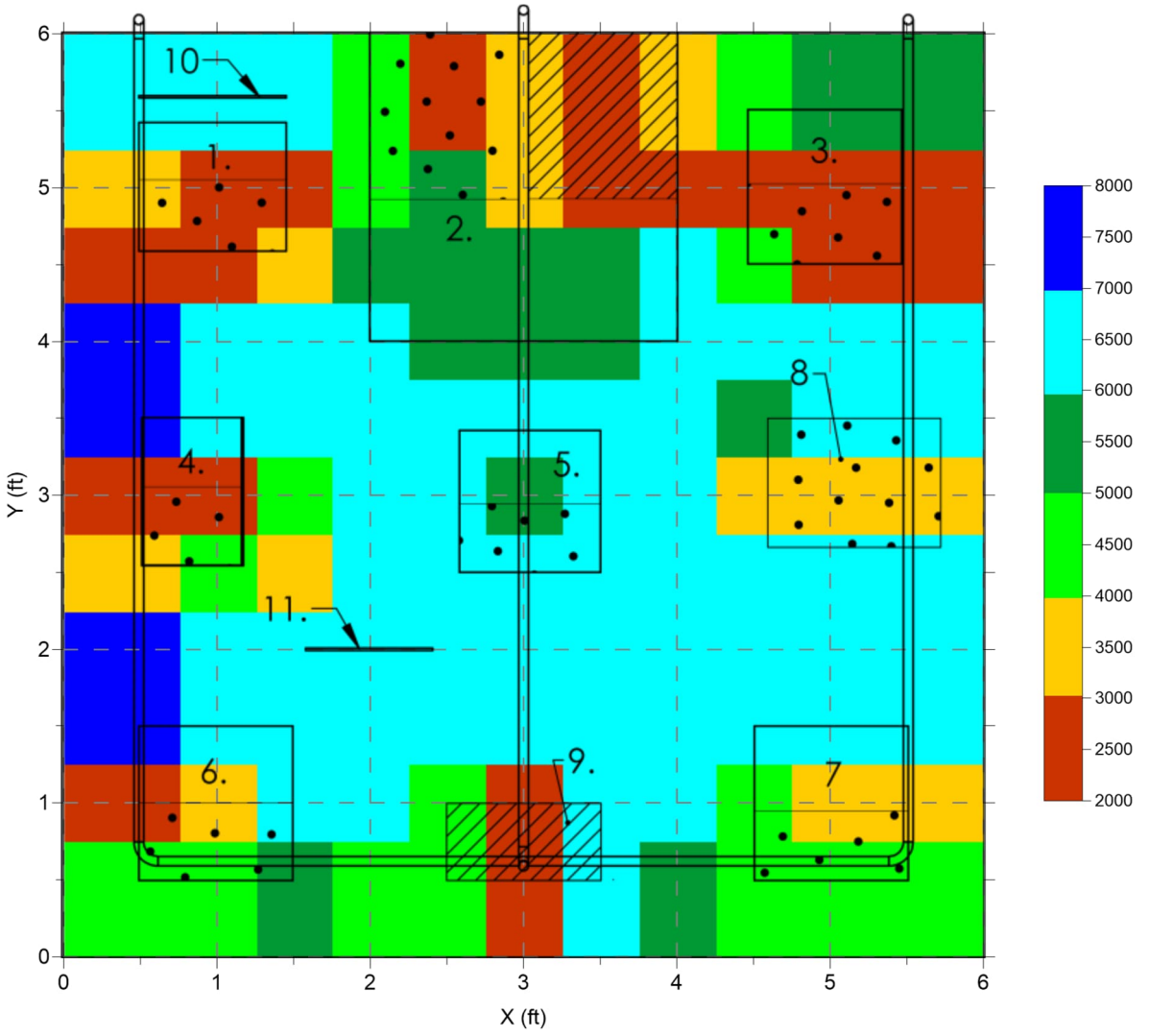

Figure 18: SASW testing results over steel plated side of Wall #1 with constructed defects overlain. Color scale surface wave velocity legend is in ft/sec. Higher velocity values indicate better concrete conditions.

It should be noted that the presented results did NOT show an effect of the two cracks which are perpendicular to the steel plate. This is due to the fact that all of the tests in the presented image results were done parallel to these cracks rather than across the cracks. Later tests done in the vertical orientation (top-bottom wave travel in the wall) did indeed show these flaws but the larger spacing between tests resulted in the actual test locations being near the ends of the flaws once overlaid.

4. CONCLUSIONS

The Impact Echo Scanning (IES), Spectral Analyses of Surface Waves (SASW), and Slab Impulse Response (SIR) test methods appear to correlate well with the embedded defects in Wall #1. The larger and more severe the defect, the easier it is to detect. All three methods are sensitive to debonding of the steel plate from the concrete, with IES likely being the method that is most sensitive, followed by the SIR method. Wall #1 appears to have debonded where planned delaminations were expected based upon all the NDE results. The ability to detect a flaw within the concrete decreases substantially if debonding of the steel plate is present. Some flaw types are difficult to distinguish from plate debonding. In summary, the following conclusions can be made:

- SIR and IE methods can be effectively applied to the steel plate side of steel lined concrete structures to evaluate the contact between the concrete and the steel plate.
- SASW and IE methods applied to the steel side of steel lined concrete structures are useful in detecting cracks, voids, and other defects deeper in the concrete if at least partial contact exists between the concrete and the steel plate.
- It is recommended to perform SASW in two directions if possible.
- Scanning techniques allow for much faster data collection than point by point measurements.
- Experienced operator is required for interpretation of test results.

ACKNOWLEDGEMENTS

The authors gratefully acknowledge the full research funding and support provided by the CANDU Owner's Group.

REFERENCES

ACI PRC-228.2-13, "Report on Nondestructive Test Methods for Evaluation of Concrete in Structures" American Concrete Institute Manual of Concrete Practice, 2013.

Haack, A., et.al. State-of-the art of Non-destructive testing Methods for Determining the State of a Tunnel Lining. Report to ITA (International Tunnelling Association in Switzerland) 1995.

Wu, Y., Cascante, G. et. al., (2011), "Ultrasonic Testing of a Grouted Steel Tank for Void Detection and Thickness Evaluation (MASW for Void and Thickness Evaluation)". MASc Thesis. University of Waterloo, Canada, 2011.

Wiggenhauser, H., et.al., (2013), "Non-Destructive Evaluation of Steel – Concrete Mock-Ups," 10th International Conference on NDE in Relation to Structural Integrity for Nuclear and Pressurized Components, October 2013. Cannes, France.

Clayton, D., Smith, C., (2013), ORNL/TM-2013/223, "Summary of Large Concrete Samples". Oak Ridge National Laboratory, USA, June 2013.

Yanagihara, A. et. al. (2015), "Application of Ultrasonic Testing to Steel-Concrete Composite Structures", International Symposium Non-Destructive Testing in Civil Engineering (NDT-CE). Berlin, Germany September, 2015.

CSNI/R(2014)1 (2015), "Non-destructive Evaluation of Thick-Walled Concrete Structures," OECD/NEA WIAGE Workshop. Prague, Czech Republic. September 2015.

Fülöp, L., (2016), "Detection Capacity of NDE Methods in Steel-Concrete –Steel Composite Elements". 12th International Conference on NDE in Relation to Structural Integrity for Nuclear and Pressurized Components October 2016. Croatia.

Tcherner, Julia and Larry Olson, Dennis Sack, Patrick Miller, "Non-Destructive Evaluation Techniques for Evaluation of Nuclear Concrete Structures with Limited Accessibility", *Transactions, SMiRT-25, 25th Conference on Structural Mechanics in Reactor Technology*, Charlotte, NC, USA, Division VIII August 4-9, 2019.

ASTM C1383-15(2022), "Standard Test Method for Measuring the P-Wave Speed and the Thickness of Concrete Plates Using the Impact-Echo Method", ASTM International, West Conshohocken, Pennsylvania, USA.

ASTM C1740-16 , "Standard Practice for Evaluating the Condition of Concrete Plates Using the Impulse-Response Method", ASTM International, West Conshohocken, Pennsylvania, USA.

Non-destructive testing of reactor containment mock-up

Zbynek Hlavac[1,*] Petr Brabec[2], Jakub Stainbruch[3], David Svoboda[4], Andrzej Garbacz[5], Ondrej Anton[6], Josef Cervenka[7] and Marek Postler[2]

[1]Centrum vyzkumu Rez s.r.o., Husinec - Rez, Czechia
[2]UJV Rez a.s., Husinec - Rez, Czechia
[3]Inset s.r.o., Liberec, Czechia
[4]Sika CZ s.r.o., Brno, Czechia
[5]PolitechnikaWarszawska, Warszawa, Poland
[6]Brno University of Technology, Brno, Czechia
[7]TZUS Praha, s.p., Praha, Czechia

ABSTRACT

Five massive concrete blocks (No. 1 to 5) in the Nuclear Research Institute UJV Rez near Prague have been used for the assessment of various non-destructive testing (NDT) techniques, along with two other blocks situated in Brno University of Technology in Brno, Czechia.

Three vertical holes were drilled into concrete block No. 3 in Rez with diameters of 50, 100 and 150 mm to simulate voids or hollows that could emerge in the containment wall of the nuclear power plant at Temelin Nuclear Power Station in Czechia. An ultrasonic pulse velocity method was used as the first NDT method for the identification of the holes in block No. 3.

Ultrasonic pulse echo from a Pundit PL-200PE and a Pulse Echo Transducer identified these holes with a precision of 2 to 45 mm. The accuracy was affected by the rough surface and the possible use of inhomogeneous concrete. Ultrasonic pulse echo's ability to detect cracks or other forms of delamination was tenuous.

Brief results of ground penetrating radar, impact-echo or electro-magnetic induction are also introduced in the article.

Keywords: massive concrete, containment, non-destructive testing, ultrasonic pulse echo, ground penetrating radar, impact-echo, ultrasonic pulse velocity, electro-magnetic induction

1. INTRODUCTION

For the purposes of this study, four massive concrete blocks and one pre-stressed reinforced concrete block were fabricated and modified in the Nuclear Research Institute UJV Rez near Prague.

Concrete block No.1 was under-reinforced and contained extruded polystyrene XPS to simulate large voids or hollows. Concrete block No. 3 was drilled with 3 vertical holes of diameters 50, 100 and 150 mm wide to simulate voids or hollows that could emerge in the 1.2 meter-thick wall of Temelin Nuclear Power Station in Czechia. The results of an ultrasonic pulse method inspection of blocksNo. 1 and 3 are given in [1].

Reinforced concrete bock No. 5 contained polyethylene ducts for pre-stressing steel, steel rebars, cracks simulation or other forms of delamination. Detection of these objects using a direct ultrasonic pulse method was carried out by David Svoboda and Petr Cikrle [2].

Non-destructive testing methods, such as direct ultrasonic pulse velocity (UPV) [1, 2], ground penetrating radar (GPR) [3, 4], electro-magnetic induction and ultrasonic pulse echo, were applied to the blocks in order to prove that hollows, voids, cracks, pre-stressing steel ducts and reinforcement in containment building walls can be detected.

*Corresponding author: phone +420 723 946 561, e-mail zbynek.hlavac@cvrez.cz

Another two blocks were fabricated in Prefa Kurim and transported to Brno University of Technology (BUT) [5, 6]. Inserted artificial defects in the form of honeycombs and badly compacted concrete were identified by NDT methods including impact-echo [7-10], GPR [3, 4, 8] and direct UPV. Additionally, steel reinforcement with diameters of 12, 22 and 32 mm were detected with the GPR or impact-echo, as described in [8 or 11].

Vast of the results were reported in [12].

2. INVESTIGATED STRUCTURES

Two sets of massive concrete blocks with modifications were used to mimicthe containment wall of a nuclear reactor with various inclusions as steel rebars or pre-stressing reinforcement polyethylene ducts and structural problems such as voids, cracks and other types of delamination, honeycombing and poorly compacted concrete.

2.1. Massive concrete blocks in Rez

Figure 1 shows concrete blocks No. 1 to 5 (from right to the left) situated at the Nuclear Research Institute UJV Rez. Block No. 5 (left one) contains polyethylene ducts, Block No. 3 was core drilled producing 3 vertical holes (Figure 2).

Figure 1. Five massive concrete blocks (2 meters tall) situated in Rez, near Prague

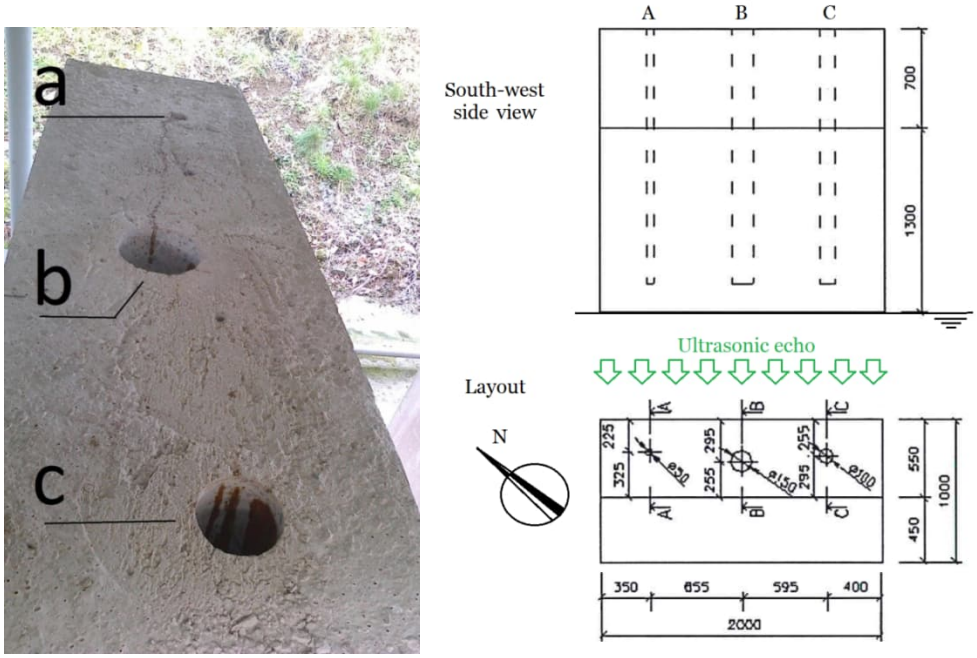

Figure 2. Top of block No. 3 with 3 vertical holes of diameter of 50 a), 150 b) and 100 mm c) (left). Adrawing of the side view and a layout of Block No. 3 (right).

The dimensions of each block were 1000×2000×2000 mm, except for block No. 5 which was 1200×2600×2000 mm. A detailed view of the moulds in block No. 5 is shown in Figure 3. This corresponds with the structure of the real containment wall (example in Figure 4).

Figure 3. Moulds in block No. 5 [2].

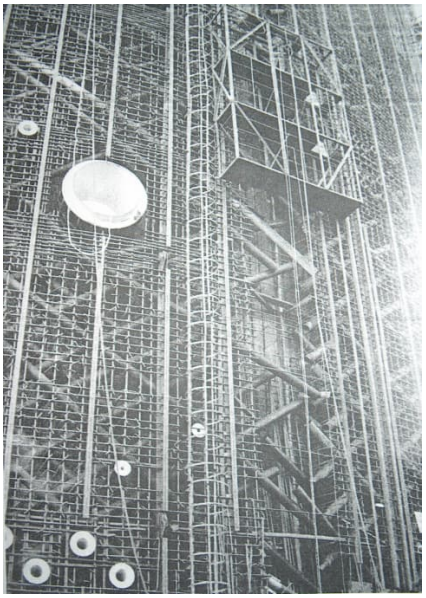

Fig. 4. Nuclear containment wall [2].

2.2. Massive concrete blocks in Brno

The two massive concrete blocks at BUT had dimensions of 1800×1800×1500 mm. One contained artificial defects and steel reinforcement, and the other acted as a reference block without any defects (Figure 5).

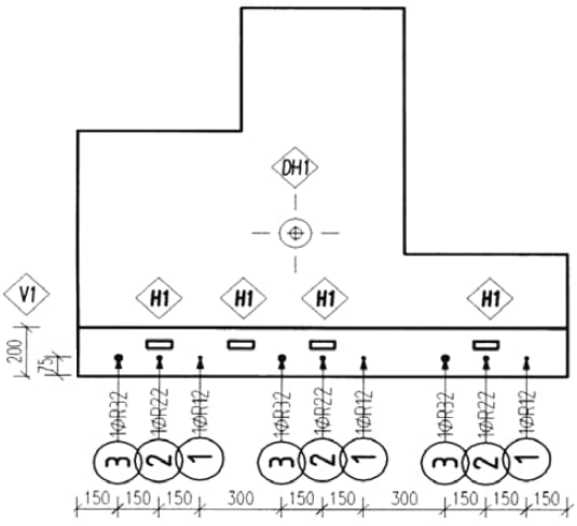

Figure 5. Photo of the massive concrete blocks at BUT [9] (left).
Drawing of the block with artificial honeycombs (H), ducts (V) and rebars [11] (right).

3. NDT METHODS

NDT techniques including UPV, ultrasonic pulse echo, GPR, an electro-magnetic induction method and impact echo were employed to analyse the massive concrete blocks mentioned in chapter 2.

3.1. Ultrasonic pulse velocity

A direct UPV method was applied from both sides of each tested block. Figure 6 shows the P-wave velocity measured in the front wall of block No. 5 at Rez, where 4 diagonally crossed polyethylene ducts (marked by red dashed lines) were inserted (see Figure 3 and 6). Figure 7 shows the results of UPV measurement in block No. 3 with drilled vertical holes (Figure 2). The UPV in the front wall of the Brno block with artificial defects (Figure 5) can be seen in Figure 8.

Apart from the delamination and the plastic duct filled by concrete, most of the objects were located with XZ coordinates.

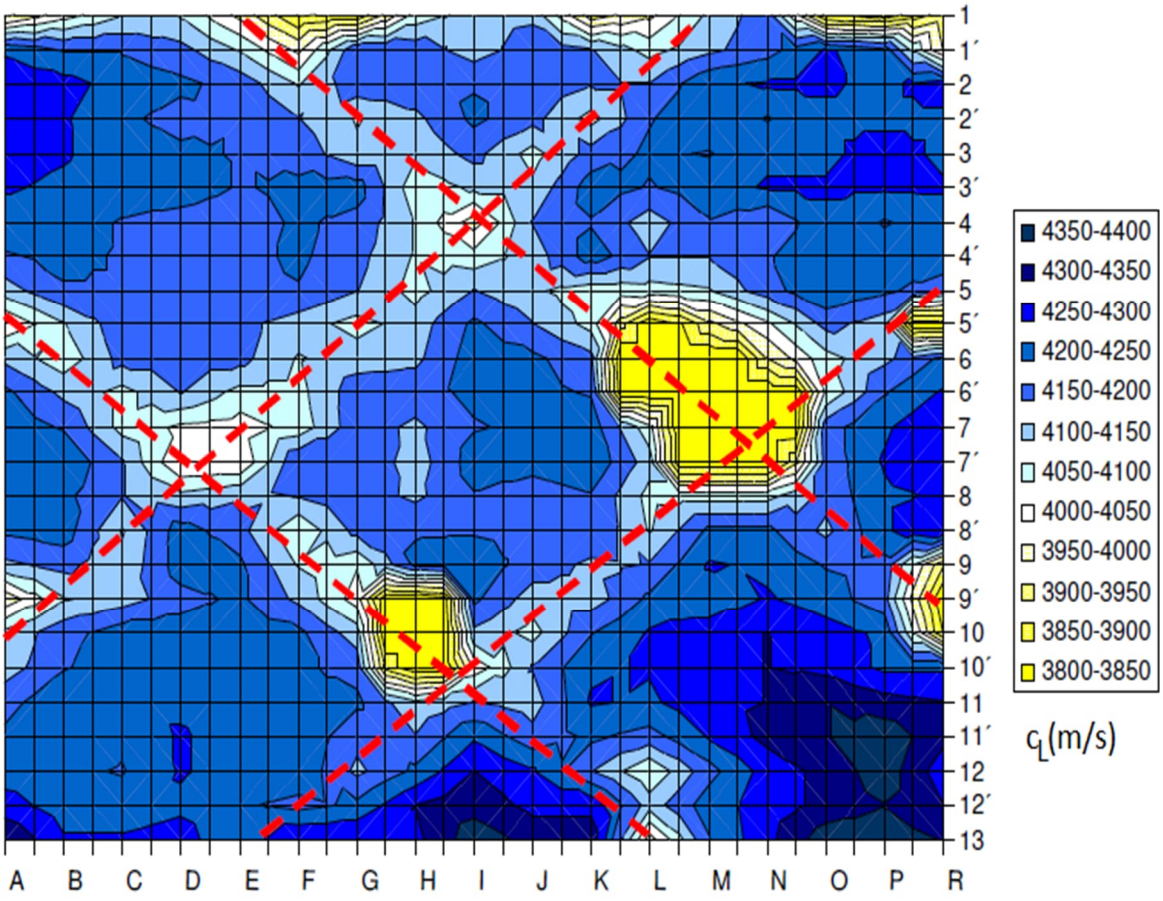

Figure 6. Front wall of concrete block No. 5 in Rez (XZ coordianates).
Results of UPV measured executed by the TICO instrument [2].
Diagonal plastic duct detected mainly at their crossing (yellow spots).
Dark blue area signalize bad compaction of the concrete due to near bottom surface.

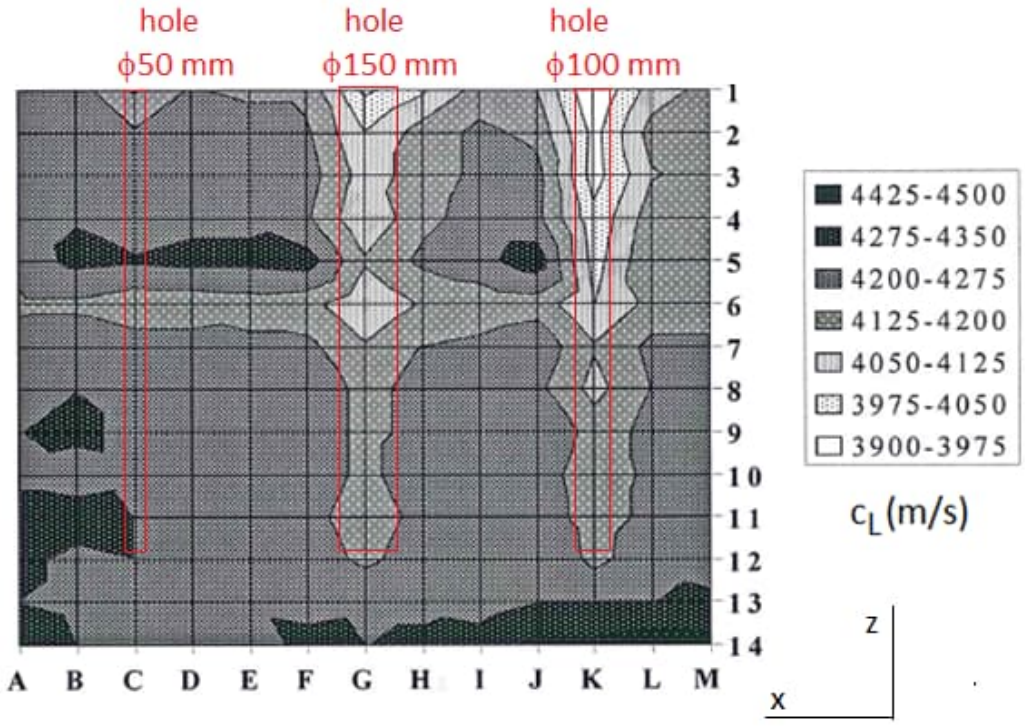

Figure 7. UPV of concrete block No. 3 in Rez [1], measured by the TICO instrument.

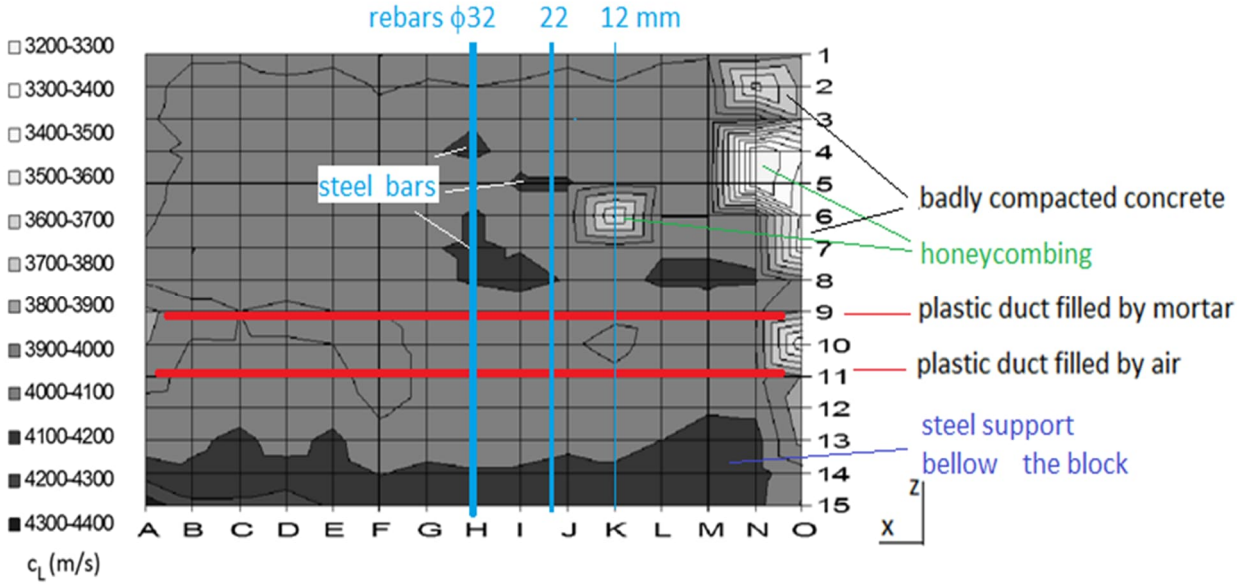

Figure 8. UPV of the Brno concrete block that contained artificial objects [10].

3.2. Ultrasonic pulse echo

The Pundit PL-200PE instrument [13] with Pulse Echo Transducer was used to determine the depth (Y) and X coordinates of the holes in block No. 3 (Figure 9). An evaluation of the results is given in Table 1. The layout of the holes is depicted in Figure 2.

This method successfully identified the location of the polyethylene (PE) duct in block No. 5 at a depth of 20 cm (Figure 10).

Table 1. The detection of vertical holes in block No. 3 by UPV.

Location	a	b	c
Diameter of hole *xy* [mm]	50	150	100
Real values			
Scan distance *x* [mm]	350	1005	1600
Depth of the hole y_h[mm]	200	220	205
Back wall depth y_b[mm]	550	550	550
Ultrasonic echo			
Scan distance *x* [mm]	350	1050	1580
Depth of the hole y_h[mm]	218	261	207
Time to the hole t_h[µs]	185	222	175
S-wave speed c_t [m/s]	2360	2360	2360
Back wall depth y_b [mm]	545	563	548

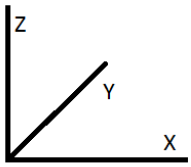

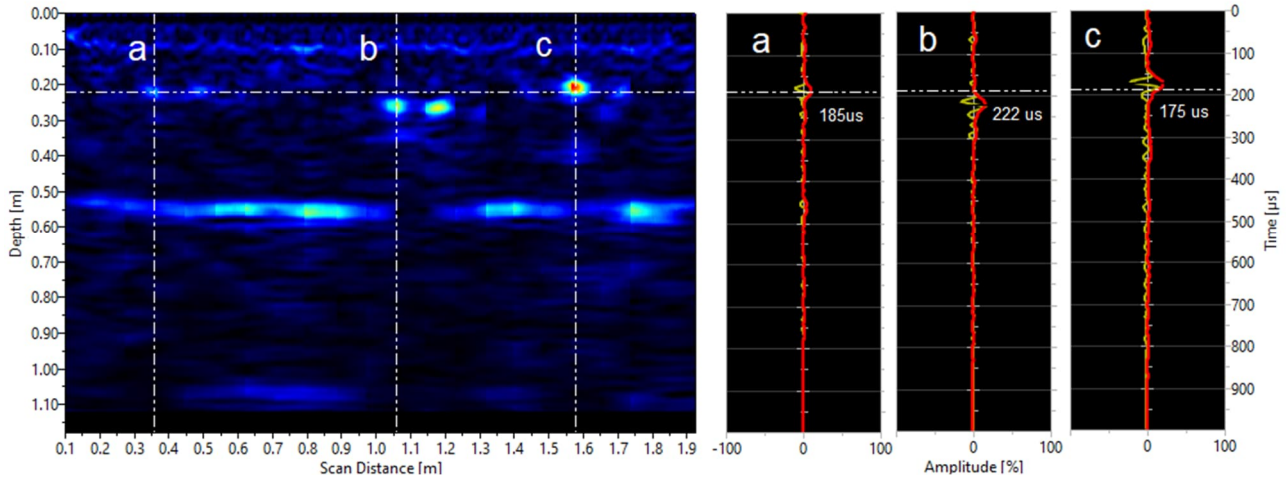

Figure 9. Ultrasonic pulse echo of 3 vertical holes (XY coordinates in block No. 3).

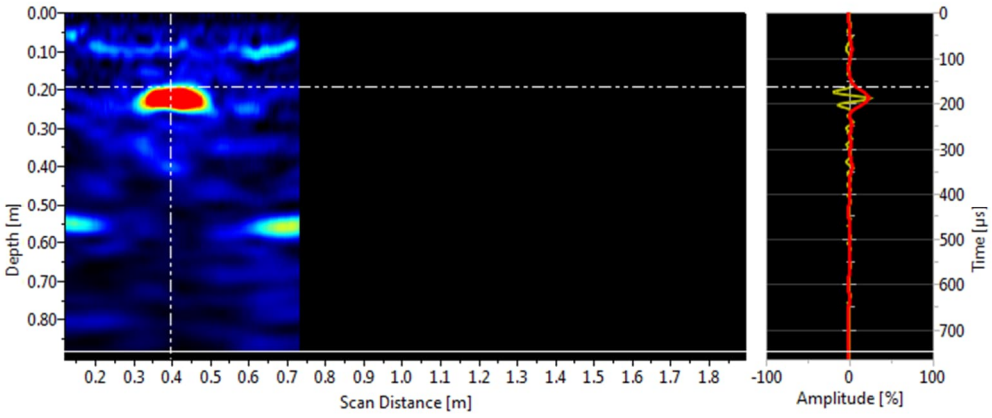

Figure 10. Ultrasonic pulse echo of diagonal PE duct (XY coordinates in block No. 5).

3.3. Ground penetrating radar

GPR measurements were carried out as part of a complex research project [12] focused on the application of different NDT techniques to scan large concrete structures. The GPR equipment used for test measurements was the commercial system RAMAC developed by MalaGeoScience, which was coupled with shielded monostatic antennas with frequencies of 500 MHz, 800 MHz and 1600 MHz (Figures 11 and 12). GPR measurements were taken from the front side of the block with artificial defects (Brno) in a grid of perpendicular lines with 10 cm separation (5 cm for measurements with 1600 MHz antenna) and from the rear side of the block in a system of parallel lines oriented vertically with 10 cm separation. Data were gathered along the lines with a step of 1 cm.

Experimental measurements proved that the GPR method can be successfully deployed for the detection of different types of structural elements and non-homogeneities. The honeycombing areas and plastic ducts were easily visible with the 800 MHz GPR antenna (Figure 11), and the higher frequency 1600 MHz antenna detected the location of the steel bars (Figure 12). For the plastic ducts, the detected locations were shifted a little (Figure 11).

GPR gave very good results in detecting anomalies when they were placed relatively close to the surface (ca 20 centimetres). For greater thicknesses of concrete a lower-frequency antenna, with a significant decrease in resolution, must be applied. [8]

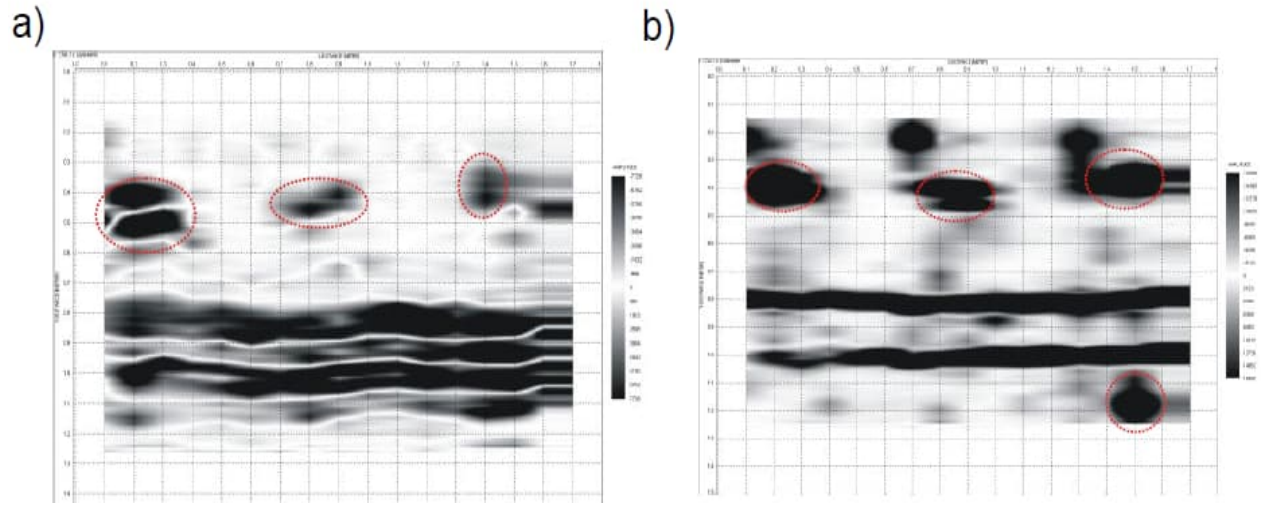

Figure 11. Front wall ofthe Brno block containing artificial defects detected by GPR and antennas with a frequency of 500 MHz a) and 800 MHz b) with the reflections of 2 horizontal plastic ducts and 4 honeycombs (red circles) [8].

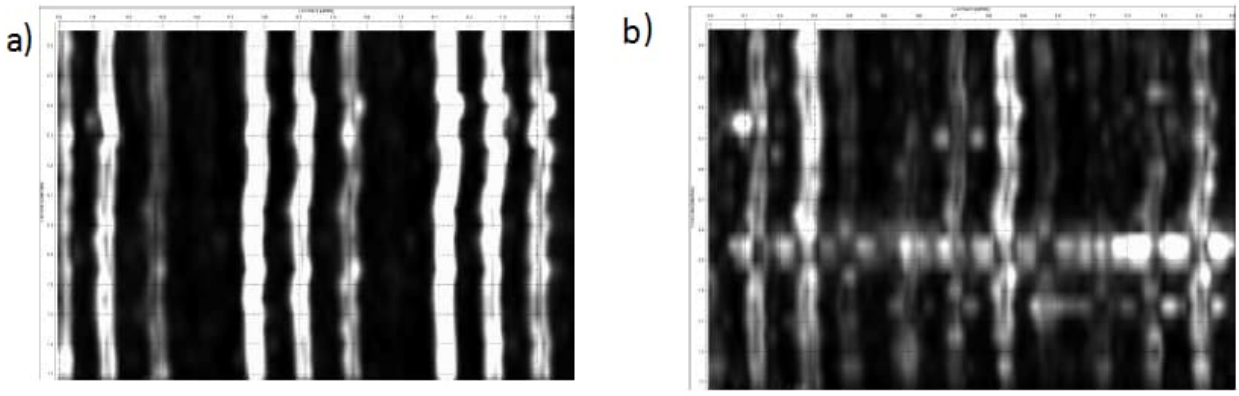

Figure 12. Front wall of the Brno block (containing artificial defects): 3D processing of GPR measurements at 1600 MHz in time t =1.6 ns at a depth of 8–10 cm a), in time t =2.0 ns at a depth of 10–12 cm b); the reinforcing steel bars can be seen as white stripes [8].

3.4. Electro-magnetic induction

The old and reliable NDT technique enabled the identification of the steel rebars and ducts in all three XYZ coordinates. The disadvantages of this technique are its limited depth and the required knowledge of at least one information point (depth or diameter). Also, when dealing with double profiles, the method loses its advantages of fast and accurate measurement.

Adepiction of the measurement process is given in Figure 13. The electro-magnetic tools Proceq Profometer 5 and 'blue Bosh' were used in Rez for steel reinforcement detection in block No. 5. Several steel rebars were located by both measuring devices and marked on the concrete surface with a piece of chalk. Both grids were compared with the design drawing of block No. 5, revealing a very close correlation of results (± 1 to 3 cm).

Each of the instruments has advantages and disadvantages, for example working better in deeper environments (Proceq) or being easier to manipulate (Bosh).

Figure 13. Locating the steel bars in block No. 5 in Rez with the Profometer 5 (right a bottom) and with the blue Bosh (top left).

3.5. Impact-echo

Impact-echo is a fairly new method with interesting applications and results. Both blocks in Brno were measured with a DOCter device (Figure 14), which enabled the detection of various object sizes at different depths using impact steel balls of diameters from 2 to 12 mm.

Figure 15 shows the results measured by the ball 12 mm in the block with the artificially inserted objects acting as honeycombs, plastic ducts or steel bars (XZ coordinates of the front wall).

Detection of the steel reinforcement is depicted along XY coordinates in Figure 16.

Figure 14. Impact-echo measurement of the front wall of block with artificial objects in Brno [9].

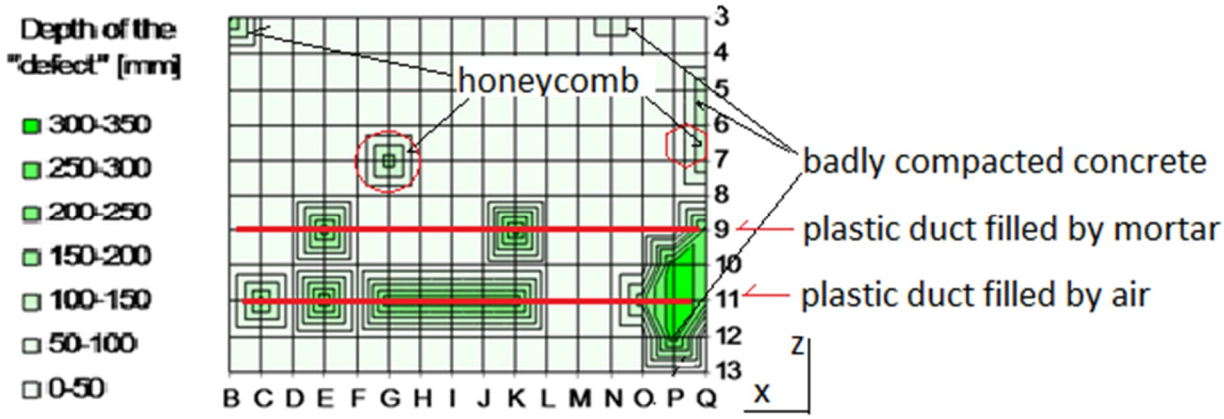

Figure 15. Artificial defects localized by impact-echo at the front wall of the Brno block [10].

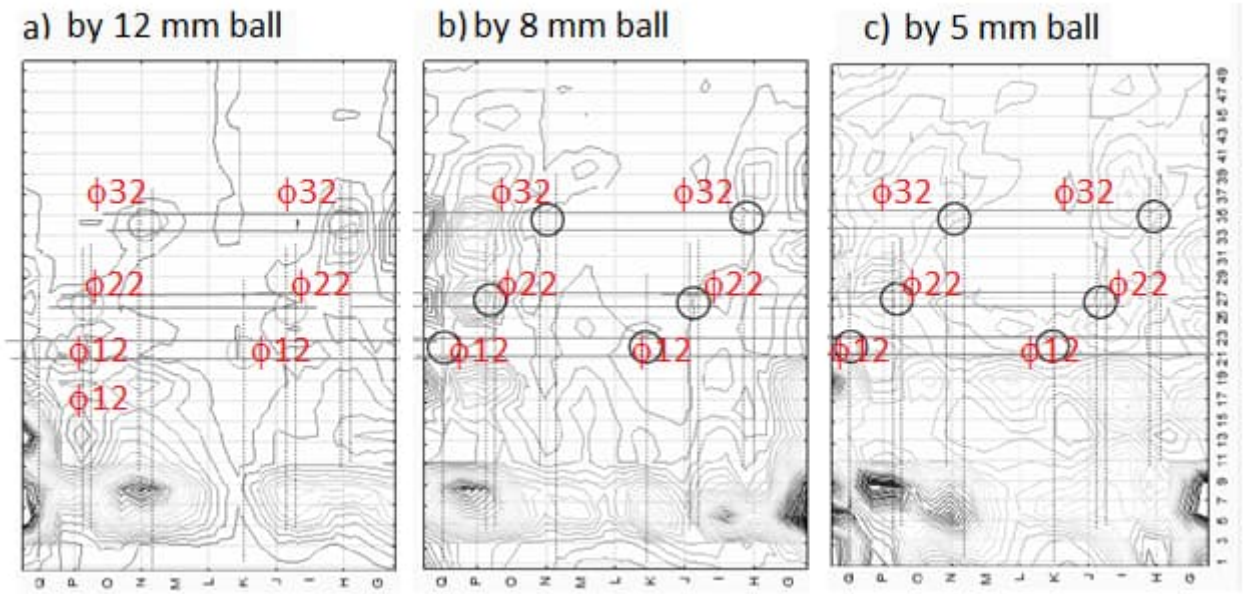

Figure 16. Horizontal b-scan of the block in Brno showing the steel rebars with a diameter 12 mm a), 8 mm b) and 5 mm c), searched by impact-echo[11].

4. CONCLUSIONS AND REMARKS

In total, 7 massive concrete blocks (five situated in Rez near Prague and two in Brno) were used to simulate the concrete containment wall at Temelin Nuclear Power Plant in Czechia. These were manipulated and inserted with various objects representing all of the potential defects and inclusions which might be found in such a wall.

Five various non-destructive testing methods were applied in order to detect these objects with sufficient accuracy.

The electro-magnetic induction was carried out using two devices manufactured by Proceq and Bosh. Both performed well in their detection of the steel bars at an appropriate depth (Figure 13). Strong results were obtained from the use of georadar with 1600 MHz antennas (Figure 12), while the impact-echo yielded poorer results (Figure 16). The ball with a diameter of 12 mm proved to be the best choice, as it detected both 32 mm rebars precisely (Figure 16 a). Unexpectedly, also UPV located some of the steel bars (32 and 22 mm, Figure 8).

The detection of holes in block No. 3 was successful with the use of both UPV (Figure 7) and ultrasonic pulse echo (Figure 9). However, the UPV method requires at least two people to hold both transducers, one on either side of the block. The results were satisfactory but they only provided information on the XZ location, yielding no information about the depth of the defect.

Honeycombs were detected significantly just by georadar (Figure 11). Neither impact-echo nor UPV yielded persuasive results (Figures 15 and 8, respectively). Ultrasonic pulse echo was not tested for this purpose.

The huge plastic ducts in block No. 5 were easily detected by both the UPV and ultrasonic pulse echo (Figures 6 and 10, respectively). Georadar did not provide any interesting results [3], perhaps due to incorrect depth vs. antenna frequency set up. However, with the block in Brno, GPR exceeded all expectations and showed clearly all inclusions (Figure 11). Impact-echo was accurate in locating the empty duct (Figure 15 - raw 11), but the duct filled with mortar was not detected by 100% (Figure 15 - raw 9). UPV identified only very low decrement of ultrasonic pulse velocity in raw 8 and 12 (Figure 8).

Unfortunately, no cracks or delamination were identified by the methods used here, perhaps due to low resolution or the low grid density.

Large hollows in block No. 1 were detected by the UPV method with sufficient accuracy [1].

Hopefully, a careful combination of these 5 methods for identifying the size and type of structural anomalies can offer fruitful NDT results with all large concrete structures, such as containment walls, dam barriers or industrial foundations [10].

ACKNOWLEDGEMENTS

The work presented here was made possible thanks to Institutional Support from the Ministry of Industry and Trade of the Czech Republic.

REFERENCES

[1] D. Svoboda, P. Cikrle, P. Suza, Z. Hlavac, "Identification of holes in concrete blocks using ultrasonic method," in *Proc. Int. conf. VVER 2007*, Praha, Czechia, Oct. 16–18, 2007, pp. 125–129.

[2] D. Svoboda, P. Cikrle, "Zjišťování poruch v masivních betonových blocích s využitím ultrazvukové impulsové metody," in *Proc. PhD stud. conf. Juniorstav 2007*, Brno, Czechia, Jan. 24, 2007,pp. 173–173.

[3] J. Stainbruch, O. Anton, T. Kordina, "Rozvoj použití georadaru při diagnostice železobetono-vých konstrukcí," in *Beton TKS*, Praha, 2011.

[4] O. Anton, V. Heřmánková, "Výzkum možnosti použití georadaru jako nedestruktivní zkušební metody při průzkumu masivních železobetonových konstrukcí," in *Proc. Int. conf. 15th Construmat 2009*, Kruh u Jilemnice, 2009, pp. 13–23.

[5] M. Luňáček, O. Anton, T. Vymazal, "Příprava masivních železobetonových bloků pro projekt 'Metodika zkoušení masivních železobetonových konstrukcí'," in *Proc. PhD stud. conf. Juniorstav 2007*, Brno, Czechia, Jan. 24, 2007, p. 166.

[6] M. Luňáček, O. Anton, "Příprava masivních bloků pro grant GAČR," in *Proc. PhD stud. conf. Juniorstav 2007,* Brno, Czechia, Jan. 24, 2007, p. 167.

[7] Z. Hlavac, A. Garbacz, O. Anton, "Defectoscopy of concrete structure by impact-echo method*,"* in *Proc. Int. conf. Concrete and Concrete Structures*, Žilina, SK, 2009, pp. 197–204.

[8] A. Garbacz, J. Steinbruch, Z. Hlavac, L. Hobst, O. Anton, "Defect detection in concrete structure with NDT methods: impact- echo versus radar," in *The e- Journal of Nondestructive Testing,* 2010, vol. 2010, no. 1, p. 21-28.

[9] Z. Hlavac, O. Anton, A. Garbacz, "Identification of Objects in Concrete Structure by Impact-Echo," in *Proc. 8th Int. conf. NDT 2010. Non-Destr. Test. Eng. Pract.,* Brno, CZ, 2010, pp. 75–80.

[10] Z. Hlavac, A. Garbacz, L. Hobst, "Detection of Defects in Massive Concrete Blocks by Impact-Echo," presented at *Online Workshop.: NDT&E of Compos. Mat. (CompNDT 2011),* May, 2011. Accessed: Dec. 1, 2022. [Online]. Available: https://www.ndt.net/search/docs.php3?id=10716

[11] Z. Hlaváč, O. Anton, A. Garbacz, "Detection of Steel Bar in Concrete by Impact- Echo," in *Trasactions on transport sciences,* 2009, vol. 2, no. 3, pp. 122–127.

[12] L. Hobst,"Metodika zkoušení masivních železobetonových konstrukcí,"Brno Univ. Tech.,Brno, Czechia, Tech. Rep. Grant Ag. Czech. Rep., 2009.

[13] Proceq SA, Schwerzenbach, Schwitzerland, *Pundit PL-200PE_Operating Instructions*. (2015). Accessed: Dec. 1, 2022. [Online]. Available:https://media.screeningeagle.com/asset/Downloads/Pundit%20PL-200PE_Operating%20Instructions_English_high.pdf

On the Multi-Frequency Electrical Impedance Measurement of Concrete

Adel Benidir[1,*], Mohamed Amara[1], Said Debbakh[1] Samir Bensaid[2]
[1] National Centre for Integrated Studies and Research in Building (CNERIB, Algeria)
[2] Materials and Sustainable Development Laboratory, Bouira University (LM2D, UMAOB, Algeria)

ABSTRACT

The paper presents a recent investigation dedicated to the multi-frequency impedance measurements of concrete performed on prismatic and cylindrical specimens by using uniaxial method. As the specimens are strongly dielectric, the equivalent electrical circuit with two parameters, where capacitance and resistance are in parallel, has been adopted. For the recording of the resistance and the capacitance of the specimens, the scanned frequency reaches the ultimate value of 5 MHz. The impedance measurements are also associated with ultrasound non-destructive method and compressive strength testing. The velocities of elastic compressive stress waves under direct and semi-direct transmissions are assessed. The results show that, under certain conditions, the capacitive effect of concrete specimens with different tortuosity fades over a frequency range. This finding is deduced after having identified a convergence of the capacitance values of the specimens over a wide frequency range. Nevertheless, on this same frequency range and even on the recommended one ranging from 0.5 to 10 kHz, the values of the resistance are dispersed. As the capacitive effect of concrete is mainly associated with constitutive elements (cement paste, aggregates) and microstructure property (unconnected pores), and by referring to the scientific literature, the study of the influence of the connected pores on the dielectric and mechanical properties of concrete could be derived. However, in the aim to express the contribution of resistivity on the impedance variation of the concrete, this study shows that the imposed measurement should be under high frequency. Furthermore, the paper discusses the strong contribution of the non-destructive tests to assess the compressive strength of concrete.

Keywords: Non-destructive test; Concrete impedance measurement; Dielectric properties; Ultrasonic wave.

1. INTRODUCTION

Concrete is considered as a highly integrated material in civil engineering due to its valuable qualities such as workability, cost, durability and resistance. The large-scale field application of that material is also accompanied by prolific investigations about the durability and the sustainability of structural elements made of concrete. Generally, the load bearing capacity of the concrete is mainly requested and the compressive strength is placed as a connecting parameter. The assessment of the compressive strength of concrete in-situ could be performed by three principal techniques: destructive, semi-destructive and non-destructive. The destructive test describes methods or techniques that breach the integrity of the structure. Principally, it consists on coring cylindrical specimens with different diameters and slenderness ratio from elements of the structure and crushing them to derive the mechanical properties of the concrete [1]. The semi-destructive tests are considered as outgrowth methods or techniques to limit the damage during the assessment of the durability of concrete structures. The most popular physical and in-field method is the pulling out testing [2, 3]. The measurement consists on the determination of the equivalent force necessary to

* Corresponding author: 00213(0)21380368; abenidir.cnerib@gmail.com

tear out an anchor previously embedded or installed in the concrete. Finally, the non-destructive tests represent methods and techniques that in any way do not impart alteration to the integrity of the structure. The testing is based on using transducers to collect information about the medium and predict some its mechanical properties. Throughout the numerous non-destructive methods, the Ultrasonic Pulse Velocity (UPV) measurement is extensively used. The transmission and the reception of elastic stress waves are performed to identify wave velocities through the medium. Consequently, models are developed to link the ultrasonic wave velocity and the compressive strength of concrete [4]. Recently, a validated approach known as the rapid chloride permeability test which is originally developed to assess the durability of concrete is used for performance-based evaluation of concrete [5]. The non-destructive method consists on subjecting a specimen to a voltage and measure the electrical charge passing through it [6,7]. The measurement of the surface electrical resistivity and bulk electrical conductivity of hardened concrete could be performed by using Wenner linear four-probe array [8] and electrodes covering the ends of the specimen [9], respectively. More interestingly, as the capacitive effect of concrete is mainly associated with constitutive elements (cement paste, aggregates) and microstructure property (unconnected pores) [10], the study of the influence of the connected pores on the dielectric and mechanical properties of concrete could be derived [11]. Subsequently, the electrical resistivity has been highlighted as an influential parameter to assess the concrete durability [12]. Furthermore, a strong relationship between the water permeability of concrete and its electrical resistivity has been reported [13, 14]. However, it has been demonstrated that there is no marked relationship between the compressive strength of various concrete mixtures and the surface electrical resistivity measured with Wenner probe [15].

This paper presents a recent investigation on the uniaxial multi-frequency measurement of the electrical impedance of concrete. This method is a non-destructive testing technique that is used in a large technological field such as a human health, biology, aeronautic structures, naval structures, concrete structures, etc. As the specimens are exclusively dielectric, the equivalent electrical circuit with two parameters, capacitance and resistance are in parallel, is used. The influence of the curing conditions of concrete on its capacitance and electrical resistance has been discussed. The experiment consists of the assessment of the impedance of specimens prepared with high strength and ordinary C25/30 concrete class. The shapes of specimens are standardized prism and cylinder. The results show that a correlation between the curing conditions and dielectric properties of concrete could be derived. Furthermore, a likely connection between the compressive strength and ultrasound pulse velocity as function of the capacitance through a frequency range is pointed out. The paper also treats the sensitivity of the ultrasound waves to distinguish various water curing conditions.

2. MATERIALS AND METHODS

2.1. Concrete mixtures

An ordinary C25/30 class and high strength concrete have been prepared for the experiment. The constitutive elements of the different concrete mixtures are listed in Tables 1 and 2. Three (03) prismatic specimens with a dimension of 28 cm in length and 7 cm in the cross-section and twelve (12) cylindrical specimens were built[16]. The diameter of the cylinder is 150 mm and the slenderness ratio of is 2.

Table 1 Mixture proportions of an ordinary concrete (cylindrical specimens)

	Cement (kg/m^3)	Natural Sand from rivers (kg/m^3)	Natural sand from dunes (kg/m^3)	Aggregates (kg/m^3)	Adjuvants (1%) (kg/m^3)	Water (kg/m^3)	Consistency class	Compressive strength, after 28 days of curing (cylindrical specimen, MPa)
Proportions	350	464	271	1058	0	210	S2 (slump range between 50 to 90 mm)	25.37

Table 2 Mixture proportions of high strength concrete (prismatic specimens)

	Cement (kg/m^3)	Natural Sand from rivers (kg/m^3)	Natural sand from dunes (kg/m^3)	Aggregates (5/16) (kg/m^3)	Aggregates (15/25) (kg/m^3)	Adjuvants (1%) (kg/m^3)	Water (kg/m^3)	Compressive strength, after 28 days of curing (cubic specimen, MPa)
Proportions	350	360	440	450	550	3.5	140	57

2.2. Curing conditions

Two distinct protocols are applied in this experiment. The prismatic specimens made of high-strength concrete were left on the water for 28 days whereas the cylindrical specimens made of ordinary C25/30 concrete class were subjected to the following curing conditions: After being demolded (24 hours after filling the molds), specimens were emerged in water and kept in a storage room. The water is at 23°C degrees and the relative humidity inside the room is 50%. The experimental plan consists of removing three (03) specimens after 0 (means not emerged), 3, 14 and 28 days of immersion. Once removed from the water, the specimens are left outside the storage room in the open air.

2.3. Ultrasound Pulse Velocity Measurement

Ultrasonic pulse velocity measurements were conducted using a portable pundit LAB ultrasonic pulse transmitter, which is non-destructive digitally showing, as depicted in Figure 1. The ultrasonic wave frequency longitudinal wave of 54 kHz is generated through a transducer kept in contact with targeted element to test. Direct and semi-direct transmissions were used to determine the ultrasonic pulse velocity, as per the procedure given in [17]. A pulse generator initiates an ultrasonic pulse, which is transmitted to the concrete through the transmission transducer, and collected by receiver transducer on the other side. The measurements are based on the time that pulse has taken to cross the concrete. The transducers were placed at the end of both opposite faces of prismatic and cylindrical specimens. The passage time of the transmitted ultrasonic waves, through the specimens was measured with the precision of 0.1 µs. The pulse velocity is the ratio of the pulse's cross distance to the time measured. The portable pundit LAB should be zeroed using the calibration rod of known time before each measurement. Three readings were taken by relocating the transducers on the opposite faces of the concrete specimens.

Figure 1. Ultrasound Pulse Velocity Measurement.

2.4. Multi-frequency impedance measurement

The impedance measurement is performed by using a precision LCRmeter (Figure 2a). The measurement consists to place two electrodes made of copper-clad laminate PCB, on both extremities of the specimen (Figure 2b). The electrodes must cover entirely the specimen cross-section. The recording of the resistance and capacitance of the specimens is done for the scanned frequency reaches the ultimate values from 100Hz to 5MHz with a step of 10kHz. To avoid the effect of the elements upstream to the electrodes, two tests given by the short circuit and the open circuit referenced to the electrodes, are carried out from 100Hz to 5MHz before starting the impedance measurement on the specimens. The adopted equivalent electrical circuit is given in figure 2c, it is constituted by a resistance and a capacitance in parallel.

a) b) c)

Figure 2. Experimental setup of impedance measurement
a) LCRmeter GW-Instek 8105G b) Electrode placement on the cylindrical specimen c) Two electrical parameter model

3. RESULTS AND DISCUSSIONS

3.1. Non-destructive testing on prismatic concrete specimen

Figures 3a and 3b show the results of the measurement of the capacitance and the electrical resistance of three concrete specimens with a prismatic shape noted S1, S2 and S3. The specimens are subjected to the same curing conditions (water curing for 28 days before crushing). The velocities

of ultrasound waves performed with direct and semi-direct methods are 5138 m/s, 5119 m/s, 5229 m/s and 5389 m/s, 5250 m/s 5377 m/s for S1, S2 and S3 respectively. The multi-frequency measurement of the two electrical parameters shows through the evolution of the capacitance that over a frequency range, the capacitive effect fades over. This frequency range is identified between 100 kHz and 300 kHz. Over this frequency range, the resistive effect traduces a slight variation in the electrical resistivity. By referring to the capacitance values accompanied with the observation of convergence over a frequency range, the presence of a likely correlation between the composition of the concrete and/or its conditions of conservation and the capacitance could be highly put under the scope. Indeed, between the three specimens, three parameters in common can be confirmed: the shape, the composition of the concrete and the curing conditions. The three specimens have the same shape, were made with the same formulation and were subjected to the same curing conditions. It is important to mention that the specimen ends are flat and the contact zones with the electrodes were carefully controlled. The variation of the electrical resistivity of the concrete over the frequency range from 100 kHz to 300 kHz can be justified by the difference in the concrete tortuosity. Due to the heterogeneity of the concrete, which is principally linked to its constitutive elements, the type of binder, the distribution of aggregates and pores are at the origin of unpredictable interconnectivity of the pores. Therefore, this specificity of the microstructure of concrete contributes to the installation of an incipient research environment and the derivation of a relationship between electrical resistivity and chloride diffusion [9]. However, to confirm a likely presence of a correlation between the concrete capacitance and the curing conditions outlined above, this point will be discussed in the following section.

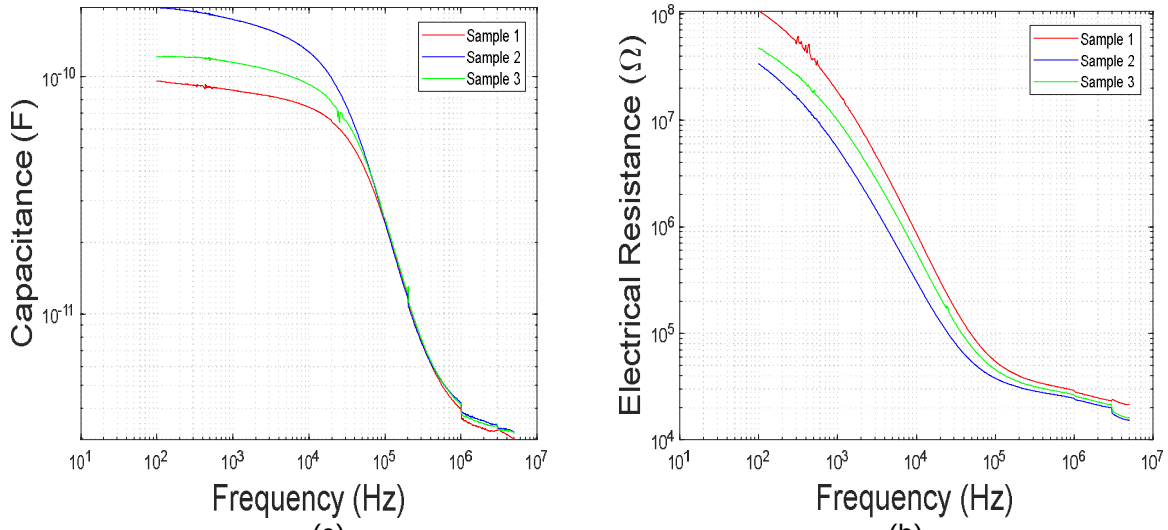

(a) (b)

Figure 3. Multi-frequency measurement of the dielectric constants of high strength concrete (a) Capacitance (b) Electrical resistance

3.2. Compressive strength and impedance measurement of concrete under different water curing durations

Imposing different curing conditions can create a radical change in the microstructure of the concrete (size and distribution of the pores, hydration, connectivity between pores, etc.) and consequently alter its performance indices (compressive strength, penetration of chlorides, thermal conductivity, etc.). To illustrate the influence of curing conditions on the dielectric constants of concrete, twelve (12) cylindrical specimens made of ordinary concrete, of the C25/30 class, were prepared and subjected to distinct curing conditions. Impedance, ultrasonic measurements and a destructive test were carried out. Table 3 shows the results of the non-destructive measurement, the crushing test and the mass density of the concrete. From that table, a positive correlation is observed between the velocities of the ultrasound elastic waves and the compressive strengths of the

cylindrical specimens. The second main observation concerns the difference in the compressive strength values between concrete specimens directly exposed to the curing conditions of an onsite implementation (zero-day water curing) and those carefully left under humid laboratory conditions (immersion up to 28 days). This dispersion from compressive strength (7.8 MPa of difference), describes the importance of the curing conditions. Thus, neglecting onsite curing conditions can be detrimental. Engineers can be misled, especially when using incompatible results during the concrete quality control process. The conclusive consequence will be at the origin of an approximate evaluation of the performance indices of the structure. It is also important to pinpoint that both compressive strength values and ultrasound wave velocities are showing limits to correctly identifying the specimens put under water for 14 and 28 days.

Table 3 Mixture proportions of an ordinary concrete (cylindrical specimens)

Specimens and water curing days	Mass density (kg/m³)	UPV (m/s)	Compressive strength (MPa)
Sp_00 day	2262	4483	17.57
Sp_03 days	2271	4561	21.81
Sp_14 days	2294	4671	25.85
Sp_28 days	2297	4660	25.37

Figures 4a and 4b show the results of the multi-frequency measurement of the capacitance and the resistance of standardized cylindrical concrete specimens. Each curve represents the average value from 03 specimens. From the evolution of the capacitance as a function of the measurement frequency, it seems to be easy to distinguish the different curing conditions applied to the specimens. The identification is even accentuated from frequencies located above 100 kHz. A positive correlation has been observed between the values of capacitance and the water curing days. However, for frequencies below 1 kHz, it is not easy to confirm which protocol of curing conditions was adopted. This illustration of the variation of the capacitance and the trend identified for frequencies above 100 kHz is confirmed for the electrical resistance values. However, for electrical resistivity, the trend is reversed. Additionally, from figure 4b, the electrical resistances of the specimens placed under different water curing durations converge to one constant value (intersection) as the frequency is approaching 80 kHz. Consequently, at that frequency the capacitance is the distinctive electrical element to identify severe curing conditions of concrete. These observations are not clearly illustrated by ultrasound test measurement or crushing test. Accordingly, impedance measurement of concrete could be used as a complementary investigation technique for the assessment of concrete strength and durability.

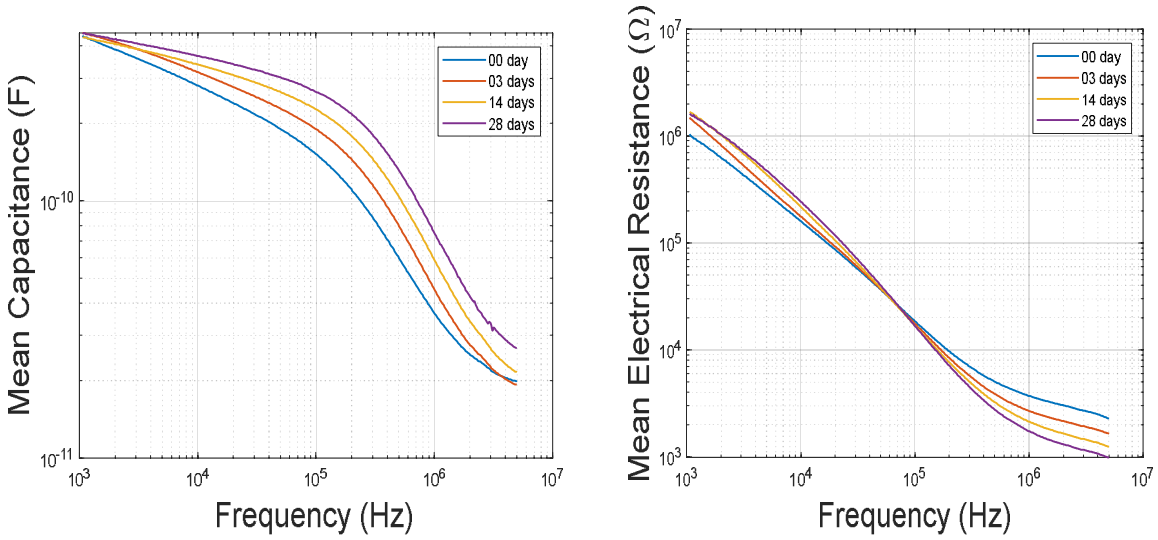

Figure 4. Multi-frequency measurement of the dielectric properties of an C25/30 concrete class concrete as function of water curing duration (a) Capacitance (b) Electrical resistivity

4. CONCLUSION

The paper presents the results of a recent investigation carried out to measure the electrical impedance of concrete. A uniaxial multi-frequency impedance measurement, ultrasound pulse velocity characterization and crushing tests were performed on standardized prismatic and cylindrical specimens. The evolution of the capacitance and the resistance as a function of the curing conditions have been discussed and the following conclusions are drawn:

- The multi-frequency impedance measurement seems to be a reliable technique to identify severe varying water curing conditions of concrete.
- The applied frequency measurement ranging from 100 kHz to 300 kHz is identified as a sensitive interval to measure the impedance variation of concrete with a uniaxial method.
- The ultrasound pulse velocity measurement is confirmed as a concise method to assess the compressive strength of concrete. However, limitations are observed to extend the use of elastic wave propagation to illustrate a variation in water curing conditions.
- At the measurement frequency of 80 kHz, the detection of the imposed water curing conditions is ensured only by the capacitance value.

ACKNOWLEDGEMENTS

The authors would like to thank all the technical stuff of the National Centre for Integrated Studies and Research in Building (CNERIB).

REFERENCES

[1] Bartlett FM and MacGregor JG. Effect of core diameter on concrete core strengths. ACI Materials Journal. 1994, 91(4), pp 339-348.

[2] ASTM C 900: Standard Method for Pullout Strength of Hardened Concrete. 1982.

[3] Bickley A. Pullout testing of concrete. Concrete Construction. 1986, 26 (7), pp 577-582.

[4] Rilem Technical Committee. Recommendation of RILEM TC249-ISC on non-destructive in situ strength assessment of concrete. Materials and Structures, 2019, 52:71.

[5] Layssi H, Ghods P, Alizadeh A. R, Salehi M. Electrical resistivity of concrete. Concrete International. 2015, pp 41-46.

[6] ASTM C1202-12, “Standard Test Method for Electrical Indication of Concrete’s Ability to Resist Chloride Ion Penetration,” ASTM International, West Conshohocken, PA, 2012, 8 pp.

[7] AASHTO T 277, “Standard Test Method for Electrical Indication of Concrete’s Ability to Resist Chloride,” American Association of State Highway and Transportation Officials, Washington, DC, 2007, 12 pp.

[8] FM 5-578. Florida method of test for concrete resistivity as an electrical indicator of its permeability. 2004.

[9] Standard Test Method for Bulk Electrical Conductivity of Hardened Concrete. C1760 – 12.

[10] Hornbostel K, Larsen C. K, Geiker M. R. Relationship between concrete resistivity and corrosion rate-a literature review. Cement and Concrete Composites. 2013, Vol. 39, pp 60-72.

[11] Gao Y, Chen M, Jiang H. Influence of unconnected pores on effective stress in porous geomaterials: Theory and case study in unconventional oil and gas reservoirs. Journal of Natural Gas Science and Engineering. 2021, vol. 88, 103787.

[12] Azarsa P. and Gupta R. Electrical Resistivity of Concrete for Durability Evaluation: A Review. Advances in Materials Science and Engineering Volume 2017, Article ID 8453095, 30 pages

[13] Andrade C, Sanjuan MA, Alonso MC. Measurement of chloride diffusion coefficient from migration tests. In: Proceedings of the NACE Corrosion'93; 1993. pp 289–98.

[14] Polder RB. Chloride diffusion and resistivity testing of five concrete mixes for marine environment. In: Proceedings of the RILEM international workshop on chloride penetration into concrete, St-Remy-les-Chevreuses, RILEM; 1997.

[15] Ramezanianpour A. A., Pilvar A., Mahdikhani M., and Moodi F. Practical evaluation of relationship between concrete resistivity, water penetration, rapid chloride penetration and compressive strength. Construction and Building Materials. 2011, vol. 25, no. 5, pp 2472–2479.

[16] NF EN 12390-3. Testing hardened concrete- part 3: compressive strength of test specimens. June 2019.

[17] NF EN 12504-4. Testing concrete in structures- part 4: determination of ultrasonic pulse velocity. July 2021.

Advanced tomographic imaging techniques for quality assessment of concrete structures by means of ultrasound

Andrey Bulavinov*, Roman Pinchuk, Andrey Samokrutov, Viktor Shevaldykin
ACS-Solutions GmbH, Saarbrucken, Germany

ABSTRACT

The novel ultrasonic data processing and image reconstruction techniques offer new opportunities for three-dimensional imaging of concrete structures. Data acquisition by matrix transducer arrays using Full-Matrix-Capture (FMC) technique with following real-time imaging capability by Total-Focusing-Method (TFM) can be successfully utilized for quality assurance in the construction industry, which is becoming the current state of the art.

Further approaches for improving the flaw detection capability and image resolution consist in advanced signal processing techniques for both transmitting and receiving signal control of the matrix transducer array when performing the data acquisition. This provides necessary matching the operating frequency to the material properties and significant improvement of the penetration capability without losing spatial resolution of the reconstructed three-dimensional inspection volume.

The active Dry-Point-Contact (A-DPC) ultrasonic transducers offer the possibility of a flexible frequency control for optimal data collecting that extends the achievable inspection range up to 4 meters and beyond.

In the present contribution both state-of-the-art and novel true-3D imaging approaches and data assessment are considered on real concrete inspection objects and the advantages of enhanced data processing with respect to improved information content and easiness of result, interpretation is discussed.

1. INTRODUCTION

The application of imaging ultrasonic testing of concrete in the civil engineering [1] has become widespread in the last decade. The reasons for this are, on the one hand, the aging infrastructure and increasing need for non-destructive quality assurance, and on the other hand, the significant advances in the development of testing technologies and the growing range of modern imaging testing systems on the market.

While the ultrasonic testing devices for metallic products and lightweight composite materials have a long history of use, the concrete testing devices belong to an “emerging market” in which there is still a lack of standards and regulations. Nevertheless, the modern testing instruments, with their two-dimensional and three-dimensional imaging, offer clear added value in terms of quantitative nondestructive testing and reliability of the condition assessment of the building construction.

The aim of the current article is to explain the latest trends in the implementation of modern ultrasonic testing instruments for concrete testing – in particular, the processing and visualization of ultrasonic measurement data—and to show the potential for expanding their area of application.

2. HARDWARE DESIGN OF THE FMC-INSTRUMENTS FOR CONCRETE TESTING

Similar to the modern ultrasonic flaw detectors for metal testing, the concrete testing instruments represent multi-channel phased array systems [2], which display the test results as images (Fig. 1).

* Dr. Andrey Bulavinov, Phone: +49-681-9659-2270, E-Mail: andrey.bulavinov@acs-international.com

Figure 1: Ultrasonic tomography system for concrete testing

The key element of such a testing instrument is the ultrasonic sensors. In contrast to conventional ultrasonic devices for metal testing, in which the piezoelectric transducers are coupled via a liquid coupling medium, the probes for concrete testing used here implement the so-called “dry point contact” principle (DPC) [3], in which a special type of excitation is used via a pin vibrating at the nominal frequency (Fig. 2).

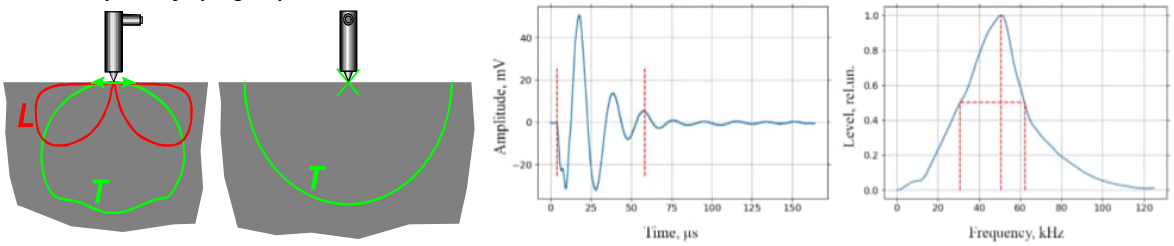

a) Beam directivity, pulse characteristic and frequency spectrum of a DPC transducer

b) Matrix aperture consisting of the spring-loaded Dry-Point-Contact transducers

Figure 2: DPC matrix aperture of the ultrasonic tomograph

Depending on the desired ultrasonic wave type (longitudinal or transverse), operating frequency and bandwidth, the construction of the transducer can vary. Broadband shear wave transducers with a center frequency of around 50 KHz are typically used for ultrasonic imaging in concrete [4].

The ultrasonic data is acquired according to the so-called “full matrix capture” (FMC) principle, where the array elements act individually as transmitters and receivers (Fig. 3).

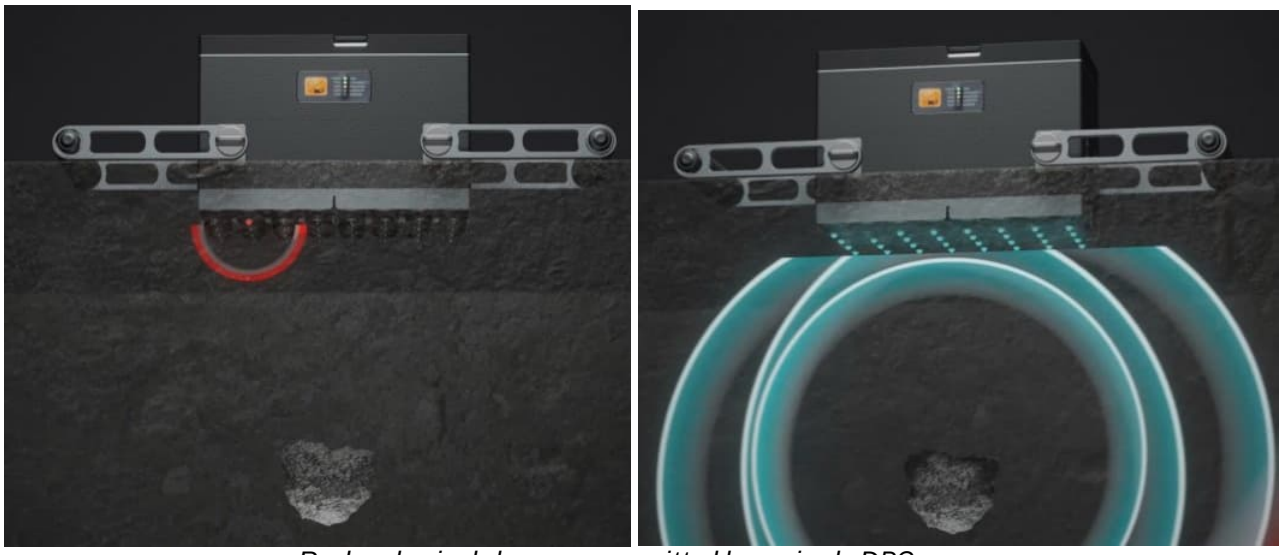

Red: spherical shear wave emitted by a single DPC sensor
Blue: spherical shear waves reflected back from the material defect

Figure 3: The principle of sequential excitation of the matrix aperture (3D-FMC)

Ultrasound data originating from the two-dimensional instrument aperture consisting of 4 x 8 DPC transducers, including all 32 x 32 = 1,024 combinations of transmitters and receivers, are superposed using the “total focusing method” (TFM). The TFM method, in turn, represents a variant of the “synthetic aperture focusing technique” (SAFT), in which the aperture to be synthesized is limited to the aperture of the phased array with alternating transmitter and receiver elements. In this way, a three-dimensional image of the component volume can be generated in each measuring position of the ultrasonic tomograph (Fig. 4).

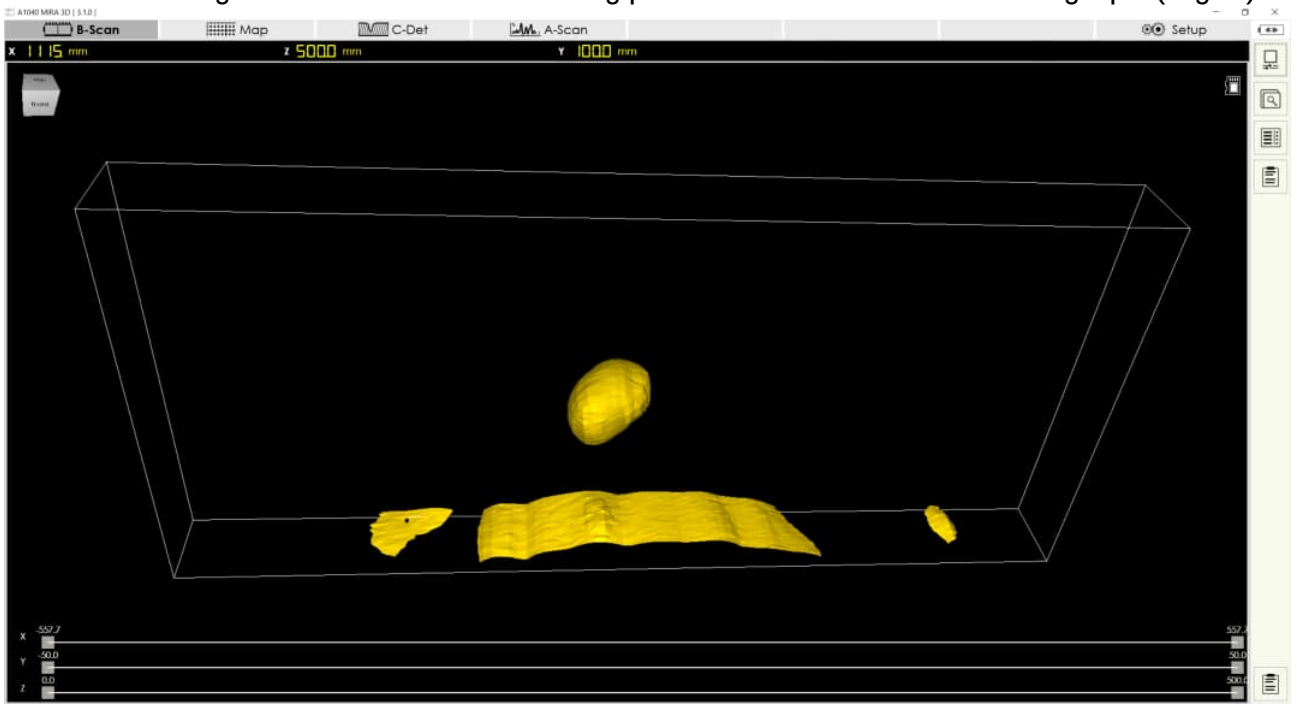

Figure 4: A 3D image of a material defect in a test position of the ultrasonic device

It must be pointed out that the spatial resolution of the imaging systems based on the low-frequency DPC transducer arrays have their physical limitations related to the ultrasonic wavelength. Supposed the instrument works in the frequency range of 20 to 100 KHz, the

resolution in concrete (shear wave sound velocity ~ 2.500 to 3.000 m/s) would lie in the range of 25 to 150 mm.

Another feature of the design structure of modern ultrasonic concrete tomographs can be mentioned, which under certain circumstances can also prove to be groundbreaking for other phased array systems, e.g., for metal testing. The image reconstruction according to the TFM principle – in particular, when calculating matrix apertures from 32 x 32 or 64 x 64-point sources – requires significant computing power in order to be able to carry it out in real-time. Modern tablet PCs have multi-core graphics processors that are perfectly capable of real-time 3D SAFT reconstruction of matrix aperture data.
The function of the data acquisition electronics is limited to the excitation and reception of the ultrasonic signals, as well as digitization and transfer of the raw ultrasonic data via a WiFi data interface. The entire data processing (incl. digital filtering), image reconstruction, visualization and evaluation (incl. reporting) is taken over by a high-performance tablet PC or, alternatively, a desktop or laptop computer. The separating DAQ and processing units communicating wirelessly opens the opportunity for automated implementation of the ultrasonic testing procedure, where not only the UT instrument, but also the scanning robot are remotely controlled by the operator (Fig. 5).

Figure 5: Possibility of an automated data acquisition via the wireless data interface

2. ADVANCED SIGNAL PROCESSING METHODS FOR EXPANDING THE UT INSPECTION RANGE

One of the unique selling points of the ultrasonic testing devices for concrete testing compared to other testing methods, such as ground penetrating radar testing systems, is their greater range with high resolution.
Even when testing reinforced concrete, inspection range of up to two meters can be implemented.
Nevertheless, ultrasonic testing also has its physical limits if the material to be tested has increased sound attenuation, e.g., due to coarse aggregates, or if particularly thick structures, such as dams, with a wall thickness of several meters are being tested. The insufficient signal-to-noise ratio does not allow the recorded ultrasonic signals to be evaluated.
If you look at the raw ultrasonic echo signals in detail, you can divide the signal noise into three categories:

- ⇒ Coherent acoustic noise due to ultrasonic backscattering
- ⇒ Quantization noise due to the limited resolution of the analog to digital conversion
- ⇒ Thermal noise

The last two types of noise occur, in particular, with very long sound paths, where one has to deal with relatively weak signals despite increased amplification values. This can be successfully overcome using a so-called pulse compression technique. For this purpose, instead of a short monochromatic excitation sequence, a long-modulated excitation sequence is used to excite the ultrasonic waves, which is then extracted again in the received and digitized ultrasonic signal (Fig. 6). As a result, a significant improvement in the signal-to-noise ratio and the spatial resolution can be achieved.

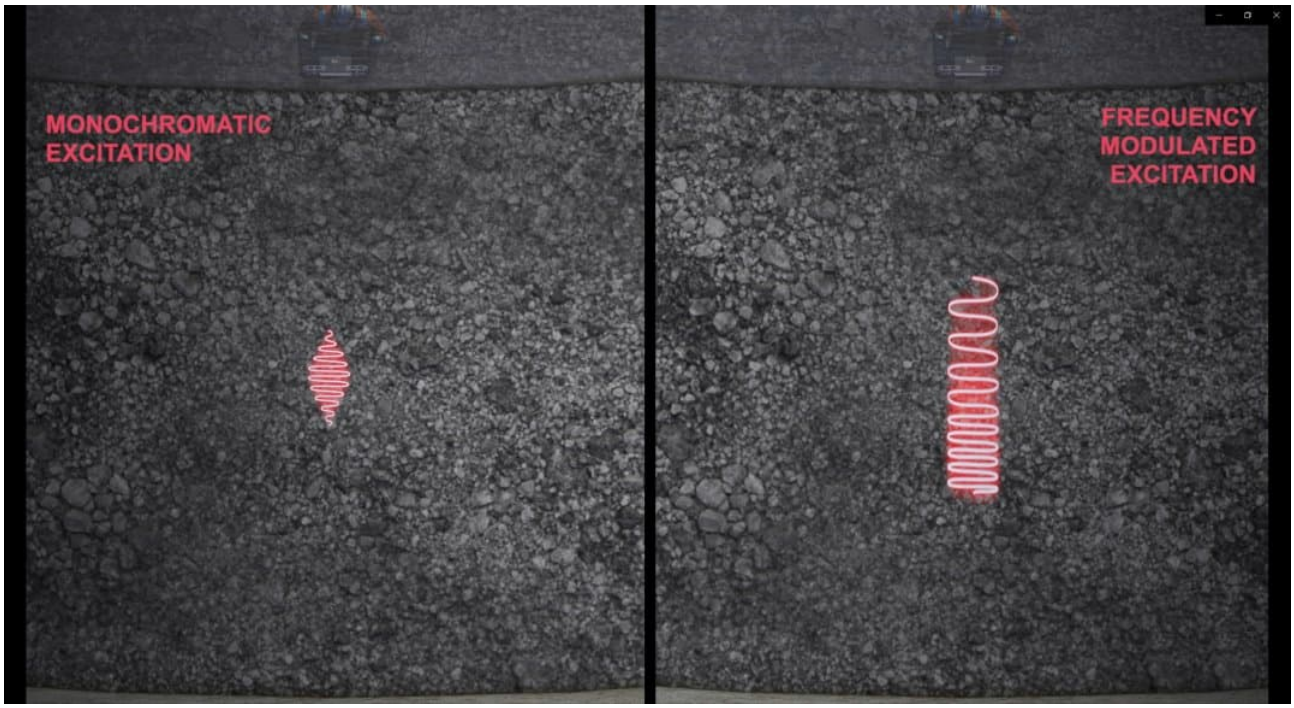

Fig. 6: Schematic representation of the types of noise (left) and the suppression principle using a modulated excitation sequence

As a result of such a decomposition of the received echo-signals before the SAFT image reconstruction, a denoised test result is obtained (Fig. 7).

a) Measurements on a concrete block with a wall thickness of 4 m

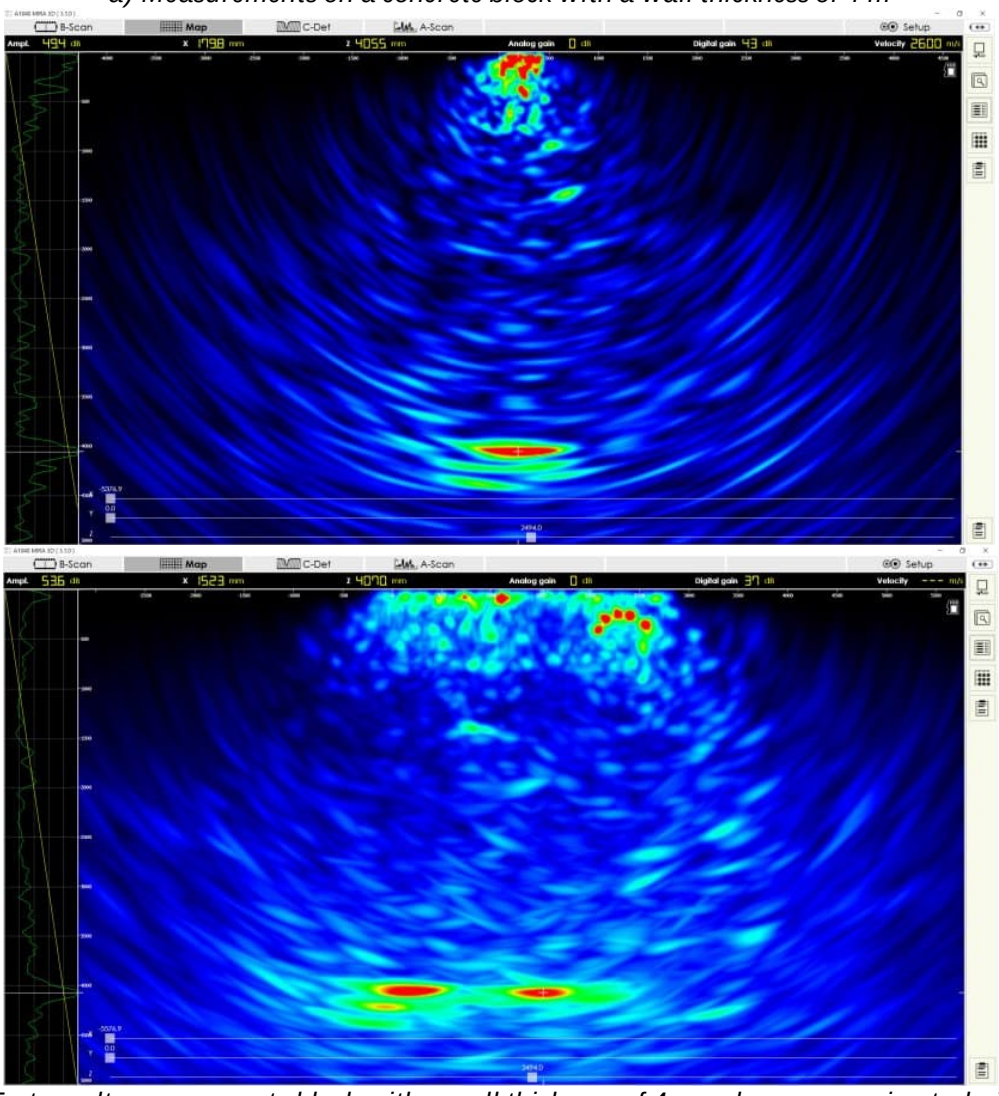

b) Test results on a concrete block with a wall thickness of 4 m pulse compression technique

Fig. 7: The test result without and with guided signal excitation on the thick concrete block*

**The results have been obtained on the reference object of the Federal Agency for Materials Research and Testing BAM at the test ground BAM-TTS at Horstwalde/Brandenburg*

4. CRECK DEPTH EVALUATION

Another significant advantage of the matrix aperture with extremely small single array elements is its very broad beam directivity characteristic, which, among other things, allows acquiring diffraction signals from unfavorably oriented material flaws, such as the tip of an outwardly open crack, to be detected. This makes it possible to determine the depth of such material defects without being able to insonify them “frontally”.
When performing such a measurement, it is necessary that the number of DPC sensors on both sides of the open crack is equal and that the crack depth does not exceed the overall aperture size of the device (Fig. 8).

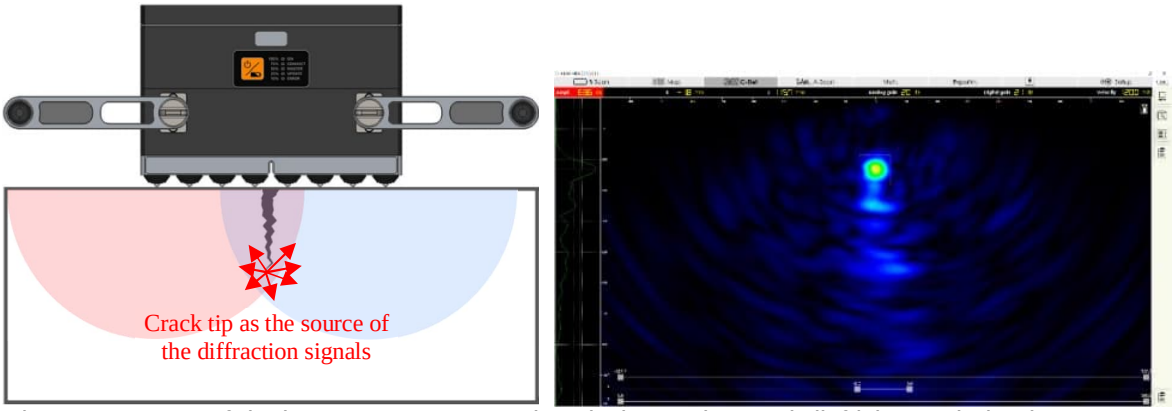

a) Arrangement of the instrument aperture in relation to the crack (left) in crack depth measurement mode of the ultrasonic tomograph (right)

b) Measurement of a natural crack in the structure

Fig. 8: Determination of the depth of an open crack using ultrasonic tomography

5. Summary and Outlook

The article presents current trends in the implementation and application of imaging ultrasonic testing systems for non-destructive concrete testing.
These mainly consist of the application of the matrix apertures based on active DPC ultrasonic transducers and the implementation of three-dimensional FMC/TFM methods

for tomographic imaging. Among other things, this sensor design allows the use of pulse compression techniques when exciting the ultrasonic waves and thus a significant expansion of the realizable inspection range to several meters.
Furthermore, the transition from the conventional line array principle to the use of matrix apertures allows three-dimensional tomographic imaging with improved spatial resolution in every position of the ultrasonic tomograph and the implementation of special functions for quantitative defect assessment in the near field of the ultrasonic sensor system, such as evaluating the crack depth.

REFERENCES

[1] V.N. Kozlov, A. A. Samokrutov, V.G. Shevaldykin. Thickness measurements and flaw detection in concrete using ultrasonic echo method, Nondestructive Testing and Evaluation 13(2): 73-84, January 1997

[2] HAZA, A. O.; PETERSEN, C. G.; SAMOKRUTOV, A. Three-Dimensional Imaging of Concrete Structures Using Ultrasonic Shear Waves. German Instruments SA, 2011, Denmark.

[3] Shevaldykin, V.; Samokrutov, A.; Kozlov, V. 2003. Ultrasonic low-frequency short-pulse transducers with dry point contact. Development and application, in International Symposium Non-Destructive Testing in Civil Engineering (NDT-CE), 1619 September, 2003, Journal of Civil Engineering and Management, 2013, 19(6): 775786 785

[4] Bishko A, Samokrutov AA, Shevaldykin VG (2008) Ultrasonic echo-pulse tomography of concrete using shear waves low-frequency phased antenna arrays. In Proceedings of the 17th world conference on non-destructive testing (Vol. 25, no. 28.10, p. 2008)

Towards corrosion assessment in steel cylinder concrete pipes using the Pulsed Eddy Current Technique

Sokratis N. Iliopoulos[1,*], Wouter Van Eesbeeck[2]
[1,2] ENGIE Laborelec, Rodestraat 125, 1630 Linkebeek, Belgium

ABSTRACT

In the framework of the ACES H2020 European Research Project the Pulsed Eddy Current (PEC) technique was evaluated for its feasibility to inspect corrosion in steel cylinder concrete pipes. The aim was twofold: a) identify commercially available PEC tools, define their technical specifications, assess their compatibility with a robotic manipulator and b) address the strengths and limitations of specific PEC probes. To address the aforementioned aim, laboratory size specimens (mockups) were designed and built. Six mockups were built in total. The mockups were replicating real pipe properties and included a steel liner and mesh. Mockups without mesh were also built for comparison purposes regarding interferences on the measurement results. Artificial defects were introduced in the steel liner of the mockups, in order to assess the detectability and the characterization potential of the technique. It was found that the Eddyfi and Maxwell systems performed equally well while small footprint probes provided more accurate results compared to larger ones. The presence of the mesh and the border effect was significant causing local distortion of the signals and misinterpretation of material thickness losses. Also, the higher the lift-off and misalignment, the lower the sensitivity. The comparison of a fine scanning grid with a coarser grid showed similar averaged thickness values and equal minimal values considering a tolerance of +/- 0.1 mm. The minimum detected defect was the one with 25 mm diameter and 2 mm depth corresponding approximately to 25% of the footprint volume of the smallest probe. A third generation of probes, which relies on array technology, is currently available on the market. Those probes improve the sensitivity by reducing the footprint.

Keywords: PEC; Corrosion; Steel Cylinder Concrete Pipes; Robot compatibility.

1. INTRODUCTION

The present paper is submitted in the framework of the European funded research project ACES “Towards improved Assessment of Safety Performance for LTO of nuclear Civil Engineering Structures” (ID 900012). ACES addresses the EURATOM Work Programme 2019-2020, dedicated to Nuclear Fission and Radiation Protection Research (H2020 NFRP-2019-2020) and more specifically the work programme related to ageing phenomena of components and structures and operational issues.

The main objective of ACES is to advance the assessment of safety performance of civil engineering structures by solving the remaining scientific and technological problems that currently hinder the safe and long-term operation of nuclear power plants reliant on safety-critical concrete infrastructure. Proper understanding of deterioration and ageing mechanisms is achieved through combined experimental and theoretical studies, following a multidisciplinary approach, and utilizing state-of-the-art experimental and modelling techniques. Material characterization at different length scales (i.e. nano, micro, meso, and macro scales) is necessary, focusing on the physical understanding of the degradation processes (e.g. neutron and gamma radiation, internal swelling reactions, liner corrosion, etc.) as well as physical phenomena (drying, creep, shrinkage, etc.), and

* Sokratis.Iliopoulos@engie.com; +32 475 63 67 13

their influence on macroscopic mechanical properties and structural/ functional integrity of the components.

ACES is divided in 7 workpackages (WP). WP2 deals with corrosion. Subtask 2.3 concerns the corrosion inspection of steel cylinder concrete pipes (SCCP), which is the subject of the current publication. An example of an SCCP pipe is shown in Figure 1.

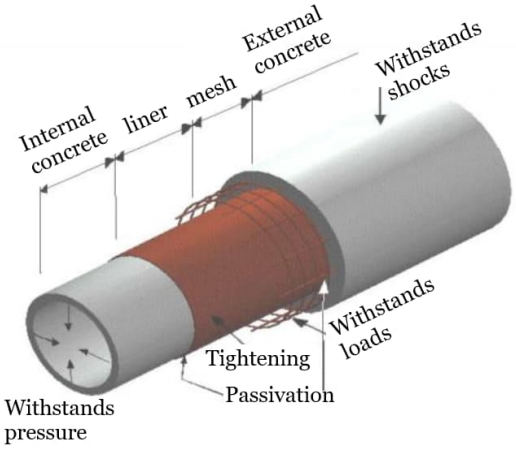

Figure 1. Steel Cylinder Concrete Pipe (SCCP)

As shown in Figure 1, the SCCP is composed of an external concrete layer, a steel liner and an internal concrete layer. The external layer of concrete protects the pipe against shocks, the steel liner ensures (water) tightness, while the internal concrete layer acts as the passivation layer of steel against corrosion. The internal concrete layer should also withstand varying pressure actions. The external concrete layer can be reinforced with a steel mesh that carries the loads, as shown in Figure 1.

The thickness of the internal concrete varies between 15 mm and 25 mm. The internal concrete diameter ranges from 600 mm to 900 mm, but, in some cases, it can be as low as 300 mm and as high as 3 m. The thickness of the steel liner is, in most cases, 4 mm. The thickness of the external concrete is 40 mm.

The internal concrete is composed of a thin passive film characterized by a high pH, protecting the steel against corrosion. This passive film can, however, be decomposed due to the reaction of the concrete with atmospheric CO2 (as carbonation results in pH decrease), or by the penetration of aggressive ions (chloride ion Cl^-) to the steel surface. At the anodic surface, ferrous ions (Fe^{2+}) are dissolved, and electrons travel through the steel to the cathodic surface, where they form hydroxide (OH^-) with water and oxygen. Anodic corrosion processes can be very localised, damaging only a small percentage of the steel surface, while large neighbouring steel surface stays passive. This indicates the separation of the anodic reaction and the cathodic reaction to form a macro-cell [1]. This principle creates a potential difference that can be measured by the half-cell method [2].

Another method that can indirectly measure corrosion is the Pulsed Eddy Current (PEC) technique. The feasibility of the aforementioned technique to inspect corrosion in SCCPs is addressed in the current publication. PEC is an electromagnetic inspection technique used to detect wall loss without the need to contact the object of interest. On the contrary, this object of interest needs to be ferromagnetic, such as carbon steel and cast iron. PEC provides a relative volumetric measurement converted into an averaged thickness measurement based on the calibration area [3].

To generate and capture PEC, first, a magnetic field is created by an electrical current in the transmitter coils of the probe. This magnetic field is called “primary field” (Figure 2). It is unaffected by the presence of any non-conducting and non-magnetic material, so it can penetrate undisturbed through the cladding, the concrete insulation, silicate insulation, insulation with weather jacket or marine growth layers until it reaches the steel surface. In this way the carbon steel directly beneath the transmitter coil can be magnetized. Since the carbon steel is ferromagnetic (i.e. it has a high relative magnetic permeability) the steel is magnetized (Figure 2).

In the second phase of the measurement, the current in the transmitter coils is switched off and, as a consequence, the primary magnetic field collapses. This abrupt change of the magnetic field induces electrical eddy currents which are decaying over depth in the bulk of the material. If the

material is thinned compared to the reference, a stronger decay of the eddy currents occurs. Based on the amount of eddy currents, a secondary magnetic field is generated which reaches the receiver coils of the PEC probe and induces a voltage (Figure 2). The PEC instrument measures the magnitude of this voltage as a function of time, or else the decay rate and an advanced signal processing algorithm translates the electromagnetic signal into an average thickness reading over the footprint of the probe [4], [5].

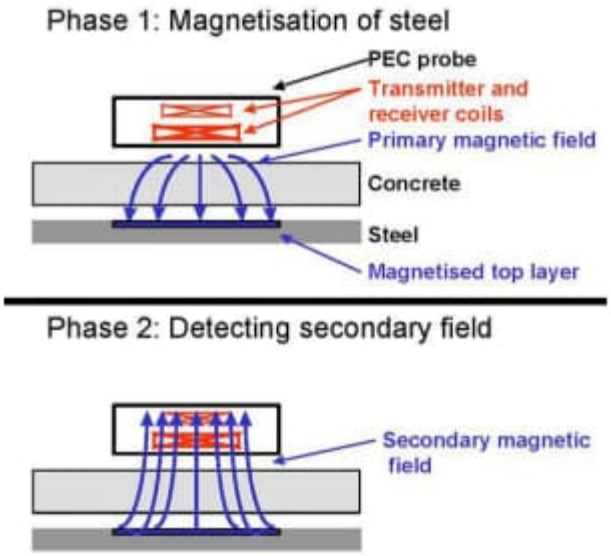

Figure 2 PEC principle

In order to address the feasibility of PEC to inspect corrosion in SCCPs, the current study is divided in two parts: a) commercially available PEC tools are identified and their technical specifications are defined b) the strengths and limitations of specific PEC probes are tested through specially designed and manufactured laboratory size specimens (mockups). Six mockups are built in total. The mockups replicate real pipe properties and include a steel liner and mesh. Mockups without mesh are also built for comparison purposes regarding interferences on the measurement results. Artificial defects are introduced in the steel liner of the mockups, in order to assess the detectability and the characterization potential of the technique.

The paper is, thus, organised as follows: Section 2 summarizes the experimental campaign (materials used, geometries, defects, test cases) and section 4 presents the results of the experiments. Section 5 provides the conclusions of the study.

2. MOCK-UP DESIGN

In order to evaluate the suitability of the most suitable single element PEC probes for corrosion detection of steel embedded in concrete, laboratory scale test specimens were produced mimicking the properties of real SCCP.

Steel plate

- Type: SS235JR
- Size: 500 mm x 500 mm
- Thickness: 4 mm
- Surface: scratches were introduced to 3 out of 6 plates to simulate roughness
- Defects: 2 different hole sizes and 2 different depths of perforation in steel for each Plate (see Figure 3).
  - o Φ25 mm – 1 & 2 mm deep &
  - o Φ50 mm – 1 & 2 mm deep or
  - o Φ75 mm – 1 & 2 mm deep &
  - o Φ100 mm – 1 & 2 mm deep

Steel mesh

Mesh (when present) is placed directly on steel liner and welded to keep the concrete in place during casting (mesh and liner are in contact). Mesh is made of B 500A steel (which is a common steel type for reinforcing steel mesh), with Φ5 mm diameter and 150 mm between individual bars.

Concrete mixture

- W/C: 0.43
- Cement: CEM I 52,5N-SR 3 CE PM NF
- Sand: 0/4
- Aggregates: 4/8 mm

Concrete cover

15 mm and 25 mm

Chlorides

Mixed-in: concentration 0.4 %. NaCl based on the mass of cement

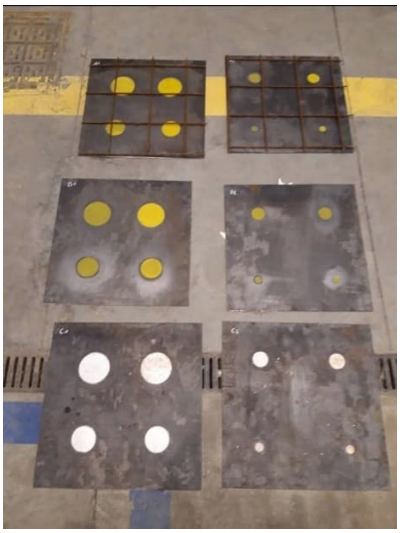

Figure 3 Presentation of the 6 mock-ups: steel liner, mesh (in 2 cases) and artificially induced defects. The defects in yellow are epoxy filled while the defects in white are polystyrene filled.

3. RESULTS

PEC analysis included the experimental study of different parameters. The following parameters were studied on the available mock-ups in an attempt to experimentally evaluate the technique (sensitivity/detection capabilities and limitations):

- Equipment brands
- Probe types
- Scanning resolution (grid size)
- Interferences (mesh, border effect)
- Lift off and misalignment

3.1. Eddyfi PEC 025 G2 vs. Maxwell small probe

Figure 4 presents the comparison of the probes with the smallest footprint of Maxwell and Eddyfi. Both probes are tested in the same mockup and with the same scanning grid (15 mm x 15 mm). The scanning with the Maxwell probe was complete, while the scanning with Eddyfi was only performed around the defects to reduce the volume of data.

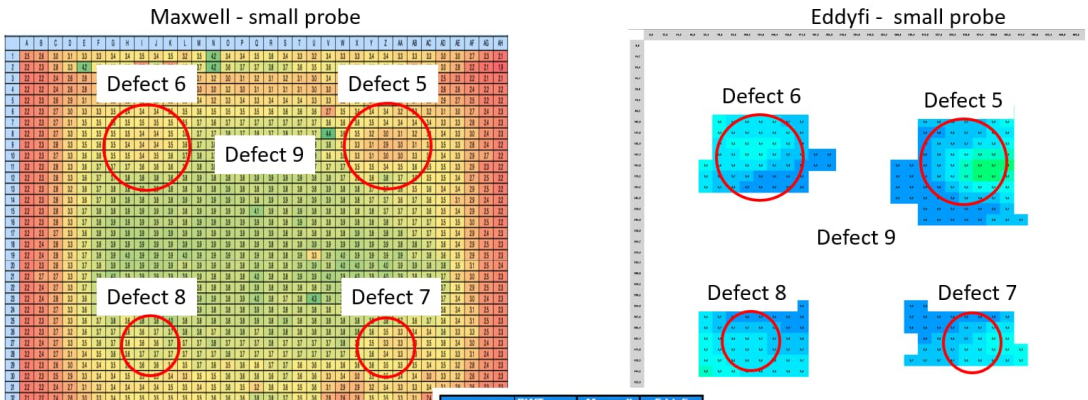

Defect no.	RWT (mm)	Maxwell (mm)	Eddyfi (mm)
5	2	2,9	3,1
6	3	3,4	3,4
7	2	3,3	3,5
8	3	3,6	3,6
9	3,9	4	4

Figure 4 Comparison of Eddyfi PEC 025 G2 and Maxwell small probe

As shown in Figure 4, despite the fact that the color palette is different, similar sensitivity to the defects was observed for both systems (see measured remaining wall thicknesses in the table of Figure 4) with a difference of +/- 0.2 mm (Maxwell probe being a little more sensitive). Defect 9 (scratches) should be considered not detectable. Similarly, defect 8 with nominal diameter 25 mm and 1 mm thickness loss should also be considered as non-detectable. Defect 7 with nominal diameter 25 mm and 2 mm thickness is barely detectable as also expected by the theoretical calculations. Defects 5 and 6 with nominal diameter 50 mm and 2mm/1mm thickness loss respectively are both detected but underestimated.

3.2. PEC 025-G2 (small) vs. PEC 089-G2 (medium probe)

The small (PEC 025-G2) and medium (PEC 089-G2) probes have different footprints and induce different powers. The footprint of the small probe for a concrete cover equal to 25 mm is 51.25 mm, while the one of the medium probe for the same concrete cover is 78.25 mm due to its coil size. For this reason and in order to compare the accuracy of the different sensors, the two probes are tested on the same mockup and with the same grid size (30mm x 30mm). As shown in Figure 5, the small probe is more accurate if we consider the complete map (defects, borders and defect free areas). When focusing on the medium probe, it is evident that the border effect is stronger (see around defects 5 & 6).

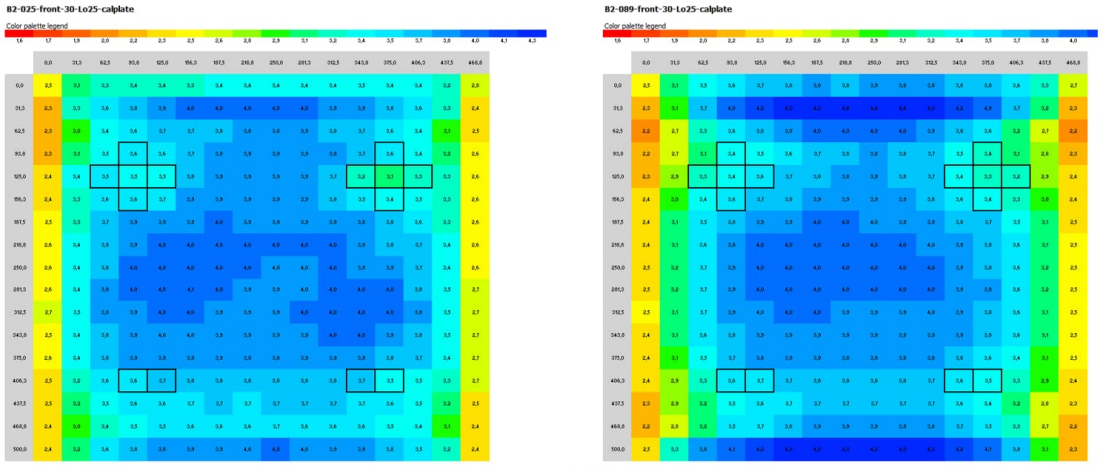

Defect no.	RWT (mm)	025 (mm)	089 (mm)
5	2	3,3	3,4
6	3	3,5	3,4
7	2	3,6	3,6
8	3	3,7	3,6

Figure 5 Comparison of small and medium Eddyfi probes

3.3. Fine vs. Coarse mesh

Two types of scanning grids were tested with the Eddyfi system in order to identify the optimal scanning resolution. The fine grid was made of 15 mm x 15 mm measuring points, while the coarser grid was 30 mm x 30 mm. In the fine grid case, scanning was only performed around the defects in order to reduce the volume of data. As shown in Figure 6, regardless of the size of the scanning grid, the averaged wall thickness values are similar, while the minimum values are the same with tolerance +/-0.1 mm. Generally, it can be concluded that the 30 mm x 30 mm is sufficient when scanning with the small probe, which is reasonable since the footprint size is larger (51.25mm)

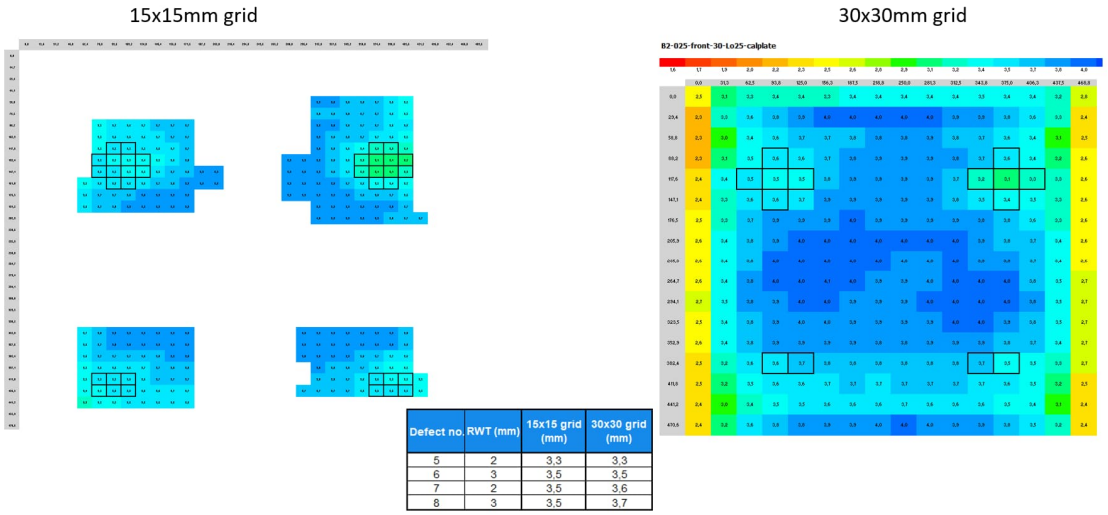

Defect no.	RWT (mm)	15x15 grid (mm)	30x30 grid (mm)
5	2	3,3	3,3
6	3	3,5	3,5
7	2	3,5	3,6
8	3	3,5	3,7

Figure 6 Comparison of fine and coarse meshes

3.4. Influence of mesh and borders

A known limitation of PEC is that plate edges affect the strength and flow of eddy currents. Therefore, readings taken at locations near or on the edges of a plate show a reduced thickness compared to the reference calibration (see Figure 7). With the defect features in these plates being quite close to the edges, the outlines of the defect features are sometimes lost in the imaging from the plate edge effects. Comparing the mockup with mesh with the one without mesh, the difference is obvious. In the second case the same defects are better detected, implying that the presence of mesh is significant (see Figure 7).

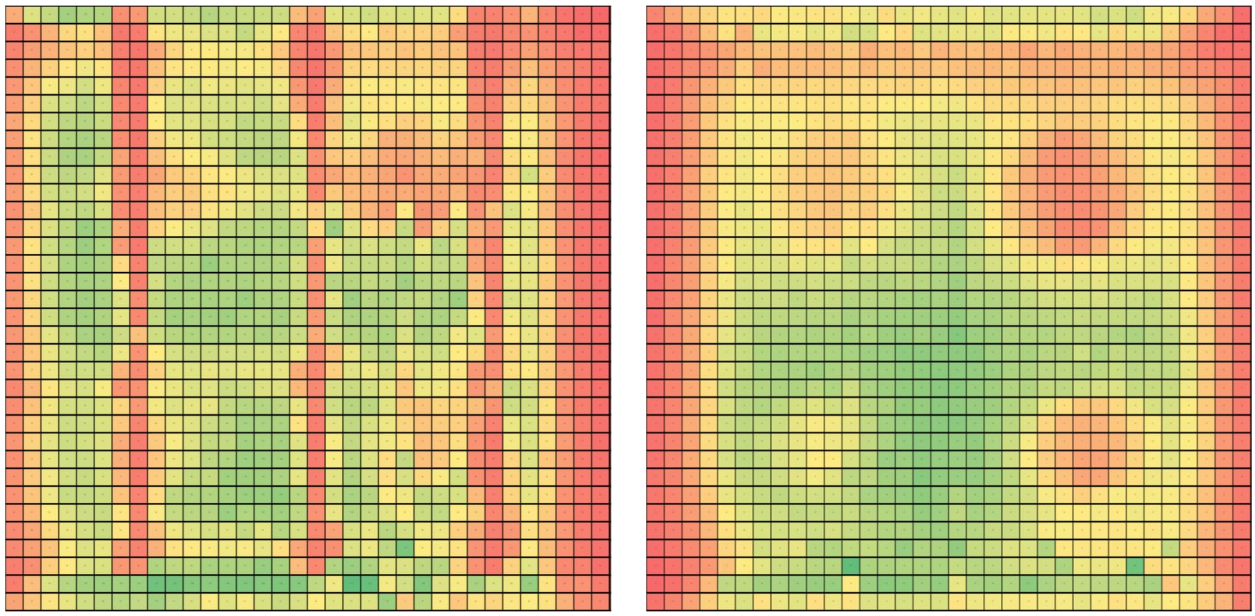

Figure 7 Influence of mesh and borders on PEC measurements

3.5. Influence of lift-off and misalignment

Figure 8 shows the results of the different applied lift-off (Lo). Generally, the sensitivity decreases with an increase in the lift-off. Same conclusions are drawn the more the PEC device is misaligned (see Figure 9).

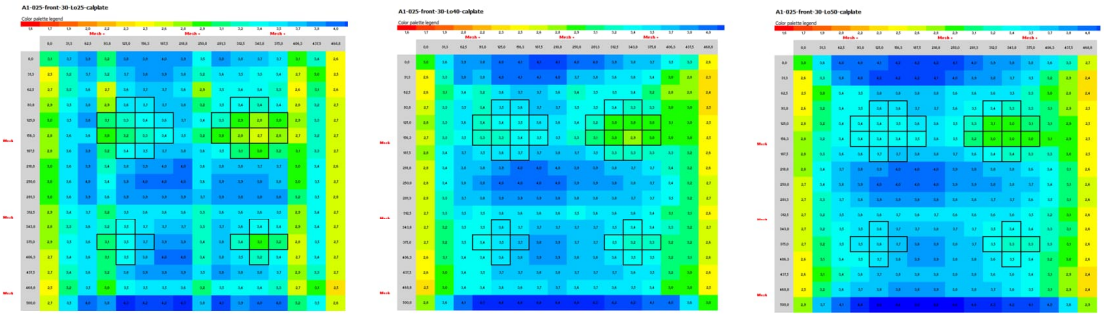

Defect no.	RWT (mm)	Lo 25 mm (mm)	Lo 40 mm (mm)	Lo 50 mm (mm)
1	2	3,0	3,1	3,2
2	3	3,4	3,5	3,5
3	2	3,2	3,4	3,4
4	3	3,4	3,6	3,6

Figure 8 Influence of lift-off on PEC measurements

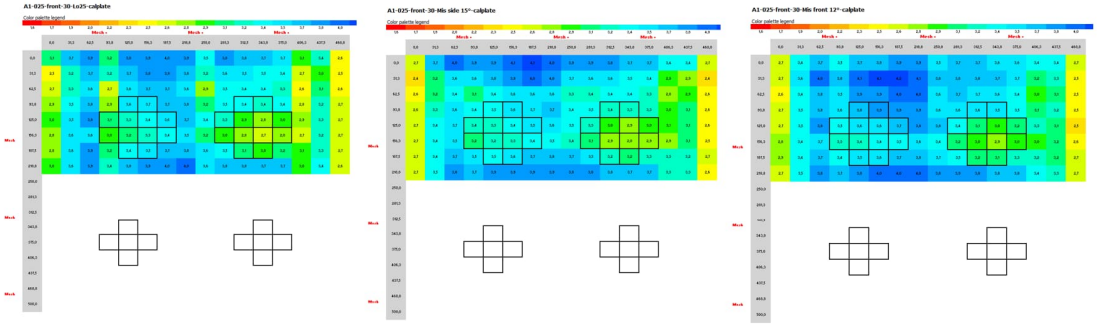

Defect no.	RWT (mm)	Lo 25 mm (mm)	Mis side 15°(mm)	Mis front 12°(mm)
1	2	3,0	3,1	3,2
2	3	3,4	3,4	3,6
3	2	/	/	/
4	3	/	/	/

Figure 9 Influence of misalignment on PEC measurements

4. CONCLUSIONS

In the current study, six mockups were designed and built. The mockups were replicating real pipe properties and included a steel liner and mesh. Mockups without mesh were also built for comparison purposes regarding interferences on the measurement results. Artificial defects were introduced in the steel liner of the mockups, in order to assess the detectability and the characterization potential of the technique. Four different sizes of defects were manufactured (100 mm, 75 mm, 50 mm and 25 mm diameter) with two different depths (1 mm and 2 mm). PEC assessment analysis included the experimental study of different parameters on the available mockups: equipment brands, probe types, interferences (mesh, border effect), lift-off and misalignment and scanning resolution (grid size). It was found that the systems of both manufacturers (Eddyfi and Maxwell) perform equally while small probes (i.e. small footprint) provide more accurate results compared to larger footprint probes. The presence of the mesh is influencing the results, causing local distortion of the signals and wrong interpretation of material thickness losses. The borders have an equally negative effect on the mapping of the remaining thicknesses, while depending on defect size and location, they show masking of these defects. Concerning lift-off and misalignment, it was found that the higher they are the lower the sensitivity. The comparison of the 15 mm x 15 mm scanning grid with the 30 mm x 30 mm grid showed similar averaged thickness values and equal minimal values considering a tolerance of +/-0.1 mm. The latter implies that a bigger scanning grid is possible to use in real applications, taking in too account the footprint size in each specific application. Concerning detectability it can be said that the minimum

detectable defect is a cylinder of 25 mm diameter and 2 mm depth, This defect equals approximately 25% of the footprint volume of the smallest probe available. A third generation of probes, which relies on array technology, is currently available on the market. The use of such probes in the future would improve the power while keeping a reduced footprint(=higher sensitivity).

ACKNOWLEDGEMENTS

This paper is submitted in the framework of the ACES project. The project has received funding from the Euratom research and training programme 2019-2020 under grant agreement No 900012. Laborelec thanks SOCEA Belgium for providing the raw materials for the creation of the mock-ups.

REFERENCES

[1] Broomfield, J.P. Corrosion of Steel in Concrete: Understanding, Investigation and Repair; CRC Press, 1996; ISBN 978-0-203-47528-7.

[2] Proceq SA Profometer - Operating Instructions Available online: https://www.screeningeagle.com/en/products/profometer-corrosion (accessed on 26 January 2022).

[3] Pulsed Eddy Current (PEC) Available online: https://www.eddyfi.com/en/technology/pulsed-eddy-current-pec (accessed on 11 March 2022).

[4] Pulsed Eddy Current Testing (PECT) Inspection Technique Available online: https://www.innospection.com/images/PDF/corrosion/Technology_-_Pulse_Eddy_Current_Testing_PECT_Technique-min.pdf (accessed on 11 March 2022).

[5] Robers, M.A.; Scottini, R. Pulsed Eddy Current in Corrosion Detection. NDT.net, The e-Journal of Nondestructive Testing 2002, 7.

Diagnostic of corrosion in liner embedded into concrete

Frederic Taillade[1]*, Fabrice Deby[2], Benoit Masson[3]
[1] EDF R&D, Chatou, FRANCE
[2] LMDC, Toulouse, FRANCE
[3] EDF DT, Lyon, FRANCE

*corresponding author: frederic.taillade@edf.fr

ABSTRACT

Nuclear Power Plants (NPP) use numerous concrete structures with embedded steel reinforcement and containment systems. Liners embedded in concrete serve as a barrier between the interior of the structure and the exterior environment to ensure leak tightness. Although concrete environment is particularly suitable for steel due to the alkaline nature that enables passivation of the steel surface, many corrosion processes take place in concrete structures, depending on the environmental conditions, geometry of the structure, the properties of concrete and the quality of construction.
The aim of this study is to provide basic information for the non-destructive inspection of the thick concrete structures and to detect the phenomenon of corrosion.

Keywords: corrosion, embedded liner, electrochemical potential

1. INTRODUCTION

Nuclear Power Plants (NPP) use numerous concrete structures with embedded steel reinforcement and containment systems. Liners embedded in concrete serve as a barrier between the interior of the structure and the exterior environment to ensure leak tightness. Although concrete environment is particularly suitable to protect the steel reinforcement due to the alkaline nature that enables passivation of the steel surface, many corrosion processes take place in concrete structures, depending on the environmental conditions and geometry of the structure.
A likely deterioration of embedded liners is due to a corrosion phenomenon. In the case of a deterioration of fully embedded liners (for example below of few tens centimeters of concrete, typically 70 cm), it isn't possible to examine directly the liner from the top of the concrete surface. In this case, the detection of the corroded area isn't easy with the common technics (guided waves, electrochemical potential…). Many nondestructive techniques (NDT) based on the measurement of the electrochemical potential, the electric resistivity, the guided waves propagation and acoustic emission are used to detect corrosion along the length of reinforced concrete [1-8]. Measuring the electrochemical potential of reinforcements in concrete is the most commonly used technique for detecting and locating areas of active corrosion in reinforced concrete structures [1-2]. However, this technique is usually used for the investigation of reinforcement embedded under a few centimeters of concrete (the cover concrete). The standard used in the scope of electrochemical corrosion measurement [1] defines the potential scale of the probability of corrosion. In our case (large thickness), this scale cannot be used to determine the probability of corrosion.

The aim of this study is to provide basic information for the nondestructive inspection of the thick concrete structure and to detect the phenomenon of corrosion.

This study will investigate inspection techniques to detect corrosion for liners embedded in concrete and to prove the efficiency of the electrochemical potential method. We have investigated only the nondestructive methods based on electrochemical potential measurement (Figure 1).

In this case, the detection of the corroded area isn't easy with the common techniques (guided waves, electrochemical potential…). The aim of this study is to provide basic information for the

nondestructive inspection of the thick concrete structure from the surface and to detect the phenomenon of corrosion.
However, this technique is usually used for on site evaluation of reinforcement embedded under a few centimeters of concrete (the cover concrete).

This paper will investigate inspection techniques to detect corrosion for liners embedded in concrete. We focus on the nondestructive methods based on electrochemical potential measurement. Simulations and experimental measurements are compared.

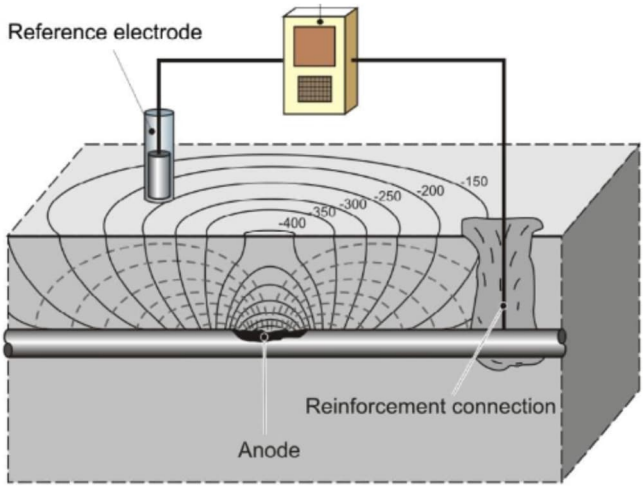

Figure 1. Electrochemical potential method [11]

2. SIMULATIONS

2.1 FINITE ELEMENT MODEL USED

To assist in the interpretation of this type of measurement in the context of the embedded liner in concrete, a finite element numerical modeling is proposed [10]. The selected modeling of the corrosion phenomenon of steel in concrete is based on the electrokinetic equations: charge conservation and local Ohm's law, coupled with specific boundary conditions, the Butler-Volmer relationship (BV).

Charge conservation equation: $\nabla i = 0$
Local Ohm's law: $i = -\frac{1}{\rho}\nabla E$
Butler-Volmer relationship: $i = i_{corr}\left[exp\left(\frac{E-E_{corr}}{\beta_a}\right) - exp\left(\frac{E-E_{corr}}{\beta_c}\right)\right]$

The conditions limits consist in taking into account the existence of nonlinear conditions at the level of the steel / concrete interface which translate the complex relations between the current density i which crosses the interface and the associated polarizations compared to its free potential E_{corr} (V). This E_{corr} corrosion potential constitutes an equilibrium potential of an anodic and cathodic reaction resulting from a uniform corrosion system. The corrosion of steel in concrete results from the electrolytic contact of 2 reversible electrodes defined by the following equations:

- Electrode 1: $Fe \leftrightarrows Fe^{2+} + 2e^-$
- Electrode 2: $2OH^- \leftrightarrows 1/2O_2 + H_2O + 2e^-$

The uniformity here results from the fact that the electrode 2 is present in dissolved form in the electrolyte (concrete) in contact with the steel. It can thus be assumed that electrode 2 is present everywhere on the surface of electrode 1. Corrosion appears because the anodic and cathodic reactions do not relate to the oxidized and reduced forms of the same electrode. Thus, the electrons released by the dissolution of iron are consumed to reduce oxygen and produce OH^- ions. The value of E_{corr} is conditioned by the balance between the anode current produced by electrode 1 and the

cathode current produced by electrode 2. This condition defines a unique E_{corr} solution. At equilibrium, the anodic current density (opposite to the cathodic current density) defines the corrosion
current density i_{corr} (A / m²).

It is then possible to define the BV equation of the uniform corrosion system. This equation is a electrochemical constitutive law that describes the response of the uniform corrosion system to an imposed polarization with respect to its free potential E_{corr}. The BV relationship is parameterized by the anodic β_a and cathodic β_c (V / Decade). All the parameters of the BV relationship used in this study are summarized in Table 1. Two distinct sets of parameters are used to distinguish the active or passive behavior of a steel.

Table 1 Butler-Volmer parameters implemented at the rebar/concrete interface for steady-state simulation

Parameters	**Corroded area**	**Not corroded area**
E_{corr} (V/Ref)	-0.6	-0.1
i_{corr} (A/m²)	0.01	0.0001
β_a (V/Decade)	0.04	1.00
β_c (V/Decade)	0.2	

The geometry used to describe the physical problem is shown on Figure 2. A slab of raft 10 meters long and 5 meters wide is used for this study. A thickness of 70 centimeters is used. The planar dimensions of the raft are taken sufficiently large in order to limit the side effects in the propagation of the corrosion current without modeling the entire raft. The length 10 m will also make it possible to check over which length the variations in potential remain measurable. The reinforcement network corresponds to 3 layers of steel, each consisting of 2 beds with a diameter of 20 mm. A first layer is positioned 10 cm from the surface of the raft, a second in the middle and the third 10 cm from the bottom, in accordance with the indications of reinforcement provided, the frame of each layer being 20 × 10 cm. Only part of these 3 layers is modeled in order to limit the complexity of the geometric model without losing precision. The density of the reinforcement around the corrosion zones which are going to be created is sufficiently important effect so that the ratio anodic surface / cathodic surface is not impacted in calculations.

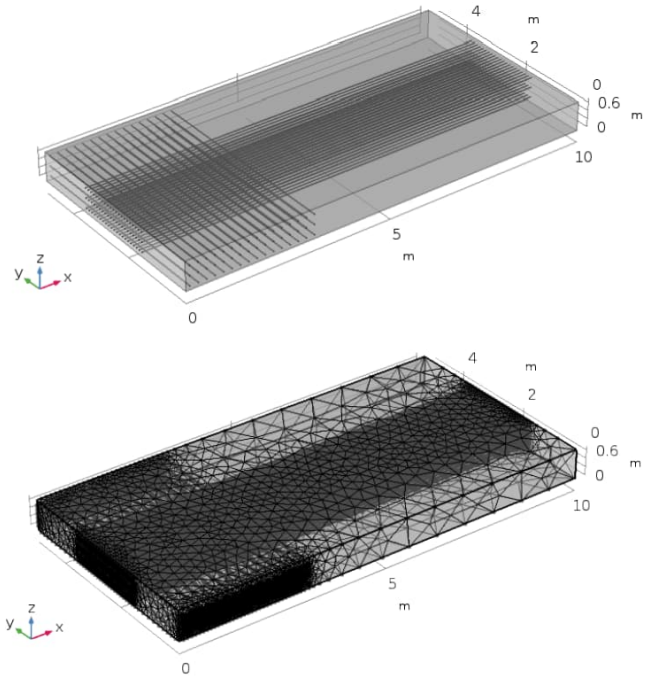

Figure 2. Geometry of the model and mesh

2.1 FINITE ELEMENT RESULTS

We considered a realistic case with the corrosion of the liner and/or the first rebar frames. Liner and rebars are considered electrically connected. In the case of the first rebar frames is corroded, the Figure 3a shows a potential mapping. The electric resistivity of concrete impacts the electric potential profile as shown in the Figure 3b.
Other corrosion scenarios are considered. Figure 4 compares the electrical profiles depending on the case considered: (i) first rebar frames corroded (blue line), (ii) liner corroded (orange line), (iii) first rebar frames and liner corroded (green line). The risk is therefore that a corrosion spot on the reinforcement, even a small one, will mask the signal returned by a corroded area on the liner.

Finally, the analysis of the electric potential measurements must take into account the value of the potentials themselves but also the potential profiles and in particular the full width at half maximum (FWHM) to detect corrosion of the liner. However, between the two cases, rebar corroded case and rebar and liner corroded case, we notice that the FWHM is not so different.

The results of simulations demonstrate the possibility to detect the corrosion using the electrochemical potential method. However, the potential gradient between a healthy and a faulty liner corroded region is low of the order of 70mV (generally, the potential gradient is of the order 300mV). These simulation studies confirm that the standard corrosion probability scale cannot be used in the case of thick concrete. Moreover, the analysis of the electric potential gradient (FWHM) enables one to detect the corrosion activity on liner. It is of the order 1 or 2 meters in the case of corroded liner and smaller in the case of corroded rebar frames.

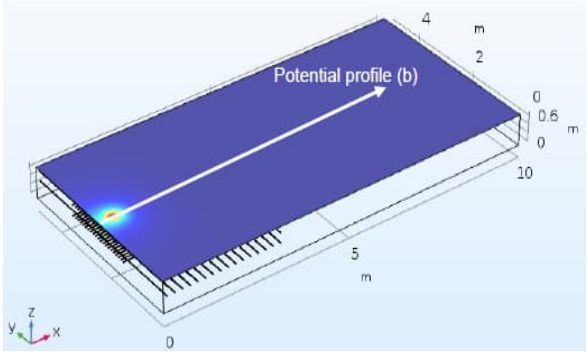

a) potential mapping in the electric resistivity of concrete case equal to 500 Ω.m

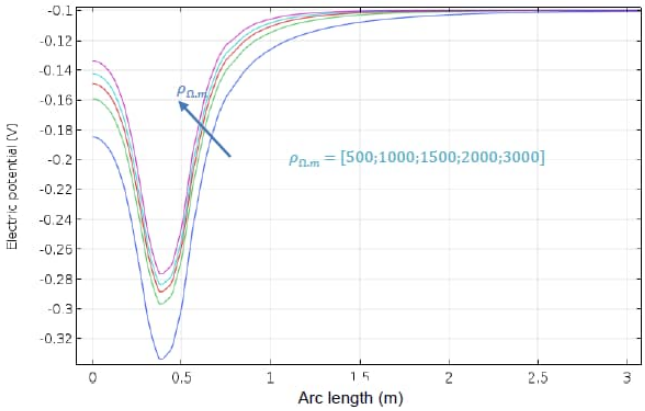

b) potential profile of figure a)

Figure 3. first rebar frame corroded and electrically connected to liner and other rebar frames healthy (corrosion length 20 cm; electric resistivity of concrete between 500 and 3000 Ω.m)

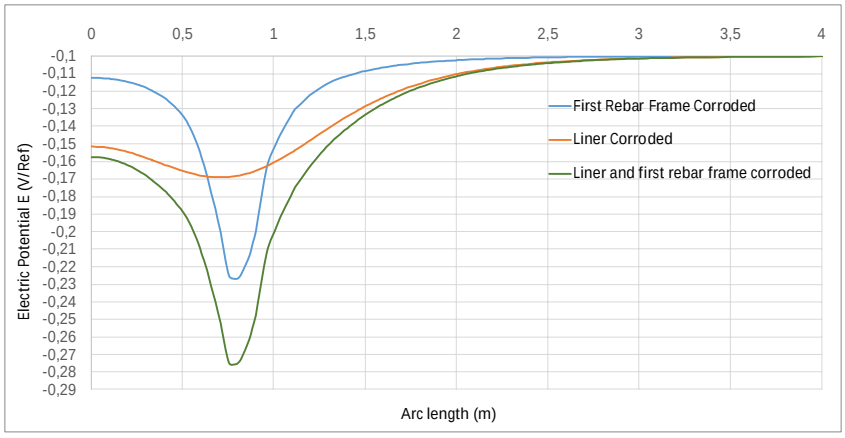

Figure 4. first rebar frame and liner corroded and electrically connected (corrosion length of rebar 5 cm and corrosion liner size 50x50cm; electric resistivity of concrete 500 Ω.m)

3. EXPERIMENTATIONS

3.1 MOCK-UP

To perform the study, a mock-up, representative of a real raft was built (Figure 5). This large mock-up (3.0 x 3.0 x 0.75 m3) built with 4 corroded representative areas: i) reference area, ii) only liner corroded, iii) first rebar frame corroded, iv) first rebar frame and liner corroded one above the other. The mock-up is made of concrete with 3 layers of reinforcement network with each layer consisting of 2 beds with a diameter of 20 mm. A steel liner (6 mm thickness) is embedded in concrete (75 cm thickness). A first layer is positioned 8 cm from the surface of the raft, a second in the middle and the third 10 cm from the bottom, the frame of each layer being 20 × 10 cm.
To produce the corrosion, we have chosen to use a salt water mixture (10 g/L concentration). To initiate a corrosion, an electric potential difference (30V) is applied between a stainless cathode in chlorides catholyte mixture and liner or rebars that we want to corrode. However, to accelerate the formation of the corrosion and control the size of the anodic zone, in particular of the liner embedded into a concrete depth of 75 cm, we have developed a system where the catholyte mixture is brought close to the liner and rebars thanks to duct embedded into concrete. The duct is filled with the mixture and the extremity of the duct is located at 5 cm of the liner or rebars. The extremity of duct is terminated by a porous material.

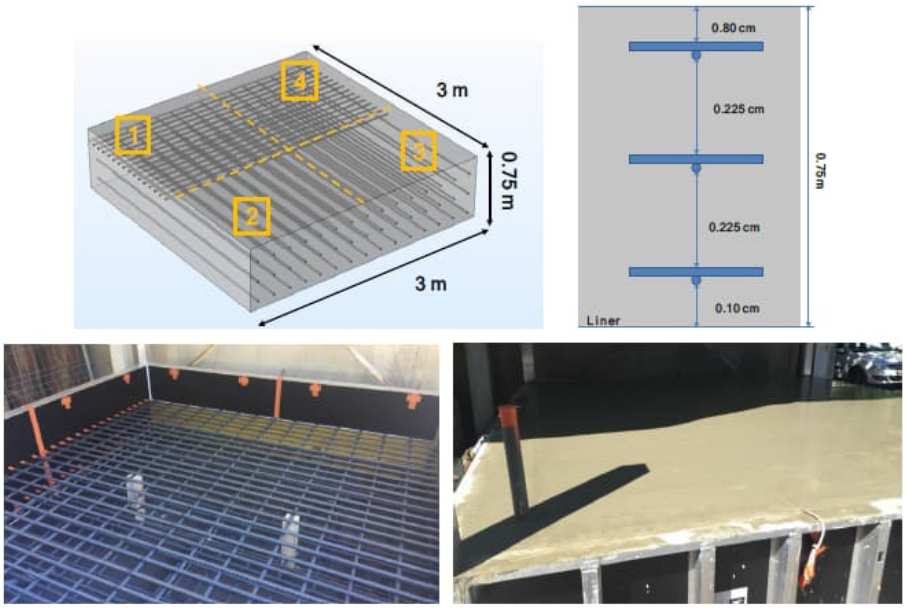

Figure 5. scheme of a large mock-up of a raft with liner embedded into concrete and four corroded areas

3.2 RESULTS

The Figure 6 shows the different potential maps measured. The first map is the reference potential map before the corrosion started (Figure 6a). The potential mean is of the order of -140 mV. After 3 weeks of applying a potential difference between steel and cathode into mixture, the corrosion started (Figure 6b). The red color shows the spot corrosion onto the first rebar frames. The corrosion due to the first frame of rebars corroded is clearly visible on the right figures (areas 3 and 4). On the area 4, where the liner is corroded too, the electronegative potential is lower (in absolute value) than the area 3 where there is just the rebars corroded. Based on the simulation results, the potential should be more electro-negative when the liner and rebars are corroded. On the corroded liner area (area 2), it is more complicated to prove the corrosion is started. Nevertheless, we notice a decrease of the potential on a large area around the area 2. After reactivating corrosion for 13 days (Figure 6c), the potential map has hardly changed. Finally, a last measurement campaign is realized after reactivating corrosion for 4 days (Figure 6c). The potential map shows a decreasing of potential into area 2 of the order of -200 mV corresponding to the liner corroded. The difference of the potential amplitudes between healthy and faulty (areas 1 and 2 respectively), of the order -60 mV is in good agreement with the simulation results (-70 mV in simulation).

Two potential profiles along the vertical lines of corrosion areas show the spatial range of potential at different dates of measures (Figure 7). We plot the potential mean (dotted line area) versus the position on the mock-up (see black arrows on Figure 6d). On the profile around area 2 (Figure 7a), we can measure the FWHM of the potential which is in range 50 cm and 1 m. On the profile around areas 3 and 4 (Figure 7b), the FWHM of the potential which is of the order of 40 cm. These experimental results are in good agreement with the simulation results (Figure 4).

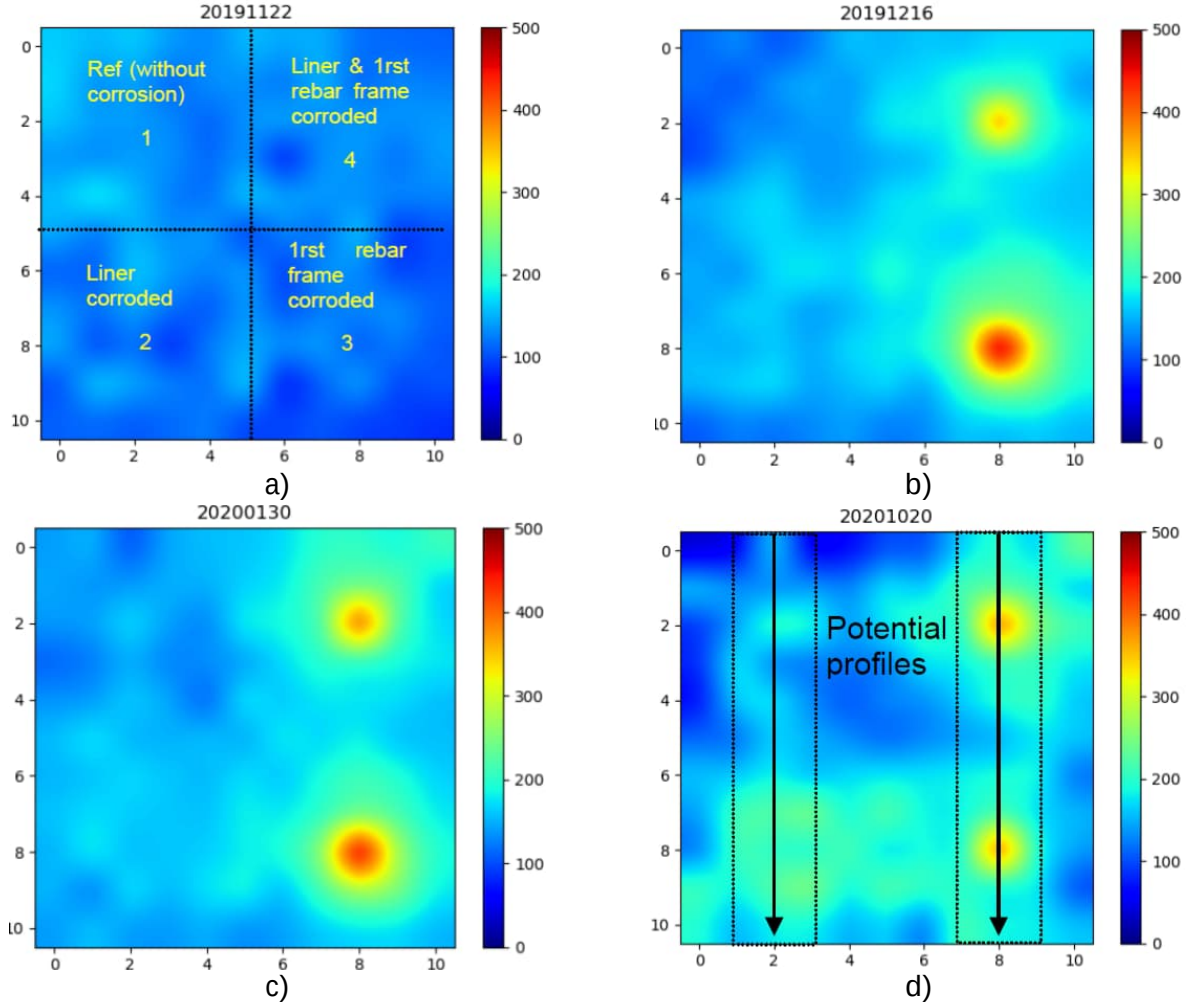

Figure 6. electrochemical potential maps (Cu/CuSO4 in -mV) at different dates

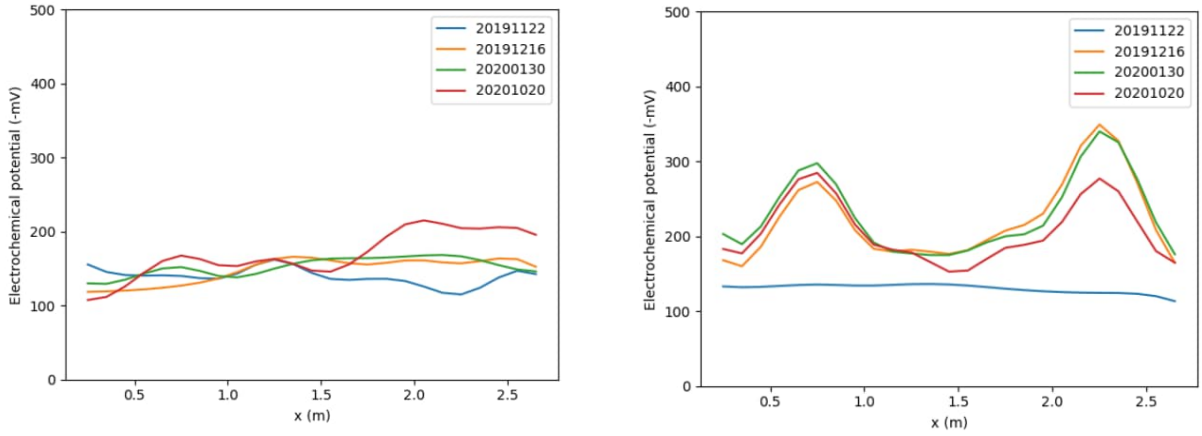

a) potential profile around areas 1 and 2

b) potential profile around areas 3 and 4

Figure 7. electrochemical profile (Cu/CuSO4 in -mV) at different dates

4. CONCLUSION

Among the existing corrosion diagnostic techniques, the measurement of the corrosion potential using a reference electrode is one of the simplest techniques in order to localize probably active corrosion areas. The use of these measured potentials in terms of absolute values is not a consensus in the scientific community which agree to work more on the gradients at the concrete surface. For massive concrete structures almost one meter thick, the investigation of the liner by the upper surface of the concrete raises questions about the technique's ability to identify potential gradients on the surface.

To tackle these issues, the study initially focused on a 3D finite element model. The simulations consider the complex geometry with several reinforcement layers and the liner at the bottom. In the same way, it allows to vary the electrical resistivity of the concrete which is a key parameter in the detection of potential gradients. Corrosion can also occur at different locations on these layers or the liner. Different scenarios are studied and the numerical results show the possibility to detect the corrosion of the liner thanks to the measurement of the electric potential from the surface (even with a concrete thickness of the order of 70 cm).

A large realistic mock-up (3.0 x 3.0 x 0.8 m) was built to compare the numerical results. The experimental results show that corrosion of the liner is effectively detectable from the concrete surface over significant thicknesses. The corrosion of the liner induces a greater extent of electronegative potential than in the case of the corrosion of the first reinforcement frame.

ACKNOWLEDGEMENTS

This work was carried out in the framework of the joint research team Exigence between EDF and LMDC labs.

REFERENCES

[1] ASTM C876-91(1999). Standard Test Method for Half-Cell Potentials of Uncoated Reinforcing Steel in Concrete

[2] RILEM TC 154-EMC. (2003). Half-cell Potential Measurements – Potential Mapping on Reinforced Concrete Structures. Mater. Struct., 36(7), 461-471

[3] Elsener, B., Andrade, C., Gulikers, J., Polder, R., & Raupach, M. (2003). Hall-cell potential measurements—Potential mapping on reinforced concrete structures. Materials and Structures, 36(7), 461-471.

[4] Patent US 2014/0210494 (A1) ELECTRICAL METHODS AND SYSTEMS FOR CONCRETE TESTING

[5] G. Samson, F. Deby, J.-L. Garciaz, M. Lassoued, An alternative method to measure corrosion rate of reinforced concrete structures An alternative method to measure corrosion rate of reinforced concrete structures, Cement and Concrete Composites 112 (2020) 103672

[6] S. Laurens F. Deby, Chapter 5 - Electrochemical Methods in book Non-Destructive Testing and Evaluation of Civil Engineering Structures 2018, Pages 173-197, ISTE Press Ltd 2018 Jean-Paul Balayssac and Vincent Garnier

[7] G. Samson, F. Deby, J.-L. Garciaz, J.-L. Perrin, F. Taillade, A. Boule, Numerical modelling and experimental investigations for corrosion state assessment of reinforced concrete structure with the DIAMOND probe, TINCE 2018 – Technological Innovations in Nuclear Civil Engineering, France, Paris-Saclay – 2018, August 29-31

[8] G. Samson, F. Deby, J.-L. Garciaz, J.-L. Perrin, New methodology for concrete resistivity assessment using the instantaneous polarization response of its metal reinforcement framework, Construction and Building Materials 187 (2018) 531–544

[9] K. Reichling, Method to determine electrochemical potential gradients without reinforcement connection in concrete structures", Cement & Concrete Composites, 4, p.3-8, 2014

[10] S. Garcia and F. Deby, Numerical and experimental development of gradient potential measurement for corrosion detection in reinforced concrete, Service Life and Durability of Reinforced Concrete Structures, RILEM Bookseries, Volume 17, 2019, Pages 71-86

Monitoring of the hydration of Portland concrete using embedded resistivity sensors: validation with modelling

Marie-Ange Eid[1,2,*], Jack Atallah[2], Géraldine Villain[1], Stéphanie Bonnet[2], Harifidy Ranaivomanana[2], Sérgio Palma Lopes[3] and François Bignonnet[2]

[1] Univ Gustave Eiffel, MAST-LAMES, Campus de Nantes, F-44344 Bouguenais
[2] Nantes Université, Ecole Centrale Nantes, CNRS, GeM, UMR 6183, F-44600 Saint Nazaire
[3] Univ Gustave Eiffel, GERS-GEOEND, Campus de Nantes, F-44344 Bouguenais

ABSTRACT

Reinforced concrete structures exposed to aggressive environments, such as nuclear and offshore structures, may be subjected to several hydric and ionic transfers that can affect their service life as well as their long-term durability. This type of structures may be sometimes difficult to access for inspection, thus several Non-Destructive testing Techniques (NDT) were developed in order to monitor and to assess such concrete structures.
The work presented in this paper consisted on studying the evolution of the hydration phase of cylindrical concrete specimens (11x18 cm^2) formulated with CEM I, by evaluating the electrical resistivity over time and depth using embedded resistivity sensors connected to a resistivity meter. Resistivity profiles obtained using these embedded sensors were compared to surface resistivity measurements carried out using a Wenner device, showing the capacity of the two techniques to assess the setting and hydration phase of concrete. Moreover, this experimental campaign was validated by numerical hydration modelling, showing a clear correlation between the experimental results and the hydration coefficient of concrete calculated using 3 different models.

Keywords: monitoring, resistivity, hydration degree, modelling

1. INTRODUCTION

Endogenous and exogenous attacks to which concrete structures can be subjected represent a major concern in the evaluation of the durability of these structures and their long-term performance. Destructive testing by local sampling of cores is not recommended for some types of structures such as offshore structures that can be subjected to the penetration of several aggressive agents (in particular chloride ions), and nuclear plants built as well in marine environments and whose required thickness must be large enough to ensure a good sealing. A major problem with this kind of structures is that they are sometimes difficult to access for inspection, especially when it affects human security. Thus, several Non-Destructive Evaluation (NDE) techniques were developed in order to carry out a specific diagnosis of structures exposed to aggressive environments [1]. The work presented below is carried out within the DEMCOM French project which pays particular attention to the durability and NDE of maritime structures, of which tidal zones may be inaccessible for inspection. One of the main causes of degradation of these structures is the corrosion of reinforcement bars due to the penetration of chloride ions from seawater. The penetration of chloride is related to the durability properties of concrete such as the chloride diffusion coefficient. This property depends on the hydration of concrete as it governs the hydrated phases, the open porosity and the composition of the poral solution [2].

In the work presented below, the evolution of the hydration phase of concrete is monitored using embedded resistivity sensors developed by Badr et. al [3], that enable to evaluate resistivity profiles over time and over the entire thickness of the structure. The electrical resistivity of a material describes its ability to resist the flow of electric current, and is highly sensitive to water and chloride contents in concrete [4-5]. The Printed Circuit Board (PCB) sensor used in this work provides a good

*Marie-Ange Eid: +33 (0)2 40 84 59 27, marie-ange.eid@univ-eiffel.fr

estimation of resistivity profiles and enables to study the gradient of the degree of saturation during the drying cycles of concrete [3].

The first part of this paper presents the experimental campaign (formulation of concrete, instrumentation with the PCB resistivity sensors and conditioning of the samples). In the second part, we report and discuss the results of the monitoring of the hydration phase, which are compared with hydration numerical modelling. This work will allow us to assess the capacity of electrical methods to follow the evolution of the hydration phase of concrete.

2. EXPERIMENTAL CAMPAIGN

2.1. Formulation of concrete

The aim of the experimental campaign is to study the behaviour of a Portland cement concrete during its hydration phase. The corresponding formulation is presented in Table 1 [6].

Table 1: Formulation of concrete

Components	kg/m^3
Gravel, 4-12 mm (Boulonnais)	1041.7
Sand, 0-4 mm (Boulonnais)	910.3
CEM I 52,5 N - SR 5 CE PM-CP2 NF HTS (Lafarge)	302.5
Superplasticizer MasterGlenium 201 (BASF)	2.94
Efficient water (Weff)	151.7
Efficient water-to-binder ratio (Weff/B)	0.5

2.2. Methods and instruments

Three cylindrical specimens with a diameter of 11 cm and a height of 18 cm were cast for the studied concrete formulation (Table 1), and were instrumented with a PCB resistivity sensor which has a ladder shape and is composed of 15 electrodes distributed on both sides of the PCB. The latter is placed at the centre of the specimen along its z axis (representing the thickness of the concrete sample), between two metal grids well anchored in concrete and serving for current injection [3] (Figure 1).

During the monitoring, one instrumented specimen is connected to a commercial resistivity meter: a Syscal Junior Switch 72 (from IRIS Instruments), that manages simultaneously up to 72 electrodes and injects an alternating current of very low frequency. The measurements were made according to the Transmission mode (Trans) [3]: an electric current is injected between two metal grids, and the potential drop is measured between two consecutive electrodes on the same side of the PCB. An additional measurement is made according to the Wenner configuration (Wen) by injecting a current and measuring the potential drop on 4 electrodes on one side of the PCB without using the grids [3].

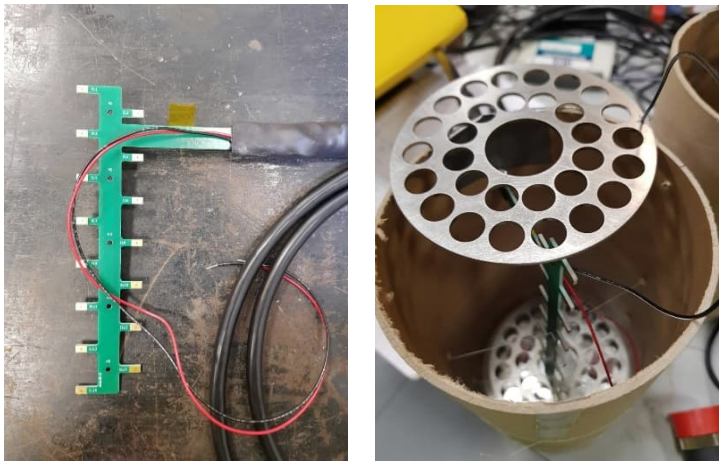

Figure 1: (a) PCB resistivity sensor with 15 electrodes, (b) instrumented mould before casting of concrete.

Moreover, 15 non-instrumented cylindrical specimens with a diameter of 11 cm and a height of 22 cm were cast and served for surface measurements using a Resipod Proceq device which operates in the Wenner configuration, and is therefore referred to as the surface Wenner device throughout this paper. The spacing between the electrodes is of 5 cm and the measurements were made along the lateral surface at mid height of the specimens. These measurements are made at different times of the curing period and are compared to the results obtained using the embedded sensors.

2.3. Curing of the specimens

The conditioning of the concrete specimens during the monitoring consisted on placing them in a tray containing a small quantity of water at a temperature of 20°C and a relative humidity of 95%. These conditions were regularly controlled using a thermo hygrometric (THR) probe along the period of cure. The latter lasted for 90 days instead of 28 days in order to allow a near stabilization of the hydration degree. Note that the period of cure was similar for both the instrumented and non-instrumented concrete specimens.

3. RESULTS AND DISCUSSION

3.1. Evolution of the apparent resistivity during the hydration phase

This part of the paper presents the results of the evolution of the apparent resistivity of concrete along its period of cure. Note that the observable measured in this experimental campaign corresponds to the apparent resistivity (ρa) given the heterogeneity of concrete (presence of water content gradients). The graph in Figure 2 shows a comparison between the apparent resistivity values obtained with the PCB embedded sensor (for both Trans and Wen configurations) and those obtained using the surface Wenner device. For surface measurements, the apparent resistivity value presented in this graph represents the average value of 15 measurements performed on each of the 15 specimens. Meanwhile, for the PCB_Trans configuration, the corresponding resistivity value represents the average value of 13 measurements obtained along the z axis, and the error bars represent ± the corresponding standard deviation.

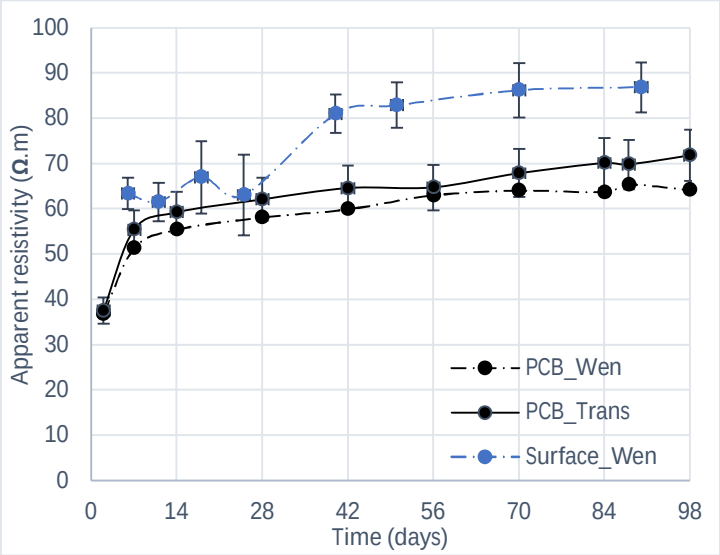

Figure 2: Evolution of the apparent resistivities obtained with the PCB sensor (Wen and average Trans) and the surface Wenner device with respect to time.

First of all, we can notice that the apparent resistivity values measured with the PCB sensor exhibit very similar magnitudes at all times for both configurations (Trans and Wen). The consistency between the two configurations was expected and validates the accurate response of the PCB sensor [3]. The apparent resistivity starts with a value of 35 Ω.m at a very young age (Tc+2 days, with Tc representing the casting time). It increases quickly during the first 28 days of cure to reach a value of 60 Ω.m. Beyond Tc+28 days, this value increases very slowly until it stabilizes approximately at 70 Ω.m at Tc+70 days. The increase in the apparent resistivity at young age and its near stabilization at Tc+70 days allow us to assess the setting and hydration phase of the concrete along its curing period.

The apparent resistivity values obtained using the surface Wenner device appear to be higher than those obtained with the PCB sensor. For example, at young age (Tc+6 days), the apparent resistivity starts with a value of 65 Ω.m. It does not seem to increase during the first 28 days of cure, although some large uncertainty bars may partly hide the real trend. Then it starts to increase until it stabilizes at 86 Ω.m. Let us note that the rate of increase is quite similar for both surface and embedded measurements from Tc+40 to Tc+86 days. We explain these differences in apparent resistivity magnitudes by the difference between the two measurement techniques, including the fact that surface measurements are more prone to variations in electrical contact quality than embedded measurements (therefore the larger uncertainty bars), as well as the fact that the samples and the observation times are not the same for both datasets. However, we can notice that the two types of curves are globally consistent, showing a similar trend for both embedded PCB and surface Wenner measurements. Thus, we believe that our experimental resistivity monitoring can be a good proxy for the hydration phase of concrete, yet the comparison between the two resistivity techniques remains qualitative in order to validate the response of the PCB sensors during the hydration phase. That is why, only resistivity measurements obtained with the PCB sensors will be compared to numerical modelling, which was the major aim of this paper.

3.2. Comparison of experimental results with numerical hydration modelling

The results obtained in the experimental campaign are compared to numerical hydration modelling, in order to validate the capacity of the electrical measurements in showing the evolution of the hydration phase of concrete. That is why, the graphs in Figure 3 show a comparison between the apparent resistivity measured experimentally and the hydration degree obtained numerically by 3 different models: VCCTL [7], Avrami's equations [14] and Bernard et al. (2003) [15]. These 3 models are widely used in literature, therefore considered as reliable models to describe the hydration degree variation in function of time.

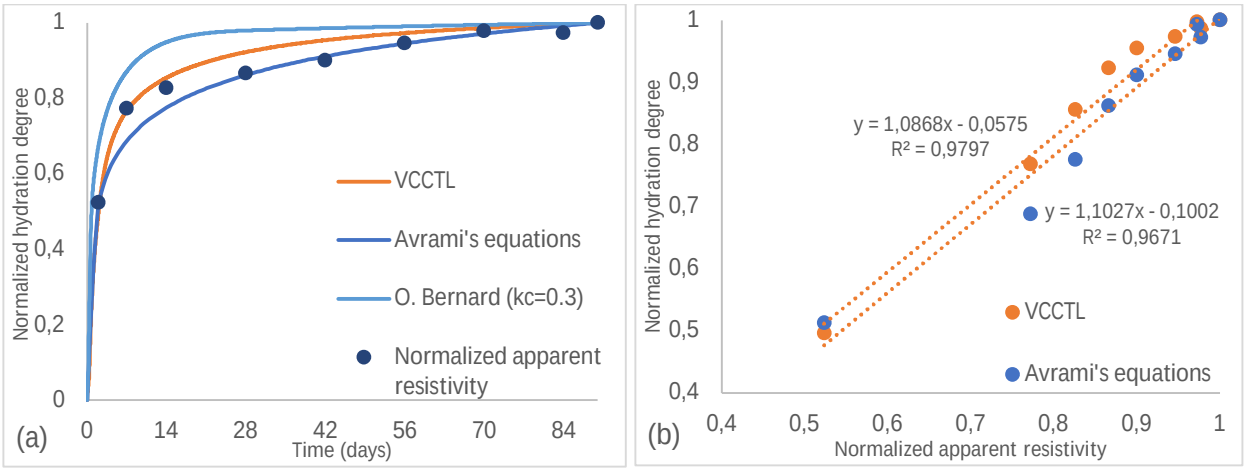

Figure 3: (a) Evolution of the normalized hydration degree and normalized apparent resistivity over time, (b) normalized hydration degree versus normalized apparent resistivity.

First of all, the Virtual Cement and Concrete Testing Laboratory (VCCTL) [7] is a virtual laboratory software based on the CEMHYD3D system where cement paste and concrete materials are computed in a virtual environment allowing the creation, hydration and estimation of the 3D cement material microstructure [8-12]. On the other hand, Avrami's equations [13- 14] are best adapted to explain nucleation and growth events established empirically. They are used as an approximation for all Portland cements; as they are expected to react at similar relative rates. These equations present a basic kinetic model that provides acceptable fits for hydrated pastes. The third model used in this work is that of Bernard et al. [15] which is a multi-phasic kinetic model that describes the variation rates of each clinker phase hydration, by kinetics laws that link the reaction rate with the chemical affinity. It is determined according to three processes: the dissolution of the phases, their nucleation and growth-controlled hydration and the diffusion of dissolved ions.

In order to provide a clear comparison while comparing the experimental results to those of the hydration modelling, both the hydration degree and the apparent resistivity (PCB_Trans) were normalized to their 90 days prediction and measured value respectively. Figure 3a shows the evolution of the normalized hydration degree and the normalized apparent resistivity during the period of cure. We can clearly observe the high correlation between the experimental and numerical data, confirming the capacity of resistivity measurements to follow the evolution of the hydration phase. Moreover, Figure 3b further validates the results above, showing a linear correlation between the normalized hydration degree (for VCCTL and Avrami's equations) and the normalized apparent resistivity.

4. CONCLUSION

The aim of the present paper is to study the hydration phase of concrete, experimentally by measuring apparent resistivities using embedded resistivity sensors, and numerically by calculating the hydration degree using 3 different models.

The experimental campaign consisted on studying the evolution of apparent resistivities measured in a Portland cement concrete during its hydration phase, using embedded resistivity sensors. Results show that the apparent resistivity increases quickly at young age of concrete, and almost stabilizes after 70 days of cure. Resistivity profiles obtained using the PCB embedded sensors were compared to surface measurements using a commercial Wenner device. Overall, both techniques were able to monitor the hydration phase of concrete, and the curves were almost close with small differences in resistivity magnitudes. Moreover, the experimental results were compared to a numerical hydration modelling using 3 different models. A clear coherence between the experimental and numerical curves was observed, showing a linear correlation between the relative hydration degree and the normalized apparent resistivity.

In the near future, a similar study will be conducted on concrete formulated with slag, a mineral addition that is particularly used in marine environments. Moreover, a diffusion campaign will be carried out in order to provide further information regarding the effect of chloride penetration on the electrical resistivity of concrete.

ACKNOWLEDGEMENTS

The authors would like to thank the French “Agence Nationale de la Recherche” for the financial support of the project ANR-20-CE22-0008-01 DEMCOM. We are also grateful to Jean-Luc Geffard from Univ Gustave Eiffel and Denis Fournol from Nantes Université for the technical support they provided.

REFERENCES

[1] Torres-Luque, M., Bastidas-Arteaga, E., Schoefs, F., Sánchez-Silva, M., & Osma, J. F. (2014). Non-destructive methods for measuring chloride ingress into concrete: State-of-the-art and future challenges. *Construction and building materials*, *68*, 68-81.

[2] El Achrafi, M. (2022). *Détermination des indicateurs de durabilité du béton en utilisant des observables d'évaluation non destructives : application aux ouvrages maritimes* (Doctoral dissertation, Nantes).

[3] Badr, J., Fargier, Y., Palma-Lopes, S., Deby, F., Balayssac, J. P., Delepine-Lesoille, S., ... & Villain, G. (2019). Design and validation of a multi-electrode embedded sensor to monitor resistivity profiles over depth in concrete. *Construction and Building Materials*, *223*, 310-321.

[4] Fares, M., Villain, G., Fargier, Y., Thiery, M., Dérobert, X., & Lopes, S. P. (2015). Estimation of water content gradient and concrete durability indicators using capacitive and electrical probes. In *International Symposium Non-Destructive Testing in Civil Engineering (NDT-CE)*.

[5] Fares, M., Villain, G., Bonnet, S., Lopes, S. P., Thauvin, B., & Thiery, M. (2018). Determining chloride content profiles in concrete using an electrical resistivity tomography device. *Cement and concrete composites*, *94*, 315-326.

[6] Fraj, A. B., Bonnet, S., & Khelidj, A. (2012). New approach for coupled chloride/moisture transport in non-saturated concrete with and without slag. *Construction and Building Materials*, *35*, 761-771.

[7] Bentz, D. P., & Bentz, D. P. (2005). *CEMHYD3D: A three-dimensional cement hydration and microstructure development modelling package. Version 3.0*.

[8] Garboczi, E. J., & Berryman, J. G. (2001). Elastic moduli of a material containing composite inclusions: effective medium theory and finite element computations. *Mechanics of materials*, *33*(8), 455-470.

[9] Bentz, D. P., & Garboczi, E. J. (1990). Digitised simulation model for microstructural development. *Ceram. Trans.*, *16*, 211-226.

[10] Garboczi, E. J., & Bentz, D. P. (1991). Digital simulation of the aggregate–cement paste interfacial zone in concrete. *Journal of materials Research*, *6*(1), 196-201.

[11] Jennings, H. M., & Johnson, S. K. (1986). Simulation of microstructure development during the hydration of a cement compound. *Journal of the American Ceramic Society*, *69*(11), 790-795.

[12] Watts, B. E., Tao, C., Ferraro, C. C., & Masters, F. J. (2018). Proficiency analysis of VCCTL results for heat of hydration and mortar cube strength. *Construction and Building Materials*, *161*, 606-617.

[13] Dalziel, J. A., & Gutteridge, W. A. (1986). *The influence of pulverized-fuel ash upon the hydration characteristics and certain physical properties of a Portland cement paste* (No. Tech Rept 560).

[14] Taylor, H. F. (1987). A method for predicting alkazi ion concentrations in cement pore solutions. *Advances in Cement Research*, *1*(1), 5-17.

[15] Bernard, O., Ulm, F. J., & Lemarchand, E. (2003). A multiscale micromechanics-hydration model for the early-age elastic properties of cement-based materials. *Cement and concrete research*, *33*(9), 1293-1309.

Inspection of corroded Concrete/Steel/Concrete pipes using ultrasound methods

Thilakson RAVEENDRAN[1]*, Arnaud RECOQUILLAY[2], Jean-Marie HENAULT[1], Jean- François CHAIX[3], Guy D'URSO[1], Denis VAUTRIN[1], Vincent GARNIER[3], Jean MAILHE[3], and Philippe BISARAH[4]

[1] EDF R&D, PRISME, Chatou, France
[2] Université Paris-Saclay, CEA, List, Palaiseau, France
[3] LMA, Université d'Aix-Marseille, CNRS, Ecole Centrale, UMR7031, Aix-en-Provence, France
[4]EDF-DI, TEGG, Aix-en-Provence, France
*Corresponding author, e-mail address: *thilakson.raveendran@edf.fr*

ABSTRACT

Non-destructive ultrasound methods are developed to inspect concrete/steel/concrete pipes affected by corrosion and especially to detect and size holes in the steel layer and to assess remaining steel thickness. In this study, we focus on hole detection and sizing on samples in laboratory using bulk waves methods. We performed measurements through concrete using pulse compression methods. A specific signature of holes in the steel layer was successfully identified. The technique allowed us to size the defect by scanning the structure with a certain measurement step and using the RMS value as an indicator.

Keywords: Concrete/Steel/Concrete pipes, ultrasounds, corrosion, pulse compression methods

1. INTRODUCTION

Concrete/Steel/concrete pipes are used in French nuclear powerplants. These pipes are composed of three layers: an internal layer of centimeter concrete, a middle layer of millimeter steel and an outer layer of centimeter reinforced concrete. Samples of these pipes are shown in Figure 1 and their dimensions in Figure 2.

Figure 1: Pictures of a sample of a concrete/steel/concrete pipe

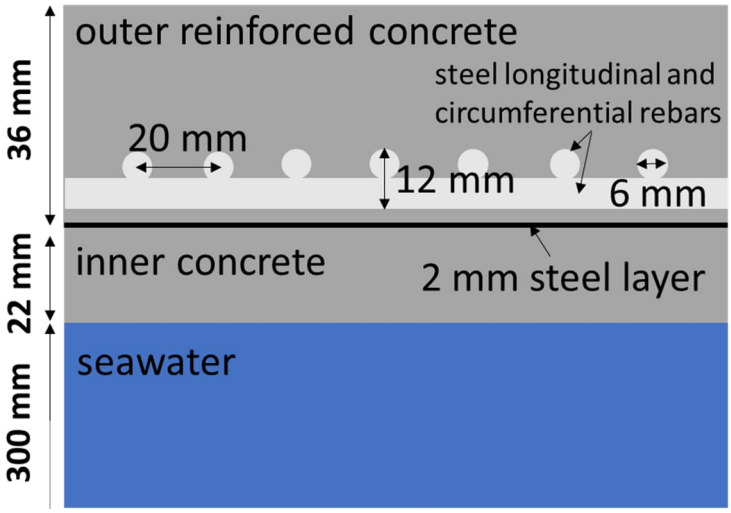

Figure 2: Dimensional data from a sectional view

When the plants are located by the sea, the pipes carry seawater. Consequently, they are affected by corrosion of the steel layer caused by diffusion of chlorides through the inner concrete layer. In Figure 3, pictures illustrate the corrosion on the inner and outer faces of a steel layer after removing the inner and outer concrete layers from a pipe sample coming from a real site. On the inner side of the steel layer, corrosion is spread over several tens of centimeters while on the outer side, corrosion is only present around a hole in the steel layer. Today, on-site inspections are carried out with electrochemical measurements from the outside of the pipe [1]. The results provide a qualitative indicator only sensitive to corrosion of the outer side of the steel layer.

(a) (b)

Figure 3: Pictures of corroded steel pieces, (a) inner side and (b) outer side

The role of the steel layer is to ensure the pipe watertightness and its mechanical strength. Watertightness is lost as soon as a hole appears in the steel layer. A mechanical study concluded that, for keeping the pipe mechanical strength, the smallest hole that needs to be detected is 1 cm diameter and that the minimum average remaining steel thickness is 800 µm. These last criteria define the goal of the non destructive technique under development. Furthermore, the inspection must be conducted from the outside of the pipe under working conditions, that is the pipe is filled with water and hence the inner concrete part is wet.

To meet this industrial goal, ultrasound bulk waves, ultrasound guided waves and vibration techniques are investigated. In this paper, results obtained with bulk waves are presented. Lab specimens (shown in Figure 4) composed by individual concrete and steel layers were used. They are 30 cm x 30 cm flat plates with thicknesses corresponding to the ones given in Figure 2. A hole of 1 cm diameter was drilled in the centre of the steel plate. Material properties are presented in Table 1. The samples can be handled easily.

Measurements can be performed on the individual samples or on assembled layers. They can be immersed in water if needed. In this preliminary study, some experimental measurements are compared to simulation results.
In general, corrosion products detach from the structure, leading to a lack of material. In our case, as the metal part is between concrete slabs, corrosion products remain traped. These products are porous and saturated by water [6]. To be representative, we hence immerse the assembly in our experimental setup. This also couples mechanically the different plates. Furthermore, it is shown in [5] that the corrosion products can be replaced by water for acoustic modeling purposes.

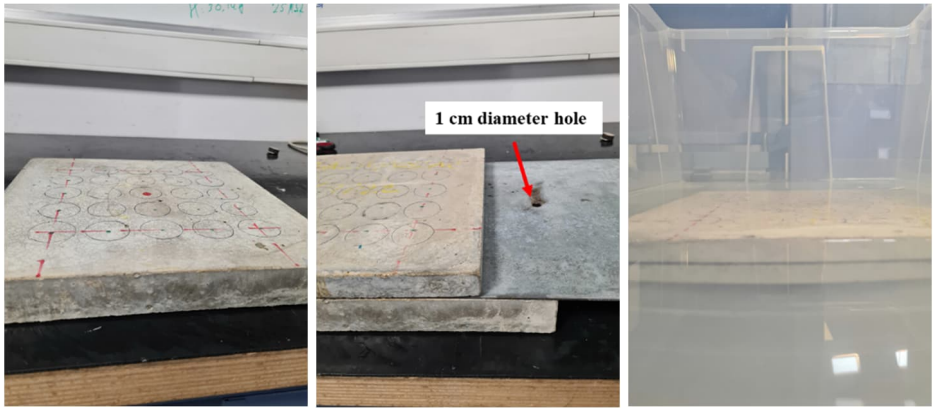

(a) (b) (c)

Figure 4: Pictures of (a) a concrete lab flat plate sample, (b) a concrete/steel/concrete assembly and (c) a concrete/steel/concrete assembly immersed in water. The steel plate has a 1 cm diameter hole in its centre

Table 1: Material properties

Material	V_p (m.s^{-1})	V_s (m.s^{-1})	ρ (kg.m^{-3})	Acoustic impedance (kg.m^{-2}s^{-1})
Concrete	4950	3150	2440	12×10^6
Steel	5710	3220	7800	44.5×10^6
Water	1480	-	1000	1.5×10^6

1 ULTRASOUND BULK WAVES, PULSE METHOD VS COMPRESSION METHOD

The traditional way to inspect a structure is to perform bulk wave measurements in reflection with a P-wave transducer. The diagram on Figure 5 presents two configurations: when the transducer is above a sound area and when the transducer is above a hole in the steel layer. Considering the material properties given in Table 1, arrival times of specific echoes can be calculated. In the sound area, the first echo comes from the outer concrete/steel interface at a time around 14.5 µs. A second interesting echo comes from the steel/inner concrete interface and its arrival time is 15.2 µs. The time difference between these two echoes is of interest because it can enable to assess the steel thickness. For this configuration, the time difference is only of 0.7 µs. To resolve these 2 echoes, the used frequency must be above 3 MHz. If the steel thickness is reduced, the echoes will be closer, and the used frequency will have to be increased. This is a real issue because at these frequencies, the wavelength is far smaller than the concrete aggregates size: multi-scattering on aggregates occurs and increases the signal attenuation [2].

When the steel layer is locally completely corroded, a hole appears. A first echo comes from the outer concrete/water interface at an arrival time of 14.5 µs. A specific echo comes from the water/inner concrete interface at an arrival time of 17.3 µs. The time difference is

then 2.8 µs. The two echoes can be resolved if the signal frequency is above 1 MHz. Such high frequency is also a challenge, even though the damping and multi-scattering are less severe.

We hence tried to use bulk waves to identify holes in the steel layer. The main challenge is to transmit enough energy to the system to identify the echoes of interest. We tested two methods, namely pulse echo method [3] and pulse compression method [4], on a concrete/steel/concrete assembly immersed in water composed by flat plate elements illustrated on Figure 4c. The steel plate has a 1 cm diameter hole in its centre. We used a 1 MHz transducer of 1 inch diameter. First, the transducer was placed above a sound area and then it was moved above the hole.

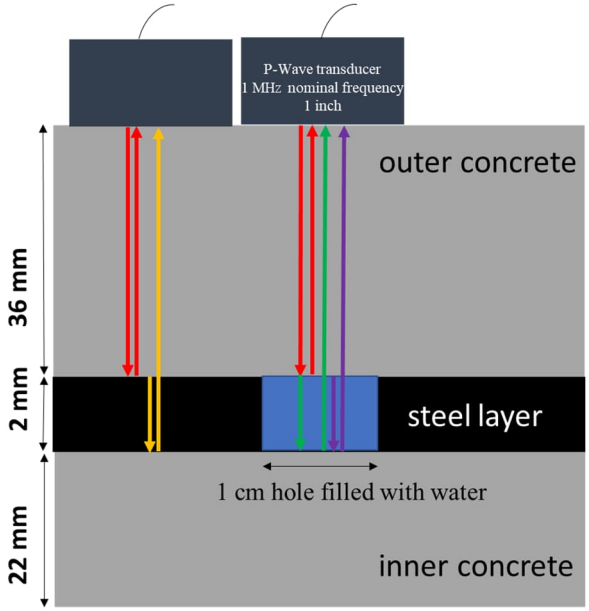

Figure 5: Diagram describing reflection measurements for two configurations: when the transducer is above a sound area and when it is above a hole in the steel layer

Figure 6 shows the experimental results for the pulse echo method where the transducer of 1 MHz nominal frequency is stimulated by a pulse signal. When the transducer is above 3 sound areas and above the hole, a common echo is observed at around 15 µs which corresponds to the outer concrete/steel and outer concrete/water interfaces. After this echo, slight differences are observed between the signals, but they remain too similar to discriminate the two cases. This method doesn't enable to detect a hole in the steel layer.

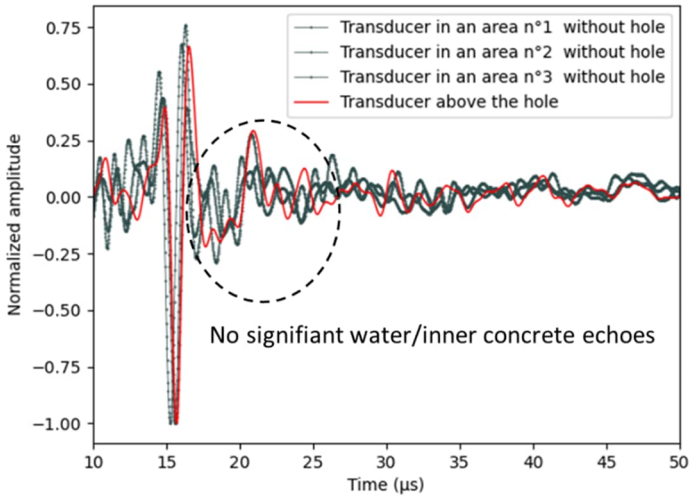

Figure 6: Pulse Echo measurement in reflection on a Concrete/Steel/Concrete assembly at 1 MHz

The signal-to-noise ratio and the signal resolution can be improved by using coded signals. The most used method of pulse compression is frequency modulation.

Typically, a Chirp signal, the instantaneous frequency of which increases linearly with time, is used to excite the transducer. The received signal is processed by an autocorrelation. The signal energy is conserved but its temporal support has been compressed and each echo is concentrated on a duration inversely proportional to the frequency band of the Chirp. Thus, the peak power after compression is significantly greater than before compression and echoes can be resolved in time. The power gain due to compression is proportional to the product of the duration of the Chirp with its frequency bandwidth.

In practice, to increase the power gain, we can therefore adjust:

- the frequency bandwidth, which is chosen as wide as possible but is limited by the bandwidth of the transducer and the attenuation and multi-scattering of the concrete,
- the Chirp duration which is chosen as long as possible. The limit here is related to the storage capacity of the devices in the measurement chain. For example, a Chirp signal of 20 ms duration sampled at 20 MHz contains 400 000 points.

To implement this method, a Chirp of 20 ms duration from 100 kHz to 2 MHz was generated. This signal was loaded on a signal generator which transmitted this signal onto a 1 MHz piezoelectric sensor of one inch diameter. The Chirp was apodized by a Hanning window to limit the amplitude of secondary lobs after autocorrelation.

In Figure 7.b, the result of a reflection measurement on concrete/steel/concrete assembly with the Chirp method is presented. A first echo from the outer concrete/steel interface is observed at about 15 µs. Besides, two other echoes can also be observed at about 19.2 µs and 22 µs. They correspond to multiple echoes from the water/inner concrete interface. The time difference between these 2 echoes is 2.8 µs which corresponds to a 2 mm water thickness considering the water velocity given in Table 1.

This is a promising result for the detection of holes larger than 1 cm in diameter in real structures. Measurements are in progress to improve this result and to have a better temporal resolution and signal to noise ratio in particular by optimizing the used excitation and the experimental setup.

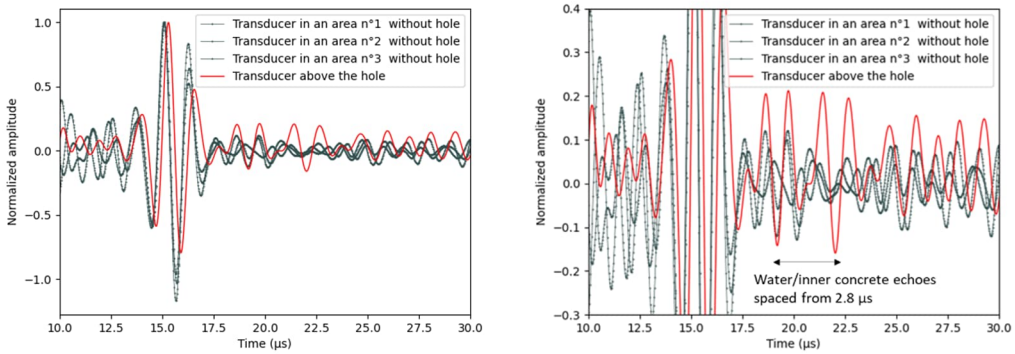

(a) (b)

Figure 7: (a) Autocorrelation of a pulse compression measurement in reflection on a Concrete/Steel/Concrete assembly above and next to a 1 cm hole in the steel part with a Chirp signal between 100 kHz and 2 MHz and (b) a zoom on the water/inner concrete echoes

2 COMPRESSION METHOD FOR DETECTION AND LOCALIZATION OF A HOLE OF 1 CM DIAMETER IN THE STEEL PLATE

In the previous section, the value of using compression techniques was demonstrated to detect a 1 cm hole filled with water in the steel layer.

With the same method a series of measurements was made along a line of 8 cm length. The measurement step was 0.1 cm. The centre of the defect is located at the origin of the measurement line as shown in Figure 8. The objective is therefore to detect and locate the hole and, if possible, to estimate its diameter. The same 1 inch transducer was used. The signal emitted is still a Chirp of 20 ms duration from 100 kHz to 2 MHz.

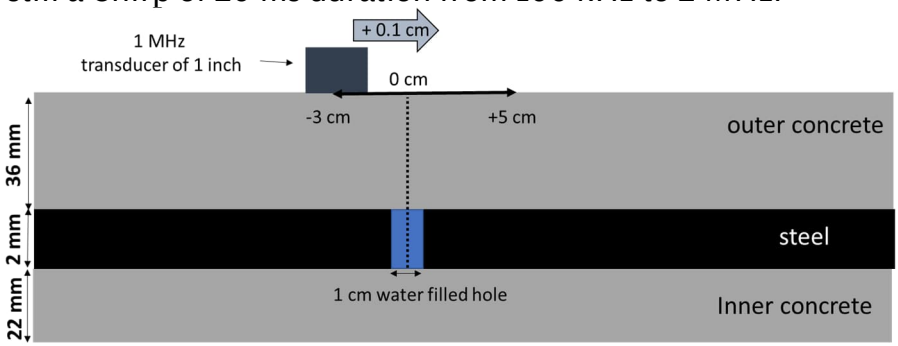

Figure 8: Diagram describing the measurement protocol: the transducer is moved along a 8 cm line by steps of 0.1 cm

The root mean square (RMS) value of the autocorrelation signal has been chosen to highlight the presence of the defect because the energy reflected when the transducer is above the hole is greater than when it is in the healthy zone. In fact, from the acoustic impedances of the media given in Table 1, the transmission and reflection coefficients in energy between two interfaces can be calculated.

In a healthy area, the wave meets concrete/steel or steel/concrete interfaces. In this case, 33% of the energy is reflected and 66% is transmitted. In a zone where the hole is filled with water, the wave meets concrete/water and water/concrete interfaces. In this case, 61% of the energy is reflected and 39% is transmitted. There is more energy reflected in the defect case so the RMS value will be higher than the measurement in a healthy area.

Before calculating the RMS values, the autocorrelation signal is normalized to the amplitude of the first echo corresponding to the outer concrete/steel (or outer concrete/water in the defect case) interface, which happens around 15 µs in our configuration, to limit the uncertainties related to the coupling between the transducer and the structure. Then in a time range between 17 µs and 23 µs where concrete/steel or concrete/water echoes are expected and before the backwall echo, the RMS values are calculated for each measurement. The result corresponding to the line of measurements is displayed on Figure 9.

In Figure 9, the RMS values are normalized to the maximum and plotted with respect to the transducer's position. The hole is clearly visible considering the amplitude of the maximum RMS value in relation to the defect-free areas. A deviation of 0.5 cm is measured compared to the theoretical position of the defect which is explained by the uncertainties related to the experimental setup. In particular, the hole is not a perfect 1 cm diameter circle, the set-up to move the transducer each 1 mm can be improved, and the hole may not be exactly at the abscissa 0 as a slight shift may have happened during the assembly. This is still consistent with the position of the hole. It should be noted that on the right-hand side of Figure 9,

significant variations of the RMS values are observable even though these are defect-free areas. This is probably due to rust defects that have appeared in these areas which may induce acoustic impedance contrasts, but this point needs further testings. Moreover, the concrete samples have flatness defects, thin layers of water may be present and return more energy than if the concrete/steel coupling had been mechanical.

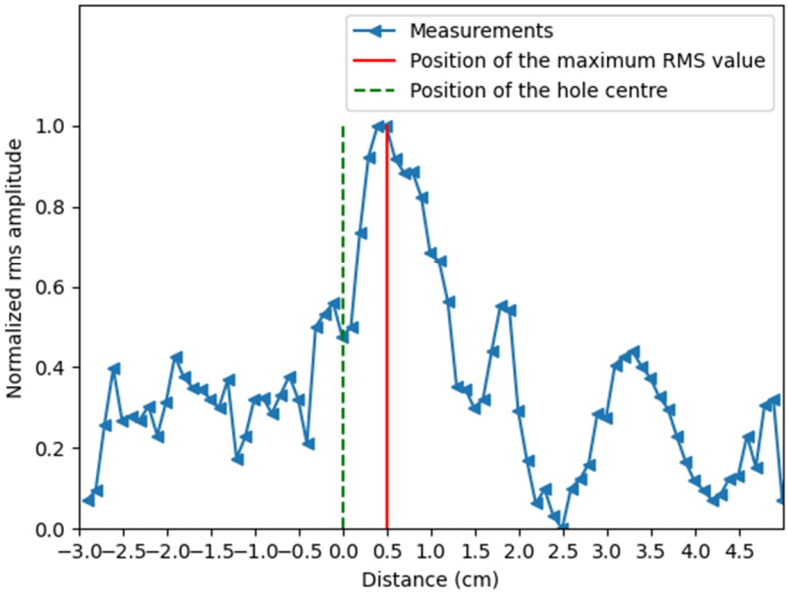

Figure 9: RMS values versus to the position of the transducer that highlights the presence of the hole

To deduce the width of the hole, the same data are displayed in logarithmic scale, and we propose here the use of a threshold at -6 dB [7], which is drawn in Figure 10. The line intersects the curve at 0.2 cm and 1.1 cm, which allows us to estimate the width of the hole at 0.9 cm. This is a consistent result with respect to the real size of the hole and the measurement uncertainties.

This result shows that we are able to detect and locate the hole by scanning the structure. More tests need to be performed to fully assess the capability of the method to estimate the width of the defect. In particular, to improve this result, the size of the transducer can be optimized. In the result presented here, the transducer has a diameter larger than the diameter of the hole, which shall enable a high sensitivity but to the cost of a less precise estimate of the width, compared to smaller sensors.

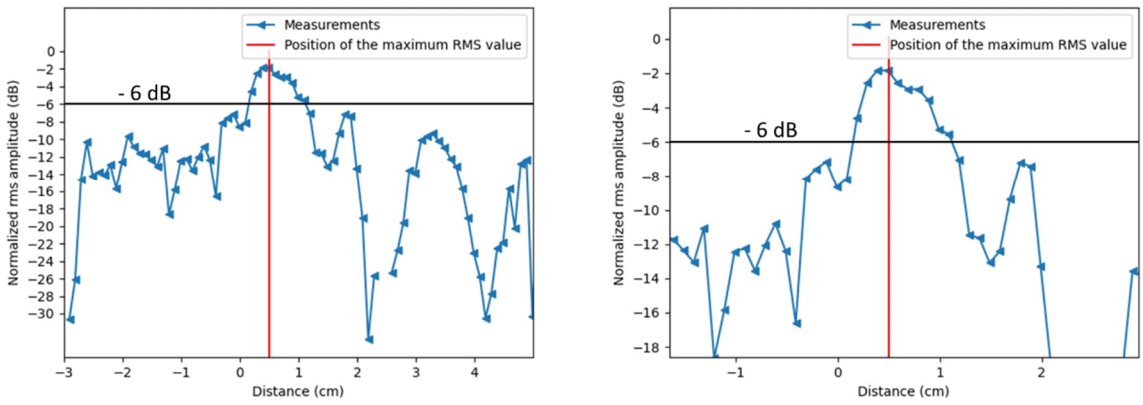

Figure 10: (a) RMS values in logarithmic scale versus to the position of the transducer to deduce the width of the hole and (b) a zoom

3 CONCLUSIONS AND PERSPECTIVES

Concrete/steel/concrete pipes are affected by corrosion because of the seawater they transport, and holes appear in the steel layer. In this paper, we focused on bulk waves methods to detect holes with a minimum diameter of 1 cm. The results presented show the interest of using pulse compression techniques. A water filled hole of 1 cm was successfully detected and located and a first coherent estimation of its size was obtained. To improve these results, in particular the temporal resolution, the implementation of Goley sequences is to be studied. This method allows to limit the sidelobes after autocorrelation [4]. A new measurement protocol is also under study by separating the transmission and reception to have a better dynamic measurement.

REFERENCES

[1] J Aimonino and S Jacq, 'Safety-classified steel cylinder reinforced concrete pipelines: mechanism of corrosion, diagnosis and maintenance strategy', Conférence Diagnobéton 2014.

[2] T. P Philippidis and D. G. Aggelis. 'Experimental study of wave dispersion and attenuation in concrete. ', Ultrasonics 43(7), 584-595, 2005.

[3] J Krautkrämer and H Krautkrämer. 'Pulse-echo method. ', Ultrasonic Testing of Materials. Springer, Berlin, Heidelberg, 193-264, 1977.

[4] J Rouyer, S Mensah, C Vasseur, P Lasaygues, 'The benefits of compression methods in acoustic coherence tomography. Ultrasonic imaging', 37(3), 205-223, 2015. https://doi.org/10.1177/0161734614553310

[5] J. M Henault, et al. "Development of a portable measuring system using ultrasound guided and surface waves to characterize concrete structures." NDT-CE Conference 2022.

[6] Zhao et al Composition and expansion coefficient of rust based on X-ray diffraction and thermal analysis (Corrosion science, 2011)

[7] ISO 5577:2017(en) Non-destructive testing — Ultrasonic testing — Vocabulary

Towards passive ultrasonic sounding of a steel-concrete-steel containment structure using embedded optical fibers

M. Lehujeur[1], T. Druet[2], C. Lefeuve[2], J. Quelene[2], O. Abraham[1], G. Laffont[2], O. Durand[1], t. Devie[1], G. Gugole[1], B. Chapuis[2], and N. Roussel[2]

[1]Gustave Eiffel University, France
[2]CEA, France

ABSTRACT

We present a Steel-Concrete wall model equipped with several embedded fiber Bragg Gratings (FBGs) and several embedded and surface piezoelectric accelerometers (PZAs). We compare the performances of these embedded sensors for several ultrasonic sources disposed on the surface of the wall and emitting at frequencies between a few tens and a few hundreds of kilohertz. We observed that a significant part of the wave energy can be transmitted to the concrete through the surface liner, despite the high mechanical contrasts between steel and concrete. Using a collection of random hammer impacts applied on the steel surface, we further attempted to reconstruct empirical Green's functions between pairs of sensors buried into the structure using passive seismic methods.

Keywords: Steel-concrete structures, Non-destructive evaluation, Embedded ultrasonic sensors, Optical Fibers, Braggs gratings.

1 Introduction

Steel-Concrete-Steel (SCS) structures are made of concrete poured between two metal plates (liners), serving both as a form-work and a mechanical reinforcement. Metal spikes anchored to the liner can be used to provide the coupling between the concrete and the steel plates. These structures are used in confinement structures in nuclear power plants. Because of the liner, visual inspection of the surface of the concrete is not possible. Non Destructive Testing and Evaluation methods (NDT, NDE) are therefore required to probe the concrete. The transmission of ultrasonic waves from the liner to the internal part of the structure is difficult due to the high mechanical contrasts between steel and concrete or when local detachments of the liner occur. This may alter the efficiency of the standard NDE approaches involving ultrasonic waves [3, 7].

In this project, we attempted to overcome this difficulty by using acoustic sensors embedded in the concrete part of a SCS module, which allows us to reduce the distance to the external sources (disposed on the liner). In particular, we focused on the use of Fiber Bragg Gratings (FBGs). This sensing technology based on state-of-the-art optoelectronics allows us to measure the dynamic strain at the location of the Bragg gratings along the fiber axis. These sensors can be used at ultrasonic frequencies over broad frequency ranges, and have proven their potential in Structural Health Monitoring applications based on passive diffuse noise correlation techniques [4, 6]. The deployment of FBGs embedded in concrete provides numerous advantages [5], their footprint on the structure is negligible, one can have several measurement points on the same fiber and the fiber are resistant to challenging environments (temperature or radiations).

We built a reduced scale model of a Steel-Concrete structure, in which we embedded several FBGs together with more conventional PZAs. Our main objectives were (a) to characterize the signals recorded with embedded FBGs, and to improve our understanding of their response in comparison to PZAs, (b) to evaluate the transmission of ultrasonic waves in the concrete for sources placed on the metal plates, and (c) to test the feasibility of using noise correlation methods in order to approximate the Green's function between pairs of embedded receivers using random sources applied on the liner.

2 Methods

1.1 Samples

A reduced scale model of a Steel-Concrete confinement wall (25 x 120 x 135 cm^3) was designed and built for the project. During the casting, 5 traversing optical fibers with a total of 36 Bragg gratings were buried in the wall, as well as 8 PZAs (Brüel & Kjær 4393). Only one side of the wall was covered with a steel liner, but studs were inserted on both sides of the wall (Fig. 1). A few additional PZA sensors were glued outside the structure, on both sides of the wall.

2.1 Sources

Several piezoelectric sources (Ultran GC30 30 kHz, Panametrics V1011-100 kHz, V1012-250 kHz, V106-2.25 MHz) were applied to the faces of the wall to test the following source functions

- a Ricker function with a center frequency incremented from 10 to 300 kHz,
- a sweep function covering all frequencies between 150 and 350 kHz

Additionally, random impacts were made with a hammer or with a robot-controlled impactor able to cover all the surface of the metal plate. The spectrum of the latter sources extended from about 5 to 70 kHz.

2.2 Data analysis

The recorded signals were visualized in the temporal and spectral domains. For the random hammer sources applied on the liner face, we implemented a correlation method initially designed to process ambient acoustic or seismic noise to recover the empirical Green's function of a medium between a pair of receivers according to the following relation [1]

$$\frac{\partial C_{AB}}{\partial t} \approx G_{A->B}(-t) - G_{B->A}(t) \quad (1)$$

In this method, the signals must be pre-processed using spectral and/or temporal normalization [2] in order to balance the contribution of every sources and to approach the ideal case of an uniform distribution of the sources or a diffusive wave-field.

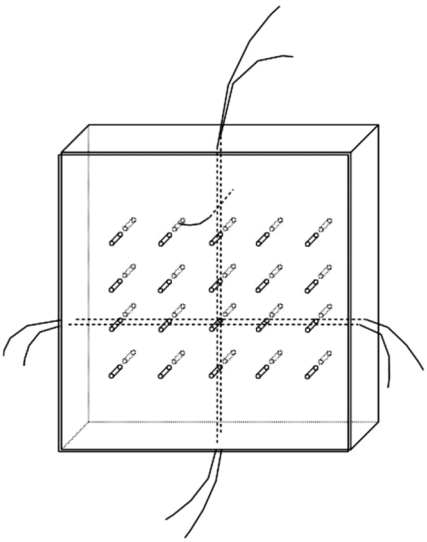

Figure 1: Scheme showing the geometry of the Steel-Concrete wall model built in this project. The front side is equipped with the steel liner. The concrete is bare on the back, lateral and upper faces of the wall. Studs were installed on both sides of the wall. The dashed lines denote the traversing optical fibers.

3 Results

3.1 Comparison of an embedded FBG and PZA

A first series of measurements was carried out using sources glued to the concrete on the upper face of the wall, in order to avoid issues related to the transmission of waves through the liner. The emitted source was a Ricker pulse, whose center frequency was gradually increased from 50 to 300 kHz (Fig. 2, red).

The longitudinal dynamic strain measured with the embedded FBG named "V2B4" (Fig. 2, blue signals) and the particle acceleration measured with the embedded PZA "A2" (Fig. 2, black signals) had a good signal to noise ratio and allowed us to identify the first arrivals clearly. The shape of the spectrum obtained with the FBG was in good agreement with the source one, while the PZA had a peak near its resonance frequency (at 55 kHz for this sensor).

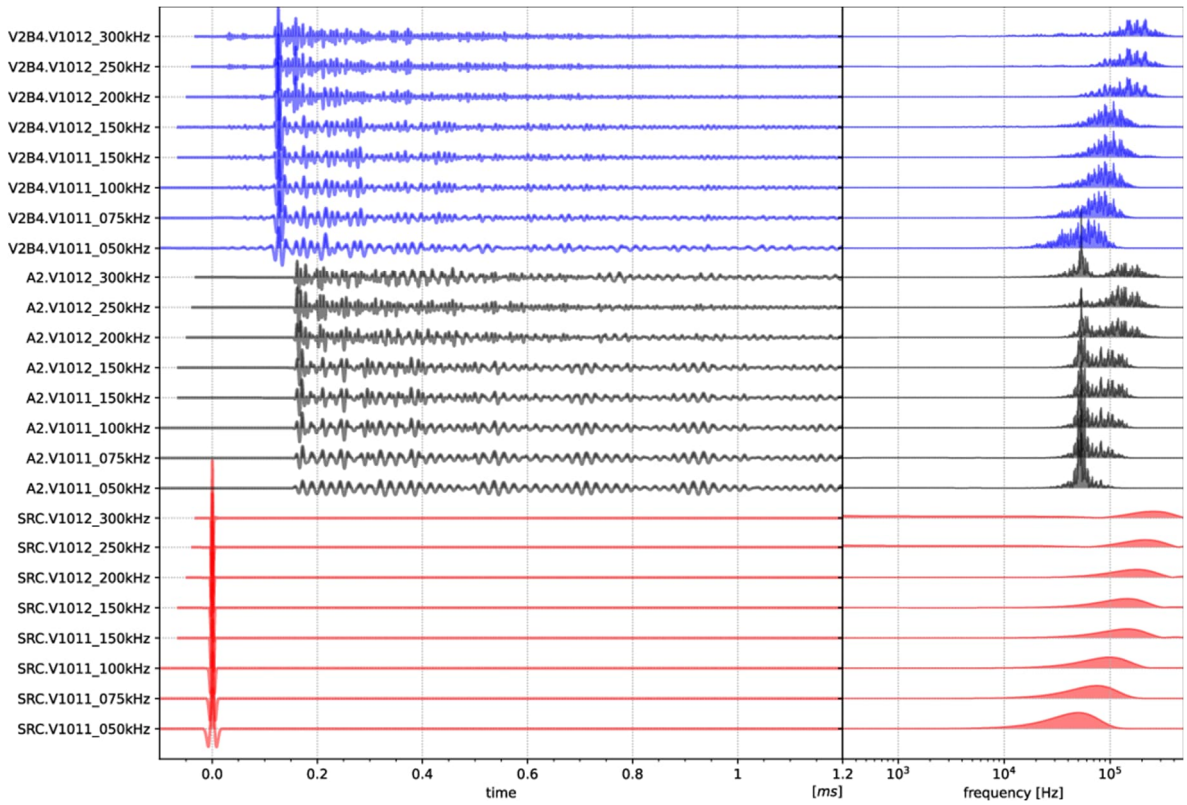

Figure 2: Signals recorded inside the wall by two nearby FBG (V2B4, blue) and PZA (A2, black) for several Ricker source functions (SRC, red) centered between 50 and 300 kHz. The signals are shown in time (left) and spectral domains (right).

3.2 Transmission of ultrasonic waves to the concrete

A second series of measurement was carried out in order to evaluate the transmission of ultrasonic waves in the concrete despite the high contrasts of impedance at the steel-concrete interface. We deployed a source emitting a sweep ranging from 150 to 350 kHz on either faces of the test wall, covered or not by the liner (Fig. 3, see source points named ”B2a” for the concrete side of the wall and ”M2a” for the liner side). The input sweep was correlated with the recorded signals in order to remove its temporal signature and to return to an impulsive record. This test showed that acoustic signals can be recorded with embedded receivers (FBGs and PZAs) at frequencies between 150 and 350 kHz. A reduction of the signal to noise ratio was observed when the source is placed on the liner (especially for the PZAs), but this did not seem to affect the waveform and the shape of the spectrum significantly.

Another potential limitation of ultrasonic methods for this application comes from the presence of local detachments of the steel plate. A possible alternative consists in placing the sources at the emerging end of the studs (Fig. 3, the source point ”ST21” corresponds to the source placed on a stud, on the concrete side of the wall and ”MST21” corresponds to the source being placed on a stud on the liner side). Here also, no clear changes in waveform and spectral shape could be observed between the two source locations. A complementary experiment in which the liner would be deliberately decoupled from the concrete would help concluding on the usefulness of placing sources at the extremity of the studs.

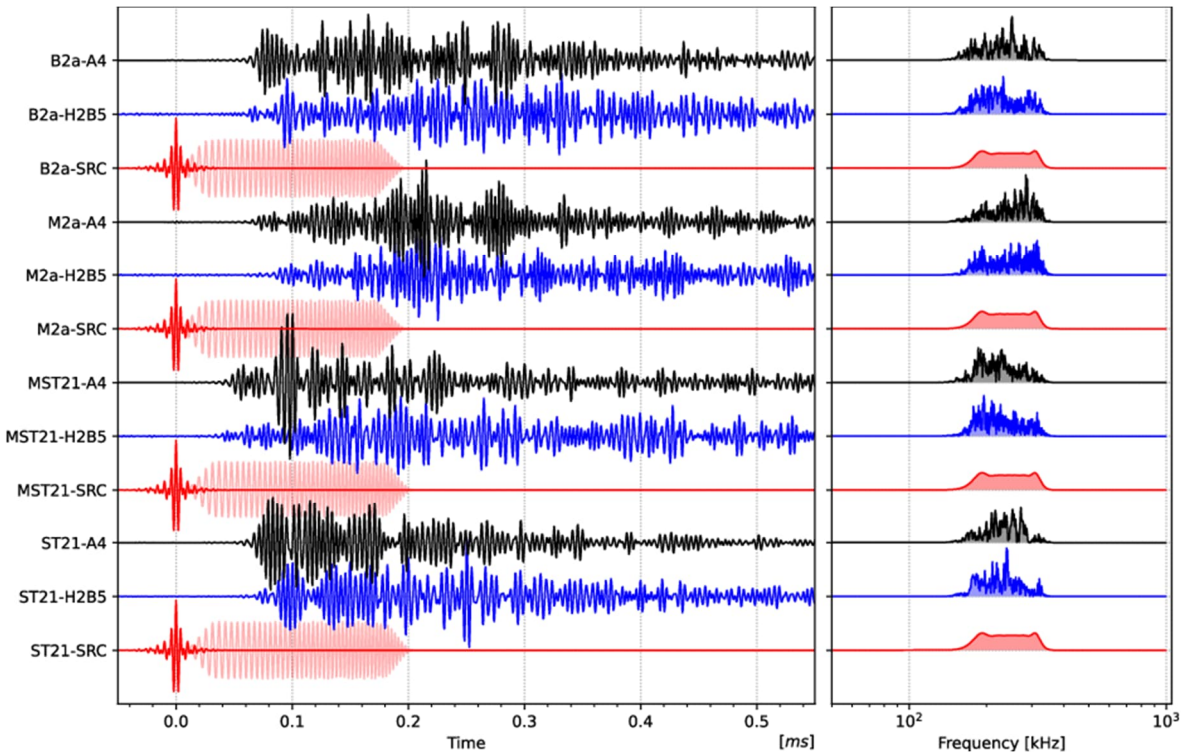

Figure 3: Signals recorded inside the wall by two nearby sensors: a Bragg grating (H2B5, blue) and a piezoelectric accelerometer (A4, black) for a source placed at various positions on the wall and emitting a sweep between 150-350 kHz (red). The signals are shown in time (left) and spectral (right) domains after correlation with the input sweep (shown in light red). The source is placed on the liner or concrete side (M2a/B2a), at the extremity of a stud on the metal or concrete side (MST21/ST21). The amplitudes are normalized for each trace individually.

3.3 Noise source correlation

Finally, we tested the possibility to obtain empirical Green's functions between pairs of embedded acoustic sensors for a collection of hammer impacts randomly distributed at the surface of the liner. Some pre-processing steps were applied to the recorded signals for each sensor individually. These steps implied spectral normalization (whitening) and the clipping of the largest amplitudes of the signal in the time domain. The signals were then correlated between pair of sensors, stacked and derivated temporally following equation 1.

For frequencies between 5 and 15 kHz, we obtained an anti-symmetrical correlation function (as expected from eq. 1), which suggests that both causal and anti-causal estimates of the Green's function are in good agreement, and that the wave-field is nearly equipartitionned. For a pair of PZAs, a good similarity between the correlation functions of each individual shot was obtained (Fig. 4a), which reveals a fast convergence of the correlation function toward the approximate Green's function. For a pair of FBGs, the signal to noise ratio is lower, but a clear pattern emerges by stacking all the source contributions (Fig. 4b).

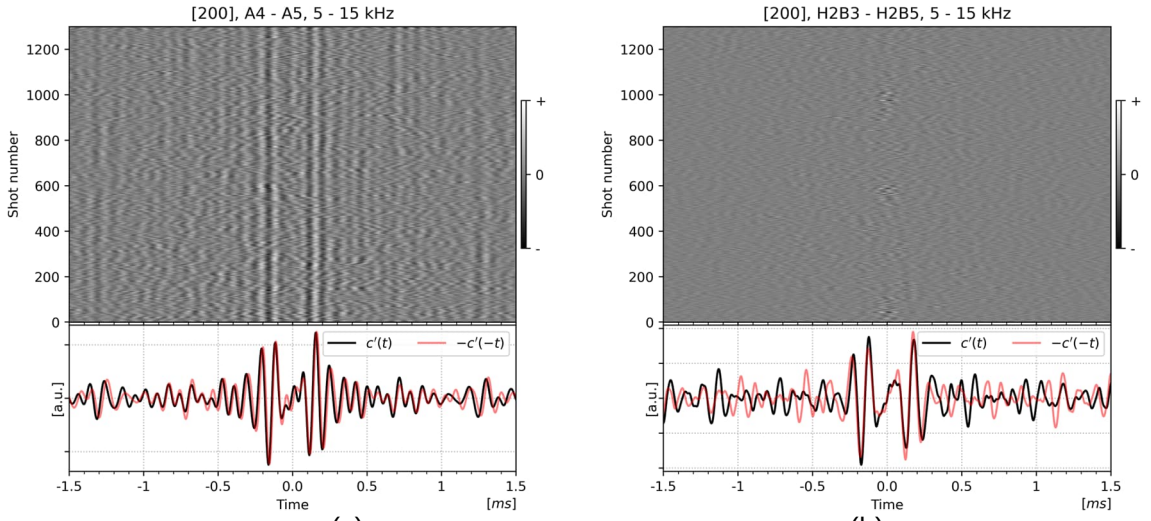

Figure 4: Estimates of the empirical Green's function by correlation of hammer shots, for a pair of PZAs (a) or FBG sensors (b). The upper part of the figures indicate the correlation functions obtained for each source individually. The stack function (black) and a reversed version of it (red) are show at the bottom of the figures.

4 Conclusions

In this work, we evaluated our ability to acquire signals using acoustic sensors embedded in concrete for the non-destructive evaluation of a Steel-Concrete-Steel module. We tested a large panel of sources with known source functions (Ricker and sweep) emitting at frequencies from 10 to 350 kHz, as well as random hammer sources applied on the liner, whose spectrum extended from 2 to 70 kHz.

Our experiments carried out in a transmission regime revealed that a significant part of the energy emitted by a source positioned on the liner can be recorded inside the concrete with both PZA and FBG sensors, which suggests that this methodology can be used to evaluate the health state of a SCS module even though only the liner is accessible. An advantage of FBG lies in the shape of the spectra, which accurately reproduces the source one in the frequency range of interest. The signals obtained with embedded FBGs are usually more noisy than those of embedded PZAs. When the source term is well known and sufficiently repeatable, this can be easily addressed by direct summation of the records. For sources with an un-controlled or weakly repeatable source function, summation of the source contributions can be achieved through the correlation method usually employed for the processing of passively acquired noise wave-fields. Using this approach, we were able to approximate the Green's function of the medium between pairs of PZAs or Bragg gratings at frequencies between 5 and 15 kHz. Future efforts will concentrate on the possibility to extend this result to ultrasonic frequencies (above 20 kHz) and to use these signals in a non- destructive evaluation process.

5 Acknowledgments

This research is conducted in the framework of the Smart-SCS project, a collaboration between Gustave Eiffel University and the French Alternative Energies and Atomic Energy Commission (CEA), and the FO-US project (ANR-21-CE04-0007) funded by the french national research agency. The authors thank F. Blaineau from the COSYS/SII laboratory (Gustave Eiffel University, France) for his numerical plans of the instrumented form-works and D. Hamon from the MAST/GPEM (Gustave Eiffel University) for his help during the casting of the concrete in the form-works.

References

[1] Oleg I. Lobkis and Richard L. Weaver. “On the emergence of the Green’s function in the correlations of a diffuse field”. In: *The Journal of the Acoustical Society of America* 110.6 (2001), pp. 3011–3017. DOI: 10.1121/1.1417528.

[2] G. D. Bensen et al. “Processing seismic ambient noise data to obtain reliable broad-band surface wave dispersion measurements”. en. In: *Geophys. J. Int.* 169.3 (June 2007), pp. 1239– 1260. ISSN: 0956-540X, 1365-246X. DOI: 10.1111/j.1365-246X.2007.03374.x.

[3] Herbert Wiggenhauser et al. “Nondestructive Evaluation of Steel-Concrete Mock-ups,” presented at the JRC-NDE, Cannes, FRANCE, 2013.

[4] Tom Druet et al. “Passive guided waves measurements using fiber Bragg gratings sensors”. eng. In: *J Acoust Soc Am* 144.3 (Sept. 2018), p. 1198. ISSN: 1520-8524. DOI: 10.1121/1.5054015.

[5] Simon Nehr et al. “Towards Embedded Fiber Optics for the Ultrasonic Monitoring of Concrete”. en-US. In: *Structural Health Monitoring 2019* 0.0 (2019). Number: 0. DOI: 10 . 12783/shm2019/32404.

[6] Arnaud Recoquillay et al. “Guided wave imaging of composite plates using passive acquisitions by fiber Bragg gratings”. In: *The Journal of the Acoustical Society of America* 147.5 (May 2020). Publisher: Acoustical Society of America, pp. 3565–3574. ISSN: 0001-4966. DOI: 10.1121/10.0001300.

[7] Ludovic Fülöp et al. “Assessing the challenges of condition assessment of steel-concrete (SC) composite elements using NDE”. en. In: *Case Studies in Construction Materials* 16 (June 2022), e00887. ISSN: 2214-5095. DOI: 10.1016/j.cscm.2022.e00887.

Studies Into the Use of Non-linear Ultrasound to Detect Corroded Steel Plates Embedded in Concrete

Markus Nilsson[1,*], Peter Ulriksen[1] and Nils Rydén[1]
[1] Lund University, Faculty of Engineering, Division of Engineering Geology, Lund, Sweden

ABSTRACT

In some nuclear power plants, the containment liners are embedded in concrete. The purpose of the containment liner is to minimize the risk of radioactive leakage by granting a leak-tight containment building. In the presence of flaws in the surrounding concrete, such as voids, or foreign objects embedded in the concrete, there is a risk that the liner plate might corrode. This could degrade the leak tightness of the containment building, leading to an increased risk of radioactive leakage. A project is being carried out at Lund University whose purpose is to assess the capability of non-linear ultrasound to detect corroded steel plates embedded in concrete. Second harmonic analysis has been used to determine if general corrosion induced an increase in acoustical non-linearity. This was done by inspecting a steel plate with varying grades of corrosion immersed in water. Results from this study indicated that severe corrosion increases the relative parameter of quadratic non-linearity (β'). β' is given by the ratio between the second harmonic amplitude and the fundamental amplitude squared. Building on this result, initial findings from modulation experiments on concrete cylinders with embedded steel plates with varying grades of corrosion are presented.

Keywords: Corrosion; containment liner; non-linear ultrasound

1. INTRODUCTION

The containment liner plates (CLP) in some Nuclear Power Plants (NPPs) are to a certain extent embedded in concrete. The purpose of the CLP is to ensure leak-tightness so that no radioactive particles are leaked into the surrounding environment. Due to the alkaline environment inside the concrete, steel should not corrode at an alarming rate. However, in the presence of flaws in the concrete or embedded foreign objects, the passivity might be compromised. This would cause the steel to corrode aggressively which will damage the leak tightness. It is therefore important to be able to detect corrosion in embedded CLP.

A project is being carried out at Lund University whose aim is to assess the feasibility of using non-linear ultrasonics to detect corroded CLP embedded in concrete. Conventional (linear) ultrasound uses parameters that are mainly linear, such as the time-of-flight, attenuation, and sound velocity. The resolution of these methods is restricted by the frequency of the ultrasound, meaning that the wavelength of the probing wave must be less than or equal to the defect size. As concrete is a highly attenuative material due to its heterogeneous nature, high-frequency (MHz-range) ultrasound is unsuitable for this application. However, research has shown that ultrasound with wavelengths some order of magnitude greater than the defect size may distort due to locally enhanced elastic nonlinearity at the defects [1], [2]. This distortion generates new spectral components in the propagated sound wave. In monochromatic ultrasound, the distortion causes the generation of higher harmonics, i.e., integer multiples of the fundamental frequency [3]. In the case of polychromatic excitations, in addition to higher-harmonics, modulation frequencies, i.e., sidebands, around the excitation frequencies are generated [4]. In non-linear ultrasound, parameters based on these spectral components are studied and used as damage indices. This work

* Corresponding author: Markus.nilsson@tg.lth.se

presents results from two investigations. The first investigation, which has been published in [5], studies second harmonic generation in a uniformly corroded steel plate. Building on those results, the second case investigates the inspection of concrete cylinders containing embedded plates using non-classical non-linearities and some initial results are presented here.

Considering that steel plates are conventionally manufactured by rolling, a metalworking process that pushes material through a series of rolls to reduce the thickness of the material, it is assumed that this process creates surface-plane parallel internal structures in the bulk material. When the plate then corrodes, the affected volume delaminates and cracks. Examples of this can be viewed in Figure 1, where X-ray tomography shows the cross-section of two corrosion products of different origins. The sheet-type corrosion product in Figure 1 a) was found on a uniformly corroded steel plate found at a scrap yard. Its thickness is roughly 2 mm. The 15 mm thick corrosion product in Figure 1 b) was extracted from the CLP in the containment building housing the nuclear reactor Ringhals 3 in Sweden. Both corrosion products exhibit similar delamination characteristics and have several cracks and voids.

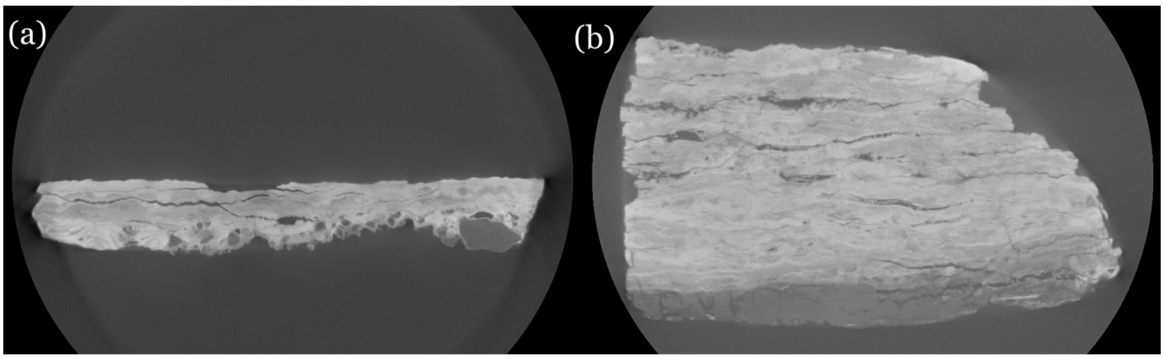

Figure 1. X-ray tomography showing; (a) the cross-section of a piece of sheet-type corrosion studied in the present work; (b) the cross-section of a corrosion product obtained from the Ringhals 3 containment wall. Reproduced from [5].

2. MEASURED PARAMETERS IN NON-LINEAR ULTRASOUND

2.1 Relative Parameter of Quadratic Non-linearity

By formulating Newton's second law of motion in terms of particle displacements (u), a non-linear wave equation can be obtained given that the stress term is expanded in a power series including first-order non-linearity. The solution will only include the fundamental component (u_1) and the second harmonic (u_2), given that the boundary condition at the source is a monochromatic excitation. This enables us to formulate an expression for the parameter of quadratic non-linearity (β) in terms of particle displacements (u):

$$\beta = \frac{8u_2}{u_1^2 k^2 x} \tag{2}$$

Where k is the wave number, and x is the propagation distance. It may be impractical to measure the particle displacement in engineering NDT applications. Fortunately, the received voltage signals from an ultrasonic transducer are proportional to the displacements, and they may be used to obtain relative measures of β. This relative parameter, given by Eq. (3), is denoted β', and is thus given by the second harmonic (A_2) and the fundamental amplitude squared (A_1^2) of the received voltage signal. Taking several measurements with increasing excitation amplitude enables the determination of averaged β'-values.

$$\beta \propto \beta' = \frac{A_2}{A_1^2} \tag{3}$$

2.2 Sideband Energy Distribution

The theory of classical power-series type non-linearity cannot adequately describe certain observed phenomena. Cross-modulation between a probe-wave and a strong amplitude-modulated (AM) wave (analogous to the Luxembourg-Gorky (LG) effect [6] in radio waves) is one such phenomenon [7], [8]. By integrating the power spectrum in appropriate intervals, the energy in the sidebands (E_{sb}) and probe-component (E_p) can be determined. This can be used to determine a parameter of non-linearity α, see Eq. (4).

$$\alpha = \frac{E_{sb}}{E_p} \tag{4}$$

3. EXPERIMENTS

3.1 Second Harmonic Analysis

3.1.1 Uniformly Corroded Steel Plate

The steel plate used to study the potential of non-linear ultrasound to detect corrosion is seen in Figure 2. The plate consisting of ordinary steel was initially uniformly corroded (*COR*) and covered by a thin sheet of corrosion (*SCOR*), here called sheet corrosion (see Figure 1 a) for a cross-sectional view of a sheet corrosion product). The sheet corrosion was separated from the steel plate during handling, and due to being very brittle, it broke into multiple pieces. One of the largest pieces was reattached to the plate by gluing it with ethyl-cyanoacrylate. As the plate was to be immersed in water, the sheet corrosion was painted in water-resistant varnish before being reattached to the plate. Half of the uniformly corroded plate was ground to remove the top corrosion layer. This was performed to achieve a region deemed flawless, thus "*OK*". Figure 2 shows the measurement point placement used in the indexed measurements. As shown, there are a total of 6 measurement points in the OK region, 4 in COR, and 2 in SCOR.

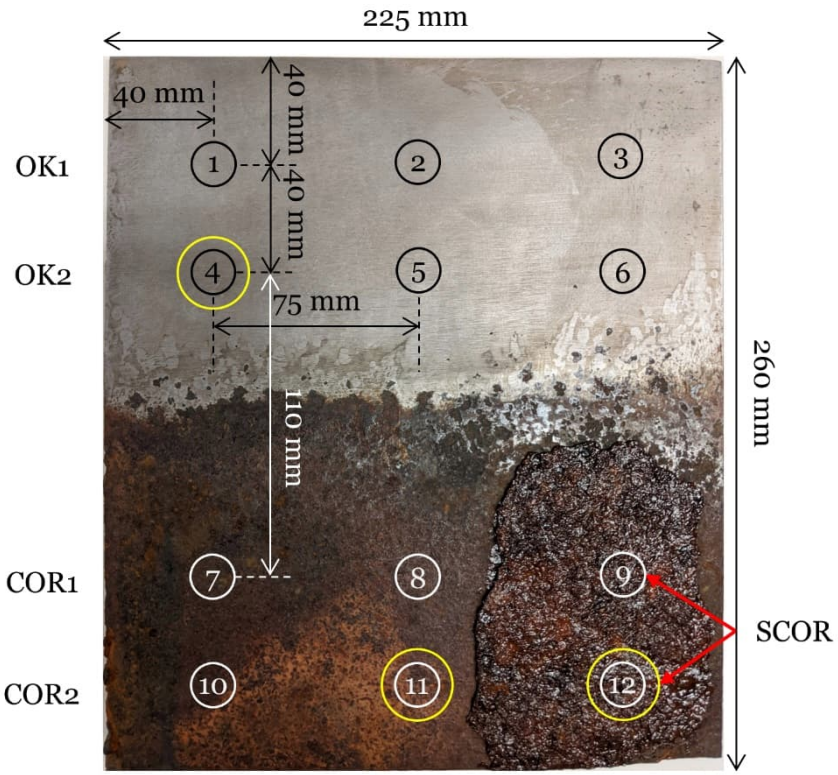

Figure 2. The corroded steel plate used in the presented work. Reproduced from [5].

3.1.2 Experimental Setup

The experimental setup for the second harmonic analysis used to inspect the steel plate (Figure 2) is illustrated schematically in Figure 3. A 4-cycle sine burst with a fundamental frequency of 4.5 MHz was used as the probe signal. The high frequency was used to avoid the generation of spurious harmonics. The signal was amplified in two steps before being sent to the transmitter (T in Figure 3). The voltage levels used were 14, 30, 47, 63, 74, and 80 V_{pp} measured at the 50 Ω load before the transducer. The transducer used was an immersion-type transducer from Olympus (V309-SU) with a center frequency of 4.5 MHz. The receiving hydrophone (SEA SPRH-S-1000, R in Figure 3) has good sensitivity in the range of 1.5 MHz - 10 MHz. The received signal was amplified before being collected in the oscilloscope. The collected data was post-processed (windowing, DFT, and more) on a PC with the MATLAB environment. A manual XY-scanner was used to move the transmitter-receiver pair equally and consistently across the plate.

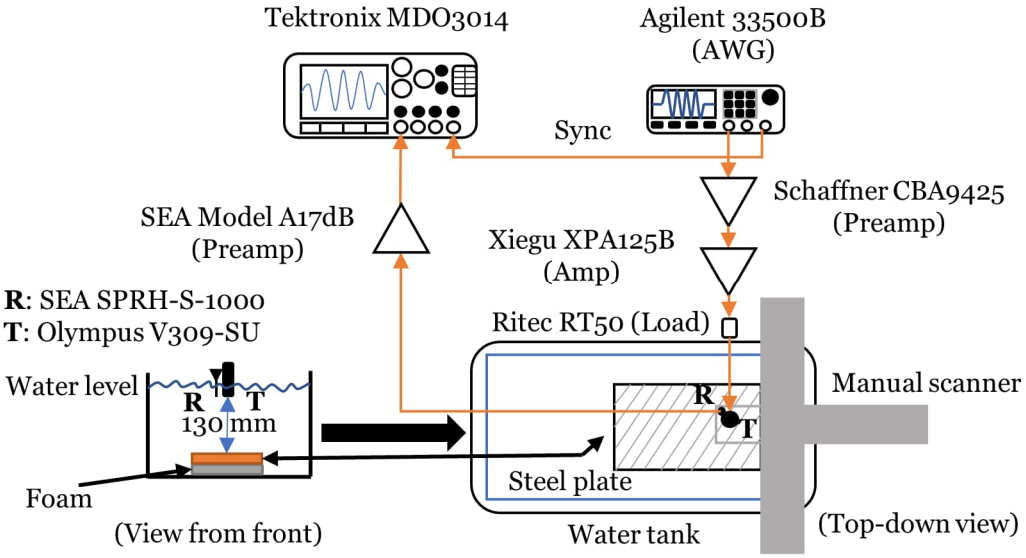

Figure 3. Experimental setup used for the measurements carried out for the second-harmonic analysis. Reproduced from [5].

3.2 Cross-Modulation Experiment

3.2.1 Concrete Cylinders with Embedded Steel Plates

A total of five concrete cylinders were prepared for the modulation experiments. One cylinder did not contain any steel plate discs, but the remaining cylinders did. The plate discs that were embedded in concrete can be seen in Figure 4. Plate COR is uniformly corroded and so was SCOR1, however, SCOR1 has a layer of sheet-type corrosion attached to it. SCOR2 is the thin sheet-type corrosion only. To ensure that the plates remain fixed in the center of the cylinders, they were attached to 250 mm long expanded metal cylinders, as shown in Figure 5 (a-b). The plates were attached to the expanded metal by using a polyurethane sealant. The specimen containing no metal plate also contained a cylinder of expanded metal, but no sealant. The concrete recipe was one part each of Portland cement and coarse aggregate, two parts fine aggregate, and enough water to achieve a water-to-cement ratio of 0.43. Details about the concrete recipe can be viewed in Table 1. PVC pipes were used as molds (see Figure 5 (c-d)) for the cylinders. The concrete cylinders were initially 250 mm long. After curing for 30 days, they were cut to lengths of 200 mm by removing 25 mm from each end. During casting the specimen containing SCOR2, it was observed that the thin corrosion product shattered. This caused multiple pieces of the corrosion product to be distributed across the entire volume.

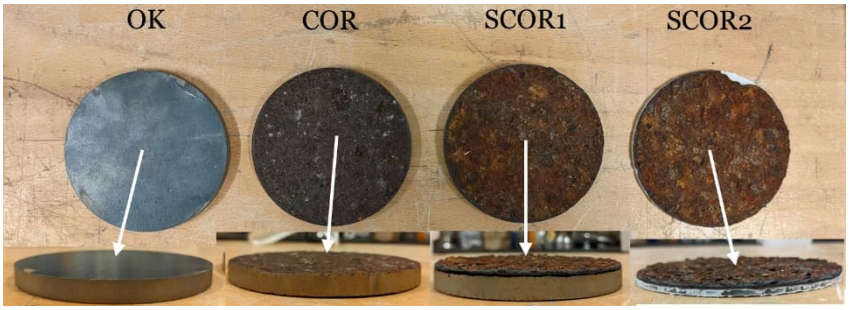

Figure 4. Plate discs that were embedded in concrete. OK is a plate with no known flaws. COR is a uniformly corroded plate. SCOR1 is uniformly corroded and has a thin sheet corrosion product attached to it. SCOR2 consists only of the sheet-type corrosion product.

Figure 5. (a) Side-view of the expanded metal cylinder with the OK-plate attached to it. (b) Top-down view of the cylinder in (a). (c) Concrete cylinder immediately after casting. The total length of the concrete cylinder is here 250 mm, but the PVC pipe is longer. (d) Shows a concrete cylinder after being cut to length of 200 mm.

Table 1. Concrete recipe.

Concrete component	Mass [kg]
Portland cement	6.038
Coarse aggregate (4-8 mm)	6.038
Fine aggregate (0-2 mm)	12.08
Water	2.597

3.2.2 Experimental Setup for measuring Cross-Modulation

A schematic of the experimental setup used for the modulation experiments can be seen in Figure 6. The probe was a continuous sine wave with a frequency of 37 kHz and amplitude of 65 V_{pp}. The pump was an AM continuous sine with a carrier frequency of 178 kHz, modulation depth of 100%, and a modulation frequency of 100 Hz. With an AM excitation, it is the modulation component that activates the defects. The carrier frequency was chosen to be significantly higher than the probe-wave to separate any modulation between the pump carrier and the probe from the

cross-modulation between the modulation component and the probe. The pump had a measured maximum amplitude of 130 V_{pp}. The equipment used is shown in Figure 6, except for the transducers. Tx1 and Rx were both Olympus X1021, and Tx2 was an Olympus X1019. Ultrasound gel was used as coupling between the transducers and the specimen. A script designed in LabView controls the instruments, collects data, and returns a power spectrum for each measurement. Additional post-processing was performed in MATLAB.

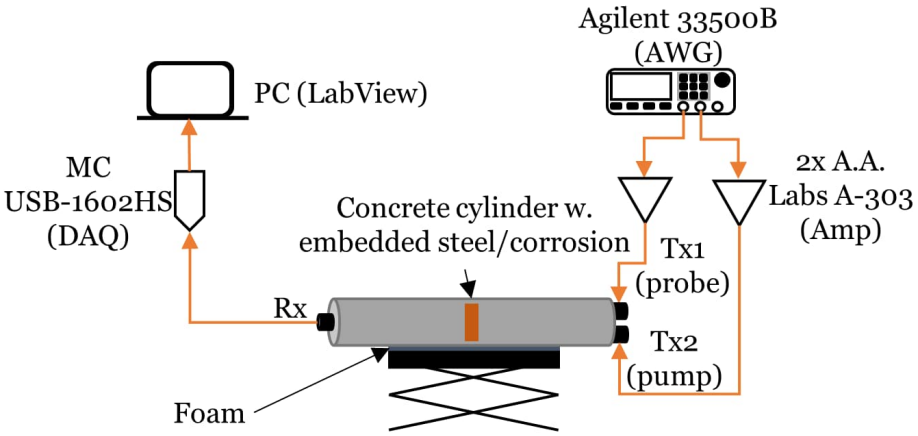

Figure 6. Schematic of the experimental setup used for the experiments on the concrete cylinders.

4. RESULTS AND DISCUSSIONS

4.1 Inspection of the Steel Plate using Second Harmonic Analysis

The magnitude spectra for the time signals recorded at points #4, #11, and #12 are plotted in Figure 7. Second harmonics (~9 MHz) are evidently generated at all measurement points. The magnitude of the second harmonic is greatest at point #4, which is located in the non-corroded region OK. Only studying harmonic amplitudes may yield erroneous conclusions as some inherent non-linearity is always to be expected. The important parameter is the energy distribution between linear and non-linear components, such as β' (Eq. 3). The β'-values averaged across all excitation levels obtained at the measurement points illustrated in Figure 2 are all plotted in Figure 8 to show the distribution across the plate. It is clear that no separation can be made between the OK and COR regions based on β'-values alone. However, there is a significant increase of β' in the SCOR region. Note that no attenuation correction has been applied.

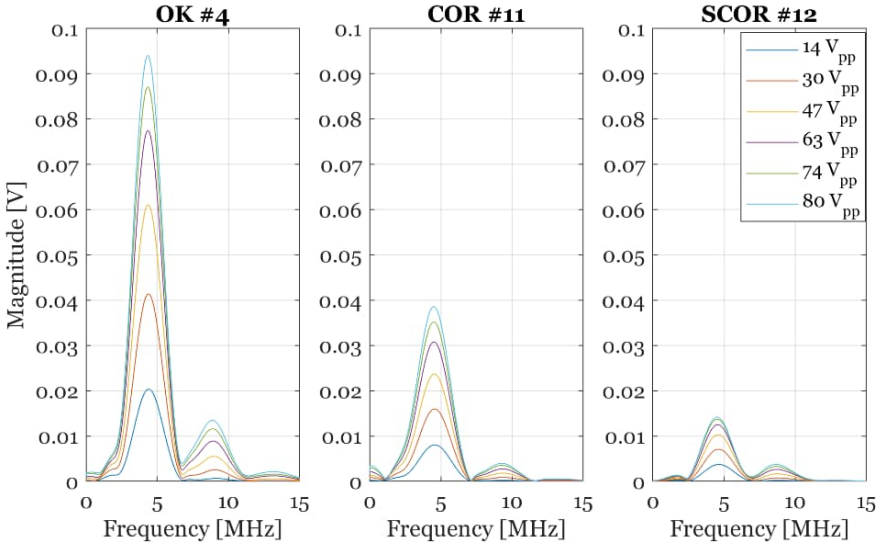

Figure 7. Magnitude spectra for the measurement points #4 (in OK region), #11 (COR region), and #12 (SCOR region). Figure reproduced from [5].

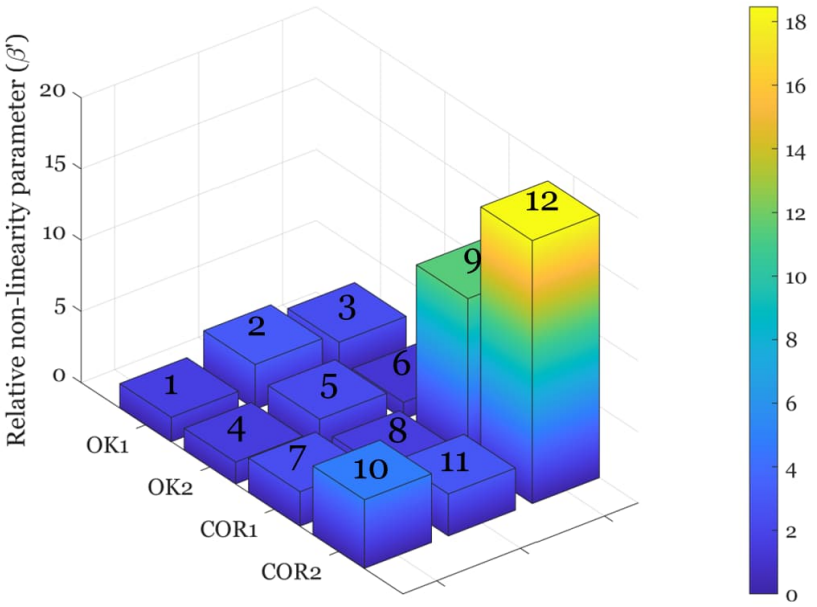

Figure 8. Averaged β'-values at all measurement points (indicated by Arabic numerals on the top surface of the bars). Figure reproduced from [5].

The interested reader is referred to Ref. [5] for additional in-depth analysis and discussion of this investigation.

4.2 Inspecting Concrete Cylinders with Cross-Modulation

The power spectra (PS) obtained from the measurements on the concrete cylinders can be viewed in Figure 9. The PS are plotted in dB-scale which makes it difficult to draw any conclusions by only studying the spectra as the magnitudes vary by several orders, but the information necessary for the determination of α (Eq. (4)) can be obtained. The sidebands appear to be ranging from 35 – 39 kHz. By integrating the linear scale PS in the regions 35 kHz – 36.94 kHz and 37.06 kHz– 39 kHz, the energy in the sidebands is obtained. The probe energy is computed by integrating the PS in the interval 36.94 kHz – 37.06 kHz. The corresponding α for each specimen can be viewed in Figure 10. It is shown that the level of non-linearity is highest for the specimen containing uniform and shell corrosion (SCOR1). SCOR2 and the specimen without embedded steel have almost equal α. The shattering of the sheet corrosion during casting likely affected the probability of detection as small pieces of the corrosion product were distributed in the entire volume. Future experiments with higher probe-wave frequency aim to investigate the feasibility of detecting this distributed 'damage' as a higher-frequency probe wave will scatter when interacting with aggregates, and possibly small corrosion products. The high level of non-linearity seen at OK could possibly be explained by the concrete not properly binding to the plate surface, as it is very smooth in comparison to the other plates. Any delamination would cause an increase in non-linearity. However, as these results are based on single measurements the variation in parameter values is unknown. Observe that no attenuation correction has been made which also affect the results. Continued work will focus on designing repeatable measurements of non-classical non-linearity on concrete samples containing embedded corrosion by investigating the impact of the experimental conditions. Investigations of the impact of couplant between sensors and the sample, the contact pressure applied to the sensors, and more will be conducted.

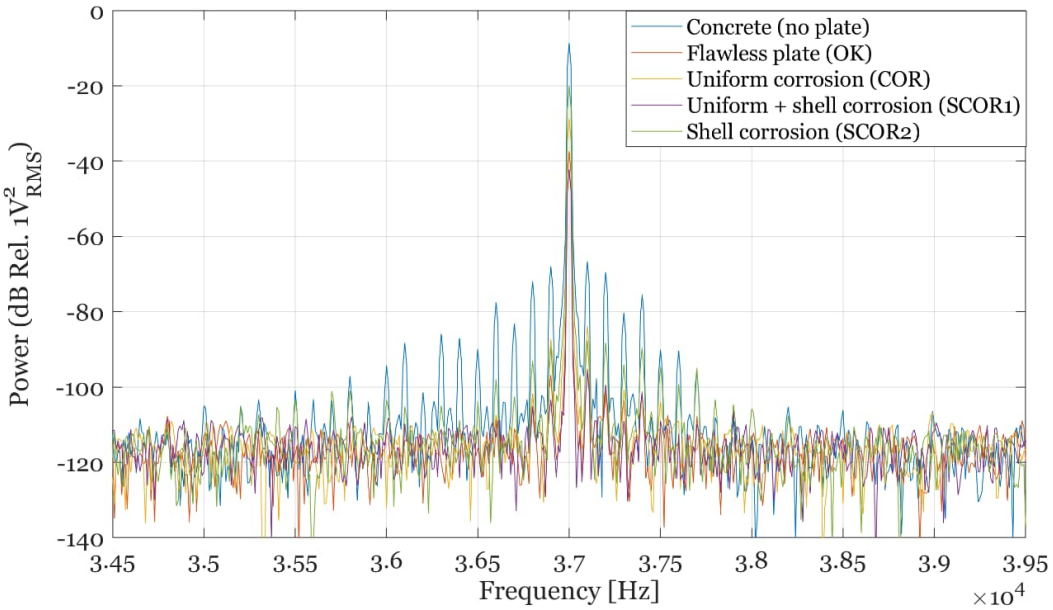

Figure 9. Power spectra for all concrete specimens.

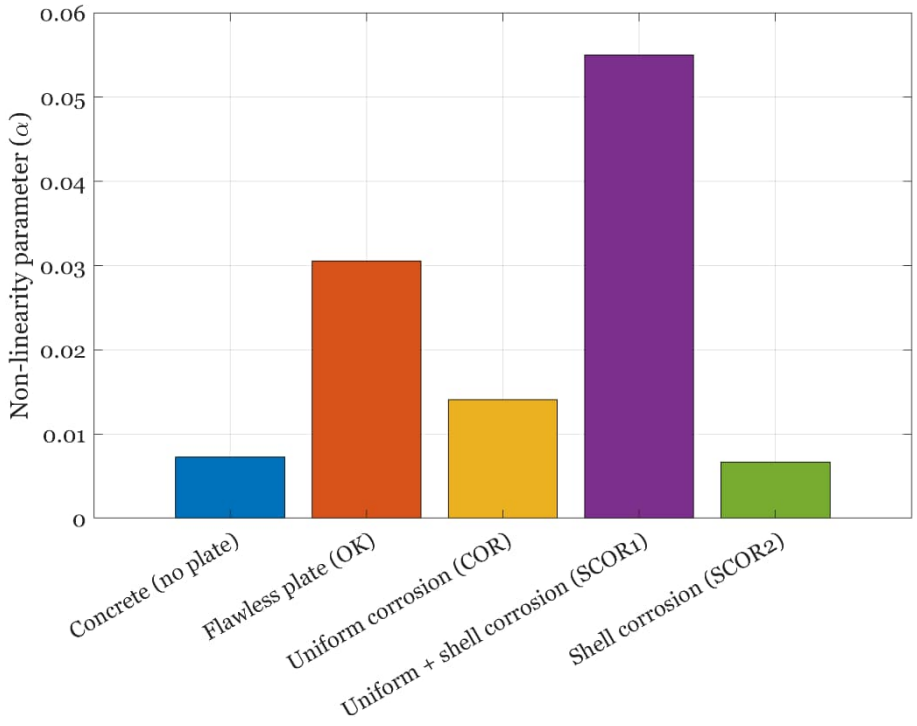

Figure 10. The non-linearity parameter α for the inspected specimens.

5. CONCLUSIONS

The current studies into the feasibility of using non-linear ultrasound to detect embedded corrosion indicate some potential of the methods. Second harmonic analysis accurately indicated the area with the most severe type of corrosion, the shell type. This corrosion product is characterized by the presence of gross damage. Initial testing on concrete specimens with embedded steel plates using the cross-modulation technique indicates further potential of non-linear ultrasonics. Due to the complexity of non-linear mechanisms, it is generally difficult to determine the exact sources of non-linearity. However, by utilizing phenomena that arise due to non-classical non-linearity, such

as the cross-modulation treated in the present work, masking effects from inherent classical non-linearities might be reduced.

ACKNOWLEDGEMENTS

This work is supported by funding from The Swedish Energy Research Centre (Energiforsk BET165) and the Swedish Radiation Safety Authority (SSM2019-1114). Gratitude is addressed towards Johanna Spåls (Ringhals AB) for granting us access to the Ringhals 3 corrosion product.

REFERENCES

[1] V. Y. Zaitsev, L. A. Matveev, and A. L. Matveyev, "On the ultimate sensitivity of nonlinear-modulation method of crack detection," *NDT E Int.*, vol. 42, no. 7, pp. 622–629, 2009, doi: 10.1016/j.ndteint.2009.05.001.

[2] C. M. Hedberg, E. Johnson, S. A. K. Andersson, K. C. E. Haller, G. Kjell, and S. E. Hellbratt, "Ultrasonic monitoring of a fiber reinforced plastic - Steel composite beam during fatigue," *Proc. 6th Eur. Work. - Struct. Heal. Monit. 2012, EWSHM 2012*, vol. 2, pp. 1254–1260, 2012.

[3] Kyung-Young Jhang, C. J. Lissenden, I. Solodov, Y. Ohara, and V. Gusev, *Measurement of Nonlinear Ultrasonic Characteristics*. Singapore: Singapore Nature Singapore Pte Ltd, 2020.

[4] T. Kundu, Ed., *Nonlinear ultrasonic and Vibro-acoustical techniques for Nondestructive evaluation*. Springer Nature Switzerland AG, 2018.

[5] M. Nilsson, P. Ulriksen, and N. Rydén, "Nonlinear ultrasonic characteristics of a corroded steel plate," *Nondestruct. Test. Eval.*, vol. 00, no. 00, pp. 1–24, 2022, doi: 10.1080/10589759.2022.2123481.

[6] B. D. H. Tellegen, "Interaction Between Radio-Waves?," *Nature*, vol. 131, p. 840, 1933.

[7] V. Zaitsev, V. Gusev, and B. Castagnede, "Luxemburg-Gorky Effect Retooled for Elastic Waves: A Mechanism and Experimental Evidence," *Phys. Rev. Lett.*, vol. 89, no. 10, pp. 2–5, 2002, doi: 10.1103/PhysRevLett.89.105502.

[8] V. Y. Zaitsev, V. Gusev, and B. Castagnède, "Observation of the 'Luxemburg-Gorky effect' for elastic waves," *Ultrasonics*, vol. 40, pp. 627–631, 2002.

Applying linear and non-linear resonant ultrasonic techniques to assess the formation of Alkali-aggregate reaction in concrete

Klayne Silva[a,b*], Vincent Garnier[b], Cedric Payan[b], Benoit Durville[a], Laurent Cantrel[a] Lounès Lahlou[c]

[a] Institut de Radioprotection et de Sûreté Nucléaire (IRSN),Saint-Paul-Lez-Durance, France
[b] Aix Marseille Université, CNRS, Centrale Marseille, LMA UMR 7031, Marseille, France
[c] École nationale des travaux publics de l'État (ENTPE), Lyon, France
* klayne.dossantossilva@irsn.fr

ABSTRACT

The Alkali-Aggregate Reaction (AAR) is an internal reaction responsible for concrete swelling due to gel formation. The main consequence of this pathology is a material expansion and in most cases the diagnosis occurs too late, when cracks appear on the structure surface.

In the nuclear reactors, concrete structures represent the third safety containment barrier and the control of their properties evolution during ageing is of key importance in the current context of service life extension beyond 40 years [1]. Several Frenchreactors are identified as possibly affected by these pathologies and shall be kept under control. Thus,concrete ageing management requires predictive numerical tools and controlling means.

In this context, specific Non-Destructive Testing methods needs to be developed and qualified to evidence and characterize early signs of swelling pathologies inside thick structures.

An innovative non-destructive methodology based on Nonlinear ultrasonic measurements for early detection of AAR is currently developed by LMA and IRSN. At first, small scale preliminary tests will be presented in this study, before a medium and full-scale qualification planned for 2023.

Small scale tests will include pathology characterization through usual expansion tests, microscopic analysis and destructive mechanical testing for a dedicated concrete formulation. At the same time, ultrasonic measurements by linear and Nonlinear Resonant Ultrasonic Spectroscopy (RUS and NRUS) will be done to establish a link between pathology nonlinear signature and its effects on the material.

These fundamental data will later allow to validate the new methodology on large scale blocks containing different levels of pathology for the same concrete.

Keywords: Alkali-Aggregate Reaction, Non-destructive Testing, Ultrasonic, Concrete, Swelling Pathologies

1. INTRODUCTION

The Alkali-aggregate reaction (AAR) is a swelling pathology which can affect concrete structures. This endogenous reaction results from chemical interactions between the components of concrete. In the case of the alkali-silica reaction (ASR), the most common AAR reaction and subject of this study, the reactions occur between the silica present in the aggregates and the alkaline hydroxides [Na^+, K^+, OH^-] presents in the cement and in the pore water of the concrete. [2-4].

Besides the chemical interactions mentioned above, other factors contribute to the occurrence and evolution of AAR in concrete, such as environmental conditions (climatic cycles and relative

humidity), permeability and water/cement ratio, air entrainment, temperature (heat of hydration and thermal gradient), reinforcements and after restraints, and others. [5] [6] The product of ASR is the formation of a gel, in this case called "alkali-silica gel", initially observed on a microscopic scale. The formation of the gel itself does not cause directly damage in the concrete. However, this gel has hygroscopic properties and expands in the presence of moisture. This expansion can cause incipient microcracks growing with the evolution of the reaction and can reach the surface of the structures, when the tensile strength supported by the material is exceeded by the gel. [7] [8] On a macroscopic scale, in addition to the structural effects resulting from ASR, which can be clearly observed in late phase of the reaction induced damage (cracks), the mechanical properties of concrete, especially compressive strength, tensile strength, and Young's modulus are directly affected, thus decreasing the service life and performance of the material. [9-11]

In nuclear power plants, containment buildings are massive concrete structures representing an important safety issue as they represent the third protective barrier of the reactor. Under accidental conditions, these massive structures limit the dispersion of radioactive material. To fulfill their function, these structures must maintain watertightness and sufficient mechanical properties throughout their service life. To verify that the containment building safety functions are not subjected to aging influence, including ASR, periodic monitoring must be performed.

The ASR was already identified in several French nuclear power plants [1]. Considering its deleterious influence on concrete, it is necessary to develop of non-destructive methods enabling early identification (as soon as possible) of this type of pathology. This strategy would facilitate the service life extension of the plants beyond 40 years.

In this context, several non-destructive ultrasonic techniques (linear and nonlinear acoustics) are evaluated in this study, initially on a small-scale samples, constituting a basis for the intermediary and next large scale transposition planned in 2023. The tests performed in the present study serve to better assess the properties evolution of concrete affected by ASR and to test at the same time the sensitivity of ultrasonic NDT for the detection of such pathologies.

2. MATERIAL AND METHODS

2.1. Concrete mixing and casting

Six prismatic samples 7x7x28cm dimensions were cast with the same concrete mixing (Table 1). The concrete is alkali-doped by adding sodium hydroxide (NaOH) to the mixing water. Alkaline doping accelerating conditions to form ASR, a content of 1.25% by mass of Na_2O equivalent in cement (including cement alkali content) was defined, following the recommendations of RILEM AAR-4 [12].

Table 1. Concrete Mix

Constituents	Designation	Ratio (kg/m^3)
Cement	CEM II Airvault 42R 2019	350
Sand	0/4 Boulonnais (NR)	731,9
Medium aggregate	CIMESCAUT (PR) 4/14	357
Coarse aggregate	CIMESCAUT (PR) 14/20	696,2
Water	Demineralised water	199,5
Alkali content	Na_2O_{eq} in mass of concrete	4.4

Of the six samples made, four are dedicated to the accelerated aging process and expansion tests and two of them are reference specimens. All of them were submitted to non-destructive acoustic testing.

2.2. Aging procedure and expansion measurements

After 24 hours of casting, the four samples dedicated to the accelerated aging process were weighed (W_0) and their initial reading on the comparator (C_0) were measured, after that they were placed in an accelerated aging process. The reference samples were weighed and then placed in a water-filled container to the concrete curing for 28 days.

The aging procedure used, consists in storing the specimens placed in a climatic chamber at a constant temperature of 40°C and 98% humidity, also constant. For the samples used in this process, the mass and expansion measurements were repeated every 2 weeks. 24 hours preceding each measurement, the specimens were left in conditions of humidity above 50% and ambient temperature for stabilization, following the recommendations of RILEM [12].

2.3. Non-destructive testing (NDT)

2.3.1. Linear Acoustics

In order to determine the damage in a concrete structure, several non-destructive testing methods can be used, but the sensitivity of each method will depend on the damage's level of the concrete. The linear acoustics techniques described in this section allow us to characterize the material acoustically and to access physical parameters such as Young's modulus and Poisson's ratio considering concrete as an isotropic material.

2.3.1.1 Waves propagation velocity measurements

The velocity measurements of longitudinal and transverse waves were performed in direct transmission on all samples with ultrasonic transducers. Resonant transducers at 500 kHz for longitudinal waves and resonant transducers 250 kHz for transverse waves were used. In both cases, the transmitter transducers are excited in an impulsive manner. The longitudinal wave arrival time is set when the amplitude of the received signal exceeds three times the standard deviation of the pre-arrival noise.

2.3.1.2 Resonant Ultrasound Spectroscopy (RUS)

The method used to access the elastic constants of concrete was RUS. This method analyses the frequencies of different free-vibration resonance modes of a solid material [13]. Initially a numerical simulation is made to identify the range that comprises the different resonance modes of the material, associating them to the resonance frequencies, from this it was possible to establish a range between 2kHz and 13 kHz.

The experimental scheme, as shown in figure 1, consists of a generator, driven by software RITA© and passing through an amplifier. The frequencies sweep between 2 and 13 kHz are driven by software at two volts per peak (Vpp). The signal is sent to the 250 kHz transmitter transducer, also used for transverse wave velocity measurements, and received by a same type of transducer, positioned at the opposite extremity of the sample. This configuration allows us to approximate the free state, where the different eigenfrequencies can be identified.

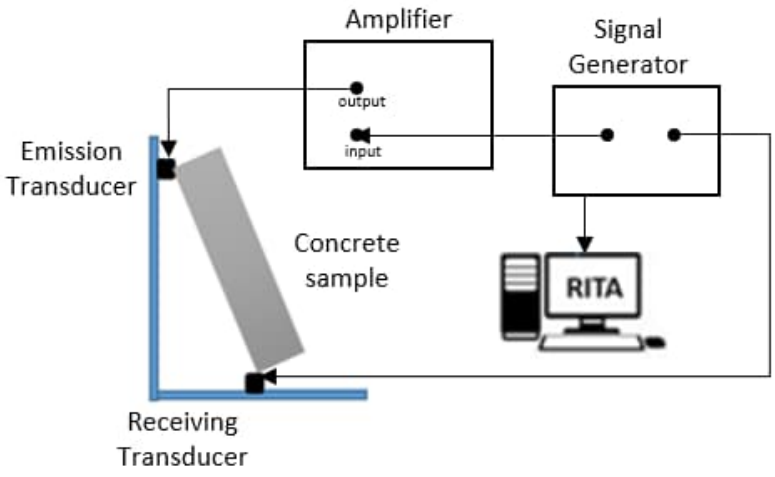

Figure 1. RUS experimental scheme

To obtain the values of the dynamic modulus and the coefficient of Poisson, an approach based on ASTM C215 [14] was used, considering the flexion and torsion resonance modes.

2.3.2. Nonlinear Acoustics

To solve several problems, we assume linear behaviour of materials, but the relationships between characteristic parameters such as pressure, density, and temperature in fluids, for example, and the relationships between material constants in solids, are nonlinear. [17] [18] Nonlinear acoustics is a part of acoustics that can be used to describe the nonlinear phenomena of materials. In inhomogeneous solids like concrete, nonlinear acoustics is useful for describing the interatomic connections (classical nonlinearity) and imperfect contacts (nonclassical nonlinearity) present in the medium, such as micro-cracks. [19] For these materials, which are highly nonlinear, their stress-strain relationship is more complex, where the Young's modulus is no more constant but is a function of strain. The equation 1 describes the nonlinear and hysteretic modulus K.

$$K(\varepsilon, \dot{\varepsilon}) = K_0 \{1 - \beta\varepsilon - \delta\varepsilon^2 - \alpha [\varepsilon + \varepsilon(t)\, \mathrm{sign}(\dot{\varepsilon})] + \cdots\} \quad (1)$$

in the above equation, K_0 is the linear modulus, β and δ are the classical nonlinear coefficient, $\dot{\varepsilon}$ is the deformation velocity and α is a measure of the material hysteresis, which is the parameter that we aim to evidence in this study. Where α is a quantitative constant representing the nonlinear non classical parameter of the material.

Considering that one of the main consequences of ASR is cracking, the alpha parameter is well suited to describe imperfect contacts in the material. Knowing that nonlinear acoustics are ten times more sensitive to concrete damage [24], a non-linear acoustics method described hereafter, was applied to evidence this parameter and to obtain information about the evolution of the non-linear behaviour of the material as a function of the pathology evolution.

2.3.2.1 Nonlinear Ultrasound Spectroscopy (NRUS)

The method applied in this work was NRUS. In recent studies, this method has been shown to be sensitive in identifying the evolution of nonlinearity due to the presence of cracks in concrete, either of thermal origin [18] or due to AAR [19].

NRUS consists in measuring the resonant frequency changes of a given mode, in this case the compression mode. Around the compressive resonance mode, we expose the material at different amplitudes in an increasing way, in this case between 100mVpp and 2.5Vpp before amplifier, at a step of 100mVpp. For the calculation of the alpha parameter, it is observed that there is a linear decrease of the resonant frequency with increasing excitation, so the frequency variation can be reasonably defined as:

$$(f - f_0)/f_0 = -\alpha\Delta\varepsilon \quad (2)$$

Where α is a quantitative constant representing the nonlinear non classical function of the material and $\Delta\varepsilon$ the maximum strain amplitude reached in the material during the resonance. f is the resonance frequency corresponding to $\Delta\varepsilon$ strain amplitude and f_0 the resonant frequency for strain amplitude tending towards zero. To generate the nonlinear concrete behaviour, the value of $\Delta\varepsilon$ could be more than 10^{-6}.

The experimental scheme used for NRUS is presented in figure 2. The same generation and acquisition system was used as in the RUS method. For the NRUS we used a cleaner transducer attached to one extremity of the specimen for the solicitation at the different amplitude levels, and an accelerometer on the opposite side of the specimen with a sensitivity of 10 mv/m/s^2.

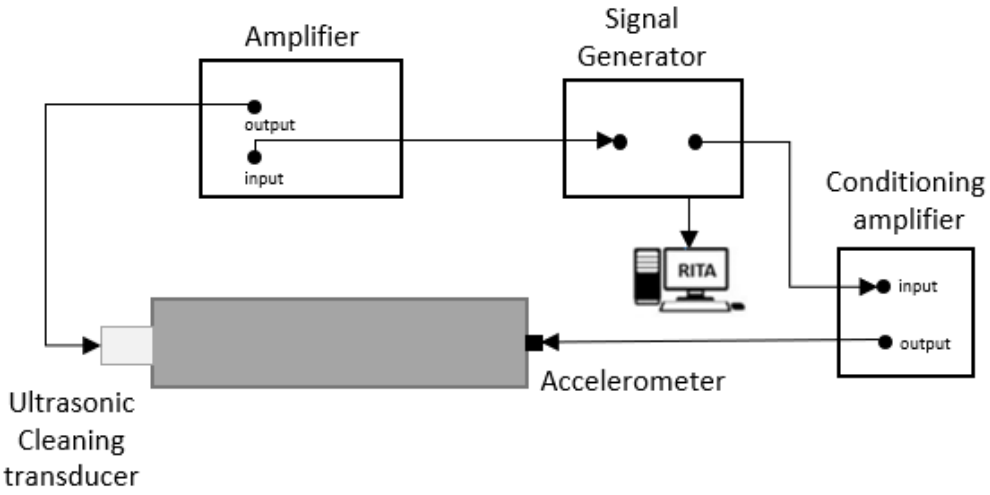

Figure 2. NRUS experimental scheme

Initially, to test the experimental setup of the NRUS test and following the information and equations provided above, concrete specimens damaged by ASR from previous tests performed at IRSN were used. The specimens were chosen based on the concrete formulation, that is very similar to the one used in this work, and due the expansion levels, which reached values above 2000µm/m (0,2% of expansion) which allowed to perform, at first, the analysis of the nonlinearity parameter α due the ASR. Thereafter, the tests were performed in the same manner on the samples dedicated to this study. The results are presented in the following section.

3. RESULTS AND DISCUSSION

This section presents the results up to date for the four types of tests being performed in this study. The results presented graphically in this section correspond to the averages of the reactive specimens and the reference specimens.

3.1. Expansion Measurements

The graph presented in Figure 3 shows the results for the expansion tests taken until up to 25 weeks. We can see that the minimum limit established by the RILEM [12] to characterize an expansion by ASR is 0,04% of expansion, and this value has not yet been exceeded. In this case the swelling is slower than expected, this is justified by the fact that every two weeks, from the removal of the specimens from the climatic chamber, until the completion of all tests, 4 days are needed, corresponding to a significant loss of accelerated aging.

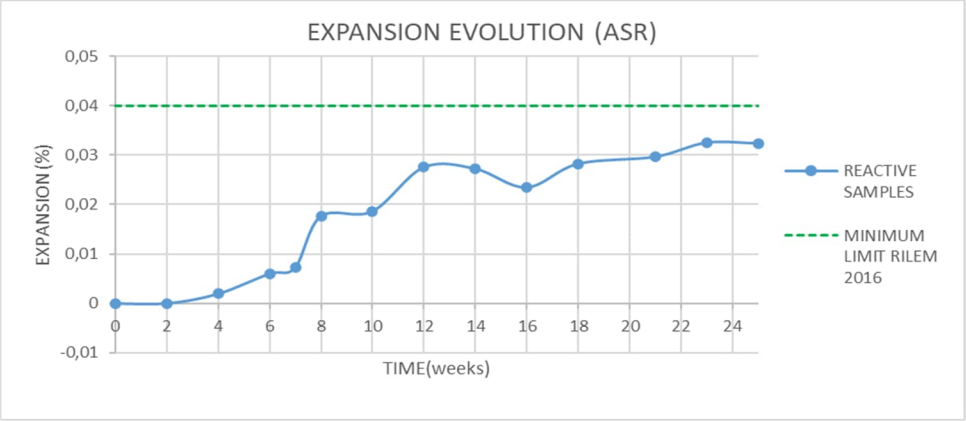

Figure 3. Expansion results for reactive samples

3.2 Transverse and longitudinal wave velocity measurements

In the linear acoustics domain, for the wave velocity measurements, the tests started at the concrete age of 8 weeks, this was due to the most important expansion evolution in this period and to exceed the curing time of the concrete in the case of the reference specimens. The obtained results are plotted in Figures 4 and 5.

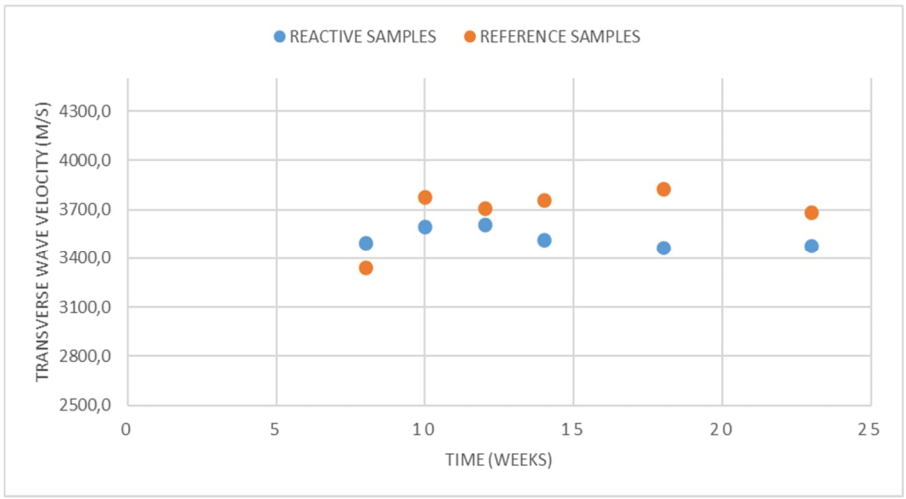

Figure 4. Transverse waves velocity results

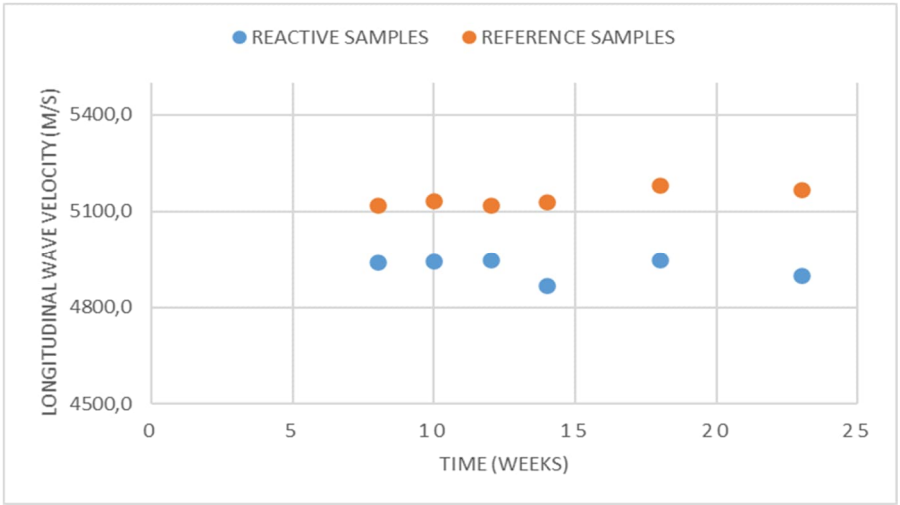

Figure 5. Longitudinal waves velocity results

For both, the longitudinal and transverse wave velocity, the results are in line with expectations, knowing that the orders of magnitude of propagation velocities in current concretes are included between 4000 and 5000 m/s in the longitudinal direction and between 1750 and 3000 m/s in the transverse direction. The obtained values are equal or very close to the typical concrete values for this type of test.

No significant variations of velocity were observed for the specimens under accelerated aging, this is also in agreement with several authors [20-22], who show that these tests can present small variations of velocity in order of 4-5% only at high expansion levels, for example 0.15% or 0.20% expansion. In other words, early detection cannot be expected using this measurement technique.

3.3 Resonant Ultrasound Spectroscopy (RUS)

Figures 6 and 7 show the results from numerical simulation of the resonance modes in bending and torsion, respectively. For the bending mode, the approximate frequency of 3.2kHz and for the torsion mode, 4.3kHz were obtained from numerical simulations. These results are compared with the experimentally values, shown in the graphs in figures 8 and 9. It can be observed that the experimental results are very close to the numerical results.

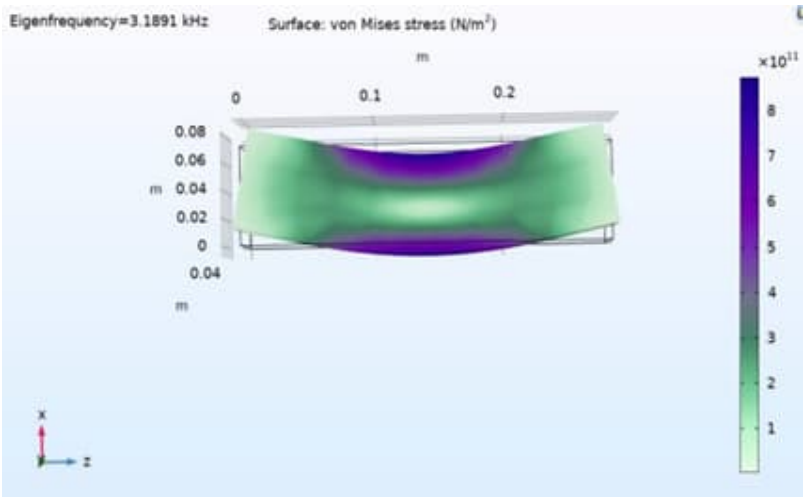

Figure 6. Bending mode

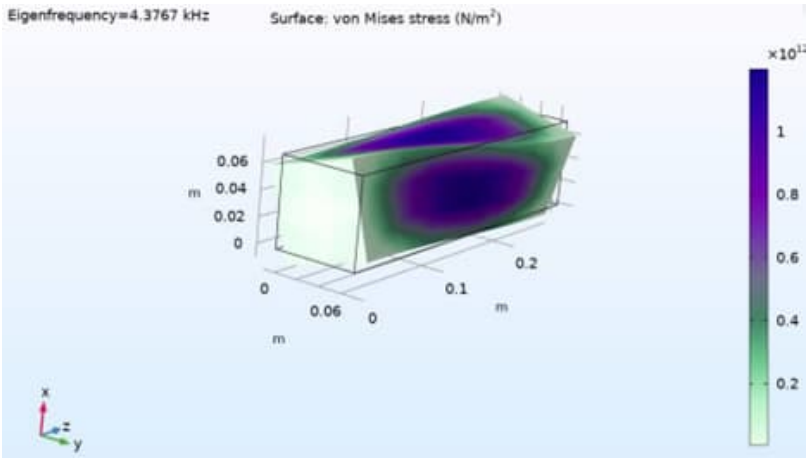

Figure 7. Torsion mode

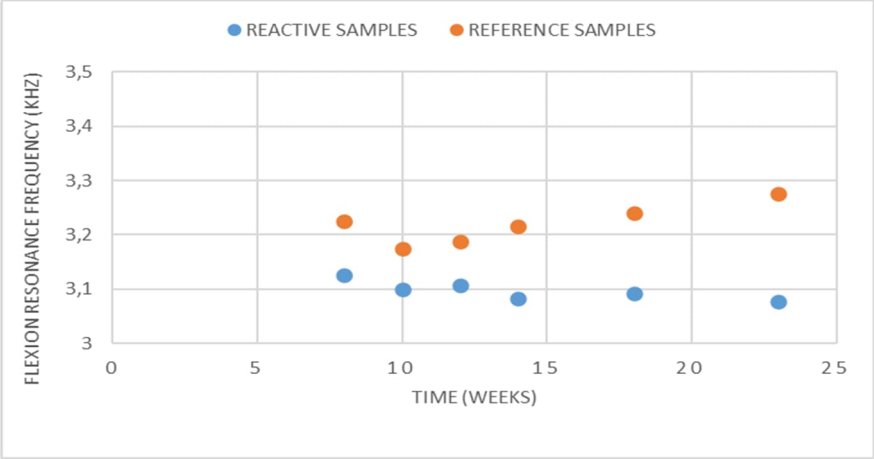

Figure 8. Experimental Bending mode results

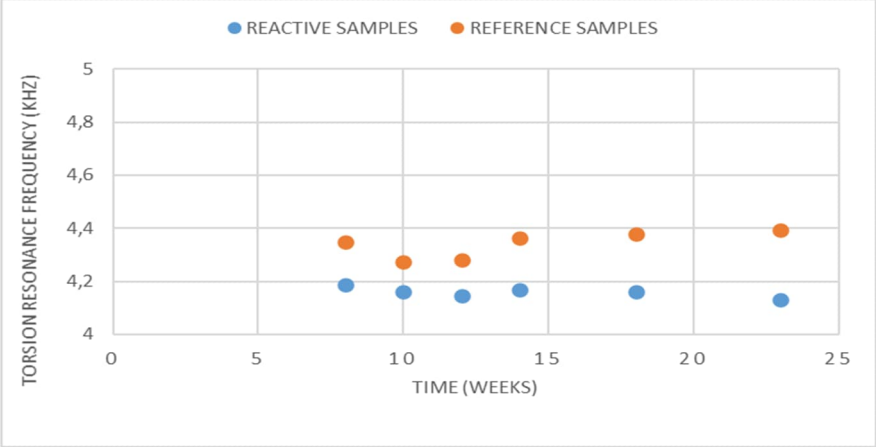

Figure 9. Experimental Torsion mode results

The evolution of the dynamic modulus of elasticity and the dynamic Poisson's ratio are plotted in figure 10 and 11 respectively. The Young's modulus is around 40GPa for reference specimens and for reactive specimens between 36 and 38 GPa, remaining in the range of expected values for the concrete. This difference can be attributed to several factors, such as the effect of heat treatment on the microstructure of the concrete.

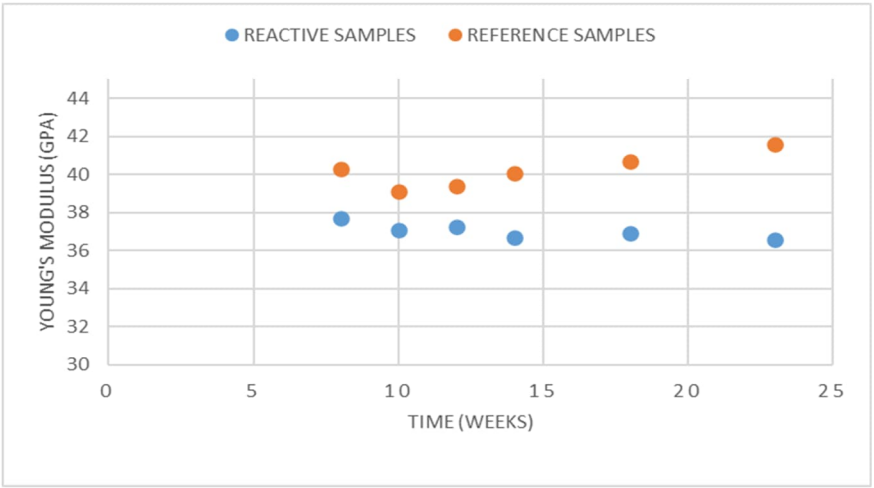

Figure 10. Young Modulus results

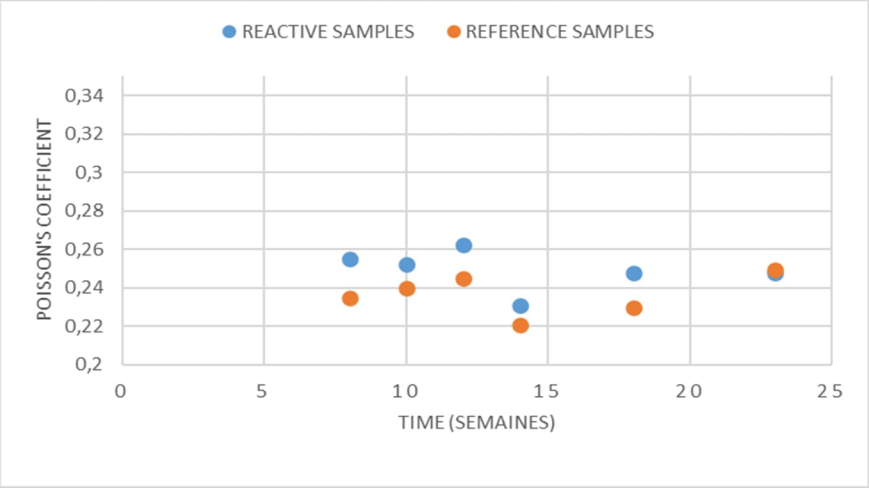

Figure 11. Poisson's coefficient results

The dynamic Poisson's ratio shows a value ranging between 0.22 and 0.26 for all specimens, which is a common value for concrete. Between the week 12 and the week 14 there was a decrease of 7% in this parameter for reactive samples, however, as the expansion levels are below the minimum limit that characterizes the presence of ASR, this variation cannot be associated to the pathology yet. A decrease of the same order is measured in the reference specimens, this is another factor that indicates that Poisson's ratio decrease cannot be attributed to the reaction.

This parameter has a smaller influence on the propagation of acoustic waves, leading to less accurate measurements. In general, no significant variation of these parameters appears following the development of the ASR, because this reaction has not exceeded the limit, as presented in section 3.1.

3.4 Nonlinear Resonant Ultrasound Spectroscopy (RUS)

The results of the initial tests, carried out with a specimen previously damaged by ASR, were obtained from post-treatment using MATLAB©, and can be seen in Figure 12.

As described in section 2.3.2.1, it is possible to observe the frequencies obtained in relation to the different amplitude levels to which the material was subjected. It is possible to see that there is a decrease in frequencies for higher deformation amplitudes, this behaviour is in accordance with equation 2, that is, the more the material is non-linear, the more the curves will tend to the left.

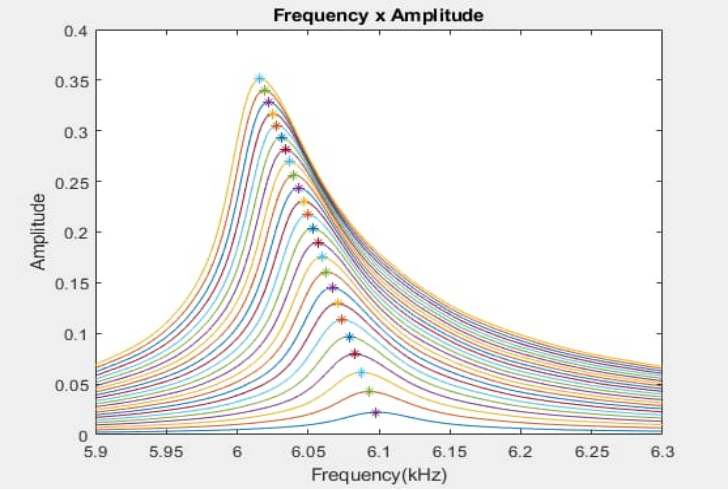

Figure 12. NRUS results for a ASR damaged specimen

In this case, for a concrete specimen with an expansion level of 0.2%, the quantitative value of the α parameter obtained was about 8000 with a strain amplitude Δε of 1.68×10^{-6}. According Boukari [23] for a similar experimental setup, concrete measurements of the α parameter (made in laboratory) can reach values ≤ 6000 at 0.09% of expansion. According to the same author, a concrete considered as healthy has α values between 1000 and 2000. The results obtained are consistent with the results found by this author and provide a parameter of comparison for the results obtained for the samples dedicated to this study, but it is very important to consider the differences between different concrete formulations and even within the same formulation.

For the samples manufactured for this work, for operational reasons, the NRUS tests started at 10 weeks concrete age. The results can be seen in figure 13.

Figure 13 shows the quantitative values obtained for the nonlinear non-classical parameter (α) are in accordance with the literature presented above and in agreement with the low levels of expansion presented at the beginning of this section.

It is possible to observe on Fig. 13 that the α parameters of reference samples reach higher values in comparison to the reactive samples, this is due to the natural drying of the reference concrete, knowing that the reactive concrete is in saturated environment (98% relative humidity) continuously until the day before the tests. It was expected that with the development of pathology, these values show a significant evolution to α, for the reactive samples, but due to the low expansion levels obtained so far, this behaviour cannot be observed.

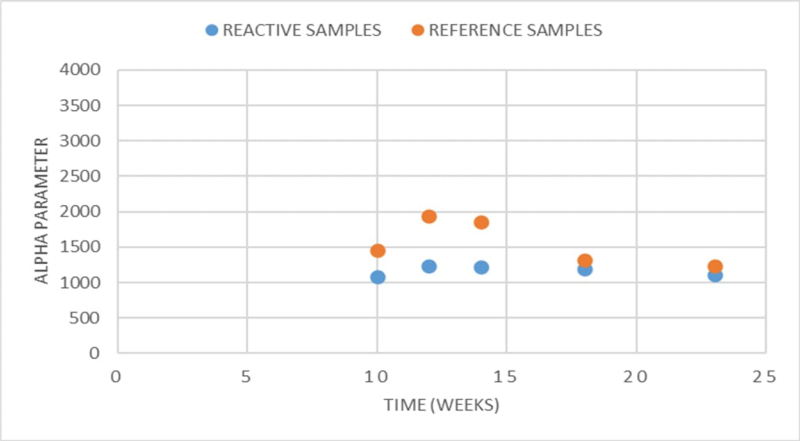

Figure 12. Nonlinear parameter results

4. CONCLUSIONS

In this work, different types of tests were applied involving linear and non-linear acoustics in the study of concrete, aiming to characterize the material and to detect an internal swelling pathology, in this case the ASR.

An evolution of the expansion of the specimens can be observed, but so in low levels until now, mainly due to the interruption of the accelerated aging of the concrete during the days of testing, corresponding to about 28% of the total time of accelerated aging.

A good agreement with the literature was obtained for all the tests (i) comparing the values found for all the parameters studied, (ii) no significant variations of the parameters was observed at the expansion levels addressed in this study.

From the linear acoustic tests (wave velocities and RUS) it was possible to characterize the material and obtain important parameters such as the elastic constants of the material, where small variations were found, due to difficulties encountered in the repeatability of the tests, a factor that requires attention to minimize the variability.

For NRUS, the experimental setup could be validated initially with the use of a concrete damaged by ASR, and the tests with de samples dedicated to this study, showed a behaviour compatible with the expansion levels obtained. An early detection of ASR from NRUS could not be obtained until now, since the minimum expansion limit to characterize ASR was not exceeded.

The same methods will be applied on aging tests under progress, for the samples presented in this study, to ensure the correlation of the parameters with the time and the pathology evolution. In parallel, the preparation of a new concrete mix, with a higher content of alkali, is envisaged. It is expected that, for the current concrete mix and for the new concrete mix planned, a significant expansion evolution will occur and consequently a non-linear parameter evolution.

The next step and next scale planned to 2023 will be to include a pathological specimen in the heart of a larger specimen with the aim to detect it by a nonlinear acoustic method. Finally, the method will be transferred on a very large specimen for “on site” scale to detect and follow ASR.

REFERENCES

[1] Décision n° 2021-DC-0706 de l'Autorité de sureté Nucléaire (ASN) du 23 février 2021

[2] Sims, I., Poole, A. B. Alkali-Aggregate Reaction in Concrete: A World Review. CRC Press, 2017

[3] J.M. Ponce, O.R. Batic, DIFFERENT manifestations of the alkali-silica reaction in concrete according to the reaction kinetics of the reactive aggregate, Cement and Concrete Research, Volume 36, Issue 6,2006

[4] Pan, J.W., Feng, Y.T.,Wang, J.T.,Sun, Q.C.,Zhang, C.H, Owen D.R.J Modeling of alkali-silica reaction in CONCRETE: a review. Frontiers of Structural and Civil Engineering, v.6, n.1, p.1-18, 2012.

[5] Fournier B., Bérubé, M. A. Alkali-aggregate reaction in concrete: a review of basic concepts and engineering implications. Can J Civ Eng. 27, 2000

[6] R.-P. Martin, C. Bazin, F. Toutlemonde, Alkali Aggregate Reaction and Delayed Ettringite Formation: common features and differences, in: Proceedings of the 14th International Conference on Alkali Aggregate Reaction, Austin, Texas, 2012.

[7] BOUZABATA, H., MULTON, S., SELLIER, A., & HOUARI, H. Swellings due to alkali-silica reaction and delayed ettringite formation: Characterisation of expansion isotropy and effect of moisture conditions. Cement and Concrete Composites, 34, 2012 https://doi.org/10.1016/j.cemconcomp.2011.10.006

[8] Ferraris, C. F. Alkali-Silica Reaction and HIGH-PERFORMANCE Concrete. Report NISTIR 5742. National Institute of Standards and Technology, Building and Fire Research Laboratory, Gaithersburg, Maryland, 1995.

[9] Dean, SW & Smaoui, N & Bissonnette, Benoit & Bérubé, M. & Fournier, B. & Durand, B. (2006). Mechanical Properties of ASR-Affected Concrete Containing Fine or Coarse Reactive Aggregates. Journal of Astm International. 3. DOI:10.1520/JAI12010

[10] Pleau, R., Bérubé, M.A., Pigeon, M., Fournier, B., Raphaël, S. Mechanical behaviour of concrete affected by ASR. 8th international conference on alkali-aggregate reaction, 1989, Kyoto, Japan: 721-726.

[11] Afshin Mohammadi, Ebrahim Ghiasvand, Mahmoud Nili, Relation between mechanical properties of concrete and alkali-silica reaction (ASR); a review, Construction and Building Materials,Volume 258,2020, 119567, https://doi.org/10.1016/j.conbuildmat.2020.119567.

[12] RILEM - Recommendations for the Prevention of Damage by Alkali-Aggregate Reactions in New Concrete Structures, 2016

[13] Hirotsugu Ogi, Keiji Sato, Takeyasu Asada, and Masahiko Hirao , "Complete mode identification for resonance ultrasound spectroscopy", The Journal of the Acoustical Society of America 112, 2553-2557 (2002) https://doi.org/10.1121/1.1512700

[14] ASTM C215-19, Standard Test Method for Fundamental Transverse, Longitudinal, and Torsional Resonant Frequencies of Concrete Specimens, ASTM International, West Conshohocken, PA, 2019

[15] Leif Bjørnø, Introduction to nonlinear acoustics, Physics Procedia, Volume 3, Issue 1, 2010, https://doi.org/10.1016/j.phpro.2010.01.003.

[16] Garrett, S.L. (2020). Nonlinear Acoustics. In: Understanding Acoustics. Graduate Texts in Physics. Springer, Cham. https://doi.org/10.1007/978-3-030-44787-8_15

[17] A. Van Den Abeele, K., Johnson, P. & Sutin, A. Nonlinear Elastic Wave Spectroscopy (NEWS) Techniques to Discern Material Damage, Part I: Nonlinear Wave Modulation Spectroscopy (NWMS). Res Nondestr Eval 12, 17–30 (2000). https://doi.org/10.1007/s001640000002

[18] Payan, Cédric & Ulrich, Timothy & Le Bas, Pierre-Yves & Saleh, Tarik & Guimarães, Maria. (2014). Quantitative linear and nonlinear Resonance Inspection Techniques and Analysis for material characterization: Application to concrete thermal damage.. The Journal of the Acoustical Society of America. 136. 537. 10.1121/1.4887451

[19] Younes Boukari, David Bulteel, Patrice Rivard, Nor-Edine Abriak, Combining nonlinear acoustics and physico-chemical analysis of aggregates to improve alkali–silica reaction monitoring, Cement and Concrete Research, Volume 67, 2015, Pages 44-51, ISSN 0008-8846, https://doi.org/10.1016/j.cemconres.2014.08.005.

[20] P. Rivard and F. Saint-Pierre, “Assessing alkali-silica reaction damage to concrete with non-destructive methods: From the lab to the field,” Constr. Build. Mater., vol. 23, no. 2, pp. 902–909, 2009

[21] F. Saint-pierre, P. Rivard, B. Sauriol, and G. Ballivy, “Étude de l ’évolution de la réaction alcalis-silice par méthodes ultrasoniques,” pp. 1–12, 2004

[22] Hwai-Chung Wu and Kraig Warnemuende "Nonlinear acoustic nondestructive testing for concrete durability", Proc. SPIE 3995, Nondestructive Evaluation of Highways, Utilities, and Pipelines IV, (9 June 2000); https://doi.org/10.1117/12.387843

[23] Younes Boukari, David Bulteel, Patrice Rivard, Nor-Edine Abriak, Combining nonlinear acoustics and physico-chemical analysis of aggregates to improve alkali–silica reaction monitoring, Cement and Concrete RESEARCH, VOLUME 67, 2015, Pages 44-51, https://doi.org/10.1016/j.cemconres.2014.08.005

[24] Garnier, Vincent & Chaix, Jean-François & Payan, Cédric. Improvement of new wave propagation techniques to characterize concrete. non-destructive testing in civil engineering nantes, france, june 30th – july 3rd, 2009

Smart Concrete Sensor for mechanical damage assessment

Shaban SHAHZAD[a], Ahmed TOUMI[a] , Jean-Paul BALAYSSAC[a]* and Anaclet TURATSINZE[a]

[a] LMDC, Université de Toulouse, INSA, UPS Génie Civil, 135 Avenue de Rangueil, 31077, Toulouse Cedex 04, France

**corresponding Author: jean-paul.balayssac@insa-toulouse.fr*

ABSTRACT

Nowadays, structural health monitoring becomes an important topic for civil engineering structures. One of the most challenging purpose is the monitoring of damage in concrete structures. Traditionally, strain gauges or optical fiber, are used for this purpose, but sometimes they are expensive and susceptible to damage under different environmental conditions. To overcome the problem of non-compatibility of the non-intrinsic sensor with cementitious materials, the development of intrinsic piezo-resistive sensor made with cementitious composites were proposed in the last years for Structural Health Monitoring (SHM). In line with the piezo-resistivity phenomenon, cement-based sensors can be used to monitor the health of the structures (mechanical strain or stress variation) by measuring the variation in the concrete electrical resistivity with external loading. However, the cementitious materials offer large resistance to current and hence it is not possible to make the cementitious materials a sensor without the inclusion of a conductive material to make cementitious material “a smart material”. Various types of conductive additions can be used to prepare the smart cementitious materials including steel fibers, carbon fibers, carbon nanotubes, slag, and carbon powder. Among them, carbon nanotubes are most frequently used conductive materials for the development of smart cementitious composites. Indeed, carbon nanotubes (CNTs) possess high electrical and thermal conductivity and having higher tensile strength. In this communication, we present the development of a smart concrete sensor using carbon nanotubes. The development and the validation of the smart concrete will be presented in a first part, in particular how was optimized the content of carbon nanotubes. Then, the sensitivity of smart concrete to mechanical stress and damage, independently of water content variations, will be described. Finally, we will demonstrate the ability of the smart concrete sensor embedded in a traditional concrete to monitor the evolution of damage and crack under flexural test. The response of the smart concrete sensor will be compared to usual measurements as Crack Mouth Opening Displacement (CMOD) and digital image correlation.

Keywords: flexural test, carbon nanotubes, resistivity, Digital Image Correlation (DIC).

1. INTRODUCTION

Damage inside concrete materials can be due to various types of loadings such as thermal stresses, earthquake, fire, and applied charges on the structures [1], but also to internal reactions like alkali–silica reaction (ASR), delayed ettringite formation or corrosion [2]. Therefore, nowadays, monitoring of the damage in concrete structures is an important subject of research. One of the most popular monitoring methods is acoustic emission technique (AET). Nevertheless AET needs to implement several sensors on the structure to detect the occurrence of damages and the number of sensors can rapidly become very important if the structure is very big and so the investigation can be very expensive.

Over the past few years, the possibility of detecting damage in concrete by measuring the change in electrical resistance of the concrete under the application of load [3], [4] has been demonstrated. Nevertheless, plain concrete being a poor conductor of electricity it shows a low sensitivity under the application of stress [5], [6]. Indeed, the ionic conduction which is prominent in plain concrete is greatly affected by moisture content. So, with the decrease in moisture content,

electrical resistivity of the concrete is increased thus making it less sensitive to assess the damage. In order to make intelligent concrete, inclusion of conductive materials such as carbon fibers, steel fibers, carbon nanotubes, slag and carbon black is an obligatory requirement. With the addition of any of the above conductive materials, resistivity of the concrete is significantly decreased and becomes quite independent of moisture content. More specifically, CNTs are being effectively used for the development of intelligent concrete due to the above highlighted properties [7].

In this study, multiwalled carbon nanotubes (MWCNTs) with concentration of 0.75 % with respect to mass of the cement were used to develop a smart concrete. The damage of the smart concrete under cyclic four-point bending test was monitored by the measurement of the electrical resistance combined to a Digital Image Correlation (DIC) method.

2. EXPERIMENTAL PROGRAM

2.1. Smart concrete

The composition of the smart concrete is shown in Table 1. 0.75 % (with respect to mass of cement) of multi-walled carbon nanotubes (MWCNTs) provided by Nanocyl were used as a conductive material to prepare an intelligent concrete. The properties of MWCNTs are shown in Table 2. For more specifications on the preparation of the smart concrete, one can refer to [7].

Table 1 Mix proportions for intelligent concrete

Material	Quantity	Unit
Ordinary Portland cement (CEM I 52.5R)	350	kg/m^3
Sand	875	kg/m^3
Aggregates	980	kg/m^3
Water	175	kg/m^3
Superplasticizer	4	%
MWCNTs	0.75	% by mass of cement

Table 2 Properties of MWCNTs

Properties	Unit	Value
Average diameter	nm	9.5
Average length	µm	1.5
Carbon purity	%	90
Surface area	m^2/g	250-300
Volume resistivity	Ω.cm	10^{-4}

2.2. Specimen under four-point bending test

Concrete beams of 100 x 100 x 500 mm with 10 mm notch at mid span were prepared as shown in Figure 1. Embedded electrodes made up of stainless-steel mesh with opening of 15 mm and wire diameter of 2 mm were used. Four electrodes were embedded in the middle of concrete specimens

with a spacing of 3 cm and 2 cm above the notch to measure electrical resistance using a four-probe method.

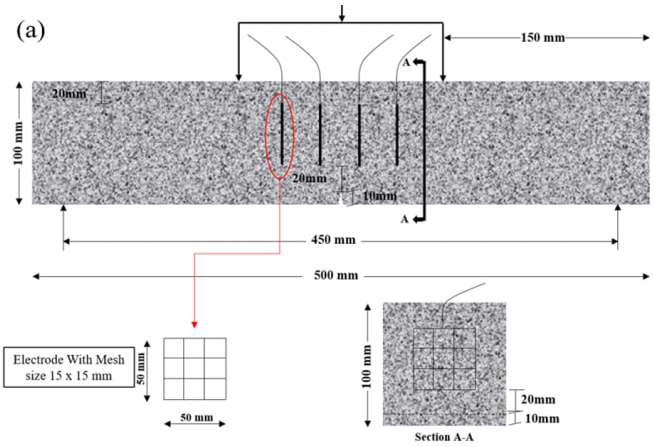

Figure 1. Specimen for four-point bending test and position of electrodes

2.3. Testing procedure

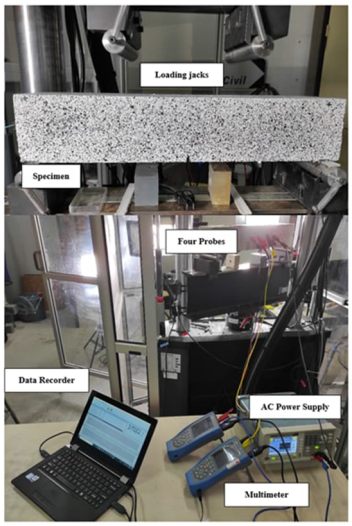

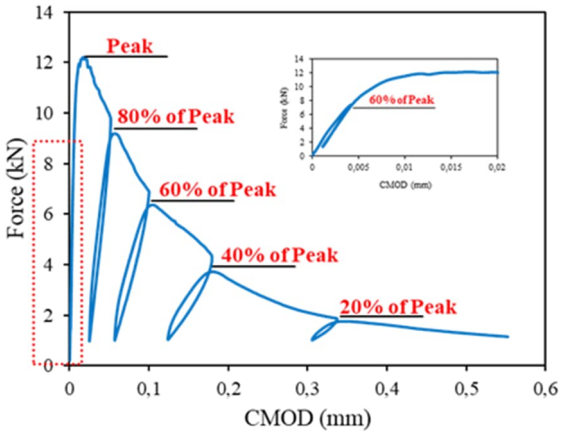

(a) (b)

Figure 2. Four-point bending test setup along four probe technique for electrical resistance measurement (a) and loading-unloading cycle (b)

Four-point bending test was carried out on the beams using MTS testing machine having a capacity of 100 kN. Crack mouth opening displacement (CMOD) at the notch of specimen was measured by a sensor. The test was controlled by the CMOD at a rate of 50 µm/min. Monitoring of crack propagation was carried out using electrical measurements and digital image correlation (DIC) techniques.

The test is presented in Figure 2-a. Five loading-unloading cycles under four-point bending were performed. The first cycle was applied in pre-peak zone starting from 0 to 60 % of the peak load. The other loading-unloading cycles were performed in the post-peak zone. The loading sequence is shown in Figure 2-b.

The variation in the electrical resistance of the smart concrete was measured by four-probe method during test. It is commonly used to find the resistance of the material by applying the current from external probes and measuring output voltage from internal probes. AC source is used for the

input (20 V peak-peak voltage and 1 kHz of frequency). The variation of resistance at each loading stage is reported to the initial value of resistance at the beginning of the test and is named Fractional Change of Resistance (FCR), expressed in percentage.

Digital image correlation (DIC) was also implemented during the test. DIC is an optical, non-contact measurement technique that is used to measure displacement fields on the surface of an object of interest. The measurement system can be seen in Figure 3.

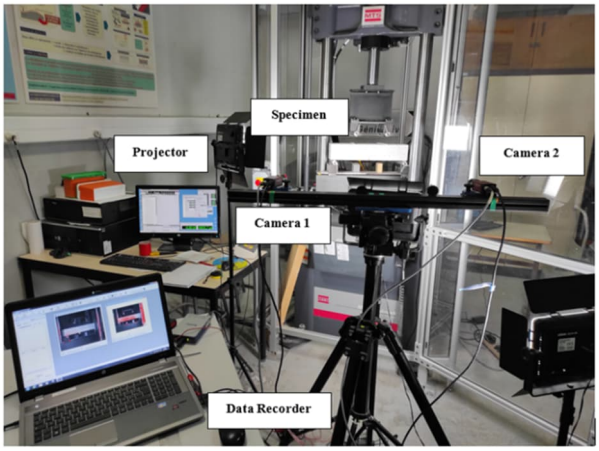

Figure 3. Setup for digital image correlation (DIC)

3. RESULTS AND DISCUSSION

Error! Reference source not found. 4 shows the relationship between load and CMOD for specimen under four point bending cyclic test. Load is increased linearly up-to the peak and the softening behaviour of the material after the peak.

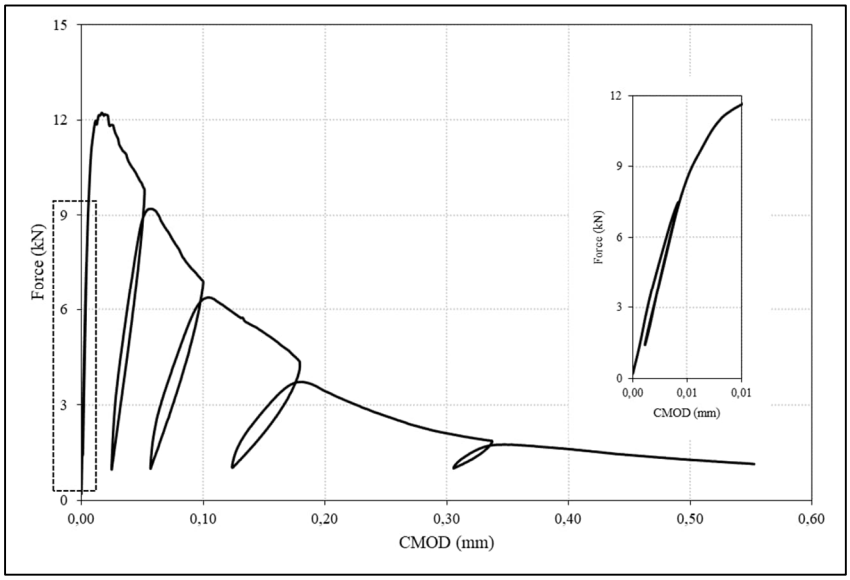

Figure 4. Force versus CMOD under cyclic loading

As seen in Figure 4, similar trend between load and FCR can be observed from the Figure 5. It can be observed that FCR increases with the increase of the load and decreases with the decrease of the load. The test was controlled by CMOD and it can be remarked that FCR quantifies the CMOD in the same pattern.

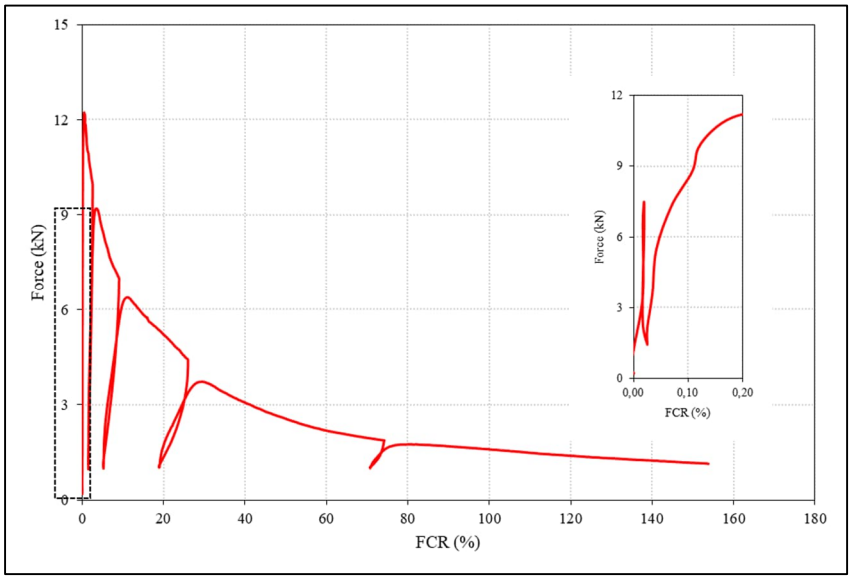

Figure 5. Load versus FCR under cyclic loading

Evolution of CMOD and FCR with time can be analysed from the results presented in Figure 6. FCR increases with opening of the crack and decreases with the closing of the crack during each cycle of loading/unloading. The FCR response of a smart concrete remains consistent with the CMOD. The magnitude of FCR is very low (< 0.04 %) at 60 % of the peak load in the pre-peak zone indicating that the material is still undamaged [8]. Moreover, it is observed that FCR significantly increases in the post-peak in line with the crack expansion at greater rate. FCR increases from 0.5% at peak-load to around 160 % at the end of the test (1 kN of load).

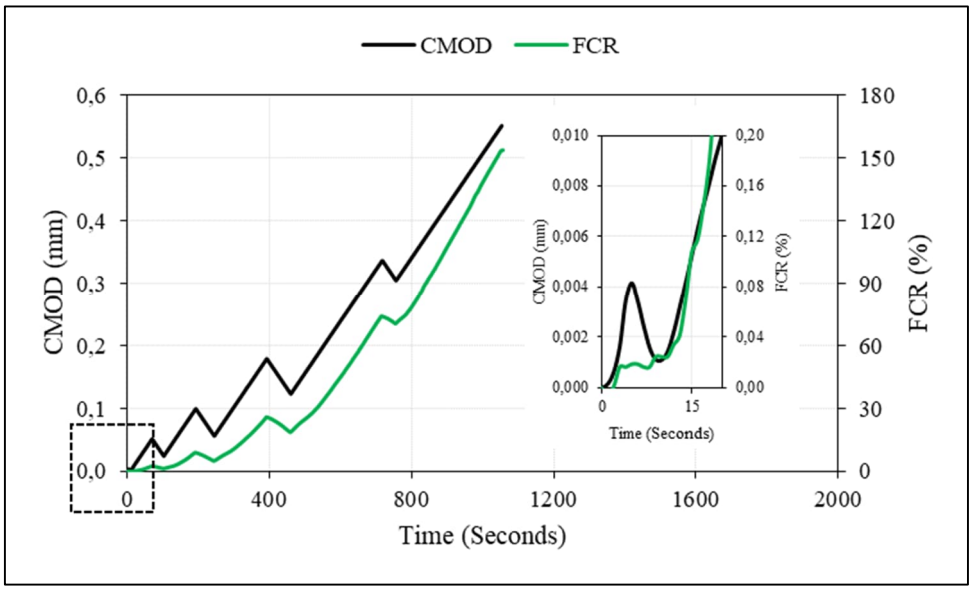

Figure 6. CMOD and FCR vs. time for the specimen

Figure 7 shows the evolution of crack at the various loading stages obtained from DIC technique. Evolution of crack is presented in the form of displacement fields according to the horizontal axis (U). Figure 7a shows the uniform displacement field indicating that the loading is not yet started. Figure 7b and 7c show the variation in the displacement field indicating the onset of a crack. At 80 % of post-peak and beyond, the propagation of macro-crack can be seen from the displacement fields as shown in the Figure 7d-h.

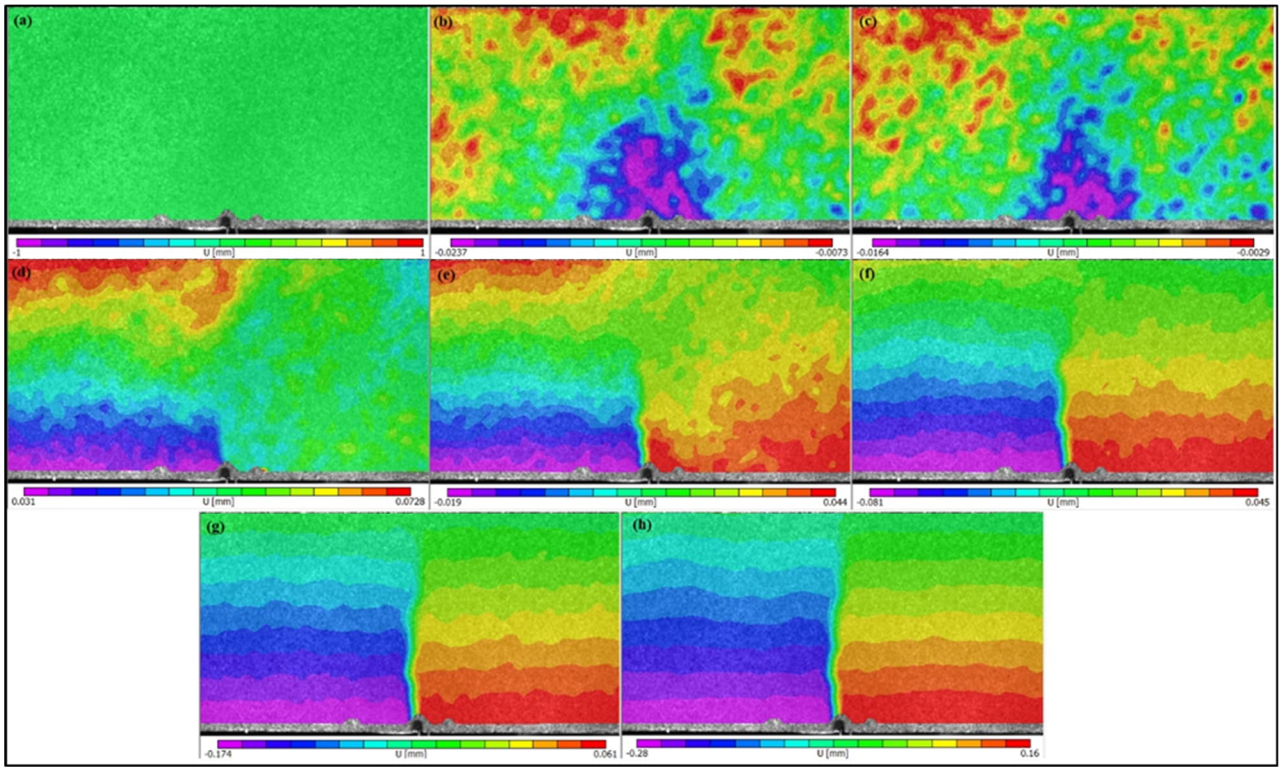

Figure 7. Displacement fields obtained by DIC at different loading stages: (a) pre-load, (b) 60% pre-peak, (c) peak-load, (d) 80% post-peak, (e) 60 % post-peak, (f) 40% post-peak, (g) 20% post-peak, and (h) failure

From the displacement fields, the crack length can be calculated by using a specific technique described in [9]. Figure 8 shows the variation of both crack length obtained by this analysis and FCR versus the ratio of the load to the failure load. DIC analysis shows that minor crack is detected at the 60 % pre-peak load which is also indicated by very small variation in electrical resistance represented by the lower value of FCR. DIC analysis showed that rate of crack length significantly increases in the post-peak zone that is also observed from large increase in the FCR. However, FCR does not significantly increase beyond 40 % of the post-peak compared to the crack length. This can be due to the bridging of MWCNTs [9] at the face of crack even though the crack is developed and detected by DIC. This can prevent the increase of FCR as the bridging of MWCNTs still provides a current conduction.

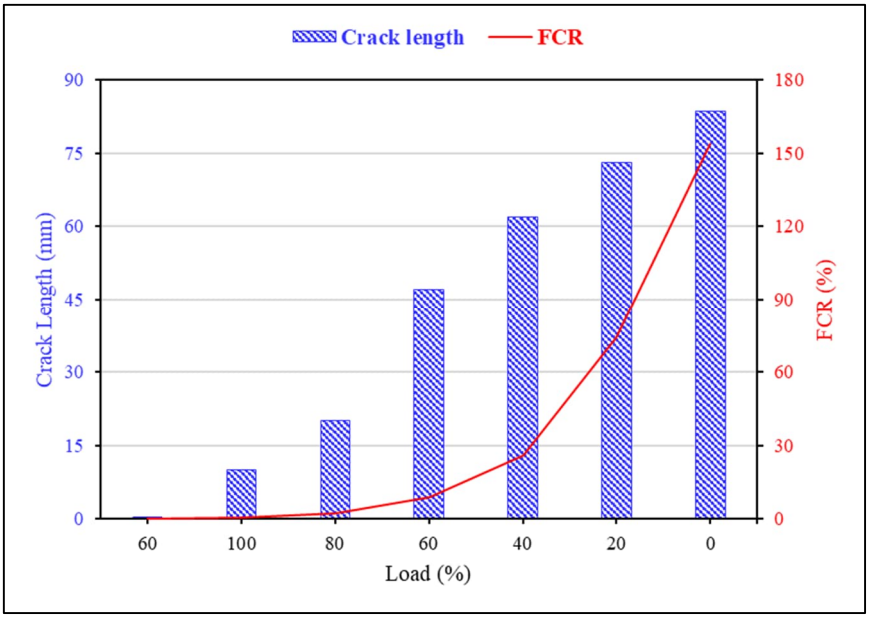

Figure 8. Crack length from DIC analysis and FCR versus load (% of peak-load)

4. CONCLUSION

In this study, a detailed experimental campaign is launched to investigate the damage of a smart concrete prepared with the addition of MWCNTs.

Results of a flexural test at a concrete beam show that the variation of electrical resistance (FCR) is well correlated to crack opening (CMOD). Digital Image Correlation (DIC) technique was also used to measure the apparent length of crack at various cycles of loading. However, the relationship between crack length measured by the DIC and FCR is not in good agreement due to the variation in the crack propagation on the surface (measured by DIC) and within the material (recorded by CMOD and FCR). This can be explained by the bridging of the carbon nanotubes as long as the crack opening is not reached beyond a certain threshold, above which bridging of MWCNTs becomes ineffective. This bridging contributes to decrease the electrical resistance in the zone seen as cracked by DIC.

ACKNOWLEDGEMENTS

The authors are thankful to the Higher Education Commission (HEC) of Pakistan for financial support of the thesis that is the source of this work.

REFERENCES

[1] K. Kovler and V. Chernov, '2 - Types of damage in concrete structures', in Failure, Distress and Repair of Concrete Structures, N. Delatte, Ed. Woodhead Publishing, 2009, pp. 32–56. doi: 10.1533/9781845697037.1.32.

[2] P. C. A. Types, 'Causes of concrete deterioration', IS536 Portland Cem. Assoc., 2002.

[3] S. Wen and D. D. L. Chung, 'Damage monitoring of cement paste by electrical resistance measurement', Cem. Concr. Res., vol. 30, no. 12, pp. 1979–1982, Dec. 2000, doi: 10.1016/S0008-8846(00)00351-3.

[4] P.-W. Chen and D. D. L. Chung, 'Concrete as a new strain/stress sensor', Compos. Part B Eng., vol. 27, no. 1, pp. 11–23, Jan. 1996, doi: 10.1016/1359-8368(95)00002-X.

[5] D. D. L. Chung, 'Damage in cement-based materials, studied by electrical resistance measurement', Mater. Sci. Eng. R Rep., vol. 42, no. 1, pp. 1–40, Oct. 2003, doi: 10.1016/S0927-796X(03)00037-8.

[6] L. Wang and F. Aslani, 'Development of self-sensing cementitious composites incorporating CNF and hybrid CNF/CF', Constr. Build. Mater., vol. 273, p. 121659, Mar. 2021, doi: 10.1016/j.conbuildmat.2020.121659.

[7] S. Shahzad, A. Toumi , J-P Balayssac, A. Turatsinze, V. Mazars, Cementitious composites reinforced with Multi Walled Carbon Nanotubes (MWCNTs): Effect of different dispersion methods on the electrical & mechanical properties, Matériaux et Techniques, Volume 110, Number 1, 2022.

[8] A. C. Ho, A. Turatsinze, R. Hameed, and D. C. Vu, 'Effects of rubber aggregates from grinded used tyres on the concrete resistance to cracking', J. Clean. Prod., vol. 23, no. 1, pp. 209–215, Mar. 2012, doi: 10.1016/j.jclepro.2011.09.016.

[9] H. F. Naji, N. N. Khalid, W. K. Alsaraj, M. I. Habouh, and S. Marchetty, 'Experimental investigation of flexural enhancement of RC beams with multi-walled carbon nanotubes', Case Stud. Constr. Mater., vol. 14, p. e00480, Jun. 2021, doi: 10.1016/j.cscm.2020.e00480.

In-situ corrosion rate measurements on reinforced concrete structures

Nuria Rebolledo[a], Julio E. Torres[a], Servando Chinchón[a], Javier sánchez[a*]
[a] Instituto de Ciencias de la Construcción "Eduardo Torroja" (IETcc-CSIC). Madrid, Spain.
* javier.sanchez@csic.es

ABSTRACT

The main cause of the reduction of the service life of structures is the corrosion of reinforcement, mainly due to the carbonation of concrete and/or the presence of chlorides. Each of these agents produces a particular type of corrosion with different corrosion kinetics.
There are different techniques for measuring corrosion rates in the laboratory which are well established and regulated. However, the measurement of in-situ corrosion in structures is a challenge as it is an intensive measurement where the area over which corrosion is being measured must be known precisely.
There are currently two different approaches to the problem. On the one hand, the guard ring can be used which, by applying a controlled current to an auxiliary electrode, allows the corrosion measurement area to be kept under control. The other approach is based on the Wenner method for resistivity using the so-called inductive or non-contact method.

Keywords: Durability; Corrosion; Rebar; Concrete.

1. INTRODUCTION

Corrosion is the primary cause of shortened reinforced concrete structure service life [1]–[3], prompting the need for costly maintenance and repair [4]–[6]. The consequences of corrosion such as cracking or even spalling of the concrete cover, loss of bonding and loss of cross-section, which can lead to brittle failure of the structures, are well known [7]–[15]. That problem acquires particular significance in offshore and geological storage structures, characterised by a long service life and inaccessibility that rules out any subsequent action [16], [17].

$Fe \rightarrow Fe^{2+} + 2e-$ (iron oxidation, anodic reaction) Equation 1
$O_2 + 2H_2O + 4e^- \rightarrow 4OH^-$ (oxygen reduction, cathodic reaction) Equation 2

The basic semi-reactions taking place in embedded steel corrosion are iron oxidation and oxygen reduction, as per Equations (1) and (2):

In underground/water environments, however, given the low levels of oxygen, the cathodic reaction is more likely to involve water reduction and hydrogen formation (Equation (3)):

$2H_2O + 2e^- \rightarrow H_2 + 2OH^-$ (water reduction, cathodic reaction) Equation 3

Reinforced concrete corrosion research often resorts to potentiodynamic polarisation tests, which deliver corrosion rates nearly instantaneously. The parameters most commonly yielded in polarisation tests are corrosion potential and corrosion current density. In processes involving polarisation activation only, corro-sion current density can be related to the potentiostat-measured current density with the following expression, known as the Butler–Volmer equation (Equation (4)):

$$i = i_a + i_c = i_{corr} \cdot \left(10^{\frac{V-E_{corr}}{b_a}} - 10^{\frac{-(V-E_{corr})}{b_c}}\right) \quad \text{Equation 4}$$

where i (μA/cm²) is the net free current density, i.e., the sum of the anodic (i_a) and cathodic (i_c) components; i_{corr} (μA/cm²) is the corrosion current density; V (V) is the steel electric potential;

E_{corr} (V) is the free corrosion electric potential; and b_a is the anodic and b_c (V/dec) the cathodic slope of the Tafel curve. Anodic current is conventionally deemed to be positive and cathodic negative.

Given the nature of corrosion itself, electrochemical techniques are the most suitable for measuring it. There are several studies and recommendations that define the methodology to be followed for a correct measurement [18]–[21]. The corrosion potential (E_{corr}) measurement helps to confine the areas with very negative potential values. This is a qualitative parameter. In the same way, the electrical resistivity (ρ) classify the areas in function of moisture content, concrete porosity and concrete microstructure [22], [23]. Between the electrochemical techniques only the polarization resistance (R_p) measurements can quantify the rate of corrosion [18].

Electrochemical techniques for calculating the corrosion rate from the measurement of polarisation resistance are described below. It should be noted that the measurement of the corrosion rate is a non-destructive and timely measure, since it provides the loss of material per unit of time and area. Therefore, in order to calculate the total loss of material over a period of time, it is necessary to integrate the corrosion rate in time, which in turn will allow an evaluation of the resistance capacity of the structure. Section 3 shows the techniques currently available to assess in-situ corrosion.

2. ELECTROTECHNICAL TECHNIQUES

2.1. Linear Polarisation Resistance (LPR or LRp)

This technique is based on a perturbation of the potential, with respect to the open circuit potential (OCP). A polarisation value ±20 mV relative to OCP and a scanning rate of 0.166 mV/s were applied to estimate linear polarisation resistance (*LPR*) and subsequently to calculate the corrosion rate [18], [21]. *Rp* was taken as the slope on the electric potential—cell current (minus the resistance drop) curve (Figure 1). Corrosion rate, i_{corr}, was found with the Stern–Geary equation [24]:

$$i_{corr} = \frac{B}{Rp\ A} \qquad \text{Equation 5}$$

where *B* is a constant equal to ~26 mV in concrete-embedded steel [18] and *A* is the lateral exposed area.

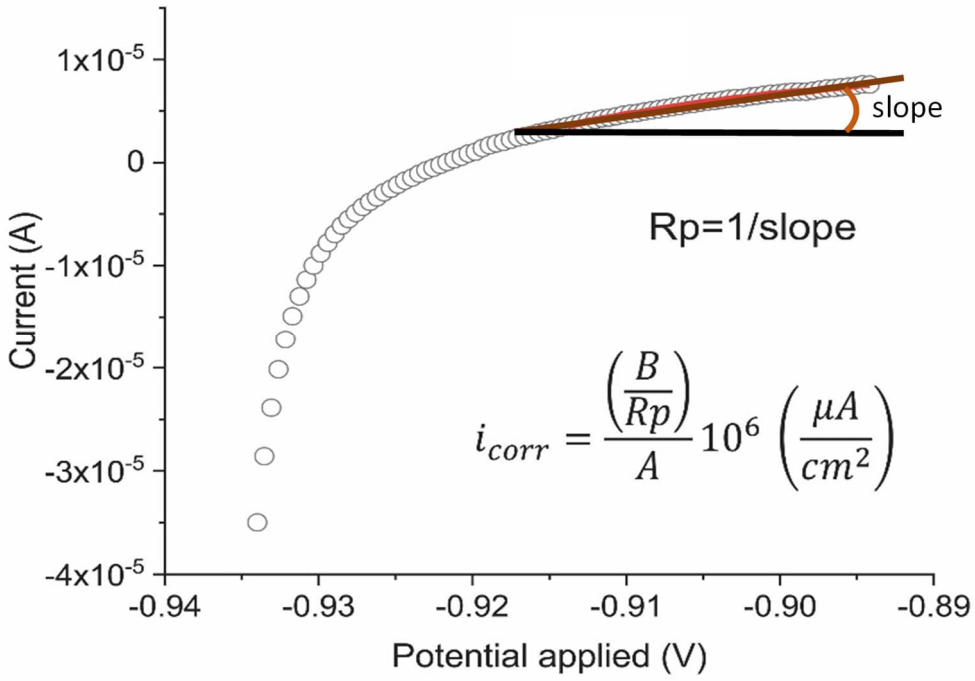

Figure 1. Example of the LPR test and Rp determination. Adapted from [21]

2.2. Electrochemical Impedance Spectroscopy (EIS)

EIS consists of applying an electric potential of varying frequency to an electrochemical cell and measuring the complex field of the resulting current [25]–[27]. Usually it is used a frequencies ranging from 10 kHz to 1 mHz with an amplitude of 0.010 V [28], [29]. The system's electrochemical response was simulated with one time-constant, Randles-type, equivalent electrical circuit (Figure 2). Resistance drop and linear polarisation resistance were found by fitting a regression line to the empirical data.

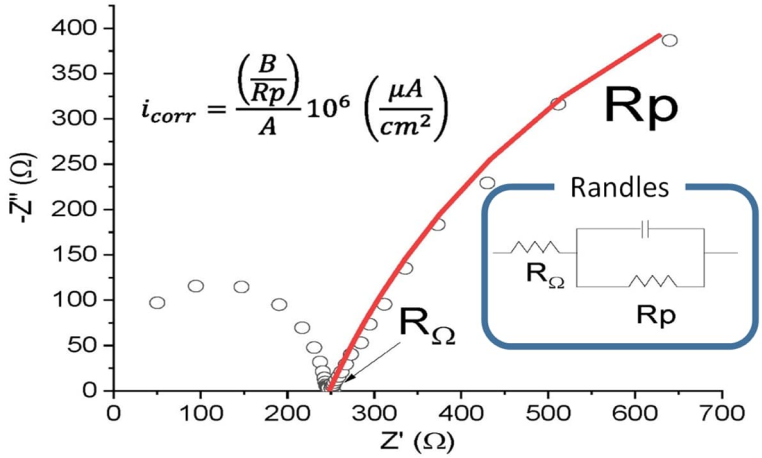

Figure 2. Example of EIS test and determination of R_Ω and Rp. Adapted from [21]

2.3. Chronopotentiometry (CP)

This technique is based on the application of a galvanostatic pulse and thus the measurement of the variation of the potential. Current is pulsed through the cell at an intensity of 1-100 µA, depending on the specimen [21], [30], [31]. The linear polarisation resistance was calculated assuming the response to fit the curve for the equivalent circuit shown in Figure 2. Since the variations in potential were obtained at constant intensity, the respective resistance could be found with Ohm's law. The initial rise in potential was associated with an ohmic drop and the remainder with linear polarisation resistance (Figure 3).

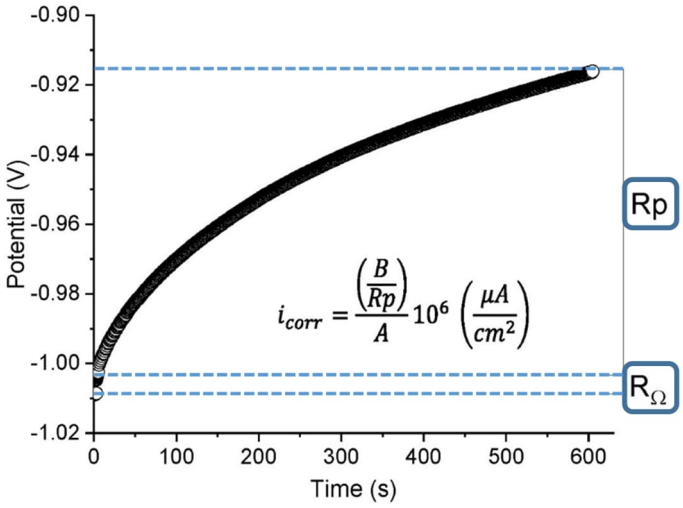

Figure 3. Example of the chronopotentiometry test and determination of R_Ω and Rp. Adapted from [21]

3. IN SITU MEASUREMENTS

For in-situ measurements it is necessary to be able to adequately control the area over which the corrosion is being measured[18], [32]. In addition, as in laboratory measurements, it is necessary to be able to estimate the ohmic drop during the measurements. Depending on the need for contact with the reinforcement, the methods can be divided into those where contact with the reinforcement is necessary and those where contact with the reinforcement is not necessary. Both types of measurement are briefly described below.

3.1. Confined current (guard ring method)

The modulated current confinement method involves contact with the armature and is based on the use of a guard ring during the measurement [32]–[35] (see figure 4).

In order to correct measurement it is necessary to incorporate a system to control that the current is always confined between the central counter electrode and the guard ring. This system consists in two reference electrodes named ‘‘confinement controller electrodes’’ whose potential difference serves to verify during the current application that the electrical field is the same than without current applied [32]. This verification has to be monitored during the current application, that is, during the 100 seconds that is necessary to wait to reach a steadystate condition, an operation, which is electronically complex. During this time, the two reference electrodes (confinement controllers) give information to the galvanostat in order it could apply more or less current through the guard ring to confine the current applied beneath the counter electrode. This is called ‘‘modulated confinement’’ because it is necessary to monitor both counters and actively vary the current applied through the guard ring during the measurement.

When the corrosion in the polarized zone is not homogeneous, but localized, two main considerations have to be made [32]:

1. The first is related to that the nominal area considered is larger than the corroding one. Then, the Rp is overestimated and the Icorr results lower. This happens not only in on-site measurements but also in laboratory tests. The best practice is then to reduce the size of the counter electrode in order to minimize the error. In any case, the a pitting factor can be applied [11], [36].

2. Another effect that also depends on the counter. The low-frequency current concentrates in and around the active spot, creating a larger electrolyte resistance. That is, in a galvanostatic pulse the current distribution on the working electrode changes from the instant-on moment, which is homogenously distributed, until the potential shift reaches a steady-state value, where the current instant-off is made. This fact suggests as best practice to measure the ohmic drop at the end of the galvanostic pulse and not at the beginning. Another possibility is to use a potentiodynamic sweep because in it the sweep rate is constant and the current distribution too.

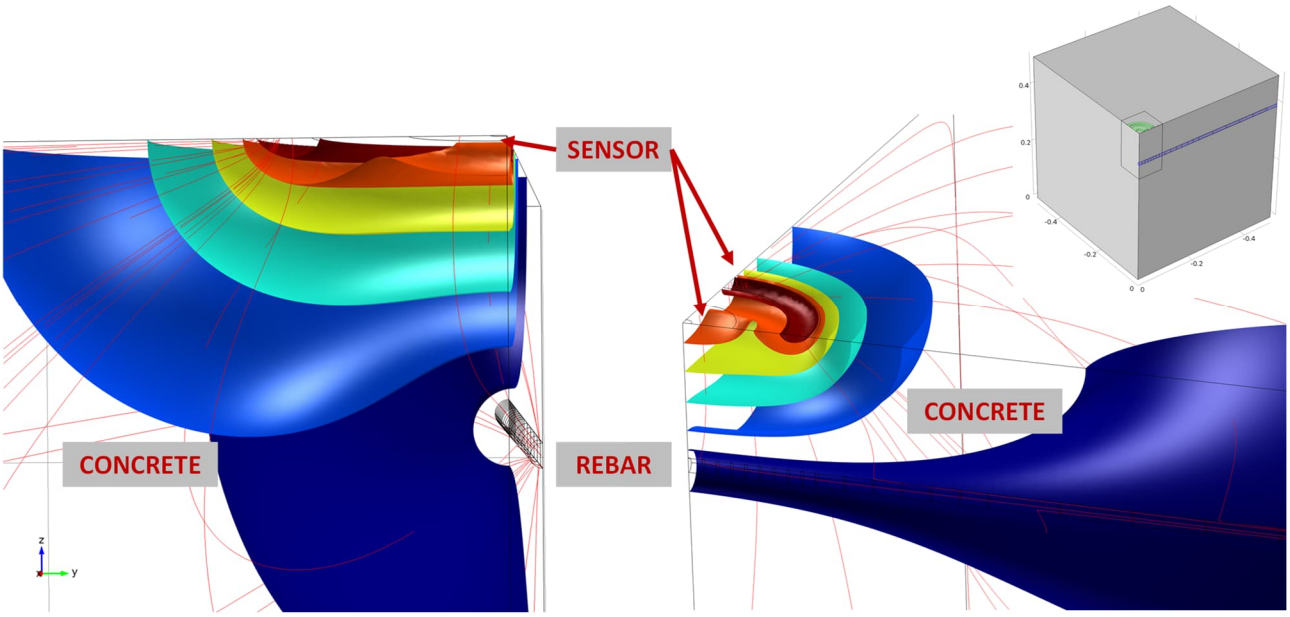

Figure 4. Simulation of modulated confinement method adapted from [37]

3.1. Non contact or induced method

Non-contact methods are based on the Wenner method for resistivity measurement [23], [31], [38]–[40]. These methods have the advantage that it is not necessary to make a connection to the reinforcement, however, it is not possible to obtain the corrosion potential of the reinforcement.

In this method the current is applied by the external electrodes and the change in potential is measured by means of the two internal reference electrodes [37], [41]–[43]. The external electrodes were small pieces of reinforcing steel and the two internal reference electrodes were Ag/AgCl (see figure 5). Currents of 10 - 500 µA were applied. The difference in potential is measured by means of the two internal reference electrodes.

The developments achieved in these studies make it possible to establish a correlation between the ohmic drop and the Rp values [41], [42]. An electrical model has also been obtained to explain the behaviour of the system with respect to an external electric field [37].

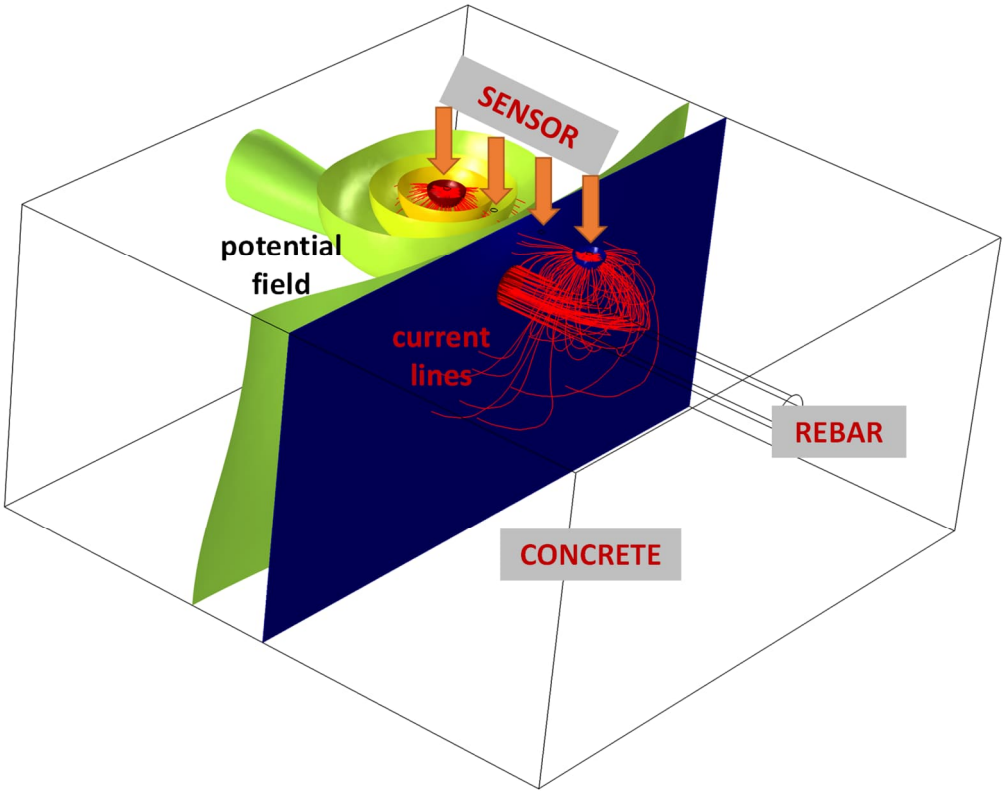

Figure 5. Simulation of non-contact in-situ corrosion rate method.

4. CONCLUSIONS

Since the nature of corrosion is electrochemical, electrochemical techniques are the most sensitive for measuring corrosion in reinforced concrete structures. The main parameters are corrosion potential, resistivity (of the concrete) and corrosion rate, which is the last one that makes it possible to quantify the loss of section of the reinforcement.

In general, in order to measure the corrosion rate, it is necessary to disturb the steel with respect to its state of equilibrium at the time of measurement. These methods are well defined and tested at the laboratory level, where small specimens are used and where the measurement area of the steel is controlled.

The challenge is to transfer the laboratory measurements to in-situ measurements on the concrete structure, where the area of reinforcement affected by the measurement is unknown. A measurement method based on modulated current confinement is already available which allows a very accurate measurement of the corrosion rate. In addition, other methods based on the Wenner method are being developed which are called non-contact or induced methods. The latter ones have

the advantage that they do not require contact with the reinforcement but have the disadvantage that they do not allow to measure the corrosion potential.

REFERENCES

[1] J. Xia, T. Li, J.-X. Fang, and W. Jin, "Numerical simulation of steel corrosion in chloride contaminated concrete," *Constr. Build. Mater.*, vol. 228, p. 116745, 2019, doi: https://doi.org/10.1016/j.conbuildmat.2019.116745.

[2] B. Hou *et al.*, "The cost of corrosion in China," *npj Mater. Degrad.*, vol. 1, no. 1, p. 4, 2017, doi: 10.1038/s41529-017-0005-2.

[3] L. Schueremans, D. Van Gemert, and S. Giessler, "Chloride penetration in RC-structures in marine environment – Long term assessment of a preventive hydrophobic treatment," *Constr. Build. Mater.*, vol. 21, no. 6, pp. 1238–1249, 2007, doi: https://doi.org/10.1016/j.conbuildmat.2006.05.006.

[4] D. V Val and M. G. Stewart, "Life-cycle cost analysis of reinforced concrete structures in marine environments," *Struct. Saf.*, vol. 25, no. 4, pp. 343–362, 2003, doi: http://dx.doi.org/10.1016/S0167-4730(03)00014-6.

[5] W. Zhu, R. François, Q. Fang, and D. Zhang, "Influence of long-term chloride diffusion in concrete and the resulting corrosion of reinforcement on the serviceability of RC beams," *Cem. Concr. Compos.*, vol. 71, pp. 144–152, 2016, doi: https://doi.org/10.1016/j.cemconcomp.2016.05.003.

[6] J. Wei *et al.*, "Corrosion evolution of steel reinforced concrete under simulated tidal and immersion zones of marine environment," *Acta Metall. Sin. (English Lett.*, vol. 32, no. 7, pp. 900–912, 2019.

[7] J. Sanchez, J. Fullea, and C. Andrade, "Corrosion-induced brittle failure in reinforcing steel," *Theor. Appl. Fract. Mech.*, vol. 92, no. Supplement C, pp. 229–232, 2017, doi: https://doi.org/10.1016/j.tafmec.2017.08.006.

[8] J. Sanchez, J. Fullea, C. Andrade, and C. Alonso, "Stress corrosion cracking mechanism of prestressing steels in bicarbonate solutions," *Corros. Sci.*, vol. 49, no. 11, pp. 4069–4080, 2007, doi: 10.1016/j.corsci.2007.05.025.

[9] J. Sanchez, J. Fullea, and C. Andrade, "Fracto-surface mobility mechanism in high-strength steel wires," *Eng. Fract. Mech.*, vol. 186, no. Supplement C, pp. 410–422, 2017, doi: https://doi.org/10.1016/j.engfracmech.2017.11.003.

[10] L. Franceschini, F. Vecchi, F. Tondolo, B. Belletti, and J. Sánchez Montero, "Mechanical behaviour of corroded strands under chloride attack: A new constitutive law," *Constr. Build. Mater.*, vol. 316, p. 125872, 2022, doi: https://doi.org/10.1016/j.conbuildmat.2021.125872.

[11] F. Vecchi, L. Franceschini, F. Tondolo, B. Belletti, J. Sánchez Montero, and P. Minetola, "Corrosion morphology of prestressing steel strands in naturally corroded PC beams," *Constr. Build. Mater.*, vol. 296, 2021, doi: 10.1016/j.conbuildmat.2021.123720.

[12] L. Franceschini, F. Vecchi, F. Tondolo, B. Belletti, J. S. Montero, and P. Minetola, "Variability in Section Loss and Maximum Pit Depth of Corroded Prestressing Wires BT - Proceedings of the 1st Conference of the European Association on Quality Control of Bridges and Structures," 2022, pp. 491–498.

[13] B. Belletti, F. Vecchi, C. Bandini, C. Andrade, and J. S. Montero, "Numerical evaluation

of the corrosion effects in prestressed concrete beams without shear reinforcement," *Struct. Concr.*, vol. n/a, no. n/a, doi: 10.1002/suco.201900283.

[14] B. Belletti, J. Rodríguez, C. Andrade, L. Franceschini, J. Sánchez Montero, and F. Vecchi, "Experimental tests on shear capacity of naturally corroded prestressed beams," *Struct. Concr.*, vol. n/a, no. n/a, Aug. 2020, doi: 10.1002/suco.202000205.

[15] F. Vecchi, B. Belletti, L. Franceschini, C. Andrade, J. Rodriguez, and S. J. Montero, "Flexural Tests on Prestressed Beams Exposed to Natural Chloride Action," 2021, December 0., pp. 205–212.

[16] P. Lu, B. Kursten, and D. D. Macdonald, "Deconvolution of the Partial Anodic and Cathodic Processes during the Corrosion of Carbon Steel in Concrete Pore Solution under Simulated Anoxic Conditions," *Electrochim. Acta*, vol. 143, no. Supplement C, pp. 312–323, 2014, doi: https://doi.org/10.1016/j.electacta.2014.08.027.

[17] P. Lu, S. Sharifi-Asl, B. Kursten, and D. D. Macdonald, "The irreversibility of the passive state of carbon steel in the alkaline concrete pore solution under simulated anoxic conditions," *J. Electrochem. Soc.*, vol. 162, no. 10, p. C572, 2015.

[18] Ø. Vennesland, M. Raupach, and C. Andrade, "Recommendation of Rilem TC 154-EMC: 'Electrochemical techniques for measuring corrosion in concrete'—measurements with embedded probes," *Mater. Struct.*, vol. 40, no. 8, pp. 745–758, 2007, doi: 10.1617/s11527-006-9219-4.

[19] R. Polder *et al.*, "Test methods for on site measurement of resistivity of concrete," *Mater. Struct.*, vol. 33, no. 10, pp. 603–611, 2000, doi: 10.1007/bf02480599.

[20] U. Angst *et al.*, "Corrosion of steel in carbonated concrete: mechanisms, practical experience, and research priorities – a critical review by RILEM TC 281-CCC," *RILEM Tech. Lett.*, vol. 5, no. 0 SE-, pp. 85–100, Dec. 2020, doi: 10.21809/rilemtechlett.2020.127.

[21] E. Garcia, J. Torres, N. Rebolledo, R. Arrabal, and J. Sanchez, "Corrosion of Steel Rebars in Anoxic Environments. Part I: Electrochemical Measurements," *Materials* , vol. 14, no. 10. 2021, doi: 10.3390/ma14102491.

[22] J. Warkus, M. Raupach, and J. Gulikers, "Numerical modelling of corrosion – Theoretical backgrounds –," *Mater. Corros.*, vol. 57, no. 8, pp. 614–617, 2006, doi: 10.1002/maco.200603992.

[23] J. Sanchez, C. Andrade, J. Torres, N. Rebolledo, and J. Fullea, "Determination of reinforced concrete durability with on-site resistivity measurements," *Mater. Struct.*, vol. 50, no. 1, Feb. 2017, doi: 10.1617/s11527-016-0884-7.

[24] M. Stern and A. L. Geary, "Electrochemical Polarization: I . A Theoretical Analysis of the Shape of Polarization Curves," *J. Electrochem. Soc.*, vol. 104, no. 1, pp. 56–63, 1957, doi: 10.1149/1.2428496.

[25] X. R. Nóvoa, "Electrochemical aspects of the steel-concrete system. A review," *J. Solid State Electrochem.*, vol. 20, no. 8, pp. 2113–2125, 2016, doi: 10.1007/s10008-016-3238-z.

[26] S. Chakri *et al.*, "Improved EIS Analysis of the Electrochemical Behaviour of Carbon Steel in Alkaline Solution," *Electrochim. Acta*, vol. 246, pp. 924–930, 2017, doi: https://doi.org/10.1016/j.electacta.2017.06.096.

[27] V. Vivier and M. E. Orazem, "Impedance Analysis of Electrochemical Systems," *Chem.*

Rev., Jun. 2022, doi: 10.1021/acs.chemrev.1c00876.

[28] S. Joiret, M. Keddam, X. R. Nóvoa, M. C. Pérez, C. Rangel, and H. Takenouti, "Use of EIS, ring-disk electrode, EQCM and Raman spectroscopy to study the film of oxides formed on iron in 1 M NaOH," *Cem. Concr. Compos.*, vol. 24, no. 1, pp. 7–15, 2002, doi: https://doi.org/10.1016/S0958-9465(01)00022-1.

[29] M. Keddam *et al.*, "Impedance measurements on cement paste," *Cem. Concr. Res.*, vol. 27, no. 8, pp. 1191–1201, 1997, doi: https://doi.org/10.1016/S0008-8846(97)00117-8.

[30] V. Feliu, J. A. Gonzalez, C. Andrade, and S. Feliu, "Equivalent circuit for modelling the steel-concrete interface. I. Experimental evidence and theoretical predictions," *Corros. Sci.*, vol. 40, no. 6, pp. 975–993, 1998.

[31] A. J. Garzon, J. Sanchez, C. Andrade, N. Rebolledo, E. Menéndez, and J. Fullea, "Modification of four point method to measure the concrete electrical resistivity in presence of reinforcing bars," *Cem. Concr. Compos.*, vol. 53, pp. 249–257, 2014, doi: 10.1016/j.cemconcomp.2014.07.013.

[32] C. Andrade, J. Sanchez, J. Fullea, N. Rebolledo, and F. Tavares, "On-site corrosion rate measurements: 3D simulation and representative values," *Mater. Corros.*, vol. 63, no. 12, pp. 1154–1164, 2012, doi: 10.1002/maco.201206775.

[33] S. Feliu, J. A. Gonzalez, and C. Andrade, "Electrochemical methods for on-site determinations of corrosion rates of rebars," in *Techniques to Assess the Corrosion Activity of Steel Reinforced Concrete Structures*, vol. 1276, N. S. Berke, E. Escalante, C. K. Nmai, and D. Whiting, Eds. 1996, pp. 107–118.

[34] S. Feliu, J. A. Gonzalez, C. Andrade, and I. Rzmaribona, *Errors introduced by the guard ring device in the on-site measurement of rebar corrosion rates*. 1990.

[35] S. Feliu, J. A. Gonzalez, M. L. Escudero, and M. C. Andrade, "Possibilities of the guard ring for electrical signal confinement in the polarization measurements of reinforcements," *Corrosion*, vol. 46, no. 12, pp. 1015–1020, 1990.

[36] E. Garcia, J. Torres, N. Rebolledo, R. Arrabal, and J. Sanchez, "Corrosion of Steel Rebars in Anoxic Environments. Part II: Pit Growth Rate and Mechanical Strength," *Materials* , vol. 14, no. 10. 2021, doi: 10.3390/ma14102547.

[37] C. Andrade, J. Sanchez, I. Martinez, and N. Rebolledo, "Analogue circuit of the inductive polarization resistance," *Electrochim. Acta*, vol. 56, no. 4, pp. 1874–1880, 2011, doi: 10.1016/j.electacta.2010.09.057.

[38] W. Morris, E. I. Moreno, and A. A. Sagüés, "Practical evaluation of resistivity of concrete in test cylinders using a Wenner array probe," *Cem. Concr. Res.*, vol. 26, no. 12, pp. 1779–1787, 1996, [Online]. Available: http://www.sciencedirect.com/science/article/B6TWG-3VSNGSB-R/2/befd7fa88eca3f02ebae907ae1bb6dba.

[39] F. Presuel-Moreno, Y. Liu, and Y. Y. Wu, "Numerical modeling of the effects of rebar presence and/or multilayered concrete resistivity on the apparent resistivity measured via the Wenner method," *Constr. Build. Mater.*, vol. 48, pp. 16–25, 2013, doi: http://dx.doi.org/10.1016/j.conbuildmat.2013.06.053.

[40] A. J. Garzon, C. Andrade, N. Rebolledo, J. Fullea, J. Sanchez, and E. Menéndez, "Shape factors of four point resistivity method in presence of rebars," in *Concrete Repair, Rehabilitation and Retrofitting III - Proceedings of the 3rd International Conference on Concrete Repair, Rehabilitation and Retrofitting, ICCRRR 2012*, 2012, pp. 695–

700.

[41] M. Keddam, X. R. Nóvoa, and V. Vivier, “The concept of floating electrode for contact-less electrochemical measurements: Application to reinforcing steel-bar corrosion in concrete,” *Corros. Sci.*, vol. 51, no. 8, pp. 1795–1801, 2009, doi: https://doi.org/10.1016/j.corsci.2009.05.006.

[42] M. Keddam, X. R. Nóvoa, B. Puga, and V. Vivier, “Impedance based method for non-contact determination of the corrosion rate in buried metallic structures,” *Eur. J. Environ. Civ. Eng.*, vol. 15, no. 7, pp. 1097–1103, Jan. 2011, doi: 10.1080/19648189.2011.9695296.

[43] A. Fahim, P. Ghods, O. B. Isgor, and M. D. A. Thomas, “A critical examination of corrosion rate measurement techniques applied to reinforcing steel in concrete,” *Mater. Corros.*, vol. 69, no. 12, pp. 1784–1799, Dec. 2018, doi: https://doi.org/10.1002/maco.201810263.

Numerical modelling of ultrasonic wave propagation in concrete using embedded sensors

Rouba Hariri[1], Vincent Garnier[2], Jean-François Chaix[2] and Odile Abraham[1]
[1]Univ Gustave Eiffel, GERS-GeoEND, F-44344 Bouguenais, France
[2]LMA UMR7031, Aix Marseille University, F-13625 Aix en Provence, France

ABSTRACT

Due to the importance of reinforced concrete for civil engineering structures, monitoring the state of concrete over time has become a special interest in non-destructive testing. Although many different studies have been performed on concrete monitoring, it is still a challenge to have valid information on the first centimeters of the structure. An ultrasonic measurement system design is proposed using pairs of ultrasound sensors that are embedded inside the concrete structures during the construction phase. This system is designed to contribute to the local evaluation of the most relevant indicators in the first 20 cm of the structure: compressive strength, Young's modulus, porosity, and water content. The design involves the development of transmitter and receiver probes embedded in concrete to measure, as a function of depth, the evolution of two parameters: ultrasonic velocity and attenuation. A frequency pulse is sent by the emitter, and the receiver records the wave after propagation. Based on the recorded signal at regular time intervals, information about the micro-structure of concrete can be monitored. A set of sensors with frequencies from 50 kHz to 200 kHz is currently being tested in small concrete samples to define a system suitable for large full-scale mock-ups. To have accurate information, the uncertainties generated by the heterogeneity on the observables must be quantified, evaluated and compared to perturbations due to indicator's properties change.

Keywords: Concrete, Non-Destructive Testing, Ultrasound, Durability indicators.

1. INTRODUCTION

Monitoring and non-destructive evaluation (NDE) have become the main focus in civil engineering as safety and environmental concerns have shown the necessity for methods to ensure structural reliability and increase the lifetime of concrete structures. NDE methods based on ultrasound propagation have shown the possibility of overcoming the limitations of traditional methods. Ultrasonic testing has some capacity to estimate the structure of different alloys of the components having different acoustic properties. The results obtained are immediate and, in several cases, only one surface requires to be accessed [1]. The velocity and attenuation of ultrasonic waves can be used to determine the elastic properties (Young Modulus, Poisson ratio) and also to characterize the micro-structural properties of concrete (porosity, grain size, micro-cracks, etc.). Although different studies have been conducted in concrete monitoring, it is still a challenge to have valid data on the first centimeters of the structure.

This work is part of a French ANR Project called "Scaning" whose main objective is to equip the structures with onboard sensors to evaluate the state of concrete as a function of time. The final purpose of this work is to design a multi-physics monitoring system (that combines ultrasonic, electromagnetic, resistivity, and capacitive methods) able to evaluate the changes in concrete property gradients over time, more specifically the saturation gradient. Recently, piezoelectric transducers have been embedded into concrete structures for non-destructive permanent monitoring of concrete ([1], [3]). Large volumes of concrete structures are monitored for changes in material properties by a limited number of transducers. Compared to usual ultrasonic transducers, using embedded transducers improves the proficiency and reproducibility of ultrasonic tests and allows measurements in unreachable places when the structure is in service ([4], [5]).

This paper focuses more particularly on ultrasonic wave measurements such as the time propagation and the maximum amplitude of the wave in concrete. A 2D numerical model is built and validated to study the ability of variable parameters, such as heterogeneity distribution and saturation ratio, represented by changes in the material properties, to influence the quality of the measurements. The variations generated by each parameter are estimated using numerical modeling in SPECFEM software [6]. A validation approach is first established to optimize the input parameters in the numerical model. This approach is detailed in the first part of the study. Then, data processing is used to calculate time propagation and amplitude in various configurations. The influence of heterogeneity and saturation ratio in concrete on the studied observables is presented. To accurately quantify all the uncertainties related to the material, no noise is added to the signal in this numerical study.

2. PROBLEM STATEMENT

An ultrasonic measurement system design is suggested using one pair of ultrasound sensors embedded inside the concrete structure. The Spectral Element Method (SEM) in the elastic domain is used to test several configurations of a concrete model in order to study the influence of physical and ultrasonic parameters on wave travel time and amplitude [8]. Significant effort will also be made to clean up information collected from the unwanted influential parameters in order to estimate the precision that can be expected in the field for travel time and attenuation measurements. First, the material properties and the frequency domain applied in the simulations are presented. The physical parameters for the simulations are similar to those used in [9]. Second, a validation of the numerical approach is presented to optimize the input parameters in the 2D model and therefore reduce the numerical uncertainties of the problem. Then, other configurations are tested to analyze the effect of the influencing factors (heterogeneity distribution, material properties change) on the observables.

3. MATERIALS AND 2D NUMERICAL MODELLING

3.1 Materials properties

The material properties used in the following numerical simulations are given (Table.1). The concrete properties in this paper are set to correspond to the values given in [8].

Table 1 Material properties for the matrix and the circular aggregates (ρ is the material density, E is the Young's modulus, ν is the Poisson's ratio, and Vp and Vs are respectively the longitudinal (pressure) and transverse (shear) wave velocities) [8]

Material properties	Mortar	Aggregate
ρ (kg/m^3)	2050	2610
E (GPa)	26	40
ν	0.26	0.25
V_p(m/s)	3950	4300
V_s(m/s)	2250	2475

To be able to generate the structure, the distribution of the aggregates should be representative of real concrete. An example of the cumulative volume fraction of aggregates as a function of the size taken in [8] is presented (Fig.1). In this study, assuming that aggregates smaller than 4 mm are homogenized in the mortar, the volume fraction of aggregates is taken at 40%. To define a random distribution of these aggregates, a Gaussian distribution is used in which the mean and variance values are respectively μ = 7 mm and σ = 2 mm (Fig.2). The aggregate radius varies between 4 mm and 10 mm.

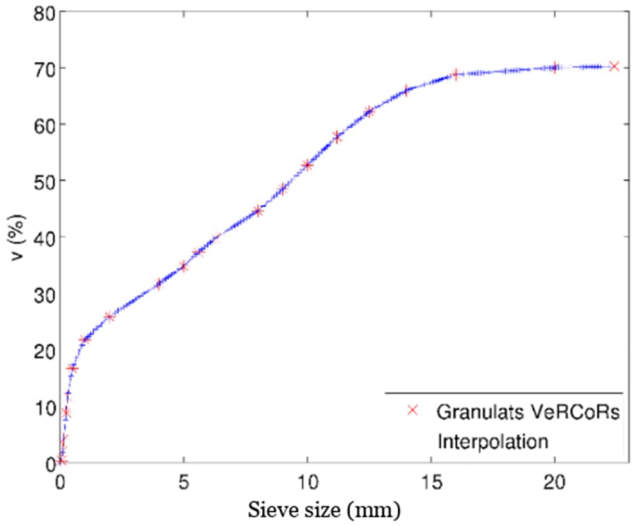

Figure 1. Cumulative volume fraction of aggregates as a function of size for VeRCoRs concrete

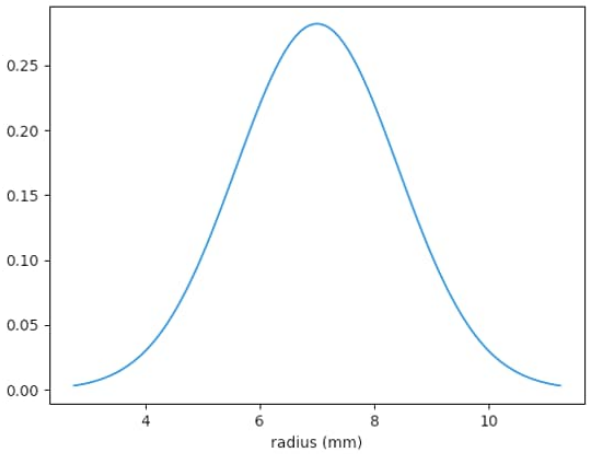

Figure 2. Gaussian distribution for random circular radii between 4 mm and 10 mm

3.2 Numerical modelling

Numerical modeling will be used to conduct a sensitivity study to evaluate the variations of the studied observables and to define the uncertainties in the experimental model. It would therefore be considered an "experiment" with digital tools that allow us to optimize the conditions of the real experiment set up. SPECFEM software is a free code based on the Spectral Element Method (SEM), allowing the simulation of wave propagation in acoustic, elastic, and viscoelastic conditions [7]. It is used in this work to simulate elastic wave propagation in both homogeneous and heterogeneous domains with randomly distributed circular aggregates [6]. We simulate a bounded computational domain by creating artificial boundaries on which absorbing conditions are imposed. The role of the absorbing boundaries is to avoid spurious waves from the reflection on the edges.

3.2.1 Geometry of a 2D numerical model.

The 2D numerical geometry is illustrated (Fig.3). An incident longitudinal wavelet propagates across the study domain [X,Y] = [18 cm, 8 cm] from the left to the right. In this paper, the emitter is a point source that generates a wave through the specimen. The emission signal which imposes the displacement corresponds to a Ricker signal that has a maximum amplitude and two minimums (Fig.4). In the snapshot, the color scale represents the displacement amplitude, with red color for a positive amplitude displacement and blue color for a negative amplitude displacement (Fig.3). The receiver is punctual and is placed in the study domain to record the displacements of the wave in both the X and Y directions of the wave field. The distance between the receiver and the emitter is d = 10 cm. This numerical geometry is meshed in the GMSH software [10]. To increase the precision

of measurements in the simulations, a function is used in SPECFEM software to optimize the mesh quality, including mesh size and element skewness.

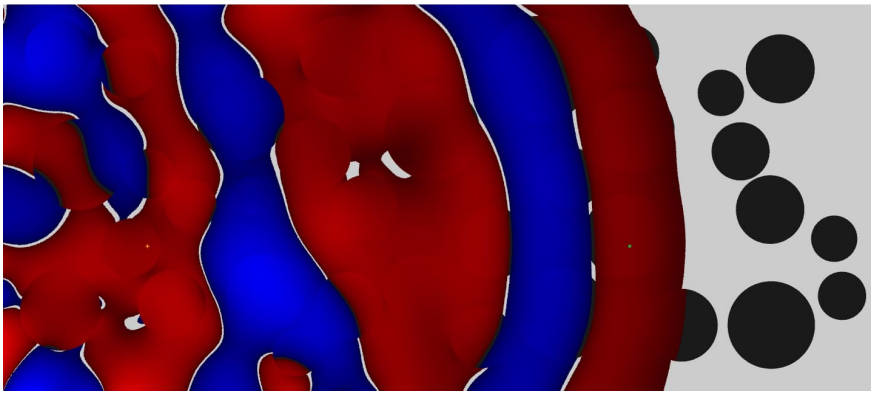

Figure 3. Numerical geometry of the study domain: Example of a heterogeneous medium with cylindrical diffusers of various radii

3.2.2 Frequency domain

In concrete, high-frequency (up to 500 kHz) is suggested [4] to carry out a faster-rising edge of the wave and therefore a reduced error when pointing its arrival time. Nevertheless, the large attenuation in concrete (due to scattering and viscous damping) controls the effective range of frequencies over which waves can be coherently propagated to a given distance. In this study, the wave frequency domain is limited to a maximum frequency of 200 kHz, which corresponds to a wavelength of around 24mm when compared with the larger aggregate size of 10mm. A Ricker wavelet with a peak frequency equal to 50kHz, 100 kHz, or 200kHz is taken as an incident longitudinal wave.

4. STUDIED OBSERVABLES AND MEASUREMENT METHODS

In this paragraph, the methodology to measure the propagation time (t_p) and the maximum amplitude (A_{max}) of coherent P-waves in a homogeneous medium is presented. Studies show that these two parameters can provide complementary information on concrete properties.

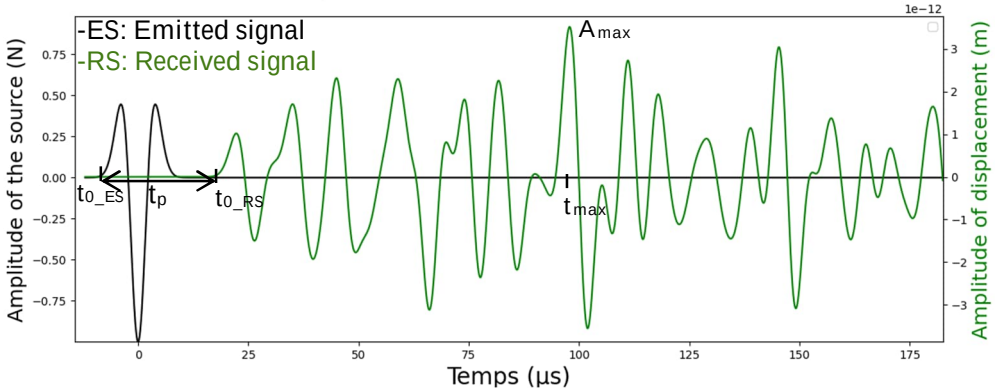

Figure 4. Displacement measurement simulation for the case of homogenized concrete

4.1 Propagation time of the longitudinal wave (t_p) and wave velocity

Wave propagation time (t_p) is the travel time from the start point of the source wavelet (t_{0_ES}) to the arrival time of the received signal (t_{0_RS}) (Fig.4).

$$t_p = t_{0\_RS} - t_{0\_ES} \quad (1)$$

Many approaches have been used to accurately pick the arrival time of the wave: The tangential line approach [11] requires drawing a tangential line from the point of the greatest gradient in front of the first peak and finding the intersection of that line with the time axis. The advantage of this approach is that only data near the rising part of the signal is necessary. However, when using this approach, the arrival time value is sometimes slightly earlier than the experimental value. Another

method is to choose the arrival time of the signal as the instant when the amplitude of the signal exceeds the noise level by a factor of 4, which makes it possible to detect the signal even if the noise is very large [8]. Because noise is not considered, a certain time range is selected between the beginning of the signal and the time corresponding to its first peak (t_{max})(Fig.4). In this range, the arrival time (t_{0_RS}) is determined as the instant when the amplitude is higher than the peak amplitude by a factor of 0.01. This method, hereafter called the threshold method, was found to give the best match between the measured value of t_p and the actual value calculated in the homogeneous medium (Fig.4).

In the following the velocity (V_{P-wave}) of the wave is determined as:

$$V_{P-wave}=\frac{d}{t_p} \quad (2)$$

In the case of a homogeneous material with the properties of the aggregates (table 1), the propagation time and the velocity of the wave are found to be in the same order as the values in the case of a homogeneous material without aggregates. When comparing the numerical values to the experimental results, the errors in time and velocities are found to be 1.3% for the tangential method and 0.6% for the threshold method. Therefore, the latter method is chosen in the following to calculate the propagation time of the wave.

4.2 Maximum Amplitude ($\mathbf{A_{max}}$)

The amplitude of a wave is a very precise tool to evaluate material changes. It is not frequently used as it requires reproducible coupling of the ultrasonic transducers, which is not always feasible. Using embedded sensors eliminates coupling complications and permits the evaluation of the ultrasonic wave amplitude. For this paper, the change in amplitude is monitored at the first peak of the received signal (Fig.4). The maximum amplitude is considered to be an ultrasonic wave propagation index that reflects variations in apparent viscosity related to changes in physical properties during the evolution of concrete [12]. Furthermore, the variation of the maximum amplitude is related to the heterogeneity of the concrete and gives information about the propagation paths of waves: a wave that propagates in the same direction as the incident wave after diffraction by heterogeneity has a lower amplitude than the one that does not interact with it. In this paper, we are interested in studying the variation of amplitude as a function of heterogeneity and material changes in concrete. The observable that is used in the following is the maximum amplitude at the first peak of the received signal.

5. RESULTS AND DISCUSSIONS

5.1 Validation of the numerical modelling at f=100 kHz

In order to validate the numerical approach used in this study, a comparison was made between the results of the simulation on a homogeneous matrix composed of mortar and a homogeneous matrix composed of mortar and aggregates with the same mechanical properties as the mortar. This computation makes possible the quantification of the errors related to the mesh only. First, aggregates are added to the homogeneous medium. The source wave frequency is 100 kHz and the wave traveling distance is 10 cm. The wave field recorded for the mortar and aggregates matrix is compared to the wave field recorded for the mortar matrix and is presented in addition to the source wave (Fig.4). Wavefronts are overlaid. The variation of the amplitude of wave displacement in one direction and the variation of the arrival time of the wave are determined as:

$$\Delta A_{max} = A_{max\ \_homo} - A_{max\ \_homo\_with\_aggregates} \quad (3)$$

$$\Delta t_{0\_RS} = t_{0\_RS\_homo} - t_{0\_RS\_homo\_with\_aggregates} \quad (4)$$

These variations are equal to ΔA_{max}= 0.02% and Δt_{0_RS} = 0.007%. The errors related to mesh generation are below 0.02 % both for time travel time and amplitude, so the numerical uncertainties are negligible compared to other variations that will be detailed in this paper, such as variations related to the heterogeneity and to property changes in concrete.

5.2 Influence of the heterogeneity of concrete on the studied observables

During their propagation time, ultrasonic waves will interact strongly with the multiple heterogeneities of the concrete. The resulting effects due to these interactions should be quantified in order to separate them from the ones related to the evolution of the saturation ratio in concrete. Aggregate distribution was found to have a significant effect on measured travel time and ultrasonic wave velocity [9]. In several studies, ultrasonic measurements were performed on concrete samples and the wave travel time was recorded and used to calculate the wave velocity, which was used as a parameter in the evaluation of concrete properties [13].

Concrete and aggregate properties are presented in Table 1, with spherical aggregates whose surface ratio is 40% and whose size distribution varies from 4 mm to 10 mm (Fig.1). Numerical simulations are performed to study wave propagation in 10 different disorder realizations using an emission frequency of 100 kHz. The aim of using multiple configurations is to quantify the uncertainty of velocity measurement related to the distribution of aggregates. For each realization, the number of aggregates between the source and the receiver is different. Therefore, in each simulation, the source-receiver distance is the same (d=10 cm) but the waves propagate along different paths. Once these variations are quantified, they will be compared to the ones related to property change in concrete in part 5.3. An example of a wave propagation snapshot taken during the simulation of the first realization is illustrated (Fig 3). Emitted and received signals are illustrated for two different disorder realizations in Fig.5 and Fig.6.

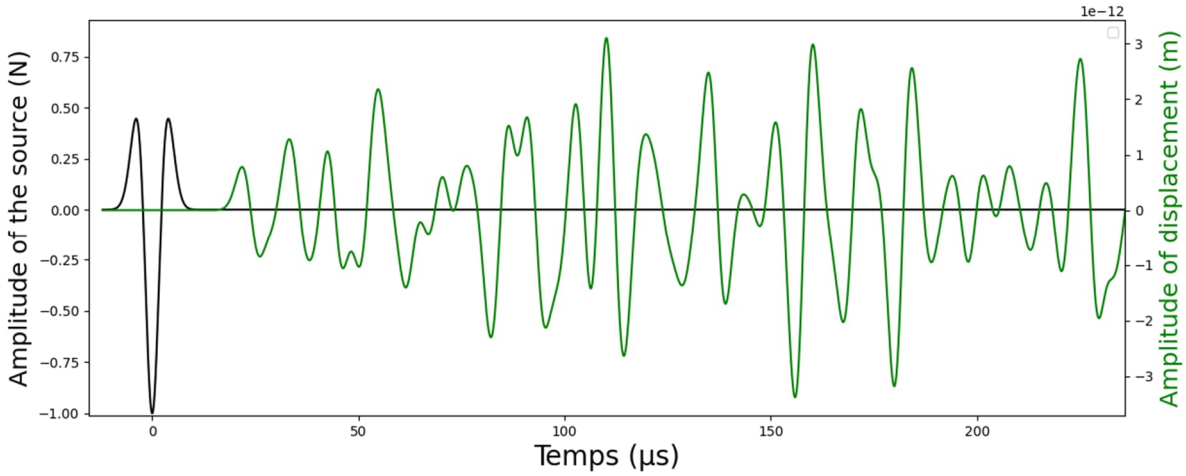

Figure 5. Displacement measurement simulation for aggregates distribution n°1

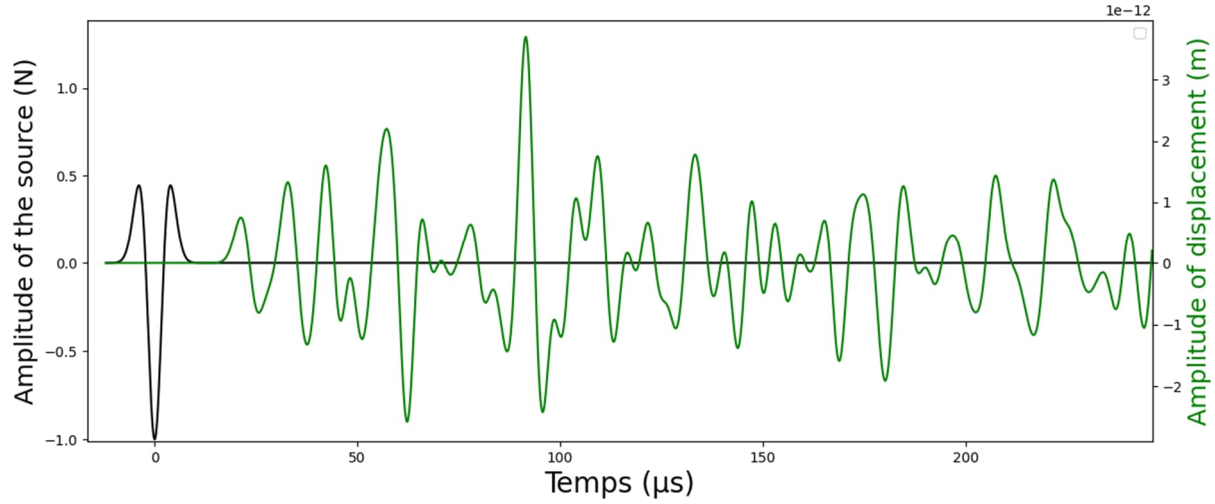

Figure 6. Displacement measurement simulation for aggregates distribution n°2

The propagation time (t_p) and maximum amplitude (A_{max}) of P-waves are calculated and Δt is the variation between the propagation time of the wave for each disorder realization (t_p) and the average travel time of all realizations (t_{ave}) (Table2).

Table 2 Variation of observable values related to the heterogeneity of concrete for 10 realizations of disorder

disorder realization number	Maximum amplitude of the received signal (A_{max}) (10^{-12} m)	Propagation time of the wave (tp) (10^{-6} s)	Δtp (%) variation of tp compared to the average travel time of the wave
1	0.88	25.07	0.83%
2	0.76	25.19	0.36%
3	0.78	25.49	0.82%
4	0.86	25.22	0.23%
5	0.87	25.27	0.03%
6	0.69	25.43	0.58
7	0.92	24.97	1.22%
8	0.67	25.37	0.35%
9	0.71	25.48	0.78%
10	0.77	25.33	0.19%
Average value	0.791	25.282	0.539 %
Standard deviation	+/- 0.08	+/- 0.164	

Results show that the variation in the propagation time of the P-wave related to the heterogeneity of concrete can be up to 1.22%. Therefore, given that these variations are quantified, the ultrasonic observables are tested to verify their ability to accurately measure other variations, related to the evolution of the water gradient in concrete, despite the observed influence of heterogeneity.

5.3 Impact of the variation of the saturation ratio on the studied observables for one disorder realization

Water saturation profiles in concrete are essential to evaluate its durability and can be determined using non-destructive measurement methods. Ultrasonic methods are applied for strength assessment through elastic modulus measurement. Several studies have been performed to establish relations between the saturation ratio and the strength of concrete [14].

The aim of this study is to examine the possibility of the NDE of concrete from a knowledge of the relationship between the saturation ratio and the ultrasonic propagation in concrete. The concrete saturation rate represents the volumetric content of free water in the material. Its value is between 0% (completely “dry” material) and 100% (completely saturated), although these extreme values are never reached in practice [15].

In the current investigation, the same configuration of concrete (disorder realization N°1 in table 2) with changes in the material properties, representing different saturation ratios, is conducted to collect reliable data for estimating the propagation time of the wave. To accurately describe the variation of the saturation ratio in concrete, the properties (ρ, Vp, Vs) are increased from 1 to 5% and are compared to the properties (ρ, Vp, Vs) of the concrete at the initial state 0. Results are presented in table 3.

Table 3 Variation of the studied observables related to variation (%)of the mortar properties (disorder realization n°1 of table 2)

Percentage of mortar properties change	Aggregates properties			Mortar properties			Maximum Amplitude of the received signal	Propagation time of the wave	$\Delta tp = \frac{t_{pi} - t_{p0}}{t_{pi}}$ With i=[1,5]
(%)	ρ (kg/m^3)	Vp (m/s)	Vs (m/s)	ρ (kg/m^3)	Vp (m/s)	Vs (m/s)	Amax (10^{-12}m)	tp (10^{-6} s)	(%)
0	2610	4300	2475	2050	3950	2250	0.88	25.07	
1				2070.5	3989.5	2272.5	0.869	24.97	0.39
2				2091	4029	2295	0.86	24.94	0.51
3				2111.5	4068.5	2317.5	0.844	24.92	0.56
4				2132	4108	2340	0.829	24.77	1.19
5				2152.5	4147.5	2362.5	0.816	24.61	1.83

Results show that when the change of the mortar properties increased from 1% to 5%, both the maximum amplitude and the propagation time of the wave decreased.

The variation of the studied observables related to the change of mortar properties is found to be comparable to that related to the heterogeneity of concrete. Only mortar variation superior to 5% gives a variation of arrival time $\Delta t_{p\_mortar\_changes} < 1.83\%$ superior to $\Delta t_{p\_heterogeneity}$ than can take values as high as 1.22%. Therefore, the measurements taken at a certain depth below the concrete surface should be compared to a reference state to be able to measure the effect of the water gradient in concrete despite the variations due to the heterogeneity of concrete.

5.4 Influence of sensors emission frequency on the studied observables

The sensor's emission frequency is an important parameter that can present sources of errors and uncertainties. The influence of this parameter on the performance of observables has been acknowledged in [13]. When changing the emission frequency, the wavefront changes and therefore the terms defining "tp" and "A_{max}" become frequency dependent.

Figures 7, 8, and 9 show waveforms of the source (Ricker signal) and the received signal of numerical simulations that are conducted for a heterogeneous medium at various excitation frequencies of 50 kHz, 100 kHz, and 200 kHz. Results are illustrated in tables 4 and 5 respectively for the homogeneous medium and the heterogeneous medium of disorder realization n°1.

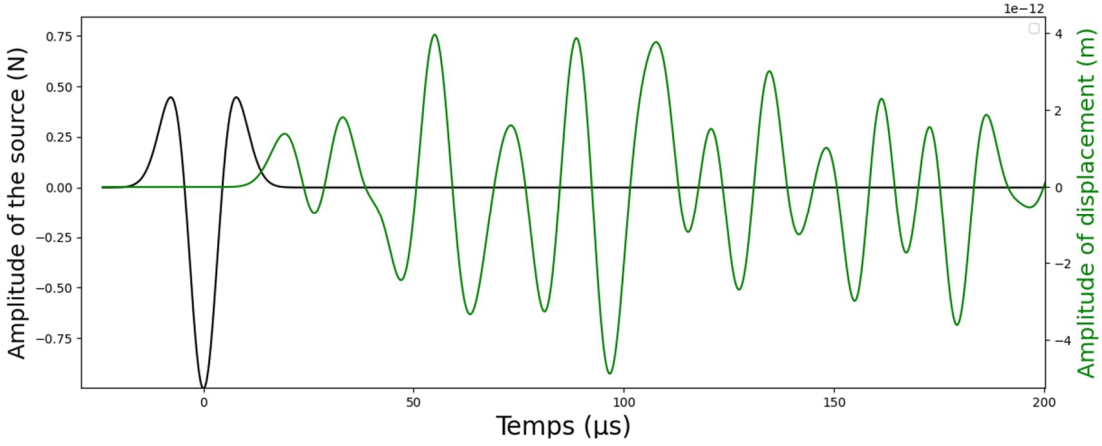

Figure 7. Displacement measurement simulation with a transmission frequency f=50 kHz

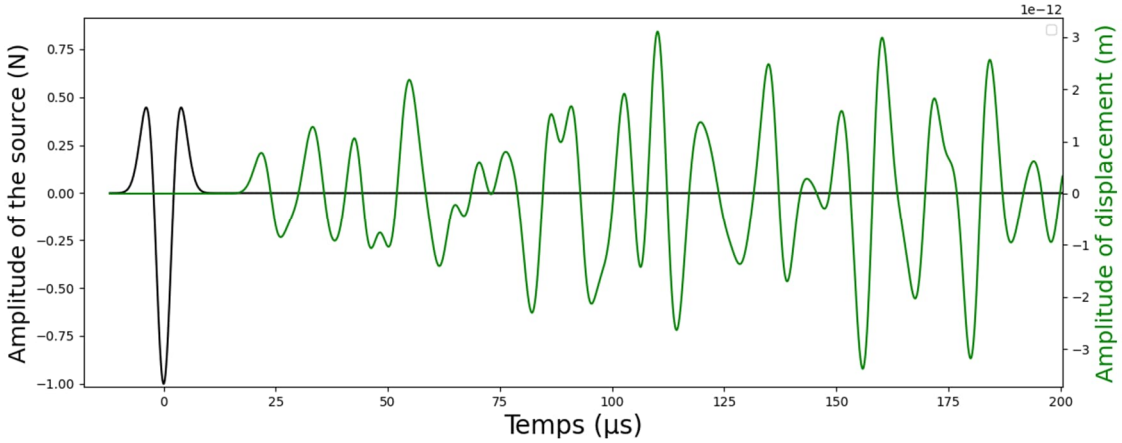

Figure 8. Displacement measurement simulation with a transmission frequency f=100 kHz

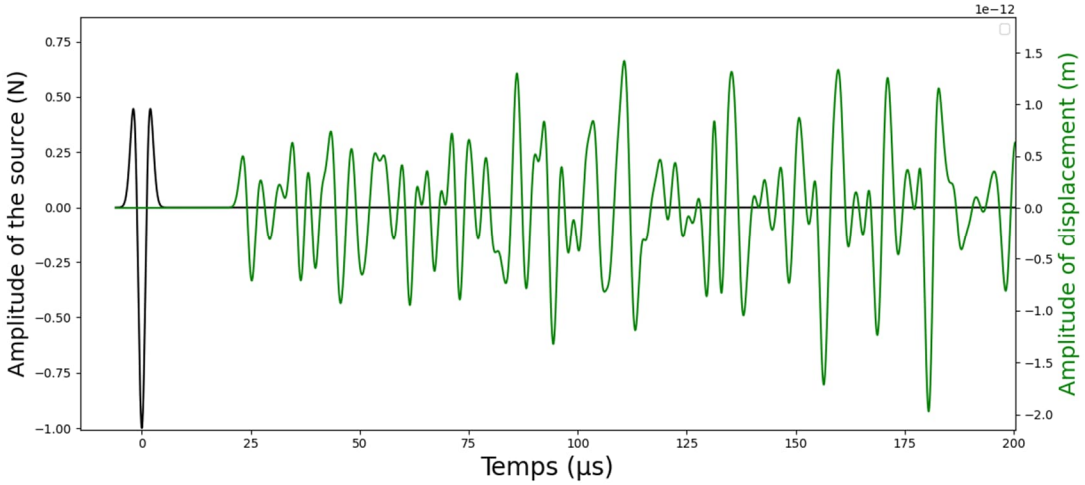

Figure 9. Displacement measurement simulation with a transmission frequency f=200 kHz

Table 4 Variation of observables related to the emission frequency in the homogeneous medium having the properties of the mortar (Table 1)

Sensors emission frequency	Maximum amplitude of the received signal (Amax) (10^{-12}m)	P-Wave propagation time (tp) (10^{-6}s)	$\Delta tp = \frac{\frac{d}{V_p} - t_p}{\frac{d}{V_p}}$
50 kHz	1.56	25.69	1.5%
100 kHz	1.03	25.47	0.63%
200 kHz	0.69	25.29	0.079%

Table 5 Variation of observables related to the emission frequency in the heterogeneous medium (disorder realization n°1 of table 2)

Sensors emission frequency	Maximum amplitude of the received signal (Amax) (10^{-12}m)	P-Wave propagation time (tp) (10^{-6}s)
50 kHz	3.96	27.76
100 kHz	3.10	26.55
200 kHz	1.42	24.79

The variation of t_p compared to the true value t=0.1/3950=25.31 µs is calculated for the homogeneous medium (Table 4). Results show that the use of a high-frequency domain is suggested

to carry out a faster-rising edge of the wave (Fig.9) and therefore a more accurate measurement when defining t_p ($\Delta tp = 0.12\%$). Results in Table 5 show that a clear correlation exists between the propagation time of the wave, hence the wave velocity, and the emission frequency. When the emission frequency increases, the maximum amplitude and the propagation time of the wave decrease. The sensor's emission frequency is shown to have a significant influence on the accuracy and reliability of picked arrival times: the use of a high frequency makes it possible to have a faster rise of the wavefront and therefore a higher precision in the detection of the arrival point.

6. CONCLUSION

Ultrasonic measurements are a commonly used and reliable form of non destructive evaluation of materials. The nature of concrete as a heterogeneous material makes it challenging to have a direct interpretation of ultrasonic data. A 2D numerical model of wave propagation in a heterogeneous medium is built and validated by the numerical comparisons in the case of two homogeneous mediums, first composed of mortar properties and the second composed of mortar and aggregates with the same properties. The simulation of numerical heterogeneous mediums, representing real concrete samples, shows that wave propagation time and amplitude evolve with two important parameters: first, the heterogeneity of concrete; and second, the variation of water gradient, which is represented in this paper by the change of mortar properties. The variation of the studied observables related to the change of mortar properties up to 1.83% is found to be comparable to that related to the heterogeneity of concrete. A comparison is also made to illustrate the influence of the emission frequency on the precision of measurements. However, in order to accurately quantify all the uncertainties related to the material, no noise is added to the signal in this numerical study. This numerical model will be extended in further studies by taking into account the size of the sensors, the aggregate distribution, and the evolution of the water gradient in the concrete and by introducing noise. Knowing that the distribution of the aggregates does not change with time, it will be possible to neglect the uncertainties due to the distribution for an identical realization. For this reason, it will be possible to follow the evolution of the saturation rate or properties of the concrete with time by making differential measurements between a reference state and a subsequent measurement.

REFERENCES

[1] Niederleithinger E, Wolf J, Mielentz F, Wiggenhauser H, Pirskawetz S, "Embedded Ultrasonic Transducers for Active and Passive Concrete Monitoring", in *Sensors*, 2015, sec. 15. https://doi.org/10.3390%2Fs150509756

[2] Anugonda P., Wiehn J., Turner J., "Diffusion of ultrasound in concrete", in *Ultrasonics*, 2001, vol.39, pp. 429-435. https://doi.org/10.1016/S0041-624X(01)00077-4

[3] Deraemaeker A., Dumoulin C., "Embedded ultrasonic transducers in concrete: A lifelong monitoring technology", in *Construction and building materials*, 2019, pp. 42-50. https://doi.org/10.1016/j.conbuildmat.2018.11.013

[4] Garnier V., Piwakowski P., Abraham O., Villain G., Payan C., Chaix J.-F., "Acoustical techniques for concrete evaluation: Improvements, comparisons and consistencies", in *JCBM*, 2013, sec. 43, pp. 598-613. http://dx.doi.org/10.1016/j.conbuildmat.2013.01.035

[5] A. Quiviger, C. Payan, J.F.Chaix, V. Garnier and J. Salin, "Effect of the presence and size of a real macro-crack on diffuse ultrasound in concrete", in *NDT&E International, 2012, sec.* 45, pp. 128–132. https://doi.org/10.1016/j.ndteint.2011.09.010

[6] Yu T., Chaix J.F., Komatitsch D., "2D numerical modeling of ultrasonic wave propagation in concrete: A parametrization study in a multiple-scattering medium", presented at the *AIP Conf. Proc.*, 2017, 080011. https://doi.org/10.1063/1.4974636

[7] Deraemaeker A., Dumoulin C., "Design optimization of embedded ultrasonic transducers for concrete structures assessment", in *Ultrasonics*, 2017, sec. 79, pp. 18-33. https://doi.org/10.1016/j.ultras.2017.04.002

[8] Yu T., Chaix J.F., Audibert L., Komatitsch D., Garnier V. and Hénault J.M., “Simulations of ultrasonic waves propagation in concrete based on a two-dimensional numerical model validated analyticallt and experimentally”, in *Ultrasonics*, 2019, sec. 92, pp. 21-34. https://doi.org/10.1016/j.ultras.2018.07.018

[9] Chekroun M., Le Marrec L., Lombrad B., Piraux J., “Time-domain numerical simulations of multiple scattering to extract elastic effective wavenumbers”, in *Waves in random and complex Media*, 2012, sec. 22, pp. 398-422. https://dx.doi.org/10.1080/17455030.2012.704432

[10] Geuzaine C., Remacle J.F., “Gmsh: A 3-D finite elemnet mesh generator with built-in-pre-and-post-processing facilities”, in *international journal for numerical methods in engineering*, 2009. https://doi.org/10.1002/nme.2579

[11] Yuji S., Zhiming G., Takuya O., Shinji N., Ryoichi M., Kazuki S., Takeshi T., “Accurate determination of the first arrival time of elastic wave traveled through rock sample by machine learning”, in *journal of Applied Geophysics,* 2022. https://doi.org/10.1016/j.jappgeo.2022.104688

[12] Kamada T., Uchida S., Rokugo K., “Nondestructive Evaluation of Setting and Hardening of Cement Paste Based on Ultrasonic Propagation Characteristics”, in *journal of Advanced Concrete Technology*, 2005, vol.3, No.3, pp. 343-353. https://doi.org/10.3151/jact.3.343

[13] Abo-Qudais S., “Effect of concrete mixing parameters on propagation of ultrasonic waves”, in *Construction and building materials*, 2005, sec. 19, pp. 257-263. https://doi.org/10.1016/j.conbuildmat.2004.07.022

[14] Lafhaj Z., Goueygou M., Djerbi A., Kaczmarek M., “Correlation between porosity, permeability and ultrasonic parameters of mortar with variable water/cement ratio and water content”, in *Cement and Concrete Research*, 2006, vol 36, pp. 625-633. https://doi.org/10.1016/j.cemconres.2005.11.009

[15] Malecot Y., Zingg L., Briffaut M., Baroth J., “*Influence of free water on concrete triaxial behavior: The effect of porosity*”, in *Cement and Concrete Research*, 2019. https://doi.org/10.1016/j.cemconres.2019.03.010

Non-destructive method to detect astate of corrosion of a tie rod and to measure thetension in a strand.

Benjamin Quentin-Froignant[1,*], Frédéric Taillade[1*]
[1] Électricité de France (EDF), department of Recherche and development, 78400 Chatou, France

ABSTRACT

Most large concrete structures in the nuclear and hydraulic fields use post-tensioning through tie rods to improve the mechanical properties of the concrete or for the support of civil engineering components. Maintaining the condition of the post-tensioning is an important part of the management of the structure. This requires periodic verifications of the state of preservation (corrosion) and an estimate of the residual stress. In this context, this study proposes a non-destructive method to detect the state of corrosion of a tie rod and to measure the tension in a strand. The main difficulty is the tensioned area of the tie rod remains inaccessible. The method proposed in this study is based on the propagation of an ultrasonic guided wave in the strand. A first step of numerical modelling is carried out to explore the influence of corrosion on the wave propagation. For this purpose, the dispersion curves are used to identify the propagation modes and their associated velocities. The first results indicate that some modes are more sensitive to corrosion-induced cross-section variations. The second step is to carry out ultrasonic measurements on non-tensioned industrial tie rods of several meters in length. Variable corrosion states are then created on bars in the laboratory. These specimens will be used to validate the ultrasonic method for locating and quantifying the level of corrosion. Finally, the dependence between the compression mode speed and the tension of the tie bar will be highlighted and will allow to find the relative tension of the tie bar. This global study combines numerical and experimental approaches to validate the auscultation method.

Keywords: Non-destructive method, strand, corrosion, tension measurement, numerical model, experimentations.

1. INTRODUCTION

The anchors are used in structures for two main goals: to anchor a concrete structure with its environment and to anchor materials with a civil engineering structure. In *Électricité de France* (EDF) many dams have a structural maintain using anchors between structure and the mountain around. The length can be up to several tens metres. However, the most common use in EDF is the attachment of materials to a structure such as valve joints on dams (Figure 1). The anchors guarantee the safety and proper functioning for the structures.

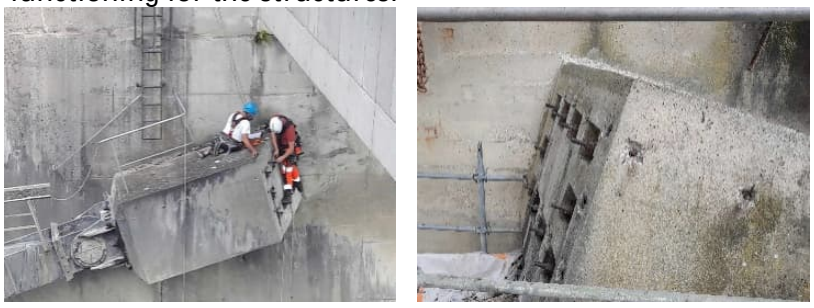

Figure 1. Tie rods to anchor rotational articulation of valve with civil engineering structure in EDF dam. On the left: tie rods are inside the concrete bloc. On the right, the head of anchorage.

* Corresponding authors: benjamin.quentin-froignant@edf.fr, frederic.taillade@edf.fr

A non-destructive measurement method must be developed to detect defects in these anchors. The main one is the occurrence of corrosion due to a corrosive environment within the concrete structure. This is because the bars are made of steel, stainless or not, and can therefore corrode over time. Their main safety function is therefore no longer guaranteed because corrosion, whether generalized on the surface or by pitting, can impact the geometry of the tie rod. The first impact of corrosion is generally a reduction in cross-section associated with a roughened surface. This will influence the tension of the bar and may even cause a breakage in the case of severe corrosion.

Several methods exist to detect defects and corrosion, but they need to have access to the tensioned area of tie rod as in [1]. In [2-4] ultrasound waves are propagated in the guide like pipes, plate or rod and use reflexions of the propagation waves to detect a defect.

This paper reports on the progress of research at EDF R&D with the aim of finding a system capable of detecting a state of corrosion and measuring the tension of an anchor.

2. GEOMETRICAL AND MATERIAL CONSIDERATIONS

Two main geometries of anchors are used in EDF structures: the first one, a strand system, is composed to a seven wires that can stand high tension over a length of several tens of metres and the second one, bar system, is a cylindrical threaded bar called Freyssibar [8-9] mainly use to low stress and length, around few meters. These bars are anchored in the structure, meaning only the top head (about 10cm long) is accessible and can be used to inspect the fully tie rod, Figure 2. In this paper, we focus on the second geometry: bar system of 3.6m length and 28.6mm diameter, allows simpler approach than the strand system.

The measuring system consists of a surface ultrasonic sensor (P-wave) to generate the wave in the bar and a point ultrasonic sensor (S-wave) for measurement. The signal is emitted from the upstream surface, normal to the direction of propagation in the bar. We use a S-wave sensor for the measurement because it can measure a particular direction of movement depending on its orientation. It can focus on the longitudinal or transverse components of the displacement. The identification of the propagation modes is thus simplified because the longitudinal mode has only a longitudinal component, the torsion mode has only a transverse component and the bending mode has components in both directions.

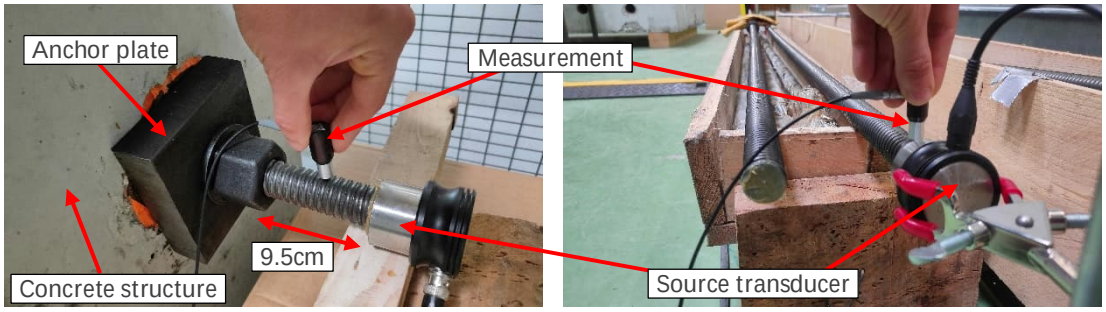

Figure 2. Experimental ultrasonic guided wave test setup. On the left, the bar is anchored in the concrete structure using anchor plates on both sides. On the right, the bars are in the air (free).

The kinetics of a corrosion phenomenon can be described in two phases:

- phase 1, the onset of corrosion wear of the prestressed reinforcement that will potentially lead to the development of stress corrosion, i.e., the appearance of a localised defect, pitting or cankers, which alter the surface protection layer of the steel. The size of these defects is sub-millimetre to millimetre.
- Phase 2, the development of stress corrosion cracking which leads, after a variable time, to the failure of the prestressed reinforcement when the defect has reached the critical size. The size of the critical defect depends on the diameter of the bar, the resilience of the steel, the mechanical stress, etc.

3. ULTRASOUND GUIDED WAVES

Guided waves are a special feature of wave propagation within a waveguide. This allows, among other things, to propagate a wave over very long distance within the waveguide. These waves, during their propagation, are sensitive to geometric defects present in the waveguide. These

phenomena are widely used in the inspection of large linear pipes and tubes for the petrochemical industry [1, 5], or in the case of searching for defects in rails [6, 7] for example. It is also based on this method that Lanza di Scalea [4] has developed a magnetostrictive transducer for detecting defects in seven-wire cable.

At high frequencies, when the wavelength is short compared to the characteristic geometrical size (diameter for a cylindrical waveguide, thickness for a plate), the wave propagation is less efficient over long distances due to attenuation and scattering [10]. In order to improve the inspection range, the frequency of wave emission must be reduced a few tens of kilohertz.

The dispersion curves are the representation of the variation of the phase and group velocities as a function of the frequency-diameter product for each propagation mode within the waveguide. The transmission signal is in the form of a windowed sine by another sine or by a rectangular window. A wave packet is thus generated in the waveguide. The time period of the window allows the transmission of between 5 and 10 periods of the sine signal. This wave packet propagates at the group velocity in the waveguide and corresponds to the real speed of the propagation. It is used in determining localizations of the end of bar (waveguide) or the defect. In our study, the real bars have a 28,6mm in diameter and 3.6m in length.

The simulated and experimental dispersion curves are represented in Figure 3 below. The experimental dispersion curves are built with the bars available in the laboratory. The simulated data are obtained using SAFE method implemented in FreeFEM software [11]. The type of steel used in the bars is not exactly known and therefore a conventional steel is used by default in the simulations. Despite this approximation, the recovery is good. It can be noticed that in the bar, with the measurement configuration, the torsion mode is not present and does not propagate. Around 50kHz (sensor frequency), the longitudinal and bending modes propagate.

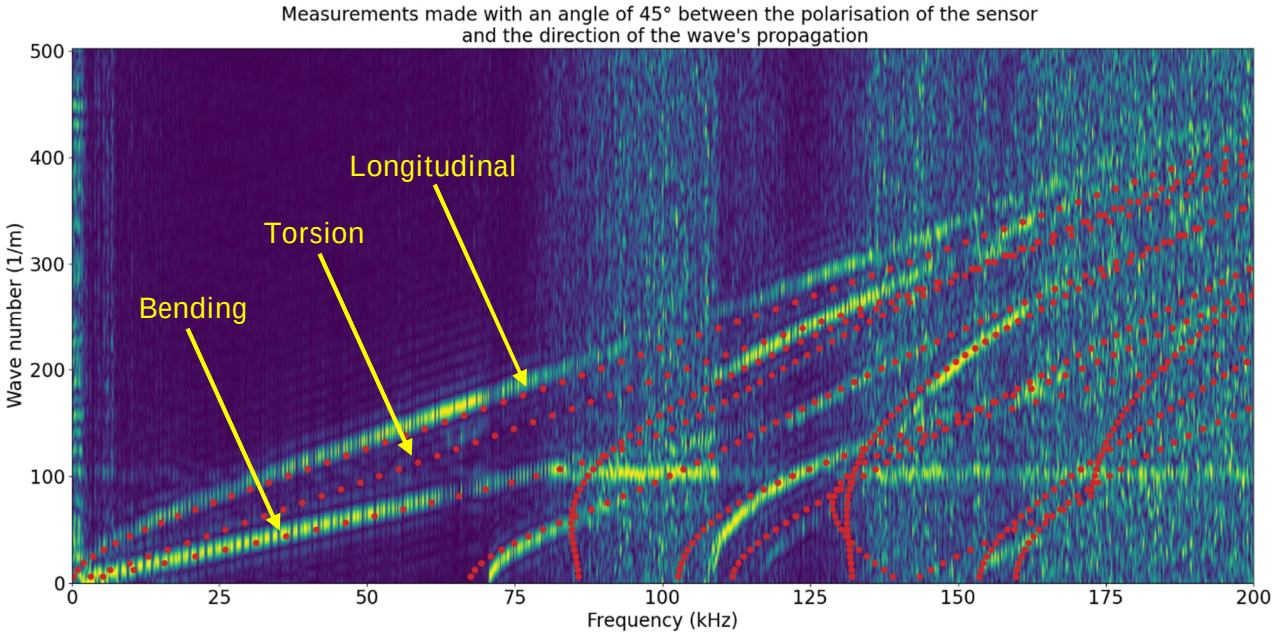

Figure 3. Simulated (red dot) and experimental dispersion curves for a bar (28.4mm in diameter and 3.6m in length).

4. COMPARISON OF UN-CORRODED AND CORRODED RODS

A Freyssibar is artificially corroded using the cathodic method. To do this, part of the bar is immersed in salt water (anode). An electrode (cathode) is placed close to the bar, under water. A current of 2A is generated between the two electrodes to accelerate the corrosion of the bar. Within a few days, the diameter was reduced by 2mm to 3mm over a length of 43cm (Figure 4)

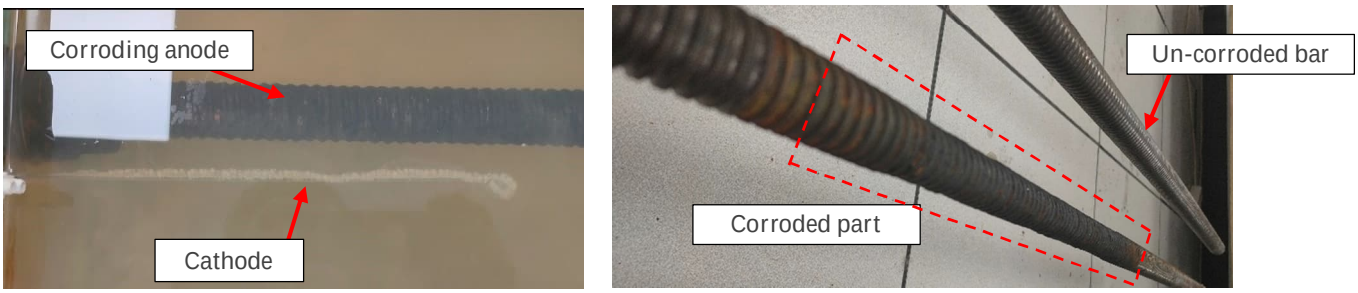

Figure 4. On left, cathodic corrosion phenomenon to create a corroded part on the rod; on right, corroded part visualisation with a diameter reduced by [2mm-3mm].

In EDF's lab in Chatou, there is a 3m concrete mock-up in which two inserts are used to install tie rods and tension them with nuts and anchor plates on each side of the inserts (Figure 2). An un-corroded bar and a corroded bar are installed in a same way, Figure 5.

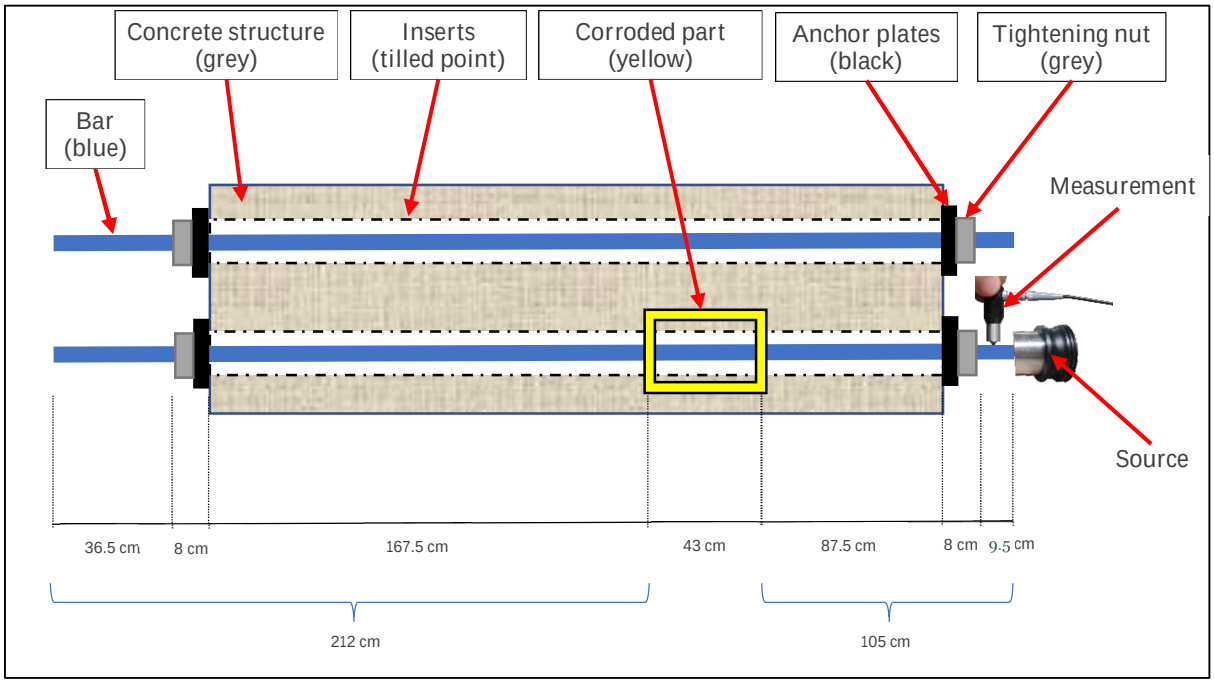

Figure 5. Configuration and dimensions of the tie rods on the 3m long concrete structure. The top bar is not corroded, and the bottom bar is corroded over 43cm. Each bar is clamped between the anchor plates using a hand spanner.

4.1. Windowed sine wave emission 30kHz

For this test, the signal is emitted from the end of the bar and the corrosion defect is located at 105cm. Two measurements are made: on the bar without defect and on the bar with corrosion. The wave is generated by a 50kHz P-type surface sensor, and the measurement is done by an S-type point sensor oriented in the direction of wave propagation, along the bar. In Figure 6 below, two echoes appear on the corroded bar signal at 0.49 ms and at 1.32 ms. At this frequency and with the measurement sensor polarised, the longitudinal propagation mode is preferentially detected. The dispersion curves are used to estimate the group velocity at 5100m/s. The corresponding distances are 1.25m and 3.37m from the emission surface.

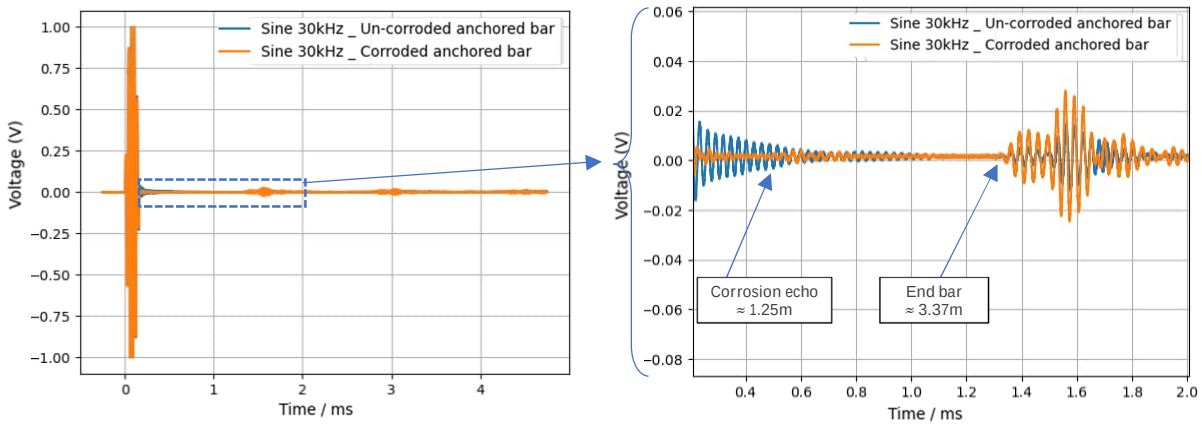

Figure 6. Corrosion detection measurements on an un-corroded bar and on a corroded bar. The emitted signal is a 30kHz windowed sine wave. On the left: the entire measured signal. On the right: zoom on the useful part of the signal.

This measurement configuration seems to be sensitive to the corrosion and allows to localise it.

4.2. Windowed sine wave emission 50kHz

With the same configuration, the sine frequency is increased to 50kHz. The results obtained are shown in the Figure 7 below. It seems that the corrosion defect is more difficult to detect with a frequency of 50kHz.

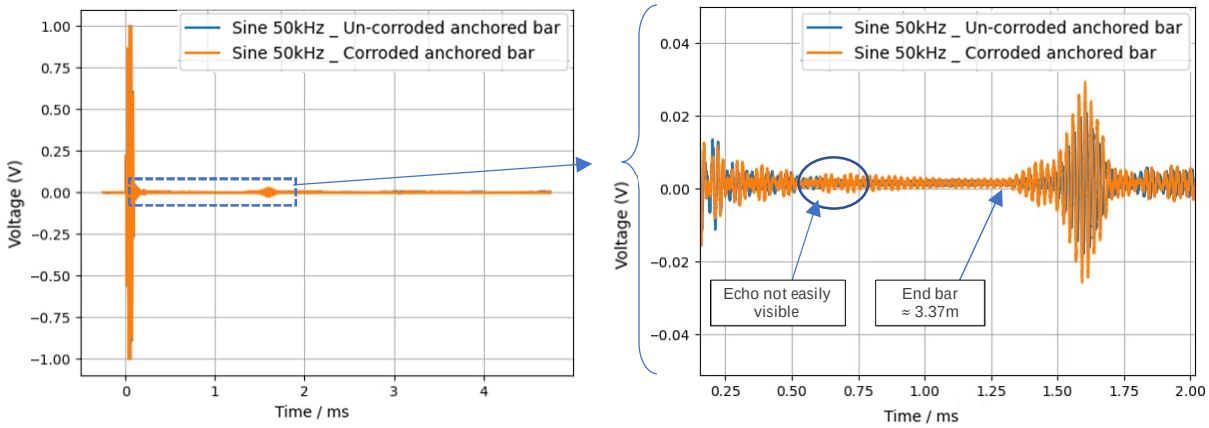

Figure 7. Corrosion detection measurements on an un-corroded bar and on a corroded bar. The emitted signal is a 50kHz windowed sine wave. On the left: the entire measured signal. On the right: zoom on the useful part of the signal.

4.3. Chirp sine wave emission [20-70kHz] in 100ms duration

A chirp signal is a linear swept sine between two frequencies, in this case [20kHz-70kHz] for 100ms duration. The measured signal is then cross-correlated to obtain a temporal signal allowing the emergence of reflections. The results in Figure 8 show an improvement in the signal to noise ratio of the measured signal. In addition, a reflection appears to emerge in the case of the corroded bar around 0.55ms but it is more dispersed than for a sine excitation. A clear separation appears on the bar end reflection at 1.3ms indicating the presence of several propagation velocities because the group velocity depends on the frequency.

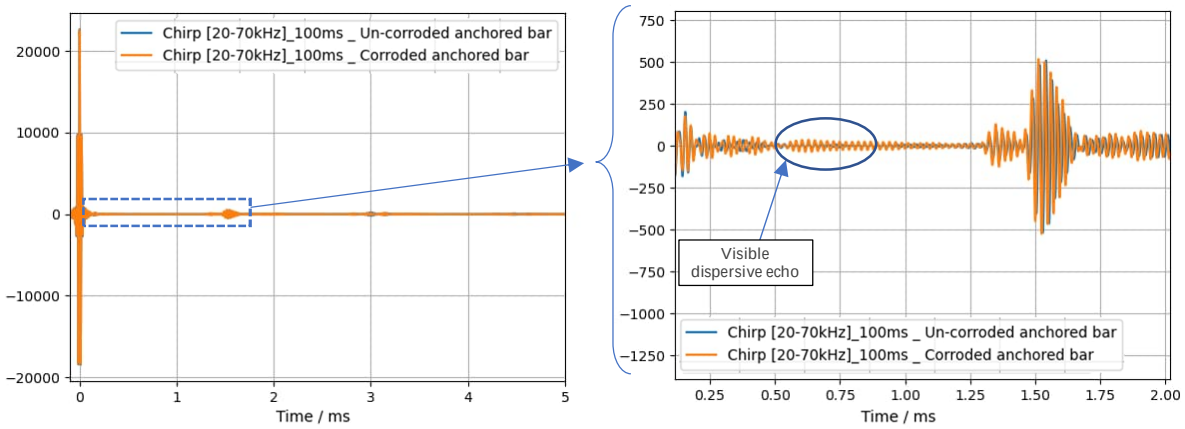

Figure 8. Corrosion detection measurements on an un-corroded bar and on a corroded bar. The emitted signal is a chirp 20-70kHz sine wave during 100ms. On the left: the entire measured signal. On the right: zoom on the useful part of the signal.

5. THE TENSION MEASUREMENT IN A TIE ROD

The tension of a tie rod varies between a few kilonewtons and a few thousand kilonewtons, depending on its use. This tension is applied with the help of anchor plates, which are present either on both sides of the anchor or on one side only (the anchor is sealed to its surroundings on the other side). For our purposes, we do not have access to the tensioned area of the tie rod. Numerical simulations using the SAFE method (Figure 9 below) allow us to analyse the influence of the tension on the group velocity of the modes propagating in the bar. It appears that the torsion and the bending modes are not sensitive to the tension, whereas the longitudinal mode has a group velocity that decreases when the tension increases, especially at low frequency.

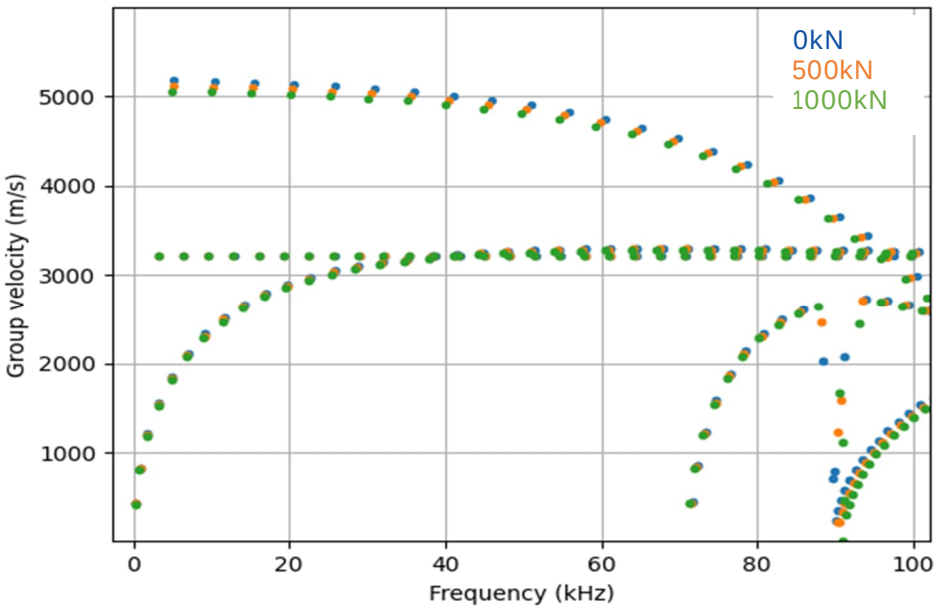

Figure 9. Simulated dispersion curves of a steel rod (diameter: 28.6mm) and comparison with three values of tension 0kN, 500kN and 1000kN.

The speed variation of the longitudinal mode is very small. It is therefore necessary to know the length of the bar precisely, which is not always the case on real sites. The reflection of the torsional and bending modes at the end of the bar can be used to know the length of the bar precisely. This length helps the numerical model to be calibrated and then the group velocity of the longitudinal mode without tension can be estimated. The last step consists in accuracy measuring the velocity of the longitudinal mode using the time of flight of the mode and the knowledge of the bar length. This velocity becomes the input data to the numerical model to determine the associated tension of the rod.

6. CONCLUSION

The work presented in this paper deals with the monitoring of tie rods in civil engineering structures. It has a double objective, based on guided waves: on the one hand, the detection of corrosion in a bar and, on the other hand, the measurement of the tension. The method uses a P-type ultrasonic surface sensor to generate a wave in the waveguide and an S-type point sensor to obtain the measurement. The wave, during its propagation, will undergo reflections due to its interaction with the end of the bar (opposite side to the emission) or due to the presence of a geometrical defect: the corrosion. The source of waves and the measurement are on the same side of the tie rod because in many situations, both sides and the tensioned part of the tie rod are not accessible. The ability to detect corrosion on a real bar, anchored in a concrete structure, was demonstrated using a 30kHz windowed sine wave. The reflection at the end of the bar is measured, allowing the propagation velocities of the generated mode to be determined and thus locating the corroded area on the bar. Some additional tests at high frequencies (1MHz) have already been carried out and seem to indicate that signal propagation is dependent on the presence of corrosion. A study should be conducted.

We have discussed the measurement of the residual stress with the help of dispersion curves. The propagation speed of the longitudinal mode is sensitive to the tension, unlike the torsional and bending modes, which can thus be used as a reference.

To further develop this measurement method, field trials are planned to test the robustness and reliability on real sites. It is also necessary to define a corrosion detection threshold. In this case, the bar has a reduction in diameter of around 10% and a study of the cross-sectional variation is to be carried out. The detection threshold found will be compared with the threshold required to ensure the correct mechanical strength of the structures.

The accuracy of the measurements will be the subject of further studies in the future.

REFERENCES

[1] D.N. Alleyne, A. Pavlakovic, M.J.S. Lowe, P. Cawley, “Rapid, Long Range Inspection of Chemical Plant Pipework Using Guided Waves,” KEM, vol. 270–273, pp. 434–441. https://doi.org/10.4028/www.scientific.net/kem.270-273.434.

[2] D. N. Alleyne, M. J. S. Lowe, P. Cawley, “The Reflection of Guided Waves From Circumferential Notches in Pipes,” J. Appl. Mech., September 1998, 65(3): 635–641.

[3] Eli Leinov, M.J.S. Lowe, P. Cawley, "Investigation of guided wave propagation in pipes fully and partially embedded in concrete", The Journal of the Acoustical Society of America 140, 4528-4539 (2016). https://doi.org/10.1121/1.4972118.

[4] F. Lanza di Scalea, P. Rizzo, F. Seible, “Stress measurement and defect detection in steel strands by guided stress waves,” J. Mater. Civil Eng. 15 (2003) 219–227, https://doi.org/10.1061/(ASCE)0899-1561(2003)15:3(219).

[5] A. Demma, “The interaction of guided waves with discontinuities in structures”, Ph.D. dissertation, Dept. Mec. Ing., Imperial College of Science, Technology and Medicine, London Univ., London, 2003.

[6] X. Xu, B. Xing, L. Zhuang et al, “A graphical analysis method of guided wave modes in rails,” Applied Sciences, 2019, vol. 9, no 8, p. 1529.

[7] I. Bartoli, A. Marzani, F. Lanza Di Scalea et al, “Modeling wave propagation in damped waveguides of arbitrary cross-section,” Journal of sound and vibration, 2006, vol. 295, no 3-5, p. 685-707.

[8] SAS Freyssinet Products Company brochure, “Anchoring systems for geotechnical engineering,” available: https://www.freyssinet.com/solution/build/anchoring-systems-for-geotechnics/

[9] SAS Freyssinet Products Company, “Freyssibar permanent ground anchors,” Ref: BGT-010, Rev 0, Nov. 2017.

[10] J. L. Rose, “Ultrasonic guided waves in solid media,” Cambridge university press, 2014.

[11] C. Hakoda, C. Lissenden, and J. L. Rose, “Weak form implementation of the semi analytical finite element (SAFE) method for a variety of elastodynamic waveguides”, AIP Conference Proceedings 1949, 230001 (2018).

Non-destructive testing of coarse aggregates irradiated by neutron and gamma radiation for the European project ACES

Zbynek Hlavac[1*], Yuliia Khmurovska[2], Patricie Halodova[1], Claudia Aparicio[1], Leos Krivsky[1] and Petr Stemberk[2]
[1]Centrum vyzkumu Rez s.r.o., Husinec - Rez, Czechia
[2] Ceske vysoke uceni technicke v Praze, Praha, Czechia

ABSTRACT

Many European and other nuclear power plants (NPPs) will soon reach their designated lifetime. Due to this fact, the crucial components of NPPs must be capable of sustaining the load they were designed for. One of the critical components is the biological shielding concrete surrounding the reactor pressure vessel. It consists of water, hardened cement paste and fine or coarse aggregates. The integrity of the shielding concrete is essential for protecting NPP staff against neutron and gamma radiation. Nevertheless, this integrity may be breached due to radiation-induced volumetric expansion caused by changes in the lattice, mainly occurring in siliceous minerals like quartz.
The presented work aims to predict changes in the coarse aggregates caused by neutron and gamma radiation with rocks typical for European NPPs. The ultrasonic pulse method was employed to determine the time of flight and dynamic E-modulus of irradiated rock cylinders of size 10 × 10 or 10 × 20 mm. Samples were core bored and brushed by special techniques to guarantee precise shapes and dimensions. A Vertex instrument measured the exact diameter and length. Density was determined with helium and water pycnometry. Amorphization and percentage content of rock-forming minerals were evaluated with X-ray diffraction and scanning electron microscopy.
Data measured by the methods mentioned above will facilitate the development of predictive models by the Czech Technical University and Oakridge National Laboratory.

Keywords: neutron and gamma irradiation; coarse aggregates; ultrasonic; X-ray diffraction.

1. INTRODUCTION

The safety of nuclear power plants (NPPs) is one of the most critical areas in energetics. The planned extension of the lifetime of NPPs needs several checks of the crucial components, e.g. the reactor pressure vessel or its immediate surroundings. One of the items that have to be checked is the concrete biological shield. The main problems of this part of the structure are variable temperatures and consequent mechanical loading and neutron radiation-induced volumetric expansion (RIVE) of coarse aggregates. RIVE is noticeable in minerals such as quartz, with a much lower expansion in calcium carbonate.

Ten different types of rocks were chosen for further inspection. Each is interesting from the point of view of the European utilities, NPP owners or regulators. Each rock was delivered to the Czech Technical University (CTU) laboratory in Prague and was precisely selected, drilled as a core, brushed and polished to a specific shape and dimension. The ready rock cylinders were brought to the Centrum vyzkumu Rez S.R.O. Special irradiation rigs were designed and manufactured for neutron and gamma irradiation in the research reactor LVR-15, whose maximum thermal power is 10 MW. The temperature during the irradiation treatment cannot exceed 70°C. The duration of irradiation in the experiment was different for the two sets of samples. A low dose and a high dose samples.

*Corresponding author: Phone +420 723 946 561, E-mail zbynek.hlavac@cvrez.cz

Irradiation rigs were removed from the reactor, cut and transported into a hot cell, shielding against gamma radiation. Rock samples were taken carefully out of the rigs, measured and tested.

The interim results of the non-destructive observations will be put together later, with the data computed by special software designed for this purpose. This comparison is not a part of this paper.

2. PREPARATION OF SAMPLES

A total of ten rock samples were selected. The preferred rocks were those found in the existing European NPPs or considered for constructing new NPPs. Therefore, the ACES partners provided samples of rocks that satisfied this preference and were large enough (Figure 1) for the subsequent production of the cylindrical rock samples (Figure 2).

The rock samples were obtained by core drilling from the provided rocks. There were two sizes for the cylindrical samples, 10 x 10 mm and 10 x 20 mm. The diameter was 10 mm and reflected the inner space dimension of the irradiation capsule. A height of 10 mm was selected to maximise the sample number. The height of 20 mm was chosen as the minimum height to validate the developed non-destructive testing (NDT) technique. In addition to the cylindrical samples, thin polished discs of the thickness of 1 mm were prepared for each rock type for optics-based analyses.

Figure 1. Example of provided rocks

Figure 2. Fabricated cylindrical samples (10 x 10 mm)

3. STRUCTURE ANALYSIS METHODS

Three methods were chosen for the structural analysis of rock sample material before and after irradiation.

2.1. Light optical microscopy

The aggregate cylindrical samples of 10 mm diameter were cut, and 1 mm thin slices were prepared and polished for light optical microscopy (LOM) and scanning electron microscopy (SEM) observations. The Stereomicroscope Zeiss 508 Stemi for fresh samples and the Dino-Lite set Professional 3.0 for irradiated samples were used to document possible optical changes after neutron irradiation. Most of the studied aggregate samples changed their appearance due to irradiation, manifested by a significant darkening. Baryte samples from the Czech Republic exhibited the most pronounced colour change. Four of the ten samples disintegrated due to irradiation along the predisposed cracks and grain boundaries present in the initial (fresh) state. Figure 3 shows the main optical changes after irradiation.

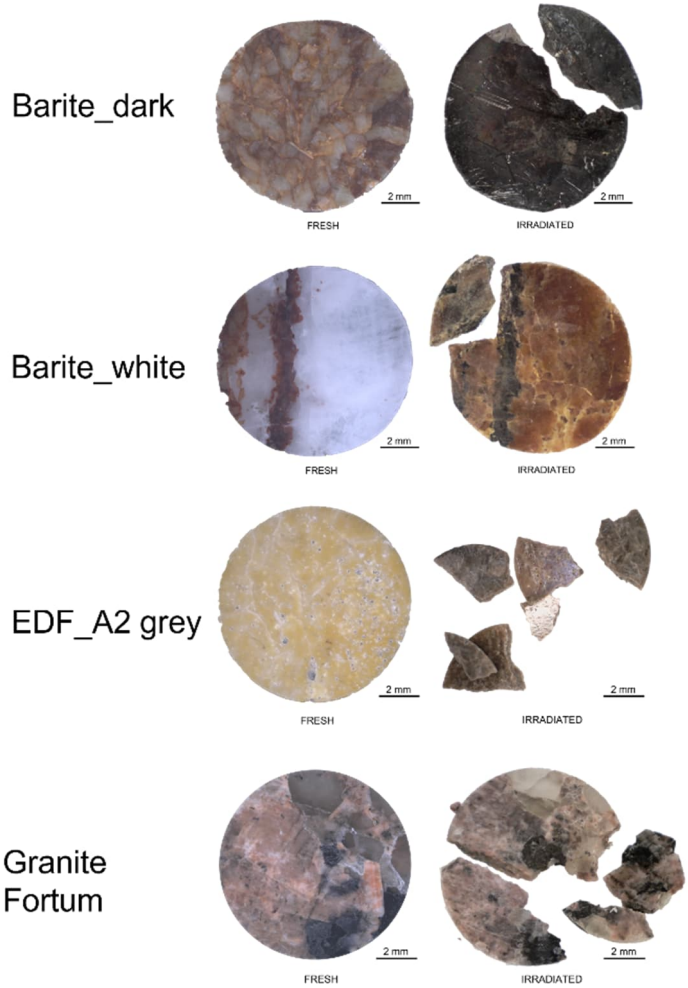

Figure 3. Light optical micrographs of the selected aggregate samples before and after irradiation.

2.2. Scanning electron microscopy

Scanning electron microscopy and microanalysis using the FEG-SEM Tescan LyraGMU equipped with the EDS analytical X-Max^N system from Oxford Instruments was used to obtain the modal mineralogical data for all aggregate samples. Large-area X-ray elemental maps were acquired, and post-processing of the obtained maps was used to identify the present mineral phases and calculate their content for each aggregate. The modal composition of the samples will be used to predict the volumetric expansion of aggregates due to neutron irradiation. Figure 4 shows a graphical summary of the main results.

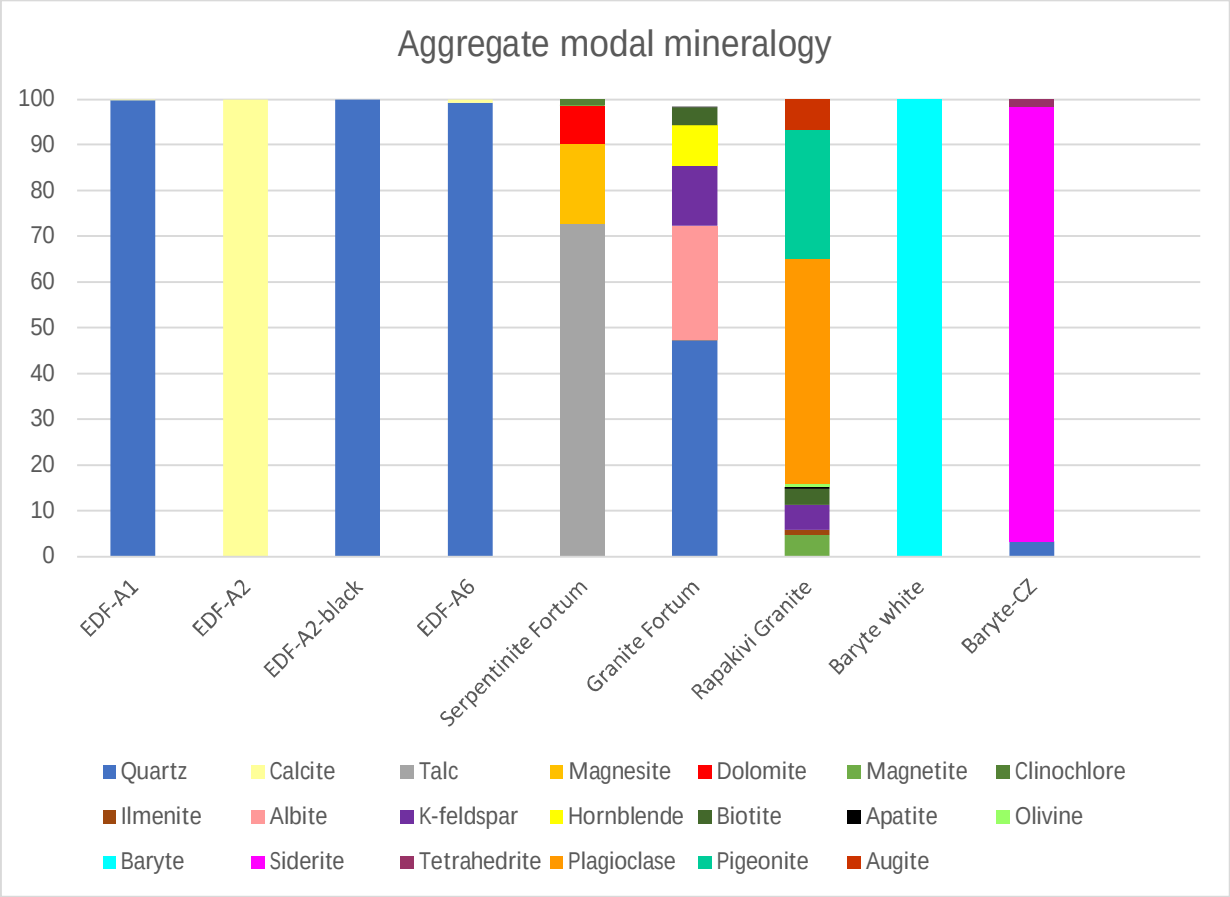

Figure 4. Modal composition of studied aggregate samples.

2.3. X-RAY DIFFRACTION

The bulk samples were hand-ground under ethanol using an agate mortar. The wet sample was drop-casted onto a foil of polyether ether ketone (PEEK), a six µm-thick plastic, transparent to X-rays and mounted on a metallic holder for XRD in transmission mode. After drying, the sample was covered with a second PEEK foil. Each sample was mixed with a convenient internal standard (cerium dioxide for baryte-white, zinc oxide for baryte-dark and aluminium oxide for other samples) in a proportion of 1:1 to estimate the amount of amorphous phase.

The data were collected at room temperature using a multipurpose diffractometer (Empyrean, Malvern-PANalytical) with a Co X-ray tube in transmission mode. All patterns were collected from 4 to 82° 2θ with a step size of 0.013° 2θ. Data analysis and Rietveld refinement were performed using the Profex 4.0.3 software package [5]. The structural models of the crystals were taken from the Profex internal database.

The samples with the highest quartz content were EDF-A1, EDF-A2 and EDF-A6, whereas EDF-A2 grey had only calcite. Baryte-white contained mainly baryte and a low percentage by weight of siderite, while baryte-dark was primarily composed of siderite and very little baryte. Granite samples differed in content; granite-Fortum was a mixture of quartz and feldspars, while granite-TVO was a mixture of mainly feldspars and pyroxene. The two serpentinite samples also had different mineral compositions. Czech serpentinite contained lizardite, forsterite, enstatite, actinolite and clinochlore. However, serpentinite-Fortum contained magnesite, talc, magnetite, dolomite and clinochlore. Serpentinite samples had the highest amorphous content of all the analysed samples. However, in the serpentinite-Fortum sample, the amorphous content may have been slightly overestimated due to a disorder in the structure of talc. Figure 5 shows the graphical results.

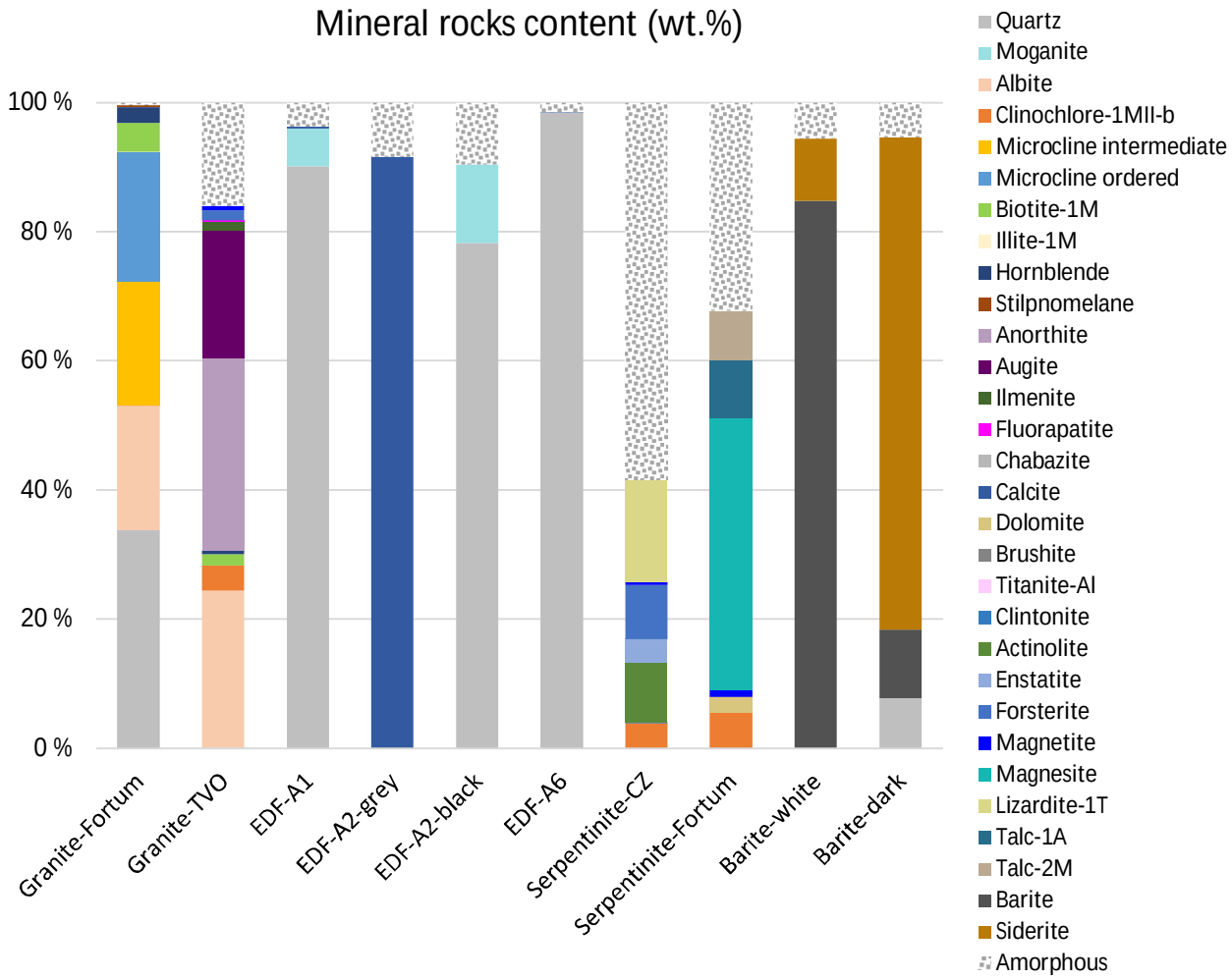

Figure 5. Mineral composition and amorphous content of selected non-active aggregate samples.

4. SIZE-CHANGE DETECTION

Three NDT methods were chosen to analyse rock samples before and after irradiation.

4.1. Vertex

Before dimension measurement, the pre-drying process and weighing were realised. Each sample was pre-dried in an electric furnace tempered for 24 h with silica gel for humidity absorption. Parameters for pre-drying were a temperature of 30°C and a pressure of 20–30 mmHg. Dimension measurement was performed using the Vertex 251HM by MicroVu with a touch probe of 6W 20 1x4 in a hot cell at the Research Centre Rez (Figure 6).

Figure 6. a) Vertex 251HM and b) furnace in hot cell

First, the sample was placed in the holder for diameter and height measurement. This holder is made of duralumin alloy. Each sample was placed in the measuring cylindrical holder adapter with holes drilled in specific locations for touch probe measurement. The results from measurements were five diameters (D1 – 5) and five heights (H1 – H5) measured at designated points. Two-cm high samples were measured using a "mill" holder, which rotates the sample. The optical method measures the diameter and height of samples at different angles of sample rotation. Figure 7 shows the results of these measurements.

In-house software for the reconstruction of the sample surface and volume calculation was created to analyse two-cm high samples. Figure 7 shows an example of these results.

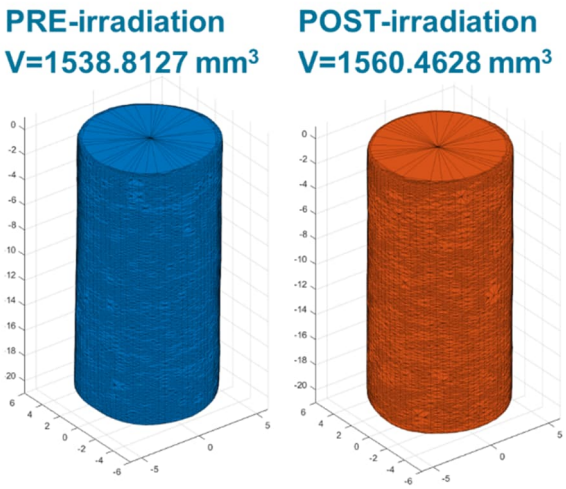

Figure 7. Reconstruction of the sample surface

Figure 8 compares the RIVE of the reference samples (quartz) measured using Vertex with that reported in the literature [1].

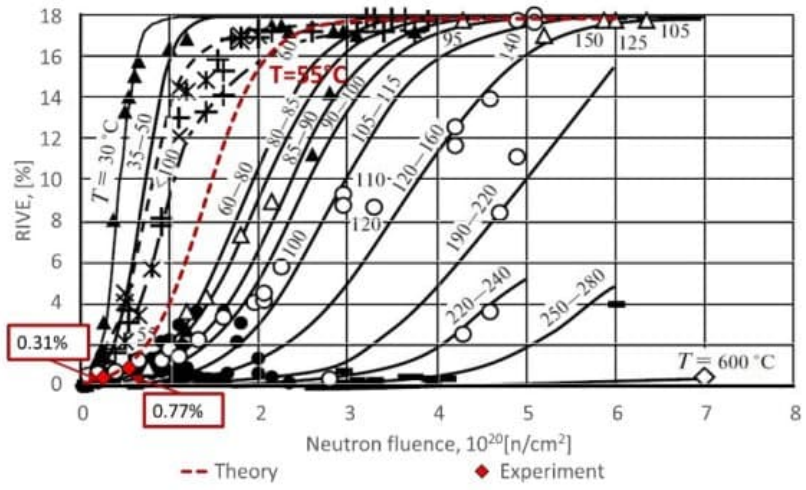

Figure 8. Comparison of RIVE for quartz obtained using Vertex with that reported in the literature [1]

4.2. Helium pycnometry

Density analysis was performed using the Pycnomatic – ATC Evo helium pycnometer from Porotec. Declared accuracy in measuring the density is ± 0.01 % and depends on the cleanliness of samples, the purity of the gas and the temperature. Samples were carefully moved in and out of the pycnometer using manipulators at a constant temperature of 20°C. Figure 9 shows the water and the helium pycnometry measurement device in the hot cell.

Figure 9. Water and helium pycnometry measurement device in the hot cell

Figure 10 shows an example of the RIVE of the reference samples (quartz) obtained using helium pycnometry.

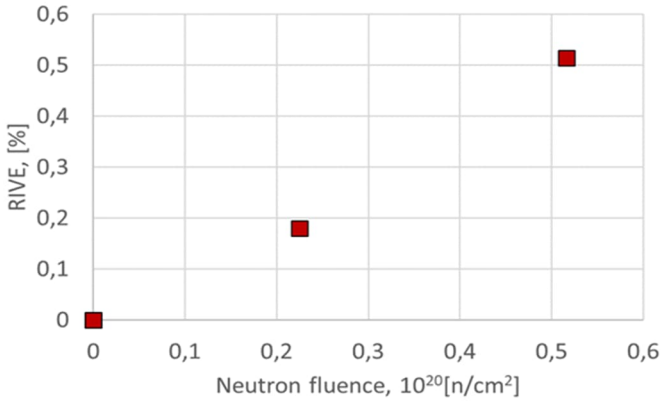

Figure 10. Example of RIVE for quartz obtained using helium pycnometry

4.3. Water pycnometry

All water (H2O) pycnometry measurements were done in the hot cell to ensure the same conditions for measuring non-irradiated and irradiated samples. An analytical balance Kern 220g x 0.1 mg ABS-N_ABJ-NM with set YDB-03 for density determination was used for water pycnometry (Figure 9). Distilled water at the same room temperature was used as a reference liquid. Each sample was measured thrice.

Figure 11 shows the comparison of the RIVE of the reference samples (quartz) measured using H_2O pycnometry with that reported in the literature [1].

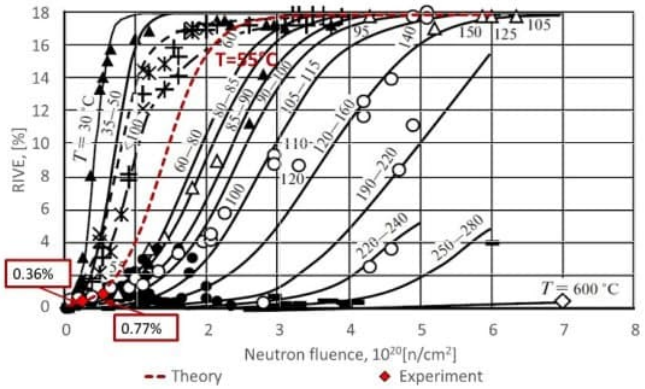

Figure 11. Comparison of RIVE for quartz obtained using H2O pycnometry with that reported in [1]

4.4. RIVE

The RIVE of aggregates is believed to be the principal mechanism of radiation-induced deterioration of concrete structures [2-4]. Thus, the measurement of RIVE is of crucial importance.

As can be seen from Figure 8, the Vertex-based method for the RIVE determination shows reliable results. The measured data corresponds to the theoretical prediction and is comparable to the data from the literature.

Similarly, Figure 11 shows that the H_2O pycnometry results are close to the theoretical prediction. Vertex and H2O pycnometry show comparable results in the reference sample since the reference samples do not have significant damage except for narrow cracks (see Figure 12). However, H2O pycnometry is a more reliable RIVE measurement tool if the sample is broken. On the other hand, if the sample is not broken but has wide cracks, the Vertex-based RIVE seems more accurate since water can penetrate the cracks.

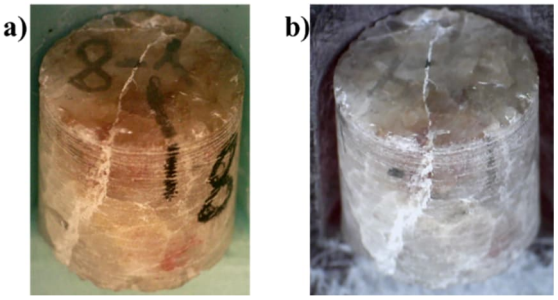

Figure 12. Photography of reference sample (quartz): a) before irradiation and b) after irradiation

The smaller RIVE of the reference sample, obtained using helium pycnometry (Figure 10), indicates the irradiation-induced opening of the closed pores and cracks. This observation brings additional information on the RIVE mechanism.

As seen above, the RIVE of the sample may vary significantly depending on the method of measurement. Thus, the appropriate experimental method should be chosen carefully. Nevertheless, the complex approach using all three methods seems to be the most promising because the Vertex, helium and H_2O pycnometry complement each other and bring more information on the RIVE and its mechanism.

5. ULTRASONIC TESTING

The direct ultrasonic pulse method (UPM) has been applied to evaluate the relative dynamic modulus (RDM) in rock samples before and after the neutron spectrum irradiation. The UPM is a robust NDT method that provides the time of flight, the velocity and the dynamic E-modulus or shear modulus. Shear modulus requires knowledge of S-wave velocity.

The P-wave and S-wave speeds are required for E-modulus determination. In exceptional cases, as in the present situation, only P-wave velocity c and bulk density of the material ρ suffice for E-modulus (E) determination:

$$E = \rho c^2 \tag{1}$$

RDM is expressed as

$$\text{RDM} = \frac{E_{\text{irr}}}{E_0} \cdot 100\%, \tag{2}$$

E_0 and E_{irr} are the dynamic E-moduli before and after neutron irradiation.

Figures 13, 14 and 15 show the photo record from the measurements before the irradiation.

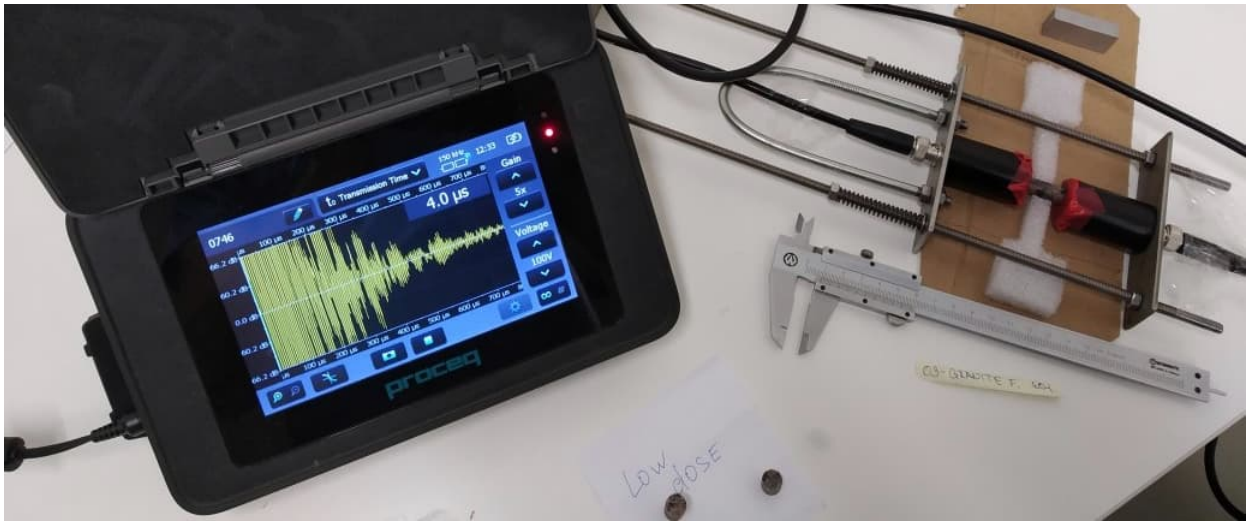

Figure 13. Ultrasonic pulse measurement by Pundit PL200 before the irradiation

Figure 14. Granite rock cylinder squeezed by two ultrasonic transducers 150 kHz (P-wave)

Figure 15. Mechanical manipulator Vendy purposed for one-axis squeezing of rock sample

Twin-layered elastic tape (Figure 14) was used as the acoustic coupling agent before and after the irradiation. This atypical solution was necessitated due to the strict rules for work in a hot lab, where no gels or other liquids are allowed.

A mechanical manipulator called Vendy (Figure 15), designed for the work in a hot lab and driven by one or two robotic arms, was targeted for manipulating small samples of diameters from 1 cm (Figure 16).

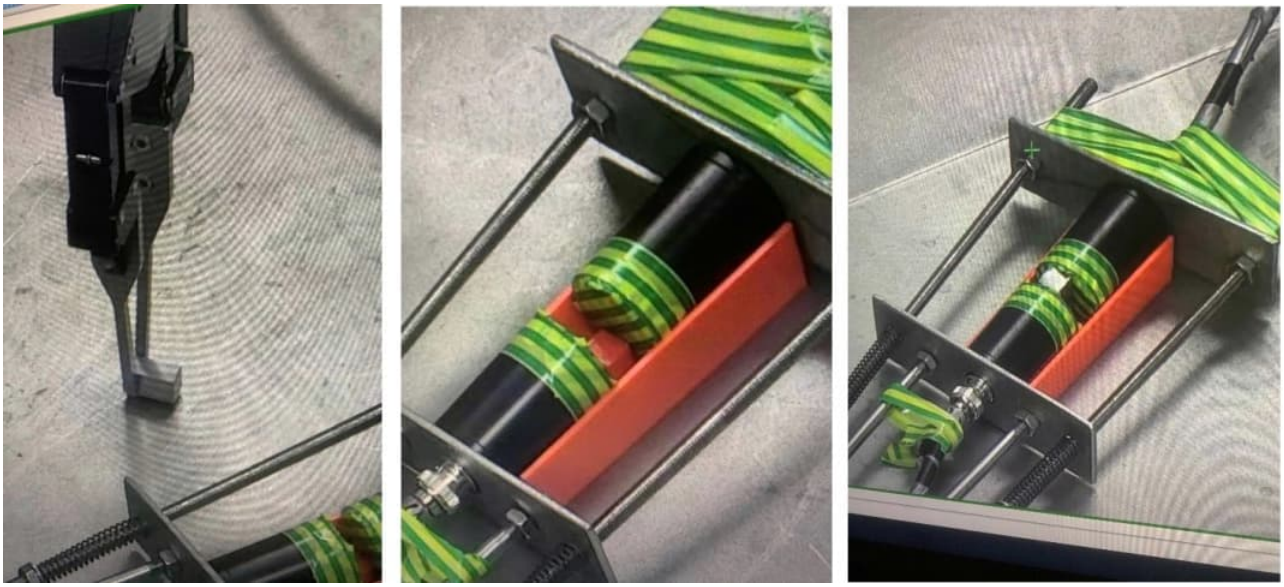

Figure 16. Manipulator Vendy (mid-right) being operated in a hot lab by a robotic arm (left)

Figure 17 provides with a comparison of RDM before and after irradiation. The bulk density for equation (1) is taken as equal for both non-irradiated and irradiated samples. Figure 10 shows that the difference between these two values is below 1% and Figure 17 performs much higher decrements than one per cent.

The decrement of RDM due to neutron radiation is most clearly visible in granites, about -80–86 %. RDM of granite TVO is higher in the case of low doses (30 % of the reference value).

Both serpentinites, granite TVO, EDF quartz A6 or white Czech Baryte (CZ) have higher values for low dose and lower for high dose. This corresponds with Figure 8 as well as FiguresFigure 10 toFigure 12. There, the higher the dose the bigger RIVE or crack width.

High discrepancy of the measurement is cause by small base length, small number of samples and big variation among each sample.

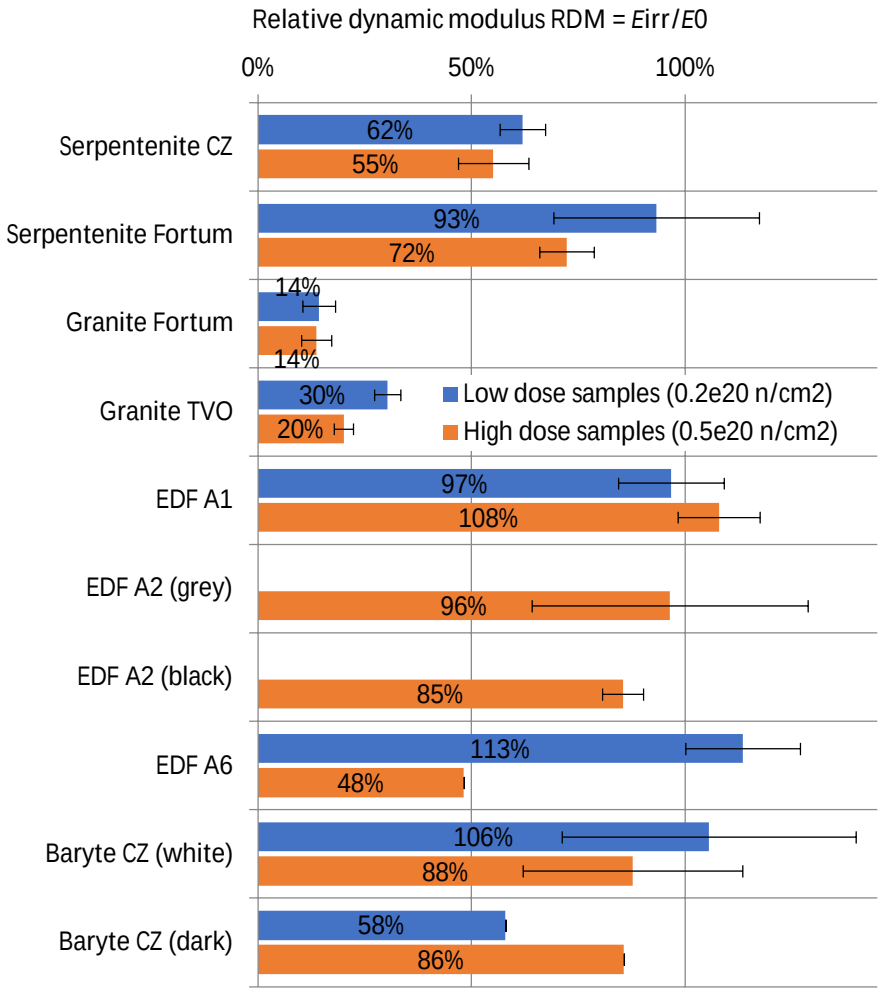

Figure 17. Relative dynamic modulus of various rocks after low- and high-dose irradiation

6. CONCLUSION

Ten different types of rocks were tested for radiation-induced changes. Three structural analysis methods were demonstrated to be effective: LOM, SEM and XRD. These methods can show cracks and modal and mineral composition, respectively.

Three methods suitable for dimension-change analysis were applied: the Vertex system and helium and water pycnometry. Vertex provides specific shapes and three-dimensional measurements. Water and helium pycnometry show the volume (and density) before and after irradiation. All three methods can determine radiation-induced volumetric expansion. Some aggregates reached +0.5 % RIVE in the neutron fluence level of 0.5 × 10^{19} neutrons per square centimetre (quartz in Figure 10).

Relative dynamic modulus was determined using direct UPM using the Pundit PL200 instrument and the mechanical manipulator Vendy (Figure 13 toFigure 16). Irradiated samples were checked in the radiation-shielded area of the hot cells (Figure 9). RDM decreased by several per cent or even tens of per cent due to the irradiation. Slight negative or even positive changes in RDM were observed between low-dose and high-dose samples (Figure 17).

Granite samples suffered a lot because of their complex modal composition (Figure 4, Figure 14). Each of the constituent reacts differently to the irradiation and extra tension causes the destruction of the internal structure of the rock.

All employed methods demonstrated their capacity to monitor radiation-induced changes (in the internal structure, outer dimension, shape, appearance and mechanical properties such as the P-wave velocity, dynamic E-modulus and RDM).

ACKNOWLEDGEMENTS

This work was conducted within the Euratom Research And Training Programme 2019–2020 under grant agreement No 900012.

REFERENCES

[1] A. Denisov, V. Dubrovskii and V. Solovyov, *Radiation resistance of mineral and polymer construction materials*. Moscow, Russia: MEI Publishing House, 2012. (in Russian)

[2] H. K. Hilsdorf, J. Kropp and H. J. Koch, “The effects of nuclear radiation on the mechanical properties of concrete.” in *Douglas McHenry International Symposium on Concrete and Concrete Structures* (ACI Special Publication SP-55), 1978, pp. 223-254, doi:10.14359/6616.

[3] K. G. Field, I. Remec and Y. Le Pape, “Radiation effects in concrete for nuclear power plants - Part I: Quantification of radiation exposure and radiation effects.” *Nuclear Engineering and Design*, 2015, vol. 282, pp. 126-143, doi:10.1016/J.NUCENGDES.2014.10.003.

[4] Y. Le Pape, A. Giorla and J. Sanahuja, “Combined effects of temperature and irradiation on concrete damage.” *Journal of Advanced Concrete Technology*, 2016, vol. 14, no. 3, pp. 70-86, doi:10.3151/jact.14.70

[5] N. Döbelin and R. Kleeberg, “Profex: a graphical user interface for the Rietveld refinement program BGMN.” Journal of Applied Crystallography, 2015, vol. 48, pp. 1573–1580, doi:10.1107/S1600576715014685.

Post-tension cables monitoring system

Frederic Taillade[1]*, Sylvie Michel-Ponnelle[1], Benoit Masson[3], Manuel Corbin[3], Alexis Courtois[3]
Mathieu Galan[2]
[1] EDF R&D, Chatou, FRANCE
[2] EDF DTG, Lyon, FRANCE
[3] EDF DT, Lyon, FRANCE

*corresponding author: frederic.taillade@edf.fr

ABSTRACT

In order to optimize or complete the monitoring device of the post-tension tendons, EDF is developing a monitoring method based on the distributed measurement of the strains along the prestressing cables [1]. This new method uses an electric coaxial cable interrogated by Frequency Domain Reflectometry. Compared to another method based on optical fiber, the robustness of the electric coaxial cable is particularly appreciated during the construction phases. This paper presents the method and the first results obtained on a prestressed concrete beam during the breaking experience of the tendons.

Keywords: post-tension, monitoring, Frequency Domain Reflectometry

1. INTRODUCTION

As in many civil engineering structures, the reactor building containment of EDF's nuclear power plants (NPP) is made of prestressed concrete. The tendons are post-tensioned. Therefore, the steel strands are threaded in ducts after the concrete has hardened. After tensioned, the residual space in duct is filled with a cement grout mixture.
This post-tensioning configuration has certain advantages from the point of view of tendons durability but during the lifetime of the structure, it does not make it possible to control the residual stress and the damage of the strands. In France, the surveillance system of the containment [4], based on the deformation measurement of the concrete, makes it possible to overcome somehow these difficulties, however the question of the actual residual force in the tendons is raised periodically by the nuclear safety authorities.

Considering the large number of prestressing tendons installed in a containment wall, the rupture of a prestressing tendon leads to relatively localized and low strains variation in the structure. To capture this localized strain information, monitoring the entire reactor building would require a large number of local sensors.

To continue using this post-tensioning technology, it is desirable to provide a real-time monitoring system (SHM). This system must be both robust during installation, and cost optimized. To minimize the cost, one of the solutions may be based on a distributed strain measurement. The common solution for distributed strain measurement uses the optical fiber sensor (OFS) [5]. It is a mature technology that provides an accurate result (around +/-20µm/m depending on the interrogation system) in agreement with the surveillance requirements of civil buildings. Depending on the monitored building and the corresponding safety / functional requirements, the design criterion and final choice is a balance between the metrological performances of the system, including robustness criteria during construction and long term operation, and the potential cost optimization.
In the case of tendon rupture detection, a solution based on acoustic emission (AE) can be considered if the metrological performances are compatible with the surveillance requirements of the buidling.

In this case, we need to be sure that the system is continuously operational in order not to miss an event. This usually requires redundant AE systems.

In this context, EDF is developing a new approach based on an electric coaxial cable (ECC) allowing the distributed strain measurement [1]. This solution allows one to minimize the cost, notably of the interrogator device, the ECC is generally more robust than the OFS. The principal disadvantage is the strain measurement which is less accurate compared to OFS but it is sufficient for our application.

2. MEASUREMENT PRINCIPLE

The coax cable is embedded into concrete structure and is interrogated by a vector networks analyzer (VNA) (see fig.1). The measurement principle is based on Frequency Domain Reflectometry (FDR): for each frequency between f_{min} and f_{max}, we measure the electric impedance coefficient, called S_{11}. S_{11} is an impedance ratio which is written as $S_{11} = (Z - Zo)/(Z + Zo)$ with $Zo = 50\Omega$ is the internal impedance of the VNA and Z the electric impedance of the ECC measured has an end of ECC.

Figure 1. measurement principle

The electric impedance Z depends on Zc the characteristic electric impedance of the ECC (here around 50Ω). Considering low electrical losses in the ECC, the characteristic impedance Zc is defined as $Zc \approx \sqrt{L/C}$ where L (H/m) and C (F/m) are the linear inductance and capacitance respectively of ECC [2] which depend on the geometric and materials characteristics of the ECC used:

$$L = \frac{\mu_0}{2\pi} ln(D/d)$$

$$C = \frac{2\pi\varepsilon_0\varepsilon_r}{ln(D/d)}$$

with ε_0 and ε_r respectively the dielectric permittivity of void and of the material embedded into the ECC (around 2.1 for PTFE), μ_0 the magnetic permeability of void and D/d the ratio of the diameter of the electric conductors.

The electric impedance (in Ohm) is given by equation:

$$Z_C = \sqrt{\frac{\mu_0}{\varepsilon_0\varepsilon_r}} \frac{ln(D/d)}{2\pi}$$

The velocity of electromagnetic wave propagation is given by equation:

$$v = \frac{c}{\sqrt{\varepsilon_r}}$$

with c the light velocity in void.

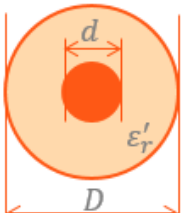

Figure 2. geometric section of the ECC

If along an ECC, at location x, a strain $\epsilon(x)$ is imposed to the ECC, the section geometry (D/d) changes at this location which induces a variation of the characteristic impedance $Zc(x)$. A localized temperature variation $\Delta T(x)$ produces a variation of geometry of the ECC and especially a variation of the local dielectric permittivity. The measurement of Z (i.e. S_{11}) allows to detect this characteristic impedance variation.

To localize the characteristic impedance variation along a cable, we use an electric inversion scheme based on inverse Fourier transform which gives the distributed characteristic impedance along the cable (along x axis). The spatial resolution and the maximum length depend on the frequency range ($f_{max} - f_{min} \approx 3GHz$) and of the frequency resolution (frequency point number, around 3000 points).

Finally, we can show that the impedance variation between two states of solicitation (strain or temperature) is written in the following form:

$$\Delta Z(x) = C_{\epsilon}.\epsilon(x) + C_T.\Delta T(x)$$

with C_{ϵ} and C_T, the sensitivity coefficients respectively to the strain $\epsilon(x)$ and temperature variation $\Delta T(x)$.

An example of the application is given on figure 3. A mass is suspended on a 1m length on an ECC ($x \in [5m; 6m]$). The measurements of S_{11} before and after applied a strain are shown on figure 3. Applying the inversion algorithm on S_{11} measurements, gives the electric impedance of the coax along the cable abscissa (x) and the difference electric impedance between two states (figure 4). The horizontal line (orange) is a theoretical variation of the characteristic impedance in this experience.

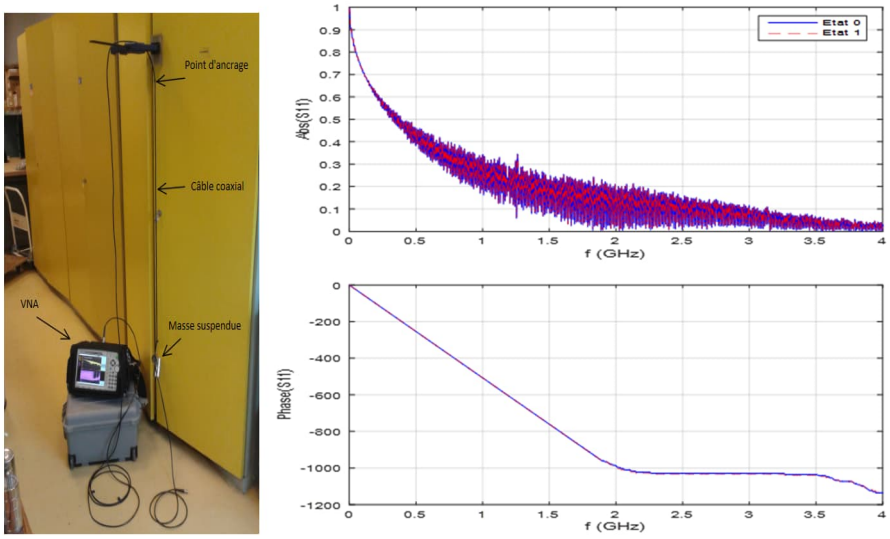

Figure 3. feasibility and typical measurement of the S_{11}

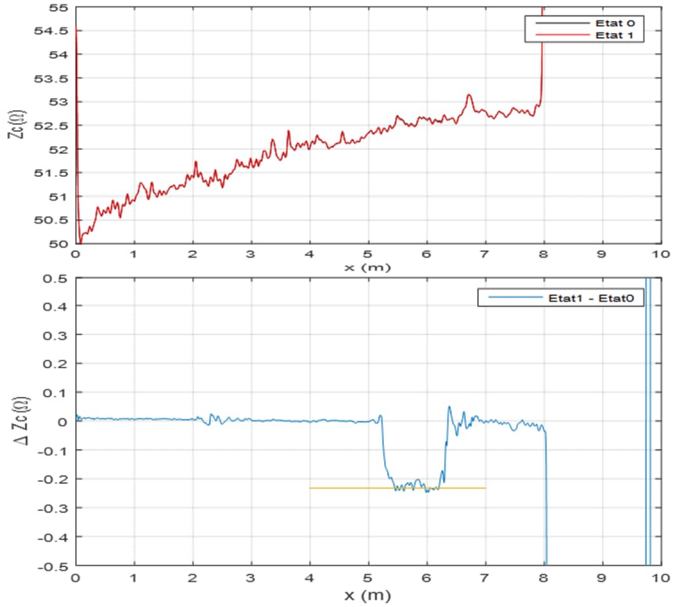

Figure 4. inversion of the characteristic impedance Zc from S_{11} measurements and impedance variation ΔZ along an ECC due to the strain applied between 5 and 6m.

3. EXPERIMENTATION

3.1 Mock-up

To simulate a breaking of a post-tension cable, we have built a concrete mock-up. The mock-up (figure 5) is a 6 m long prestressed reinforced concrete beam equipped with a 7C15 tendon consisting of 7 clear T15.7 strands of class 1860 (section 150 mm^2). The force of the post-tension strand is of the order 970kN.

A notch is made in the upper part of the beam to allow the strands to be cut. Numerous sensors were installed in the mock-up to monitor the strain of the concrete and the steels during the tensioning and the breaking test. In particular, we have installed 3 strain sensors based on vibrating wire (VW) and associated temperature sensors , 2 tensiomag® sensors to measure the stress applied on the strands. OFS and ECC sensors have been installed on different paths along the beam allowing a distributed measurement of the concrete strain. The OFS and ECC can be easily fixed on the rebars (or post tension duct) into a concrete structure (see figure 6). The OFS and ECC used in this experience are respectively referenced as AFL-DNS0470 and RG58.

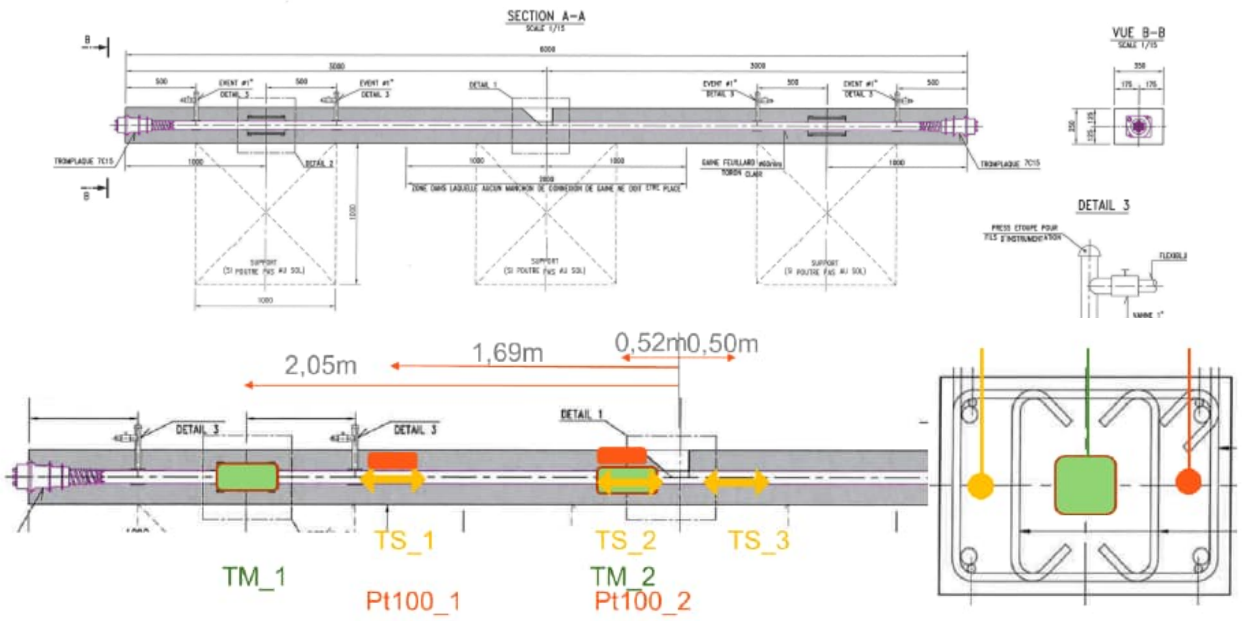

Figure 5. scheme of mock-up

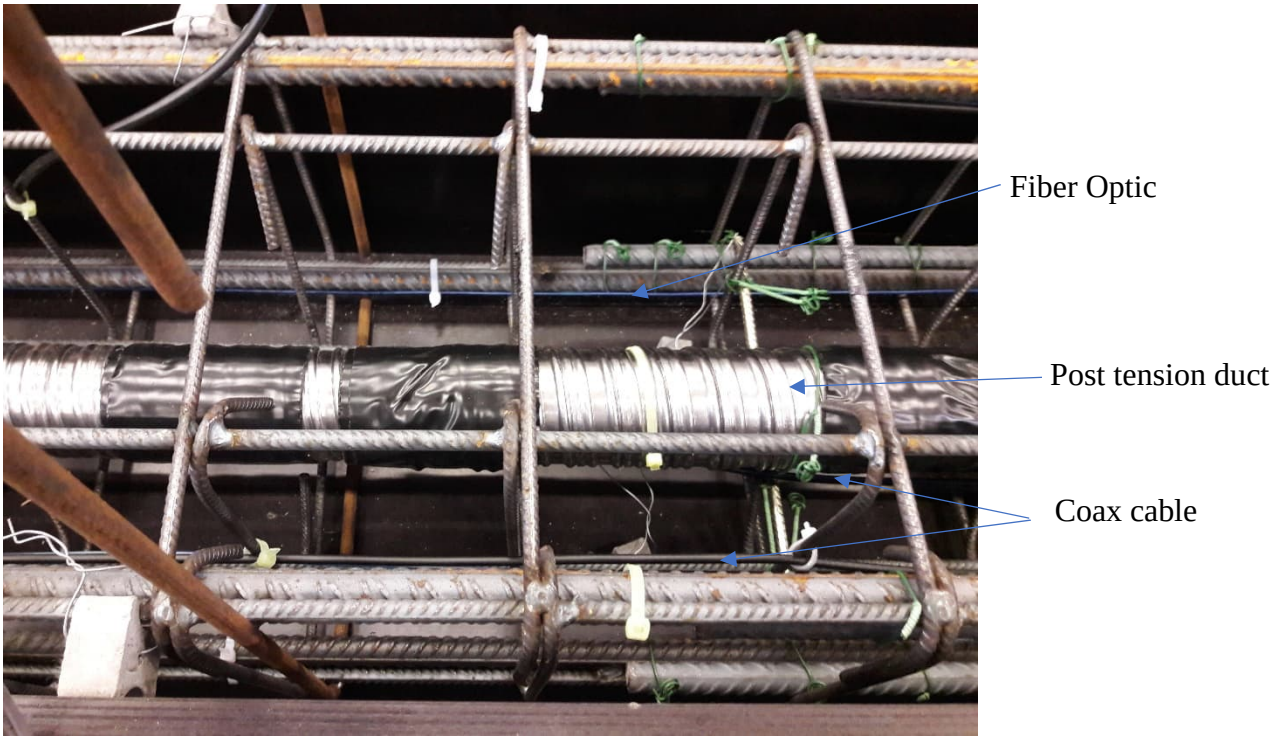

Figure 6. sensors implementation

3.2 Breaking test

Following the tensioning of the strands and the injection of the cement grout, the strand breakage test of the strands was carried out. The strands were cut by means of a disc saw (Figure 7) according to the sequence defined: wire by wire for the first two strands on the surface of the opening then strand by strand. A total of five strands out of seven were cut.

Figure 7. cutting of strands with disc saw and definition of the cutting sequence

During the breaking test, the measurement sequence consists of measuring the strain state of the concrete beam before the first step (reference state) and then measuring the deformation after each wire or strand cut. The strain is then compared to the reference strain state.

3. RESULTS AND DISCUSSIONS

Several optical and electrical lines were positioned in the beam section. All results are given in the beam reference frame with the tendon rupture located at position $x = 3m$. We consider the strain measurements from these OFS and VW as the reference. We are particularly interested in the lines positioned just below the prestressing duct and in the one positioned in the concrete.

In figure 8, we compare the distributed strains along the beam during the cutting sequence. We note that the strains measured by the ECC and by the OFS are relatively comparable. However, spreading of the strain measured by the ECC is more pronounced than with the OFS. This spread comes from the mechanical transfer function of the ECC (itself equivalent to an anchoring length of the coax in the concrete) which is undoubtedly larger than that of the OFS used in this test (of the order of 10 cm according to the [3]). Moreover, the differences in amplitude of the strains can come from the ignorance of the real sensitivity coefficient to the strain C_ϵ of the coaxial cable.

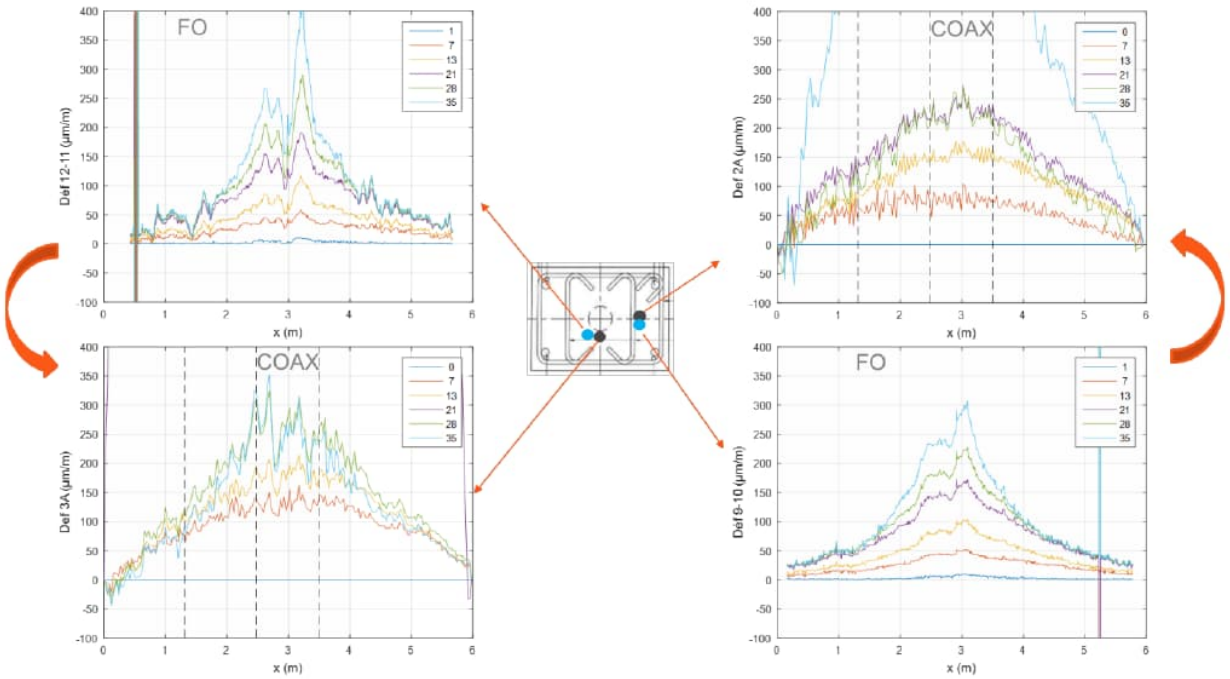

Figure 8. comparison of concrete strain measurements from embedded OFS and ECC as a function of the number of broken wires

We compare the strain measurements from the VW to the measurements from the OFS and ECC (Figure 9). The OFS strain values are in good agreement with the VW measurements. The strain of the concrete at the breaking zone for each broken strand is about 50 $\mu m/m$/strand. The strain values from the ECC are noisier than the OFS strain measurements but remain overall of the same order of magnitude. Nevertheless, depending on the use case, this accuracy can be sufficient to detect and locate strand failures.

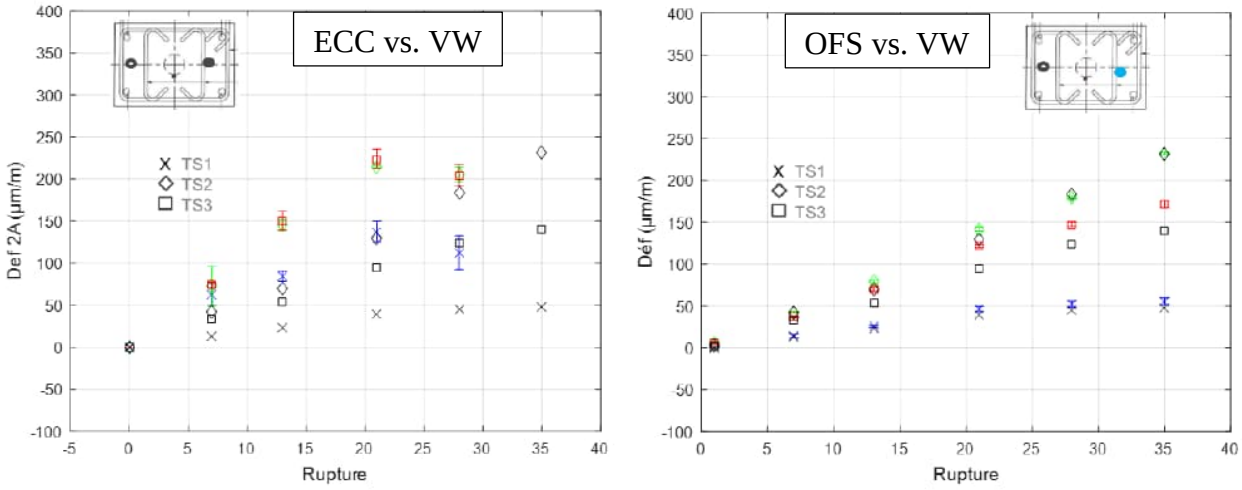

Figure 9. comparison of concrete strain measurements from embedded OFS, ECC and VW (here called TS) as a function of the number of broken wires

Taking into account the measurement uncertainties, of the order of 10µm/m for the VW, we can see that a monitoring solution based on a local measurement strain would require the use of many sensors to cover the entire structure. The ECC solution seems to be a good compromise between the cost of instrumentation and the accuracy needed to monitor the large prestressed structures.

4. CONCLUSIONS

We have presented a new monitoring device based on electric coaxial cable able to measure the distributed strain of concrete along the cable. A 6-meter long concrete beam have been built with an embedded post-tensioned tendon.

The ECC solution seems to be a good compromise between the cost of the instrumentation and the accuracy needed to monitor the large prestressed structures.

Depending on the monitored building and the corresponding safety / functional requirements, the design criterion and final choice between one surveillance technology and another, is a balance between the metrological performances of the system, including robustness criteria during construction and long term operation, and the potential cost optimization.

If the ECC solution allows detecting and locating qualitatively the rupture phenomenon, additional analyses should be made in order to quantify precisely its metrological performances for measuring strain variations due to rupture and potentially the re anchorage phenomenon,.

REFERENCES

[1] Patent FR3059780B1, Method and system for monitoring civil engineering construction, EDF, F. Taillade

[2] David M. Pozar, Microwave Engineering, Fourth Edition, John Wiley & Sons, Inc., 2012.

[3] J-M Henault & al., Quantitative strain measurement and crack detection in RC structures using a truly distributed fiber optic sensing system, Construction and Building Materials, 2012(37), pp. 916-923

[4] M. Galan & al., Structural monitoring of prestressed concrete containments of nuclear power plants for ageing management, SMiRT-26, 2022

[5] M. Galan & al., Concrete distributed strain measurements feedback on civil structures based on VEROCRS mockup – potential application for new NPP's, SMiRT-26, 2022

Using non-destructive testing methods for locating the steel reinforcement in reinforced concrete structures

Fahim Al-Neshawy, Abobaker Ba Ragaa and Jari Puttonen
Department of Civil Engineering, Aalto University School of Engineering, Espoo, Finland

ABSTRACT

Concrete cover for reinforcement steel is required to protect the steel rebar against corrosion and to provide resistance against fire. Determining the precise location, cover depth, and diameter of concrete reinforcement in existing structures can be rather difficult. Especially in densely reinforced elements, where there are several layers of reinforcement. The most common non-destructive methods for locating reinforcement are the electromagnetic cover meters and the ground penetrating radars (GPR) methods.

This paper describes the possibilities of non-destructive determination of the location and depth of reinforcement in concrete structures using electromagnetic ProfoScope cover meter and GPR. The paper describes the use of the two methods for in-situ measurement of a steel-reinforced-thick-walled concrete mock-up, presents the results of measurements of cover depth and the location of the reinforcement, and discusses the strong and weak points of the two methods.

The results indicate that the cover meter is suitable for measuring the concrete cover depth while the GPR is very good in identifying and locating the rebar position in reinforced concrete structures.

Keywords: Reinforced concrete, mock-up, cover meter, GPR, Non-Destructive Testing.

1 INTRODUCTION

Reinforcement corrosion is a major concern that causes extensive damage to the reinforced concrete structures. For new or freshly constructed reinforced concrete structure, adequate concrete cover to reinforcement bar (rebar) is essential to protect it from external aggressive chloride or carbon-di-oxide (CO_2) induced environments. For the quality assessment of reinforced concrete structures, it essential to locate the reinforcement bars, measure the concrete cover thickness and the rebar diameter. Also, for core sampling and extraction, rebar location is important to avoid cutting of the rebar. A reliable estimation of rebar location, concrete cover thickness and rebar diameter, non-destructively, is very much important for the quality assurance of new and for the condition assessment of existing reinforced concrete structures [1].

The thickness of cover depends on environmental conditions and type of structural member. The Eurocode 2 (EN 1992-1) [2] establishes the cover of reinforced concrete structural members and the dispersion of this variable in relation to its execution is also considered.

In order to secure the structural performance and durability of steel-reinforced concrete, the arrangement of rebars in the concrete and cover depth are critical variables. It is also important to assess these variables when evaluating the integrity of existing structures. When non-destructive inspections are used to determine the in-place locations and diameters of rebars in concrete, two techniques that are most commonly used in the field for the rebar identification, cover thickness and rebar diameter estimation are cover meter and the ground-penetration radar (GPR) techniques [3].

The cover meter and rebar locator can be used to find the depth from the face of the concrete to the top of reinforcement, to locate steel within the concrete, and to estimate the rebar diameter [4]. Ground Penetrating Radar (GPR) is a rapid, non-destructive testing method for a wide range of applications. GPR is based on the propagation of short electromagnetic (EM waves) impulses having a pulse duration of <1 ns (1×10^{-9} s) in the structure to be investigated and detects the reflected signals from reflectors (boundaries related to a mismatch of electric properties) in subsurface structures. GPR can identify and map areas with a high likelihood of corrosion-based deterioration, assess construction quality, determine structural reinforcement layout, and estimate thickness of reinforcement cover [5].

	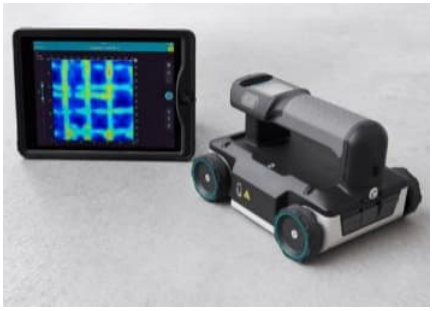	
Metal rebar locator Profoscope, Proceq	GPR Live concrete scanner, Proceq	HILTI PS-1000 GPR concrete scanner

Figure 1. The NDT devices used for rebar identification and cover thickness measurement.

In this paper, we will present the concrete electromagnetic cover meter and GPR methods for measurements of the concrete cover and identification of the reinforcement location of a thick-walled reinforced concrete mock-up wall.

2 EXPERIMENTAL PROGRAM

For the NDT measurement of the concrete cover depth and mapping of the steel reinforcement, the surface of mock-up wall was divided into a 10×10 cm grid area as presented in Figure 2. The measurements were performed in the south side of the wall except within a distance of 10 cm from the edges.

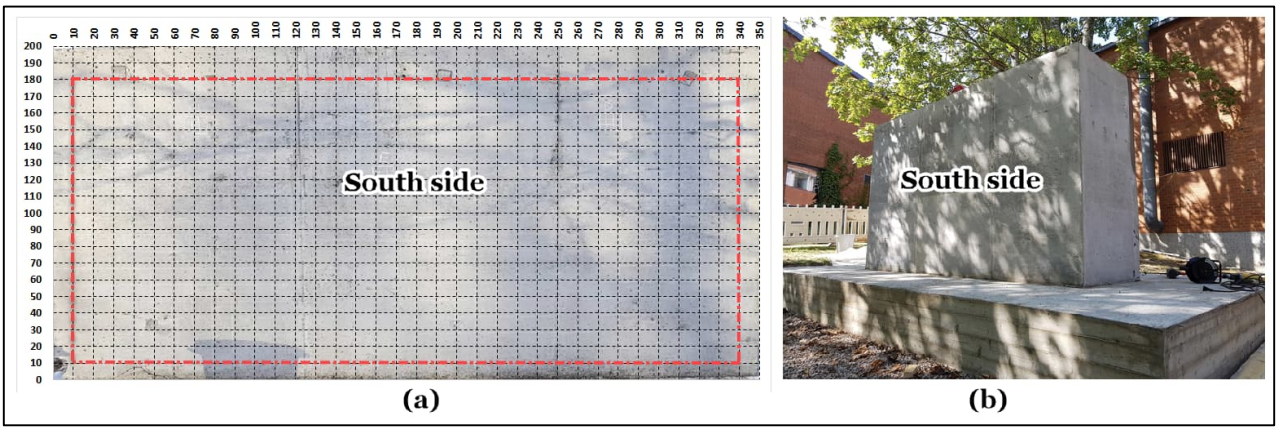

Figure 2. (a) Measurement area with 0.1 m mesh density and grid points used in the procedure [6] and (b) the south side of the mock-up wall.

2.1 Mock-up wall reinforcement design

The general approach to the reinforcement design for the mock-up wall was based on the cross-section design of the containment wall of TVO's NPP Olkiluoto 2. The reinforcement design for the main wall is characteristic by two areas, one of higher reinforcement density, and one with lower

reinforcement density. The reinforcement diameter used is 25 mm. The nominal reinforcement concrete cover is 50 mm.

The outer layer of reinforcement is characterized by a reinforcement grid with the following characteristics, as shown in Figure 3:

Left half side of the mock-up when facing the wall

- Horizontal reinforcement spaced 150 mm apart
- Vertical reinforcement spaced 150 mm apart

Right half side

- Horizontal reinforcement spaced 300 mm apart
- Vertical reinforcement spaced 200 mm apart

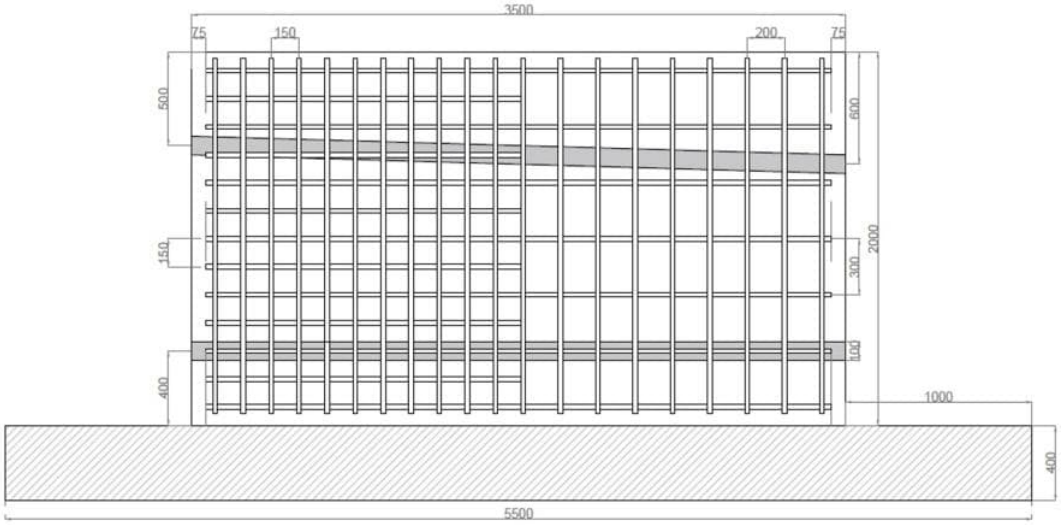

Figure 3. Side view of the mock-up main wall reinforcement.

The secondary reinforcement layer exists only on the left side of the mock-up when facing the wall. The reinforcement grid has the following characteristics:

- Horizontal reinforcement spaced 150 mm apart
- Vertical reinforcement spaced 150 mm apart

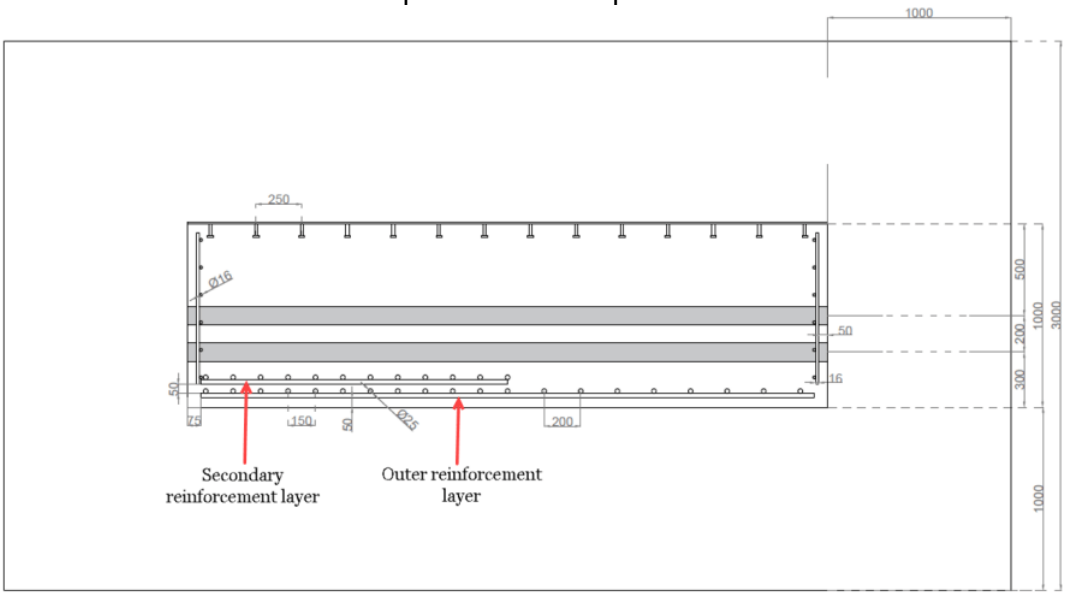

Figure 4. Plan view of the mock-up main wall reinforcement.

2.2 Measuring the concrete cover depth

For measuring the concrete cover depth, the cover meter method was used. Cover meters use the principle of eddy currents that occur in conductors placed in an electromagnetic field. Originally, the method exploited the magnetic properties of the material being detected. The ProfoScope cover

meter operates on the pulse induction principle. The probe houses coil without a magnetic core, which means it is unaffected by magnetic fields in the surrounding area. Advanced signal processing allows locating a rebar as well as measuring of concrete cover depth. Some of the strong points of the ProfoScope cover meter include immediate visual output, high accuracy, the option to make corrections for the distance of adjacent reinforcement, and the considerable speed of measurement. Measurements can suffer e.g., by mis-detecting rebars that are too close, whether next to or behind one another. Another limiting factor can be the instrument's range (in normal probes about 60 – 100 mm, in depth probes approximately 150 mm to 220 mm). The measurements can also be impaired by strong electromagnetic fields near the structure being tested [7].

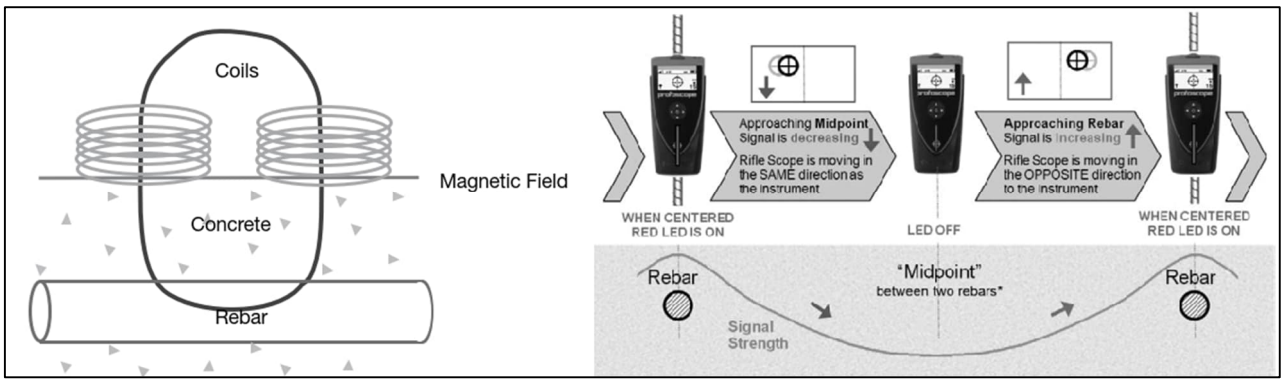

Figure 5. Measurement principle of the concrete ProfoScope which uses Eddy current [8].

The Profoscope cover meter was calibrated using the calibration test block, presented in Figure 6. The location and cover of the reinforcement of the test block were measured at different locations by using the cover meter to check the calibration accuracy. The calibration measurement data was compared with the standard values prescribed on the test block. The recorded data and the standard values were matching.

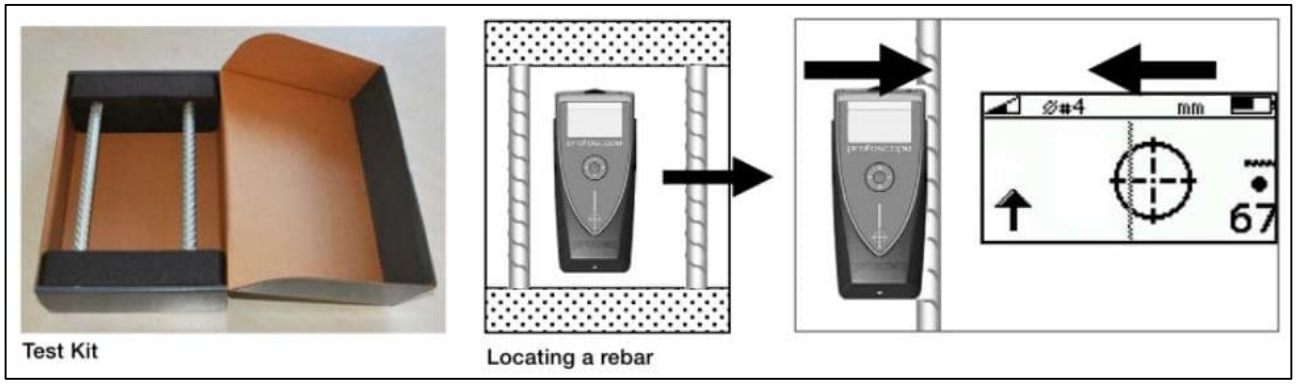

Figure 6. The calibration of the Profoscope cover meter using the calibration test block.

The Profoscope cover meter was used to measure the cover from the south side of the mock-up wall, in horizontal and vertical direction to detect the concrete cover depth. As soon as the Profoscope cover meter was above rebar or nearest to it, it gave an audio signal through a short beep and visual red colour display. Simultaneously, the measured concrete cover was recorded. To ensure that the positioning of the probe at the measurement position, the probe was continuously dragged along the surface.

2.3 Mapping of the reinforcement steel bars

For mapping and locating the positions of the mock-up reinforcement, GPR Live scanner (shown in Figure 1b) was used. The GPR method is a radar-based technology that uses antennas to transmit and receive pulses of electromagnetic energy through a medium such as the ground or concrete. As the radar receives the transmitted pulses it registers "echoes" from objects based on their different electromagnetic conductivity. A simple illustration of the principle is shown in Figure 7. When the Scanner is moved along a concrete surface, electromagnetic waves are reflected from objects beneath this surface. These objects are indicated immediately on the display.

The data is taken by a unique transceiver antenna at a fixed position (x, y) as presented at Figure 8. The propagation duration of the electromagnetic wave (in the Z axis direction) varies depending on the GPR speed. The GPR (A - Scan) signals can be used to detect locations of buried objects via propagation duration. GPR (B – scan) images consist of (A – scan) signals along the x axis measured at regular intervals. The vertical axis (y) represents the depth of the scanning area in relation to the signal time (t), while the horizontal axis (x) symbolizes the surface distance. Buried objects in B – scan image is displayed as hyperbola. GPR (C – scan) is three-dimensional image which is generated by combining simultaneous B scan images on the (x-y) plane [9].

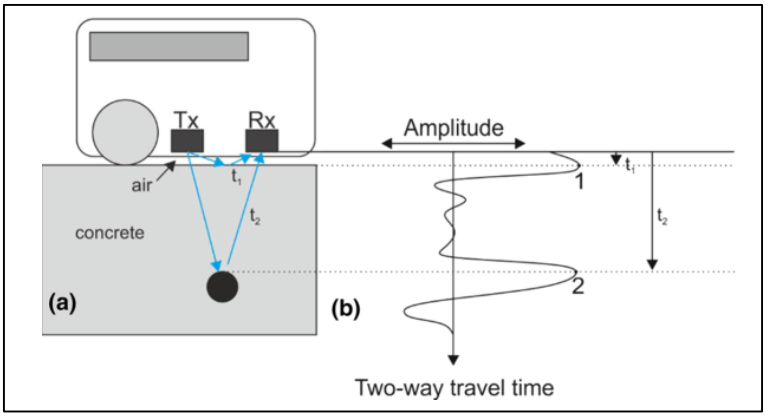

Figure 7. (a) Layout of a survey on a reinforced concrete structure using a GPR system, and (b) corresponding GPR signal output [10]

The survey of the south side of the mock-up wall was undertaken by experienced GPR surveyors. The scanning was undertaken on a regular orthogonal grid spacing areas (1200x1200 mm areas) as shown in Figure 8.

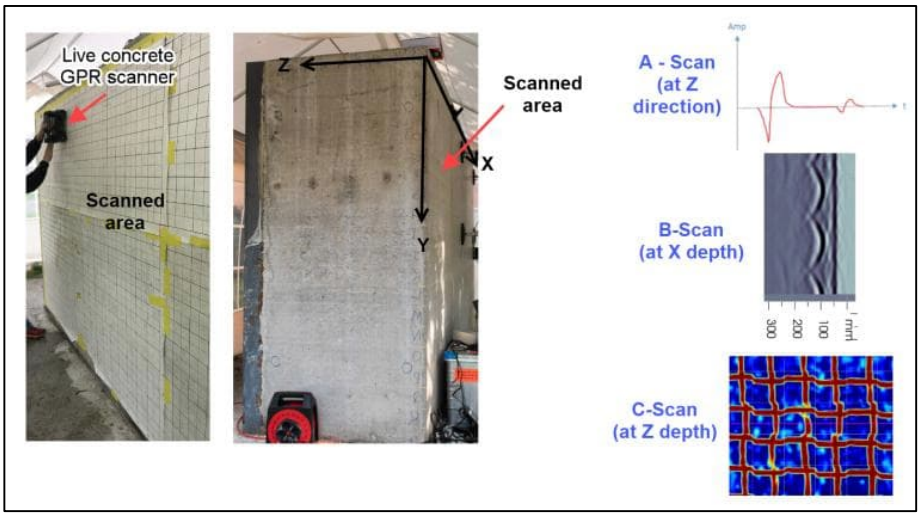

Figure 8. The grid scanned areas of the south side of the mock-up wall.

The size of the GPR measurement field examined on the south side of the mock-up wall were 350 cm x 180 cm using the Proceq live concrete scanner (see Figure 9a) and 120 x 120 cm area at the middle of the wall using Hilti PS-1000 concrete scanner (see Figure 9b). The penetration depth with the GPR systems used was approximately 30 cm.

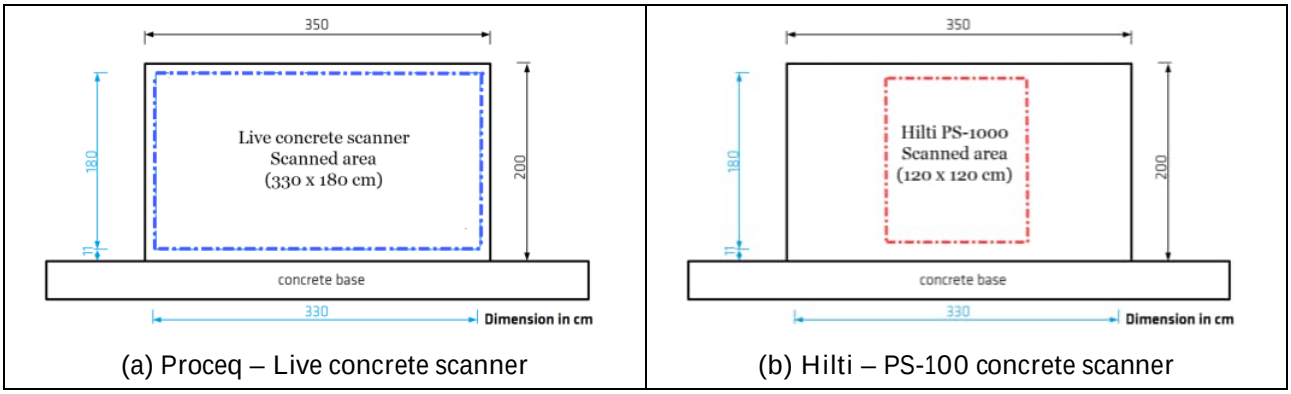

(a) Proceq – Live concrete scanner (b) Hilti – PS-100 concrete scanner

Figure 9. Location of the GPR data sets on the south side of the mock-up reinforced concrete wall.

3 RESULTS AND DISCUSSION

3.1 Concrete cover depth

The cover meter was set to identify the clear cover above the rebar of 25 mm diameter. Examples of the concrete cover measurement obtained from the scans on the south side of the mock-up wall for horizontal and vertical reinforcement direction are presented in Figure 10 and Figure 11 respectively.

As shown in Figure 10, the concrete cover depth in the left side of the wall varies from 39 mm to 51 mm and the right side of the wall varies from 40 mm to 48 mm. The results show that the measured cover depth is close to the design concrete cover depth value of the wall which is 50 mm on the left side and the right side of the wall.

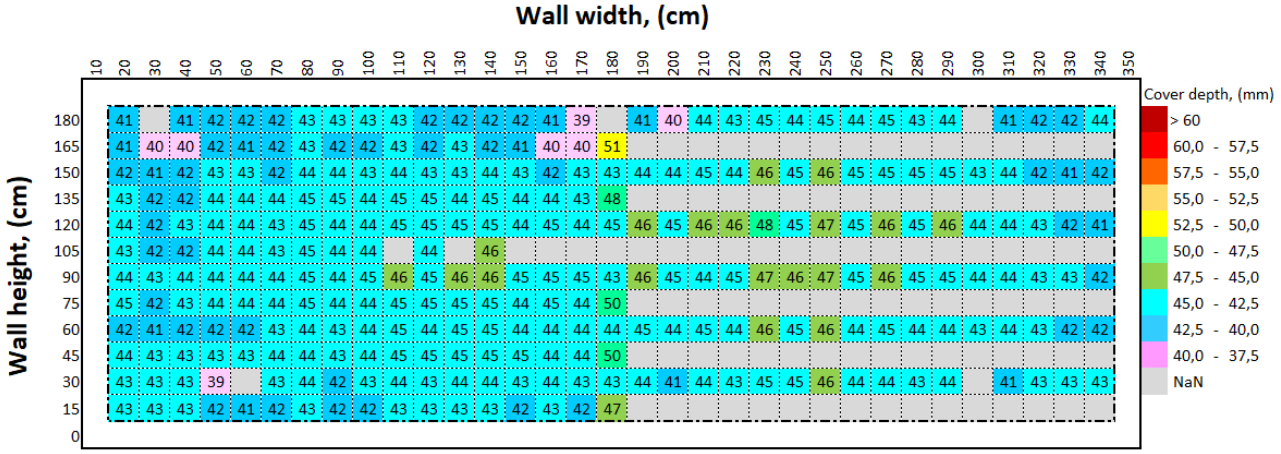

Figure 10. Concrete cover depth (south side, horizontal reinforcement scanning).

The measurements presented in Figure 11 show the variation of the concrete cover depth in the left side of the wall from 41 mm to 57 mm and the right side of the wall from 45 mm to 59 mm. The variation of the measurements in the right half side could be due the lower number of measurements. It is noticed the measurements are not close to the design concrete cover depth value of the vertical reinforcement of the primary reinforcement layer which is 75 mm on the left half side of the wall. The results also show that the cover depth of the secondary layer of the reinforcement bars could not be detected using the cover meter.

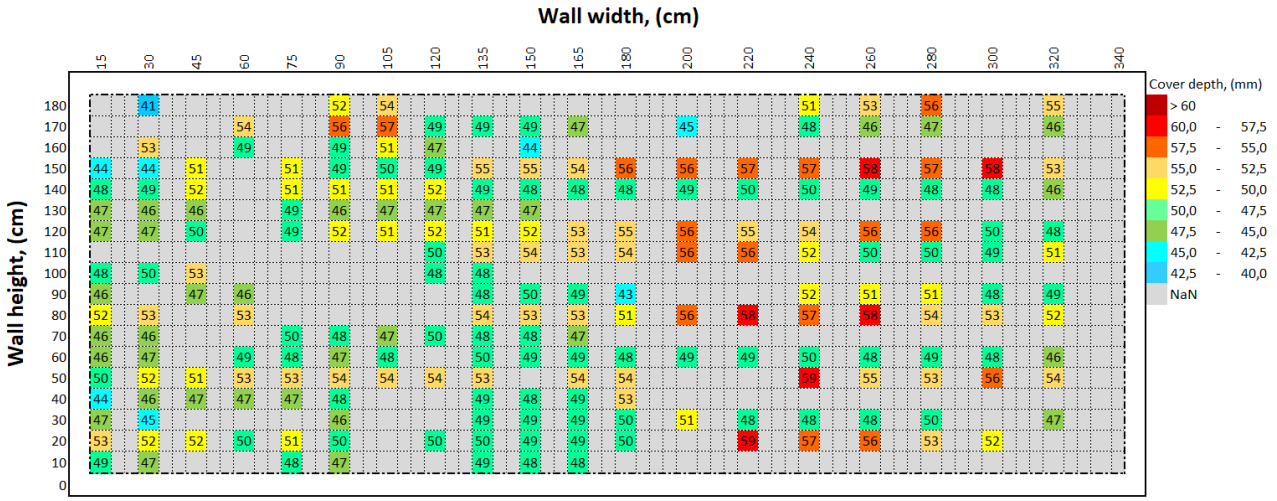

Figure 11. Concrete cover depth (south side, vertical reinforcement scanning).

Table 1 shows the results of the detected cover for the south side of the reinforced concrete mock-wall. The data in the table show that Profoscope can effectively be used to measure the cover depths. The relative error in detection of the cover depth increases in the left half side where higher reinforcement density located.

Table 1. Details of the detected clear cover depth for both horizontal and vertical reinforcement scanning.

Reinforcement	South wall side area	Average detected cover, (mm)	Actual location of bar from top surface, (mm)	Accuracy (Relative Error), (%)	Standard deviation, (mm)	Coefficient of variation, (%)
Horizontal reinf. bars	Left half side	43	50	-14,0	1,7	4,0
	Right half side	44	50	-12,0	1,6	3,6
Vertical reinf. bars	Left half side	50	57,5	-13,0	2,9	5,8
	Right half side	52	57,5	-9,6	3,9	7,5

Figure 12 presents the normal distribution of the verified concrete cover depths for the horizontal and vertical reinforcement bars. For the horizontal reinforcement bars, the mean (μ) of the verified concrete cover depth is about 43 – 44 mm with standard deviation (σ) is 1.6 – 1,7 mm and the coefficient of variation is 4,0 – 3,6% for left and right half side of the wall. The variation of the measurements was higher for the vertical reinforcement bars than the horizontal bars.

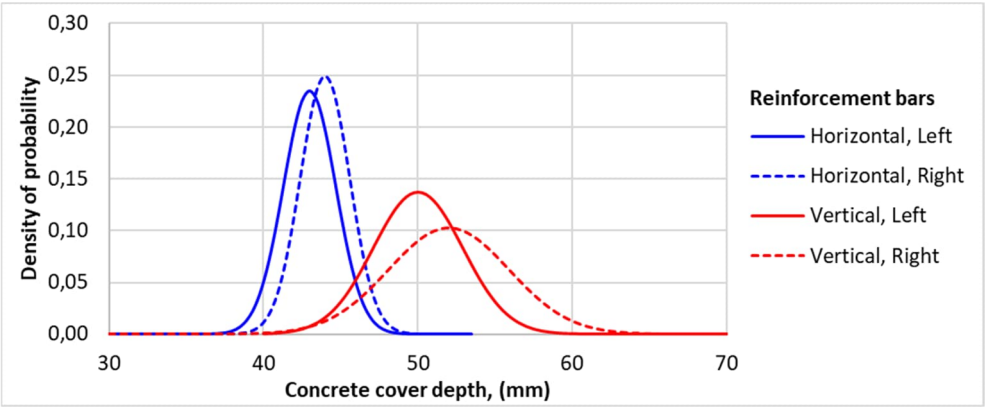

Figure 12. Normal distribution of the concrete cover depth measurement in the south surface of the mock-up wall.

3.2 Mapping of the reinforcement

Examples of the Live concrete GPR scanner measurements are presented at Figure 13. At a depth of 4 – 6 cm, the near-surface primary reinforcement is visible, with the reinforcement on the left half side of the specimen being approximately twice as dense as on the right side. The secondary reinforcement surface is visible at the depth of 13 – 15 cm.

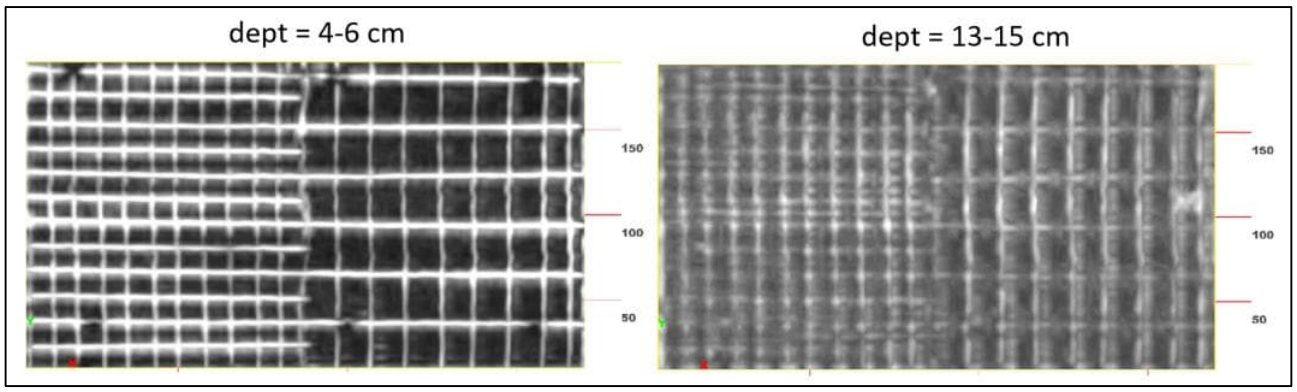

Figure 13. Depth sections, captured with the Live concrete GPR scanner on the south side of the mock-up (measuring field size = 330 cm x 180 cm).

Figure 14 presents the Hilti PS-1000 GPR scanning results of the scanning area (1200 x 1200 mm) on the middle of south direction. The estimated concrete cover depth is approximately 50 mm. Because of the data noise the exact value of concrete cover depth was difficult to determine. A dense reinforcement is shown in the scanning data. The concrete cover depth of the right scanning area is approximately 60 mm. The space between vertical steel rebar is about 150 mm at the right half side and 200 mm at the left half side. The space between horizontal steel rebar is about 150 mm at the right half side and 300 mm at the left half side.

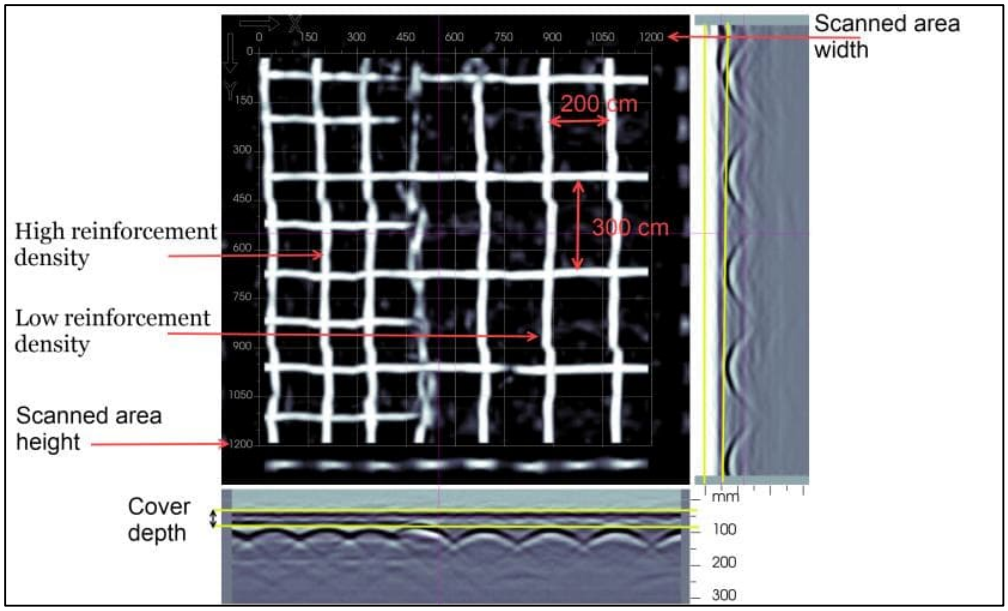

Figure 14. C-scan maps of the inspected area (depth z = 5 cm).

The benefits of the application of the GPR technique to concrete include the identification and mapping of embedded reinforcement rebars. One of the major disadvantages of the GPR technique is related to the difficulty that is associated with interpreting and understanding the resulting data. The data interpretation is technician (operator) dependent, and the human error is a factor of the reliability of the results.

4 CONCLUSION

In this paper, we presented two techniques that are used for locating and mapping of the steel reinforcement bars in thick-walled reinforced concrete wall. These techniques are magnetic methods using concrete cover meter and Ground Penetrating Radar (GPR). Two GPR devices were used: (i) the Proceq Live concrete scanner and (ii) the Hilti PS-1000 concrete scanner. The Following conclusions can be drawn from the experimental study:

- Cover meter and GPR techniques can be used for rebar identification and cover thickness estimation. In general, Cover meter technique is simple to use and easy to interpret the results when compared to that of GPR technique. The concrete cover depth measured by the cover meter is almost close to the design values of the cover depth.
- By using the real rebar diameter details during the calibration of the cover meter, the results of the cover thickness are reliable and correct.
- Structural members with deep cover and heavily reinforced sections with metal inserts, rebar identification using Cover meter is difficult. In such cases, GPR technique is effective in identifying rebar locations and cover thickness estimations.
- One of the limitation of the GPR techniques that it needs an experienced technician for the use of the scanner and interpretation of the results. Another limitation is that the penetration depth with the GPR system used was approx. 30 cm.

ACKNOWLEDGEMENTS

The authors of this paper would like to thank the following people who have helped us undertake this research:

- Timo Kukkola and Ilmari Ranta from Teollisuuden Voima Oyj (TVO), for their performing of the Hilti PS-1000 concrete scanner (GPR) measurements, data analysis and reporting the results.
- Jens Wöstmann, Marco Lange, Ute Effner from BAM (Federal Institute for Materials Research and Testing, Berlin, Germany), Division 8.2, for their performing of the GPR measurements, data analysis and reporting the results.

REFERENCES

[1] S. Bhaskar and S. Vasanthakumar, “A study on the applicability of cover meter and GPR survey for cover thickness and rebar identification in reinforced concrete structures,” in *NDE 2017 Conference & Exhibition of the society for NDT (ISNT), 14-16 December 2017, Chennai, T.N., India (NDE-India 2017)*, 2017. Accessed: Sep. 03, 2022. [Online]. Available: http://www.ndt.net/?id=22341

[2] EN 1992-1-1, “Eurocode 2: Design of concrete structures - Part 1-1: General rules and rules for buildings,” *305/2011 Directive 98/34/EC*. The European Union Per Regulation 305/2011, 2004.

[3] H. Hamasaki *et al.*, “Identification of Reinforced in Concrete by Electro-Magnetic Methods,” in *International Symposium (NDT-CE 2003)*, 2002. Accessed: Sep. 03, 2022. [Online]. Available: https://www.ndt.net/article/ndtce03/papers/v006/v006.htm

[4] K. Sivasubramanian, K. Jaya, and M. Neelemegam, “Covermeter for identifying cover depth and rebar diameter in high strength concrete,” *International Journal of Civil and Structural Engineering*, vol. 3, pp. 557–563, 2013.

[5] J. F. C Sham, H. Kong Janetsham, polyueduhk Wallace, W. L. Lai, and H. Kong Wallacewai, “Diagnosis of reinforced concrete structures by Ground Penetrating Radar survey - case study,” 2017. doi: 10.1109/IWAGPR.2017.7996058.

[6] F. Al-Neshawy, Y. Chen, I. Ranta, and J. Wöstmann, “Report on round robin NDE testing for concrete cover measurements,” Espoo, 2021. Accessed: Sep. 03, 2022. [Online]. Available: https://aaltodoc.aalto.fi/handle/123456789/110938

[7] S. Hüblová, P. Cikrle, O. Karel, and D. Kocáb, “Experimental measurement of the diameter and cover depth of steel reinforcement using an electromagnetic concrete cover meter,” *IOP Conf Ser Mater Sci Eng*, vol. 549, no. 1, p. 012011, Jun. 2019, doi: 10.1088/1757-899X/549/1/012011.

[8] Proceq, “PROFOSCOPE - Operating instructions.” 2017. Accessed: Sep. 03, 2022. [Online]. Available: https://media.screeningeagle.com/asset/Downloads/Profoscope_Operating%20Instructions_English_high.pdf

[9] U. Özkaya, Ş. Öztürk, L. Seyfi, and B. Akdemir, “Region analysis of buried object based on fully automated image processing.” [Online]. Available: https://www.researchgate.net/publication/343548181

[10] F. Tosti and C. Ferrante, “Using Ground Penetrating Radar Methods to Investigate Reinforced Concrete Structures,” *Surv Geophys*, vol. 41, no. 3, pp. 485–530, May 2020, doi: 10.1007/S10712-019-09565-5/FIGURES/20.

SFCW GPR Array concrete inspection on nuclear sites

Houssame El Ghanami, Manuela Kaufmann and Alexanre Novo
[1] Screening Eagle Technologies, Zurich, Switzerland

ABSTRACT

Ground Penetrating Radar (GPR) is an effective method to test concrete structures in a non-destructive way. However, traditional pulsed GPR systems come with limitations, including depth penetration constraints, laborious 3D data collection, and complicated post-processing [1]. Working on nuclear sites, on the other hand, requires fast and accurate 3D data collection and significant depth penetration to evaluate structural elements.

To overcome the depth penetration and the long collection and processing curve, we use a Stepped Frequency Continuous Wave (SFCW) GPR array. While a traditional pulsed GPR system uses time-domain measurements of the reflected waves, a SFCW system collects data in the frequency domain and converts these to time-domain via computer processing [2]. This approach gives better resolution and depth penetration, eliminating the common frequency dilemma of a GPR inspection.

Collecting 3D data with GPR is a procedure that requires a significant amount of time, including grid data collection over specific lengths and widths and with predefined spacing between the lines. This method creates delays, limits your ability to see and visualize data and comes with a high cost for post-processing the data. We use a compact GPR array, that comes with six antennas in line with 5cm separation, which allows us to see targets in real-time, with high resolution, and without additional post-processing. This makes our NDT inspection of nuclear sites safer and more effective.

Keywords: ground penetrating radar, stepped frequency continuous wave

1. INTRODUCTION

Reinforced and prestressed concrete is the main material used for the structure of nuclear power plants: reactors, cooling towers, raft foundation, operations buildings, and pipes. The structure is not only critical for safety reasons but also for the operations during the specified asset life which is exposed to an aggressive environment and potential accident. Any defect such as spalling, crack, deflection, or potential water pipe leakages needs to be located early and requires adequate monitoring. Next to sensors continuously measuring the structure health, non-destructive testing (NDT), plays a key part in finding defects early. In the specific case of concrete structures imaging, three main technologies are available: Ground Penetrating Radar (GPR), ultrasonic pulse-echo, and eddy current testing.

Handheld high-frequency GPR is increasingly used in the construction and inspection industry for three main applications. These are a) the location of reinforcement, post-tensioning elements (ducts and cables), and other features before coring/sawing/drilling operations, b) the as-built verification of concrete structures (i.e., to test if the construction was built according to specification), and c) the blank-slate investigation of concrete structures and facilities for which little or no information is available in the form of drawings.

Overall, GPR systems have seen significant advances in high performance and user-friendliness, allowing direct on-site reporting and helping non-GPR experts to assess the health of

the infrastructures. However, with one single GPR line, it is often not clear, what is detected and how the objects/anomalies extend. To obtain a complete image of the concrete, multiple parallel lines are normally measured [1]. Normally, this process is time-consuming post-processing might be needed to combine all data.

In subsurface GPR application such as utility location or archelogy, GPR systems with multiple parallel antennas, so-called arrays, are frequently used to measure large areas fast while maintaining good lateral resolution [3]. So far, these arrays are heavy and lack due to the used frequency range resolution for concrete imaging. Recently, a novel handheld small GPR array system for concrete application was developed. The GP8100 (see Figure 1) measures in one pass 6 scan lines with 5 cm separation. The system uses Stepped Frequency Continuous Wave (SFCW) to achieve better resolution and depth penetration compared to a traditional pulsed GPR system [4].

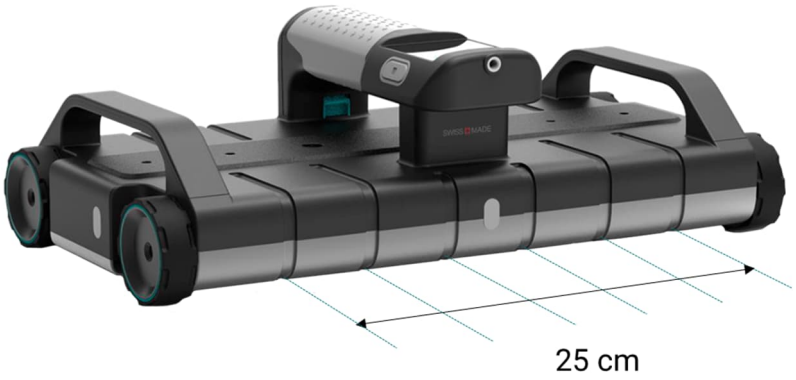

Figure 1. Compact handheld GPR array: GP8100

In this paper, we discuss the benefit of SFCW GPR handheld array. Showing results of a case studies. Additionally, we briefly show how combining GPR data with pulse-echo-based Ultrasonic data and eddy current testing helps to achieve an even more comprehensive image of the concrete structure.

2. METHODS

2.1. Stepped Frequency Continuous Wave (SFCW) GPR

Ground Penetrating Radar (GPR) sends high-frequency electromagnetic waves into a subsurface. The GPR unit measures the time needed for a wave to travel down to a target and get back to the unit. This two-way travel time gives the user a precise picture of the concrete subsurface, of foreign elements, like rebars and pipes.

Instead of operating by using pulses cantered around a single nominal frequency, an SFCW GPR system broadcasts electromagnetic wave trains and receives reflection signals by stepping through frequency steps across a modulation-frequency range. For concrete-scanning applications, a frequency range between 0.2 and 6.0 GHz and a triple-digit number of steps demonstrably deliver excellent resolution down to larger depths compared to directly-comparable handheld pulsed-GPR devices targeting the same applications [4].

Beneficially to a user who has become accustomed to interpreting radargrams of pulsed-GPR devices, the radargrams resulting from using an SFCW GPR device can be interpreted in the same way as those resulting from pulsed-GPR devices. As a result, switching from pulsed to SFCW GPR is straightforward for users, benefiting from the two main documented and published advantages of SFCW GPR compared to pulsed GPR. These are 1) a bandwidth wider than the typical definition of “UWB”, and 2) a signal-to-noise ratio that is up to approx. 20 dB higher [5]. The end result of those advantages is a reduction of salt-and-pepper noise (especially at larger depths), a larger penetration depth, and an improved resolution.

2.2. The benefit of an array

The GP8100 is SCWF GRP with a 400-4000MHz modulated frequency range and measures 6 scan lines at once with a line spacing of 5 cm, so in one pass an area of 25 cm is covered. Due to this, the software can show in real time a map of the features within the concrete (an exemplary data sample is shown in Figure 2a). The C-scan allows non- GPR expert to see targets in real-time. Additionally, in one single pass, a 25 cm width is covered, reducing the passes needed to measure a specific area. However due to the polarization of the antenna [6], only linear objects perpendicular to the measurement's direction can be detected (dark green objects Figure 2b) to map objects in all directions, perpendicular measurements should also be performed.

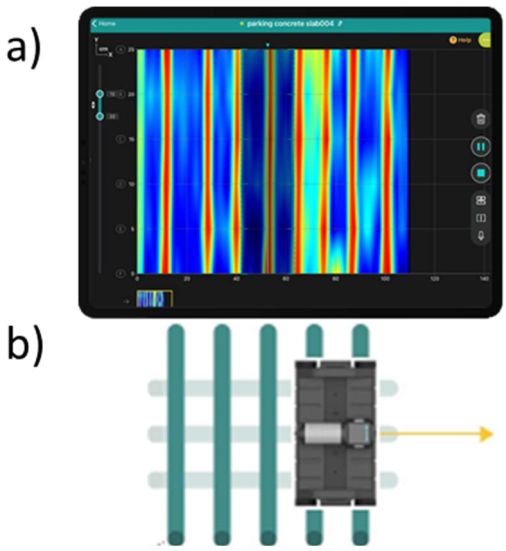

Figure 2. a) Data example of Single pass b) Exemplary image explain the visibility of only perpendicular objects (dark green) perpendicular to the measurement direction.

3. CASE STUDY

3.1. GPR measurements for rebars and cable

To verify the location of a cable in a concrete slab, a single pass with the GP8100 was performed. A C-scan was obtained with a focus on a depth range from 0 -20 cm (Figure 3 top). On the C-scan, red areas show the presence of a reflector and blue areas represent areas of concrete. Through the C-scan, it can be noted that there are 4 rebars (straight lines) and one pipe (slanted line).

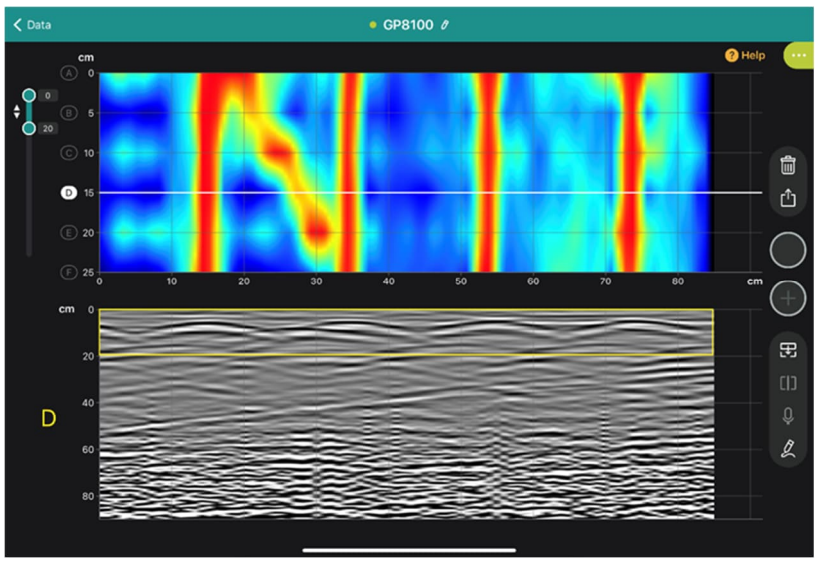

Figure 3. Measured Live data showing a C-scan of 1 pass with Gp8100, bottom a corresponding single GPR line

A single measurement with conventional GPR system would be similar to the data shown in Line D, in the lower part of Figure 3. An experienced user might use the visible hyperbolas to locate rebars and pipe, but without the information of the neighbouring scan, it would not be clear how they expand latterly, unless additional scans were performed.

3.2. Large Areas

Often on nuclear sites, not only small areas as described above may have to be monitored and mapped. To map large areas, data collection with dense horizontal and vertical lines may be necessary. In the following example, 5 mm small deflection of a concrete slab was observed, resulting in the need to verify the rebar spacing and find any other anomalies within the 3 by 3 m large area.

With a common single channel handheld GPR 108 singles lines with 5 cm spacing, would be needed to be marked on the ground and measured. Additionally, most GPR devices and their field software struggle to process that many lines live, so while measuring only a traditional B-scan would be visible to the user, allowing no live data interpretation. To obtain the full 3D image, all lines would have needed to be saved separately and then exported to a computer for some basic processing to generate a C-scan [7].

With the GP8100 the 3 m by 3 m-area was measured with 18 passes in 20 minutes. The data was directly visualized while measuring in the field. On the complete C-scan (Figure 4), it is recognizable that rebar spacing is varying from 12 cm on the left to 15 cm on the right side of the area. Additionally, on the top (around x=120 cm and y= 200 cm) an anomaly is present. To identify the anomaly, the corresponding single GPR lines were checked (Figure 5).
While doing measurement accurate placement of the GPR array at the start of a new pass/line is essential to avoid small misalignment between passes (as visible at Line 17) which can be corrected with a post-processing software.

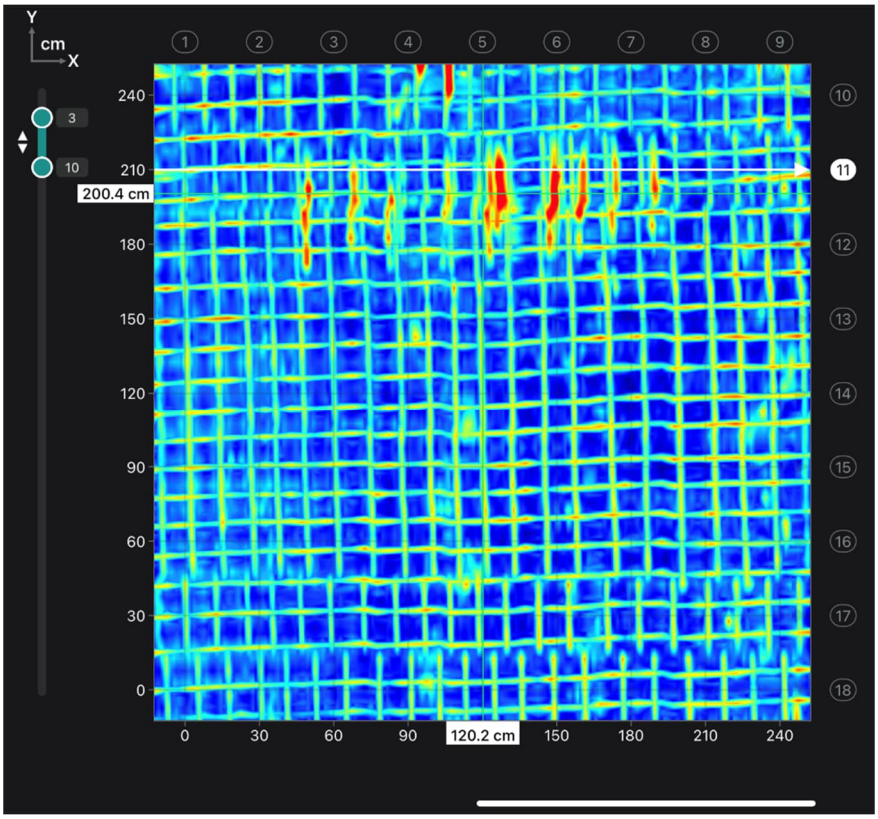

Figure 4. C-scan of the Area Scan showing the rebars.

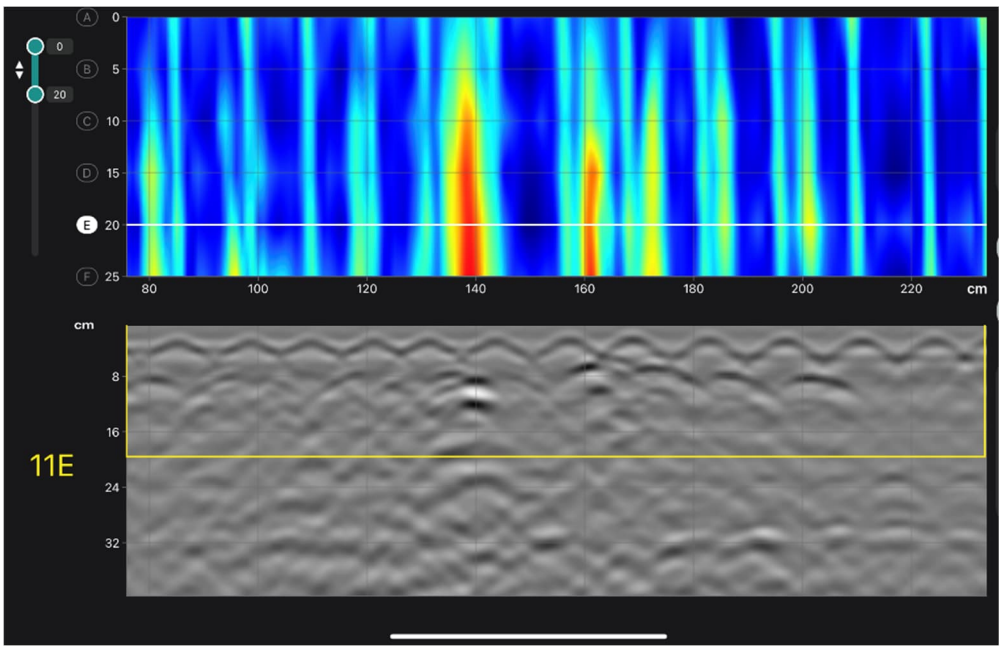

Figure 5 Superline for detail identification

After the measurement, with AR the data can be directly broadcasted onto the measured location (Figure 6) and the found results can be directly marked on the ground. Additionally, the 3D images help to show and share the results with non-GPR users

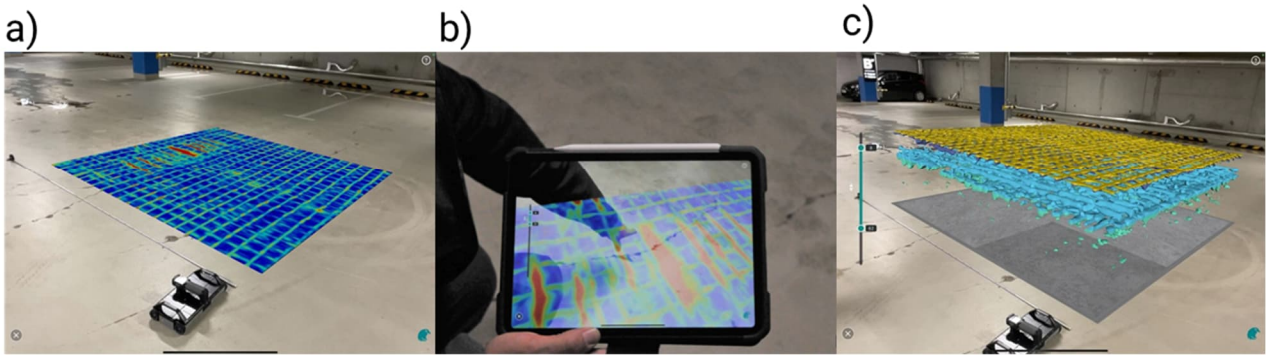

Figure 6. a) Measured Data (C-scan) shown at the real location. b) AR feature to help locate critical areas c) 3D image

3.3. Combining Eddy Current, GPR, and Ultrasonic data for a more comprehensive image

In the above example, the GP8100 clearly showed the ability to efficiently map metallic and non-metallic objects within a concrete structure. However, GPR often fails to detect air voids or delamination which can be easily detected with pulse-echo-based Ultrasonic Tomography (UT). The potential of combining both methods is shown on an 85 x 85 cm large area on a demo block containing rebars, delamination, tendon duct, plastic pipes, and varying backwall depths.

In a first step, an eddy current device (PM8000) was used to determine the rebar cover depth. This information was than later used to calibrate the velocity of GPR and UT.

The area was measured with 6 passes with GP8100 and post-processed within GPR-SLICE to obtain a 3D image (Figure 7a) showing rebars, tendon duct, and the shallow backwall. However, GPR failed to detect the delamination. On the other hand, the Ultrasonic data (Pundit PD8050: 8 stripes scan) shows the delamination but was not able to map the shallow rebars (Figure 7b).

In the last step, the GPR and UT results were combined, by taking for each cell the maximum amplitude of either GPR or ultrasound. The 3D image (Figure 7c) is a comprehensive image of the concrete block.

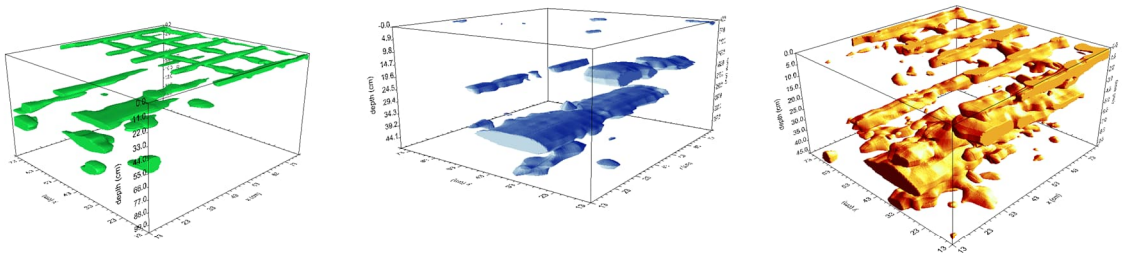

a) GPR b) Ultrasonic c) Combined

Figure 7. 3D image mapped with a) GPR b) Ultrasonic and c) combined of both methods

CONCLUSION

We demonstrate the benefits of using a handheld GPR array, to obtain fast a comprehensive, and detailed image of the nuclear concrete infrastructure. Conventionally, collecting 3D data with GPR is a process that requires a significant amount of time, limits your ability to see and visualize data and comes with a high cost for post-processing the data. However, with the handheld GPR array, GP8100 the process is 6 times faster and moreover, easy access to 3D GPR data in the field with new software capabilities that helps non-GPR experts visualize the results. Additionally combining different NDT technology can help with obtaining a more comprehensive understanding of the concrete structure.

. ACKNOWLEDGEMENTS

REFERENCES

[1] What to Know About Ground Penetrating Radar (GPR), M. Arvanitis, 2021, For Construction Pros, September 2021.

[2] Comparison of pulsed and stepped frequency continuous wave (SFCW) GPR systems, Tronca et al., 2018, 17th International Conference on Ground Penetrating Radar (GPR).

[3] Trinks, I., Hinterleitner, A., Neubauer, W., Nau, E., Löcker, K., Wallner, M., ... Schiel, H. (2018). Large-area high-resolution ground-penetrating radar measurements for archaeological prospection. Archaeological Prospection, 25, 171– 195.

[4] G. Tronca, S. Lehner, L. Raj, I. Tsalicoglou, J. Meier and R. Mennicke, “Looking into concrete – multiple frequency usage in radar products to detect structural parameters and defects faster and more accurately”, 15th Asia Pacific Conference for Non-Destructive Testing (APCNDT2017), Singapore.

[5] Pieraccini M. [2017] Noise Performance Comparison Between Continuous Wave and Stroboscopic Pulse Ground Penetrating Radar. IEEE Geoscience and Remote Sensing Letters, pp (99):1-5, 10.1109/LGRS.2017.2781458.

[6] Jol, H. M. [1995] Ground penetrating radar antennae frequencies and transmitter powers compared for penetration depth, resolution and reflection continuity. Geophysical prospecting, 43(5), 693-709.

[7] Rebar Detection Methodology, M. Arvanitis, 2021, For Construction Pros, November 2021.

Laser-induced breakdown spectroscopy to investigate the chemical composition of concrete

Gerd Wilsch, Tobias Völker, Tim Klewe and Sabine Kruschwitz

Bundesanstalt für Materialforschung und -prüfung (BAM), Berlin, Germany
Gerd.Wilsch@bam.de

ABSTRACT

Laser-induced breakdown spectroscopy (LIBS) is a spectroscopic method for the analysis of the chemical composition of sample materials. Generally, the measurement of all elements of the periodic table is possible. In particular, light elements such as H, Li, Be, S, C, O, N and halogens can be measured. Calibration with matrix-matching standards allows the quantification of element concentrations. In combination with scanner systems, the two-dimensional element distribution can be determined. Even rough surfaces can be measured by online adjustment of the laser focus. LIBS can also be used on-site with mobile systems. Hand-held systems are available for point measurements.

Common applications include the investigation of material deterioration due to the ingress of harmful ions and their interaction in porous building materials. Due to the high spatial resolution of LIBS and the consideration of the heterogeneity of concrete, the determination of precise input parameters for simulation and modelling of the remaining lifetime of a structure is possible. In addition to the identification of materials, it is also possible to assess the composition for example of hardened concrete, which involves the cement or aggregate type used. Other important fields of application are the detection of environmentally hazardous elements or the material classification for sorting heterogeneous material waste streams during dismantling. Non-contact NDT for “difficult to assess” structures as an example application through safety glass or in combination with robotics and automation are also possible.

In this work, an overview of LIBS investigations on concrete is given based on exemplary laboratory and on-site applications.

Keywords: *concrete, laser induced breakdown spectroscopy, damage processes, on-site, recycling.*

1 INTRODUCTION

Laser-induced breakdown spectroscopy (LIBS) is a developing technique whose advantages include the ability to measure directly at the surface of solids (with less or no sample preparation), the possibility to detect all elements (including light elements such as H, Li or Na) in one measurement, the high frequency of the measurements and thus the possibility to map the element distributions on surfaces. This enables users to consider the heterogeneity of the concrete and to relate the measurement results directly to the binder content. The measurement can be performed under atmospheric pressure without the need for a vacuum.

In a LIBS measurement, a few nano- to micrograms of the sample material are ablated with a high-energy laser pulse and a plasma is ignited. The emitted radiation from the plasma is then examined using the familiar techniques of optical emission spectroscopy.

The potential applications of the LIBS technique are diverse, ranging from quality assurance in production to the identification of various materials or the exploration of foreign planets such as Mars.

In our institute, we have been using the method for many years to examine various building materials and their damage caused by the ingress of different ions. Both laboratory setups and commercially available instruments are used for the investigation. In addition, there is also the possibility to measure directly on the construction site with a mobile LIBS system that was developed together with project partners. In this case, the time between taking a sample and acquiring the element distribution is only a few minutes.

The fact that the measurement can be performed automatically and without time-consuming sample preparation saves time and effort. To detect ion ingress, cores are usually taken, split in the middle and the cross-sectional area is measured. Typically, a core with a diameter of 50 mm and a length of 100 mm is scanned in a few minutes with a resolution of 0.25 mm. First engineering companies in Europe are using the technology commercially for their investigations of damage processes.

In order to quantify the concentration of individual elements, a system calibration with matrix matching standards is required. Together with project partners, we have prepared a leaflet for the quantitative determination of the chloride content in concrete. A first successful interlaboratory comparison for the determination of the chloride content in homogenized cement paste samples was carried out.

In this work, an overview of LIBS investigations on concrete is presented using exemplary laboratory and on-site applications.

2 LIBS

In this section, the principle of the method and the procedure for a measurement as well as a typical result are presented. As an example, a system for daily use in the laboratory and a mobile system are presented. Afterwards, some examples of typical applications are given.

2.1 Principle and devices

In a LIBS-System (see Figure 1) a pulsed laser beam (e.g.: wavelength: 1064 nm, pulse energy: 1-10 mJ, pulse width: 1-10 ns, and repetition rate of up to 1000 Hz) is focused on the sample surface, some material is ablated and a plasma is ignited (see also Figure 2, left).

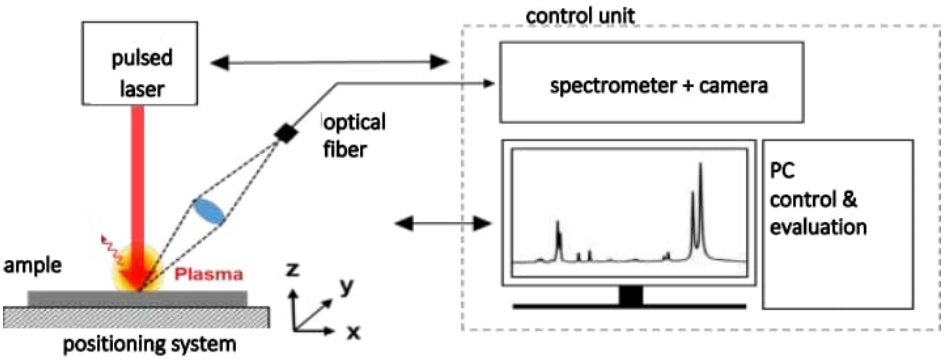

Figure 1. Schematic design of a LIBS device

The radiation emitted by the plasma is then guided through an optical fibre to a spectrograph and the intensity recorded as a function of wavelength (see Figure 2, right). The wavelength and intensity of a respective peak provide information about the element in the vaporized volume. Figure 2 shows on the left a typical measurement on a concrete surface with a plasma, process gas supply and a dust extraction nozzle. The detection sensitivity for individual elements and the reproducibility are determined by the selection of the individual components.

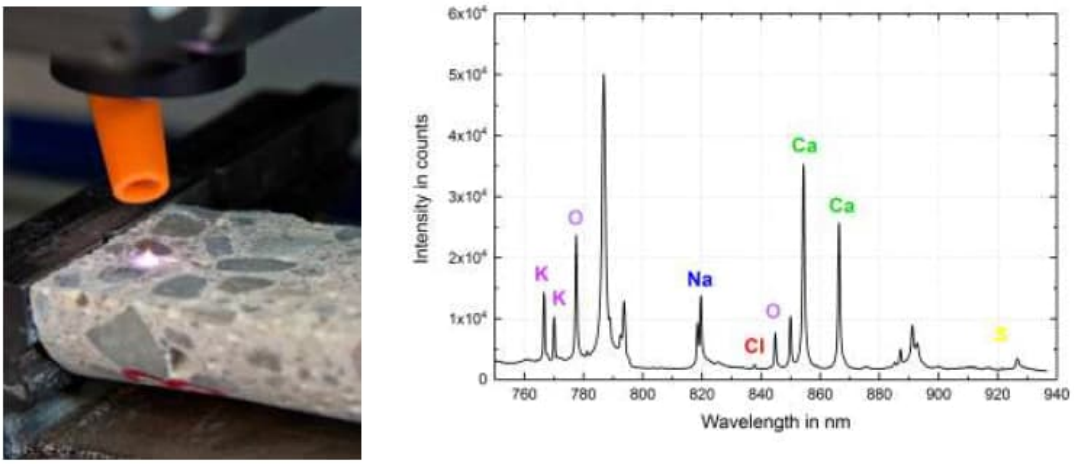

Figure 2. Left: concrete sample with plasma on the surface. Right: Typical spectrum measured on cement paste in the near-infrared wavelength range. Important peaks are marked by the element symbol.

The sample under investigation can be moved in a plane perpendicular to the laser beam which enables an imaging representation of the element distribution. Spatial resolution is determined by the design of the translation stage, the time available for a measurement, the laser energy and the laser spot size. The system also has a third axis that allows the distance between the laser head and the sample to be kept constant. This makes it possible to examine samples with a roughness of a few millimeters. Since it is a multi-element method, the contents of different elements (see Figure 3) can be recorded at the same time. This information can then in turn be used to separate individual phases of a heterogeneous system and thus, e. g. to indicate the chloride content in relation to the cement content. The measurement was carried out with a resolution of 0.5 mm × 0.5 mm and a total of 20,800 spectra were recorded. Three results were averaged for each measuring point.

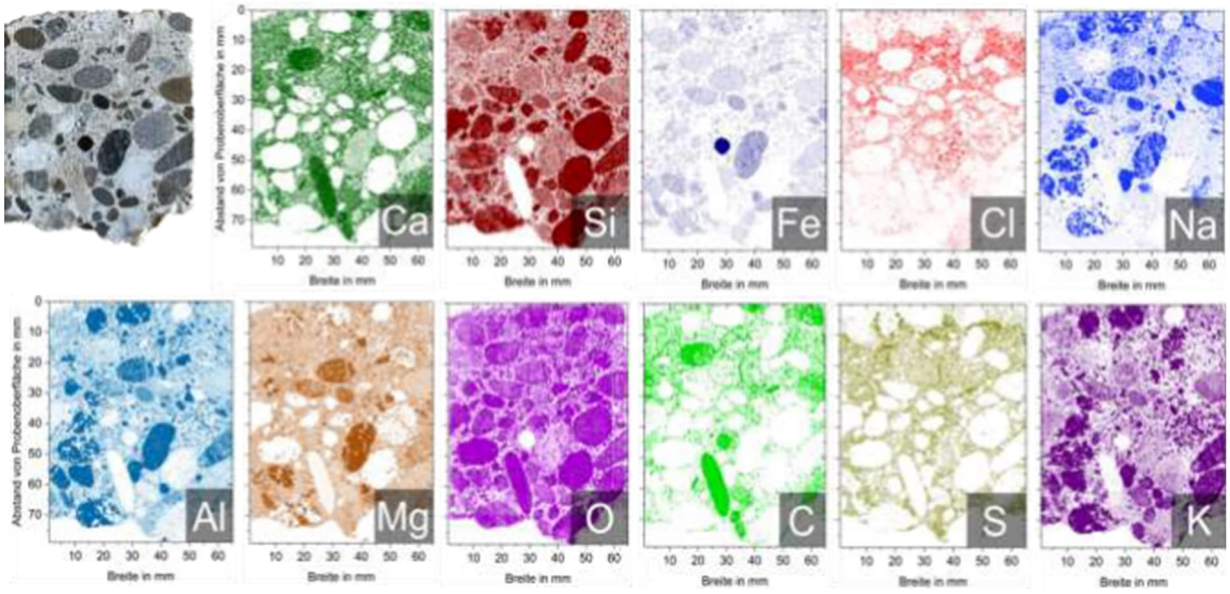

Figure 3. Color-coded qualitative grades for individual elements as a result of a scanned measurement on the cross-sectional area of a concrete drill core (see picture first row left). Darker colours correspond to higher levels

Permanently configured systems are used for day-to-day tasks (see Figure 4 left). These are also available commercially. Individual components can be optimally assembled for special applications, but this requires appropriately trained personnel and more effort.

A prototype exists for the on-site scanning measurement (see Figure 4 right). This was developed together with project partners and is specially optimized for examining concrete.

Figure 4. Left: Laboratory system for daily use. Right: Mobile system for on-site measurements.

2.2 Chloride and carbonation

On the left side, Figure 5 shows the chlorine distribution as determined on the cross-sectional area of a concrete core. Only the measurement results on the binder matrix are considered. The aggregates are excluded and marked in black. The ingress profile is shown on the right side. It is formed by taking the weighted average for each measurement line

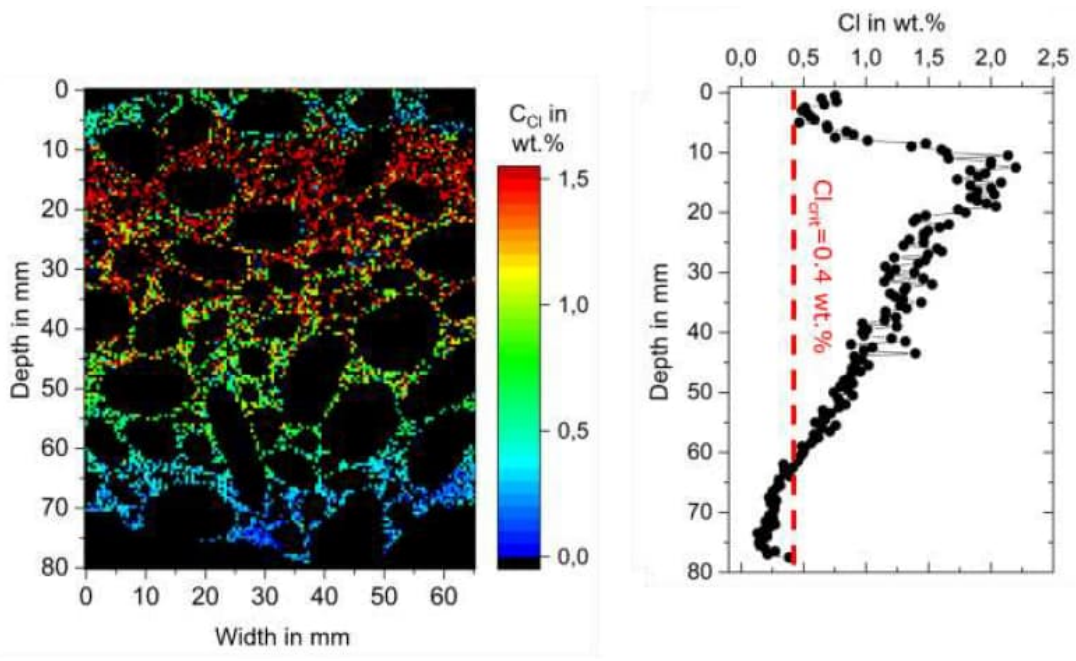

Figure 5. Left: Chlorine distribution determined on the binder matrix on the cross-sectional area of a concrete core (area of 80 mm x 65 mm). The aggregates are excluded and marked in black colour. Right: Ingress profile formed from the weighted average of the chlorine signal for each measurement line.

In addition to determining the chlorine distribution, the carbon distribution can also be evaluated. The corresponding result is shown I n Figure 5 for comparison. On the left side the carbon distribution is shown. An increased carbon content in the first 5 mm is clearly visible, indicated by the red colour. On the right, Figure 5 shows the ingress profiles of carbon and chlorine for comparison. It becomes clear that the chlorine concentration decreases in the carbonization area and reaches its maximum in the adjacent area.

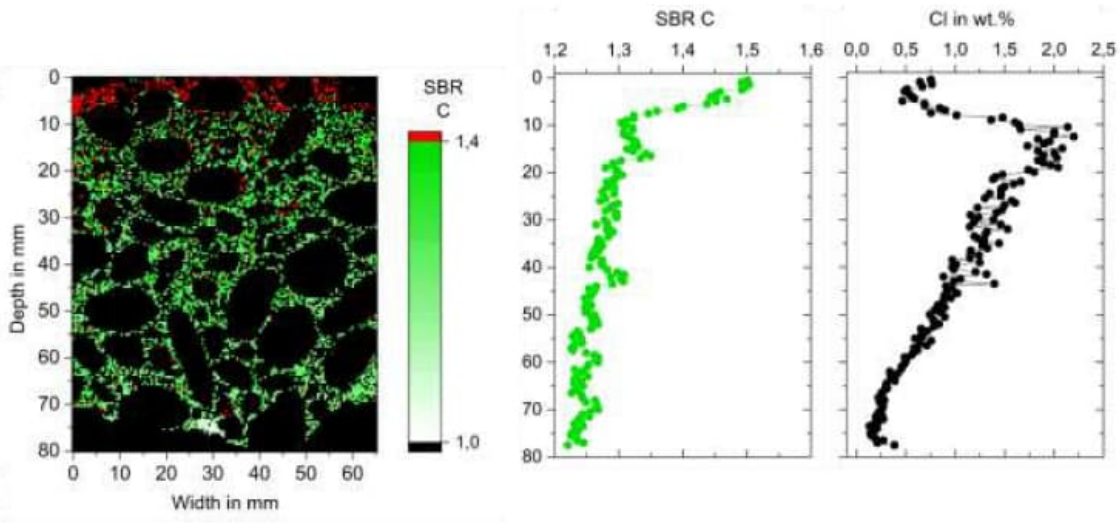

Figure 6. Left: Qualitative carbon distribution indicated by the signal to background ratio (SBR) of the carbon spectral line. Values are only determined at the binder matrix on the cross-sectional area of a concrete core (area of 80 mm x 65 mm). Increased carbon values can be seen in the first 5 mm, indicating the depth of carbonation. Right: Ingress profiles of carbon and chlorine in comparison.

2.3 Ingress through a crack

The advantages of the imaging process are shown in the following example, which deals with the enhanced chloride ingress through a crack in the structure (see Figure 7). The results obtained on drill core taken in the area of the fracture are presented below. The increased chloride values around the crack are clearly visible in the image.

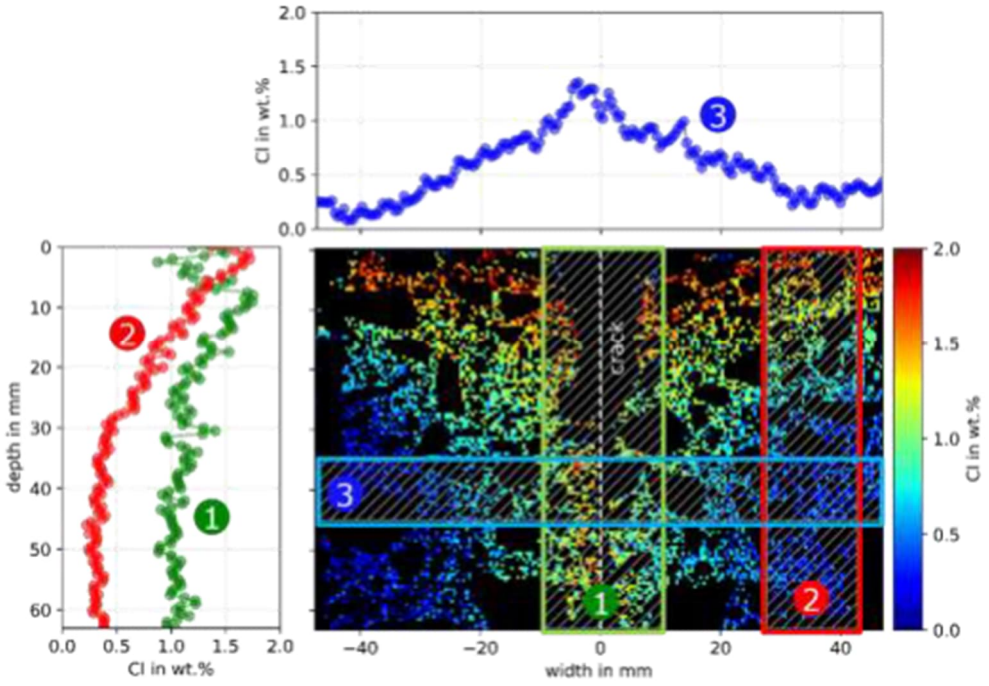

Figure 7. Imaging representation of the chloride concentration in the area of the crack in a concrete core. The areas in which the corresponding profiles were determined are identified by numbers in the image. The horizontal profile (blue) through the crack is shown above the image, and the penetration profiles in the area of the crack (green) and in a more distant area (red) are shown on the left for comparison.

2.4 Ingress of Sulphur

Sewage structures are particularly exposed to attack by biogenic sulfuric acid. Over time, this leads to the destruction of the concrete structure and a repair measure must be carried out. In order to evaluate the quality of a repair measure, a drill core was taken from a repaired sewage structure. It was assumed that all concrete with elevated sulphate levels at the sampling point had been removed and that a suitable substrate was available for the application of the repair mortar. However, the LIBS measurement clearly shows that the contaminated concrete was not completely removed. Increased sulphur levels can still be seen at a depth of 5 mm - 20 mm. Consequently, the repair mortar was applied to an unsuitable substrate, and it is to be expected that the repair will have to be carried out again in the near future.

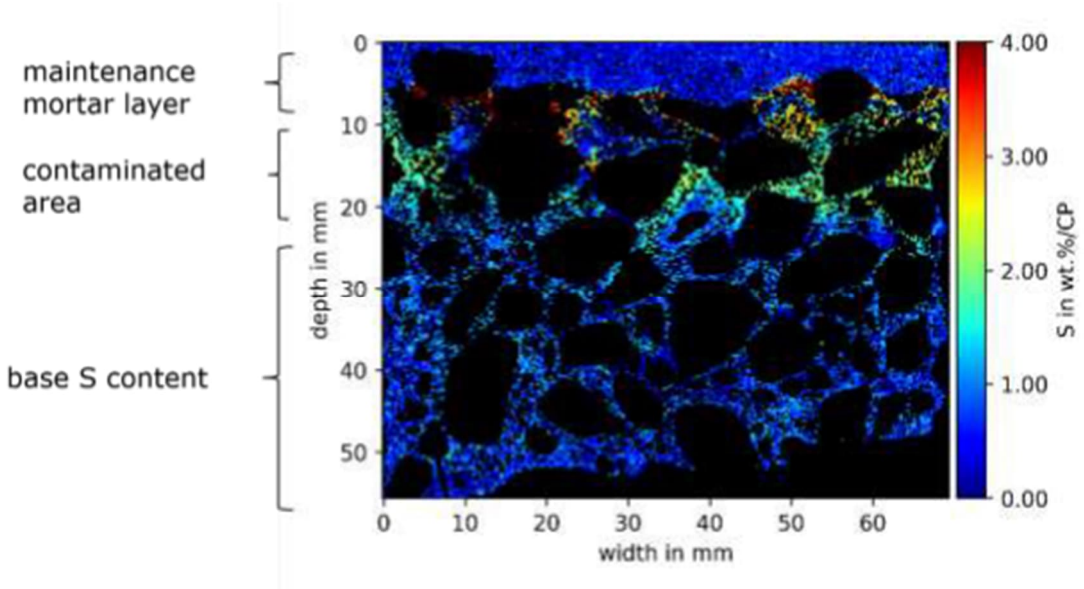

Figure 8. Imaging of the quantitative sulphur distribution in a concrete drill core taken from a sewage water treatment structure after repair.

2.5 Mobile system

If the time between the measurement and the provisioning of the result plays a decisive role, measurements directly on the construction site with a mobile system are also possible. Figure 9 shows the transport of the instrument to the construction site and in use.

Figure 9. Left: Transport of the mobile LIBS system in a parking garage. Right: The system during operation. A typical result can be seen on the screen.

Normally, measurements are first taken on the surface and then, based on the obtained results, the positions to take cores are determined. Figure 10 shows the comparison of two measurements at different positions on the surface of a parking deck.

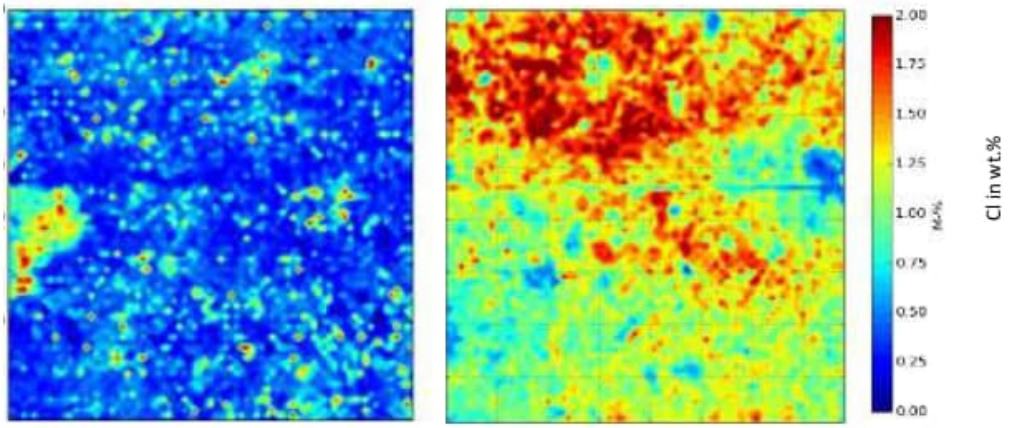

Figure 10. Comparison of the results obtained on the surface at two different positions (measuring area is 80 mm x 80 mm). The chlorine concentration is shown colour coded. Left: Result for position A. Mean value of chlorine concentration (1.26 ± 0,37) wt.%. Right: Result for position B. Mean value of chlorine concentration (0.49 ± 0,32) wt.%.

It is obvious, that the chloride concentration at position B (Figure 10, right) is much higher. A core was then drilled at position B and cut on-site in the direction perpendicular to the surface. Then the cross-sectional area was examined with LIBS. The results are shown in Figure 11.

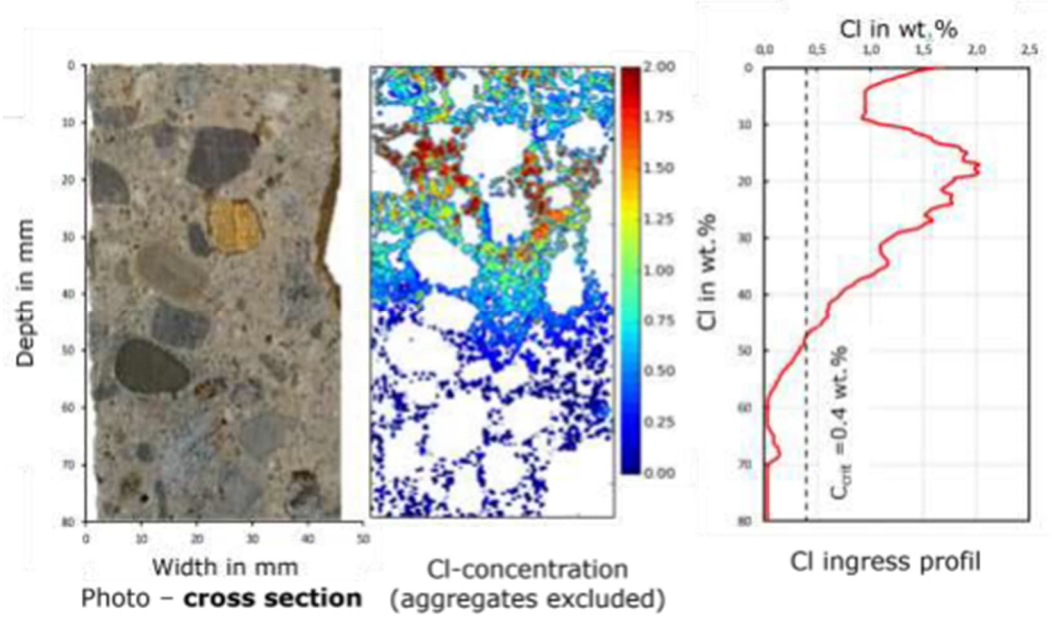

Figure 11. From left to right: Photo of the cross section, colour coded quantitative chlorine concentration in the binder matrix, and chlorine ingress profile in relation to the cement.

2.6 Dismanteling and recycling

The potential of LIBS for the recycling of construction and demolition waste (CDW) is currently investigated in a research project. In an alliance of industrial partners, small companies, and research institutions, it is to be shown that the recycling rate can be significantly increased by using a combination of sensors (see Figure 12, right). A video camera and a hyperspectral camera are used for the image-based classification of the materials before an additional LIBS system performs chemical investigation at selected points. The results are then combined and used for the classification with the help of machine learning methods. The diversity and heterogeneity (see Figure 12, left) of the material flow pose a particular challenge in this respect.

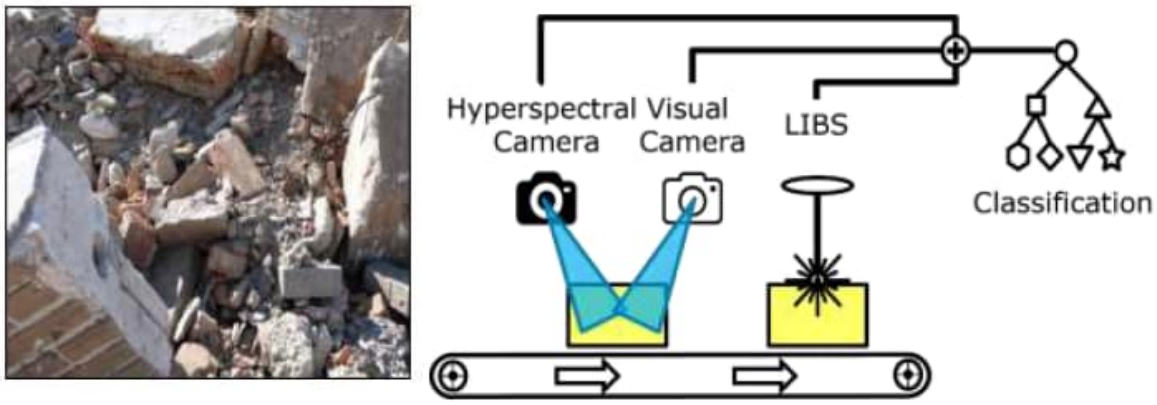

Figure 12. Left: Example for the diversity and heterogeneity of CDW. Right: Illustration of the multi-sensor approach for the classification of different materials.

The LIBS method also has potential to be used in the selective deconstruction of buildings. For example, materials can be classified directly on site and recycled accordingly. Additional potential is also the combination with other analytical methods such as Raman spectroscopy or RFA-analyses.

3 SUMMARY AND CONCLUSION

LIBS enables rapid imaging analysis of element distributions in building materials. Quantitative results are possible by calibrating the system with matrix matching reference samples; qualitative results are obtained by default. Different element distributions can be detected simultaneously during a single measurement. Generally, all elements can be detected, typical detection limits are less than 0.1 wt.%. The heterogeneity of the concrete can be considered, and the determined element concentration relate directly to the binder matrix.

LIBS is currently finding its way from research into practice. Commercial systems for daily use are available on the market and first engineering companies offer services for regular testing of building materials.

In a joint project, a leaflet on the “Quantification of chloride in concrete with laser-induced breakdown spectroscopy (LIBS)” was developed and will be published by the “German Society for Non-Destructive Testing e.V. “ by the end of 2022.

ACKNOWLEDGEMENTS

We appreciate the funding from the Federal Ministry for Economic Affairs and Energy in the framework of WIPANO (grant number 03TNK013) in Germany and from the Federal Ministry for Economic Affairs and Energy in the framework of ReMin (grant number 033R259) in Germany.

REFERENCES

[1] D. W. Hahn and N. Omenetto, “Laser-Induced Breakdown Spectroscopy (LIBS), Part II: Review of Instrumental and Methodological Approaches to Material Analysis and Applications to Different Fields”, Applied Spectroscopy, Vol 66, Issue 4, pp 347-419, April 2012.

[2] R Noll, “Laser-induced Breakdown Spectroscopy - Fundamentals and applications”, Springer Verlag, Berlin Heidelberg, 2012

[3] G. Wilsch, F. Weritz, D. Schaurich, and H. Wiggenhauser, “Determination of chloride content in concrete structures with laser-induced breakdown spectroscopy”, Constructions and Building Materials, Vol 19, Issue 10, pp 724-730, December 2005.

[4] F. Weritz, S. Ryahi, D. Schaurich, G. Wilsch, “Quantitative determination of sulfur content in concrete with laser induced breakdown spectroscopy”, Spectrochimica Acta Part B-Atomic Spectroscopy, Vol 60, Issues 7-8, pp 1121- 1131, August 2005.

[5] T. A. Labutin, A. M. Popov, S. N. Raikov, S. M. Zaytsev, N. A. Labutina, N. B. Zorov, “Determination of chlorine in concrete by laser-induced breakdown spectroscopy in air”, Journal of Applied Spectroscopy 80 (3) (2013) 315–318. doi: 10.1007/s10812-013-9766-8.

[6] S. Eto, T. Matsuo, T. Matsumura, T. Fujii, M. Y. Tanaka, “Quantitative estimation of carbonation and chloride penetration in reinforced concrete by laser-induced breakdown spectroscopy”, Spectrochimica Acta Part B: Atomic Spectroscopy 101 (2014) 245–253. doi: 10.1016/j.sab.2014.09.004.

[7] S. Millar, S. Kruschwitz, G. Wilsch, “Determination of total chloride content in cement pastes with laser-induced breakdown spectroscopy (LIBS)”, Cement and Concrete Research, 2019, 117, 16-22, https://doi.org/10.1016/j.cem-conres.2018.12.001

[8] T. Völker, S. Millar, C. Strangfeld, G. Wilsch, “Identification of type of cement through laser-induced breakdown spectroscopy”, Construction and Building Materials, 2020, Vol. 258, https://doi.org/10.1016/j.conbuildmat.2020.120345

[9] G. Wilsch, T. Eichler, S. Millar and C. Gottlieb, “Quantitative Determination of Chloride-to-Cement Content of Concrete by Laser-Induced Breakdown Spectroscopy (LIBS)”, Concreep 10: Mechanics and Physics of Creep, Shrinkage, and Durability of Concrete and Concrete Structures 2015 Pages 815-822, Accession Number: WOS:000378045400098

Ultrasonic parameters evolutions with concretes saturation states

**J-François Chaix[1*], Jean Mailhé[1], Cécile Saïdi-Muret[1], Vincent Garnier[1]
Thilakson Raveendran[2] and J-Marie Hénault[2]**

[1] LMA, Aix Marseille University, CNRS, Ecole Centrale, UMR7031, F-13625 Aix en Provence, France
[2] EDF PRISME, Quai Watier, F-78400 Chatou, France

*Corresponding author, e-mail address: *jean-francois.chaix@univ-amu.fr*

ABSTRACT

The non-destructive characterization of concrete containments of energy production systems is often carried out by ultrasonic methods [1]. If these are useful for the detection of damage linked to variations in geometries (defects) and/or materials, these measurements are sensitive, for concrete, to the variations in the water saturation rate [2]. This parameter depends on the environmental conditions and the porosity rate of the cementitious matrices. This phenomenon is observed but it's not well documented and can present a bias in the context of the ultrasonic auscultation of concrete and the evaluation of its mechanical strength. The concrete is very heterogeneous, it is composed of a porous cementitious matrix, aggregates of medium and large size (4/20) and aggregates of small size (0/4) also called sand. Multiple scattering is often observed for the propagation of waves. Ultrasonic measurements are very complex in concrete media.

In this study we work on several formulations of cement, mortar and concrete for saturation degrees ranging from dry concrete to saturated concrete. The observation of the coherent ultrasonic waves transmitted in the different samples makes it possible to extract the parameters of propagation, that is to say ultrasonic velocity and attenuation versus frequency for different saturation rates of the specimens. Only few studies provide attenuation that is a very sensitive parameter in the concrete.

These data can be implemented in the context of the procedure for adjusting the measurements to improve the diagnosis integrating environmental humidity conditions. Furthermore, in the context of precise modelling, as accurate as possible, the cement water saturation can be taken into account to converge toward experimental results on real concrete structures.

Keywords: *concrete, non-destructive testing, ultrasound, attenuation and velocity.*

1. INTRODUCTION

Concrete is a material widely used in the civil engineering infrastructures. This material is subjected to numerous stresses of various kinds (mechanical, thermic and/or sometimes chemical). To be sure about the evolution of the structures and to can conclude on the mechanical strength in the time, a follow-up of the concrete structures state is therefore necessary. The LMA is working on Non-Destructive Testing (NDT) methods using ultrasound with the aim of making the link between changes in concrete and the parameters of elastic waves [1]. Numerical propagation models adapted to concrete are being developed and make it possible to establish the links between the material parameters (composition but also damage) and the ultrasonic parameters [3]. However, concrete is a highly heterogeneous material which has variable porosities from one composition to another, in which the free water will be more or less present depending on the environmental conditions. This is the saturation rate of the concrete which also influences the ultrasonic parameters [2].

It is therefore a bias parameter of ultrasonic measurements which is currently difficult to take into account in numerical modeling by finite elements. The proposed empirical approach will provide basic data to judge the influence of the saturation rate on the ultrasonic parameters. We first present the experimental protocols and the materials tested, then the results obtained for 2 different compositions at various water saturation rates.

2. ULTRASOUND MEASUREMENTS OF CEMENT BASED MATERIALS BY IMMERSION SET-UP

For this study, two compositions similar to classical concretes used in civil engineering constructions are tested. These formulations correspond to a micro-concrete and a mortar. The specimens are saturated with water and then gradually dried, and at each state of saturation are tested by ultrasound on a bench for measuring velocity and attenuation by immersion technique. Signal processing by frequency analysis makes it possible to monitor the behavior of the parameters according to the frequency and the rate of water saturation.

2.1. Cement based materials and saturation ratio

The retained formulations are presented in table 1. The micro-concrete will be representative of the final concretes, the fact of having replaced the large aggregates 8/20 by medium aggregates 4/11 makes it possible to work on samples of smaller dimensions. The mortar is representative of both cementitious matrix and sand included in the specimens. This medium and its parameters are taken into account in numerical modelling as the homogeneous matrix in which we add the medium and large aggregate (4/20). This is done according to keep reasonable mesh sizes with respect to the calculation times and because small aggregates have small effects on ultrasonic propagation in the observed frequency range in numerical simulation.

Table 1: Material formulations *(for $1m^3$)*

	Micro-concrete	**Mortar**
Cement CEM I 52.5 *(kg)*	316	596
Sand 0/4 *(kg)*	819	1267
Aggregate 4/11 *(kg)*	978	-
Sikaplast Techno 80 *(kg)*	3	5
Water/Cement ratio	0.525	0.525

The produced specimens are parallelepipedic with dimensions of 200x150x40mm^3 and 200x150x70mm^3. This makes it possible to have surfaces (200x150mm^2) sufficient large to carry out several ultrasonic shots (see figure 3) for the same specimen and to carry out tests on specimens of different thicknesses (40 and 70mm) to apply a measurement principle by comparison to eliminate the errors which could be induced by the ultrasonic measurement chain. The volume and mass remain reasonable so that the specimens can be handled and can be accommodated in the various necessary devices (ultrasonic measuring tank, oven).

During the study, these specimens will be subjected to different degrees of saturation. For this, the specimens are placed in total immersion for a period of one month (time required for hydration to the core). The mass is then checked and when it has stabilized at its high value, called M_{100}, the specimen is considered to be totally saturated with water (saturated state at 100% of water).

The specimens are placed in an oven to dry them gradually. The drying time is about 40 days for a temperature of 75°C, chosen as not to induce strong damage of the specimens during heating. The exact drying time cannot be predicted, the specimens are regularly weighed until their masses are stabilized. When the mass is stabilized at its low value, called M_0, the specimens are considered to be dry (dry state) and have a degree of water saturation close to 0%; The absolute point 0% of water saturation could be never reach because of water that could be confined in closed porosities; this point is discussed in the literature, it may be that all the water contained cannot be evacuated.

To reach other degrees of saturation, the specimens are rehydrated, and the mass is measured to follow the hydratation kinetic. Rehydration will target an intermediate saturation rate (i/100) for a mass M_i :

$$M_i = M_0 + (M_{100} - M_0) \times \frac{i}{100} \quad (1)$$

Once the mass M_i is reached, the specimens are wrapped with a layer of cellophane film and a layer of aluminum tape to prevent moisture loss. They are then left to rest for a month so that the water is homogenously distributed in the specimen. During this phase, mass monitoring is carried out to monitor that no mass is lost.

For each "homogenized" saturation rate, the specimens are quickly unpacked and then inserted into the ultrasonic measurement device to obtain velocity and attenuation values.

2.2. Immersion Set-up

The ultrasonic measurements are made in water immersion in order to overcome the conditions of coupling of the transducers to the specimen. Immersion is not a problem with regard to the control of the saturation rate of the specimens given the lap of the measurements (a few minutes) with regard to the time required to rehydrate the specimens. This factor is also checked by measuring the mass of the specimen before and after immersion for the ultrasonic measurement phase.

The measurements are made in transmission (figure 1) respecting the positioning of the specimen in the far field of the transmitter sensor. The transmitter and receiver sensors (Panametric®, with a nominal frequency of 500kHz and a diameter of 1 inch) as well as the specimen support are adjustable around the y and z axes in order to ensure an ultrasonic beam perpendicular to the faces of the specimens. Face parallelism defects of the specimens are limited to a few 1/10 of a mm.

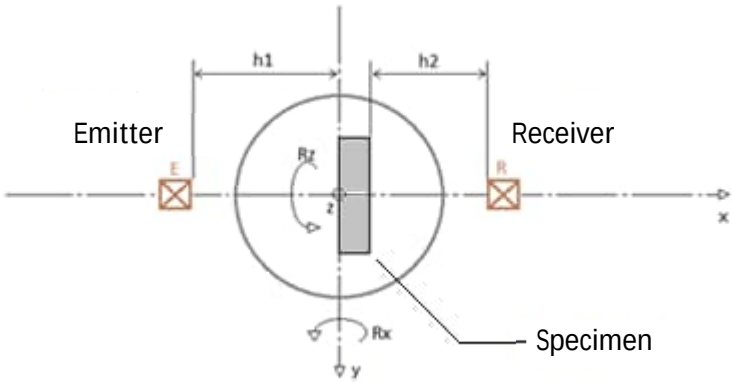

Figure 1: Ultrasound experimental set-up

The measurements are based on the principle of comparison between two signals obtained for ultrasonic shots through the specimens of different thicknesses (40 and 70mm) and same composition and water saturation state. These thicknesses make it possible to have a propagation over a sufficient distance to be able to consider the inspected area representative of the material with respect to the average size of the aggregates. To improve this, the signals used are the result of averages obtained over 16 positions for each specimen (figure 3).

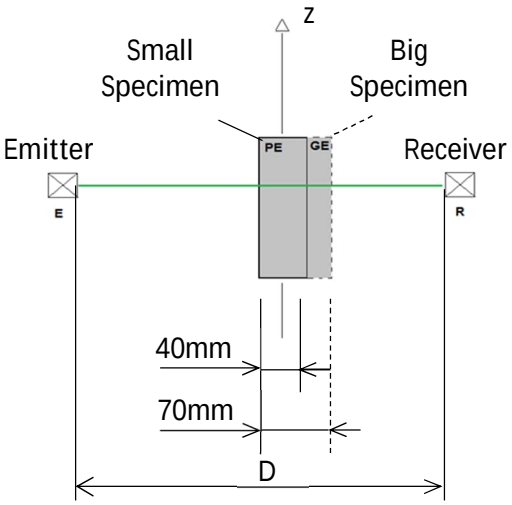

Figure 2: Comparison measurement between two specimens of different thicknesses

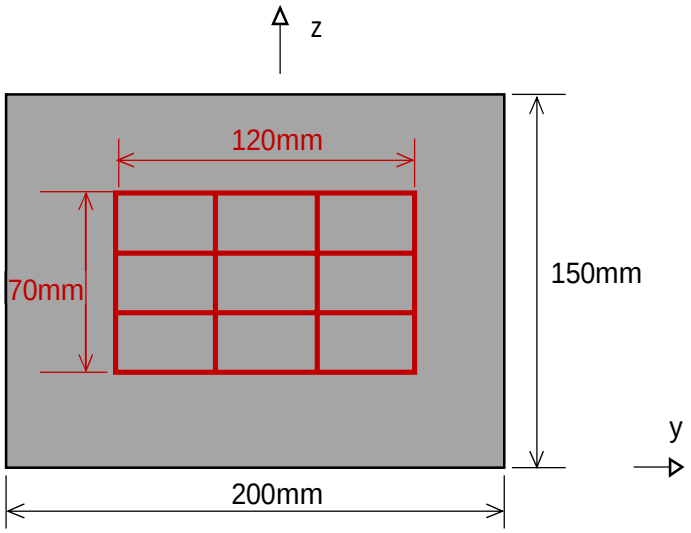

Figure 3: Positions of the ultrasonic shots

Pulsed ultrasonic signals are generated and received by a Mistras® IPRad-PCI2 system coupled with UTWin software. The signals are then extracted to be processed under Matlab®.

2.3. Ultrasonic signals processing

The average temporal signals are obtained and windowed around the first transmitted echo (figure 4) for each specimen. The signals are then analyzed (figure 5) by Fourier transform to extract the frequency data from the transmitted waves.

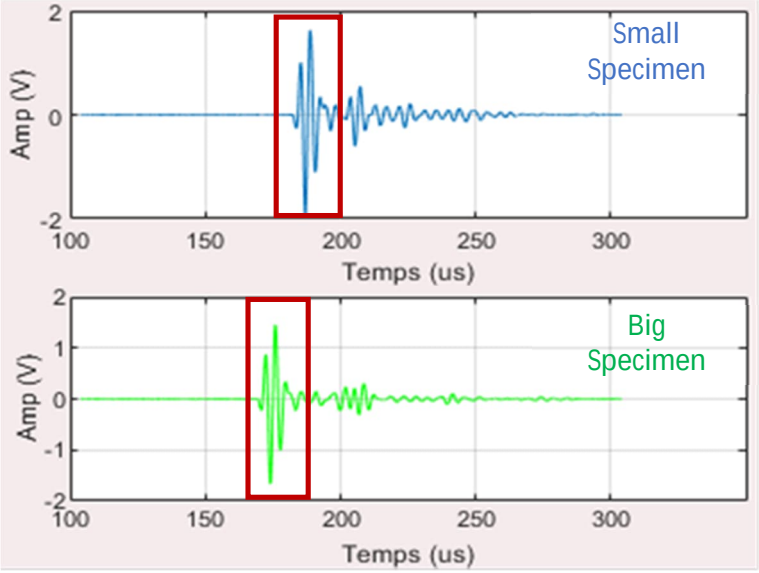

Figure 4: Temporal signals for the mortar specimens of different thicknesses

The signal arrives late on the small specimen because the wave crosses more distance in water in this case (propagation on a distance (D-40mm) in water instead of (D-70mm), see figure3) and less in cementitious based materials (high speed of 3200 to 4700m/s depending on the materials).

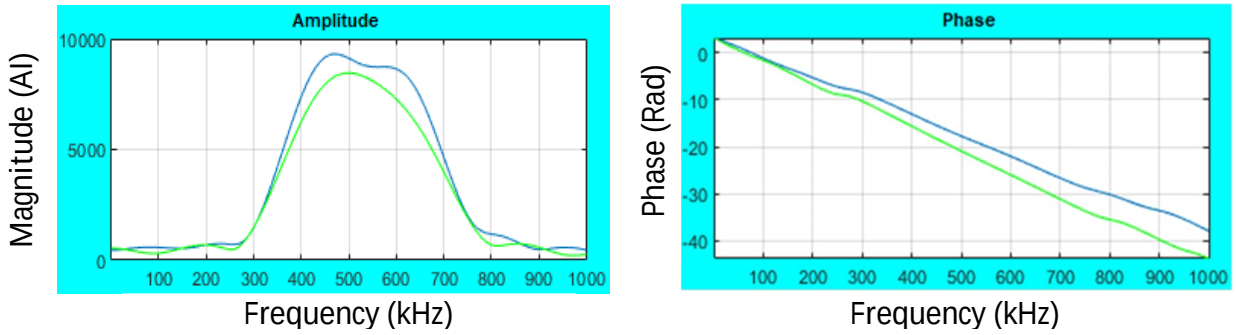

Figure 5: Example of Fourier analysis for the mortar specimens of different thicknesses

Overall the range from 300 to 700kHz can be analyzed and corresponds to a drop of around 12dB compared to the maximum. The maximum has been found around 500kHz depending on the specimens tested, frequency which corresponds to the nominal frequency of the transducers used.

The longitudinal wave velocity c_l is then given as a function of frequency by :

$$c_l = \frac{\omega \cdot \Delta e}{\varphi_2 - \varphi_1 + 2k\pi + \omega \cdot \Delta t + \omega \cdot \frac{\Delta e}{c_{eau}}} \quad (2)$$

where ω (=2π.f) is the pulsation, Δe is the difference in thickness between the two specimens tested, φ_1 and φ_2 are the phases obtained by Fourier transform for the 2 signals, Δt is time shift between the two observation windows, c_{eau} is the wave velocity in the water, measured during the test ; it is around 1490m/s for tests carried out at 23°C.

The attenuation of longitudinal waves α_l is calculated as a function of frequency by :

$$\alpha_l = \frac{1}{\Delta e} \times ln\left(\frac{A_2}{A_1}\right) \quad (3)$$

where A_1 and A_2 are the amplitudes obtained by Fourier transform for the 2 signals.

3. VARIATIONS OF ULTRASOUND VELOCITY AND ATTENUATION WITH THE EVOLUTIONS OF THE WATER SATURATION RATO

Two types of materials are tested for different saturation rates. We firstly present the results in phase velocity and attenuation for each material over the frequency range measured for the different saturation states. Then we compare the results for a representative frequency for the different saturation rates.

3.1. Ultrasound behavior in micro-concrete

Figure 6 shows the changes in ultrasonic velocity and attenuation as a function of frequency for two water saturation states (0 and 100%) of the micro-concrete specimens.

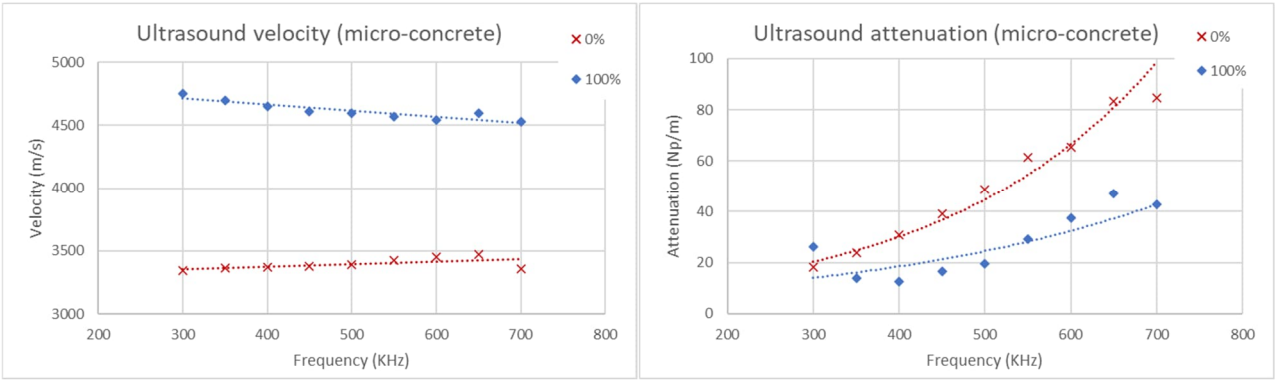

Figure 6: Ultrasound velocity and attenuation versus frequency for micro-concrete at two different water saturation states (0 and 100%)

One can notice two different behaviors of the velocity according to the frequency and to the states of saturation. At 0% the velocity is slightly increasing while at 100% we find a rather decreasing behavior with the frequency. The evolutions are close to a linear evolution with little dispersion of the measurements. However, these velocity variations as a function of frequency are very small. For the attenuations we find a rather exponential behavior with the frequency and a strong increase with the frequency whatever the saturation rate ; the attenuation measurements seem more dispersed than the velocity measurements.

The velocity is significantly higher in the saturated state than in the dry state with differences between these two states greater than 1000m/s regardless of the frequency. This represents an increase of more than 30% in velocity between the dry state and the saturated one. The attenuation presents an opposite evolution, it is much lower in the saturated state than in the dry state with differences of 50% order of the value in the dry state. Dispersions are greater, especially at low frequency where the value at 300 kHz for the saturated state deviates from the measurements at higher frequencies.

These results are in agreement with what was expected: an increase in velocity [1, 4] combined with a drop in attenuation when going from a dry state to a saturated state. The variation values are large and significant for both velocity and attenuation.

3.2. Ultrasound behavior in mortar

Figure 7 shows the changes in ultrasonic velocity and attenuation as a function of frequency for three states of water saturation states (0, 30% and 100%) of mortar specimens.

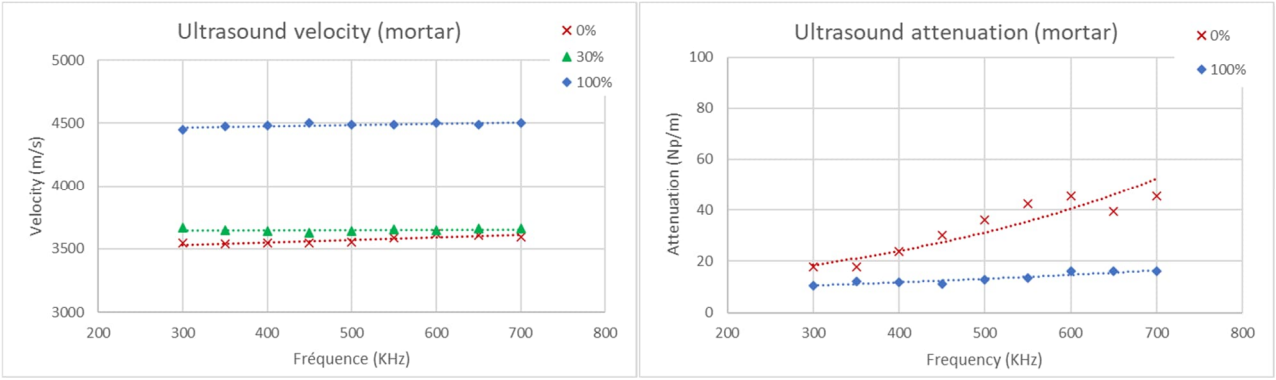

Figure 7: Ultrasound velocity and attenuation versus frequency for mortar at three different water saturation states (0, 30 and 100%)

One can notice increasing behaviors (0 and 100%) or constant one (30%) of the velocity according to the frequency and to the states of saturation. The evolutions are close to a linear evolution with very little dispersion of the measurements. The variations in velocity as a function of frequency are very small. For the attenuations we find a linear or exponential behavior with the frequency and also an increase with the frequency whatever the saturation rate ; the attenuation measurements seem more dispersed than the velocity measurements, especially for the measurements for a water saturation rate of 0%.

The velocity is significantly higher in the saturated state than in the dry state with differences between these two states of the order of 900m/s regardless of the frequency. This represents an increase in the order 25 to 30% of the velocity between the dry state and the saturated one. That can be explain by the stronger sound velocity in the water than in the air. The case at 30% water saturation is close to that at 0% but the differences observed are still significant, stronger at low (120m/s at 300kHz) than at high frequency (70m/s at 700kHz). The attenuation presents an opposite evolution, it is clearly lower in the saturated state than in the dry state with differences of 50% order of the value in the dry state. This result was expected due to the fact that ultrasounds have strong attenuation in the air. Dispersions are greater, especially for the dry state.

These results show the same evolutions as those of the micro-concrete and the differences observed are in the same orders of magnitude.

3.3. Ultrasound evolutions versus water saturation ratio

Figure 8 presents the evolutions of velocity and ultrasonic attenuation as a function of the saturation rate for a frequency of 500 kHz. This is the nominal frequency of the transducers and the observed curves are representative of the behaviors for the other frequencies of the bandwidth observed.

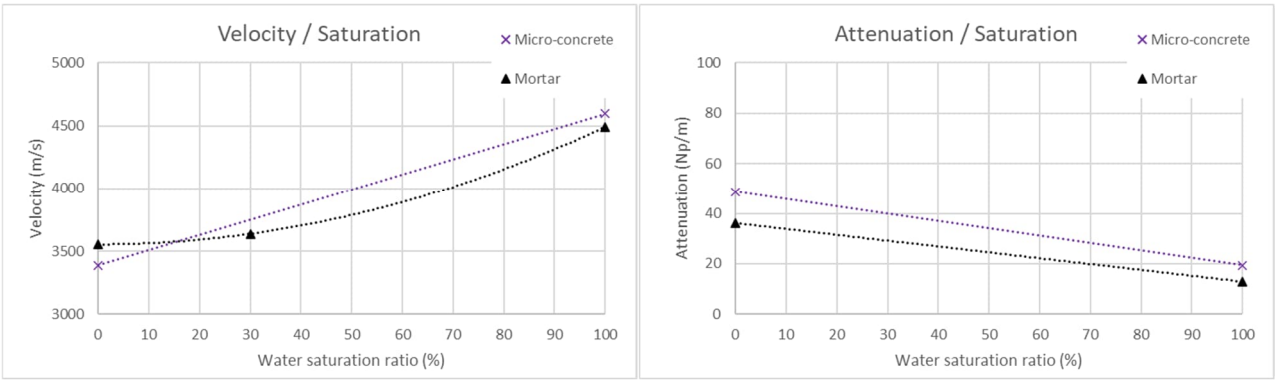

Figure 8: Ultrasound velocity and attenuation, for a frequency of 500kHz, versus water saturation state for a mortar and a micro-concrete

The changes in velocity and attenuation as a function of the saturation rate are similar and in the same orders of magnitude for the two compositions tested (mortar and micro-concrete). An increase in velocity and a drop in attenuation are observed with the increasing water saturation rate of the specimens. The evolutions in velocity are of 25 to 35% order, those of attenuation of 50 to 55% order. The only intermediate value tested shows that the behavior of velocity as a function of the saturation rate is not linear but rather polynomial or even exponential.

4. CONCLUSION AND PERSPECTIVES

This study shows the changes in velocity and ultrasonic attenuation as a function of the water saturation rate of the specimens. Knowing the water saturation rate of the specimens before any ultrasonic inspection is therefore important in the context of non-destructive evaluation. The objective of which is often the evaluation of the material from a mechanical strength point of view. This saturation rate may have a bias that should be corrected for a fair assessment. The evolutions of the classic ultrasonic parameters of velocity and attenuation according to the frequency are established in term of maximum amplitude but the behavior of the ultrasonic waves at intermediate rates are necessary to refine this study, just like the work at lower frequencies and the multiplication of this measurements on other formulations to confirm these initial results.

REFERENCES

[1] V. Garnier, B. Piwakowski, O. Abraham, G. Villain, C. Payan, J.F. Chaix. Acoustical techniques for concrete evaluation: Improvements, comparisons and consistencies, *Construction and Building Materials 43* (2013) 598–613.

[2] V. Garnier & all. Containment Nuclear Plant Structures Evaluation by Non Destructive Testing: Strategy and Results, *3rd Conference on Technological Innovations in Nuclear Civil Engineering*, Paris, France, September 5-9, 2016

[3] T. Yu, J.F. Chaix, L. Audibert, D. Komatitsch, V. Garnier, J.M. Hénault. Simulations of ultrasonic wave propagation in concrete based on a two dimensional numerical model validated analytically and experimentally, *Ultrasonics 92* (2019) 21–34.

[4] Wang, Wei. (01.2017). Effects of pore water saturation on the mechanical properties of fly ash concrete, *Construction and Building Materials 130* (2017) 54–63.

Combined NDT methods to determine the variations in compressive strength throughout concrete structures

Fahim Al-Neshawy[1], Miguel Ferriera[2] and Jari Puttonen[1]
[1] Department of Civil Engineering, Aalto University, Espoo, Finland
[2] Structural materials, VTT, Espoo, Finland

ABSTRACT

Compressive strength is an essential characteristic of reinforced concrete structures. Standards and codes of practice give rules for the assessment of the structural compressive strength of hardened concrete in situ, which are to be compared with the strength class used in design. In this paper, Non-Destructive Testing (NDT) methods were used to map the compressive strength variations of a concrete mock-up wall.

A combination of Ultrasonic Pulse Velocity (UPV) and Rebound (Schmidt) Hammer were used to estimate the in-situ compressive strength of concrete. Compressive strength estimation models were generated using NDT methods with a minimal number of drilled concrete cores in order to calibrate the NDT methods. Reliability of the estimated compressive strength values was a challenge when assessing the in-situ strength of the mock-up wall. The factors affecting the compressive strength estimation models include the number of test location for cores used to identify the model, quality of measurements, the type of NDT technique, the use of single or combined NDT techniques, and the model identification approach.

This article presents the on-site evaluation of concrete compressive strength using combined NDT techniques. The investigation was carried out on a thick-walled reinforced concrete mock-up wall. The test results show some variation in the compressive strength when applying the combined NDT techniques. The prediction of compressive strength carried out shows how the use of known destructive methodologies associated with a combined non-destructive method improves the accuracy of the estimation of the concrete compressive strength if the NDT methods are calibrated using enough test samples.

Keywords: Concrete structures; Ultrasonic Testing; Rebound Hammer; Compressive Strength.

1 INTRODUCTION

Reinforced concrete structures are normally designed for a specified target service life based on the functional and economical aspects. Generally, quality and performance of concrete have traditionally been assessed by its compressive strength. Compressive strength is an essential characteristic of concrete structures. Standards and codes of practice give rules for the assessment of the structural compressive strength of hardened concrete in situ, which are to be compared with the strength class used in design [1].

The in-situ compressive strength of concrete can be influenced by numerous factors, such as carbonation, amount of reinforcing steel, the location of the reinforcing steel or the aggregate size. It has been shown that the most accurate compressive strength estimation can be determined by combining different testing techniques. The correlation of data from the Schmidt hammer and Ultrasonic Pulse Velocity (UPV) tester to the existing compressive strength data has been found to be a more accurate predictor of compressive strength [2]–[4].

Researchers have developed an algorithm whereby the values from the Schmidt hammer and the compression wave velocity from the UPV can be correlated with actual compressive strength of the concrete. The algorithm can then be applied to either the Schmidt hammer or UPV alone. The

correlation of the different testing methods with actual compressive strength is commonly known as the SONREB (SONic REBound) method [5]–[7].

The Schmidt hammer test is a low-cost method used to assess the concrete hardness surface based on the European standard for testing concrete in structures – EN 12504-2 [8]. When the hammer is pushed onto the surface of the concrete, an impact on the surface is generated by the plunger. The measured distance by the sliding indicator is the rebound number [9]. The UPV test is performed by using the ultrasonic velocity transit through the concrete to estimate its strength based on standards specified in EN 12504-4 [10]. UPV device have a transmitter and a receiver which provides waves that goes through concrete specimen.

Combining the Ultrasonic Pulse Velocity (UPV) and Rebound Hammer with core test data is the most popular combination for estimating in-situ strength. Ideally, the NDT testing survey should be undertaken prior to coring to make easier to select the positions for coring. The results measured are substituted into the empirical formula obtained by the multiple regression analysis to estimate the compressive strength of the existing concrete structure based on the European standard for assessment of in-situ compressive strength in structures and precast concrete components – EN 13791 [11].

This paper summarizes the estimation of the compressive strength of thick-walled reinforced concrete mock-up wall representing Nuclear Power Plant NPP containment using combined NDT methods.

2 EXPERIMENTAL PROGRAM

For conducting this research work, data was obtained from testing the thick-walled reinforced concrete mock-up wall. The data obtained consists of non-destructive test (UPV and RH) and destructive test conducted core samples taken from a concrete slab cast concurrently with the mock-up wall using the same concrete. The slab was stored in the same outdoor condition as the mock-up wall. The mock-up wall of reinforced concrete, presented in Figure 1, is 1.0 m thick, 2.0 m high and 3.5 m long [12].

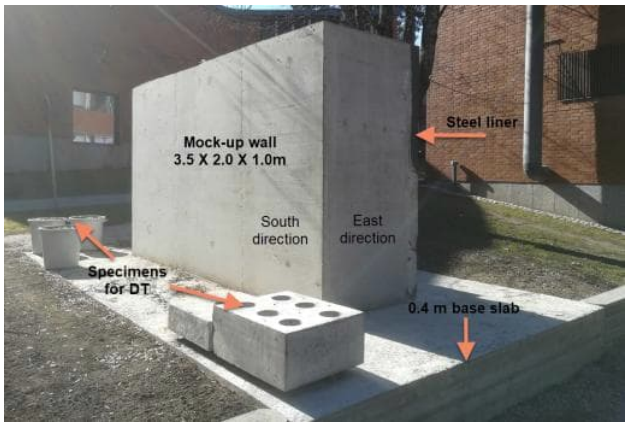

Figure 1. Overview of the thick-walled concrete structure [12].

The mix design of the concrete was based on the C35/45 compressive strength class and S3 consistency class. A total of two truck batches were delivered for the casting of the mock-up wall. The mix designs were the same on both batches and average amounts of the realized constituents are shown in Table 1.

Table 1. Mix design of concretes for C35/45 concrete

Concrete mix		ingredients (kg/m³)
Cement (CEM II/B-M (S-LL) 42,5 N)		365
Aggregates	(0/8 mm)	1045
	(8/16 mm)	902
Water	Recycled Water	50
	Cold Water	102
Effective water content		170
Super-plasticizer (Master Glenium SKY 600)		2.74

Fresh concrete tests were performed during the cast prosess and three cubes ($100 \times 100 \times 100$ mm) were prepared for 28 and 91 days compressive strength. The test results of the fresh and hardened concrete are presented in Table 2.

Table 2. Summary of the fresh and hardened concrete test results.

		Batch I	Batch II
Temperature	[°C]	21	20
Slump	[mm]	170	180
Air content	[%]	3.7	1.0
28d Compressive strength	[MPa]	43	44
91d Compressive strength	[MPa]	51	52

Two rebound hammers were used for the measurements: (i) the original Schmidt Rebound Hammer (R – Rebound Hammer) and (ii) the Silver Schmidt Rebound Hammer (Q – Rebound Hammer), as presented in Figure 2. The measurements were performed on the smooth, clean and dry surface of the wall during July – August 2019 with the original Schmidt Rebound Hammer and during July – August 2020 with the Silver Schmidt Rebound Hammer.

Figure 2. Rebound hammers equipment used for the measurements.

The measurements were performed using the UPV indirect transmission. The pulse velocity based on the indirect transmission was determined by recording the transit times by placing the receiver at different distances (100, 200, 300 and 400 mm) from the fixed position of the transmitter and then obtaining the mean pulse velocity as inverse of slope of a best fit line plotted using spacing versus transit time data.

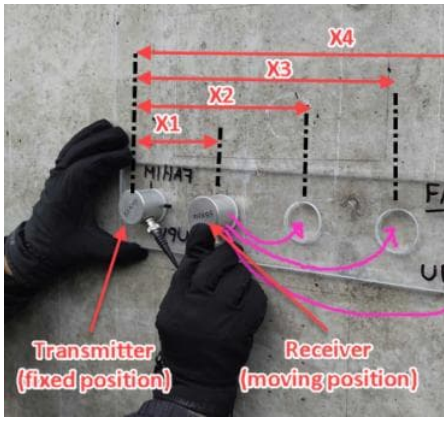

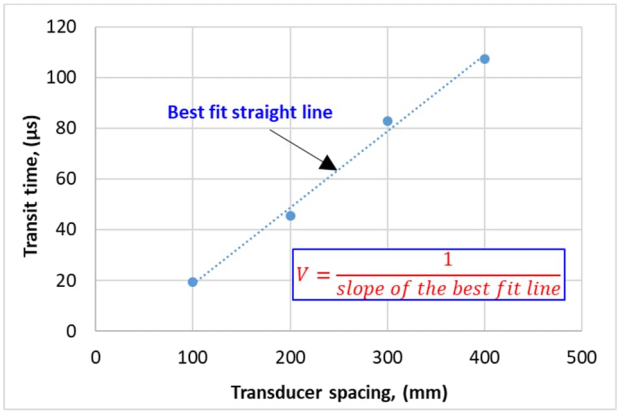

Figure 3. Illustration of the indirect (surface transmission) measurement and example of obtaining the mean pulse velocity.

Drilled cores of 100 cm diameter were retrieved from a concrete slab, as shown in Figure 4, and tested in compression to establish a relationship between the compressive strength estimated by NDT methods and the in-situ strength measured by core testing. The concrete slab was cast concurrently with f the mock-up wall using the same concrete. The slab was stored in the same outdoor condition as the mock-up wall. After extracting the cores, they were placed inside a curing chamber with temperature of 20±2°C and relative humidity of 95±5%. The cores were sawed into a length of 100 mm and the testing surfaces were grinded and tested in compression in the following day.

Figure 4. Drilling of core from the concrete slab cast of the concrete used in the wall concrete and stored in the same condition.

3 RESULTS AND DISCUSSION

For assessing of the compressive strength of drilled cores, the concrete slab (presented in Figure 4) was divided into 12 areas. Concrete cores with 100 mm diameter and height of 100 mm were drilled at the centre of each test area. The average compressive strength and the density of the drilled samples are represented in Table 10.

Table 3. Summary of the compressive strength and density values for the drilled concrete specimens.

Sample code	Density (kg/m3)	Core compressive strength, (MPa)	Equivalent compressive strength, (MPa)
A	2380	46	49
B	2391	47	47
C	2364	43	46
D	2373	48	50
E	2328	39	41
F	2342	48	51
G	2321	47	49
H	2332	41	44
I	2338	49	52
J	2335	41	54
K	2329		
L	2336	45	49

The equivalent in-place compressive strength of the concrete at the location from which a core test specimen can be computed using the following equation [13]:

$$f_c = F_{l/d} * F_{dia} * F_{mc} * F_d * f_{core} \quad (1)$$

Where F_c is the equivalent in-place strength [MPa], F_{core} is the core strength [MPa]. The strength correction factors are:

- $F_{l/d}$ Facor account for the effect of the length (l)-to-diameter (d) ratio.

$$F_{l/d} = \frac{2.5}{1.5 + \left(\frac{1}{l/d}\right)} \; if \; 1.0 \leq \frac{l}{d} \leq 1.2 \; (cube \; strength) \quad (2)$$

- F_{dia} is diameter factor. For 100 mm diameter, F_{dia} = 1.0.
- F_{mc} is the moisture condition of the core factor. F_{mc} = 1.0 for the as-received core specimens
- F_d damage due to drilling factor = 1.06

A combined Ultrasonic Pulse Velocity and Rebound Number (SonReb) method gives a general relationship between compressive strength of concrete, rebound hammer number, and ultrasonic pulse velocity. The basis of SonReb technique is given as tentative recommendations for "in-situ concrete strength estimation by combined non-destructive methods" published by RILEM Committee TC 43 CND, 1993 [14].

SonReb method is an empirical correlation formula is proposed to relate the concrete compressive strength to the rebound hammer number (RN) and the ultrasonic velocity (V).

$$f_c = f_0 \cdot e^a \cdot V^b \cdot RN^c \quad (3)$$

Where:

f_c is the concrete compression strength, [MPa],
f_0 is the unit conversion factor, [usually f_0 = 1 MPa·s/m],
V is the ultrasonic pulse velocity [m/s],
RN is the rebound number (either R-value or Q-value) and
a, b, c are dimensionless correlation parameters.

The equation describing the compressive strength f_c(MPa) as functions of the pulse velocity V (m/s) and the original rebound hummer number R is

$$f_c = 0{,}32035 \cdot V^{0{,}49282} \cdot R^{0{,}27346} \quad (4)$$

The coefficient of determination R^2 for Equation (1) is 0,8862.

Using the silver rebound hummer number Q, the corresponding equation is

$$f_c = 0{,}0507 \cdot V^{0{,}6138} \cdot Q^{0{,}467} \quad (5)$$

The coefficient of determination R^2 for Equation (5) is 0,8466..

Example of the compressive strength obtained by combining the UPV measurements and the Original Schmidt Rebound Hammer measurements for the west surface of the mock-up wall are represented in Figure 5. The improvement of the accuracy of the strength prediction using SonReb method is as shown in Table 4 and Figure 6. For the west surface example, the probability of the combination of rebound hammer and ultrasonic pulse velocity results in the peak probability 0.15. The coefficient of variation of concrete strength decreases from 11.4% by the original rebound hammer (R-value) to 5.9% when combined with the UPV measurements. It is very important to notice that the accuracy of each and every relationship depends on the calibration and correlation that is made with destructive tests, i.e., core samples.

Ased on the example presented, SonReb results seems to be more accurate and reliable than any individual test performed on the same concrete surface. It can help to assess concrete performance more accurately and it will be easier to track concrete behaviour after long period of service.

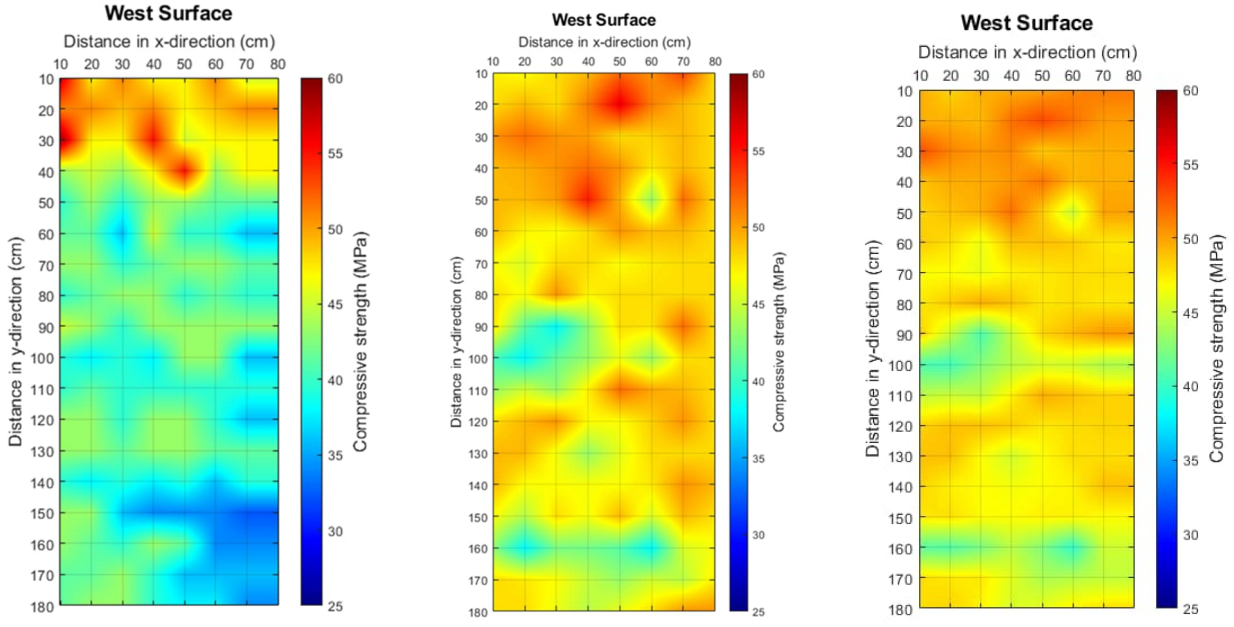

(a) (b) (c)

Figure 5. Compressive strength values for the west surface of the mock-up wall received by (a) R-Value hammer, (b) UPV measurements and (c) combining the results of the UPV and R-value Hammer.

Table 4. Summary of the SonReb method estimated compressive strength results for the west surface of the mock-up wall.

	R-hammer West	UPV-West	Drilled specimens	SonReb (UPV+R) West
Maximum strength	59,3	56,0	45,5	55,7
Minimum strength	32,3	30,3	34,9	40,3
Median	41,4	39,3	44,8	44,6
Average	39,1	42,2	45,4	45,0
Standard deviation	5,0	4,8	3,7	2,7
COV (%)	11,4	12,8	8,2	5,9

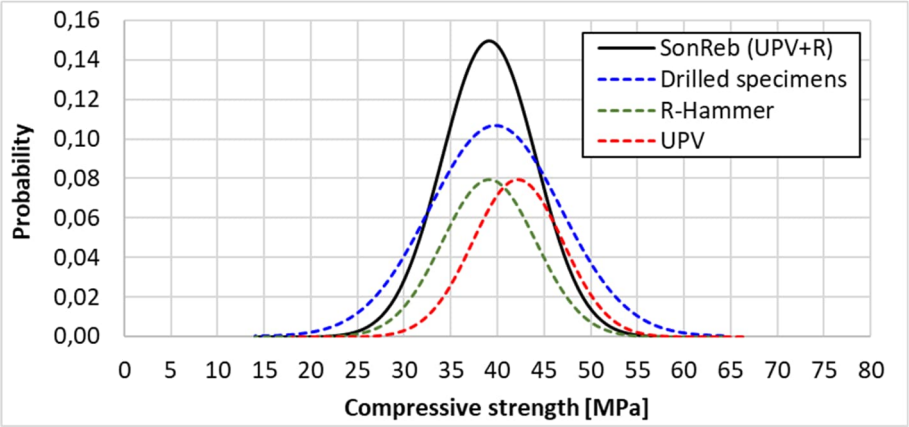

Figure 6. Normal distribution of the concrete compressive strength.

4 CONCLUSION

Non-destructive testing (NDT) of existing reinforced concrete structures is an essential part and an active area of research in the construction engineering industry for the evaluation of existing condition. rebound hammer (RH) and ultrasonic pulse velocity (UPV) tests are the two easy-to-perform NDT methods that are widely used. This research work is focused on evaluation of a reinforced concrete thick-walled concrete mock-up. The objective was to gather information about the usefulness of combining of the two NDT methods (RH and UPV) for assessing the compressive strength of the mock-up wall.

Based on the experimental observations and results, following conclusions can be drawn:

- Extracting concrete cores and testing for compressive strength is considered the most reliable solution for evaluating the compressive strength of concrete. Drilling the core samples is fast procedure, but location and properties (moisture, aggregate content, reinforcement, cracking during the drilling process, etc.) of the cores are affecting the compressive strength results. Coring is not an option for owners of important structures, especially when there are concerns about further damaging the structure.
- The Rebound Value (number) can be used to assess the surface hardness and estimate strength of hardened concrete in situ. The rebound hammer can be used to assess the variation of concrete strength.
- The use of UPV in evaluating of the compressive strength of concrete should be associated with drilling the cores for testing, which is not an attractive option with the critical concrete structures. The UPV method has not enough results and reliable models for assessing the quality of the results in the field.

- The compressive strength of the concrete using combined UPV, rebound hammer measurements and testing of drilled core samples (SonReb method) could be predicted with a decent accuracy.

In conclusion, the prediction of compressive strength carried out shows how the use of known destructive methodologies, i.e. core samples, associated with a non-destructive method (SonReb) make it possible to improve the accuracy of the estimation of the concrete compressive strength in situ if the NDT methods are calibrated by using enough test samples.

REFERENCES

[1] M. R. Garcez, A. B. Rohden, and L. G. Graupner de Godoy, "The role of concrete compressive strength on the service life and life cycle of a RC structure: Case study," *J Clean Prod*, vol. 172, pp. 27–38, Jan. 2018, doi: 10.1016/j.jclepro.2017.10.153.

[2] G. Uva, F. Porco, and A. Fiore, "The sonreb method: Critical review and practical aspects," in *Lecture Notes in Civil Engineering*, vol. 10, Springer, 2016, pp. 161–171. doi: 10.1007/978-3-319-78936-1_12.

[3] M. Breccolotti and M. F. Bonfigli, "I-SonReb: An improved NDT method to evaluate the in situ strength of carbonated concrete," *Nondestructive Testing and Evaluation*, vol. 30, no. 4, pp. 327–346, Oct. 2015, doi: 10.1080/10589759.2015.1046872.

[4] M. T. Cristofaro *et al.*, "Mechanical Characterization of Concrete from Existing Buildings with SonReb Method," in *15th world conference on earthquake engineering*, 2012, pp. 24–28. Accessed: Nov. 30, 2018. [Online]. Available: http://www.iitk.ac.in/nicee/wcee/article/WCEE2012_4185.pdf

[5] F. Papworth, D. Corbett, and R. Barnes, "In-situ concrete strength assessment based on ultrasonic pulse velocity (UPV), rebound, cores and the sonreb method," in *Proceedings of the 4th International Conference on Concrete Repair, Rehabilitation and Retrofitting, ICCRRR 2015*, Sep. 2016, pp. 55–56. doi: 10.1201/b18972-36.

[6] M. T. Cristofaro, S. Viti, and M. Tanganelli, "New predictive models to evaluate concrete compressive strength using the SonReb method," *Journal of Building Engineering*, vol. 27, Jan. 2020, doi: 10.1016/j.jobe.2019.100962.

[7] N. R. Chandak and H. R. Kumavat, "SonReb Method for Evaluation of Compressive Strength of Concrete," in *IOP Conference Series: Materials Science and Engineering*, Apr. 2020, vol. 810, no. 1. doi: 10.1088/1757-899X/810/1/012071.

[8] EN 12504-2, *Testing concrete in structures - Part 2 : non-destructive testing - Determination of rebound number*. 2021.

[9] V. M. Malhotra and N. J. Carino, *Handbook on Nondestructive Testing of Concrete 2nd Edition* , 2nd ed. CRC Press , 2003.

[10] EN 12504-4, *Testing concrete - Part 4: Determination of ultrasonic pulse velocity*. 2004.

[11] EN 13791, *Assessment of in-situ compressive strength in structures and precast concrete components*. 2019.

[12] F. Al-Neshawy, T. Ojala, M. Ferreira, and J. Puttonen, “Mock-up wall for non-destructive testing and evaluation of thick reinforced concrete structures in nuclear power plants,” *The e-Journal of Nondestructive Testing & Ultrasonics*, vol. 23, no. 8, 2018, Accessed: Dec. 05, 2020. [Online]. Available: https://cris.vtt.fi/en/publications/mock-up-wall-for-non-destructive-testing-and-evaluation-of-thick-

[13] A. R. Grubbs, A. C. Carroll, A. K. Schindler, and R. W. Barnes, “Evaluation of in-place concrete strength by core testing.,” Auburn University. Highway Research Center, Auburn, Alabama, Nov. 2016. doi: 10.21949/1503647.

[14] RILEM TC 43-CND, “Draft recommendation forin situ concrete strength determination by combined non-destructive methods,” *RILEM Materials and Structures*, vol. 26, no. 1. pp. 43–49, Jan. 1993. doi: 10.1007/BF02472237.

INDEX

L

M

N

O

P

Q

R

S

T

U

V

W

Z

While non-destructive evaluation (NDE) of reinforced concrete structures (RCS) in civil engineering applications has a long history, as well as NDT of the pressurized (metallic) components of a nuclear power plant, testing of concrete constructions in nuclear installations has partly been neglected. At the same time there are many specific challenges to NDE that justify a dedicated international event.

The International Conference on Non-destructive Evaluation of Concrete in Nuclear Applications (NDE NucCon) was co-organized by VTT Technical Research Centre of Finland, Aalto University, Finland, and Bundesanstalt für Materialforschung und -prüfung (BAM), Germany. The event was sponsored by the Euratom projects ACES and PREDIS. In January 2023 about 70 participants gathered for three days in the Dipoli convention center in Espoo, Finland to listen to about 50 presentations from 15 countries, complemented by an exhibition with international instrument manufacturers and service providers.

This book includes all peer reviewed manuscripts submitted to the conference. The reader will find a large variety of subjects from basic research, new inspections methods and case studies in actual facilities. We, the organizers m hope you will enjoy the read.

Aalto University
School of Engineering

VTT

BAM
Bundesanstalt für Materialforschung und -prüfung

ISBN (pdf)
ISSN 1799-490X (pdf)

Aalto University
School of Engineering
Department of Civil Engineering
www.aalto.fi

BUSINESS + ECONOMY

ART + DESIGN + ARCHITECTURE

SCIENCE + TECHNOLOGY

CROSSOVER

DOCTORAL THESES